Gutemberg B. França
Francisco L. de Albuquerque Neto
Haroldo F. de Campos Velho

NOWCASTING USING MACHINE LEARNING AND DETERMINISTIC MODELS: A BRAZILIAN INITIATIVE TO IMPROVE AVIATION METEOROLOGY

EDUNIFA

Nowcasting using Machine Learning and Deterministic Models:
A Brazilian Initiative to improve aviation meteorology

Editors:

Gutemberg Borges França

Francisco Leite de Albuquerque Neto

Haroldo Fraga de Campos Velho

The authors assume full responsibility for the texts published in this book.

UNIFA Library catalog sheet

NOWCASTING USING MACHINE LEARNING AND DETERMINISTIC MODELS: A BRAZILIAN INITIATIVE TO IMPROVE AVIATION METEOROLOGY

Summary

CONTEXTUALIZATION

Gutemberg Borges França, Francisco Leite de Albuquerque Neto, Vinícius Albuquerque de Almeida, Antonio Vicente Pereira Neto, Haroldo Fraga de Campos Velho e Enio Pereira de Souza

CONVECTIVE WEATHER

Yasmin Uchôa da Silva, Gutemberg Borges França, Heloisa Musetti Ruivo e Haroldo Fraga de Campos Velho

Jimmy Nogueira de Castro, Gutemberg Borges França, Vinícius Albuquerque de Almeida e Valdonel Manoel de Almeida

Caroline Menegussi Soares, Gutemberg Borges França, Manoel Valdonel de Almeida e Vinícius Albuquerque de Almeida

Vinícius Albuquerque de Almeida, Gutemberg Borges França, Haroldo Fraga de Campos Velho e Nelson Francisco Favilla Ebecken

Vinícius Albuquerque de Almeida, Gutemberg Borges França e Haroldo Fraga de Campos Velho

Suzanna Maria Bonnet, Alexandre Evsukoff e Carlos Augusto Morales Rodriguez

Tales Bernardes Paulucci, Gutemberg Borges França, Renata Libonati e Alexandre M. Ramos

Gutemberg Borges França, Manoel Valdonel de Almeida e Alessana C. Rosette

CEILING AND VISIBILITY

Fabricio Cordeiro, Gutemberg França, Francisco Leite de Albuquerque Neto e Ismail Gultepe

Summary

Presentation

The development of studies in the field of Aeronautical Meteorology is of paramount importance to maintain the safety and efficiency of air navigation. To improve the provision of the Aeronautical Meteorological Service, the Department of Airspace Control (DECEA) reinforces the need to understand the behavior of meteorological phenomena in the Brazilian airspace region and how they affect air operations.

The works developed by the "Cátedra" of Aeronautical Meteorology helped in the improvement of scientific knowledge related to turbulence, visibility, ceiling, data assimilation, severe weather, en-route convective weather, among others. Providing a meteorological service with accurate weather forecasts is a challenge that involves the analysis of meteorological data and the application of sophisticated mathematical models, which are in full development and improvement, aiming at excellence in results.

Good planning, based on accurate weather information and assertive forecasts, is critical to provide safe and efficient flights. With the experience of having been a military pilot, I can say that a good prognosis of such meteorological phenomena is essential for decision making.

Finally, I express my satisfaction with the partnership of DECEA with the Air Force University (UNIFA) and the Federal University of Rio de Janeiro (UFRJ) for the realization of this book. It is the result of an arduous study, with tireless dedication on the part of doctors, masters, students, managers, meteorologist officers of the Brazilian Air Force and other professionals involved, that consolidates a cycle of academic production of notable contribution to Meteorology.

Lieutenant-Brigadier Alcides Teixeira Barbacovi
Director-General of DECEA

Preface

The present book is a compilation of recent research dedicated to the applications of prediction models for weather nowcasting linked to aeronautical meteorology. Models embrace differential equations for atmospheric dynamics, as well as data-driven approaches.

Convective weather, wind, clear air turbulence, visibility, and ceiling are the significant phenomena affecting aviation events investigated by the "Cátedra" project of aeronautical meteorology. The project is a joint effort between the graduate meteorology program from the Federal University of Rio de Janeiro (UFRJ), the Department of Airspace Control (DECEA) and the Air Force University (UNIFA). The book focuses on aviation operational meteorology and deals with numerical weather forecast simulation results obtained by deterministic and hybrid models. The latter is based on the composition of deterministic modeling and computational intelligence techniques. The studies presented in this publication make use of data from remote sensing sensors, such as satellite, radiometer, ceilometer, and sodar, as well as information from in-situ observations for monitoring and developing short-term forecast models. These aim to predict convective weather, surface wind shifts, wind gusts, clear air turbulence, low visibility due to fog, and low ceilings. All these are important for landing and takeoff procedures, as well as for scheduling flights and increasing safety on Brazilian air routes.

This volume provides a comprehensive overview of research results, including comments on the currently existing knowledge, and the numerous remaining difficulties in predicting and measuring issues related to aforementioned meteorological events at different time and space scales.

It will be helpful to academics with an interest in operational meteorology and aviation as well as weather offices, pilots, meteorologists, aviation experts, scientists, college students, postgraduates, and others.

Most of the chapters are produced by "Cátedra" project´s researchers and published in scientific journals.

Gutemberg B. França
Francisco L. de Albuquerque Neto
Haroldo F. de Campos Velho
Editors

Brazilian initiative to improve aviation meteorology

Gutemberg Borges França[1]

Francisco Leite de Albuquerque Neto[1]

Vinícius Albuquerque de Almeida[1]

Antonio Vicente Pereira Neto[1]

Haroldo Fraga de Campos Velho[2]

Enio Pereira de Souza[3]

1. CONTEXTUALIZATION

Atmospheric conditions can have an impact on aviation in any location and at any time, according to Ahrens (2008). Although meteorological information is required on the airways between departure and destination airports, aircraft are most sensitive to weather conditions during take-off and landing procedures. Pilots and air traffic controllers require an accurate weather forecast for intervals ranging from a few minutes to 6 hours - the timescale of nowcasting - for them to make immediate or short-term decisions. Several initiatives to improve aviation forecasting are underway around the world, such as those developed in Canada by Isaac et al. (2006), Isaac et al. (2011), and Isaac et al. (2014), which use data from numerical models, surface observations, radar, satellite, and a microwave radiometer to generate forecasts for major airports in Canada down to approximately 6 hours.

A series of studies has recently been developed in the United States to investigate the use of deep/machine learning algorithms for specific weather forecasting improvements. NextGen Weather Processor (NWP) and Offshore Precipitation Capability (OPC) are two initiatives run by MIT Lincoln Laboratory. The first (NWP) identifies potential threats to aviation safety by combining meteorological data from multiple sources, including weather radars, environmental satellites, lightning, meteorological observations from surface stations and aircraft, and numerical forecast model output, to forecast route closures and airspace capacity restrictions up to eight hours in advance (Newell et al., 2010). The OPC project combines data from satellite imaging, atmospheric discharges, and numerical weather forecast models to estimate the location and intensity of precipitation where radar coverage is unavailable (Veillette et al., 2016). This data is converted into an image that resembles radar using machine learning algorithms. A hybrid model that combines discriminatory trained prediction algorithms with a deep neural network was put out by Grover et al. (2015). In order to offer wind data throughout a flight in real time, Kim et al. (2021) created a hybrid wind forecasting methodology that combines a supervised learning algorithm with the inverse distance weighting technique. Both produced encouraging outcomes that could help weather forecasting systems become more sophisticated.

SIRIUS, a NextGen-like system, was implemented in Brazil to improve the organization and operational safety of Brazilian air traffic management (Gavazzi, 2018). However, the meteorologist at the Integrated Center for Aeronautical Meteorology (CIMAER in Portuguese) is still using his experience to integrate different information from RADAR-satellite images, in situ meteorological observations, and/or outputs from atmospheric models, as well as using conceptual models about how the atmosphere works to issue, with a certain level of subjectivity, warnings of significant weather.

---

[1] Federal University of Rio de Janeiro.

[2] The National Institute for Space Research.

[3] Federal University of Campina Grande.

The aeronautical meteorology service in Brazil is managed by the Department of Airspace Control (DECEA, in Portuguese) and supported by the Institute for Control of Air-Space (ICEA in Portuguese) and CIMAER. The latter was established to meet the new requirements established in the air traffic management (ATM) system implementation plan. In order to meet these new demands from civil and military aviation, DECEA needed to establish new processes for managing and optimizing resources. The services provided by the main regional meteorological centers were combined and are now provided by CIMAER, which, through defense meteorology, supports defense activities, particularly those aimed at military aviation.

The World Meteorological Organization (WMO) and the International Civil Aviation Organization (ICAO) both made recommendations that served as the foundation for the activities of aeronautical meteorology as well as the current organization of Meteorological Centers and Stations of the Brazilian Airspace Control System (SISCEAB). The aeronautical meteorology service still has a contemporary structure considering recent technological advancements and user demands for greater service effectiveness. Operational meteorology, which involves the generation, conception, and dissemination of meteorological information supported by the networks of meteorological centers and stations, and aeronautical climatology are the primary activities related to aeronautical meteorology within the scope of SISCEAB.

The International Civil Aviation Organization (ICAO) issued the Global Air Navigation Plan (GANP) for Aeronautical in 2013, which includes three-time blocks that establish the guidelines for global aeronautical meteorology, as briefly described below. The GANP is a rolling, 15-year strategic methodology that makes use of current technologies and foresees future developments in accordance with operational goals established by the government and the industry. The block upgrades are arranged in separate, non-overlapping six-year time periods beginning in 2013 and running through 2031 and beyond. This methodical approach lays the groundwork for wise investment plans and will inspire support from governments, equipment suppliers, operators, and service providers. To put things in perspective, the ICAO work program is approved by the ICAO assembly on a triennial basis. The GAMP, on the other hand, provides a long-term vision that assists the ICAO, countries, and industries in ensuring continuity and harmonization among their modernization programs. It investigates the need for more integrated aviation planning at both the regional and state levels, as well as addresses the necessary solutions by introducing the consensus-driven

aviation system block upgrades systems engineering modernization strategy. Along with the financial aspects of modernizing the aviation system, it also pinpoints problems that need to be resolved soon. It is also emphasized how crucial partnerships and collaboration are as aviation recognizes and responds to its future multidisciplinary challenges.

The three GANP´s meteorology blocks are as follows:

1. The first block includes elements that should be viewed as a subset of all available meteorological information that can be used to support enhanced operational efficiency and safety. It is divided into three modules, the first of which depicts the meteorological information made available by world area forecast centers, volcanic ash advisory centers, and tropical cyclone advisory centers that can be used by the ATM community to support dynamic and flexible airspace management, improved situational awareness and collaborative decision making, and dynamically opportunistic operations.

2. The second module depicts meteorological information issued by aerodrome meteorological offices in the form of aerodrome warnings, wind shear warnings, and alerts (including those generated by automated meteorological systems) that help to improve safety and maximize runway capacity. In some cases, wind shear detection systems (such as ground-based LIDAR or SODAR) have proven useful in wake turbulence detection and tracking/monitoring, and thus contribute to improving safety and maximizing runway capacity from a wake turbulence encounter prevention standpoint.

3. The third module discusses SIGMET, which is meteorological information provided by meteorological watch offices on the occurrence and/or expected occurrence of specified en-route weather phenomena (such as severe turbulence, severe icing, and thunderstorms) that may affect aircraft safety. This module also describes other operational meteorological information (such as METAR/SPECI and TAF) provided by aerodrome meteorological offices on observed or forecast meteorological conditions at the aerodrome. The second meteorology block builds upon the first block, which detailed a subset of all available meteorological information that can be used to support enhanced operational efficiency and safety. This block is concerned with

enabling the reliable identification of solutions when forecasted or observed meteorological conditions have an impact on aerodromes, airspace, or operations in general. Full ATM-Meteorology integration is required to guarantee that meteorological data is incorporated into decision making logic and that the effects of meteorological conditions on operations are automatically deduced, comprehended, and taken into account. The supported decision time horizons range from a few minutes to several hours or days prior to the operation of the ATM. This includes optimal flight profile planning and execution, as well as assistance with tactical in-flight avoidance of hazardous meteorological conditions (improved in-flight situational awareness) to typical near-term and planning (>20-minute) decision making. It also encourages the creation of guidelines for the international exchange of meteorological data that are consistent with other data domains and strictly adhere to a single reference. It also encourages the improvement of meteorological data in terms of a variety of quality-of-service factors, such as the reliability and consistency of the data when applied to linked operational decision making processes. In summary, the goal is to improve global ATM decision making in the context of decisions that should take immediate effect in the face of hazardous meteorological conditions. The capabilities created in the second block and the initial information integration concept are built upon in this module. The following are key considerations, a) tactical avoidance of hazardous meteorological conditions, particularly in the 0–20-minute time window; b) increased use of aircraft-based capabilities to detect meteorological parameters (e.g., turbulence, winds, and humidity); and c) display of meteorological information to improve situational awareness. This block also promotes further the establishment of standards for the global exchange of information.

It is well known that the creation of precise models for the forecasting of high-impact aviation weather events, such as precipitation type, clean air turbulence (CAT), turbulence, wind, gust, low visibility, ice formation, and ceiling, as required by air operations, en route and during landing and takeoff, depends primarily on observations made by radar, radiosondes (traditional and via current meteorological satellites), sodar, lidar, radiometers, meteorological station, and remote sensing orbital platform.

In 2017, the DECEA, a division of the Brazilian Aeronautics Command, encouraged researchers to form the "Cátedra de Meteorologia Aeronáutica" or "Cátedra," which was approved by the University of the Brazilian Air Force (UNIFA, in Portuguese) in the National Council for Scientific and Technological Research (CNPq in Portuguese). The "Cátedra" has three goals for modernizing aeronautical meteorology in Brazil:

1. Ongoing research based on the characterization of aviation meteorological events on the required time scales via observations recorded by state-of-the-art in-situ and remote sensors;
2. Development and testing of specific forecast models for meteorological events affecting aviation in Brazil, with the goal of reducing the current level of subjectivity to CIMAER forecasts; and
3. Continuing education for personnel at all levels, including undergraduate, master's, doctoral, and post-doctoral investigations.

To meet the ICAO´s GANP standards, the Cátedra recognizes the importance of developing accurate models for forecasting weather events that affect aviation. Therefore, apart from ice formation, most of the aforementioned weather events are in detail studied throughout this book's chapters using observations made by cutting-edge in-situ instruments, reconstructions made using a numerical weather model, and machine learning-based algorithms.

Figure 1a depicts the main causes of flight delays in Brazil from 2014 to 2016, according to the DECEA. Weather accounts for 63% of these delays, while flight demand accounts for 27%, runway closures account for 6%, equipment accounts for 2%, and other technical factors account for 2%. The percentage of flights in Brazilian airspace that were delayed because of meteorological conditions is specifically shown in Figure 1b. According to the records each meteorological event has the following percentage impact:

- 31%, the convective cells (or complexes) because they can affect takeoff and landing procedures as well as flights en-route;
- fog and low visibility accounted for 27%,
- moderate to heavy rain for 19%,
- the ceiling for 15%,
- wind gust and wind shear for 7%, and
- turbulence and CAT for 1%.

Figure 1 - The primary causes of flight delays in Brazil between 2014 and 2016 (a) and the percentage of each weather event's impact on flights (b).
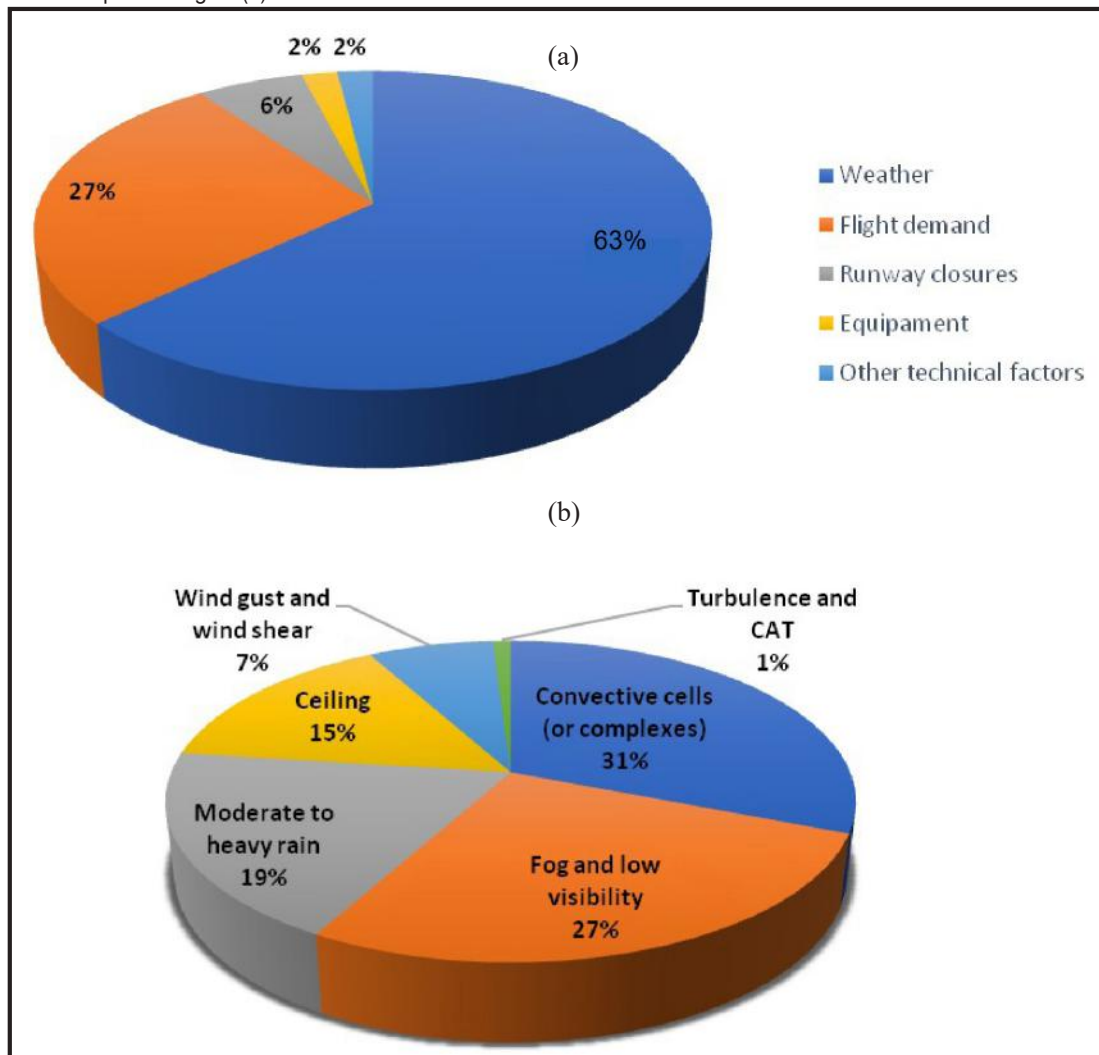
Source: DECEA.

2. MODELLING

The scientific community has used a variety of approaches to develop models for predicting meteorological events that have an impact on aviation. There are three types of models that can be classified as numerical weather prediction (NWP) (Haltiner-Williams, 1983; Kalnay, 2002), data-driven models (Scher and Messori, 2018; Schultz et al, 2021), and hybrid models (Krasnopolsky and Fox-Rabinovitz, 2006; Silva et al., 2022).

The time integration of differential equations is used in numerical weather prediction models, which group all of the physics of the atmosphere and its interactions with the land surface and the hydrosphere (lakes, rivers, and oceans). Based on initial conditions, these models attempt to calculate mathematically how atmospheric conditions will evolve over time (hours, days, months, or years). These models perform well for forecasts of up to 7 days at a regional level (e.g., city, state, country, continent), but have significant limitations for forecasts of minutes to hours at a local level (e.g. airport).

Data-driven models attempt to extract mathematical patterns from historical series of a variety of meteorological variables related to aviation impact phenomena. These models can also provide a high-accuracy short-term local forecast. The requirement for long historical observation series is a constraint to this approach (not always available). Multivariate regressions and the use of computational intelligence fall into this category of models.

The final type of model is a "hybrid," which uses the outputs of numerical weather prediction models as input to data-driven models. In this case, it is possible to extract patterns from numerical model outputs and relate them to high-impact phenomena in aviation. This last category has great potential to be a milestone for modeling, given that it will allow the replacement of numerical parameterizations with several limitations by models based on observational data.

2.1 Prediction models

As mentioned, there are two approaches to addressing a scheme to predict atmospheric dynamics. One method is to establish a relationship between the quantities involved in the phenomenon, and then use mathematical equations to quantify how this balance will change over time. These mathematical equations are known as partial differential equations because they relate all of the quantities involved. Another option is to create a massive database that collects time series for those various quantities from multiple measured points in the domain of interest and/or measurements from remote sensing.

The first strategy is to use numerical methods to solve the collection of mathematical equations, integrating time in the future to compute forecasts. A second strategy involves calibrating an algorithm to forecast the future state of the desired quantity, with some attributes being chosen as algorithm inputs. A data-driven formulation is the second framework. To create a prediction model, linear regression techniques can be used. Machine learning has recently been used as a competitive forecasting technique. Both schemes can be combined into hybrid schemes.

All the techniques are used in this book, with a focus on the use of machine learning techniques. Two sections ahead will present brief comments to give an overview of the two modeling schemes as forecasting tools for atmospheric dynamics.

2.1.1 Prediction by solving mathematical differential equations

Numerical integration of the Navier-Stokes (N-S) equations is the approach adopted for operational centers focused on weather prediction. The N-S equations can be expressed in different forms, namely primitive variables (using wind components (u, v, w)) (Figueroa et al., 2016) or prognostic variables – where derived variables are used (such as vorticity and divergence (ζ, D) approach). Most of the regional or limited area models employ primitive variables (e.g., WRF and BRAMS model). For the vorticity-divergence formulation, in general, the velocity vector is split into $\vec{V_3} = \vec{v} + w\vec{k}$, where $\vec{v} = u\vec{i} + v\vec{j}$ is the horizontal wind velocity. The variable separation is employed in all fields: $\Gamma(\lambda, \theta, r, t) = \Lambda(\lambda, \theta, t)Z(r)$, where t is time, (λ, θ, t) are spherical coordinates – the longitude, co-latitude, and radial coordinates, respectively. After that, the set of equations with dependency on (λ, θ) can be expressed as - see: Haltiner and Williams (1980) Washington and Parkinson (1986), and Krishnamurti and co-authors (1998):

$$\frac{\partial \zeta}{\partial t} = -\nabla \cdot (\zeta + f)\vec{V} - \vec{k} \cdot \nabla \times \left(RT\nabla q + \dot{\sigma}\frac{\partial \vec{V}}{\partial \sigma} + \vec{F} \right) \tag{1}$$

$$\frac{\partial D}{\partial t} = -\vec{k} \cdot \nabla \times (\zeta + f)\vec{V} - \nabla \cdot \left(RT\nabla q + \dot{\sigma}\frac{\partial \vec{V}}{\partial \sigma} + \vec{F} \right) - \nabla^2 \left(\phi + \frac{1}{2}\vec{V} \cdot \vec{V} \right) \tag{2}$$

$$\frac{\partial T}{\partial t} = -\nabla \cdot (T\vec{V}) + TD + \dot{\sigma}\gamma - \frac{RT}{c_p}\left(D + \frac{\partial \dot{\sigma}}{\partial \sigma} \right) + H_T \tag{3}$$

$$\frac{\partial q}{\partial t} = -\vec{V} \cdot \nabla q - D - \frac{\partial \dot{\sigma}}{\partial \sigma} \tag{4}$$

$$\sigma\frac{\partial \phi}{\partial \sigma} = -RT \tag{5}$$

$$\frac{\partial r_h}{\partial t} = -\nabla \cdot (r\vec{v}) + rD - \sigma\frac{\partial \phi}{\partial \sigma} + M \tag{6}$$

where f is the Coriolis parameter, $\zeta \equiv \vec{k}\nabla \times \vec{V}$ is the vertical component of the vorticity, $D \equiv \nabla \cdot \vec{v}$ is the divergence, $\sigma = p/p_s$ is used as a vertical coordinate, p_s is the surface pressure, $\dot{\sigma} = d\sigma/dt$ is the sigma vertical velocity, T is the air temperature, R is the gas constant for dry air, c_p is the heat capacity of dry air at constant pressure, $\vec{F}$ is the friction force, q is the specific humidity, $\gamma \equiv RT/(c_p\sigma) - \partial T/\partial \sigma$ is the static stability, $H_T \equiv \dot{Q}/c_p$ is the diabatic heat source/sink, and M is the moisture source/sink. The relation between $\vec{V}$ and (ζ, D) is linked to the Helmholtz theorem, $\vec{V} = \vec{k} \times \nabla\psi + \nabla\chi$, where ψ and χ are the stream function and the velocity potential, respectively. Therefore, the vertical component of vorticity and the divergence are computed by solving the Poisson equations:

$$\zeta = \vec{k} \cdot \nabla \times \vec{V} = \nabla^2\psi \ , \tag{7}$$

$$D = \nabla \cdot \vec{v} = \nabla^2\chi \ . \tag{8}$$

Equations (1)-(6) are integrated by numerical methods. Initially, the finite difference method was employed (Holton and Hakim, 2012; Krishnamurti et al., 1998). But new algorithms reducing the computational complexity in the calculations were developed, becoming competitive with the spectral methods. One relevant example is the fast Fourier transform (FFT) (Cooley and Tukey, 1965) for speeding up the discrete Fourier transform (DFT) for computing the finite Fourier transform with N terms by $O(Nlog_2 N)$ operations – instead of $O(N^2)$.

The finite difference method expands a space-dependent variable α^1 the field $\Lambda(\alpha_i)$ in a truncated Taylor's series:

$$\Lambda(\alpha_i \pm \Delta\alpha_i) = \Lambda(\alpha_i) \pm \frac{\partial \Lambda(\alpha_i)}{\partial \alpha_i}\Delta\alpha_i \pm \frac{\partial^2 \Lambda(\alpha_i)}{\partial \alpha_i^2}\frac{\Delta\alpha_i^2}{2!} \pm O\left(\Delta\alpha_i^3\right) \tag{9}$$

where $O\left(\Delta\alpha_i^n\right)$ indicates the magnitude of truncation order – third order in the worked example, and $\Lambda = \psi$, χ, u, v, ζ, D, T, r_h, q, φ. It is possible to have a numerical representation for the derivatives:

---

[1] Space variable $\alpha = (\alpha_1, \alpha_2)$, where $\alpha_1 = x$ and $\alpha_2 = y$ for cartesian coordinates; or $\alpha_1 = \lambda$ and $\alpha_2 = \theta$ in the spherical coordinate system.

$$\frac{\partial \Lambda(\alpha_i)}{\partial \alpha_i} \approx \frac{\Lambda(\alpha_i + \Delta\alpha_i) - \Lambda(\alpha_i)}{\Delta\alpha_i} + O\left(\Delta\alpha_i\right) \ ,$$

$$\frac{\partial \Lambda(\alpha_i)}{\partial \alpha_i} \approx \frac{\Lambda(\alpha_i) - \Lambda(\alpha_i - \Delta\alpha_i)}{\Delta\alpha_i} + O\left(\Delta\alpha_i\right) \ ,$$

$$\frac{\partial \Lambda(\alpha_i)}{\partial \alpha_i} \approx \frac{\Lambda(\alpha_i + \Delta\alpha_i) - \Lambda(\alpha_i - \Delta\alpha_i)}{2\,\Delta\alpha_i} + O\left(\Delta\alpha_i^2\right) \ ,$$

$$\frac{\partial^2 \Lambda(\alpha_i)}{\partial \alpha_i^2} \approx \frac{\Lambda(\alpha_i + \Delta\alpha_i) - 2\Lambda(\alpha_i) + \Lambda(\alpha_i - \Delta\alpha_i)}{\Delta\alpha_i^2} + O\left(\Delta\alpha_i^2\right) \ .$$

Basically, the derivatives in the predictive equations are substitutes by the finite difference operators – some of them are shown above, transforming the system of partial differential equations into a non-linear vector ordinary differential equation:

$$\frac{d\mathbf{\Lambda}_F}{dt} + \mathbf{D}\,\mathbf{\Lambda}_F + N^F(\mathbf{\Lambda}_F) + \mathbf{K} = \mathbf{0} \ . \tag{10}$$

The vector $\Lambda_F = [\Lambda_{mn}]^T$ represents the values of the fields Λ on the discrete grid points (αi), L is a (sparse) matrix associated to the linear part from the system (1)-(6), N^F is the non-linear vector, and K is a constant vector.

In the spectral method, the space dependency is pre-described assuming spherical harmonics expansions (Washington and Parkinson, 1986):

$$\Lambda(\lambda, \mu, t) = \sum_{m=-J}^{+J} \sum_{\ell=|m|}^{|m|+J+\alpha} c_\ell^m \Lambda_\ell^m(t) Y_\ell^m \tag{11}$$

$$Y_\ell^m = Y(\lambda_\ell, \mu_m) = P_\ell^m(\mu)\, e^{im\lambda}$$

$$c_\ell^m = \begin{cases} a^2 \ , & \text{for:} \ \psi \ , \ \chi \ , \ \phi \\ a \ , & \text{for:} \ u \ , \ v \\ 1 \ , & \text{for:} \ T \ , \ r_h \ , \ q \end{cases}$$

$$\alpha = \begin{cases} 1 \ , & \text{for:} \ u \ , \ v \\ 0 \ , & \text{otherwise} \end{cases}$$

again $\Lambda = \psi, \chi, u, v, T, r\_h, q, \Phi$; $P_\ell^m(\mu)$ is the associated Legendre polynomial of degree l; $\mu = sin\,\theta$; and a is the Earth's average radius. For computing the expansion coefficients $\Lambda_\ell^m(t)$, the weighted residuals method is applied. Substituting the expression (11) in the system (1)-(6), there will be a residual since the discrete formulation (11) is only an approximation of the exact solution. The discrete system is multiplied by a weight function ψ_l^m and the resulting system is integrated over the entire space domain. Therefore, the expansion coefficients $\Lambda_\ell^m(t)$ are determined by becoming the residual equal to zero. The Galerkin approach is verified when the weight function is the same as the basis function used in the expansion (11), i.e., $\psi_l^m = Y_l^m$. Finally, the Galerkin-spectral method drops into a vector ordinary differential equation expressed by:

$$\frac{d\mathbf{\Lambda}_S(t)}{dt} + \mathbf{L}\,\mathbf{\Lambda}_S + N^S(\mathbf{\Lambda}_S) \tag{12}$$

where vector $\mathbf{\Lambda}_S(t) = [\Lambda_\ell^m(t)]^T$ represents the expansion coefficients of expression (11), L is the matrix associated to the linear components in the system (1)–(6) after discretization by the spectral approximation, N^S is a non-linear vector, and C is a constant vector. There are several options for time integration to be applied to Equations (10) or (12). Options include explicit, implicit, or semi-implicit

methods (Krishnamurti et al., 1998). Beyond finite difference and spectral methods for space representation, using structured meshes, nowadays other formulations have been proposed based on finite volume and finite element schemes have been proposed with the use of unstructured grids.

Irrespective of the method employed to solve the set (1)–(6) there will always be physical mechanisms whose representation is related to higher-order terms in Taylor's expansion or to harmonics in the spectral form that are not taken into account due to truncation – subgrid process.

Usually, those are important physical mechanisms for the atmosphere's energetics. The way to properly consider meaningful physical mechanisms is to develop physical models that relate them to the variables explicitly resolved in the model grid. This procedure is called parameterization. The most important parameterized processes include turbulence, radiation, surface, and saturated processes (Holton and Hakim, 2012; Washington and Parkinson, 1986). A physical model used to parametrically represent some process is called a parameterization scheme.

Some parameterization schemes can rely on a solidly established theory. This is the case of the short-wave and long-wave radiation schemes, whose parameterizations are rooted in the radiative transfer equation. Therefore, the several different types of radiation parameterization are a specific solution of the radiative-transfer equation.

Saturated processes, on the other hand, cannot profit from a unifying theory. Therefore, any parameterization for convection or cloud microphysics depends on a closure hypothesis, which is a particular (physically meaningful, though) way to relate clouds to some triggering function or a cloud model.

2.1.2 Prediction by Machine Learning Approach

Machine learning (ML) is a set of computational (machine) techniques with a focus on identifying and understanding patterns from databases. The learning process is a kind of algorithm configuration applied to calibrate the computer model, in general, a non-linear mapping among different types of data. ML is considered as part of artificial intelligence. Computational statistics and data mining can be related to the field of machine learning.

A sample data used to configure a ML algorithm is called the training data. After that – the learning process – the ML model can make predictions or decisions, employing data out of the training data, in other words, the ML model can produce good results without being explicitly programmed for those new data. For the training – or learning – processes, optimization schemes are applied to identify a set of parameters by searching for the best performance of the ML algorithms. Data mining is also an associated area of study.

The ML algorithms can be identified according to our goal as regression or classification (clustering) models. Another separation for the ML algorithms is linked to the learning process, where the main schemes are as follows:

– Supervised learning;
– Unsupervised learning;
– Semi-Supervised learning;
– Reinforcement learning.

Some ML algorithms can be classified as supervised or unsupervised schemes. One example is the restricted Boltzmann machine (RBM), and the classification algorithm depends on the application goal. For the RBM there are visible processing units (v_i) and hidden processing units (h_j), where the units v_i and h_j are unconnected among themselves. Bias for visible (a_i) and hidden (b_j) units, the energy $E(v, h)$ for the RBM configuration is given by (Hinton, 2010):

$$E(v,h) = -\sum_i a_i v_i - \sum_j b_j h_j - \sum_i \sum_j v_i w_{i,j} h_j \quad (13)$$

with the joint probability distribution for both unit types (v, h) is expressed as

$$P(v,h) = \frac{1}{Z} e^{-E(v,h)} \quad (14)$$

being Z the partition function - a normalization constant. For p visible units and q hidden units, $P(h \lor v)$ (conditional probability) of a configuration of the visible units v - given a configuration of the hidden units h, and $P(h \lor v)$ of h given v are

$$P(v|h) = \prod_{i=1}^{p} P(v_i|h), \qquad P(h|v) = \prod_{j=1}^{q} P(v|h_j).$$

The individual activation probabilities are given by (Hinton, 2010).

$$P(v_i = 1|h) = \sigma\left\{ a_i + \sum_j w_i h_j \right\} \quad (15)$$

$$P(h_j = 1|v) = \sigma\left\{ b_j + \sum_i w_i v_i \right\}$$

Finally, the training for the RBM is obtained by maximizing the product probabilities $P(v)$:

$$\arg\max_W \prod_{v \in V} P(v) \iff \arg\max_W E\{\log P(v)\} \quad (16)$$

where $E\{.\}$ is the expected value.

Supervised learning

A set of pairs(x, y) of labeled values is used for a training process, being x a set of input attributes, and y the observed/measured/desired values. The goal is to calibrate for the ML model could produce an output y similar to the label values y. In general, the training process is a set of parameters W that minimizes an objective function J:

$$J(W) = \|\bar{y} - y(W)\|_L + \lambda_1 \Omega_1[W] + \lambda_2 \Omega_2[W] \quad (17)$$

where $\|.\|_L$ is a L-norm (square difference, for example) to evaluate the similarity between the ML output and the labeled values y, λ_1 and Ω_j ($j = 1, 2$) are regularization parameters and regularization operators, respectively. The algorithm calibration is carried out by minimizing a objective function $J(W)$.

Unsupervised learning

There is no data label to be followed as a reference. The idea is to extract patterns from the environment by considering some criteria. Therefore, the algorithm is forced to date up its parameter set – calibration cycle – following the established criterion. There are several criteriums to be selected: minimizing a dynamical energy function – equilibrium point (Hopfiled neural network (Hopfield, 1982)), self-similarity map (Kohonen neural network (Kohonen, 1982)), or classification by similarity intra-class with maximum difference inter-classes (K-means approach (Everitt et al., 2011)). Wassermann (1989) presents different algorithms for this training approach.

Semi-Supervised learning

This is a training strategy where there is an amount of tagged data and unlabeled data — in general, labeled data is in smaller numbers than untagged data. The labeled data is used for training by minimizing a regularized functional (Chapelle et al., 2006), similar to the objective operator in Eq. (17), including Tikhonov of zeroth and second-order or entropy regularizations. The unlabeled data can be used as a testing set. Vapnik (1998, 2006) introduced the problem as transductive learning (predictions only for the test points). Different from inductive learning: the prediction addresses all input space. Most methods for semi-supervised are transductive approaches.

Reinforcement learning

A source of inspiration for this strategy is the optimal control problem (OCP), The OCP idea is to design a control project forcing the system to follow a reference according to a control action u_k. The control action works as a constraint in the optimization control problem. Dynamic programming is a method to address optimal control by solving time-backward equations (Kröse and van der Smargt, 1996). A solution for optimal control without the formal use of a system model and environment is called the dynamic programming technique. Reinforcement learning sometimes is also called a heuristic dynamic programming technique. The most directly related RL technique to DP is Q learning. The basic idea in Q learning is to estimate a function Q of states and actions where Q is the minimum discounted sum of future costs $J_{min}(x_k, u_k, k)$. For convenience, the notation with J is continued here:

$$\hat{J}(x_k, u_k, k) = \gamma J(x_{k+1}, u_{k+1}, k+1) + r(x_k, u_k, k) \quad (18)$$

$$\epsilon(K) = \left[\gamma \min_{u \in U} \hat{J}(x_k, u_k, k) + r(x_k, u_k, k) \right] - J(x_k, u_k, k) \quad (19)$$

where u_k is the control action. The weights can be computed following different strategies for the ML control framework (Kröse and van der Smargt, 1996), minimizing a cost function as expressed by Eq. (18) above.

3. PURPOSE

Gather the collection of scientific works produced by researchers throughout the Cátedra project between April 2018 and March 2023 and make them available in this on five major topics studied: convective weather, ceiling and visibility, clear air turbulence, wind, and a review of all weather and events that impact aviation.

REFERENCES

Ahrens, C. D.: Meteorology Today – Introduction to Weather Climate and Environment, 9th Edition, Brooks/Cole, CA, USA, 2008.

Chapelle, O., Schölkopf, B., Zien, A. Semi-Supervised Learning. The MIT Press, 2006.

Cooley, J. W., Tukey, J. W.. An Algorithm for the Machine Calculation of Complex Fourier Series. Mathematics of Computation, vol. 19, n. 90, 297–301, 1965.

Everitt, B. S., Landau, L., Leese, M., Stahl, D. Cluster Analysis, 5th edition edn. John Wiley and Sons, 2011.

Figueroa, S.N., Bonatti, J.P., Kubota, P.Y., Grell, G.A., Morrison, H., Barros, S.R.M., Fernandez, J.P.R., Ramirez, E., Siqueira, L., Luzia, G., Silva, J., Silva, J.R., Pendharkar, J., Capistrano, V.B., Alvim, D.S., Enor ́e, D.P., Diniz, F.L.R., Satyamurti, P., Cavalcanti, I.F.A., Nobre, P., Barbosa, H.M.J., Mendes, C., Panetta, J.: The Brazilian Global Atmospheric Model (BAM): Performance for tropical rainfall forecasting and sensitivity to convective scheme and horizontal resolution. WeatherandForecasting 31(5), 1547–1572 (2016).

Gavazzi, A. B. (2018). *Programa SIRIUS e o uso racional do espaço aéreo brasileiro*. Unpublished Bachelor Thesis. Universidade do Sul de Santa Catarina.

Grover, A., Kapoor, A., & Horvitz, E. (2015). A Deep Hybrid Model for Weather Forecasting. *Proceedings of the 21th ACM SIGKDD International Conference on Knowledge Discovery and Data Mining*, 379–386. https://doi.org/10.1145/2783258.2783275

Haltiner, G. J.; Williams, R. T. Numerical Prediction and Dynamic Meteorology. John Wiley & Sons, 1983.

Hinton, G.: A practical guide to training restricted boltzmann machines. Technical Report University of Toronto, Toronto, Canada (2010). URL: https://www.cs.toronto.edu/~hinton/absps/guideTR.pdf

Holton, J. R., Hakim, G. J. An introduction to dynamic meteorology - Fifth edition, 2012.

Hopfield, J. J.: Neural networks and physical systems with emergent collective computational abilities. Proceedings of the National Academy of Sciences, vol. 79, n. 8, 2554-2558, 1982.

Kohonen, T.: Self-organized formation of topologically correct feature maps. Biological Cybernetics. vol. 43, n. 1, 59–69, 1982.

Kalnay, E. Atmospheric Modeling, Data Assimilation and Predictability. Cambridge University Press, 2002.

Kim, J.-H., Zhang, C., Briceno, S. I., & Mavris, D. N. (2021). Supervised Machine Learning-based Wind Prediction to Enable Real-Time Flight Path Planning. *AIAA Scitech 2021 Forum*. American Institute of Aeronautics and Astronautics. https://doi.org/10.2514/6.2021-0519

Krasnopolsky, V. M.; Fox-Rabinovitz, M. S., Complex hybrid models combining deterministic and machine learning components for numerical climate modeling and weather prediction. Neural Networks, v. 19, n. 2, 122-134, 2006. https://doi.org/10.1016/j.neunet.2006.01.002

Krishnamurti, T. N., Bedi, H. S., Hardiker, V. M. An Introduction to Global Spectral Modeling, 1998.

Kröse, B., van der Smargt, P. An Introduction to Neural Networks. University of Amsterdam, 1996.

Newell, O. J., Wolfson, M. M., & Ducot, E. R. (2010). NextGen Weather Processor Architecture Study. *Project Report ATC-361*, MIT Lincoln Laboratory, 67.

Schultz, M. G., Betancourt, C., Gong, B., Kleinert, F., Langguth, M., Leufen, L. H., Mozaffari, A., Stadtler, S., Can deep learning beat numerical weather prediction? Philosophical Transactions of the Royal Society A: Mathematical, Physical and Engineering Sciences, v. 379, n. 2194, 2021, https://doi.org/10.1098/rsta.2020.0097

Scher, S.; Messori, G. Predicting weather forecast uncertainty with machine learning. Quarterly Journal of the Royal Meteorological Society, v. 144, n. 717, 2830-2841, 2018.

Silva, Y. U., França, G. B., Ruivo, H. M., Campos Velho, H. F., Forecast of convective events via hybrid model: WRF and machine learning algorithms. Applied Computing and Geosciences, v. 16, 100099, 2022, https://doi.org/10.1016/j.acags.2022.100099.

Vapnik, V. N., *Statistical Learning Theory*. New York: Wiley.1998.

Vapnik, V. N., Transductive Inference and Semi-Supervised Learning. Chapter 24, Book: *Semi-Supervised Learning* (Editors: O. Chapelle; B. Schölkopf; A. Zien), 453-472, MIT Press, 2006.

Veillette, M., Iskenderian, H., Wolfson, M., Mattioli, C., Hassey, E., & Lamey, P. (2016). TheOffshore Precipitation Capability. Project Report ATC-430,MIT Lincoln Laboratory, 39.

Washington,W. M., Parkinson, C. L. An Introduction to Three-Dimensional Climate Modeling. University Science Books, 1986.

Wasserman, P. D. Neural Computing: Theory and Practice. Van Nostrand Reinghold, 1989.

Convective Weather

Forecast of Convective Events Via Hybrid Model: WRF and Machine Learning Algorithms

Yasmin Uchôa da Silva[1]

Gutemberg Borges França[1]

Heloisa Musetti Ruivo[2]

Haroldo Fraga de Campos Velho[2]

ABSTRACT

This presents a novel hybrid 24-hour forecasting model of convective weather events based on numerical simulation and machine learning algorithms. To characterize the convective events, 13-year from 2008 up to 2020 of precipitation data from the main airport stations in Rio de Janeiro, Brazil, and atmospheric discharges from the surrounding area of around 150 km are investigated. The Weather Research and Forecasting (WRF) model was used to numerically simulate atmospheric conditions for every day in February, as it is the month with the greatest daily rate of atmospheric discharge for the data period. The p-value hypothesis test (with $\alpha = 0.05$) was applied to each grid point of the numerically predicted variables (defined as an independent attribute) to find those most associated with convective events using the output of the 3-D WRF grid. This one identified 36 attributes (or predictors) that were used as input in the machine learning algorithms' training-test process in this study. Several cross-validation training and testing experiments were carried out using the nine-selected categorical machine learning algorithms and the 36 defined predictors. After applying the boosting technique to the nine previously trained-tested algorithms, the results of the 24-hour predictions of convective occurrences were deemed satisfactory. The Random Forest method produced the best results, with statistics values close to perfection, such as POD=1.00, FAR= 0.02, and CSI= 0.98. The 24-hour hindcast utilizing the nine algorithms for the 28 days of February 2019 was very encouraging because it was able to almost recreate the maturation phase of events and their eventual failures were noted during the formation and dissipation phases. The best and worst 24-h hindcast had POD=0.97 and 0.88, FAR = 0.02 and 0.12, and CSI = 0.94 and 0.78, respectively.

Keywords: Convective event. Data mining. Machine learning. Atmospheric discharge. Forecast.

1. INTRODUCTION

Atmospheric conditions affect aviation at any time and in every location (Ahrens, 2009). The region that corresponds to an airport's TMA (Terminal Maneuvering Area), where planes begin their approach procedures for landing, is thus highly susceptible to weather conditions. The Rio de Janeiro TMA (TMA – Rio) - the subject of this study - is made up of five airports: Galeão, Santos Dumont, Santa Cruz, Afonsos, and Jacarepaguá (internationally coded as SBGL, SBRJ, SBSC, SBAF, and SBJR, respectively), whose flights are significantly affected during landing or take-off approaches due to instabilities and adverse phenomena typically associated with convective systems.

Between 1960 and 1980, data extrapolation techniques were developed and tested, giving rise to studies such as Wilson (1966), Wilk and

Gray (1970) and Battan (1973), which utilized radar and satellite data to forecast convective occurrences. Subsequently, Wilson et al. (1998) then proposed utilizing numerical prediction models to assimilate radar and/or satellite data. Nascimento (2005) examined the use of atmospheric indices (or parameters) developed in the northern hemisphere (in non-tropical latitudes) in identifying atmospheric conditions favorable to the appearance of severe convective storms in the tropics in Brazil. Teixeira and Satymurty (2007) investigated the dynamic and synoptic factors that distinguish heavy rainfall periods from non-heavy rainfall events in southern Brazil from 1991 to 2001 using reanalysis data. It is concluded that the mean flow patterns preceding the events are associated with the presence of a mean tropospheric trough east of the South Pacific approaching the coast three days earlier, a low-pressure center in northern Argentina one day earlier, a low-level jet over Paraguay two days earlier, and moisture flow convergence over southern Brazil (1 day before). Pinto et al. (2006) investigated the spatial-temporal distribution of atmospheric discharge data collected from 1999 to 2004 in the southeastern region of Brazil, which is the study area of this investigation, and found that the high-frequency incidence of AD, which occurs in the summer, is coupled to urban heat islands. Paulucci et al. (2019) investigated the Spatial-temporal variability of cloud-to-ground atmospheric discharges in the Rio de Janeiro metropolitan region and observed that the largest incidence occurs in the summer (64.3%) and the minimum is in the winter (2.3%).

Currently, the prediction of convective events is based on meteorologist's local experience since there is no accurate numerical model to predict the occurrence and severity of these events (Anquetin et al., 2005; Meißner et al., 2007) with the accuracy required by various sectors of our society, such as civil defense and aviation. McGovern et al. (2017), Zhou et al. (2019), Shirali et al. (2020), Teixeira et al. (2020), Sayeed et al. (2021), and Dupuy et al. (2021) are examples of recent studies that use hybrid models and IA techniques to improve forecasts based on numerical models and/or in situ observations.

A series of studies has recently been developed to investigate the application of deep/machine learning algorithms for specific weather forecasting improvements. MIT Lincoln Laboratory projects include the NextGen Weather Processor (NWP) and Offshore Precipitation Capability (OPC). The first identifies potential threats to aviation safety by combining meteorological data from various sources (such as weather radars, environmental satellites, lightning, meteorological observations from surface stations and aircraft, and output from the numerical forecast model) to forecast route closures and airspace capacity restrictions up to eight hours in advance (Newell et al., 2010). In Brazil, a system similar to NextGen, called SIRIUS, was implemented to improve the organization and operational safety of Brazilian air traffic management (Gavazzi, 2018). The OPC project combines information from satellite imaging, atmospheric discharges, and output numerical weather forecast models to estimate the position and intensity of precipitation in places where radar coverage is not available (Veillette et al., 2016). This data is converted into an image that resembles radar using machine learning algorithms. Guikema et al. (2010) developed a technique based on regression and data mining to predict the number of electric poles that will need to be replaced. The results of the created tool indicate that hurricane-related damage to electricity poles can be properly detected. A hybrid model that combines discriminatory trained prediction algorithms with a deep neural network was put out by Grover et al. (2015). In order to offer wind data throughout a flight in real time, Kim et al. (2021) created a hybrid wind forecasting methodology that combines a supervised learning algorithm with the Inverse Distance Weighting technique. Both produced encouraging outcomes that could help weather forecasting systems become more sophisticated. França et al. (2016), Almeida et al. (2020), Freitas et al. (2019), and Soares et al. (2021) developed models with aeronautical purposes based on deep/machine learning algorithms that provide successful convective event forecasting for specific regions in southern Brazil. Likewise, França et al. (2018) used a regressive neural network-based nowcasting model to forecast low wind profiles at Guarulhos airport in São Paulo, Brazil, with favorable performance for up to 45 minutes. Gultepe et al. (2019) presented a comprehensive literature review that describes weather information understanding for aviation maneuvers and provides suggestions for major improvements in weather-related measurement and prediction, numerical weather techniques, and next-generation integrated systems.

According to the statistical overview of air traffic (CENIPA, 2022), in the last 10 years, almost 58% of the meteorological conditions that influenced the flow of air navigation in Brazil are associated with the occurrence of severe convective events. In general, frontal systems (Derecynski et al., 2009), the existence of the South Atlantic convergence zone (Andrade et al., 2015), or isolated convection is associated with the genesis of these events (Teixeira and Satyamurty, 2007). Reliable forecasting of convective events remains to be a difficulty and a critical component of aviation meteorology. So, the goal here is to predict a severe convective event. As a result, it intends to use the output of the reconstruction of the atmospheric conditions of convective events (before, during, and after) via a numerical model based on machine learning algorithm training to create a hybrid model of local convective event prediction.

The present study uses outputs from the WRF model to provide attributes for feeding a machine learning algorithm to classify the convective events. The meteorological attributes are selected by using a p-value statistical hypothesis testing, where the p-value is computed with the help of software package BRB-ArrayTool, developed from the Biometrics Research Branch (BRB) team of the National Cancer Institute (NCI) – USA. Choosing the attributes with the smallest p-values, the process allows dealing with a significant reduction of the attribute dimension.

The main novelties of this work can be summarized as follows:

- A hybrid approach is applied, combining WRF simulation with a machine learning algorithm.
- The hybrid approach is executed in two steps:
  Step-1: WRF simulations
  Step-2: from the WRF simulations some attributes are selected as the inputs for the machine learning (ML) algorithms.
- The precipitation events are identified into different severity classes.
- The method for the attribute selection is based on the statistical p-value scheme.
- A better configuration of the ML algorithms was obtained by using the Adaptive Boosting approach.

2. STUDY AREA AND DATA

This represents the irregular polygon in Figure 1 that depicts the boundary of TMA – Rio and displays the approximate location of the airports Galeão (SBGL), Santa Cruz (SBSC), Jacarepaguá (SBJR), Afonsos (SBAF), and Santos Dumont (SBRJ).

Figure 1 - TMA-Rio study area and the location of its five main airports.
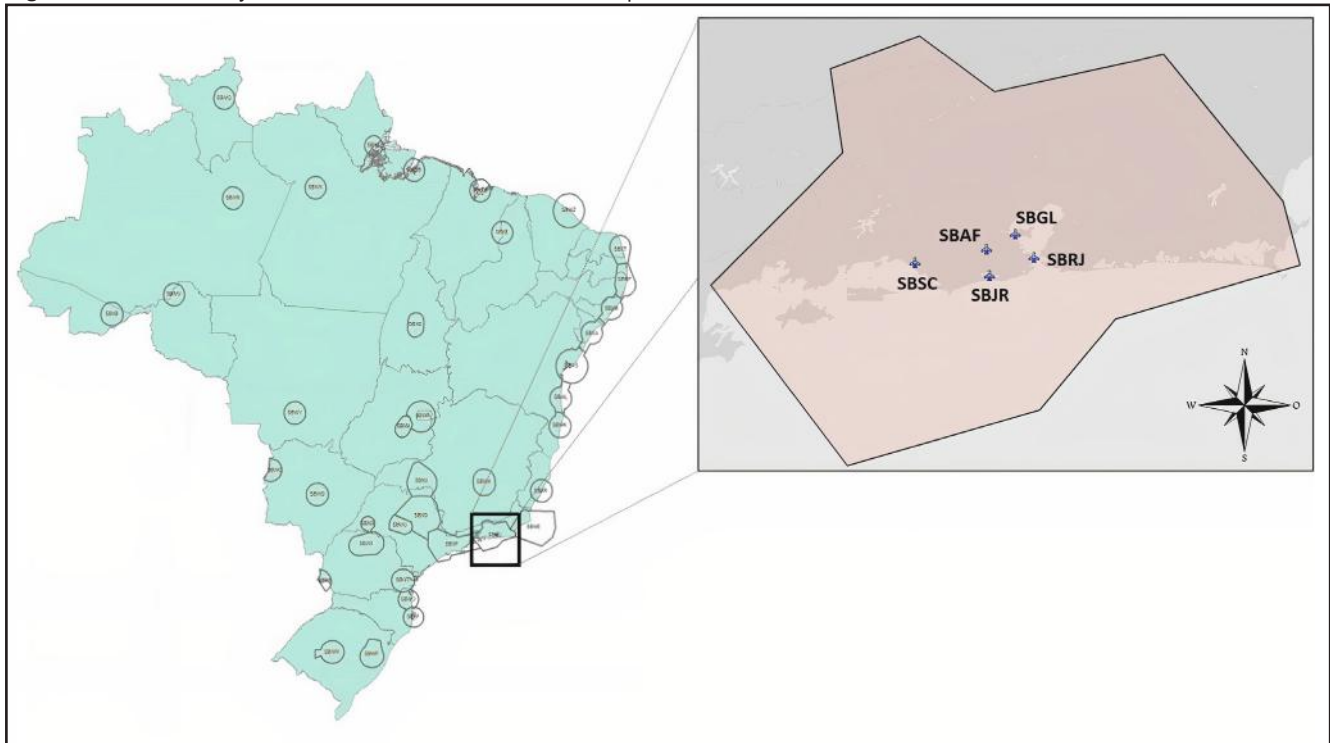
Table 1 shows the four-time series that had been used: 1) atmospheric discharge (AD) collected by the national lightning detection network (RINDAT) from 2008 to 2018, which were used to characterize the severity of the convective events studied; 2) maps and synoptic fields are used to understand the atmospheric conditions that origin convective events; 3) For the RINDAT data period, data from the Global Forecast System with a resolution of 50 km (GFS 0.5) is available and was utilized as the initial condition for the WRF forecast model in simulations of the reconstructed events and, 4) precipitation data from surface weather stations are used to observe precipitation distribution.

3. METHOD

The difficulty at hand is connected to identifying the predicted atmospheric patterns provided by the WRF (numerical simulation) that correlate to the start and finish of a convective event. In short, the method evaluates each point of the grid of meteorological variables (defined as an independent attribute) of the WFR output to select the set of attributes that has the highest influence on the occurrence of a convection event using the statistical hypothesis of the p-value (see Ruivo et al., 2018). The selected attributes will serve as predictors (or input) for the deep/machine learning algorithms, which will be trained and tested to forecast the aforementioned atmospheric patterns.

3.1 Numeric Simulation

The WRF model was used to conduct numerical reconstruction of the investigated convective and no convective events. The modeling period was based on an analysis of the spatial-temporal distribution of atmospheric discharges (section 4.1), which considers the atmospheric volume with a radius of 150 km centered at the SBGL airport, which corresponds roughly to the TMA – Rio. The AD distribution analysis revealed that February has the highest occurrence, consequently, numerical simulations of February were conducted from 2008 to 2018, excluding the twenty-nineth day of leap years. at 22.8°S and 43.27°W (SBGL) inserted at coordinates 15°S – 30°S and 36°W – 51°W with a grid of 9 km (d01), 3 km (d02), and 1 km (d03), each one with 60×60, 127×112 and 277×277 points for horizontal respectively, with 33 levels at vertical coordinate, and using a Mercator map projection (Figure 2).

The initial and boundary conditions were generated from the Global Forecast System (GFS) model of the National Centers for Environmental Prediction (NCEP), which has a horizontal resolution of 0.5° and 33 integrated vertical levels. The model starts the analyses at 00 UTC and extends them for 36 hours, however, the first 12 hours are disregarded due to a process known as spin-up, which is defined as the time necessary to adapt the model

Table **1** - Data source, description, frequency, and availability of the data used.

Source	Description	Temporal resolution	Availability period
Lightning detection network (RINDAT) http://www.rindat.com.br	The geographical location (latitude, longitude) of atmospheric discharges using remote sensing detectors.	300 ns	2000-present
Surface synoptic charts (CPTEC) http://tempo.cptec.inpe.br/cartas.php?tipo=Superficie	Synopticanalysis.	6 h	2008-present
GFS 0.5 https://catalog.data.gov/dataset/global-forecast-system-gfs-0-5-deg	Initial and boundary atmospheric conditions with 0.50 resolution.	3 h	2006-present
4. BNDMET https://bndmet.inmet.gov.br/mapa	Observational Rainfall data from the DECEA/INMET network stations.	1 h 24 h Monthly	2000-present

regardless of the initial and boundary conditions. The simulations employed the following settings, as proposed by Silva et al. (pre-print): 1) Grell-Freitas (Grell and Freitas, 2014); 2) microphysics, WSM6 (WRF Single-Moment 6-class Schema) (Hong and Lim, 2006); 3) Boundary layer - Yonsei University (Hong et al., 2006); and 4) radiation- for long-wave and short-wave radiation, the RRTM (Rapid Radiative Transfer Model) (Mlawer et al., 1997) and Dudhia (Dudhia, 1989) models are used.

Figure 2 - Domains of the used simulation grids that are centered in SBGL.
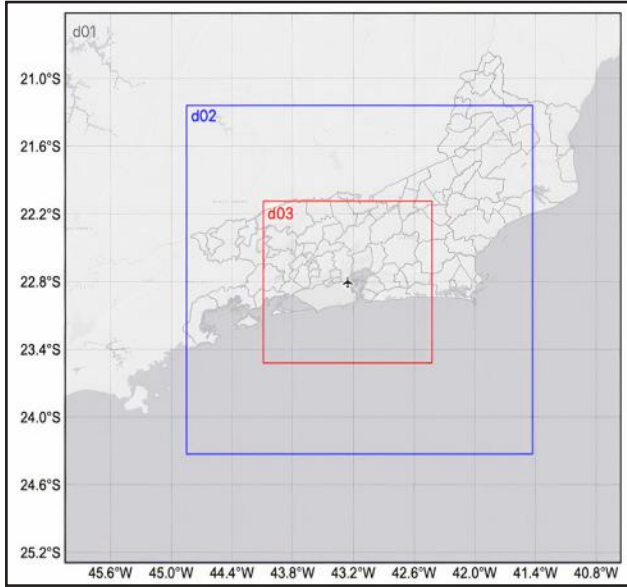
3.2 Data mining

Data mining is a subfield of database study that incorporates techniques and concepts from several disciplines such as machine learning, statistics, pattern recognition, and data visualization (Fayyad et al., 1996). Its goal is to find patterns and extract information from a set of data by converting it into smaller subsets to promote better interpretation and minimize the processing time of existing data. This data mining approach is known as dimensionality reduction. (Hair et al., 1995) According to Alppaydin (2010), simpler models are more robust in the face of smaller data sets, and if we can reduce the amount of the data without losing information, the structure and bias can be plotted and studied more readily, improving interpretation. Dimensionality reduction approaches include principal component analysis, associative neural networks, and p-value, the latter often known as hypothesis testing.

In the meteorological context, Wang et al. (2013), Ganguly et al. (2014), Ruivo et al. (2014), Anochi

and Campos Velho (2015) are works that apply data mining approaches connected with a significant weather forecast, although it is still a little-studied methodology. The p-value was chosen as the dimensionality reduction strategy in this study, which, according to the literature, is an innovative approach for developing a hybrid forecasting model, as in this study, integrating data from a meteorological numerical model, data mining techniques, and machine learning categorical algorithms.

3.3 Attribute analysis: P-value

The p-value hypothesis testing is calculated for each attribute of 3D WRF grid, and a georeferenced map of p-values for each 3D coordinate of each meteorological variable is constructed. The idea is to choose attributes from a set of data that act differently in predefined classes of precipitation intensity, and then determine their significance for the occurrence of severe convective events, or, in other words, the lower the p-value, the more probably the attribute is associated with the phenomenon under investigation. The p-value statistical analysis is codified in the BRB-ArrayTools (version 4.6.1), free software available at http://linus.nci.nih.gov/brb/download.html. It has a comprehensive collection of tools for constructing predictive classifiers and performing thorough cross-validation. In this research, the software was adapted to environmental problems; the following steps were taken in line with the strategy employed by Ruivo et al. (2014, 2015, and 2018):

i. Examine the statistical consistency for outline detection of the hourly rainfall data at TMARio of the five airports (SBSC, SBGL, SBRJ, SBJR, SBAF);

ii. The convective event time series is chosen based on the existence of AD, and the pentad precipitation series is calculated in anomalies (average of 5 days). Rainfall classes are determined by thresholds heavy ($\geq$ 3.0mm) and moderate/weak (< 3.0mm), so, the most significant pentad is selected for simulation with the WRF;

iii. For the 13-Yr period 2008-2018, atmospheric dynamics is simulated employing WRF with the settings specified in 3.1 for February;

iv. The predicted WRF variables are preliminarily selected (as shown in Table 2), as a guide, to be used to determine the p-values, taking into account the previous successful experiments conducted by Ruivo et al. (2015 and 2018) for extreme rainfall events in Brazil;

Table 2 - Predicted variables and their attributes obtained by Ruivo et al. (2015), used here as guide to determine the best predictors (or input) of the machine learning algorithms to be trained and tested.

No	Predicted Variable	Attribute observation level (hPa)
1	Sea level pressure (SLP)	1000
2	Air temperature (T)	2 meter, 925, 850, 700, 600, 500, 300
3	Specific humidity (SH)	925, 850, 700, 600, 500, 300
4	Omega (ω)	925, 850, 700, 600, 500, 300, 200
5	Geopotential height (GH)	1000
6	Zonal Wind (U)	925, 850, 700, 600, 500, 300
7	Meridional Wind (V)	925, 850, 700, 600, 500, 300

Table 3 - The characteristics of the selected algorithms.

Classifier	Description	Reference
BayesNet	Based on the construction of a Bayesian network, using various search algorithms and quality measures.	Witten et al. (2016)
NaiveBayes	Naive Bayes standard probabilistic classifier. Numerical estimator precision values are chosen based on the analysis of training data.	G.H. John and P. Langley (1995)
MultilayerPerceptron	Uses backpropagation to learn a multilayer perceptron to classify instances. It has a hidden layer with a customs number of units also hidden.	Witten et al. (2016)
SimpleLogistic	Construction of linear logistic regression models. LogitBoost with simple regression functions as basic learners is used to fit the logistic models.	Landwehr et al. (2005)
LMT	Classifier for building classification trees with logistic regression functions on leaves.	Landwehr et al. (2005)
J48	Creates a single decision tree based on all available input resources.	Ross Quinlan (1993)
RandomForest	Creates decision trees trained on different subsets of input features.	Leo Breiman (2001)
RandomTree	Construction of a tree that considers k attributes randomly chosen at each node. Do not perform pruning.	Witten et al. (2016)
REPTree	Quick decision tree. Build a decision or regression tree using information gain/variance and pruning using reduced error pruning (with backfitting).	Witten et al. (2016)

v. Datasheets are structured with characteristics – variables at different levels and coordinates – precipitation classes, and time series (in pentads) for simulated events;

vi. Data dimension reduction: Considering the grids (d01, d02, d03) applied to the WRF model, the number of attributes for each time-step for seven (7) meteorological variables (temperature, pressure, moisture, wind components: (u,v,w), geopotential height) will be: $7_{variables} * 464_x * 449_y * 33_z = 48,125,616$. These are too many inputs for a machine learning tool, requiring a supercomputer for configuring and training a supervised machine learning algorithm. Therefore, a methodology can be employed to reduce the number of inputs, without losing the information capacity to estimate a quantity from the reduced number of attributes. Table 2 indicates some meteorological variables for specific coordinates for several levels. This set of attributes was used by Ruivo et al. (2015), the companion paper, to identify extreme events in Brazil. Here, the same strategy is also applied, where the p-value hypothesis test is computed. Firstly, classifying if there is (YES) or not (NOT) the AD. Secondly, events with the presence of AD are classified into different

precipitation classes. The p-value is calculated at several levels of significance (α = 0.5, 0.1, 0.05, 0.01) of seven meteorological variables at each WRF grid point. The BRB software package was designed to examine genetic propensity to certain types of cancer. The adaption of this approach and classification of features for convective events is detailed further below.

a) For the application of the BRB-arraytool, the following analogy was adopted: genes and diseases are associated to meteorological attributes and extreme events, respectively.

b) According to Simon et al. (2004), there are several schemes to evaluate significant statistical diference of classes. Here, the t-student testing is used as a metric to quantify the difference (distance) between two samples, considering standard deviation units – see equations (1) and (2a-b). For an established threshold, it is determined the difference significance between two samples or classes.

c) The multivariate permutation test (MPT) is used for mapping the t-statistics into p-values, by NP random permutations for Nattributs. The MPT is regularly employed to compute the statistical significance (p-values) of a sample (Knijnenburg et al.,2009; Ernst, 2004). The t-test value is computed randomly by changing entries among classes. For two classes C1 and C2, entries of both classes are changed. So, changing an entry from class C1 is now to class C2, the same situation for a randomly selected entry from class C2. With these new classes, a new t-test score (t*) is calculated, and the operation is repeated for Np permutations. The computation of the t-test score between two classes is determined by the formula:

$$t\text{-test} = \frac{\langle x_1 \rangle - \langle x_2 \rangle}{\sqrt{s_p^2 \left[\frac{1}{J_1} + \frac{1}{J_2} \right]}}, \qquad (1)$$

where $\langle x_i \rangle$ $(i = 1,2)$ are the means of classes, and s_p^2 is given by:

$$s_p^2 = \frac{(J_1-1)s_1^2 + (J_2-1)s_2^2}{J_1 + J_2 - 2}, \qquad (2a)$$

$$s_i^2 = \frac{1}{J_i} \sum_{k=1}^{J_i} [x_{ik} - \langle x_i \rangle]^2 . \qquad (2b)$$

The p-value from the MPT is calculated by the ratio between the number of t-test scores (t*)greater or equal to the reference value (t) and the total number of permutations plus one, as expressed in the formula below:

$$\text{p-value} = \frac{1 + \text{random pertabation where } |t^*| \geq |t|}{1 + N_p} . \qquad (3)$$

vii. The fields of the most relevant attributes, as well as their respective p-values, are plotted for analysis and selection and normalized of attributes to be utilized as predictors.

viii. Training and testing: it is expected that the machine learning-based algorithms that will be trained and tested, with the aforementioned attributes as input, would be capable of distinguishing atmospheric patterns associated with convective (YES) and non-convective (NO) events. WEKA (version 3.7.12), a machine learning-based categorical algorithm developed by the University of Waikato in New Zealand (Witten et al., 2016), was used for algorithm training and testing. By randomly dividing the data in training and testing samples into different proportions, the algorithms were trained and tested via a cross-validation that consists of testing machine learning algorithms by training them on subsets of the input data and then evaluating them on the complementary subset. This technique is recommended to avoid overfitting.

ix. Case study.

3.4 Algorithms Evaluation

The predicted vs observed can be evaluated using the confusion matrix or contingency table (Table 4). The columns reflect the observed values, and the rows indicate the forecast values, in this NxN order matrix. The statistical metrics used are: (1) Probability of detection (POD) is a statistical term that evaluates the percentage of observed events that were correctly predicted. A perfect score is 1; (2) False alarm rate (FAR), which is the percentage of YES forecasts that were incorrect. (3) Critical Success Index (CSI), the ratio of correct forecasts to the number of times events were predicted and observed; The ideal score is one (Wilks, 2005). In addition, the results of the algorithms' predictions were evaluated using ROC (Relative Operating Characteristic) diagrams, which represent the joint plot of POD Vs FAR values.

Table 4 - Contingency table described as: a (Hit) – the phenomenon was predicted and observed; b (False Alarm) – the phenomenon was predicted and not observed; c (Miss) – the phenomenon was not predicted, but it was observed; and d (Correct Negatives) – phenomenon was not predicted and was not observed.

		Observation		
		Yes	No	Total
Prediction	Yes	a	b	(a+b) Predicted
	No	c	d	(c+d) NotPredicted
Total		a+c	b+d	

4. RESULTS

4.1 Characterization of events

The AD data were analyzed following the steps of the method in section 3 for the 11-yr period (2008-2018)in the cycle centered on SBGL with a radius of 150 km, where the TMA-Rio is inserted. The hourly and monthly distributions of AD are shown in figures 3a and 3b. Between 18:00 and 20:00 (local time) is throughout December to March, 56% of AD events occur, when there is more energy available for convection, enhancing the production of convective clouds and the incidence of lightning (Christian et al. 2003; Paulucci et al., 2019). The data was chosen for simulations with WRF and test-training of machine learning algorithms because of the higher density of AD that occurs in February.

4.2 Analysis by p-value

The aim is to identify those predictor attributes of the set of variables predicted by the WRF that have higher correlations with the occurrence of convective events, as suggested by Ruivo et al. (2015), to reduce the number of them used as input for machine learning algorithms to be trained and tested in this study.

Figure 3 - Distribution of atmospheric discharge for the period 2008–2018: (a) Hourly, and (b) Monthly.
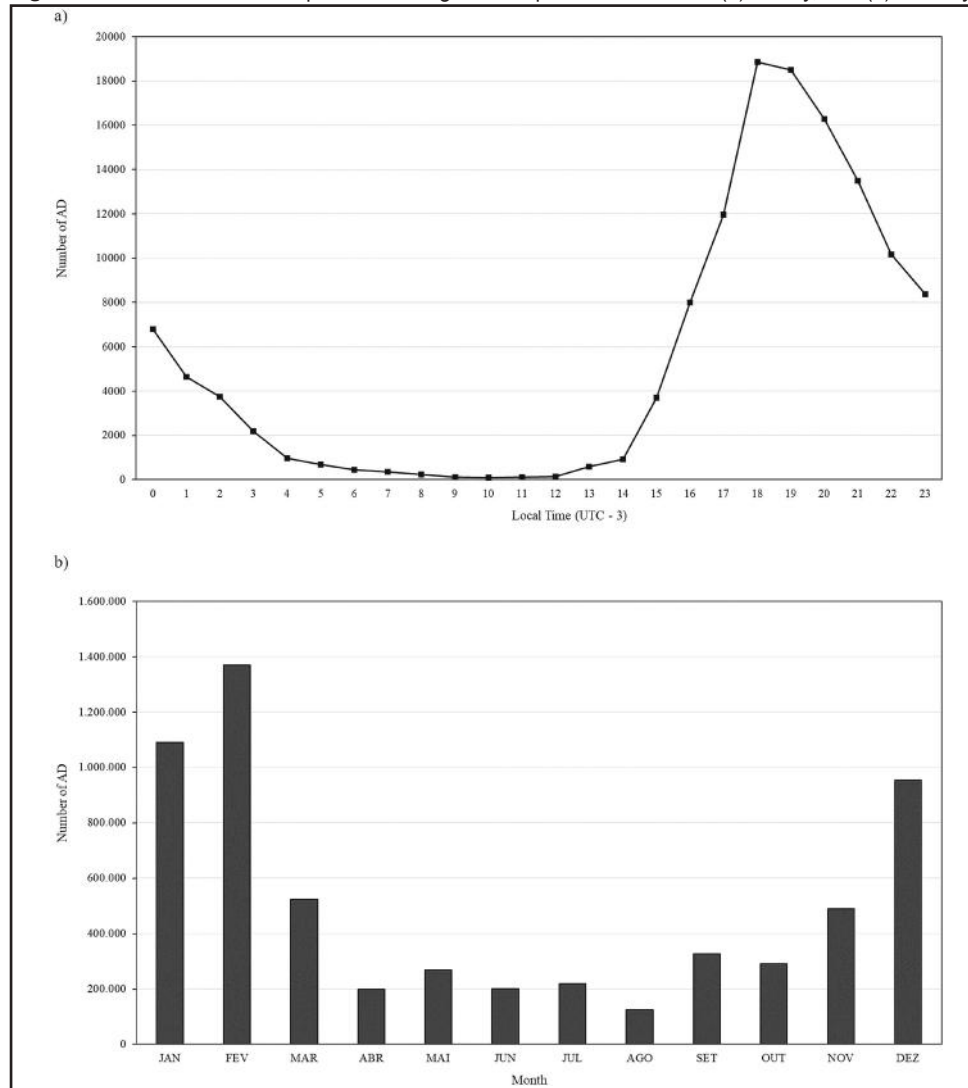
Figure 4 shows a series of anomalies in average precipitation from the five TMA-Rio airport meteorological stations in pentads, including if AD occurred within this time interval, throughout an 11-year period (2008-2018), classifying those pentads that are heavy (rainfall ≥ 3.0 mm) and moderate-weak (precipitation < 3.0 mm). The red highlighted rainfall pentad from February 13-17, 2018, was selected for WRF simulation as it recorded the highest positive rainfall anomaly and AD=15,939 occurrence in TMA-Rio.

Following to method´s step vi, the total number of attributes (N-attributes) is equal to 48,125,616 (which represents 7-variables*464-x* 449-y*33-z) that are stimulated by the WRF. Each attribute's p-value (Eq. 1) was calculated using 10,000 random permutations (Np) with a significance level $\alpha = 0.05$, which represents a probability of less than 5% being a false positive. The following section discusses the behavior patterns of the p-value field for some of the predicted variables (Table 2). Figure 5 (a-d) depicts the p-value of specific humidity average predicted at various levels (925, 850, 600, and 300 hPa) at 00 hs (local time) for February 15, 2018. It observes that the area surrounding the airports (red dots) shown in Figure 5 (a-d) (at 925, 850, 600, and 300 hPa), corresponding approximately to TMA-Rio area, has a p-value of SH less than 0.05 (as shown in the dark regions in the figures).

This means that the SH values at the aforementioned levels (attributes) can be considered

strong predictors of convective events. Similarly, the p-values of the mean omega (vertical movement) at 600 and 300 hPa (Figure 6, a-b) and the mean wind at 925 hPa (Figure 7) are plausible predictors for the selected event, since their values are low in the TMA-Rio region, where the airports are located (red dots). Table 5 summarizes the characteristics (variable, level, latitude, longitude, and p-value) of the 36 selected attributes, which are the result of several experiments and are used as input (predictors) to machine learning algorithms.

4.3 Training and testing

A numerical experimentation process, changing the algorithm configuration parameters and verifying the performance, is one of the most used strategies for configuring machine learning algorithms. This procedure is typically costly. The success of an ML algorithm is strongly dependent on the predictors (inputs) chosen, as well as the training set. As inputs, the thirty-six attributes with the lowest p-values from the preceding section (Table 5) are employed, which are hypothesized to be associated with atmospheric conditions of the thermodynamic state in the development and maintenance of convective events. The training strategy consists of determining algorithm parameters that can perform the best mapping between input data (inputs) and ML algorithm outputs, for minimizing the difference between predicted and observed values.

Figure 4 - Average precipitation in anomaly (mm) in pentad and its amount of AD in TMA-Rio for February between 2008 and 2018 (average of meteorological stations at 5 airports).
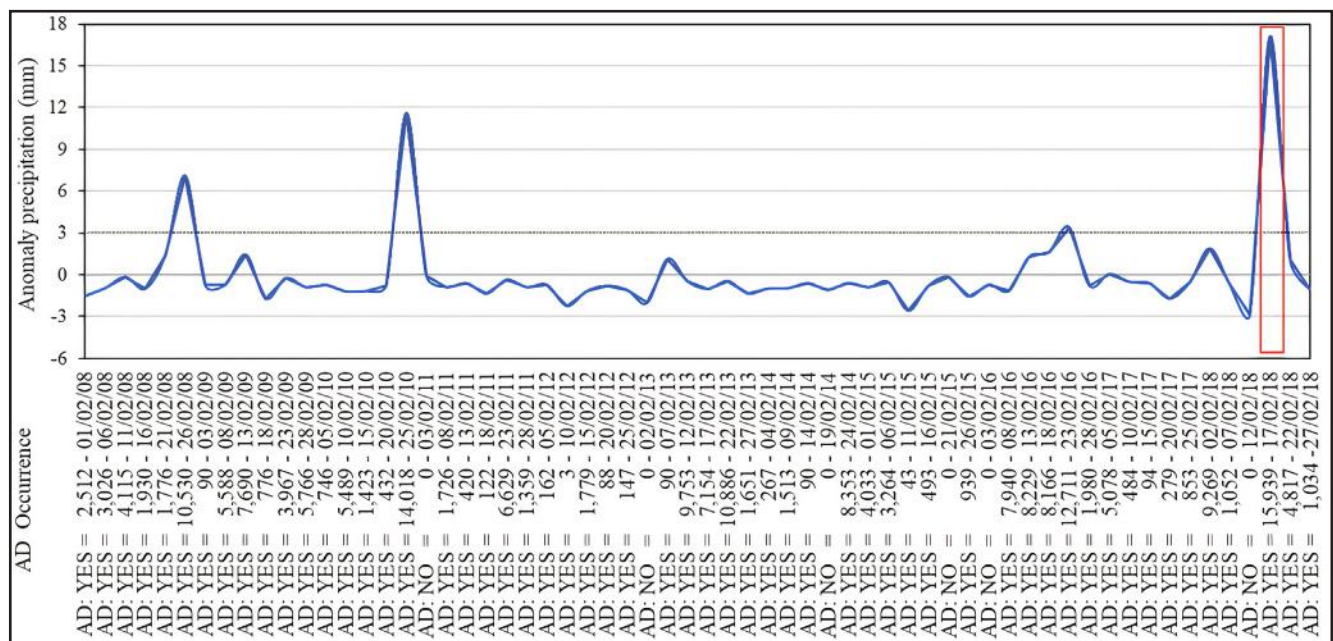
Figure 5 - P-value of specific humidity at levels of 925, 850, 600, and 500 at 00 h s (local time) for the event on February 15, 2018.at 5 airports).
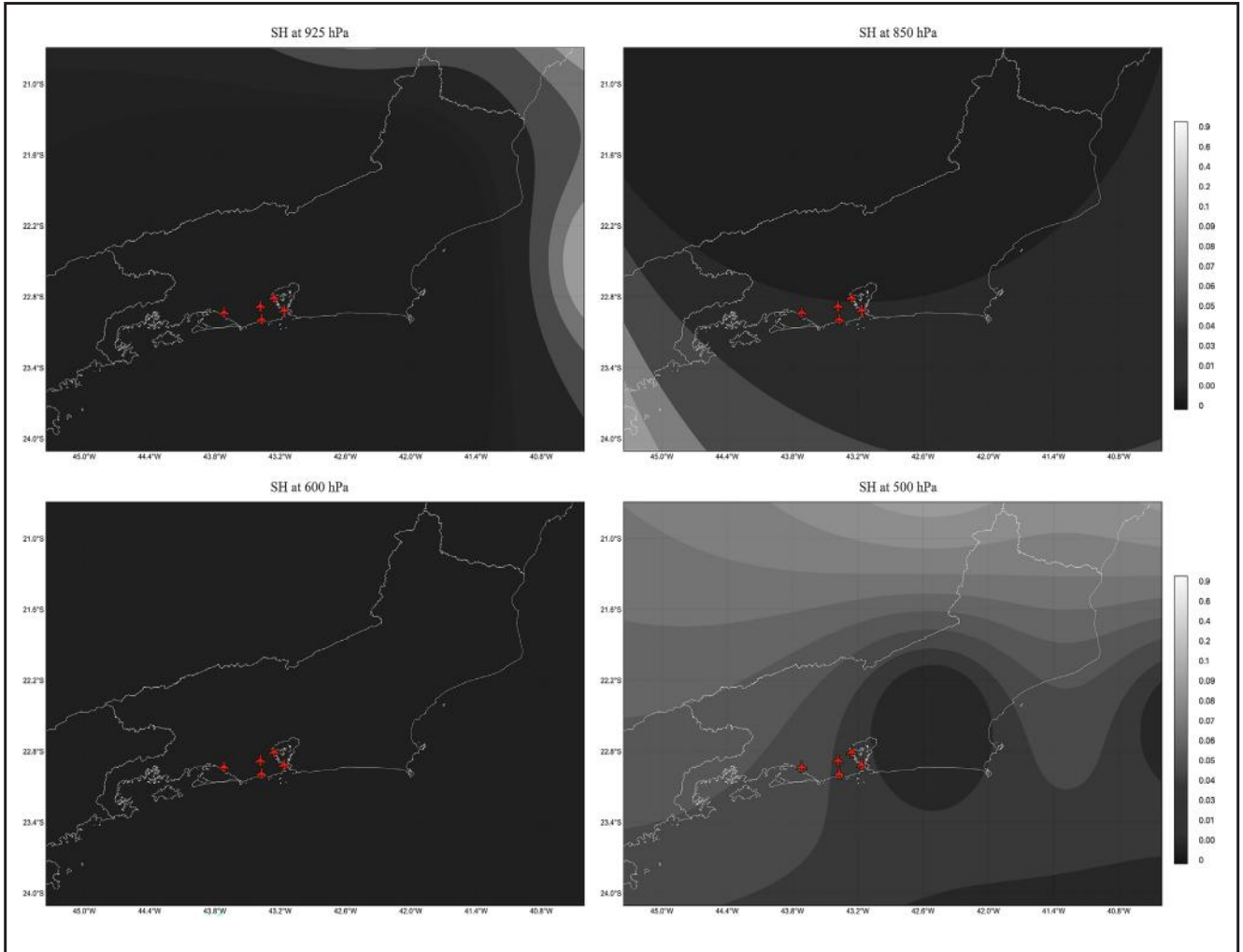
Figure 6 - P-value of omega at levels of 600 and 300 hPa at 00 h s (local time) for the event on February 15, 2018.
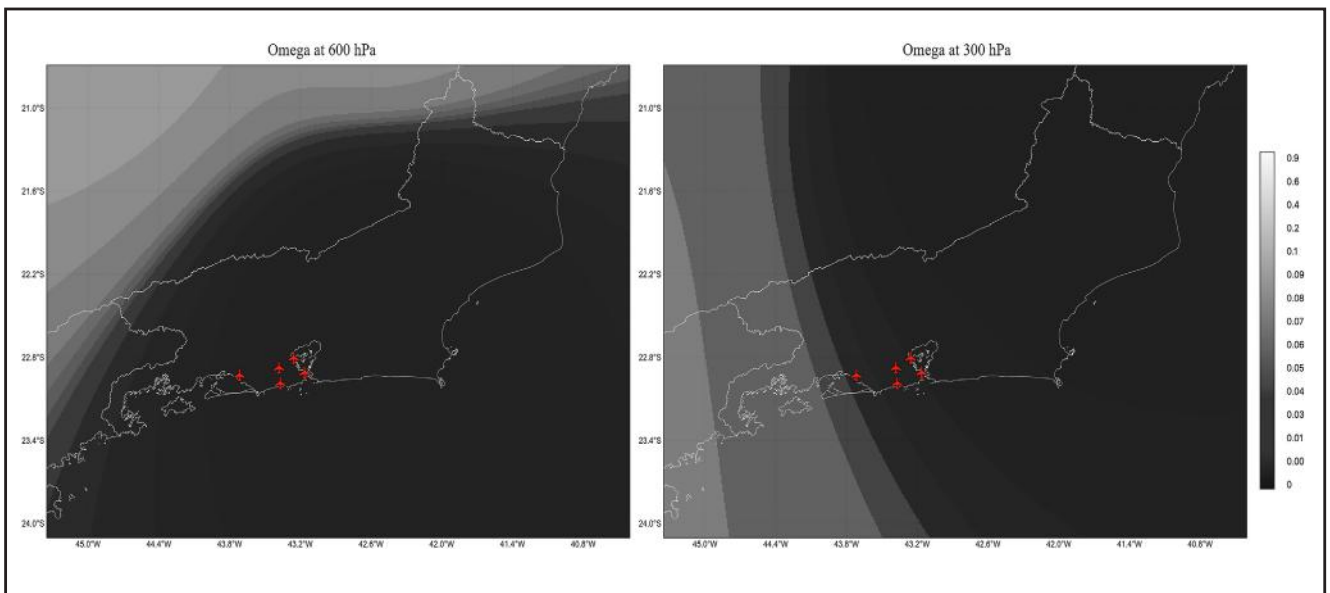
Figure 7 - It shows the p-value representation of the wind at 925 hPa at 00 h s (local time) for the event on February 15, 2018.
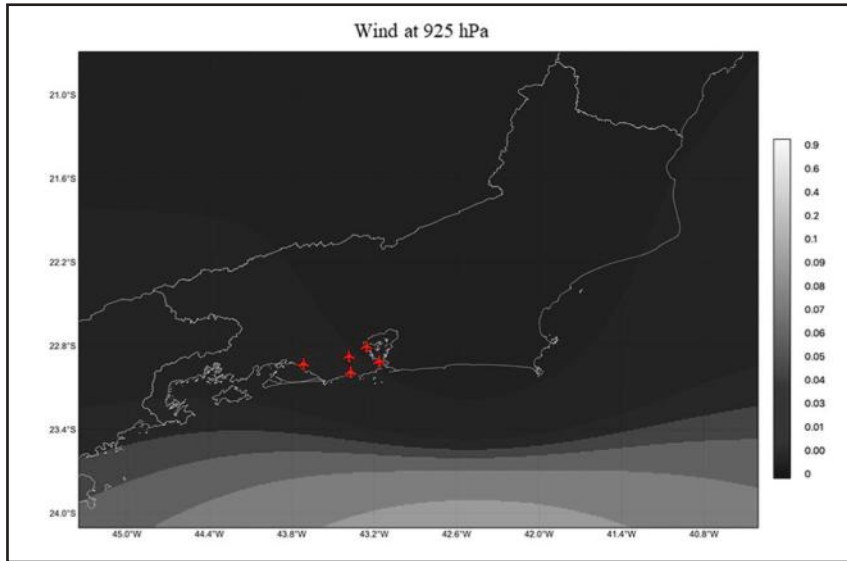
Table 5 - The POD, FAR, and CSI statistics for predictions of nine selected algorithms trained (* with boost) using cross-validation for six conditions of established data partitions (1: unaltered data, 2: 50% YES and 50% NO, 3: 55 % YES and 45 % NO, 4: 60% YES and 40 % NO, 5: 65% YES and 35 % NO, and 6: 70% YES and 30 % NO) in 438 experiments.

No	Variable	Level (hPa)	Latitude	Longitude	P-value
1	sh	400	-22.5S	320W	9.2E-05
2	sh	300	-20S	317.5W	1.7E-04
3	sh	400	-25S	322.5W	3.2E-04
4	sh	850	-20S	315W	4.2E-04
5	sh	850	-20S	312.5W	8.5E-04
6	sh	300	-20S	320W	1.4E-03
7	sh	400	-25S	320W	1.4E-03
8	sh	400	-27.5S	322.5W	1.4E-03
9	sh	300	-22.5S	320W	1.5E-03
10	omega	600	-20S	317.5W	1.6E-03
11	omega	300	-20S	315W	2.0E-03
12	u	925	-25S	317.5W	2.3E-03
13	v	925	-25S	317.5W	2.5E-03
14	sh	925	-22.5S	317.5W	3.2E-03
15	omega	600	-20S	317.5W	3.4E-03
16	sh	300	-22.5S	322.5W	3.4E-03
17	sh	400	-22.5S	322.5W	4.4E-03
18	omega	600	-20S	315W	4.7E-03
19	sh	500	-27.5S	322.5W	4.8E-03
20	sh	600	-22.5S	317.5W	4.9E-03
21	omega	700	-20S	312.5W	5.7E-03
22	omega	500	-27.5S	312.5W	6.0E-03
23	omega	600	-27.5S	312.5W	6.5E-03
24	omega	700	-27.5S	312.5W	6.7E-03
25	v	400	-27.5S	322.5W	6.8E-03
26	sh	400	-20S	320W	7.1E-03
27	sh	850	-20S	317.5W	7.2E-03
28	v	700	-25S	322.5W	8.0E-03
29	sh	500	-25S	320W	8.1E-03
30	v	500	-25S	322.5W	8.6E-03
31	omega	850	-20S	310W	8.8E-03
32	sh	700	-27.5S	322.5W	8.8E-03
33	u	500	-27.5S	322.5W	8.9E-03
34	u	700	-22.5S	322.5W	8.9E-03
35	omega	400	-27.5S	312.5W	9.2E-03
36	u	850	-22.5S	317.5W	9.4E-03

Using the WRF hourly output of 9:00 (local time), the lead time is defined as 30 hours for the forecast period from 18:00 to 23:59 (local time), which is the most likely time for AD to occur (Figure 4a). Thus, if the trained category algorithms predict YES and AD consciously occurs between 18:00 and 23:59, the forecast is determined to be right (HIT); otherwise (ERROR). Most of the category algorithms provided in the WEKA package were used in several experiments. Because of their observed performance, the nine algorithms shown in Table 3 were chosen for further investigation.

Table 6 presents the values of the statistical metrics (POD, FAR, CSI) for 438 experiments of best predictions made by nine algorithms using cross-validation, taking into account six partitions namely: (1) unaltered data, (2) data adjusted (repeating or withdrawing) to 50% YES = convective event, 50% NO = no convective event, (3) 55% YES and 45 % NO, (4) 60% YES and 40 % NO, (5) 65% YES and 35 % NO, and (6) 70% YES and 30 % NO, for training and test data, applying the boosting (*prediction with boost) procedure using AdaBoost.M1 algorithm and without boost. The latter is accomplished by sequentially combining several weaker predictor models. As a result, the next weak learner considers the previous weak learner's predictions, giving higher weight to the more difficult predictions (those that the current iteration's weak learner predicted incorrectly), resulting in increased optimization of the final algorithm. Models are trained in this manner to reduce the errors of previous models. In this investigation, the algorithm is considered acceptable (or model) if its prediction outcomes achieve POD$\geq$80, FAR$\leq$20, and CSI$\geq$80. Thus, given an acceptable model criterion, it is seen that none of the algorithms used, without boost, achieved the required performance. On the other hand, the results demonstrate that using the boost process improved most of the predictions made by the nine algorithms regardless of the data partition. Only the Naive Bayes algorithms with data partition (6), Multilayer Perceptron, partition (1), LMT, condition (4), and RandomForest for partitions from (2) to (6) achieved results that met the established criterion for a model. As a result of these findings, it can be stated that the predictions produced by the group of five models (set: G1) based on the RandomForest* algorithm are statistically superior to those produced by the three other models (set: G2) based on the Naive Bayes*, Multilayer Perceptron*, and LMT*, as the average POD, FAR, and CIS statistics values and deviation are a little closer to perfection (i.e., POD (G1) = 0.97$\pm$0.02 and POD (G2) = 0.90$\pm$0.01; FAR (G1) = 0.07$\pm$0.032 and FAR (G2) = 0.12$\pm$0.01; CSI (G1) = 0.92$\pm$0.05 and CSI (G2) = 0.80$\pm$0.02).

Table 6 - The POD, FAR, and CSI statistics for predictions of nine selected algorithms trained (* with boost) using cross-validation for six conditions of established data partitions (1: unaltered data, 2: 50% YES and 50% NO, 3: 55 % YES and 45 % NO, 4: 60% YES and 40 % NO, 5: 65% YES and 35 % NO, and 6: 70% YES and 30 % NO) in 438 experiments.

Algorithm	Data partition																
	(1)			(2)			(3)			(4)			(5)			(6)		
	POD	FAR	CSI	POD	FAR	CSI	POD	FAR	CSI	POD	FAR	CSI	POD	FAR	CSI	POD	FAR	CSI
BayesNet	0.61	0.38	0.45	0.63	0.35	0.46	0.71	0.42	0.53	0.77	0.50	0.23	0.85	0.65	0.63	0.91	0.81	0.67
BayesNet*	0.70	0.35	0.51	0.55	0.44	0.47	0.61	0.26	0.50	0.64	0.35	0.58	0.70	0.44	0.52	0.82	0.23	0.77
NaiveBayes	0.62	0.39	0.45	0.64	0.34	0.48	0.66	0.38	0.50	0.68	0.43	0.53	1.00	0.99	0.65	0.99	1.00	0.70
NaiveBayes*	0.67	0.26	0.55	0.63	0.37	0.56	0.60	0.32	0.52	0.68	0.32	0.50	0.71	0.32	0.60	**0.89**	**0.11**	**0.80**
MultilayerPerceptron	0.86	0.50	0.58	0.78	0.32	0.59	0.72	0.35	0.56	0.80	0.44	0.62	0.85	0.53	0.66	0.92	0.65	0.72
MultilayerPerceptron*	**0.91**	**0.13**	**0.84**	0.74	0.26	0.67	0.72	0.28	0.65	0.70	0.34	0.59	0.85	0.43	0.67	0.75	0.48	0.63
SimpleLogistic	0.62	0.40	0.44	0.64	0.35	0.47	0.69	0.42	0.51	0.75	0.53	0.56	0.86	0.71	0.62	1.00	1.00	0.60
SimpleLogistic*	0.64	0.36	0.48	0.62	0.36	0.55	0.70	0.31	0.53	0.75	0.24	0.66	0.66	0.31	0.56	0.91	0.59	0.67
J48	0.44	0.21	0.37	0.81	0.21	0.67	0.84	0.27	0.69	0.84	0.27	0.72	0.87	0.33	0.74	0.90	0.46	0.75
J48*	0.61	0.30	0.42	0.48	0.32	0.37	0.84	0.22	0.77	0.80	0.22	0.75	0.87	0.37	0.70	0.90	0.46	0.75
LMT	0.52	0.23	0.42	0.82	0.19	0.69	0.87	0.26	0.72	0.87	0.26	0.74	0.89	0.29	0.77	0.91	0.46	0.76
LMT*	0.66	0.17	0.60	0.60	0.41	0.48	0.74	0.14	0.66	**0.91**	**0.13**	**0.83**	0.90	0.37	0.75	0.92	0.39	0.78
RandomForest	0.61	0.32	0.47	0.86	0.16	0.75	0.88	0.20	0.75	0.91	0.25	0.78	0.94	0.36	0.79	0.96	0.44	0.81
RandomForest*	0.86	0.18	0.78	**0.93**	**0.08**	**0.84**	**0.96**	**0.06**	**0.90**	**0.97**	**0.09**	**0.92**	**1.00**	**0.02**	**0.98**	**0.99**	**0.11**	**0.96**
RandomTree	0.57	0.45	0.39	0.82	0.17	0.70	0.85	0.21	0.72	0.89	0.26	0.75	0.90	0.28	0.78	0.91	0.32	0.80
RandomTree*	0.79	0.21	0.74	0.65	0.34	0.54	0.82	0.18	0.75	0.83	0.20	0.77	0.89	0.28	0.80	0.93	0.27	0.84
REPTree	0.56	0.30	0.43	0.71	0.27	0.56	0.78	0.32	0.62	0.80	0.38	0.64	0.84	0.45	0.68	0.87	0.55	0.71
REPTree*	0.82	0.23	0.71	0.70	0.29	0.62	0.73	0.28	0.67	0.80	0.38	0.62	0.84	0.45	0.68	0.89	0.29	0.79

4.4 Hindcast

This is the hindcast of the nine models that satisfied the acceptance criterion for hourly data at TMA-Rio between February 1-28, 2019. The hourly 24-h hindcast of each model is shown in Figures 8 (a-d). The green and red squares denote HIT if the hindcast YES and the occurrence of AD within one hour, and ERROR otherwise. Observe that there were convective events on all of the investigated month's days. The following is a diagnosis from a hindcast analysis:

Figure 8 - (a), (b), (c), (d) Convective events 24-h hindcast for the nine algorithms chosen. for February 1–28, 2019.

a)

b)

Figure 8 - (continued).

c)

d)

DAY 1 – 8 AD was recorded during an event that lasted from 19:00 to 21:00 hours, and only one RandomForest*(6) model was able to do the hindcast for the entire event. At 00:00 and 14:00, the NaiveBayes*(6) model generated two false alarms;

DAY 2 - 208 AD were recorded between 16:00 and 22:00 hours, and three models from the RandomForest*(2-6) family were revealed to have detected the event. Some false alarms were generated; however, because they occurred during the event's genesis and/or dissipation, when atmospheric conditions were still highly unstable, these models cannot be held responsible for the inaccuracy.

DAY 3 - There were 1389 AD, with 100 and 1289 falling between 13:00-14:00 and 17:00-23:00 hours.

The RandomForest *(3-6) models detected every event perfectly, but the other models generated occasional false alarms during the event's genesis and dissipation stages;

DAYs 4 and 5 – The discharges were distributed in two events, the first with 69 AD, which occurred at 07:00 h, and the second with 993 AD, which happened from 17:00 h on DAY 4 to 4:00 h on DAY 5 and was accurately detected by the RandomForest* models (4)- (5). As in prior examples, it is conceivable to observe the models producing false alarms throughout the event formation and/or dissipation phases;

DAYs 6 and 7 - On the 6th, there were recordings of 1330 AD between 05:00 and 23:59 h, with no AD at 18:00 h. The event lasted until 04:00, when 19 AD occurred, in its dissipation phase. The event was detected at all times by

the set of models, and it was noted that the performance of some models dropped during the event's formation and dissipation phases. On the 7th, between 16:00 and 23:00 h, another event with 962 AD occurred, which was caught by RandomForest models (3-5), which generate YES at 17:00 h when no AD occurs. Another event with 962 AD happened on the 7th, between 16:00 and 23:00 h, which was caught by RandomForest models (3-5), which generate YES at 17:00 h when no AD happens. On the 7th, between 16:00 and 23:00 h, another event with 962 AD happened, which was recognized by RandomForest models (3-5), which generate YES at 17:00 h when no AD occurs. The latter cannot be regarded as an error because atmospheric conditions remained unstable and 907 AD occurred within the next few hours.

DAYs 8 to 28 - During this time, it can be seen that, similar to the previous events, the model performances that recreate the maturation phase of convective events are nearly entirely consistent with the observations, with the eventual inaccuracies found in the event genesis and dissipation phases.

Table 7 displays the POD, FAR, and CSI statistics for each model. The models RandomForest*(5) and NaiveBayes*(6) had the best and poorest hindcast performance, with POD=0.97 and 0.88, FAR = 0.02 and 0.12, and CSI = 0.94 and 0.78, respectively.

Finally, it is worth noting that the time required to run the WRF simulations, configured as described in section 3.1, on a cluster (CPU Intel, Core (TM) i7-4770, with 8 processing cores and architecture of 64 bits) is approximately 240 hours. Whereas, the nine machine learning models were able to predict whether or not, using the input (chosen parameters) generated by the WRF simulation, a convective event would occur in roughly 0.57 seconds on an hourly basis up to 24 hours in advance.

Table 7 - The POD, FAR, and CSI statistics for hour hindcast of February of 2019 using the algorithms of defined groups G1 and G2.

Algorithm	POD	FAR	CSI
NaiveBayes* (6)	**0.88**	**0.12**	**0.78**
MultilayerPerceptron* (1)	0.89	0.11	0.80
LMT* (4)	0.90	0.07	0.84
RandomForest* (2)	0.93	0.05	0.88
RandomForest* (3)	0.94	0.04	0.90
RandomForest* (4)	0.95	0.03	0.92
RandomForest* (5)	**0.97**	**0.02**	**0.94**
RandomForest* (6)	0.95	0.09	0.86

5. CONCLUSIONS

A hybrid model is presented here that uses WRF numerical simulation and machine learning algorithms to 24-h predict convective events in the TMA-Rio. The simulated events were reconstructed using data from atmospheric discharge, precipitation, and initial and boundary conditions (GFS).According to 13-year lightning data from 2008 to 2019, February had the highest occurrence of convective events in the area under study. The following are the key findings, which are based on a simulation of February for the data period:

- The WRF data simulation's p-value hypothesis testing was able to identify (lower the dimensionality of the predictors to be used by the machine learning algorithms) a set of attributes, among millions, that are most associated with the occurrence of a convective event;
- Nine trained algorithms including boosting were selected, and these were able to accurately 24-predict the time of occurrence of convective events due to near-perfect POD, FAR, and CSI statistical values;
- The time 24-h hindcast for February 2019 by the generated set of models nearly exactly recreated the maturation phase of convective events, with any inaccuracies noted in the genesis and dissipation phases of the events studied.
- Assuming that any prediction meteorological center can generate the input required (selected attributes) by the nine machine learning-based models employed in this paper, it is reasonable to state that the set of these models can be an important tool for various sectors of society (e.g., aviation, civil defense, tourism, and so on) because convective events can be predicted within 24 hours with good performance.

In summary, the various strategies used to develop hybrid forecasting models here demonstrated to be a viable strategy for the prediction of convective occurrences.

ACKNOWLEDGMENTS

REFERENCES

Ahrens, C. D. (2009). *Meteorology today: An introduction to weather, climate, and the environment* (9th ed). Brooks/Cole, CengageLearning.

Almeida, V. A. de, França, G. B., & Campos Velho, H. F. de. (2020). Short-range forecasting system for meteorological convective events in Rio de Janeiro using remote sensing of atmospheric discharges. *International Journal of Remote Sensing*, *41*(11), 4372–4388. https://doi.org/10.1080/01431161.2020.1717669

Alpaydin, E. (2010). *Introduction to Machine Learning*. MIT Press.

Andrade, K. M., & Pinheiro, H. R. ([s.d.]). Análise sinótica e simulação numérica de um evento extremo de chuva sobre o litoral de São Paulo e do Rio de Janeiro em dezembro de 2011. *XVII Congresso Brasileiro de Meteorologia, 2012, Gramado-RS. Anais… 2012. DVD. Disponível em*.

Anochi, J. A., & Campos Velho, H. (2016). Meteorological data mining for climate precipitation prediction using neural networks. *Journal of Computational Interdisciplinary Sciences*, *6*(2). https://doi.org/10.6062/jcis.2015.06.02.0096

Anquetin, S., Yates, E., Ducrocq, V., Samouillan, S., Chancibault, K., Davolio, S., Accadia, C., Casaioli, M., Mariani, S., Ficca, G., Gozzini, B., Pasi, F., Pasqui, M., Garcia, A., Martorell, M., Romero, R., & Chessa, P. (2005). The 8 and 9 September 2002 flash flood event in France: A model intercomparison. *Natural Hazards and Earth System Sciences*, *5*(5), 741–754. https://doi.org/10.5194/nhess-5-741-2005

Breiman, L. (2001). Random Forests. *Machine Learning*, *45*(1), 5–32. https://doi.org/10.1023/A:1010933404324

Christian, H. J., Blakeslee, R. J., Boccippio, D. J., Boeck, W. L., Buechler, D. E., Driscoll, K. T., Goodman, S. J., Hall, J. M., Koshak, W. J., Mach, D. M., & Stewart, M. F. (2003). Global frequency and distribution of lightning as observed from space by the Optical Transient Detector. *Journal of Geophysical Research: Atmospheres*, *108*(D1), ACL 4-1-ACL 4-15. https://doi.org/10.1029/2002JD002347

Dereczynski, C. P., Oliveira, J. S. de, & Machado, C. O. (2009). Climatologia da precipitação no município do Rio de Janeiro. *Revista Brasileira de Meteorologia*, *24*, 24–38. https://doi.org/10.1590/S0102-77862009000100003

Dudhia, J. (1989). Numerical Study of Convection Observed during the Winter Monsoon Experiment Using a Mesoscale Two-Dimensional Model. *Journal of the Atmospheric Sciences*, *46*(20), 3077–3107. https://doi.org/10.1175/1520-0469(1989)046<3077:NSOCOD>2.0.CO;2

Dupuy, F., Mestre, O., Serrurier, M., Burdá, V. K., Zamo, M., Cabrera-Gutiérrez, N. C., Bakkay, M. C., Jouhaud, J.-C., Mader, M.-A., & Oller, G. (2021). ARPEGE Cloud Cover Forecast Postprocessing with Convolutional Neural Network. *Weather and Forecasting*, *36*(2), 567–586. https://doi.org/10.1175/WAF-D-20-0093.1

Ernst, M. D. (2004). Permutation Methods: A Basis for Exact Inference. *Statistical Science*, *19*(4). https://doi.org/10.1214/088342304000000396

Fayyad, U., Piatetsky-Shapiro, G., & Smyth, P. (1996). From Data Mining to Knowledge Discovery in Databases. *AI Magazine*, *17*(3), 37–37. https://doi.org/10.1609/aimag.v17i3.1230

França, G. B., de Almeida, M. V., Bonnet, S. M., & Albuquerque Neto, F. L. (2018). Nowcasting model of low wind profile based on neural network using SODAR data at Guarulhos Airport, Brazil. *International Journal of Remote Sensing*, *39*(8), 2506–2517. https://doi.org/10.1080/01431161.2018.1425562

França, G. B., de Almeida, M. V., & Rosette, A. C. (2016). An automated nowcasting model of significant instability events in the flight terminal area of Rio de Janeiro, Brazil. *Atmospheric Measurement Techniques,* *9*(5), 2335–2344. https://doi.org/10.5194/amt-9-2335-2016

Freitas, J. H. V. de, França, G. B., & Menezes, W. F. (2019). Previsão de Convecção Profunda Usando Árvore de Decisão na Região Metropolitana do Rio de Janeiro. *Anuário do Instituto de Geociências*, *42*(1), 127–134. https://doi.org/10.11137/2019_1_127_134

Ganguly, A. R., Kodra, E. A., Agrawal, A., Banerjee, A., Boriah, S., Chatterjee, S., Chatterjee, S., Choudhary, A., Das, D., Faghmous, J., Ganguli, P., Ghosh, S., Hayhoe, K., Hays, C., Hendrix, W., Fu, Q., Kawale, J., Kumar, D., Kumar, V., … Wuebbles, D. (2014). Toward enhanced understanding and projections of climate extremes using physics-guided data mining techniques. *Nonlinear Processes in Geophysics*, *21*(4), 777–795. https://doi.org/10.5194/npg-21-777-2014

Gavazzi, A. B. (2018). *Programa SIRIUS e o uso racional do espaço aéreo brasileiro.* Unpublished Bachelor Thesis. Universidade do Sul de Santa Catarina.

Grell, G. A., & Freitas, S. R. (2014). A scale and aerosol aware stochastic convective parameterization for weather and air quality modeling. *Atmospheric Chemistry and Physics*, *14*(10), 5233–5250. https://doi.org/10.5194/acp-14-5233-2014

Grover, A., Kapoor, A., & Horvitz, E. (2015). A Deep Hybrid Model for Weather Forecasting. *Proceedings of the 21th ACM SIGKDD International Conference on Knowledge Discovery and Data Mining*, 379–386. https://doi.org/10.1145/2783258.2783275

Guikema, S. D., Quiring, S. M., & Han, S.-R. (2010). Prestorm estimation of hurricane damage to electric power distribution systems. *Risk Analysis: An Official Publication of the Society for Risk Analysis*, *30*(12), 1744–1752. https://doi.org/10.1111/j.1539-6924.2010.01510.x

Gultepe, I., Sharman, R., Williams, P. D., Zhou, B., Ellrod, G., Minnis, P., Trier, S., Griffin, S., Yum, S. S., Gharabaghi, B., Feltz, W., Temimi, M., Pu, Z., Storer, L. N., Kneringer, P., Weston, M. J., Chuang, H. ya, Thobois, L., Dimri, A. P., … Neto, F. L. A. (2019). A Review of High Impact Weather for Aviation Meteorology. *Pure and Applied Geophysics*, *176*(5), 1869–1921. https://doi.org/10.1007/s00024-019-02168-6

Hair, J. F. (1995). *Multivariate Data Analysis with Readings*. Prentice Hall.

Hong, S. & Lim, J. (2006) The WRF Single-Moment 6-Class Microphysics Scheme (WSM6). *Journal of the Korean Meteorological Society*, 42, 129-151.

Hong, S.-Y., Noh, Y., & Dudhia, J. (2006). A New Vertical Diffusion Package with an Explicit Treatment of Entrainment Processes. *Monthly Weather Review*, *134*. https://doi.org/10.1175/MWR3199.1

John, G. H., & Langley, P. (2013). Estimating Continuous Distributions in Bayesian Classifiers. *arXiv:1302.4964 [cs, stat]*. http://arxiv.org/abs/1302.4964

Kim, J.-H., Zhang, C., Briceno, S. I., & Mavris, D. N. (2021). Supervised Machine Learning-based Wind Prediction to Enable Real-Time Flight Path Planning. *AIAA Scitech 2021 Forum*. American Institute of Aeronautics and Astronautics. https://doi.org/10.2514/6.2021-0519

Knijnenburg, T. A., Wessels, L. F. A., Reinders, M. J. T., & Shmulevich, I. (2009). Fewer permutations, more accurate P-values. *Bioinformatics*, *25*(12). https://doi.org/10.1093/bioinformatics/btp211

Landwehr, N., Hall, M., & Frank, E. (2005). Logistic Model Trees. *Machine Learning*. https://doi.org/10.1007/s10994-005-0466-3

McGovern, A., Elmore, K. L., Gagne, D. J., Haupt, S. E., Karstens, C. D., Lagerquist, R., Smith, T., & Williams, J. K. (2017). Using Artificial Intelligence to Improve Real-Time Decision-Making for High-Impact Weather. *Bulletin of the American Meteorological Society, 98*(10), 2073–2090. https://doi.org/10.1175/BAMS-D-16-0123.1

Meißner, C., Kalthoff, N., Kunz, M., & Adrian, G. (2007). Initiation of shallow convection in the Black Forest mountains. *Atmospheric Research*, *86*(1), 42–60. https://doi.org/10.1016/j.atmosres.2007.03.003

Mlawer, E. J., Taubman, S. J., Brown, P. D., Iacono, M. J., & Clough, S. A. (1997). Radiative transfer for inhomogeneous atmospheres: RRTM, a validated correlated-k model for the longwave. *Journal of Geophysical Research: Atmospheres*, *102*(D14), 16663–16682. https://doi.org/10.1029/97JD00237

Nascimento, E. (2005). Previsão de tempestades severas utilizando-se parâmetros convectivos e modelos de mesoescala: Uma estratégia operacional adotável no Brasil? *Revista Brasileira de Meteorologia*, *20*, 121–140.

Newell, O. J., Wolfson, M. M., & Ducot, E. R. (2010). NextGen Weather Processor Architecture Study. *Project Report ATC-361*, MIT Lincoln Laboratory, 67.

Paulucci, T. B., França, G. B., Libonati, R., & Ramos, A. M. (2019). Long-Term Spatial–Temporal Characterization of Cloud-to-Ground Lightning in the Metropolitan Region of Rio de Janeiro. *Pure and Applied Geophysics*, *176*(11), 5161–5175. https://doi.org/10.1007/s00024-019-02216-1

Pinheiro, H., Andrade, K., & Moura, C. (2011). A maior catástrofe climática do Brasil sob a visão operacional do CPTEC/INPE. *Anais do IV Simpósio Internacional de Climatologia*.

Pinto, O., Naccarato, K., Pinto, I., Fernandes, W. A., & Neto, O. P. (2006). *Monthly distribution of cloud-to-ground lightning flashes as observed by lightning location systems*. https://doi.org/10.1029/2006GL026081

Quinlan, J. R. (1993). Programs for Machine Learning (1° ed). Morgan Kaufmann Publishers. https://doi.org/10.1016/C2009-0-27846-9

Radar observation of the atmosphere. L. J. Battan (The University of Chicago Press) 1973. PP X, 324; 125 figures, 21 tables. £7 15. (1973). *Quarterly Journal of the Royal Meteorological Society*, *99*(422), 793–793. https://doi.org/10.1002/qj.49709942229

Ruivo, H. M. (2015). Analysis of Extreme Precipitation Events Using a Novel Data Mining Approach. *American Journal of Environmental Engineering*, 10.

Ruivo, H. M., Sampaio, G., & M. Ramos, F. (2014). Knowledge extraction from large climatological data sets using a genome-wide analysis approach: Application to the 2005 and 2010 Amazon droughts. *Climatic Change*, *124*(1), 347–361. https://doi.org/10.1007/s10584-014-1066-7

Ruivo, H. M., Velho, H. F. de C., Ramos, F. M., & Freitas, S. R. (2018). Data Mining for Flooding Episode in the States of Alagoas and Pernambuco—Brazil. *American Journal of Climate Change*, *07*(03), 420–430. https://doi.org/10.4236/ajcc.2018.73025

Sayeed, A., Choi, Y., Jung, J., Lops, Y., Eslami, E., & Salman, A. K. (2021). A Deep Convolutional Neural Network Model for Improving WRF Simulations. *IEEE Transactions on Neural Networks and Learning Systems*, 1–11. https://doi.org/10.1109/TNNLS.2021.3100902

Shirali, E., Nikbakht Shahbazi, A., Fathian, H., Zohrabi, N., & Mobarak Hassan, E. (2020). Evaluation of WRF and artificial intelligence models in short-term rainfall, temperature and flood forecast (case study). *Journal of Earth System Science*, *129*(1), 188. https://doi.org/10.1007/s12040-020-01450-9

Simon, R., Korn, E., Mcshane, L., Radmacher, M., Wright, G., & Zhao, Y. (2004). Design and analysis of DNA microarray investigations. *Springer Verlag*. https://doi.org/10.1007/b97583

Soares, C. M., França, G. B., de Almeida, M. V., & de Almeida, V. A. (2021). Study of GOES-R Thermodynamic Indices for Short-Term Forecasting of Convective Weather Events Using Machine Learning. *Pure and Applied Geophysics*, *178*(11), 4651–4663. https://doi.org/10.1007/s00024-021-02889-7

Teixeira, M. S., & Satyamurty, P. (2007). Dynamical and Synoptic Characteristics of Heavy Rainfall Episodes in Southern Brazil. *Monthly Weather Review*, *135*(2), 598–617. https://doi.org/10.1175/MWR3302.1

Teixeira, R. S., Conterato, F. S., Dias, P. M. A., Kitagawa, Y. K. L., Moreira, D. M., & Nascimento, E. G. S. (2020). Hybrid model of wind speed prediction in short time range using WRF and artificial neural networks. *Blucher Engineering Proceedings*, *7*(2), 617–625. https://doi.org/10.5151/siintec2020-HYBRIDMODEL

Veillette, M., Iskenderian, H., Wolfson, M., Mattioli, C., Hassey, E., & Lamey, P. (2016). TheOffshore Precipitation Capability. *Project Report ATC-430*, MIT Lincoln Laboratory, 39.

Wang, D., Ding, W., Yu, K., Wu, X., Chen, P., Small, D. L., & Islam, S. (2013). Towards long-lead forecasting of extreme flood events: A data mining framework for precipitation cluster precursors identification. *Proceedings of the 19th ACM SIGKDD international conference on Knowledge discovery and data mining*, 1285–1293. https://doi.org/10.1145/2487575.2488220

Wilks, D. (2005). *Statistical Methods in the Atmospheric Sciences, Volume 91, Second Edition (International Geophysics)*.

Wilson, J. W., Crook, N. A., Mueller, C. K., Sun, J., & Dixon, M. (1998). Nowcasting Thunderstorms: A Status Report. *Bulletin of the American Meteorological Society*, *79*(10), 2079–2099. https://doi.org/10.1175/1520-0477(1998)079<2079:NTASR>2.0.CO;2

Wilson, J. W., United States, Environmental Science Services Administration, Institutes for Environmental Research, & National Severe Storms Laboratory. (1966). *Movement and predictability of radar echoes*. U.S. Dept. of Commerce, Environmental Science Services Administration, Institutes for Environmental Research, National Severe Storms Laboratory.

Witten, I., Frank, E., Hall, M. A., & Pal, C. J. (2016). *Data Mining: Practical Machine Learning Tools and Techniques* (p. 621).

Zhou, K., Zheng, Y., Li, B., Dong, W., & Zhang, X. (2019). Forecasting Different Types of Convective Weather: A Deep Learning Approach. *Journal of Meteorological Research*, *33*(5), 797–809. https://doi.org/10.1007/s13351-019-8162-6

Severe Convective Weather Forecast using Machine Learning models

Jimmy Nogueira de Castro [1]

Gutemberg Borges França [2]

Vinícius Albuquerque de Almeida [2]

Manoel Valdonel de Almeida [2]

ABSTRACT

This work developed models, based on machine learning, for severe convective weather forecasts characterized by remotely sensed atmospheric discharge (AD) in the approaching landing region of airports in the vicinity of São Paulo. In the training and testing of machine learning algorithms, classical thermodynamic indices (input), derived from the atmospheric profiles of the Marte-São Paulo soundings, and ADs were used to characterize the convective severe weather (output), considering the period 2001 to 2017. The statistical distribution defined the locations, times, and severity of the convective events. The POD, 1-FAR, BIAS, kappa, and f-measure statistics were used to evaluate the 5-hour prediction of convective event detection (and in parentheses for whether it is severe when the occurrence of lightning is greater than or equal to 1,000), yielding values of 0.91 (0.85), 0.95 (0.94), 0.92 (0.89), 0.74 (0.77), and 0.88 (0,95), respectively. The results of applying the model to thirty days (hindcast), show that it is effective since it hit 96.7% of occurrence and 86.7% if they are severe. The detection errors of the model are presented and discussed.

Keywords: convective meteorological event, machine learning, thermodynamic instability indices, atmospheric discharge.

1. INTRODUCTION

A severe convective meteorological event can inflict significant damage to society (Barthlott et al., 2006), including the loss of human life in some cases. As it is often linked with severe rain (and/or hail), gusts, and ADs, this frequently forms floods, landslides on slopes, residences demolition, power outages, and other problems in metropolitan areas (Banta, 1990, Barthlott et al., 2006). Aviation, in particular, is a sector that is essentially vulnerable to convective events, as evidenced by reduced visibility due to heavy rain and the appearance of gust and wind shear during landing and takeoff, as well as large deviations that result in high fuel consumption en route, and sometimes discomfort on board due to the presence of clear air convection-induced turbulence (Gultepe et al., 2019).

Meteorological convective events are increasingly becoming the focus of research in order to improve forecasts to avoid or limit damage. The atmospheric requirements for the genesis of convective events are generally known to be wet at low levels, instability across a significant depth layer, strong vertical wind shear, and a lifting mechanism (Dowell, 1987, Houze, 1993).

Initially, the investigations about convective events, such as those by Battan (1953) and Wilson (1966), employed meteorological radar data as the major source for monitoring convective cells associated with severe storms. In the 1980s and 1990s, remotely detected lightning data and sampling atmospheric profiles obtained by soundings became more accessible and therefore began to be used in convective storm studies. For example, Weisman and Klemp (1986) used thermodynamics instability indices (TII) determined using sounding data to differentiate storm types. And Turman and Tettelbach (1980), Williams et al. (1989), and Kane (1991) used a similar system capable of monitoring lightning in real-time and therefore used this to study and monitor convective storms. Subsequently, McCann (1992) proposed a three-to-seven-hour prediction method for the occurrence of severe storms based on two neural networks from variables

[1] Integrated Center of Aeronautical Meteorology. Ponta do Galeão, s/n, Ilha do Governador, Rio de Janeiro, RJ, Brazil, CEP 21941-520.
[2] Federal University of Rio de Janeiro. Av. Brigadeiro Trompowski, s/n, Ilha do Fundão, Rio de Janeiro, RJ, Brazil, CEP 21941-890.
E-mails: jimmynogueira@gmail.com; gutemberg@lma.ufrj.br; vinicius@lma.ufrj.br

based on surface moisture convergence, which resulted in the analysis of atmospheric patterns that precede severe events, in addition, to demonstrate the potential impact of neural networks in forecasting weather events. Mueller et al. (2003) developed a 1-hour forecast system to locate areas of likely storm occurrence based on different data sources, i.e., surface weather stations, radars, satellites, and numerical modeling. More recently, Isaac et al. (2006, 2011, 2012, and 2014) presented several aviation-related studies for nowcasting of restricted weather based on data from numerical models, surface observations, radar, satellite, and a microwave radiometer for major airports in Canada.

In Brazil, Nascimento (2005) presented work on the severe weather forecast, highlighting atmospheric TII applicable to the identification of the occurrence of severe convective storm events, through the outputs of the mesoscale models. Furthermore, Nascimento (2005) demonstrated that some parameters used in the midlatitudes of the northern hemisphere for the prediction of severe weather can be applicable in the prediction of convective systems in Brazil, also allowing the use of these parameters for the development of improved indices for the South hemisphere. Nascimento (2005) stated that the use of lightning records strongly contributes to nowcasting forecasts and weather monitoring. Queiroz (2009) developed the severity index for the immediate prediction (nowcasting) of severe convective storms using weather radar data. Paulucci et al. (2019) analyzing the spatial-temporal distribution of cloud-to-ground ADs events based on data from 2001 to 2016 in the metropolitan area of Rio de Janeiro, observing polarity, peak currents, geographic distributions, diurnal and interannual and identified that the occurrences of ADs, in the studied area, are concentrated in the summer (64.3%) and spring (20.5%) periods, and in the autumn (12.9%) and winter periods (2.3%) of lower incidence, in addition to identifying the hours of 6 pm and 7 pm as the peak of occurrences and that most of the observed ADs derived from the orographic effect, which stimulates the formation of convective storms along the southern part of the slope.

Meteorological convective events are widely known to have an influence on air traffic management, and there are presently no reliable numerical models to estimate these occurrences with exact accuracy (Anquetin et al., 2005; Meißner et al., 2007) to airport regions. This forecast remains a challenge that must be overcome. Artificial intelligence-based models are increasingly being used in a wide range of fields. In particular, Guikema et al. (2010), França et al. (2016), Bhuiyan et al. (2017), Bhuiyan et al. (2019), Freitas et al. (2019), Ehsan et al. (2019), Almeida et al. (2020) and Soares et al. (2021), employ these models to conduct weather forecasting, which is the subject of this paper.

Schulz (1989), Lee and Passner (1993), Huntrieser et al. (1997); Manzato (2005), Nascimento (2005), and Kunz (2007) investigated the behavior of the TII values data for convective event prediction. Recently, Freitas et al. (2018), Almeida et al. (2020), and Soares et al. (2021) developed specifically short-term forecasting models that generate encouraging predictions of convective events using machine learning algorithms and TII values as predictors, with a specific focus on the interests of Brazilian aviation.

Using this strategy and keeping in mind that TMA-SP, the study's target region, operates about 800,000 flights per year, according to the statistical yearbook of air traffic (DECEA, 2019), and that they are heavily impacted by frequent convective occurrences, the goal of this study is to use TII values, determined from atmospheric sounding data, as predictors to test the WEKA categorical algorithms (default versions without any specific hyper optimization algorithm) to identify the thermodynamic atmospheric pattern that precedes the occurrence of convective activity in the TMA-SP.

2. STUDY AREA AND DATA

The study region is depicted in Figure 1 as a 137-kilometer-radius circle centered on Marte Airport (23° 30' 24" S, 46° 38' 02" W), whose international location aviation indicator is the SBMT (ICAO, 2021). Two data sources are used to train and test ML classification algorithms, as shown in Table 1, namely, atmospheric soundings, from which daily TIIs at 12 (UTC) are determined, and ADs, recorded by the Brazilian Lightning Location System (RINDAT), through which convective events are characterized.

Figure 1: The circle that roughly encircles TMA-SP represents the study region.
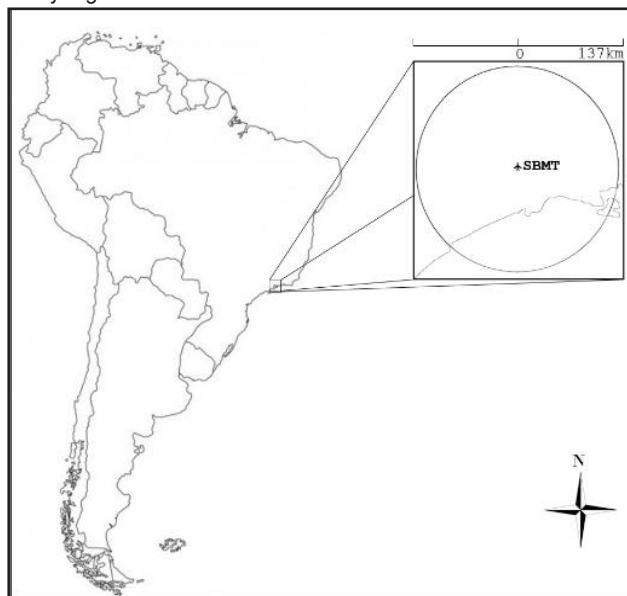
Table 1: Data characteristics.

Source	Quantity	Description	Temporal resolution	Period
Atmospheric Soundings (weather.uwyo.edu/upperair/sounding)	4,717	The value of the set of 25 instability thermodynamic indices[1]	Daily at 12 (UTC)	2001 to 2017
RINDAT (www.inpe.br/webelat/rindat/)	6,576,737	Location (latitude, longitude) and time (UTC) of atmospheric discharge	300 ns	December 2000 to June 2017

[1] Instability Thermodynamic Indices: (1) Showalter (SH), (2) Lift (LI), (3) Lift computed by using virtual temperature (LITV), (4) Sweat (SW), (5) K index (K), (6) Cross Totals (CT), (7) Vertical Totals (VT), (8) Total Totals (TT), (9) Convective Available Potential Energy (CAPE), (10) CAPE computed by using the virtual temperature (CAPV), (11) Convective Inhibition (CINS), (12) CINS computed by using virtual temperature (CINV), (13) Equilibrium level (EQLV), (14) EQLV computed by using virtual temperature (EQTV),(15) Level of Free Convection (LFCT), (16) LFCT computed by using the virtual temperature (LFCV), (17) Bulk Richardson number (BRCH), (18) BRCH computed by using the virtual temperature (BRCV), (19) Temperature (K) at the LCL (LCLT), (20) Pressure (hPa) at the LCL, (21) the lifting condensation level, from an average of the lowest 500 meters (LCLP), (22) Mean mixed layer THTA (MLTH), (23) Mean mixed layer MIXR (MLMR), (24) 1000 mb to 500 mb thickness (THTK) and (25) Precipitable water (mm) for the entire sounding (PW) (see http://weather.uwyo.edu/upperair/sounding.html).

3 METHOD

Based on WM0 (2010), the TII values represent the thermodynamic state of the atmosphere of the volume corresponding to a cylinder with a radius of about 150 km. The concept behind this research is that ML classification algorithms can be trained using the TII as input, resulting in models capable of classifying the atmospheric pattern that causes convective events to arise in TMA-SP. The following five steps were created to do this:

1. **Data processing** - based on the possible time of determination of TII values from the atmospheric profile (sounding) at 12 UTC, the hourly and monthly distribution of historical AD data is studied and, thus, the leading time for convective events prediction is defined;

2. **Input and output** - the redundant values are eliminated from the collection of 25 TIIs available (detailed in Table 1) utilizing cross-correlation analysis of TII data, and the n-input vector (or predictor variables represented by selected n-TII) of the ML algorithms to be trained is determined. The vector input then is concatenated into a binary output (or target), which is either YES or NO depending on whether or not there is AD;

3. **Training and Validation** - Cross-validation is used to train and validate the ML 25-classification algorithms available in WEKA (version 3.8.5), using the inputs and outputs defined in the previous step (which entails dividing the total data set into k mutually exclusive subsets of the same size, with one subset used for testing and the remaining k-1 used for parameter estimation and calculating the algorithm's accuracy, Holmes et al., 1994). When the values of the probability of detection (POD) and false alarm ratio (FAR) statistics, specified in Table 2, meet the conditions of POD≥ 0.80 and FAR≤ 0.15 (or 1- FAR ≥ 0.85), an algorithm is called an optimal model;

4. **Classification of convective events** - the severity index (SI), is defined as the weighted average ($SI = \frac{\sum_{i=1}^{n} P_i TII_i}{\sum P_i}$) of the selected n-TII, and their optimal weights (P_i) are determined through trial and error, varying the weight of 0.1 to k, in increment of 0.1, observing the results of the ML classification algorithms considering with the inputs, now, the values of the selected n-TII and SI, for n-AD intervals per event (for example, without AD, 1-10, 11-100, 101-500, 501-1,000, 1,001-2,000, 2,001-3,000, 3,001-4,000, 4,001-5,000, 5,001-6,000, 6,000-10,000 and >10,001);

5. **Case study** - The purpose is to use an independent sample of convective and non-convective events to do a hindcast with the best model(s).

Table 2: The statistics utilized are from the contingency table (WILKS, 2006), where a, b, c, and d stand for true-positive, false-negative, false-positive, and true-negative, respectively.

Statistic	Equation	Description
Probability of Detection (POD)	$POD = \dfrac{a}{a+c}$	Provides the correct prediction rate for the desired event.
False Alarm Ratio (FAR)	$FAR = \dfrac{b}{b+d}$	Corresponds to the ratio of the number of false alarms divided by the total of non-observed events.
F-measure	$F-measure = \dfrac{2P \cdot POD}{P+POD}$ where, $p = \dfrac{a}{a+b}$	Harmonic measure between accuracy and sensitivity.
KAPPA	$KAPPA = \dfrac{p_o - p_e}{1 - p_e}$ where $p_o = \dfrac{a+d}{a+b+c+d}$ and $p_e = \dfrac{[(a+b)(a+c)] + [(c+d)(b+d)]}{(a+b+c+d)^2}$	The measure of agreement between predicted and observed.
BIAS	$BIAS = \dfrac{a+b}{a+c}$	Measures the proportion of the frequency of predictive events by the frequency of observed events, used to indicate whether the prognosis is overestimated or underestimated.

4 RESULTS

4.1 AD distribution

For the data period investigated 2001-2017, Table 1 demonstrates that only 76% (4,717) of the projected soundings were conducted in the SBMT at 12 (UTC). It reveals that the average, minimum and maximum percentages of days without observed data (or soundings) are expressive equal to 24.1%, 19.2%, and 31.5%, respectively.

Figure 2 shows the spatial distribution of AD occurrences for the period from December 1st, 2000 to June 30th, 2017, and it can be seen that the highest concentrations of AD are strongly associated with the presence of heat islands corresponding to the urban regions where the main airports of TMA-SP, i.e., Guarulhos (SBGR), Congonhas (SBSP), Marte (SBMT), Campinas (SBKP) and São José dos Campos (SBSJ), are located.

The AD monthly and hourly distributions are shown in Figure 3 (a) and (b). Figures 3 (a) show that more than 81% of AD occurrences are concentrated between December and March and Figure 3 (b) has shown that period between 3 and 11:59 pm (local time) is the one with the highest AD occurrences (more than 84%). Then, it can perhaps be stated that the genesis of convective events that generate AD are chiefly due to local convection, rather than frontal systems. Finally, based on previous analysis of Figure 3 (b), the forecast period (or leading time), as required in step 1 of the method, will be approximately 5 hours, representing the time interval between 10 am (when the TII will be determined) and 3 pm (local time), when the period of the greatest AD occurrence begins.

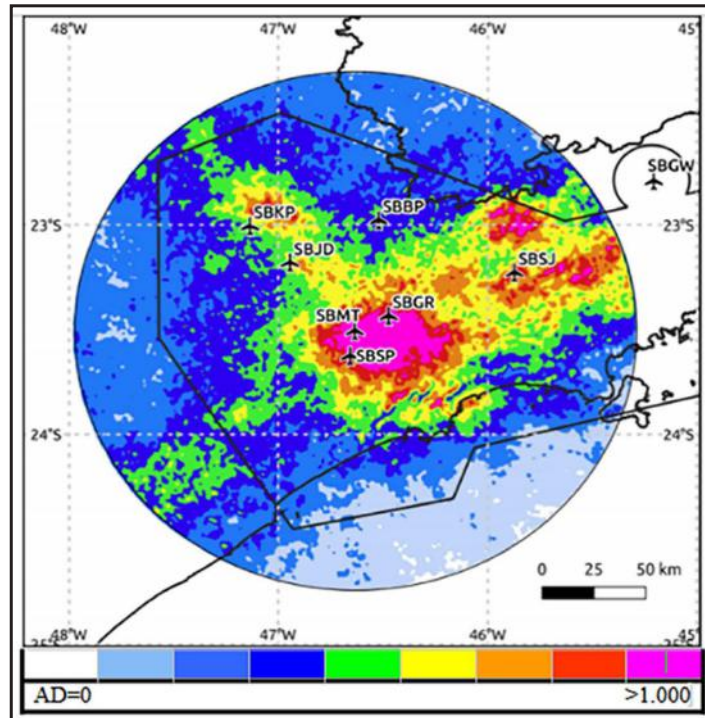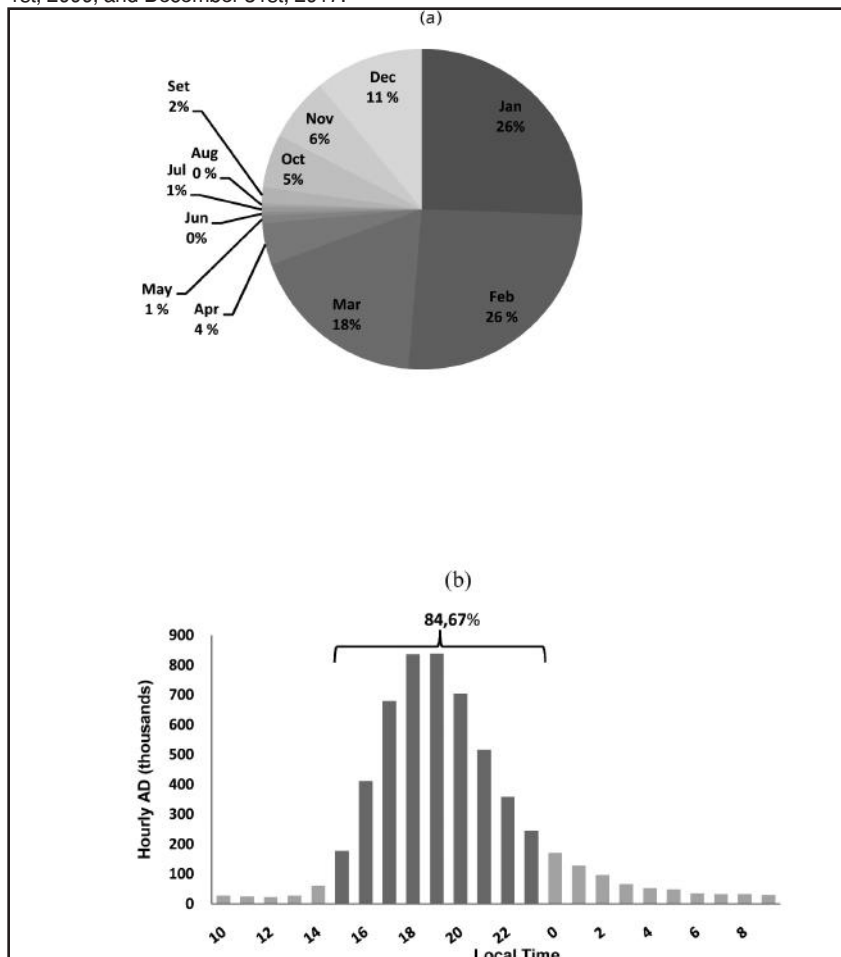**Figure 2:** The density of AD between December 1st, 2000, to June 30th, 2017.

Figure 3: Monthly (a) and hourly (b) distribution of AD occurrences in the period from December 1st, 2000, and December 31st, 2017.

4.2 Forecast model

The process of training and testing ML algorithms is well acknowledged to be difficult and time-consuming. The success of this procedure is mainly associated with the choice of variables (input), which here characterize the local thermodynamic state of the atmosphere that precedes the occurrence of convective events in the study area. Similar to the studies developed by Freitas et al. (2019) and Almeida et al. (2020), according to step 2 of the method, the cross-correlation of the twenty-five TII available (numbered in section 2, Table 1) was performed, resulting in six TIIs, namely, SH, LI, SW, K, TT, and PW, which will be used with predictor variables (input) of the ML classification algorithms in the training and testing process until reaching the optimal model.

Following step 3 of the method, 1,025 experiments were developed using twenty-five classificatory algorithms available in WEKA that were trained and tested by 10-fold cross-validation for each sixteen AD intervals as in column 2 of Table 3. Table 3 shows the statistics (POD, 1-FAR, BIAS, Kappa, and F-measure) from 10-fold cross-

validation for 5-hour detection forecasting of the highest performing method (column 3). In other words, the results provide a 5-hour prediction (YES OR NO) of whether a convective event will occur, and if YES, if AD will exceed the interval's limit. When employing the optimal model criterion established in step 3 (that is, when its findings yield POD $\geq$ 0.8 and 1-FAR $\geq$ 0.85), only the optimal models are limited to completing the 5-hour forecast of convective events up to the limit of AD = 100).

Thus, the $SI = \frac{\sum_{i=1}^{n} P_i TII_i}{\sum_{i=1}^{n} P_i}$ was designed to

improve the 5-hour forecast of the most impactful convective events (those more severe with the highest number of AD), according to step 4 of the method, which is defined as the weighted average of the 6-TIIs selected (i.e., SH, LI, SW, K, TT and PW). Twelve AD intervals (i.e., 0, 1-10, 11-100, 101-500, 501-1,000, 1,001-2,000, 2,001-3,000, 3,001-4,000, 4,001-5,000, 5,001-6,000, 6,001-10,000, and > 10,001) have been established to determine the weight (P_i) of each TII_i, and the plot of each of the six ITTs

Table 3: The best-performing models (column 3) for 5-hour forecasting using the selected 6-TII as input for each the AD interval.

Result	AD interval per event	Model	POD	1-FAR	BIAS	Kappa	F-measure
1	0	RandomForest	0.91	0.95	0.92	0.74	0.88
2	>10	RandomForest	0.94	0.88	0.91	0.83	0.84
3	>100	RandomForest	0.83	0.85	0.97	0.74	0.84
4	>200	BayesNet	0.74	0.91	0.82	0.71	0.82
5	>300	BayesNet	0.76	0.80	0.96	0.68	0.78
6	>400	BayesNet	0.68	0.92	0.74	0.67	0.78
7	>500	RandomForest	0.75	0.67	1.12	0.62	0.71
8	>600	BayesNet	0.67	0.77	0.88	0.61	0.72
9	>700	LMT	0.60	0.91	0.66	0.62	0.73
10	>800	AdaBoostM1	0.63	0.77	0.82	0.60	0.69
11	>900	AdaBoostM1	0.58	0.83	0.70	0.58	0.69
12	>1,000	Multilayer Perceptron	0.70	0.56	1.25	0.55	0.63
13	>2,000	Multilayer Perceptron	0.66	0.71	0.94	0.60	0.68
14	>3,000	JRip	0.56	0.49	1.15	0.45	0.52
15	>4,000	BayesNet	0.26	0.84	0.31	0.31	0.40
16	>5,000	BayesNet	0.21	0.83	0.26	0.27	0.34

versus AD intervals was analyzed, as shown in Figure 4. It shows that the behavior of all TII values is highly correlated to AD values, with absolute correlation values ranging between 0.96 and 0.99. The convective event is then classified as severe with AD ≥ 1,000 based on behavior all TIIs seem to be similar.

The ideal weights (P_i) for each TII are determined by trial and error, varying o P_i from 0.1 to k=3, in increment of 0.1, and observing the results of the algorithms regarding defined optimal POD and FAR values, as described in step V of the method. The SH, LI, PW and SW, K, TT received weights of 2 and 1, respectively, as a result of this approach. As a result, the SI is used as a predictive variable in the training and testing of the twenty-four algorithms, together with the chosen TII.

Figure 4: SH (a), LI (b), SW (c), K (d), TT (e), and PW (f) atmospheric indices versus the twelve AD intervals.
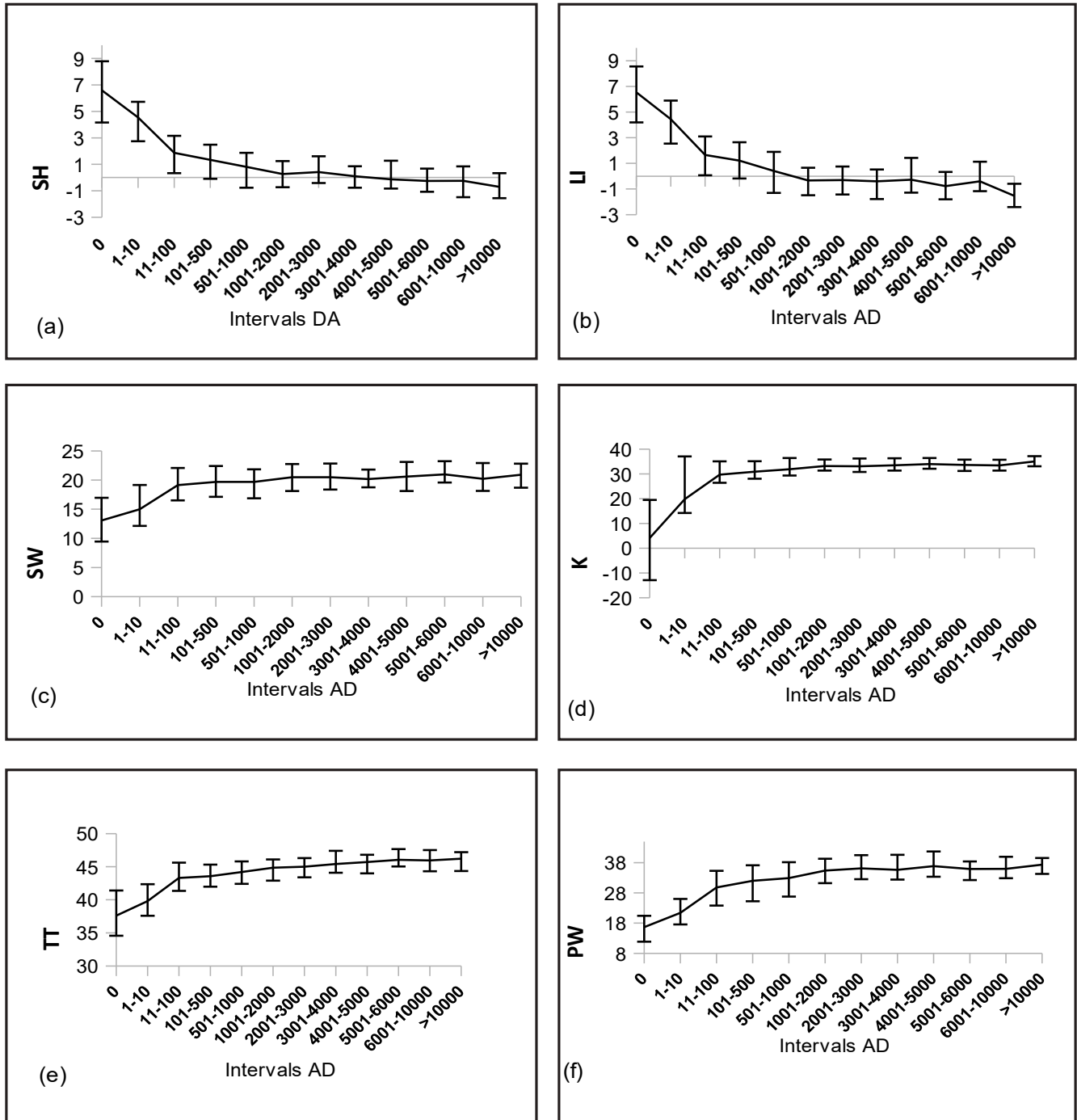
Table 4 shows the statistics of the best results of 10-fold cross-validation for 5-hour prediction models of convective events for TMASP based on the results of 38,401 tests with AD intervals, similar to the results in Table 3. The 5-hour best-models of convective occurrences up to the limit of DA≥1,000 are reliable because the values of POD, 1-FAR, BIAS, KAPPA, and F-measure are expressive and equal to 0.85, 0.94, 0.89, 0.77, and 0.95. This implies that integrating SI as a predictive characteristic considerably improved the 5-hour prediction models of convective event severity, as they can accurately discriminate the severity of convective events up to 1000 AD occurrences. According to Landis (1977), Kappa values of more than 0.6 indicate high agreement between forecasts and observations, hence the 5-hour prediction models may be considered credible up to AD=3,000.

Finally, Table 5 illustrates the best model with 5-hour hindcast for event detection (HIT: H − ERROR: E, column 4) and severity (column 5 for thirty convective and non-convective events where the predictor variables are the TII and SI

values. The results reveal that the best model was capable of nowcasting 96.66% of the events will be convective or not (column 3) and if 86.66% of those will be severe ones. As previously stated, most of the convective events that occur in the study area are caused by local convection, with the exception of events 2, 6, 23, and 27, which all had their origins owing to a frontal system through the region, as shown, for example, in Figure 6, which shows images from the GOES-13 satellite (infrared channel) at two moments during the passage of a cold front through studied region (red circle) for the events 6 and 27 that occurred on February 22nd, 2013, and March 13th, 2013, respectively. To attempt to explain, it is important to note that the learning process of ML algorithms is dependent on the data sample representation of the studied phenomenon, and since the proportion of frontal origin convective events is smaller when compared to local convection ones, it is possible that therefore the ML learning algorithms, using as input TIIs were unable to capture the advection atmospheric pattern generated by a frontal system.

Table 4: The best-performing models (column 3) for a 5-hour forecast using the selected 6-TII and SI as input for each the AD interval.

Result	AD interval per event	Model	POD	1-FAR	BIAS	Kappa	F-measure
1	0	DecisionTable	0.92	0.91	1.00	0.83	0.90
2	>10	RandomForest	0.93	0.97	0.96	0.89	0.95
3	>100	RandomForest	0.91	0.93	0.98	0.84	0.94
4	>200	RandomForest	0.90	0.93	0.97	0.82	0.94
5	>300	LMT	0.92	0.93	0.99	0.83	0.95
6	>400	LWL	0.96	0.90	1.07	0.80	0.94
7	>500	LogitBoost	0.88	0.92	0.95	0.79	0.94
8	>600	DecisionTable	0.84	0.93	0.90	0.76	0.94
9	>700	RandomForest	0.85	0.92	0.91	0.75	0.94
10	>800	J48	0.84	0.92	0.91	0.73	0.94
11	>900	LMT	0.82	0.94	0.86	0.74	0.95
12	>1,000	REPTree	0.85	0.94	0.89	0.77	0.95
13	>2,000	JRip	0.73	0.92	0.77	0.59	0.94
14	>3,000	JRip	0.68	0.97	0.69	0.60	0.97
15	>4,000	MultilayerPerceptron	0.66	0.95	0.68	0.52	0.97
16	>5,000	KStar	0.63	0.94	0.65	0.43	0.97

Table 5: Results of optimum model hindcast-5h for thirty events randomly selected in the dataset.

Event	DAY	AD number per event	RESULT OF PREDICTIVE MODELS (HIT: H – ERROR: E)	
			EVENT DETECTION	SEVERITY
1	10/Aug/2004	0	H	H
2	17/Jan/2006	208	E	H
3	09/Jul/2007	0	H	H
4	12/Sep/2007	0	H	H
5	14/Aug/2013	0	H	H
6	22/Feb/2013	12950	H	E
7	05/Mar/2013	22796	H	H
8	17/Apr/2005	199	H	H
9	15/Apr/2002	106	H	H
10	28/Dec/2003	609	H	H
11	26/Jan/2003	473	H	H
12	23/Feb/2005	620	H	H
13	24/Dec/2002	2865	H	H
14	29/Nov/2013	1640	H	H
15	16/Jan/2005	3361	H	H
16	07/Feb/2006	7103	H	H
17	17/Feb/2011	3619	H	H
18	21/Apr/2004	2190	H	H
19	03/Mar/2006	4844	H	H
20	23/Mar/2006	1843	H	H
21	28/Nov/2001	8095	H	H
22	22/Feb/2017	1370	H	H
23	11/Jan/2012	18	H	E
24	19/Feb/2013	14715	H	H
25	17/Jan/2010	2763	H	H
26	16/Jan/2014	17556	H	H
27	13/Mar/2013	77	H	E
28	14/Feb/2008	13497	H	H
29	09/Jan/2016	6933	H	H
30	15/Feb/2016	16398	H	H

Figure 6: Infrared images from the GOES-13 satellite, channel 4, taken at (a) 12:30 and (b) 20:00 on February 22nd , 2013, and (c) 12:30 and (d) 20:30 (UTC) on March 13th, 2013.

(a)   (b)

(c)   (d)
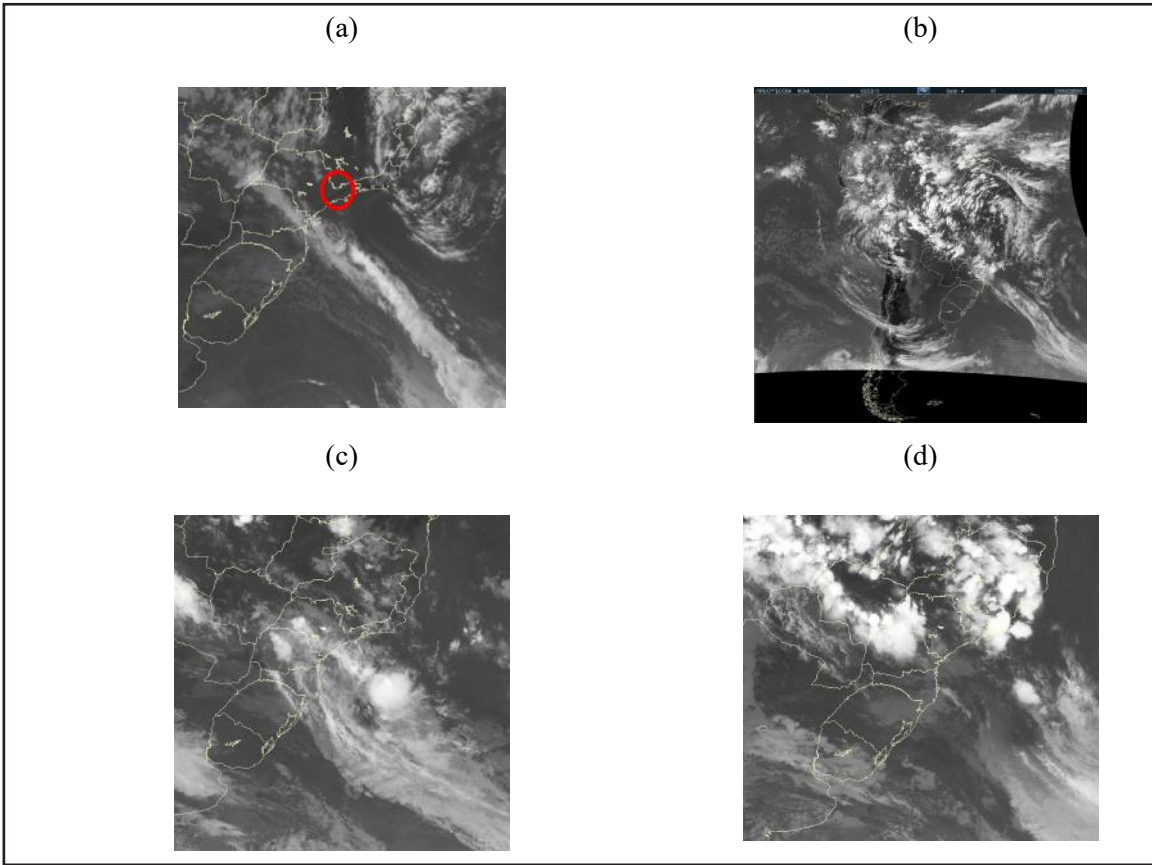
5. CONCLUSION

In this study, prediction models based on machine learning were created with the goal of detecting severe convective events in the TMA-SP. The main findings are summarized below:

- Atmospheric discharges occur more frequently in the summer and are primarily associated with heat islands located in the cities of São Paulo (represented by the aerodromes identified by: SBGR, SBSP and SBMT), Campinas (SBKP), São José dos Campos (SBSJ), in Serra da Mantiqueira and along the Dutra Highway, located, respectively, to the north and east of São José dos Campos (SBSJ);

- The time period from 3 pm to 11:59 pm (local) was identified as having the highest occurrence of convective activity. The developed models were able to predict and classify the severity (up to 5 hours in advance), with high probability of detection, low rate of false alarm and little bias;

- The hindcast results of the analyses show that the models do not currently have a satisfactory performance in predicting convective events with frontal origin.

Adjusting models to predict frontal genesis convective events, testing them outside of the TMA-SP, and training ML algorithms to develop a hybrid model using the result of the reconstruction of atmospheric conditions of convective events via a numerical model are all topics that will be investigated in the future.Future studies intend to improve the performance of current machine learning models using different regularization techniques, including ensemble methods (e.g. bagging, boosting), dropout, among others (Goodfellow et al., 2016).

ACKNOWLEDGEMENT

REFERENCES

Almeida, V. A., França, G. B., and Velho, H. F. C. (2020). Short-range forecasting system for meteorological convective events in Rio de Janeiro using remote sensing of atmospheric discharges, International Journal of Remote Sensing, 42 (0), 4372-4388, DOI: 10.1080/01431161.2020.1717669.

Anquetin, S., Yates, E., Ducrocq, V., Samouillan, S., Chancibault, K., Davolio, S., Accadia, C., Casaioli, M., Mariani, S., Ficca, G., Gozzini, B., Pasi, F., Pasqui, M., Garcia, A., Martorell, M., Romero, R., and Chessa, P. (2005). The 8 and 9 September 2002 flash flood event in France: a model intercomparison, Nat. Hazards Earth Syst. Sci., 5, 741–754, 2005, http://www.nat-hazards-earth-syst-sci.net/5/741/2005/.

Banta, R. (1990). The role of mountain flows in making clouds, Meteorol. Monographs., Amer. Meteorol. Soc.

Battan, L. J. (1953). Duration of convective radar cloud units. Bull. Amer. Meteor. Soc., 34, 227-228.

Barthlott, C., Corsmeier, U., Meißner, C., Braun, F., and Kottmeier, C. (2006). The influence of mesoscale circulation systems on triggering convective cells over complex terrain, Atmos. Res., 81, 150–175.

Bhuiyan, M.A.E., Anagnostou, E.N., Kirstetter, P.E. (2017). A nonparametric statistical technique for modeling overland TMI (2A12) rainfall retrieval error. IEEE Geosci. Remote S 14, 1898–1902.

Bhuiyan, M.A., Nikolopoulos, E.I., Anagnostou, E.N. (2019). Machine learning-based blending of satellite and reanalysis precipitation datasets: a multi-regional tropical complex terrain evaluation. J. Hydrometeorol. https://doi.org/10.1175/JHM-D-19-0073.1.

DECEA (2019). Anuário estatístico de tráfego aéreo, p. 222. [Available from http://portal.cgna.decea.mil.br]

Doswell, C. I.: The distinction between large-scale and mesoscale contributions to severe convection: A case study example, Wea. Forecasting, 2, 3–16, 1987.

Ehsan, B. M. A., Begun, F., Ilham, S. J., Khan, R. S. (2019). Advanced wind speed prediction using convective weather variables through machine learning application, Apllied Computing and Geoscineces, 1, https://doi.org/10.1016/j.acags.2019.100002.

França, G. B., de Almeida, M. V., and Rosette, A. C. (2016). An automated nowcasting model of significant instability events in the flight terminal area of Rio de Janeiro, Brazil, Atmos. Meas. Tech., 9, 2335–2344, https://doi.org/10.5194/amt-9-2335-2016.

Freitas, J. H; França, G. B. Menezes, W. F. (2019). Deep Convection Forecasting Using Decision Tree in Rio de Janeiro Metropolitan Area, Anuário de Igeo, 42, DOI: http://dx.doi.org/10.11137/2019_1_127_134.

Goodfellow, I.; Bengio, Y; Courville, A. (2016). Deep Learning. MIT Press. 785 pp. DOI: http://www.deeplearningbook.org.

Gultepe, I., Sharman, R, D.williams, P.; Zhou, B., Ellrod, G., Minnis, P.; Trier, S., Griffin, S.; Yum, S. S., Gharabaghi, B., Feltz, W. Temimi, M., Pu, Z., Storer, L. N., Kneringer, P., Weston, M. J., Chuang, H., Thobois, L., Dimri, A., Dietz, S.,França, G. B., Almeida, M. V. ; F. L. Albuquerque Neto (2019). A review of high impact weather for aviation meteorology. Pure and Applied Geophysics. https://doi.org/10.1007/s00024-019-02168-6.

Guikema, S.D., Quiring, S.M., Han, S., 2010. Prestorm estimation of hurricane damage to electric power distribution systems. Risk Anal. ttps://doi.org/10.1111/j.1539-6924.2010.01510.

Holmes, G., Donkin, A. and Witten, I. H. (1994). "WEKA: a machine learning workbench, Proceedings of ANZIIS '94 - Australian New Zealnd Intelligent Information Systems Conference, pp. 357-361, doi: 10.1109/ANZIIS.1994.396988.

Houze, R. A.: Cloud Dynamics, no. 53 in International Geophysics Series, Academic Press, San Diego, 1993.

Huntrieser, H., Schiesser, H., Schmid, W., Waldvogl, A. (1997). Comparison of traditional and newly developed thunderstorm indices for Switzerland. Weather Forecast. 12, 108–125.

ICAO. Global Air Navigation Plan. 6ª ed. (2016). 142 f., International Civil Aviation Organization, Montreal, Canada.

Isaac, G. A., Bailey, M., Cober, S. G., Donaldson, N., Driedger, N., Glazer, et al. (2006) Airport Vicinity Icing and Snow Advisor (AVISA). 44th AIAA Aerospace Sciences Meeting and Exhibit, https://doi.org/10.2514/6.2006-1219.

Isaac, G. A., Bailey, M., Boudala, F., Cober, S. G, Crawford, R., Donaldson, N., et al. (2011) Decision making regarding aircraft de-icing and in-flight icing using the Canadian airport nowcasting system (CAN-Now). SAE International, https://doi:10.4271/2011-38-0029.

Isaac, G. A., Bailey, M., Boudala, F., Burrows, W. R., Cober, S. G., Crawford, R. W., el al. (2012) The Canadian airport nowcasting system (CAN-Now). Meteorological Applications, https://doi.org/10.1002/met.1342.

Isaac, G. A., Burrows, W. R., Cober, S. G., Crawford, R. W., Donaldson, N., Gultepe, I., Hansen, B., Heckman, I., Huang, L. X., Ling, A., Mailhot, J., Milbrandt, J. A., Reid, J., and Fournier, M. (2014). The Canadian airport nowcasting system (CANNow), Meteorol. Appl., 21, p. 30–49.

Kane, R. J., (1991). Correlating lightning to severe local storms in the northeastern United States. Wea. Forecasting, 6, p. 3-12.

Kunz, M. (2007). The skill of convective parameters and indices to predict isolated and severe thunderstorms. Nat. Hazards Earth Syst. (NHESS) 7, 327–342.

Landis, J.R., Koch, G.G. (1977). The measurement of observer agreement for categorical data. Biometrics. Vol. 33, p. 159–174.

Lee, R.R., Passner, J.E. (1993). The development and verification of TIPS: an expert system to forecast thunderstorm occurrence. Weather Forecast. 8, 271–280.

Manzato, A. (2005). The use of sounding-derived indices for a neural network short-term thunderstorm forecast. Weather Forecast. 20, 896–917.

McCann, D. (1992). A neural network short-term forecast of significant thunderstorms. Wea.Forecasting, 7, 525–534, https://doi.org/10.1175/1520-0434.

Meißner, C., Kalthoff, N., Michael, Adrian, G. (2007). Initiation of shallow convection in the Black Forest Mountains, Atmos. Res., in press, doi:10.1016/j.atmosres.2007.03.003.

Mueller, C., Saxen, T., Roberts, R., Wilson, J., Betancourt, T., Dettling, S., Oien, N., Yee, J. (2003). NCAR auto-nowcast system, Weather Forecast, 18, p. 545–561.

Nascimento, E.D.L. (2005). Forecasting severe storms using convective parameters and mesoscale models: an adoptable operational strategy in Brazil. Brazilian Journal of Meteorology, 20(1), p.121-140.

Paulucci, T. B., Gutemberg, B. F., Libonati, R., Ramos, A. M. (2019). Long-Term Spatial– Temporal Characterization of Cloud-to-Ground Lightning in the Metropolitan Region of Rio de Janeiro. Pure and Applied Geophysics, 176, 5161-5175. Doi:10.1007/s00024-019- 02216-1.

Queiroz, A. P. (2009). Monitoring and Immediate Prediction of Severe Storms Using Radar Data. Master's Dissertation of the Postgraduate Course in Meteorology. INPE.

Soares, C. M., França, G. B., Almeida, M. V., Almeida, V. A. (2021). Study of GOES-R Thermodynamic Indices for Short-Term Forecasting of Convective Weather Events Using Machine Learning, Pure and Applied Geophysics, 178, 4651-4664. Doi: 10.1007/s00024-021-02889-7.

Schulz, P. (1989). Relationships of several stability indices to convective weather events in northeast Colorado. Weather Forecast. 4, 73–80.

Turman, B.N., Tettelbach, R. J. (1980). Synoptic scale satellite lightning observations in conjunction with tornadoes. Mon. Wea. Rev., 108, p. 1878-1882.

Weisman, M. L., and J. B. Klemp (1986). Characteristics of isolated convective storms. Mesoscale Meteorology and Forecasting, P. S. Ray, Ed., Amer. Meteor. Soc., p. 331-358. Wilks, S. D. (2006). Statistical Methods in the Atmospheric Sciences. 2ª ed., New York, USA, Academic Press.

Williams, E.R., M.E. Weber, and R.E. Orville (1989). The relationship between lightning type and convective state of thunderclouds. J. Geophys. Res., 94, p. 13213-13220.

Wilson, J. W. (1966). Movement and predictability of radar echoes. Tech. Memo ERTM-NSSL-28, National Severe Storms Laboratory, 30 pp. [Available from National Information Service, Operations Division, Springfield, VA 22161.].

Study of the Goes-R Thermodynamic Indices for Short-Term Forecasting of Convective Weather Events using Machine Learning

Caroline Menegussi Soares

Gutemberg Borges França

Manoel Valdonel de Almeida

Vinícius Albuquerque de Almeida

ABSTRACT

Forecast models(6 – 8 h) are proposed forpredicting meteorological convective events(MCEs) based on machine learning algorithms for two pre-established areas I and II that correspond to the flight routesfrom Rio de Janeiro to São Paulo, Brazil. As input data, the models havefive atmospheric instability indices, extracted from remotely sensed data retrieved from the GOES-R satellite, for January to March of 2018 and 2019. Temporal characterisation for the events was carried out using lightning (i.e.,atmospheric discharge) data from 2001 to 2019, and the hourly distribution defined the forecast period of the study. Five machine learning algorithms were selected and trained using 400 experiments aimed at forecasting MCEs and their severity. Statistics indicated that the multilayer perceptron and simple logistic algorithms had the best forecast performance,with the probability of detection being 0.86 and 0.94, false alarm rate being 0.14 and 0.08, bias being 1.00 and 1.01, F-measure being 0.86 and 0.94, and Kappa values being 0.72 and 0.85 in areas I and II, respectively. The hindcast results for April 2020 reveal that the models were able to capture physical characteristicsrelated to the convective event patterns and correctly forecast 96% of the days, and are toolsthat can be used to improve operational forecasts for aviation purposes in the region and elsewhere.

Keywords: flight routes, atmospheric discharges, convective events, machine learning.

1. INTRODUCTION

Severe meteorological convective events (MCEs) have a serious impact on aviation and are often responsible for accidents and incidents worldwide (CENIPA, 2018; Gultepe et al., 2019). MCEs can impact a flight in its different phases; that is, during landing and take-off with the presence of hail and/or heavy rain, gusts, and wind shear, and en route, by the formation of ice and/or clear air convection-induced turbulence (Gultepe et al., 2019).

Aviation meteorology aims to contribute to ensuring the safety standards, economy, and efficiency of flights. Therefore, it is necessary to determine whether these weather conditions will cause significant variations, such as ice formation, turbulence, thunderstorms (cumulonimbus clouds), low ceilings, low visibility, and wind gusts (or the appearance of wind shears), which may result in deviations in the route and, consequently, higher fuel consumption. As a result, traffic control requires assertive predictions regarding the estimated time for the beginning of these variations and the expected period of their duration.

With the aim of improving short-term predictions, several early studies regarding weather forecasting, such as the ones by Wilson (1966) and Wilk and Gray (1970), suggested forecasting approaches based on extrapolations of radar data limited to subjective interpretation to predict storms.

For applications in aviation, Isaac et al. (2006), Isaac et al. (2011), and Isaac et al. (2012) presented a sequence of analyses that resulted in a refined forecasting system for aviation using data from numerical models, surface observations, radar, satellite, and a microwave radiometer to generate projections of up to approximately 6 h for major airports in Canada.

Nascimento (2004) used profiles of numerical models and radiosonde data to verify atmospheric conditions for the prediction of severe storms and concluded that the convective parameters and indices used in mid-latitudes can be used to elaborate or adjust indices that are more appropriate to the tropical region. Nascimento (2005) presented a comprehensive discussion on the issue of severe weather forecasting in Brazil, a description of atmospheric parameters useful to help identify atmospheric conditions conducive to the occurrence of severe convective storms and stated that atmospheric discharge (AD) is essential for weather forecasting and climate monitoring. Pinto et al. (2006) presented a description of the spatial-temporal distribution of AD considering data recorded from 1999 to 2004 in the southeast region of Brazil, where the Rio de Janeiro to São Paulo air route studied here is located. They concluded that high frequency occurrence of AD is associated with the effects of urban heat islands and orography, which enhance the convection mechanism.

Recently, Bender (2018) studied the atmospheric conditions that generate strong storms in the metropolitan region of São Paulo and analysed the potential for increased convective activity with urban expansion until 2030, and concluded that vertical and horizontal urbanisation will generate increased precipitation and displacement of severe storms for the region of São Paulo city considering the current projections. Conversely, Paulucci et al. (2019) studied the spatial and temporal variability of cloud-to-ground rays in the metropolitan region of Rio de Janeiro using data from to 2001-2016 and observed that, of 258,794 ADs, 64.3% occurred in summer, 20.5% in spring, 12.9% in autumn, and 2.3% in winter.

The area between Rio de Janeiro and São Paulo, located in south-eastern Brazil, is highly impacted by MCE, characterised by AD records, primarily during the hottest months of the year between November and April (Pinto et al., 2006).

Presently in Brazil, the nowcast for MCEs is done by meteorologists, who uses their experience to integrate different *in situ* meteorological observations and/or atmospheric model outputs using conceptual models of how the atmosphere works. It is known that this nowcasting procedure results in a high degree of subjectivity and uncertainty. Therefore, the objective of this work is to study the occurrence of MCEs in the Rio de Janeiro – São Paulo air route and evaluate the use of machine learning (ML) algorithms as a tool for short-term forecasting of these events and their severity, based on remotely sensed atmospheric thermodynamic indices from satellites.

This article is part of a sequence of related studies successfully delivered by the Laboratory of Applied Meteorology of the Federal University of Rio de Janeiro (Almeida et al., 2009; Silva et al., 2016; França et al., 2016; França et al., 2018; Hermsdorff, 2018; Almeida et al., 2020a; and Almeida et al., 2020b) that have utilized machine learning techniques for forecasting convective events.

2. DATA AND METHOD

2.1 Study Region

The study region was a rectangular area of 160.908 km², corresponding to the Rio de Janeiro – São Paulo route, which is approximately represented by the geographical position of the two airports, Antonio Carlos Jobim (Rio de Janeiro) and Guarulhos (São Paulo). Considering the representativeness of the atmospheric profile in a 150 km radius circle, according to the World Meteorological Organization, the area was divided using the computational package, free software, QGIS (version 3.14.0, available at https://qgis.org/en/site/), for study purposes, into two areas, I and II, as shown in Fig. 1.

Figure 1: Representation of areas I and II.
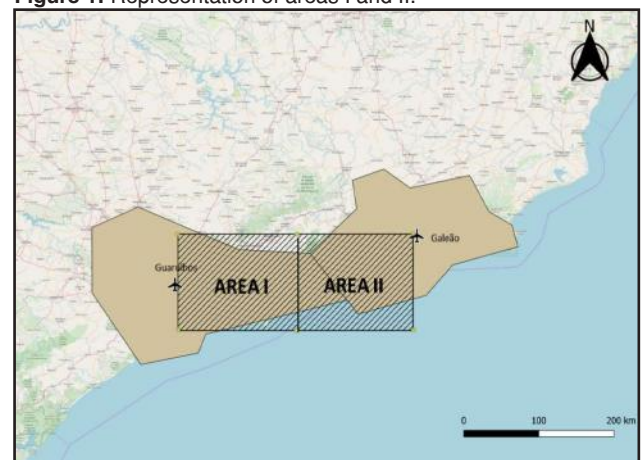
2.2 Data

The data used are from two sources, as described in Table 1.

1) The Geostationary Operational Environmental Satellite (GOES) series formally began on 16 October 1975 with the GOES-A or GOES I launch. This series is a joint effort between the National Aeronautics and Space Administration (NASA) and the National Oceanic and Atmospheric Administration (NOAA) for the development of idealised geostationary meteorological satellites, of which 19 have been produced (GOES A–U). GOES-Q was not built and GOES-T and U are planned to be launched in 2021 and 2024, respectively. All previous satellites were successfully launched (https://www.nasa.gov/content/goes-overview/index.html). The GOES-R Algorithm Working Group (www.star.nesdis.noaa.gov/goesr/documentation_ATBDs.php) provides information that can be used to calculate derived stability indices from the retrieved atmospheric profiles, such as the lifted index (LI), convective available potential energy (CAPE), total totals index (TT), Showalter index (SI), and K index values (K). In order to determine the favourable sites for the formation of intense storms that give rise to heavy rains, the following indices and thresholds were considered for this study: K index values (George, 1960) above 30 °C have a high potential for the occurrence of storms; LI negative values (Galway, 1956) are related to unstable conditions; low or negative values of SI (Showalter, 1953) indicate more atmospheric instability; TT values above 40 °C (Miller, 1972) imply storm formation potential; and values greater than 1,000 J/kg of CAPE (Houze, 1993) are related to instability. The indices are determined using only non-cloud profiles, represent a 10 km × 10 km pixel, and have been available for download since December 2017. In this study, the listed indices were used as predictor variables of the atmospheric conditions that characterise the potential occurrence of MCE in the regions of interest, areas I and II of Figure 1.

2) The National Network of Atmospheric Discharge Detection (RINDAT) has been continuously recorded since December 2000, according to the information available at http://simepar.br/rindat/internas/institucional.shtml. The AD data are used here for the MCE characterisation.

2.3 Method

Considering the potential of GOES-R indices as MCE predictors, two important aspects were addressed: 1) Local thermodynamic indices are not, by themselves, unique predictors to identify the atmospheric pattern of severe MCEs, which have complex thermodynamic formation mechanisms, since some other aspects such as advection, shear, and others could contribute to the mechanisms. Thus, the idea is that the model based on ML can be identified in the set of values of the indices related to MCE atmospheric patterns. 2) If a given MCE appeared at the edge of the area of interest and could impact the area, it is assumed here that the averages of each index used by area, representing the volume of the atmosphere as approximately recommended by the World Meteorological Organization (2013), are a potential predictor of severe MCEs for areas I and II.

Table 1: *Data used in the study.*

Source	Description	Temporal resolution	Time (UTC)	Qty	Period
Atmospheric profiles from GOES-R (https://www.ncdc.noaa.gov/airs-web/search).	The values of the set of indices K, Showalter, Lifted Index, Total Totals and CAPE represent a 10 km x 10 km pixel in areas I and II.	15 min	hourly from 12 to 16	96,400*	Jan – Mar, 2018 and 2019
Atmospheric discharge from RINDAT (http://www.rindat.com.br)	Time and location (lat., long.) of atmospheric discharges in areas I and II.	300 ns	----	9,945,882 (AD)	2001 – 2019

*The number 96,400 means the number of thermodynamic index values extracted in the period established for the study. On the other hand, 9,945,882 are the numbers of AD that occurred in the period and in the study area.

Therefore, the challenge in this work was to identify the atmospheric conditions that precede the onset of an MCE for a given period of the day, which in other words represents a classification of YES or NO for the MCE occurrence. The WEKA software package (version 3.7.12) developed by the University of Waikato in New Zealand (Witten et al., 2016) was chosen because it has several classification algorithms based on ML. These algorithms can be trained and tested to identify the atmospheric thermodynamic patterns associated with MCE onset in target areas I and II. The steps of the applied method are as follows:

1. The nowcasting period was analysed and defined based on the distribution of daily AD occurrence using the data set in Table 1.
2. The spatial average of the GOES-R instability indices at 12, 13, 14, 15, and 16 UTC were calculated for areas I and II (Table 1).
3. The dataset of average thermodynamic indices (input of the algorithms to be trained) were concatenated hourly, for 12, 13, 14, 15 and 16 UTC, by area I and II and classified according to the number of recorded AD (YES when AD>0 and NO when AD=0). In other words, the cumulative number of AD were computed between 18-23:59h local time. If the cumulative value was greater than zero the event was classified as "YES" (MCE event); if there is no atmospheric discharge the classification will be "NO" (non-MCE event).
4. Testing was carried out via a classical cross-validation procedure that consists of dividing the total data set into k mutually exclusive subsets (folds) of the same size; from there, a fold is used for testing and the remaining k-1 folds are used for training. For training and testing of all of ML classification algorithms of WEKA, the weights of the occurrence of YES and NO events are adjusted (class balance) in the training dataset considering the following event proportions (where the MCE and non-MCE occurrence are artificially replicated or reduced considering the behaviour of the observed value indices); (1) original data, (2) 50% YES and 50% NO, (3) 60% YES and 40% NO, (4) 70% YES and 30% NO, (5) 80% YES and 20% NO for the different forecast lead times from 12, 13, 14, 15, and 16 UTC, respectively. In order to balance the output of the model, so that the model learns efficiently the physical patterns related to MCE and non-MCE events, the output weights of each model were artificially varied. That is, if the model output has many more values of "NO", a greater weight at the "YES" output is applied. The output weights were chosen randomly based on trial and error. Many tests were carried out in order to find the proportion of weight variation at the output of the model so that it obtained the best performance.
5. The optimal ML classification algorithms (or model that means that a given algorithm was trained and evaluated via the statistics in Table 4) with the best performance in the previous step were selected, considering the values of the statistics specified in Table 3, for further analysis of the results and discussion.
6. Using a trial-and-error procedure, the AD per hour (AD/h) limit for the MCE was determined by gradually varying the value of AD/h (threshold) and observing the performance of the ML algorithms in classifying an MCE with an AD $\geq$ the limit until reaching the optimum severity limit.
7. Finally, an optimal model was applied to a hindcast experiment using independent data sampling.

2.4 Selected ML algorithms

The ML algorithms used in step 5 are briefly described in Table 2.

2.5 Evaluation

The ML algorithms had their predictions evaluated in comparison to the target values using a two-dimensional contingency table (Table 3) according to Wilks (2006). Thus, it was possible to determine five categorical statistics, namely, 1) probability of detection (POD), 2) false alarm (FAR), 3) BIAS, 4) F-measure, and 5) KAPPA, as detailed in Table 4.

Table 2: *Classifiers used.*

Classifier	Description	Reference in Weka
Random forest	A collection of tree classifiers that are trained on different subsets of input features and the one with the best performance is chosen.	Breiman (2001)
J48	Creates a single decision tree based on all input resources available.	Quinlan (1993)
MPL	Multilayer perceptron; one or more hidden layers and an output layer of computational nodes.	-
Hoeffding Tree	Grants a certain level of confidence in the best attribute to split the tree.	Hulten et al. (2001)
Logistic	Predicts the probability of an event belonging to the standard class, which can be of type 0 or 1.	Brownlee (2016)
Simple Logistic	Builds linear logistic regression models. LogitBoost with simple regression functions as base learners was used for fitting the logistic models.	Sumner et al. (2005)

Table 3: *Contingency Matrix.*

		Observed		
		Yes	**No**	**Total**
Forecast	Yes	Hits (a)	False alarm (c)	
	No	Misses (b)	Correct negatives (d)	
Total		Observed Yes	Observed No	Total

Tabela 4: *Statistics retrieved from the contingency matrix.*

Statistict	Formulat	Descriptiont	Referencet
Probability of detection (POD)	$POD = \dfrac{a}{a+c}$	Measures the fraction of observed events that were correctly predicted. A perfect score is 1.	(Wilks, 2006)
False alarm (FAR)	$FAR = \dfrac{b}{b+d}$	Measures the fraction of "YES" predictions in which the event did not occur. A perfect score is 0.	-
BIAS	$B = \dfrac{a+b}{a+c}$	Measures the proportion of the event frequency prediction by the observed events frequency. The perfect score is 1.	-
F-measure[1]	$F = \dfrac{2P.POD}{P + POD}$	It is a measure of the accuracy of a test.It considers the accuracy and recall of the test to calculate the score.The F-Measure is the harmonic average of precision and recall, where it reaches its best value at 1 (perfect precision).	(Sasaki, 2007)
Kappa[2]	$k = \dfrac{p_0 - p_e}{1 - p_e}$	It is a way of measuring the performance of the classification process where the perfect agreement is 1. This coefficient can be defined as a measure of association. It is used to describe and test the degree of agreement in the classification, that is, its reliability and accuracy.	(Cohen, 1960)

[1]where the statistics used are defined as $P = \dfrac{a}{a+b}$,

[2]$k = \dfrac{a+d}{a+b+c+d}$ and $= \dfrac{[(a+b)(a+c)]+[(c+d)(b+d)]}{(a+b+c+d)^2}$

3. RESULTS

To train and test the classificatory algorithms for MCE short-term forecasting, as described in Section 2.3, the distribution of the occurrence of ADs was initially analysed for the Rio de Janeiro – São Paulo route. Fig. 2(a) shows the seasonal distribution of ADs from 2001 to 2019. As expected, it was observed that in the spring-summer period, due to the greater availability of energy, approximately 89% of ADs occur: 57.1% and 31.7% in summer and spring, respectively. In autumn, 6.3% of ADs occurred, whereas 4.8% occurred in winter. This decrease in the number of ADs compared to spring-summer can be explained by the absence of local convective forcing, as these seasons are usually drier. They are characterised by a westward displacement of the South Atlantic Subtropical High and the associated subsidence hinders convective activities in the study area; thus, ADs are typically related to mass passages (cold or hot fronts).

Fig. 2(b) represents the hourly distribution of AD in the study area and indicates that convective activity increases from 3 pm and peaks at 6 pm local time. It is noteworthy that most ADs occurred between 6 pm and 0 am local time which was also found by Almeida et al. (2020) for the flight terminal area of Rio de Janeiro. Remotely sensed data from GOES-R were retrieved for January–March, 2018 and 2019 (Table 1). Fig. 3 shows the number of MCE and AD range for 413 occurrences in the study area. Notably, 79.4% of the events had AD of 130 or less. In this study, severe MCE was defined when an MCE had more than 130 AD.

Figure 2: (a) Seasonal and (b) hourly distribution of atmospheric discharge (AD) for the Rio de Janeiro –São Paulo flight route.
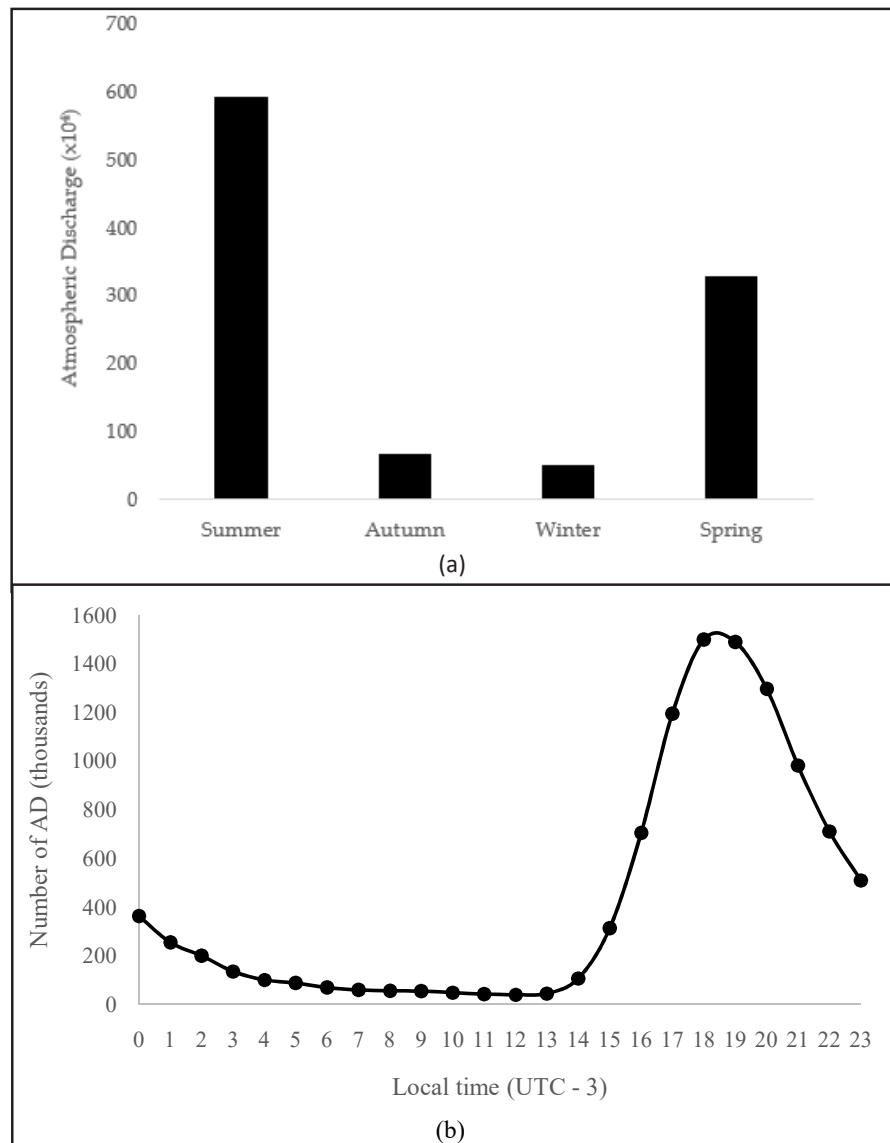
Training and testing any computational intelligence algorithms are time-consuming tasks (França et al., 2016). Following the method, fifty-six classification algorithms available in WEKA were trained and tested via cross-validation. To select the classifier(s) algorithm(s) to be explored in detail, all were initially evaluated with input (from to 12-16 UTC for areas I and II. After 280 experiments, the algorithms called naive Bayes (John and Langley, 1995), multilayer perceptron (Quinlan, 1993), Hoeffding tree (Hulten et al., 2001), logistic (Brownlee, 2016), and simple logistic (Sumner et al., 2005) algorithms obtained superior statistical results and were thus selected.

The experiments are described separately for the MCE forecast (or detection) (method steps 7 and 8) and the severity forecast.

3.1 MCE forecast

A total of 400 MCE prediction experiments were performed considering the following four aspects: (1) five selected algorithms; (2) (1) − (5) dataset configurations as per the method's step 4; (3) different lead times (i.e. 12, 13, 14, 15, and 16 UTC); and (4) two areas (I and II), step 4 of the method.

Table 5 shows the best test results (cross-validation) for the input times at 12, 13, 14, 15, and 16 UTC, identifying the configuration of the training dataset. Therefore, all of the statistics have the unit as the ideal value; 1-FAR was adopted instead of the classic statistic FAR (whose ideal value is zero). The performances of the five algorithms were similar regardless of the lead time or area, because the values of the POD, 1-FAR, F-measure, BIAS, and KAPPA statistics were in the small ranges of [0.81, 0.94], [0.80, 0.92], [0.81, 0.94], [0.95, 1.01], and [0.61, 0.85], respectively. However, the class weight variation used in step 4 of the method proved to be an interesting strategy for improving the training of the algorithms because the best result (the MLP algorithm whose 6 h probability of detection was of the order of 86%, with a 6 h false alarm rate of 13% and its forecast was still slightly skewed, because it is noted only in the third decimal place of the BIAS value) for area I is with the 15 UTC inputs and dataset configuration (2). For area II, all algorithms had better performance (the simple logistic algorithm can generate an 8 h forecast of slightly skewed MCE with BIAS = 1.01, a high detection probability value and low false alarm rate with values 94% and 8%, respectively) with the inputs of 13 UTC and dataset configuration (4).

3.2 Storm severity

In summary, here two models were developed. The first is a model to predict whether there is condition favorable to convective events. And the second is a model to predict the severity of the convective event, considering that the first model predicted conditions favorable to its formation. For the severity of these events, several procedures were performed, by percentiles, by trial and error, analysing how the distribution of significant events behaved. It was identified that most events, that is, those with the lowest or least significant impacts occur more frequently (which can be observed in Fig. 3). And

Table 5: *Tests of the five selected algorithms at 12, 13, 14, 15, and 16 UTC (and dataset configuration) for areas I and II. The columns represent the statistics Probability of Detection (P), the difference of False Alarm from unit (1-F), F-measure (F1), Bias (B) and Kappa (K).*

AREA I	Dataset Configuration: (3) for 12 UTC					Dataset Configuration: (2) for 13 UTC					Dataset Configuration: (2) for 14 UTC					Dataset Configuration: (2) for 15 UTC					Dataset Configuration: (2) for 16 UTC				
Algorithm	P	1-F	F1	B	K	P	1-F	F1	B	K	P	1-F	F1	B	K	P	1-F	F1	B	K	P	1-F	F1	B	K
Naive bayes	0.82	0.80	0.81	1.00	0.61	0.82	0.82	0.82	0.98	0.64	0.81	0.81	0.81	1.00	0.63	0.83	0.83	0.83	1.00	0.66	0.82	0.82	0.82	1.00	0.64
Logistic	0.83	0.80	0.83	0.98	0.64	0.81	0.81	0.81	1.00	0.62	0.82	0.82	0.82	1.00	0.63	0.85	0.85	0.85	1.00	0.69	0.83	0.83	0.83	1.02	0.65
MPL	0.86	0.80	0.85	0.96	0.69	0.85	0.85	0.84	1.00	0.69	0.82	0.82	0.82	1.00	0.63	0.86	0.86	0.86	1.00	0.72	0.84	0.84	0.84	1.00	0.69
Simple Logistic	0.82	0.78	0.82	0.98	0.62	0.81	0.81	0.81	1.01	0.62	0.82	0.82	0.82	1.00	0.64	0.83	0.83	0.83	1.00	0.67	0.85	0.85	0.85	1.00	0.70
Hoeffding Tree	0.82	0.80	0.82	1.00	0.61	0.82	0.82	0.82	1.00	0.64	0.81	0.81	0.81	1.00	0.63	0.83	0.83	0.83	1.00	0.66	0.82	0.82	0.82	1.00	0.64

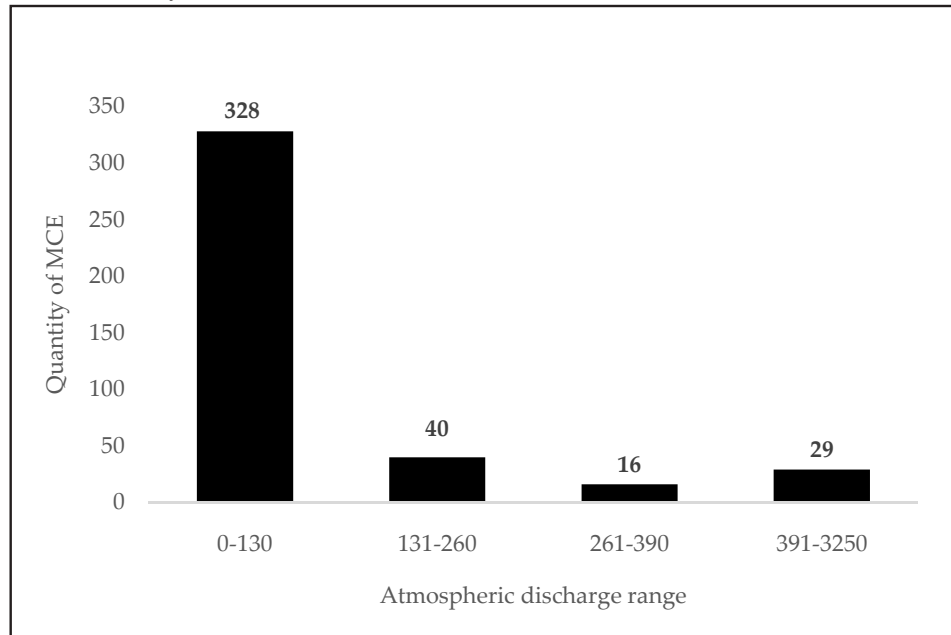| AREA II	Dataset Configuration: (2) for 12 UTC					Dataset Configuration: (4) for 13 UTC					Dataset Configuration: (3) for 14 UTC					Dataset Configuration: (2) for 15 UTC					Dataset Configuration: (4) for 16 UTC				
Algorithm	P	1-F	F1	B	K	P	1-F	F1	B	K	P	1-F	F1	B	K	P	1-F	F1	B	K	P	1-F	F1	B	K
Naive bayes	0.83	0.84	0.83	1.00	0.66	0.90	0.84	0.90	0.98	0.76	0.87	0.85	0.87	1.00	0.73	0.84	0.84	0.84	1.00	0.68	0.86	0.82	0.86	1.00	0.67
Logistic	0.82	0.82	0.82	1.00	0.64	0.91	0.85	0.91	0.98	0.77	0.86	0.83	0.85	0.98	0.69	0.83	0.83	0.83	1.00	0.66	0.88	0.81	0.87	0.95	0.70
MPL	0.82	0.82	0.81	1.00	0.63	0.90	0.79	0.90	0.92	0.74	0.91	0.87	0.91	0.97	0.80	0.83	0.83	0.83	1.00	0.66	0.93	0.86	0.93	1.00	0.83
Simple Logistic	0.83	0.83	0.83	1.00	0.65	0.94	0.92	0.94	1.01	0.85	0.86	0.84	0.86	0.99	0.71	0.86	0.86	0.85	1.00	0.71	0.88	0.79	0.88	0.96	0.70
Hoeffding Tree	0.83	0.83	0.83	1.00	0.66	0.90	0.84	0.90	0.98	0.75	0.87	0.85	0.87	0.99	0.73	0.84	0.84	0.84	1.00	0.68	0.87	0.82	0.87	1.01	0.68

after several tests it was identified that the threshold higher than 130 AD (those of lower occurrence), is the threshold found to verify whether the event is severe or not. That said, when there is an AD number greater than 130 AD/h, there is a severe event.

Following the method´s step 6, the variation of AD/h from 1 to 3,000 was considered in increments of 10 AD/h intervals, to calculate the evaluation statistics in Table 4. The distribution presented in Fig. 3 shows that the highest occurrence of AD was in the range of up to 130 discharges per hour. Therefore, 81 and 328 convective meteorological events were classified as severe and non-severe, respectively (according to Table 6). This meant that the training record sets generated an output of "YES" for severe MCE, and "NO" for all others. Step 4 was then used to generate five

dataset configurations. Finally, the algorithms were trained and tested until the optimal algorithms were obtained.

The J48 (Breiman, 2001) and RF (Quinlan, 1993) algorithms were the ones that obtained the best performances and the values of these statistics are presented in Table 6. Generally, the results for area II are superior to those of area I. Both algorithms are capable of a 6-h forecast of severe MCE (with dataset configuration 2) with POD = 0.78 and FAR = 0.23, with low bias for area I. The same algorithms produced more expressive results in the forecast of the severity of MCEs for area II. The RF generated an 8 h prediction of severe MCE with POD = 92% (14% higher than area I) and a false alarm rate of 7% (16% higher than area I) with a positive bias of 6% (approximately 6% less than area I).

Figure 3: Distribution of the 413 convective meteorological events by atmospheric discharge range per hour from January to March, 2018 and 2019.

Table 6: *Tests of performance of the two selected algorithms at 15 UTC (for area I) and 13 UTC (for area II) with a specific dataset configuration.*

AREA I	Dataset Configuration: (1) for 15 UTC					Dataset Configuration: (2) for 15 UTC				
Algorithm	POD	1-FAR	F-MEASURE	BIAS	KAPPA	POD	1-FAR	F-MEASURE	BIAS	KAPPA
J48	0,90	0,56	0,89	0,80	0,58	0,78	0,78	0,77	1,00	0,58
Random Forest	0,90	0,56	0,89	0,80	0,58	0,78	0,78	0,77	1,00	0,58
AREA II	Dataset Configuration: (1) for 13 UTC					Dataset Configuration: (2) for 13 UTC				
Algorithm	POD	1-FAR	F-MEASURE	BIAS	KAPPA	POD	1-FAR	F-MEASURE	BIAS	KAPPA
J48	0,88	0,90	0,89	1,08	0,73	0,92	0,92	0,92	1,00	0,84
Random Forest	0,92	0,93	0,92	1,06	0,80	0,93	0,93	0,93	1,00	0,85

3.3 Hindcast results

Considering the definition of severe MCE, the RF algorithm was applied to both areas. Tables 7 and 8 show the daily records of the thermodynamic index values at 15 UTC (Area I) and 13 UTC (Area II), corresponding to columns 2 to 6, the amount of AD recorded (column 7), and the MCE forecast output (column 8) for days with data available for areas I and II in April 2019, respectively. The results reveal that the models obtained expressive and similar hindcasts and could correctly identify, 8 h in advance, 100% of non-MCE days, and 96% of MCE days. The observed forecast errors correspond to only one MCE day for each area, that is, day 13, in area I, and day 28 in area II, as seen in column 8 of Tables 7 and 8, respectively. To evaluate the model failures, the instability index values were analysed, and it is noteworthy that these are compatible with those that occur in typical MCE days, except for the CAPE index value, which was null and positive LI (atypical for MCE days according to the data in Section 2.2). Intuitively, a plausible reason is that there was little quality control in the data and, as "YES", the calculation of the CAPE and LI values were obtained with corrupted data resulting in erroneous hindcast for the specific days.

4. CONCLUSIONS

In this study, a forecast model based on machine learning algorithms for short-term meteorological convective event forecasting was developed for the Rio de Janeiro – São Paulo route. The main results are summarised below.

- The 6 pm local time period was identified as the period with the highest convective activity.
- The models with input data at 10 am and 12 pm local time are the models with the best performances.
- The developed models demonstrate the ability to predict and classify the severity of MCE and non-MCE with a high probability of detection, low false alarm rate, and a bias close to unity (unbiased model).
- Atmospheric profiles extracted from orbital remote sensors are promising for characterising the thermodynamic states of the atmosphere at high frequency (every 15 min); thus, essential input data for any predictive models for MCEs, since the results of the 6 h and 8 h hindcasts of the model (trained algorithms) are satisfactory for nowcasting prediction performances in identifying MCE and non-MCE for the studied area.

To use these models in the future as an operational tool by Brazilian aviation, the data period has been extended. In addition, the methodology developed here will be applied to other flight routes and areas with scarce sounding data.

A great advantage of using machine learning is that numerical time models do not solve phenomena on a spatial and time (nowcasting) scale. In addition, it can be utilized to obtain a local forecast without using parameterisations, using only the observed data. Another advantage is that ML models require lower computational costs, in addition to reducing the forecast uncertainty.

Atmospheric physics and dynamics suggest a good representation, because the model is fed with local thermodynamic conditions.

Studies such as those by Almeida et al. (2020) and Anochi et al. (2021), among others, show how important it is to consider machine learning models for forecasting in operational centres to improve the quality of forecasts and reduce computing costs.

DECLARATIONS

Conflicts of interest/Competing interests
There is no conflict of interest.

Availability of data and material
All data and materials as well as software application or custom code support their published claims and comply with field standards.

Code availability

Author Contributions
Caroline Menegussi spent more effort writing the original draft and suggested corrections. In addition, Gutemberg França played a critical role in funding acquisition and project administration, in addition to his technical contributions. The remaining authors have contributed equally to the manuscript: review, editing, and investigation. All authors have read and agreed to the published version of the manuscript.

Table 7: *Values of thermodynamic indices and atmospheric discharges for area I in April 2019.*

DAY	CAPE	KI	LI	SI	TT	AD	FORECAST RESULT
01	4.54	26.47	0.52	4.73	40.66	0	CORRECT
02	0.00	13.23	4.68	8.35	35.49	0	CORRECT
03	0.00	20.81	2.00	6.95	37.89	0	CORRECT
04	0.00	22.28	3.75	6.00	37.21	0	CORRECT
05	44.78	35.28	-0.99	0.25	44.45	985	CORRECT
06	65.06	35.61	-1.06	-0.30	43.66	29271	CORRECT
07	159.55	35.32	-1.94	-0.02	43.94	3655	CORRECT
08				NO INFORMATION			
09	4.98	32.04	0.01	0.66	43.16	9	CORRECT
10	1.62	25.81	1.43	3.22	41.29	3	CORRECT
11	0.01	23.10	2.63	5.06	38.61	0	CORRECT
12	0.00	18.55	3.16	6.27	37.06	0	CORRECT
13	0.00	24.24	0.54	3.56	41.09	175	NOT CORRECT
14				NO INFORMATION			
15				NO INFORMATION			
16	92.83	31.97	-0.88	0.98	43.85	26244	CORRECT
17	247.71	25.40	-0.33	1.54	43.63	5450	CORRECT
18	2.24	1.49	4.38	8.83	36.48	0	CORRECT
19	2.59	-9.03	5.32	10.94	35.96	0	CORRECT
20	0.00	3.89	7.44	10.90	31.99	0	CORRECT
21	0.00	23.85	3.77	3.85	40.04	88	CORRECT
22	5.25	32.04	0.41	1.39	43.59	0	CORRECT
23				NO INFORMATION			
24				NO INFORMATION			
25	20.84	27.45	0.66	4.16	39.51	4	CORRECT
26	78.03	29.23	-0.60	2.31	42.23	849	CORRECT
27	5.32	31.71	-0.03	1.23	42.92	0	CORRECT
28	7.45	29.49	-0.05	1.98	43.30	6286	CORRECT
29	0.00	18.86	2.42	5.70	38.34	4	CORRECT
30	0.00	3.28	3.53	8.37	37.46	0	CORRECT

Table 8: *Values of thermodynamic indices and atmospheric discharges for area II in April 2019.*

DAY	CAPE	KI	LI	SI	TT	AD	FORECAST RESULT
01	16.30	25.71	0.37	5.60	40.80	0	CORRECT
02	0.00	12.21	3.61	9.02	35.42	0	CORRECT
03	0.27	15.31	0.66	7.59	38.97	0	CORRECT
04	0.00	15.44	2.31	8.75	33.70	0	CORRECT
05	21.07	31.21	-0.77	2.46	42.41	2620	CORRECT
06	16.70	35.89	-0.75	-0.02	43.42	345	CORRECT
07	282.99	26.86	-2.57	2.87	43.59	5735	CORRECT
08				NO INFORMATION			
09	55.59	33.98	-0.66	0.91	42.94	1743	CORRECT
10	5.18	29.42	0.25	2.66	41.72	0	CORRECT
11	0.00	23.31	2.13	6.83	36.82	0	CORRECT
12	0.00	18.25	3.40	8.46	34.02	0	CORRECT
13	4.89	25.47	0.62	4.07	39.55	0	CORRECT
14				NO INFORMATION			
15				NO INFORMATION			
16	31.69	29.03	-0.29	2.58	41.99	28	CORRECT
17	410.52	27.65	-1.44	1.34	44.29	17407	CORRECT
18	23.58	9.39	2.58	7.67	36.42	11	CORRECT
19	53.33	0.81	2.35	7.71	39.74	0	CORRECT
20	0.00	-18.02	3.66	14.15	29.21	0	CORRECT
21	0.00	19.00	5.12	5.92	37.27	0	CORRECT
22	1.72	29.14	0.40	3.09	41.75	0	CORRECT
23				NO INFORMATION			
24				NO INFORMATION			
25	37.47	25.44	0.24	5.38	38.68	0	CORRECT
26	16.43	24.55	0.43	5.52	39.09	0	CORRECT
27	3.36	28.72	1.25	3.72	40.22	0	CORRECT
28	0.00	26.38	1.67	3.78	40.56	1205	NOT CORRECT
29	1.82	21.07	0.72	4.72	39.72	5	CORRECT
30	0.70	10.60	2.93	5.72	38.16	0	CORRECT

REFERENCES

Almeida, M. V. (2009). Aplicação de técnicas de redes neurais artificiais na previsão de curtíssimo prazo da visibilidade e teto para o aeroporto de Guarulhos – SP. Doctoral thesis. Federal University of Rio de Janeiro. http://www.coc.ufrj.br/teses-de-doutorado/153-2009/1186-manoel-valdonel-de-almeida. Accessed 20 August 2020.

Almeida, V. A., França, G. B., & Velho, H. F. C. (2020a). Short-range forecasting system for meteorological convective events in Rio de Janeiro using remote sensing of atmospheric discharges. *International Journal of Remote Sensing*. https://doi: 10.1080/01431161.2020.1717669

Almeida, V. A., França, G. B., & Velho, H. F. C. (2020b). Data assimilation for nowcasting in the terminal area of Rio de Janeiro. *Ciência e Natura*. https://doi:10.5902/2179460X53224

Almeida, V. A., França, G. B., Velho, H. F. C. & Ebecken, N. F. F. (2020c). Artificial Neural Network for Data Assimilation by WRF Model in Rio de Janeiro, Brazil. *Revista Brasileira de Geofísica*. http://dx.doi.org/10.22564/rbgf.v38i2.2042

Anochi, J. A., Almeida, V. A. & Velho, H. F. C. (2021). Aprendizado de máquina para modelagem de previsão de precipitação climática na América do Sul. *MDPI: Remote Sensing*. https://doi.org/10.3390/rs13132468

Bender, A. (2018). Condições Atmosféricas Conducentes a Tempestades Severas e sua Relação com a Urbanização na RMSP. Doutoral thesis. Universidade de São Paulo, São Paulo. https://doi.org/10.11606/T.14.2019.tde-18042019-101002

Breiman, L. (2001). Random Forests. *Machine Learning*. https://doi.org/10.1023/A:1010933404324

Brownlee, J. (2016). *Master Machine Learning Algorithms*. Melbourne, VIC: Machine Learning Mastery.

CENIPA. (2018). Aeródromos - Sumário Estatístico 2008-2017. Available online: file:///C:/Users/Windows%2010/Downloads/sumario_estatistico_aerodromos.pdf. Accessed 08 July 2020.

Cohen, J. (1960). A Coeficient of agreement for nominal scales. *Educational and Psychological Measurement*. https://doi.org/10.1177/001316446002000104

França, G. B., Bonnet S. M., & Albuquerque Neto F. A. (2018). Nowcasting model of low wind profile based on neural network using SODAR data at Guarulhos Airport, Brazil, *International Journal of Remote Sensing*. https://doi:10.1080/01431161.2018.1425562

França, G. B., Almeida M. V., & Rossete A. C. (2016). An Automated Nowcasting Model of Significant Instability Events in the Flight Terminal Area of Rio De Janeiro, Brazil. *Atmospheric Measurement Techniques*. https://doi:10.5194/amt-9-2335-2016

Galway, J.G. (1956). The lifted index as a predictor of latent instability. *Bulletin of the American Meteorological Society*. https://doi:10.1175/1520-0477-37.10.528

George, J. J. (1960). *Weather Forecasting for Aeronautics*. Atlanta, GA: Academic Press.

Gultepe, I., Sharman, R., Williams D., Zhou P., Ellrod, B., Minnis, G., et al. (2019). A review of high impact weather for aviation meteorology. *Pure and Applied Geophysics*.

Hall, M., Frank, E., Holmes, G., Pfahringer, B., Reutemann, P., & Witten, I. H (2009). The WEKA Data Mining Software: an Update. *ACM SIGKDD Explorations*. https://doi.org/10.1145/1656274.1656278

Hermsdorff, J. (2018). Previsão de instabilidade atmosférica significativa usando árvore de decisão na região metropolitana do Rio de Janeiro. Masters' dissertation. Federal University of Rio de Janeiro. Accessed 20 August 2020.

Houze, R. A. (1993). *Cloud Dynamics*. Waltham, MA: Academic Press.

Hulten G., Spencer L., & Domingos, P. (2001). Mining time-changing data streams. KDD '01: *Proceedings of the seventh ACM SIGKDD international conference on Knowledge discovery and data mining*. https://doi.10.1145/502512.502529

Isaac, G. A., Bailey, M., Boudala, F., Burrows, W. R., Cober, S. G., Crawford, R. W., et al. (2012). The Canadian airport nowcasting system (CAN-Now). *Meteorological Applications*. https://doi.org/10.1002/met.1342

Isaac, G. A., Bailey, M., Boudala, F., Cober, S. G, Crawford, R., Donaldson, N., et al. (2011). Decision making regarding aircraft de-icing and in-flight icing using the Canadian airport nowcasting system (CAN-Now). *SAE International*. https://doi:10.4271/2011-38-0029

Isaac, G. A., Bailey, M., Cober, S. G., Donaldson, N., Driedger, N., Glazer, et al. (2006). Airport Vicinity Icing and Snow Advisor (AVISA). *44th AIAA*

Aerospace Sciences Meeting and Exhibit. https://doi.org/10.2514/6.2006-1219

John, G., H. & Langley, P. (1995). Estimating continuous distributions in bayesian classifiers. *Proceedings of the 11th Conference on Uncertainty in Artificial Intelligence*, San Mateo, CA: Morgan Kaufmann.

Miller, R. C. (1972). Notes on analysis and severe storm forecasting procedures of the Air Force Global Weather Central. *Technical Report 200.* Air Weather Service: United States Air Force.

Mueller, C., Saxen, T., Roberts, R., Wilson, J., Betancourt, T., Dettling, S., el al. (2003). NCAR auto-nowcast system. *Weather and Forecast* (pp. 545–561). Retrieved August 10, 2020, from https://www.weather.gov/media/mdl/Mueller_ANC2003.pdf

Nascimento, E. L. (2004). Identifying Severe Thunderstorm Environments in Southern Brazil: Analysis of Severe Weather Parameters. Proceedings of the 22nd Conference on Severe Local Storms. Hyannis, MA, EUA: American Meteorological Society. Retrieved June 26, 2021, from file:///C:/Users/Windows%2010/Downloads/81745.pdf

Nascimento, E. L. (2005). Previsão de tempestades severas utilizando-se parâmetros convectivos e modelos de mesoescala: uma estratégia operacional adotável no Brasil? Revista Brasileira de Meteorologia, 20 (1), 121-140.

Paulucci, T. B., França, G. B., Libonati, R., & Ramos, A. M. (2019). Long-Term Spatial– Temporal Characterization of Cloud-to-Ground Lightning in the Metropolitan Region of Rio de Janeiro. *Pure and Applied Geophysics.* https://doi.org/10.1007/s00024-019- 02216-1

Pinto, O. J., Naccarato, K., P., Pinto, I. R. C. A., Fernandes, W.A. & Pinto, O. N. (2006). Monthly distribution of cloud-to-ground lightning flashes as observed by lightning location systems. *Geophysical Research Letters.* https://doi.org/10.1029/2006GL026081

Quinlan, J. R. (1993). *C4.5. Programs for Machine Learning*, San Mateo, CA: Morgan Kaufmann.

Sasaki, Y. (2007). The truth of the F-measure. Retrieved August 15, 2020, from https://www.cs.odu.edu/~mukka/cs795sum09dm/Lecturenotes/Day3/F-measure-YS-26Oct07.pdf

Showalter, A. K. (1953). A stability index for forecasting thunderstorms. *Bulletin of the American Meteorological Society.* https://doi.org/10.1175/1520-0477-34.6.250

Silva, W. L., Albuquerque, F. A. N., França, G. B. & Matschinske, M. (2016). Conceptual model for runway change procedure in Guarulhos international airport based on SODAR data. *The Aeronautical Journal.* https://doi:10.1017/aer.2016.33

Sumner M., Frank E., & Hall M. (2005). Speeding Up Logistic Model Tree Induction. *Springer-Verlag.* https://doi:10.1007/11564126_72

Wilk, K. E. & Gray, K. C. (1970). Processing and analysis techniques used with the NSSL weather radar system, *Preprints, 14th Conf. on Radar Meteorology* (pp. 369–374). Tucson, AZ: American Meteorological Society.

Wilks, S. D. (2006). Statistical Methods in the Atmospheric Sciences.

Wilson, J. W. (1966). Movement and predictability of radar echoes. *National Severe Storms Laboratory.*

WMO (2013, March). *The GCOS Reference Upper-Air Network (GRUAN) GUIDE.* Retrieved July 7, 2021, from https://library.wmo.int/doc_num.php?explnum_id=7196

FIGURE CAPTIONS

Fig. 1 Representation of areas I and II.

Fig. 2 (a) Seasonal and (b) hourly distribution of atmospheric discharge (AD) for the Rio de Janeiro – São Paulo flight route.

Fig. 3 Distribution of the 413 convective meteorological events by atmospheric discharge range per hour from January to March, 2018 and 2019.

Data assimilation using WRFDA over the terminal area of Rio de Janeiro

Vinícius Albuquerque de Almeida[1]

Gutemberg Borges França[1]

Haroldo Fraga de Campos Velho[2]

Nelson Francisco Favilla Ebecken[3]

ABSTRACT

The impact of the data assimilation process of air temperature and relative humidity from surface meteorological stations and sounding at airports in the terminal area of Rio de Janeirois evaluated using the *Weather Research and ForecastData Assimilation* system. Synthetic data of temperature, relative humidity and wind are generated in the locations of airport sensors by applying a white-noise perturbation in the forecast data. Results show a positive overall impact of the assimilation process with the removal of part of the noise in the observation data but keeping the effect of local conditions in the later timesteps of the simulation. In addition, with the assimilation process there is a global reduction of the error between the analysis data and the observation data. In the future, a neural network will be trained to emulate the data assimilation process to speed-up the assimilation process in the WRF model.

Keywords: data assimilation, 3d Var, surface data, profile data.

1. INTRODUCTION

Numerical weather forecasting is considered an initial-value problem where the present state of the atmosphere is used as input to a numerical model for simulating or forecasting its evolution on space and time. The problem of the initial condition determination for a forecast model is essential and complex, and has become a science in itself (Daley, 1991). Several methods have been developed since the 1950s to tackle this problem. Lorenc (1986), Daley (1991), Talagrand (1997), Zupanski and Kalnay (1999), Kalnay (2002), Barker *et al.* (2004), Barker *et al.* (2012), Lorenc and Jardak (2018), among others provide a broader review on data analysis and assimilation techniques.

In meteorology, there is a wide variety of data sources to be assimilated to accurately estimate the state of the atmosphere, which includes conventional and non-conventional data. Conventional data include surface meteorological stations, balloon soundings, aircraft and ship observations. On the other hand, data retrieved from satellites (e.g. radiance), wind profilers (e.g. SODAR, LIDAR), and radar are usually known as non-conventional. Conventional data are commonly assimilated in global models, but very often the local conditions they represent are smoothed due: low-resolution models, data quality control that let some data sources out of the global model run1 due to missing data or errors, delay in data transmission to the global operational centers, many data sources are not part of the Global Telecommunication System (GTS), such as local wind profilers (SODAR, LiDAR) and RADAR. interpolation methods and quality control routines. Also, not all observations are part of the global observation network and thus are not processed by data assimilation routines of global models. Therefore, to accurately determine the state

[1] Laboratório de Meteorologia Aplicada, Universidade Federal do Rio de Janeiro, Rio de Janeiro, RJ, Brasil.

[2] Laboratório de Computação e Matemática Aplicada, Instituto Nacional de Pesquisas Espaciais, São José dos Campos, SP, Brasil.

[3] Instituto Alberto Luiz Coimbra de Pós-Graduação e Pesquisa de Engenharia, RJ, Brasil.

of the atmosphere it is mandatory not to rely only on the global model's analysis, but also, to assimilate all the available local data.

The present article is part of a sequence of studies related to nowcasting that have been executed by the Applied Meteorological Laboratory at the Federal University of Rio de Janeiro, following Almeida (2009), Silva *et al.* (2016), França, Almeida, and Rossete (2016), França *et al.* (2018), Paulucci *et al.* (2019), and Almeida *et al.* (2020a, 2020b). All these studies encompass researches based on artificial intelligence and methods of limited-area numerical weather forecasts. This work relates to the latter, exploring the sensibility of the Weather Research and Forecasting (WRF) regional model for surface and upper-air data assimilation in the metropolitan area of Rio de Janeiro.

2. MATERIAL AND METHODS

The study area in the present work is the metropolitan area of Rio de Janeiro and its surroundings (Fig. 1) located approximately at latitude 22°55'44.3" S and longitude 43°24'21.1" W. The most import airports in the region are highlighted in Fig. 1 by their International Civil Aviation Organization (ICAO) codes: Santos Dumont Airport (SBRJ), Galeão International Airport (SBGL), Santa Cruz Air Force Base (SBSC), Jacarepaguá Airport and Afonsos Air Force Base (SBAF).

Figure 1: Domain and computational grid. The labels SBSC, SBAF, SBJR, SBRJ and SBGL are the locations of the airports in the metropolitan area of Rio de Janeiro.
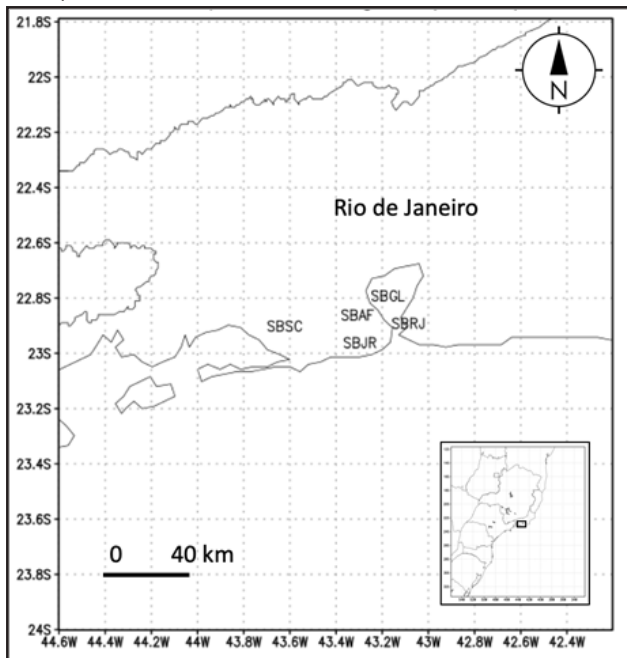
Each airport is responsible for local hourly routine and special reports surface observations of several meteorological parameters as surface wind (direction and speed), visibility, significant weather, cloud cover, air and dewpoint temperature, and station pressure. Besides, the SBGL airport has an upper-air (or sounding) station that produces regularly atmospheric soundings twice a day, the atmospheric profile of pressure, air and dewpoint temperature, relative humidity, and wind (direction and speed), from the surface up to more than 25 km.

The numerical experiments performed using the NCEP FNL (Final) Operational Global Analysis data for initial and boundary conditions. The FNL data are available on 1-degree grids prepared operationally every 6 h. This product is from the Global Data Assimilation System (GDAS), which continuously collects observational data from the Global Telecommunications System (GTS), and other sources.

2.1. WRF model

The WRF Model is a mesoscale numerical weather prediction system designed for both atmospheric research and operational forecasting applications. It features two dynamical cores, a data assimilation system, and a software architecture supporting parallel computation and system extensibility. The effort to develop WRF began in the latter 1990s and was a collaborative partnership of the National Center for Atmospheric Research (NCAR), the National Oceanic and Atmospheric Administration (represented by the National Centers for Environmental Prediction (NCEP) and the Earth System Research Laboratory), the U.S. Air Force, the Naval Research Laboratory, the University of Oklahoma, and the Federal Aviation Administration (FAA). Please refer to the WRF Users Guide and the Technical Note document available at WRF website for completeness of the description of WRF (Skamarock *et al.*, 2019).

The WRF model solves a set of equations that control the state and evolution of the atmosphere, including: (i) conservation of momentum; (ii) thermodynamic energy conservation; (iii) mass conservation; (iv) geopotential relation; and (v) the equation of state. Also, several physical processes are parameterized (e.g. short and longwave radiation transfer, surface modeling, turbulence, cumulus convection, cloud microphysics and precipitation), because these ones are too small, too brief, too complex, too poorly understood, or too computationally costly to be explicitly represented.

In our numerical experiments, the WRF model is integrated into a 2-km grid with 35 levels in vertical, generating hourly outputs from the surface and pressure-level variables. Regarding the parametrizations the

following options were chosen: Microphysics - WRF Single-moment 3 (Hong *et al.*, 2004), Cumulus - Grell-Freitas Ensemble Scheme (Grell and Freitas, 2014), Radiation - Dudhia Shortwave Scheme (Dudhia, 1989)/ RRTM Longwave Scheme (Mlawer *et al.*, 1997), Planetary Boundary Layer - Yonsei University Scheme (YSU) (Hong, 2006) and Land-Surface model - Unified Noah Land Surface Model (Tewari *et al.*, 2004).

2.2. Data assimilation method: 3D-Var

The 3D-Var approach was used as implemented in the Data Assimilation component of the WRF framework. The basic ideas of variational data assimilation and specifically the WRF Data Assimilation (WRFDA) system is deeply discussed in Barker *et al.* (2004) and Barker *et al.* (2012).

Among various data assimilation methods, the variational approaches have been widely used in meteorology, specifically the method 3D-Var. In the 3D-Var approach, a cost function (Eq. (1)) is defined which is proportional to the square of the distance between analysis ($\vec{x}^{a}$) and both the background($\vec{x}^{b}$) and the observations ($\vec{y}^{0}$) (Sasaki, 1970; alnay, 2012). The analysis field is computed by the direct minimization of such function. Important to notice that the error matrices for both the background*(B)* and observation*(R)* are considered in the minimization process. The operator H mapped the gridded analysis to the observation space for comparison against the observation matrix $\vec{y}^{0}$. The analysis $\vec{x}^{a}$ is computed by minimizing the cost function (J) expressed below:

$$J = \frac{1}{2}\{[\vec{y}^{0} - H(\vec{x})]^{T}R^{-1}[\vec{y}^{0} - H(\vec{x})] + (\vec{x} - \vec{x}^{b})^{T}B^{-1}(\vec{x} - \vec{x}^{b})\} \quad (1)$$

where R is the covariance matrix of the observation errors, and B is the covariance of the background errors matrix. The latter matrix is computed as a vector product from the difference of two WRF executions for a certain initial condition (Barker *et al.*, 2004). Here, the B matrix was computed by the NMC method (Parrish and Derber, 1992) and the R matrix entries are the same from a table of observation errors for each major observation type, as used in the US Air Force Weather Agency applications (Barker *et al.*, 2012).

The 3D-Var approach is described in the details in Barker *et al.* (2004), and also in chapter 6 of the WRF User's Guide.

2.3. Description of Experiments

Experiments with 6h-cycle for 7 days with data assimilation are performed using the WRFDA in 2014 and 2015 starting on February 1st with 168 h for time-integration (seven days). February is a very important month in Southern Hemisphere summer. This month is characterized by a peak of atmospheric discharges in Rio de Janeiro (Paulucci *et al.*, 2019) and the development of intense convective events. Lastly, after the end-of-the-year holidays, February has a peak of movements in airports, becoming the period relevant - since our study is a joint research between the Federal University of Rio de Janeiro and the Department of Airspace Control (DECEA), a division of the Brazilian Air Force. The data assimilation is carried out every 6 h for surface variables (air temperature, relative humidity, and wind direction and speed) at the airport locations, and every 12 h for upper-air variables (air temperature, relative humidity, and wind direction and speed) at SBGL location.

The experiment was performed in the following steps:

(i) White-noise perturbation is applied to GFS analysis field on Feb, 1st 00 UTC at the airport locations for surface and upper-air data generating synthetic observations;

(ii) Synthetic observations are placed on the exact coordinates where real sensors are located;

(iii) New analysis field is generated from synthetic observations and background field using the 3D-Var data assimilation technique;

(iv) WRF model is integrated for 6-h;

(v) Steps (i)-(iii) are repeated until Feb, 8th 00 UTC with surface data assimilation every 6h and upper-air data assimilation every 12h;

(vi) Steps (i)-(iv) are repeated for the same period of 168h for 2014 and 2015.

3. RESULTS AND DISCUSSIONS

This section presents the results of the experiments performed in this work showing the characteristics of data assimilation in the study area.

Before presenting the results, a discussion is necessary regarding the domain definition and the use of a single domain instead of nested domains. An experiment comparing 6-h assimilation cycle was performed considering a nested experiment (with three grids of 32 km, 8 km and 2 km for horizontal resolutions, respectively), and a single-domain experiment (with a 2-km grid). Figure 2 shows the result of a 6-h assimilation cycle for the single-domain (Fig. 2a) and the nested-domain (Fig. 2b) experiments at each airport within the study area. The comparison was performed on the 2-km horizontal resolution grid. Figure 2 shows the effect of the assimilation process is very similar for both experiments, in other words, there is a reduction of the white-noise perturbation for both analysis. Therefore, the mentioned experiments allow us to use a single-domain (computationally cheaper) instead of using nested domains.

Figure 2: Experiments for 6-h assimilation cycle at each airport for (a) single domain and (b) nested domain.


(a)

(b)
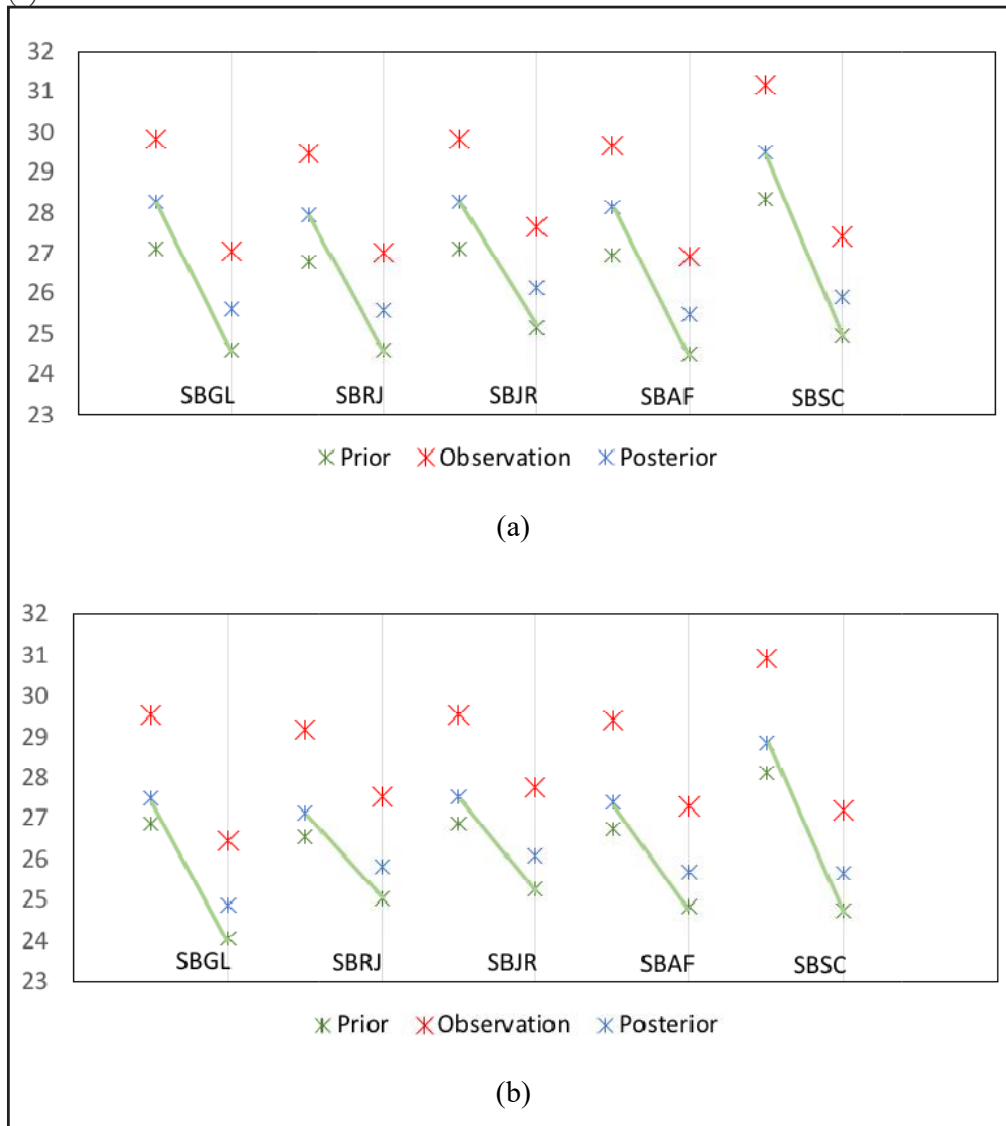
Any data assimilation method consists basically in optimally merging observation and forecast fields to generate the best approximation of the true state of a dynamic system. The observations do not represent "the reality" but the closest estimate of the true state superimposed with some noise due to the nature of the sensors. Therefore, a good strategy to evaluate a data assimilation algorithm is to apply some perturbation in the location of the sensors and perform a data assimilation process. If this algorithm is working, the expected result is that the perturbation would be partially removed and the analysis field would be closer to the original field (before the perturbation application), that is, our "true" state of the dynamical system.

Figures 3 to 6 present the results of the assimilation process for air temperature, relative humidity, wind speed and wind speed profile at SBGL. All figures have the following structure: (a) control - 6-h forecast from initial field without assimilation; (b) background - 6-h forecast from initial field with assimilation; (c) analysis - initial field with surface and upper-air assimilation; and (d) the difference from analysis and control field.

Figure 3a shows that on Feb 1st, 2014 06 UTC the process of data assimilation generated an analysis field (Fig. 3c) with greater temperature values in the surroundings of the station locations, mainly close to SBAF. Considering that the white-noise perturbation magnitude was a real number between 0 and 3 K the differences between analysis and control field (Fig. 3d) show that the data assimilation process removed 80-90% of the noise, and the resulting magnitude of innovation was not greater than $|0.6|$.

Figure 3: Air temperature field for (a) control and observation points, (b) background, (c) analysis and (d) difference from analysis and control, for Feb 1ˢᵗ, 2014 06 UTC.

Control and observation points (a)

Background (b)
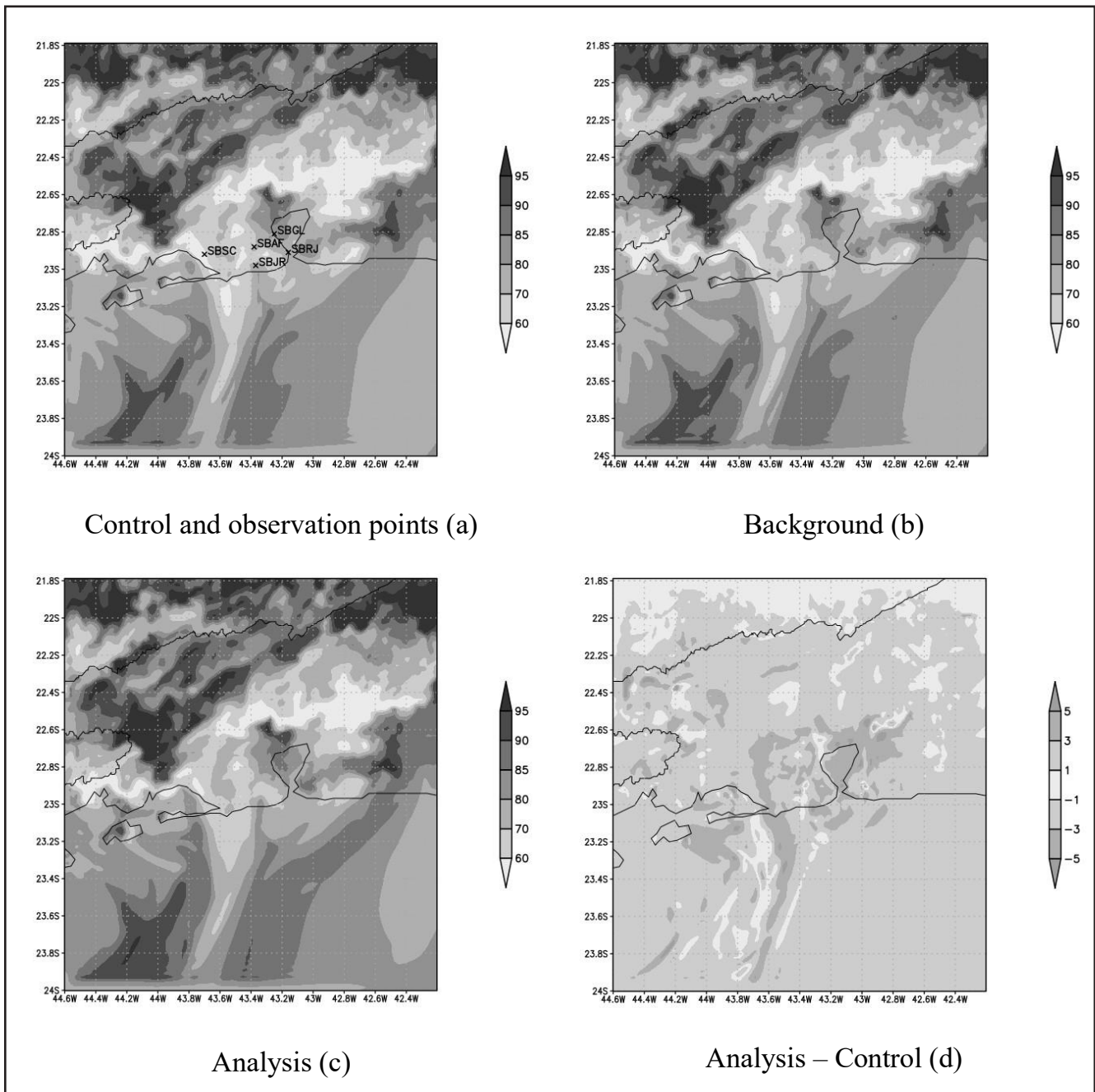
Analysis (c)

Analysis – Control (d)
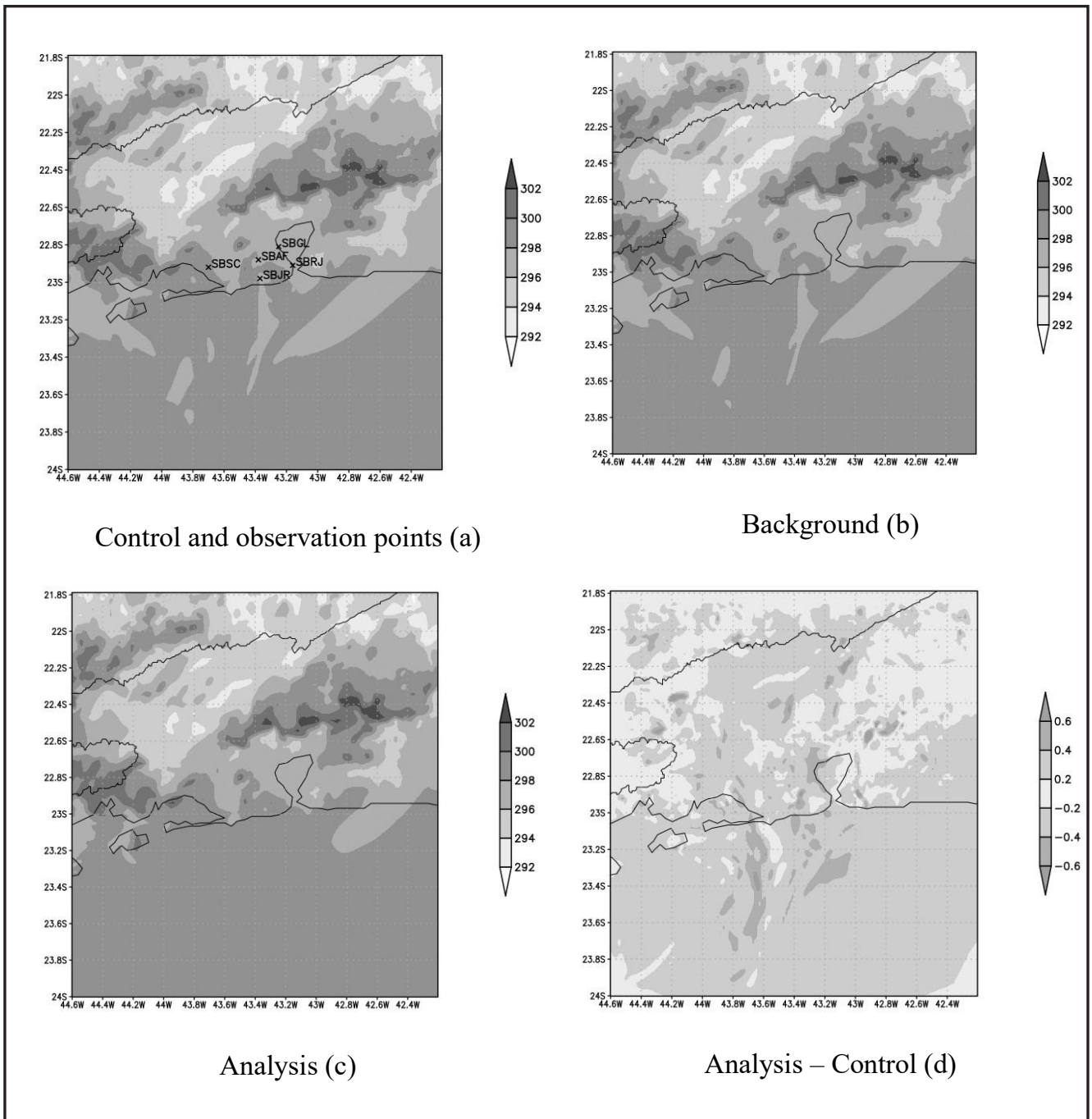
In a similar analysis, Fig. 4 show the impact of data assimilation process to the 2-m relative humidity field. Differently from what was observed for the temperature field in Fig. 3, the resulting innovation matrix generated by the 3D-Var (Fig. 4d) reached greater values, with regions with innovations up to 50% of the initial perturbation.

The wind speed (Fig. 5) shows that the data assimilation process generated an innovation

(Fig. 5d) of up to 60% of the white-noise perturbation applied to the control field – which had a magnitude of up to 1 m s-1. The difficulties involved into analyzing a vector field (the wind variable) in comparison to scalar variables (e.g. air temperature and relative humidity) are noteworthy. As shown in Fig. 5d, small perturbations in vector fields seem to cause perturbation in almost the whole domain

Figure 4: Relative humidity field for (a) control and observation points, (b) analysis and (c) background and (d) difference from analysis and control field, for Feb 1st, 2014 06 UTC.

Control and observation points (a)

Background (b)

Analysis (c)

Analysis – Control (d)

whereas the innovation in scalar fields (Fig. 3d and 4d) are more restricted to surroundings of stations – where the perturbation was applied. The analysis of wind speed profile (Fig. 6) shows that the difference between analysis and control (Fig. 6d) was close to zero from 850 hPa upward, with small increase in the layer between 800 and 650 hPa. Greater positive impact is observed close to surface, possibly related to the contribution of the surface data assimilation. Differently from the surface field, the impact in the vertical profile does not exceed 20% of the white noise perturbation. The small effect of the assimilation process might be related to the way that 3D-Var computes the impact of the station data in its surroundings, that is, the process of interpolation from observation grid to the model grid by the H operator (see eq. 1) after the innovation calculation.

Figure 5: Wind speed field for (a) control and observation points, (b) analysis and (c) background and (d) difference from analysis and control field, for Feb 1st, 2014 06 UTC.

Control and observation points (a)

Background (b)

Analysis (c)
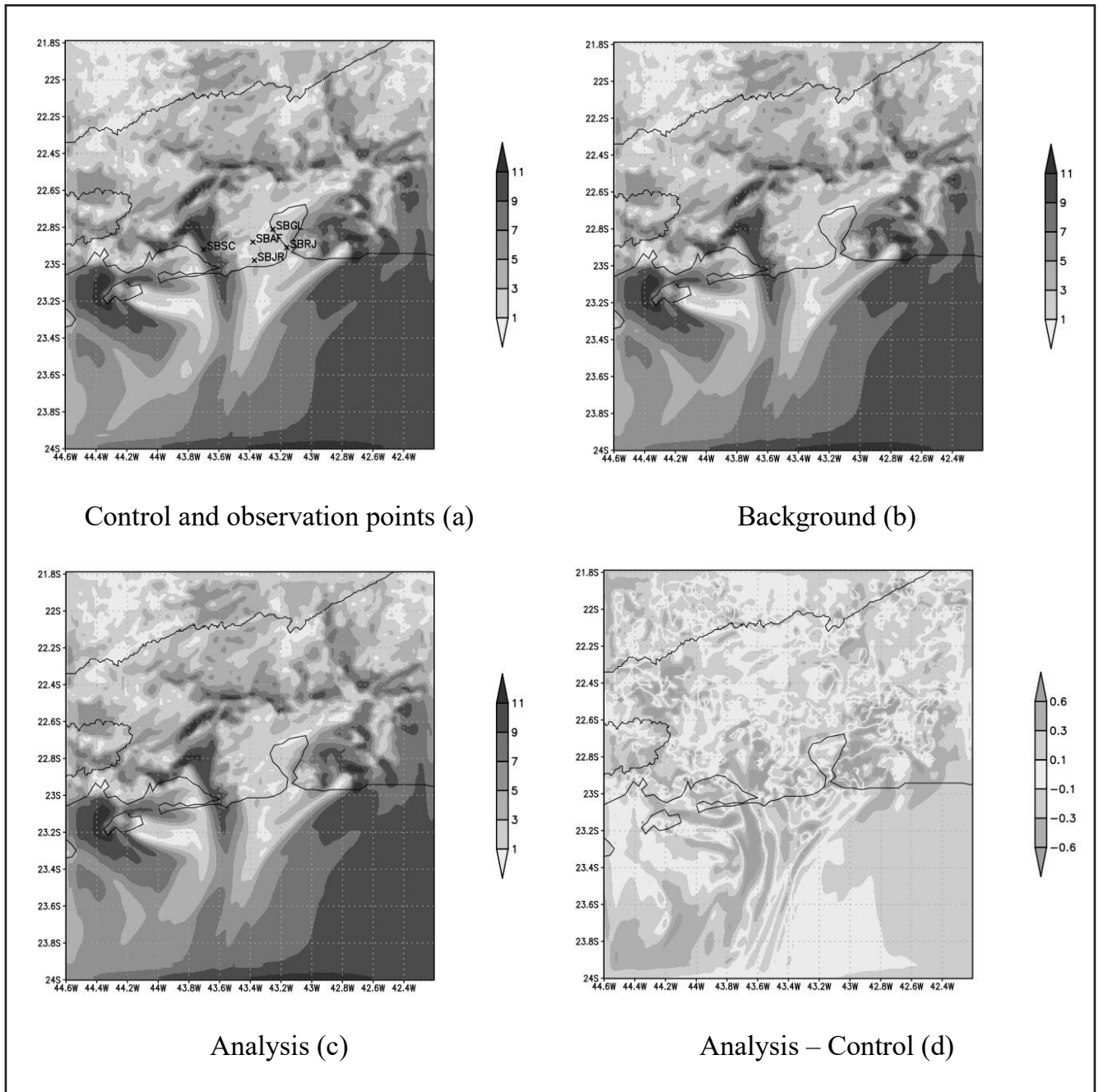
Analysis – Control (d)

In summary, all figures show a similar behavior, with small errors between analysis and control field, as expected, showing that the assimilation process removed most of the white-noise perturbation existent on the observation data.

Therefore, the results of data assimilation process using synthetic data (air temperature, relative humidity and wind speed), show that the 3D-Var method in the WRFDA system is able to perform a good estimate of the control field, here representing the "true" state of the dynamic system. The implications of such results are important since it implicitly states that only by using local data in the regional atmospheric model initialization the weather forecasts are to be improved. Currently, many observational data are not used because they are not considered by the global model assimilation system or because they are not part of the global observation system.

Figure 6: Profile field of wind speed for (a) control field, (b) analysis (c) background and (d) difference from analysis and observation field at SBGL, for Feb 1st, 2014 06 UTC.

Control (a)

Background (b)

Analysis (c)

Analysis – Control (d)
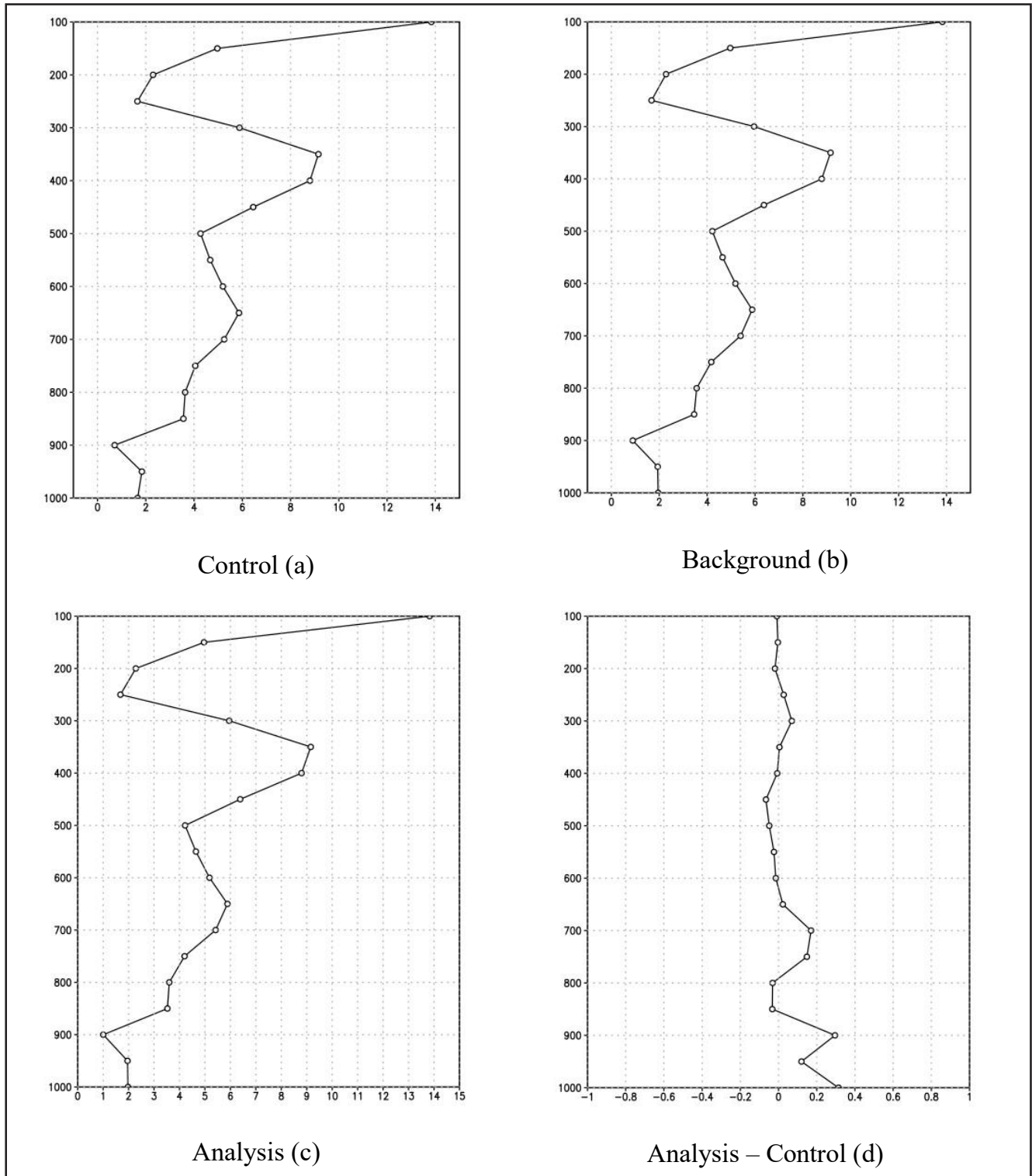
Figures 7 presents the result of the background and analysis errors (against synthetic observations) of air temperature assimilation process at SBGL for every 6-h between Feb 1st to 7th, 2014, and Feb 1st to 7th, 2015. As expected, the assimilation process removes most of the white-noise perturbation existent on the observation data, represented by lower errors in the data (solid line) compared to the forecast (or background) values (dashed line), as previously discussed in the analysis of Fig. 3.

Figure 7: Error on the air temperature field from synthetic observation to background (dashed line) and analysis (solid line) at SBGL between Feb 1st to 7th, 2014, and from Feb 1st to 7th, 2015.

Table 1 displays the statistics for all grid points and surface variables used on the assimilation process. The overall impact of the assimilation is posi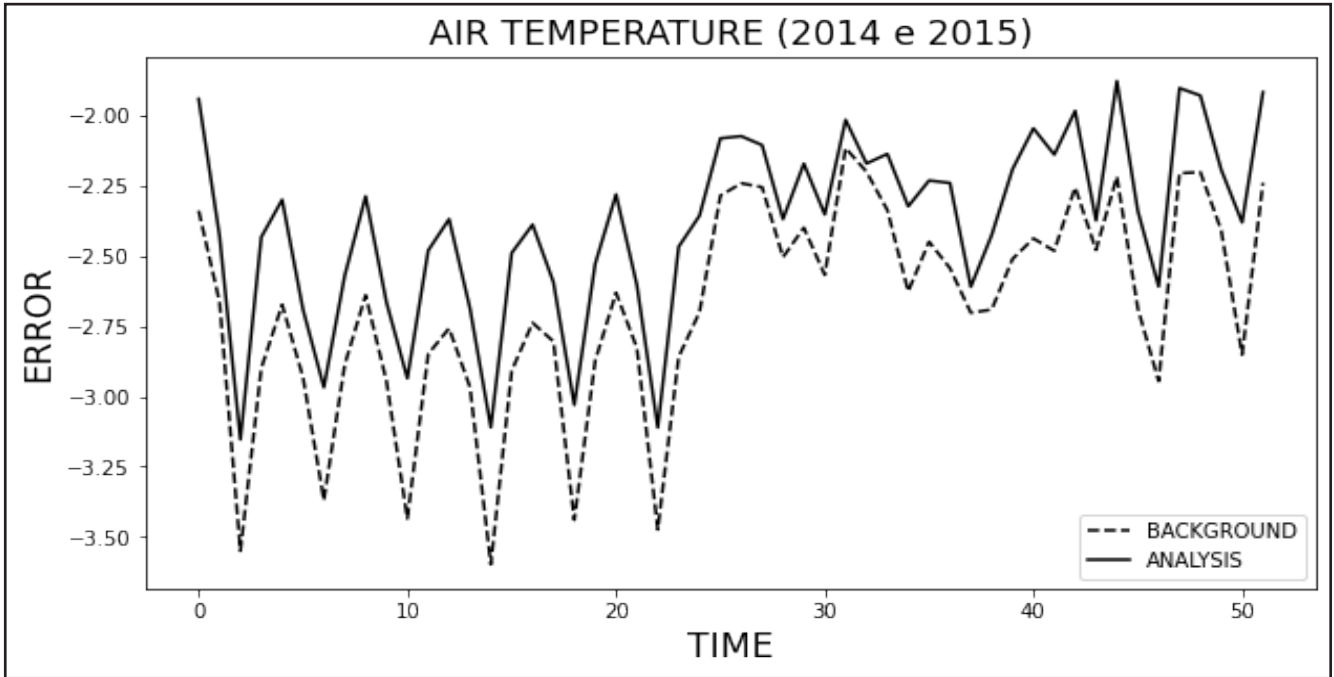tive for scalar variables (air temperature and relative humidity) as shown by the smaller values of analysis error compared to the forecast error. As discussed in the analysis of Fig. 5-6 there is a difference in the assimilation for vector fields in comparison to scalar variables. While the standard deviations of scalar variables are around 10% and 30% of the mean for air temperature and relative humidity, respectively, the standard deviation for wind speed is of the order of the mean. Although the error is relatively small for wind speed, the innovation in the wind speed is spread for almost the whole domain - see from Fig. 5d, whereas the innovation for scalar variables was closed to the station locations and their surroundings.

4. CONCLUSIONS

The 3D-Var approach for data assimilation from the WRF framework was evaluated for the surface and upper-air data assimilation of METAR and TEMP at different airports of the metropolitan area of Rio de Janeiro for a 168-h period in February 2014 and 2015.

Results showed that the assimilation routine was able to adjust the background field of the airport temperature, relative humidity, and wind, providing a better estimate of the true state of the atmosphere - closer to the control field. Even though conventional data are commonly assimilated in global models, the local conditions are smoothed. Therefore, meteorological fields can be adjusted for improvements in mesoscale forecasts.

This results are in accordance to the results in the experiments commonly carried out by University

Table 1: Statistics for all grid points and surface variables in the study domain. In the table, "std" refers to the standard variation and "error" to the difference between the background and analysis field to the synthetic observation.

	Observation		Background			Analysis		
	Mean	Std	Mean	Std	Error	Mean	Std	Error
Air temperature	30.13	3.84	27.48	3.45	9.00%	27.74	3.49	**8.00%**
Relative humidity	69.81	18.71	63.63	17.56	9.00%	65.22	17.46	**7.00%**
Wind speed	4.80	3.37	4.81	3.40	0.21%	4.79	3.38	0.21%

Corporation for Atmospheric Research (UCAR) and the National Center for Atmospheric Research (NCAR), where numerical experiments are described for 1D systems and also to the results presented in Almeida *et al.* (2020b). From the cited UCAR-NCAR experiments, they conclude that the data assimilation process reduces the added noise in the prior forecast and makes the posterior field closer to the "actual dynamics", that is, closer to the true state of the system.

The assimilation method can be effective for the short-range forecast and nowcasting time-window, under 24-h, removing the white-noise perturbation that is present in real observations and also adjusting the meteorological fields to local information.

In the future, the assimilation for real data using neural networks (Cintra and Campos Velho, 2012) will be tested to speed up the assimilation process, allowing for high-frequency assimilation processes (e.g. rapid update cycle) in the operational environment. The neural network approach will be trained to emulate the 3D-Var, as described in the framework described here.

ACKNOWLEDGMENTS

REFERENCES

Almeida, M.V. Aplicação de Técnicas de Redes Neurais Artificiais na Previsão de Curtíssimo Prazo da Visibilidade e Teto para o Aeroporto De Guarulhos - SP. Doctoral Dissertation, COPPE/UFRJ, Federal University of Rio de Janeiro, Brazil, 2009.

Almeida, V.A.;França, G.B.; Campos Velho; H.F. Short-range forecasting system for meteorologicalconvective events in Rio de Janeiro using remotesensing of atmospheric discharges. International Journal of Remote Sensing, v. 41, n. 11, p. 4372-4388, 2020a.

Almeida, V.A.;França, G.B.; Campos Velho, H.F.Data Assimilation for Nowcasting in the terminal area of Rio de Janeiro. Ciência e Natura, v. 42, 2020b.

Barker, D.M.; Huang, W.;Guo, Y.-R.;Bourgeois, A.;Xiao, X.N.A Three-Dimensional Variational Data Assimilation System for MM5: Implementation and Initial Results. Mon. Wea. Rev., v. 132, p. 897-914, 2004.

Barker, D.M.; Huang, X.-Y.; Liu, Z.;Auligne, T.; Zhang, X.; Rugg, S.; AL KATHERI, A.A.;Bourgeios, A.; Bray, J.; Chen, Y.;Demirtas, M.; Guo, Y.; Henderson, T.; Huang, W.; Lin, H.-C.;Michalakes, J.; Rizvi, S.; Zhang, X.-Y. The Weather Research and Forecasting (WRF) Model's Community Variational/Ensemble Data Assimilation System: WRFDA. Bull. Amer. Meteor. Soc., v. 93, p. 831-843, 2012.

Cintra, R.S.; Campos Velho, H.F. Global Data Assimilation Using Artificial Neural Networks In Speedy Model. Proceedings of the 1st International Symposium on Uncertainty Quantification and Stochastic Modeling, 2012.

Daley, R.Atmospheric data analysis. Cambridge University Press, 466 p., 1991.

Dudhia, J. Numerical study of convection observed during the Winter Monsoon Experiment using a mesoscale two-dimensional model. J. Atmos. Sci., v. 46, n. 20, p. 3077-3107, 1989.

França, G.B.; Almeida, M.V.; Rossete, A.C. An Automated Nowcasting Model of Significant Instability Events in the Flight Terminal Area of Rio De Janeiro, Brazil. Atmospheric Measurement Techniques, v. 9, p. 2335-2344, 2016.

França, G.B.; Almeida, M.V.; Bonnet, S.M.; Albuquerque Neto, F.A. Nowcasting Model of Low Wind Profile Based on Neural Network Using SODAR Data at Guarulhos Airport, Brazil. International Journal of Remote Sensing,v. 39,n. 8, 2506-2517, 2018.

Grell, G.A.; Freitas,S.R. A scale and aerosol aware stochastic convective parameterization for weather and air quality modeling.Atmos. Chem. Phys.,v. 14, p. 5233-5250, 2014.

Hong, S.-Y.;Dudhia, J.; Chen, S.H. A revised approach to ice microphysical processes for the bulk parameterization of clouds and precipitation. Mon. Wea. Rev., v. 132, p. 103-120, 2004.

Hong, S.-Y.; Noh, Y.;Dudhia, J. A new vertical diffusion package with an explicit treatment of entrainment processes. Mon. Wea. Rev., v. 134, n. 9, p. 2318-2341, 2006.

Kalnay, E.Atmospheric Modeling, Data Assimilation and Predictability. Cambridge University Press, 368 p., 2002.

Lorenc, A.C. Analysis methods for numerical weather prediction. Q.J.R. Meteorol. Soc., v. 112, n. 474, p. 1177-1194, 1986.

Lorenc, A.C.;Jardak, M. A comparison of hybrid variational data assimilation methods for global NWP. Q. J. R.Meteorol. Soc.,v. 144, n. 717,p. 2748-2760, 2018.

Mlawer, E.J.; Taubman, S.J.; Brown, P.D.;Iacono, M.J.; Clough, S.A. Radiative transfer for inhomogeneous atmospheres: RRTM, a validated correlated-k model for the longwave. J. Geophys. Res., v. 102, n. D14, p. 16663-16682, 1997.

Parrish, D.F.;Derber, J.C. The National Meteorological Center's Spectral Statistical Interpolation analysis system. Mon. Wea. Rev.,v. 120, n. 8, p. 1747-1763, 1992.

Paulucci, T.B.;França, G.B.;Libonati, R.; Ramos, A.M.Long-Term Spatial-Temporal Characterization of Cloud-to-Ground Lightning in the Metropolitan Region of Rio De Janeiro. Pure and Applied Geophysics, v. 176, p. 5161–5175, 2019.

Silva, W.L.; Albuquerque Neto, F.A.;França, G.B.;Matschinske, M. Conceptual Model for Runway Change Procedure in Guarulhos International Airport Based on SODAR Data. The Aeronautical Journal,v. 120, n. 1227, p. 725-734, 2016.

Skamarock, W.C.;Klemp, J.B.;Dudhia, J.; Gill, D.O.; Liu, Z.; Berner, J.; Wang, W.; Powers, J.G.;Duda, M.G.; Barker, D.M.; Huang, X.-Y.A Description of the Advanced Research WRF Version 4. NCAR Tech. Note NCAR/TN-556+STR, 145 p., 2019.

Talagrand, O.Assimilation of observations, an introduction. J. Met. Soc., v. 75, n. 1B, p. 191-209, 1997.

Tewari, M.; Chen, F.; Wang, W.;Dudhia, J.;LeMone, M.A.; Mitchell, K.;Ek, M.;Gayno, G.;Wegiel, J.; Cuenca, R.H. Implementation and verification of the unified NOAH land surface model in the WRF model. 20th conference on weather analysis and forecasting/16th conference on numerical weather prediction, p. 11-15, 2004.

Zupanski, M.; Kalnay, E. Principles of data assimilation. In: Global energy and water cycles, K.A. Browning and R. J. Gurney, (eds) Cambridge: Cambridge University Press, p. 48-54, 1999.

Internet Resources

WRF website http://www2.mmm.ucar.edu/wrf/users/.

WRF User's Guide, http://www2.mmm.ucar.edu/wrf/users/docs/ user_guide_V4/WRFUsersGuide.pdf

Short-range forecasting system for meteorological convective events in Rio de Janeiro using remote sensing of atmospheric discharges

Vinícius Albuquerque de Almeida[1]

Gutemberg Borges França[1]

Haroldo Fraga de Campos Velho[2]

ABSTRACT

In this study, a method is presented for meteorological convective event forecasting at the terminal control area of the Galeão International Airport, Rio de Janeiro, Brazil, using machine learning, sounding and remotely sensed atmospheric discharge data from 2001 to 2016. A monthly and daily climatology were computed for the atmospheric discharge temporal distribution in the study area. Six machine learning models were trained and cross-validated for 10 years (2001-2010), and a test was produced for 6 years (2011-2016). The results showed that the deep learning fully-connected (dense) algorithm achieved the best results for storm forecast and severity based on the following statistics: probability of detection (0.91 and0.85), BIAS (1.03 and 1.07), false-alarm ratio (0.12 and 0.20) and CSI (0.81 and 0.69), respectively. The 6-year test analysis showed that the model has increasing performance for high-impact events, and this performance decreases gradually as the events become weaker and more frequent. The models presented here could be useful tools for air traffic management purposes.

Keywords: convective events, aeronautical meteorology, Galeão International Airport– Brazil, machine learning models, atmospheric discharge.

1. INTRODUCTION

Meteorological convective events (MCE) are usually related to many harmful effects to society, such as transportation disruption, interruption of energy distribution, landslides, flash floods, other financial impacts, and ultimately loss of lives. In particular, aviation may be severely affected by such events both in terminal control area (TCA), mainly in landing and take-off procedures, and in-flight routes. It is evident that for secure air traffic management, there is a high demand for precise short-range forecasts (minutes to hours), normally referred to as nowcasts, to guide TCA operations in particular.

Mass (2012), Sun et al. (2014), França et al. (2016), and Gultepe et al. (2019) presented comprehensive reviews regarding efforts that have been made in the context of nowcasting since the 1960s. The earliest work on nowcasting was mainly limited to the subjective interpretation and temporal extrapolation of meteorological radar (Wilson 1966; Battan 1973; Wilson and Wilk 1982) and satellite (Purdom 1976). To follow up this idea, the convective tracking approaches were improved by including the cell evolution in time and intensity

[1] *Laboratório de Meteorologia Aplicada, Departamento de Meteorologia-IGEO-CCMN, Universidade Federal do Rio de Janeiro (UFRJ), Rio de Janeiro, Brazil.*

[2] *Laboratório Associado de Computação e Matemática Aplicada (LABAC), Instituto Nacional de Pesquisas Espaciais (INPE), São Paulo, Brazil.*

using radar data, the TITAN algorithm (Dixon and Wiener, 1993). Johnson et al. (1998) presented the Storm Cell Identification and Tracking algorithm (SCIT), a centroid tracking algorithm with improved methods of identifying storms (both isolated and clustered). Wilson et al. (1998) reviews the status of forecasting convective precipitation for nowcasting showing two promising methods for thunderstorm evolution: knowledge-based expert systems and numerical forecasting models that are initialized with radar data (data assimilation). Lately, the data assimilation problem has been largely studied, e.g. Xue et al. (2003), Sun and Wilson (2003), Schroeder et al. (2006), Liu et al. (2008), and others. Mueller et al. (2003) presented a nowcast (up to 1 h) method to forecast thunderstorm locations based on a combination of different data types (surface, radar, satellite, and numerical modelling. Han et al. (2009) presented advances in the identification, tracking, and forecast of convective storm cells with enhancements to the aforementioned TITAN algorithm.

Some field experiments have been conducted to allow further development of nowcasting, such as the Chesapeake Bay Nowcasting Experiment (Scofield and Weiss 1977), the summer Olympics in Atlanta (Rothfusz et al. 1998), the Spring Forecast Experiment (Coniglio et al. 2010; Kain et al. 2003, 2010), and an experiment in Helsinki, Finland (Koskinen et al. 2011). Considering the aviation applications, Isaac et al. (2006, 2011, 2014) presented a sequence of works that resulted in a refined nowcasting system for aviation using data from numerical models, surface observations, radar, satellite, and a microwave radiometer to generate nowcasts of up to approximately 6 h for principal airports in Canada. Recently, França et al. (2018) presented a nowcast model for low-level wind profiles at Guarulhos International Airport, São Paulo, Brazil.

According to França et al. (2016), in Brazil, a meteorologist is currently using his experience (conceptual models on how the atmosphere works) to integrate different site-specific meteorological observations and/or atmospheric model outputs to generate nowcasts at principal airports. In particular, the TCA of Rio de Janeiro, the focus of this study, has five airports whose flights are significantly affected (by delays and trajectory changes), especially during the approximations for landing or take-off, by significant MCE, which are normally associated with convective weather. Groisman et al. (2005) discussed trends in intense precipitation in the

climate records, showing a systematic increase of very heavy precipitation since the 1940s in subtropical part of Brazil an increase of 58% in 100 years. França et al. (2016) presented a model based on neural network techniques to produce short-term and local-specific forecasts of significant instability for flights in the TCA of Rio de Janeiro with a performance for three forecast hours: BIAS (1.10, 1.42, and 2.31), the probability of detection (POD) (0.79, 0.78, and 0.67) and the false-alarm ratio (FAR) (0.28, 0.45, and 0.73). Paulucci et al. (2019) studied the spatial-temporal variability of cloud-to-ground atmospheric discharges in the metropolitan region of Rio de Janeiro, revealing that most atmospheric discharges observed over Rio de Janeiro were derived from the orographic effect, which spurs the formation of convective storms along the southern part of the slope. Additionally, this work shows that the peak levels of electrical activity were observed from 18:00 to 19:00 local time and most of the cloud-to-ground lightning events recorded over the analyzed period (2001-2016) occurred in austral summer.

The objective of the current study is to develop MCE nowcasting models (approximately 6 h in advance) for the TCA of Rio de Janeiro based on machine learning algorithms considering the characterizations of MCEs and their genesis via atmospheric discharges (AD) data and instability indices (extracted from the sounding profiles).

The present article is part of a sequence of studies related to nowcasting that have been successfully executed by the Applied Meteorological Laboratory at the Federal University of Rio de Janeiro, following Almeida (2009), Silva et al. (2016), França et al. (2016), França et al. (2018), and Paulucci et al. (2019).

2. DATA AND STUDY AREA

The Galeão International Airport (SBGL) is located in the city of Rio de Janeiro (RJ), Brazil, where latitude and longitude are approximately 22°48'18.9"S and 43°15'23.9"W, respectively. Figure 1 shows the study area and the influence of SBGL soundings. This area represents the approximate limit of influence of the airport sounding data to evaluate atmospheric conditions on the neighborhood. Also, Figure 1 shows the domain from which the remotely sensed atmospheric discharges were extracted. The time period of data used in this work was from January 2001 to December 2016. Table 1 describes the data characteristics.

Figure 1: Study area and region of influence of SBGL soundings.
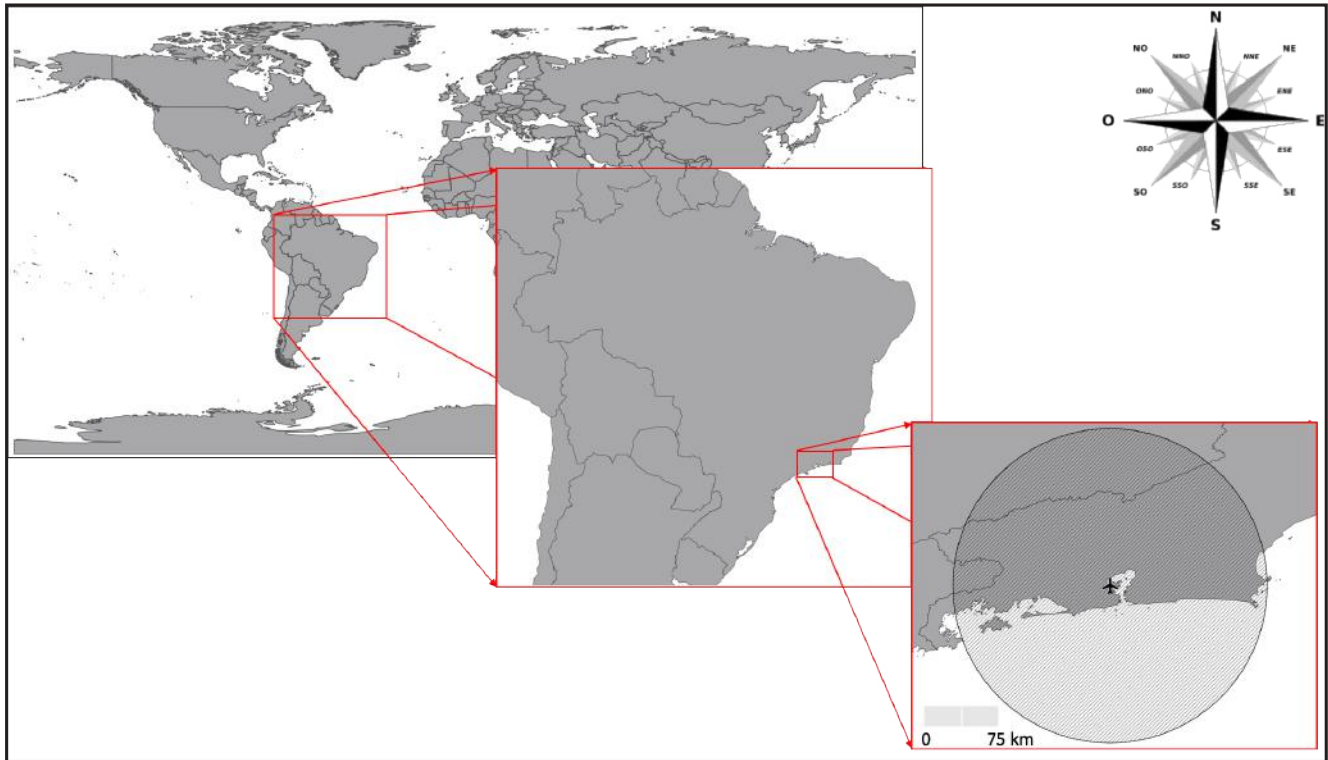
Table 1: Data source, description, and frequency of the data used for the events classification, training, validation and test for the forecast method proposed in this study.

Source	Description	Frequency	Data availability
Lightning detection network (RINDAT) http://www.rindat.com.br/	RINDAT is a network of detectors for the remote sensing of atmospheric discharges that covers most of the South-Central Brazil.	300 nanoseconds	2000-present
Atmospheric Sounding https://www.redemet.aer.mil.br	Atmospheric profiles of SBGL of temperature, relative humidity, atmospheric pressure, winds and sounding-derived atmospheric instability indices.	daily (12Z)	1977-present

3. METHODS

Figure 2 shows the steps sequence to obtain the optimum models, depictedin the following subsections.

3.1 Data Preprocessing

The main objective of this step was to initially review the data characteristics and to detect whether there were outliers and errors present.

According to Naccarato (2005), there are three main types of remotely sensed AD: (1) intracloud (IC), which occur inside the same storm cloud; (2) cloud-to-cloud (CC), occurring between different clouds; and (3) in the air (AIR), starting from a cloud and ending in the atmosphere, without reaching another cloud or the ground. AD striking the ground, also known simply as lightning, is classified into two basic types: (1) cloud-to-ground (CG), characterized by discharges that start from a cloud and reaching the surface of the Earth; and (2) ground-to-cloud (GC), occurring from the ground toward the cloud.

Figure 2: Methodological steps followed in this study.
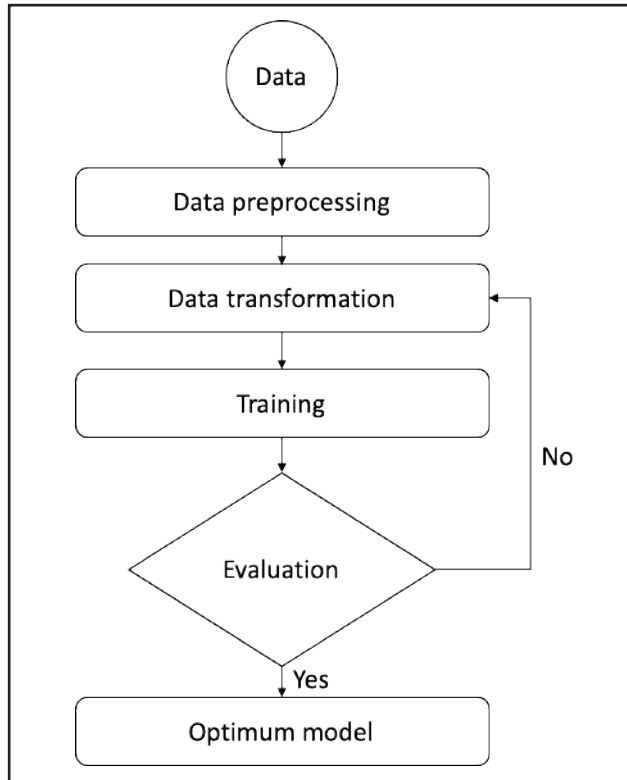
To understand the atmospheric discharge distribution in the study area, a monthly climatology spanning the 16 years of data was constructed. Figure 3 shows the monthly atmospheric discharge distribution curves for a region of 150-km radius centered at SBGL. From the distribution curve, it is possible to infer the following: (i) atmospheric discharge more often occurs from September to April, i.e., from austral spring to austral autumn; (ii) the maximum number of atmospheric discharge strikes is observed between December and March (region within the dashed black lines in figure 3), due to more energy available for convection and consequently the formation of convective clouds and atmospheric discharges occurrence (Christian et al. 2003; Paulucci et al., 2019); and (iii) the minimum is observed during austral winter.

Nascimento (2005) presents a review regarding the atmospheric indices normally used to identify favorable atmospheric conditions for MCE occurrence and maintenance, which highlights intense convective instability and vertical wind shear conditions in the atmosphere in South America (and specifically, in Brazil). Among other indices presented by the author, the following indices and thresholds were considered in the current paper: low or negative Showalter index (Showalter, 1947) values indicate more atmospheric instability; negative values of the Lifted index (Galway, 1956) are related to unstable conditions; Severe WEather Threat (SWEAT) index (Miller, 1972) values higher than 300 are considered favorable to severe storm formation. Total Totals Index (Miller, 1972) values higher than 40°C are related to storm formation. K Index (George, 1960) values higher than 30°C have a high potential for storm occurrence. Convective available potential energy (CAPE) (Houze, 1993) values higher than 1,000 J/kg are related to instability. Convective inhibition energy (CINE) (Houze, 1993) values close to zero are considered more favorable to atmospheric instability. In the current study, these seven atmospheric indices were selected and used to describe the thermodynamic state of the atmosphere for characterizing MCE genesis. Table 2 details the formulation of each index.

Figure 3: Monthly distribution of atmospheric discharge (AD) at the TCA along the 16 years of data for the region of 150-km radius centered at SBGL.
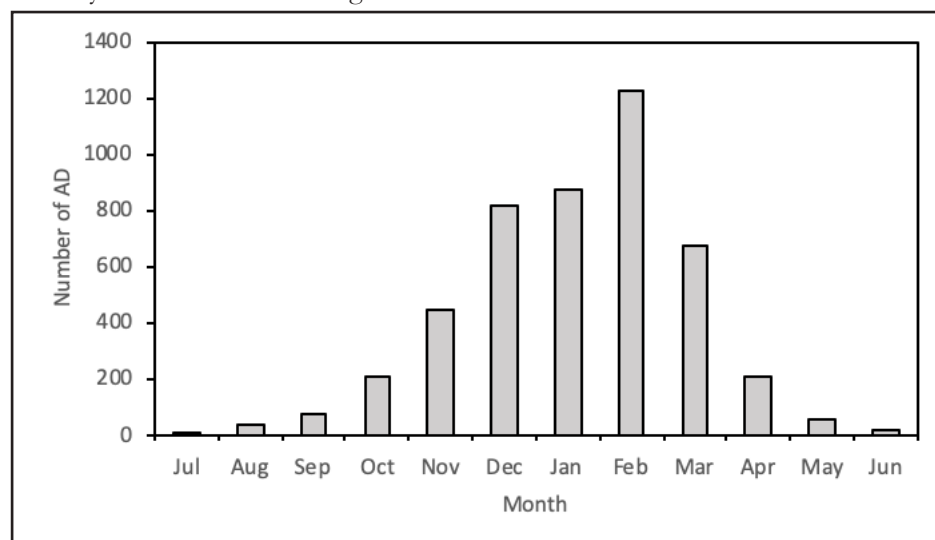
Table 2: Formulas and reference of the used atmospheric instability indices.

Indext	Formulationt	Referencet
Showalter	$S = T_{500} - T_{500\,(parcel)_{from\ 850hPa}}$	Showalter (1947)
Lifted Index	$LI = T_{500} - T_{(parcel)500}$	Galway (1956)
SWEAT	$SWEAT = 12 \times T_{d850} + 2 \times V_{850} + V_{500} + 20$ $\times (TT - 49) + 125 \times f(\alpha)$ $f(\alpha) = \exp\left(-\left(\frac{(\alpha - 90)}{40}\right)^2\right)$	Miller (1972)
Total Totals	$TT = T_{850} - T_{d850} - 2 \times T_{500}$	Miller (1972)
K	$K = (T_{850} + T_{d850}) - (T_{700} - T_{d700}) - T_{500}$	George (1960)
CAPE	$CAPE = g \int_{LFC}^{EL} \frac{T_{vp} - T_{va}}{T_{va}}\,dz$	Houze (1993)
CINE	$CINE = g \int_{SUP}^{LFC} \frac{T_{vp} - T_{va}}{T_{va}}\,dz$	Houze (1993)

*Observations: In equations, *T* and *Td* represent the air temperature and the dewpoint temperature, respectively. The values next to those variables refer to the isobaric levels (hPa) in which the variables should be measured. The index parcel refers to the parcel lifting, from an isobaric level to the assigned level. *Tvp* and *Tva* refer to the virtual temperature of a parcel and of the environment. EL refer to the equilibrium level, LFC the level of free convection and SUP the surface level. *V* refers to the wind at a specified isobaric level (hPa).

For completeness of the text and its brevity, the discussion about the statistical behavior of the atmospheric indices is not presented here. Some outliers and error records were found and highlighted to be treated on the data preparation step.

In this phase, a correlation analysis was also performed between AD and the atmospheric indices to verify which variables would be most related to AD and among themselves.

Correlation analysis among atmospheric instability indices showed high intercorrelation among some of them. Additionally, each index contains different information for the genesis and development of convective storms, and thus, all indices were used in the learning process of the predictive models used here.

3.2 Data Transformation

Following, there is an objective list of activities performed on this study for data preparation to the modeling step:

- Remotely sensed AD data were grouped in days and hours defining the events to be studied;
- Days without storms were added to the dataset defining 0 for the AD number. This procedure was applied to allow the model to differentiate between atmospheric conditions with and without AD;
- An integration was performed between atmospheric sounding derived indices and AD data;
- According to the 16-year hourly AD climatology (Figure 4), most AD occurs at night. Therefore, only AD records between 6 pm and midnight were retained. This period accounts for more than 65% of the recorded AD;
- A new binary variable (0: no-storm; 1: storm) was created to classify the events for the occurrence or absence of AD;

- The percentiles from 0.5 to 0.9 of AD for storm events were computed to determine the optimum threshold for storm severity classification;

- A new binary variable (0: no; 1: yes) was created classifying whether the AD records were above or below the severity threshold;

- All input variables were normalized to a common interval [-1,+1];

- Finally, the data were divided into two different datasets: (i) 2001-2010 for training and cross-validation and (ii) 2011-2016 for testing.

Table 3 summarizes the final input and output variables set used in the modeling step.

Table 3: Input and output variables and description.

Variable	Type	Description
Julian day	Input	Numeric value representing the number of days in the year after Jan 1st
Monthly mean		Numeric value representing the monthly mean of AD for that month etween 6pm and midnight
Showalter index		Numeric value extracted from SBGL sounding
Lifted index		
K index		
Total totals		
CAPE		
CINE		
Sweat		
Precipitable water		
Indices(julian day – 1)		Numeric value extracted from SBGL with a lag of one day
Storm? (yes/no)	Output	Boolean value representing the presence (yes) or absence (no) of AD on that record
SeverityP0.X? (yes/no)		Boolean value representing if the number of AD on that record is over (yes) or under (no) the percentile 0.X of the number of AD in storm events

Figure 4: Atmospheric discharge (AD) hourly cumulative probability density function (pdf). The upper-right region - defined by the intersection between the black dashed lines - shows that the AD cumulative probability from 18 to 23:59h (local time) is greater than 65%.
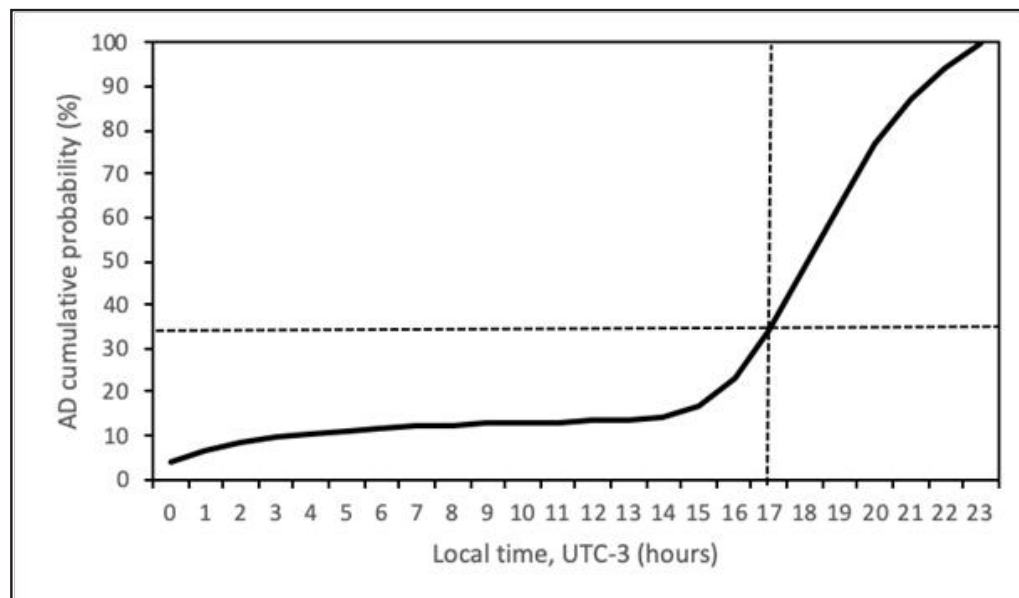
3.3 Training

The models were based on artificial intelligence to create the relation between the thermodynamic state of the atmosphere and storm occurrence and severity..

There are several classifiers in the Weka software package (developed by the University of Waikato, Frank et al., 2016), but for the present study, only the five classifiers described intable 4 (line 2-6) were used.A python routine was developed for the Deep Learning Fully-Connected (DL-FC) algorithm, which architecture is presented in Figure 5a and 5b, for storm forecast and severity, respectively.

Figure 5: Architecture for the DL-FC model for storm (a) forecast and (b) severity.
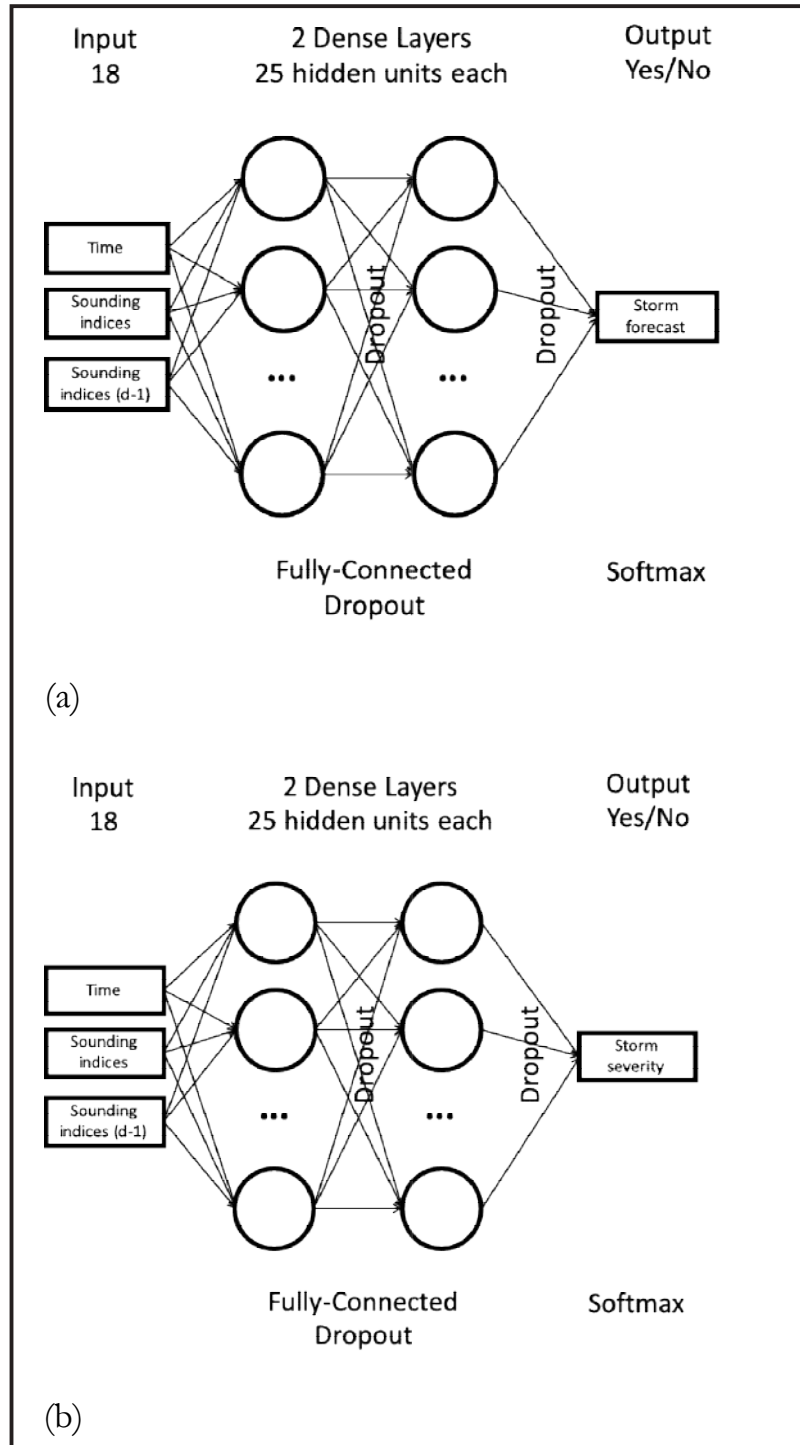
3.4 Evaluation

There are several strategies for evaluating machine learning algorithm performance to find the optimum model for the classification problem.

Here, the cross-validation method was chosen as a strategy for evaluating model performance. This evaluation method consists of the following steps:

- Split training set into N arbitrarily chosen folds. In general, ten folds is enough, and this number is the Weka's default;
- The training cycle runs Ntimes, and, at every iteration, N-1 folds are used for training, with the remaining fold used for validation. This procedure is repeated until every fold has been used both for training and validation.

- Statistics metrics are generated for every single fold, and the model performance is the average among them.

The statistical metrics are evaluated from the confusion matrix. This matrix has order N×N, where the columns represent the observed values, and the rows represent the forecast values (see Table 5 for a matrix example). Ideally, a perfect result occurs when only values on the main diagonal are verified, representing that all the forecasted and observed values match. Values out of the main diagonal from the confusion matrix imply that our model has an error, which should be well known for those who will use the results.

Table 6 shows the statistics obtained from the confusion matrix, which are shown in the Results section for the forecast model analysis. Table 6 presents the statistical values used in our study.

Table 5: Confusion Matrix.

			Observed		
			Yes	**No**	**Total**
Forecast	**Yes**		Hits (a)	False Alarm (b)	Forecast Yes
	No		Misses (c)	Correct Negatives (d)	Forecast No
Total			Observed Yes	Observed No	Total

Table 6: Statistics retrieved from the confusion matrix.

Statistic	Formula	Description
Probability of detection (POD)	$POD = \dfrac{a}{(a+c)}$	Measures the fraction of observed events that were correctly forecast. A perfect score is 1.
False alarm Ratio (FAR)	$FAR = \dfrac{b}{(a+b)}$	Measures the fraction of "yes" forecasts in which the event did not occur. A perfect score is 0.
BIAS	$BIAS = \dfrac{(a+b)}{(a+c)}$	Measures the ratio of the frequency of forecast events to the frequency of observed events. A perfect score is 1.
Critical Success Index (CSI)	$CSI = \dfrac{a}{(a+b+c)}$	This statistic combines hit rate and falser alarm ration in one statistic. It does not consider the "not forecast/ not occurred" (d) events. This score ranges from zero (0) from one (1), the perfect score.

3.5 Test

After finding the optimum models for storm forecast and severity a test was performed for the period from 2011 to 2016. The test is a simulation of what can be expected as the model's performance after its operational deployment.

4. RESULTS AND DISCUSSION

This section summarizes the testresults for storm forecasts (4.1) and storm severity (4.2) models built on the training dataset (2001-2010). Additionally, the results from a 6-year test (2011 to 2016) are presented (4.3).

4.1 Storm forecast

This section describes the results for the 9-h storm forecast based on the 9-h local time sounding at the International Airport of Rio de Janeiro. Positive events indicate the occurrence of forecasted convective activity at the TCA of Rio de Janeiro with atmospheric discharge.

Figure 6a and Table 7 present the cross-validation results on the training dataset (2001-2010) for storm forecast using algorithms defined inTable 4.

Analyzing the model performance, most of the results are on or above the optimum threshold– here defined as the region where both POD and (1-FAR) statistics are greater than 80%.

(a)

(b)
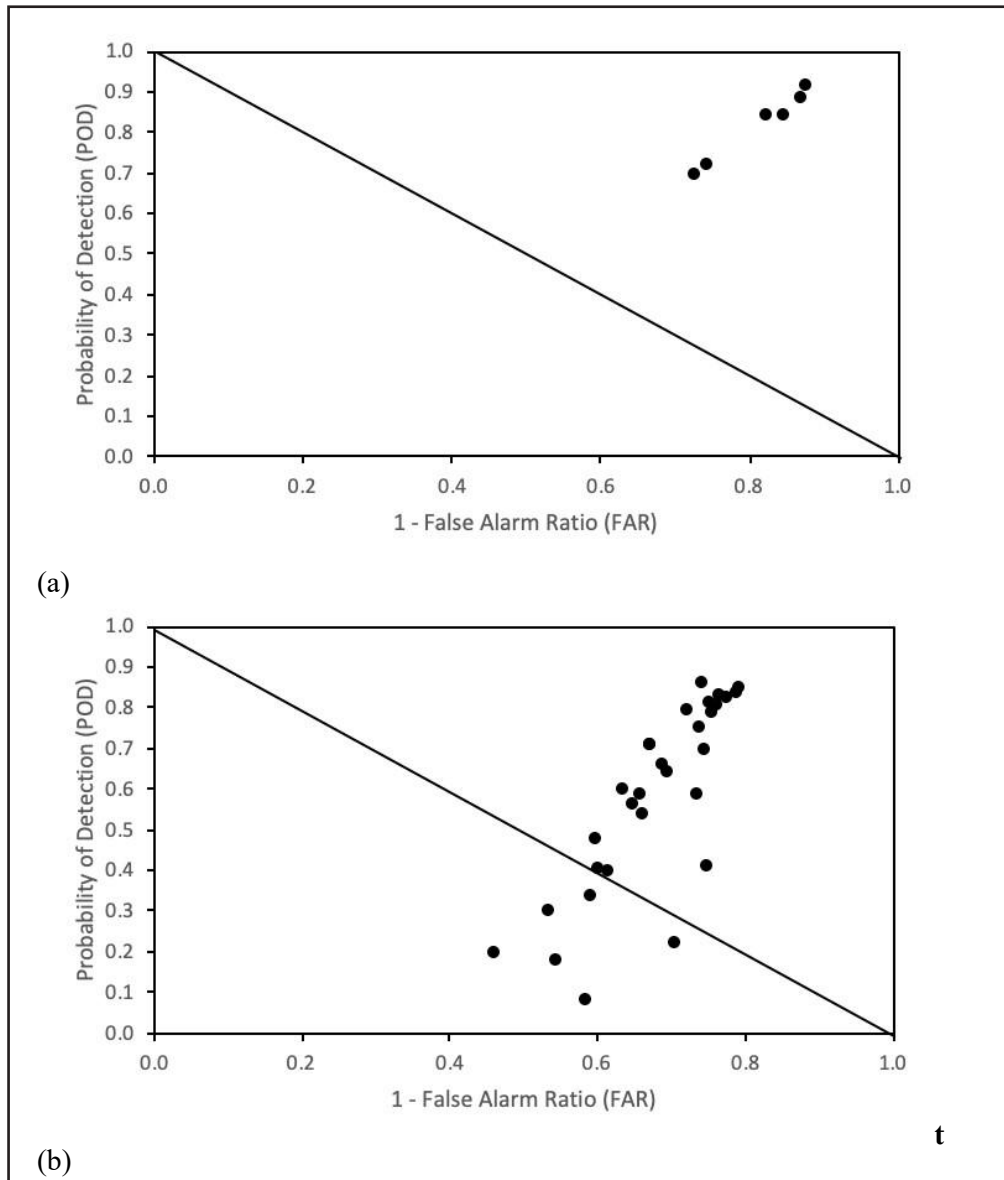
The DL-FC model showed results with values of 0.91, 0.12 and 0.809 for POD, FAR and CSI, respectively. Also, the decision tree algorithms (J48 and Random Forest) and the Voting committee achieved CSI values greater than 0.70.

Comparing the results, they are divided in decision trees (J48 and random forest) and neural networks (Multilayer Perceptron - MLP, Radial Basis Function - RBF and Deep Learning - DL) algorithms, respectively. In relation to the decision tree algorithms (lines 1 and 2, Table 4), the increase of performance from the single decision tree (J48) to the random forest is related to the skill of the latter to learn more patterns since it consists of multiple trees trained from different combination of input parameters. Regarding to the neural network algorithms (lines 3, 4 and 6, Table 4), it is evident that the DL algorithm outstands the other methods (MLP and RBF) since, e.g., POD of DL is higher than MLP and RBF by 20% and 22%, respectively. The reason for the learning improvements on the DL versus MLP and RBF (shown in statistics of Table 4) are mainly due to the use of (i) more layers and hidden units; (ii) regularization method (dropout); and (iii) Adam optimizer (Kingma and Lei Ba, 2014). Also, the DL results are slightly better than the decision tree, as shown by POD, FAR and CSI values in Table 4. Finally, the voting committee performs worse than the Random Forest, penalized by the poor performance of the MLP and RBF methods.

4.2 Storm severity

Figure 6b presents the cross-validation results on the training dataset (2001-2010) for storm severity using algorithms defined in Table 4 for all possible percentiles of AD in storm events.

As may be noted, most of the models are located in the optimum region – here defined as the region where both POD and (1-FAR) statistics are greater than 70%. However, there is a greater dispersion of results compared with the results presented in Table 7, which was expected, since here the percentile thresholds for storm severity from 50% to 90% were used, which has gradually increased the difficulty of modeling.

The models performed poorly to classify events with more than 438.0 h-1 (90% percentile) with CSI values mostly under 0.6. The performance gradually increases for lower thresholds, since the events get more frequent. For the of 91 h-1 (70% percentile) threshold the DL-FC algorithm shows values of 0.845, 0.207 and 0.69 for POD, FAR and CSI, respectively.

4.3 Test results for the 2011-2016 data period

To clarify how the 6-h MCE forecast model results were analyzed, the following steps were carried out:
- The thermodynamic indices were computed using 12Z sounding, which are regularly available at SBGL approximately 13:30Z;
- Considering the 16-year hourly AD climatology (Figure 4), the storm occurrence was defined based on the existence of at least one AD between 6 pm and midnight;
- Based on the 0.7 percentile of AD on storm events (91 h-1 AD), the severity parameter was defined.

Figure 7 presents a hit and error rate for all events on the test dataset, using the DL-FC algorithm, that was selected here based on the analysis of the maximum POD and minimum FAR for storm forecasting and severity. It is noteworthy that as the events become more intense and rarer, the prediction model becomes more precise on storm forecast. However, weaker events tend to be more frequent, leading to greater prediction errors. As noted, for weaker events (under 1,000 AD), the model performance decreases for storm forecast. As the events became stronger, progressively, there was an increase in performance. Events with more than 3,000 AD are almost always predicted (only 3 errors).

Table 7: Results of storm forecast with approximately 6 h in advance.

Algorithm	POD (Ideal value 1)	FAR (Ideal value 0)	1-FAR (Ideal value 1)	BIAS (Ideal value 1)	CSI (Ideal value 1)
J48	0.84	0.17	0.83	1.01	0.71
Random Forest	0.88	0.13	0.87	1.01	0.78
MLP Classifier	0.71	0.26	0.74	0.96	0.57
RBF Classifier	0.69	0.27	0.73	0.94	0.55
Vote	0.84	0.15	0.85	0.99	0.73
DL-FC	0.91	0.12	0.88	1.03	0.81

Figure 7: Test analysis for 2011 to 2016 considering different thresholds for atmospheric discharge (AD) events.
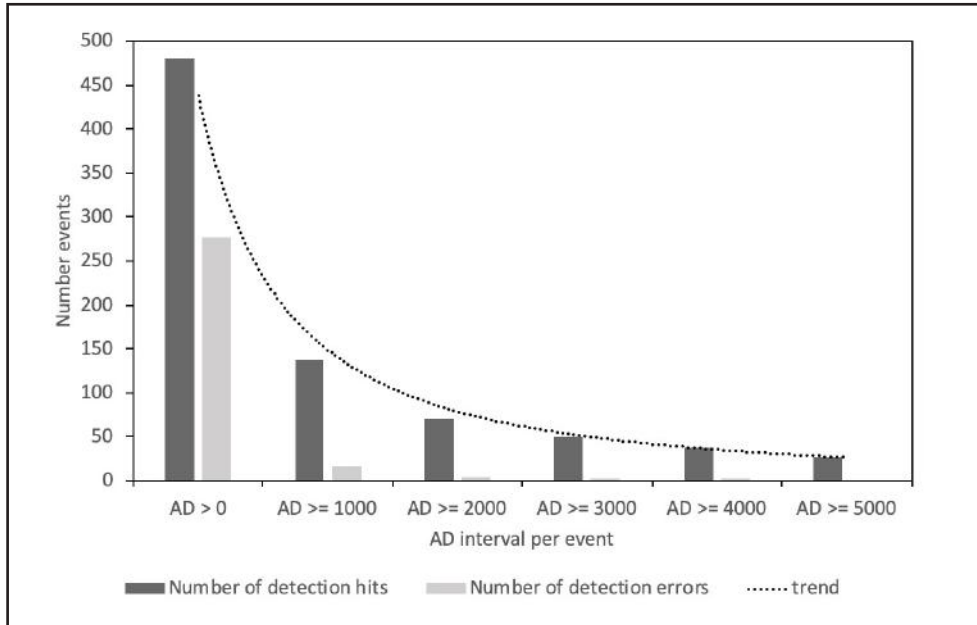
For the completeness of this work, Table 8 presents the most intense events on the test dataset – ordered in decreasing order by the daily accumulated AD between 6 pm and midnight. It is important to note, for the selected events, the AD ranged between 4,966 and 15,122; that is, these were relevant events that occurred in the study area.

Considering this subset, the optimum model (DL-FC) correctly predicted all storm occurrence.

5. CONCLUSIONS

This study developed techniques for forecasting meteorological convective events in theflight terminal area of Rio de Janeiro using different computational intelligence algorithms, remotely sensed atmospheric discharge data for classifying storm occurrence and severity, and atmospheric instability indices. The main conclusions of this work are summarized as follows:

- The analysis of the results showed that the deep learning fully-connected model presented the highest results for storm forecast and severity, respectively, considering POD, FAR and CSI values;
- The error analysis showed that most of the incorrect predictions were related to low-intensity events. Therefore, the models presented here can be used for high-intensity events, which have the greatest potential to disrupt aviation operations;
- The 6-year test analysis showed that the model can be used for operational application by the aviation sector;

- The model can be a potential tool for elaborating the standard meteorological messages of significant weather (with six hours in advance) for aviation in the TCA of Rio de Janeiro;
- The results presented a development from our previous work (França et al., 2016) with increase (decrease) of POD (FAR) for storm forecast and included storm severity forecasts of AD events;
- It is important to highlight the importance of remotely sensed data (e.g. atmospheric discharges) for the development of improved models for weather forecasts aligned to the aviation purposes.

In the future, these models will be improved to predict the most likely areas (or sector of the TCA) to be affected by MCEs. A complete analysis of the synoptic conditions related to the most intense events should be studied to develop a conceptual model of storm genesis and intensification. In addition, the use of remotely sensed atmospheric profiles and derived atmospheric instability indices from high-frequency satellite data may be useful for applying this forecasting technique to flight routes and areas in which there is no sounding available.

ACKNOWLEDGEMENTS

Table 8: Results of storm forecast for the top 30 events of the test dataset.

Year	Month	Day	Forecast	DA
2016	2	20	yes	15122
2016	2	17	yes	12973
2014	1	16	yes	11075
2012	12	30	yes	10988
2013	3	5	yes	10478
2016	3	6	yes	10053
2016	3	23	yes	9750
2012	12	27	yes	9026
2016	12	12	yes	8936
2016	12	22	yes	8437
2016	12	8	yes	8129
2012	12	29	yes	7922
2015	11	8	yes	7720
2016	2	22	yes	7518
2016	2	15	yes	7359
2014	2	28	yes	6956
2016	2	28	yes	6696
2012	12	13	yes	6525
2016	12	31	yes	6198
2013	3	4	yes	5867
2013	12	10	yes	5809
2016	2	25	yes	5753
2013	3	9	yes	5681
2016	2	27	yes	5568
2013	2	26	yes	5541
2012	12	12	yes	5473
2012	12	17	yes	5436
2013	1	15	yes	5358
2013	1	14	yes	4980
2012	12	14	yes	4966

REFERENCES

Albers, S. C.: The LAPS wind analysis. Wea. Forecasting, 10, 342–352, 1995.

Almeida, M. V.: Aplicação de Técnicas de Redes Neurais Artificiais na Previsão de curtíssimo prazo da Visibilidade e Teto para o Aeroporto de Guarulhos – SP. Doctoral dissertation, COPPE/UFRJ, Federal University of Rio de Janeiro, Brazil, 2009.

Battan, L. J.: Radar Observations of the Atmosphere. University of Chicago Press, 324 pp, 1973.

Christian, H. J., Blakeslee, R. J., Boccippio, D. J., Boeck, W. L., Buechler, D. E., Driscoll, K. T., ... & Stewart, M. F. (2003). Global frequency and distribution of lightning as observed from space by the Optical Transient Detector. Journal of Geophysical Research: Atmospheres, 108(D1), ACL-4.

Coniglio, M. C., Elmore, K. L., Kain, J. S., Weiss, S. J., Xue, M. and M. L. Weisman: Evaluation of WRF model output for severe weather forecasting from the 2008 NOAA Hazardous Weather Testbed spring experiment. Wea. Forecasting, 25, 408–427, 2010.

Dixon, M. and G. Wiener: TITAN: Thunderstorm identification, tracking, analysis and nowcasting—A radar based methodology. J. Atmos. Oceanic Technol., 10 (6): 785-797, 1993.

França, G. B., Almeida, M. V., and Rossete, A. C.: An Automated Nowcasting Model of Significant Instability Events in the Flight Terminal Area of Rio De Janeiro, Brazil. Atmospheric Measurement Techniques 9: 2335–2344. doi:10.5194/amt-9-2335-2016, 2016.

—, —, Bonnet S. M., and Albuquerque Neto F. A.: Nowcasting model of low wind profile based on neural network using SODAR data at Guarulhos Airport, Brazil, International Journal of Remote Sensing, 39:8, 2506-2517, doi: 10.1080/01431161.2018.1425562, 2018.

Frank, E., Hall, M. A., and Witten, I. H.: The WEKA Workbench. Online Appendix for "Data Mining: Practical Machine Learning Tools and Techniques", Morgan Kaufmann, Fourth Edition, 2016.

George, J. J.: Weather Forecasting for Aeronautics. Academic Press, 673 pp, 1960.

Golding: Quantitative precipitation forecasting in the UK. J. Hydrol., 239, 286–305, 2000.

Groisman, P. Y., Knight, R. W., Easterling, D. R., Karl, T. R., Hegerl, G. C., and Razuvaev, V. N.: Trends in intense precipitation in the climate record, J. Climate, 18, 1326–1350, 2005.

Gultepe, I. ; Sharman, R. ; D.williams, P. ; Zhou, B. ; Ellrod, G. ; Minnis, P. ; Trier, S. ; Griffin, S. ; Yum, S. S. ; Gharabaghi, B. ; Feltz, W. ; Temimi, M. ; Pu, Z. ; Storer, L. N. ; Kneringer, P. ; Weston, M. J. ; Chuang, H. ; Thobois, L. ; Dimri, A. ; Dietz, S. ; França, G. B. ou Gutemberg Borges França ; Almeida, M. V. ; F. L. Albuquerque Neto . A Review of High Impact Weather for Aviation Meteorology. PURE AND APPLIED GEOPHYSICS , v. xxx, p. 1-53, 2019.

Han, L., S. X. Fu, L. F. Zhao, Y. G. Zheng, H. Q. Wang and Y. J. Lin: 3D convective storm identification, tracking, and forecasting-An enhanced TITAN algorithm. J. Atmos. Oceanic Technol., 26 (4): 719-732, 2009.

Haykin, S.: Neural Networks: A Comprehensive Foundation. New Jersey, NJ: Prentice Hall, 1999.

Houze, R. A: Cloud Dynamics. Academic Press, 573 pp, 1993.

Isaac, G. A., Bailey, M., Cober, S. G., Donaldson, N., Driedger, N., Glazer, A., Gultepe, I., Hudak, D., Korolev, A., Reid, J., Rodriguez, P., Strapp, J. W., and Fabry, F.: Airport Vicinity Icing and Snow Advisor, in: AIAA 44th Aerospace Sci. Meeting and Exhibit, Reno Nevada, AIAA-2006-1219, 2006.

—, —, Boudala, F., Cober, S. G, Crawford, R., Donaldson, N., Gultepe, I., Hansen, B., Heckman, I., Huang, L., Ling, A., Reid, J., and Fournier, M.: Decision Making Regarding Aircraft De-Icing and In-Flight Icing Using the Canadian Airport Nowcasting System (CAN-Now), in: SAE 2011 International Conference on Aircraft and Engine Icing and Ground Deicing, 13–17 June 2011, Paper Number: 2011-38-0029; doi:10.4271/2011-38-0029, 2011.

—, —, —, Burrows, W. R., Cober, S. G., Crawford, R. W., Donaldson, N., Gultepe, I., Hansen, B., Heckman, I., Huang, L. X., Ling, A., Mailhot, J., Milbrandt, J. A., Reid, J., and Fournier, M.: The Canadian airport nowcasting system (CAN-Now), Meteorol. Appl., 21, 30–49, 2014.

Johnson, J.T., P.L. Mackeen, A. Witt, E.D. Mitchell, G. Stumpf, M.D. Eilts, and K.W. Thomas: The Storm cell identification and tracking algorithm: an enhanced WSR-88D algorithm. Wea. Forecasting, 13, 263-276, 1998.

Kain, J. S., P. R. Janish, S. J. Weiss, R. S. Schneider, M. E. Baldwin, and H. E. Brooks: Collaboration between forecasters and research scientists at the NSSL and SPC: The spring program. Bull. Amer. Meteor. Soc., 84, 1797–1806, 2003.

— , and Coauthors: Assessing advances in the assimilation of radar data and other mesoscale

observations within a collaborative forecasting–research environment. Wea. Forecasting, 25, 1510–1521, 2010.

Diederik P. Kingma and Jimmy Lei Ba. Adam : A method for stochastic optimization. 2014. arXiv:1412.6980v9

Koskinen, J. T., and Coauthors: The Helsinki testbed: A mesoscale measurement, research, and service platform. Bull. Amer. Meteor. Soc., 32, 325–342, 2011.

Liu, Y., Warner, T. T., Bowers, J. F., Carson, L. P., Chen, F., Clough, C. A., Christopher, A. D., Craig, H. E, C. h., Halvorson, S. F., Terrence, W. H. Jr., Lachapelle, L., Malone, R. E., Daran, L. R., Sheu, R.-S., Swerdlin, S. P., and Weingarten, D. S.: The opera- tionalmesogamma-scale analysis and forecast system of the US Army Test and Evaluation Command. Part I: Overview of the modeling system, the forecast products, and how the products are used, J. Appl. Meteorol. Clim., 47, 1077–1092, 2008.

Mass, C.: Nowcasting the promise of new technologies of communication, modelling, and observation, B. Am. Meteorol. Soc., 93, 797–809, 2012.

Miller, R. C.: Notes on analysis and severe storm forecasting procedures of the Air Force Global Weather Central. Tech. Report 200, Air Weather Service, United States Air Force, 190 pp, 1972.

Mueller, C., Saxen, T., Roberts, R., Wilson, J., Betancourt, T., Det- tling, S., Oien, N., and Yee, J.: NCAR auto-nowcast system, Weather Forecast, 18, 545–561, 2003.

Naccarato, K. P.: Lightning Characteristics In Southeastern Brazil. INPE, São José dos Campos, INPE-8380-TDI/770,(PhD Thesis), 2005.

Nascimento, E. L.:Severe Storms Forecasting Utilizing Convective Parameters And Mesoscale Models: An Operational Strategy Adoptable In Brazil? RevistaBrasileira de Meteorologia, v. 20, p. 121-140, 2005.

Paulucci, T. B.; Gutemberg, F.; Libonati, R.; Ramos, A. M.: Long-Term Spatial–Temporal Characterization of Cloud-to-Ground Lightning in the Metropolitan Region of Rio de Janeiro. Pure and Applied Geophysics. 10.1007/s00024-019-02216-1, 2019.

Purdom, J.: Some uses of high-resolution GOES imagery in the mesoscale forecasting of

convection and its behavior. Mon. Wea. Rev., 104, 1474–1483, 1976.

Rothfusz, L. P., M. R. McLaughlin, and S. K. Rinard: An overview of NWS weather support for the XXVI Olympiad. Bull. Amer. Meteor. Soc., 79, 845–860, 1998.

Schroeder, A., Stauffer, D. R., Seaman, N. L., Deng, Gibbs, A., Hunter, G. K., and Young, G. S.: An automated high-resolution, rapidly relocatable meteorological nowcasting and prediction system, Mon. Weather Rev., 134, 1237–1265, 2006.

Scofield , and C. C. Weiss: A report on the Chesapeake Bay region nowcasting experiment. NOAA Tech. Memo. NESS 94, 52 pp, 1977.

Silva, W. L., Albuquerque Neto, F. A., França, G. B. and Matschinske, M.: Conceptual Model for Runway Change Procedure in Guarulhos International Airport Based on SODAR Data. The Aeronautical Journal 120 (1227): 725–734. doi:10.1017/aer.2016.33, 2016.

Showalter, A. K.: A stability index for forecasting thunderstorms. Bulletin of the American Meteorological Society, v. 34, p. 250-252, 1947.

Sun, J., M.Xue, J. W. Wilson, etc.: Use of NWP for Nowcasting Convective Precipitation: Recent Progress and Challenges. Bull. Amer. Meteor. Soc., 95, 409–426, 2014.

Dixon, M. and G. Wiener, 1993: TITAN: Thunderstorm identification, tracking, analysis and nowcasting—A radar based methodology. J. Atmos. Oceanic Technol., 10 (6): 785-797.

Wilson, J. W.: Movement and predictability of radar echoes. National Severe Storms Laboratory Tech. Memo ERTM-NSSL-28, 30 pp, 1966.

Wilson , and K. E. Wilk: Nowcasting applications of Doppler radar. Nowcasting, K. Browning, Ed., Academic Press, London, 87–105, 1982.

Wilson, J.W., N. A. Crook, C. K. Mueller, J. Sun and M. Dixon: Nowcasting Thunderstorms: A Status Report. Bull. Amer. Meteor. Soc., 79, 2079-2099, 1998.

Xue, M., Wang, D., Gao, J., Brewster, K., and Droegemeier, K. K.: The Advanced Regional Prediction System (ARPS), storm-scale numerical weather prediction and data assimilation, Meteorol. Atmos. Phys., 82, 139–170, 2003.

Precipitation Nowcasting with Weather Radar Images and Deep Learning in São Paulo, Brasil

Suzanna Maria Bonnet [1]

Alexandre Evsukoff [1]

Carlos Augusto Morales Rodriguez [2]

ABSTRACT

Precipitation nowcasting can predict and alert for any possibility of abrupt weather changes which may cause both human and material risks. Most of the conventional nowcasting methods extrapolate weather radar echoes, but precipitation nowcasting is still a challenge, mainly due to rapid changes in meteorological systems and time required for numerical simulations. Recently video prediction deep learning (VPDL) algorithms have been applied in precipitation nowcasting. In this study, we use the VPDL PredRNN++ and sequences of radar reflectivity images to predict the future sequence of reflectivity images for up to 1-h lead time for São Paulo, Brazil. We also verify the feasibility for the continuous use of the VPDL model, providing the meteorologist with trends and forecasts in precipitation edges regardless of the weather event occurring. The results obtained confirm the potential of the VPDL model as an additional tool to assist nowcasting. Even though meteorological systems that trigger natural disasters vary by location, a general solution can contribute as a tool to assist decision-makers and consequently issue efficient alerts.

Keywords: *precipitation nowcasting; spatiotemporal forecast; video prediction deep learning; weather radar.*

1. INTRODUCTION

The occurrence of severe weather events, such as storms, tornadoes, lightning, strong winds, can cause damage to human lives and social, economic and environmental assets of communities and countries [1–3]. According to Golnaraghi et al. [1], between 1970 and 2012, floods, mass movement, and storms accounted for 85% of disasters linked to weather, climate and water extremes, responsible for more than 1 million deaths and caused an economic loss of about USD 2 billion across the globe. Moreover, floods are expected to be more complex and affect more people with temperature rise due to climate change [4,5].

In addition to people in situations vulnerable to severe weather phenomena, floods also affect decision-makers in disaster management, energy, agriculture and aviation agencies, which are responsible for safety and administration. The possibility of obtaining accurate hazardous weather warnings at least one hour in advance could help in the planning and mobilization of the responsible agencies and may contribute to reducing losses, mitigating damage and saving lives.

Precipitation nowcasting tools have been used to forecast severe weather events. Briefly, this comprises a detailed description of the current weather to make predictions for a small range (meters to few kilometers) and for a short period of time (0 to 6 h) [6]. In general, severe storms are localized, with a small spatial area and a short duration (life cycle). One type of precipitation nowcasting is based on weather radars, due to its high spatial (~1 km) and temporal resolutions (~5 min) [6–10].

Several methodologies applicable to nowcasting can be found in the literature, from the analysis of meteorological variables, such as the evaluation of images from weather radars or satellites [9,11–14], evaluation of observed meteorological variables like wind and precipitation, and instability indexes from radiosonde [9,11–14], to predicting methods, such as models of Eulerian persistence [10,15], models of Lagrangian persistence (e.g., optical flow) [10,15], models of mathematical extrapolation of images from weather radars or satellites [9–11,15–18] and

[1] *Civil Engineering Program/COPPE, Federal University of Rio de Janeiro, Rio de Janeiro 21941-909, Brazil; alexandre.evsukoff@coc.ufrj.br, suzanna@coc.ufrj.br*

[2] *Department of Atmospheric Sciences, University of São Paulo, São Paulo 05508-090, Brazil; carlos.morales@iag.usp.br*

computational intelligence models [19–21]. Nowcasting systems can use only one of these methods or combine several of them [11,12,18].

The most-used predicting method for nowcasting is the extrapolation model: either based on cell tracking or based on area tracking. The former is principally designed to locate severe weather objects (mostly convective), while the latter is better for stratiform precipitation. These models use many radar products, such as volume scan, the definition of the movement field for system advection, fixed reflectivity, precipitation relationship, and fixed thresholds for system detection (such as size and intensity) [10,17].

Extrapolation models conserve the elements in the image and advect these elements by a motion field or vector, so they only change the position of the storm cells; taking a cloud as an example of an image element, these models cannot predict dissipation due to rain, or the formation of a new cloud where there was nothing before [22]. In addition, observed storms cannot significantly deviate from their path [13]. Pierce et al. [15] enumerated some limitations in nowcasting models. For example, a typical error is the identification of the storm, leading to tracking errors (speed and direction) and the wrong estimate of intensity. Additionally, because of mistakes in the estimation of size and lifetime, the forecast quality decrease.

Extrapolation models do not take physical processes into account, unless the nowcasting system uses a field of a numerical weather prediction model as input, the usage of this method is restricted in time (~60 min) and space, due to the nonlinearity of meteorological systems and cloud dynamics [10]. So, only very complex nowcasting systems (e.g., the Auto Nowcast system [23]), that combine many techniques and observational data, are able to predict storm initiation or decay. Furthermore, some points that limit the predictability of nowcasting are: intrinsic features of weather events [24]; model definition and parameterizations [24]; topography [24]; observational data, that may contain uncertainty, noise, spurious data, and insufficient spatial and temporal coverage [20,24]; computational resources, which are still limited to evaluate and integrate information to solve these problems in time to be used for decision-making [20].

Apart from conventional methods, recent applications of video prediction deep learning (VPDL) algorithms using weather radar images have shown good possibilities for precipitation nowcasting [25]. These are data-driven models that show promise for the building and integration of understanding the weather system [26]. VPDL combines computer vision (convolutional layers) with the memory of temporal aspects of the time series (recurrent layers) in a data-driven spatiotemporal model. Most of these solutions are not specific for precipitation nowcasting, and they have

been used for diverse datasets such as moving-MNIST [27], people movement [28], and animal migration [29].

Shi et al. [27] proposed the Convolutional Long Short-Term Memory (ConvLSTM) neural network unit to model the spatiotemporal relationships between frames of a video, extending the idea of fully connected LSTM to convolutional structures. The ConvLSTM model was applied to precipitation nowcasting [27].

Wang et al. [28] proposed the Predictive Recurrent Neural Network (PredRNN) model, composed by spatiotemporal LSTM (ST-LSTM) as the basic unit. Different from the ConvLSTM unit, which has only temporal memory, the ST-LSTM unit memorizes both spatial appearances and temporal variations. As in Shi et al. [27], PredRNN was also applied to the weather radar sequences of images.

Shi et al. [30] proposed the Trajectory Gated Recurrent Unit (TrajGRU) algorithm, which learns the location-variant structure—intrinsic of natural motion, as an improvement of the ConvLSTM. Tran, and Song [31], following the suggestions of Klein et al. [32] and Mathieu et al. [33], adapted the TrajGRU model using image quality assessment metrics as the loss function for the same problem of precipitation nowcasting, in order to reduce the blurry image issue.

Franch et al. [25] presented a method to improve the nowcasting skills of VPDL models, in particular for extreme rain rates, by combining orographic features with a model ensemble. They used the TrajGRU algorithm as a baseline model to build the ensembles, where the ensemble members have different rain thresholds as input. The proposed method doubled the forecasting skill of the VPDL model in extreme precipitations.

Purely VPDL models are subject to the same restriction as any model using just mathematical extrapolation of images. Both lack the physics and dynamics behind cloud formation and dissipation that would differentiate the application of video prediction for nowcasting problems from common video prediction problems, such as the movement of digits [34]. Nevertheless, we expect the VPDL to learn the effect of the topography and dynamics of the cloud life cycle from a series of reflectivity images.

In this study, we evaluate the applicability of a VPDL model as a tool to support nowcasting. We also evaluate the feasibility of the continuous use of the VPDL model, providing the meteorologist with trends and forecasts in precipitation edges regardless of the weather event occurring. We predict reflectivity images and precipitation edges from weather radar images for up to 1-h lead time using the PredRNN++ model [35] as a VPDL model and radar reflectivity at only one level of measurement (0.5° Plan Position Indicator—PPI) as a single input. The PredRNN++ model is compared to the conventional

precipitation nowcasting model, Ensemble NowCASTing (ENCAST), which is the model operationally used by the Hydraulic Technology Center Foundation (FCTH, Portuguese acronym), in three case studies. We evaluate the model's performance and propose a number of improvements. Even though meteorological systems that trigger natural disasters vary by location, a general solution can contribute as a tool to assist decision-makers and consequently issue efficient alerts.

This paper is organized as follows. The next section presents the datasets used in this work and briefly discusses the models. Section 3 presents the experimental setup and evaluation measures. Section 4 presents results and discussion, and Section 5 the conclusions of the work.

2. MATERIALS AND METHODS

2.1 Dataset

This study uses a dual-polarization S-band (SPOL) Doppler weather radar from the Department of Water and Electric Energy, DAEE (Portuguese acronym), manufacture Selex ES GmbH, installed at Ponta Nova [36], State of São Paulo, Brazil, at latitude 23°36' S, longitude 45°58'20" W (Figure 1a). The radar is operated by the Hydraulic Technology Center Foundation, FCTH (Portuguese acronym) and it is configured to cover a distance of 240 km with 250 m gate resolution (gate or bins are discrete illuminated volume that are sampled by pulsed weather radars). It makes measurements at eight elevation angles and completes a volume scan every 5 min. As a note, one sweep represents a Plan Position Indicator (PPI). At each sweep the radar beam rises in the atmosphere as it moves away from the radar due to Earth curvature and variation
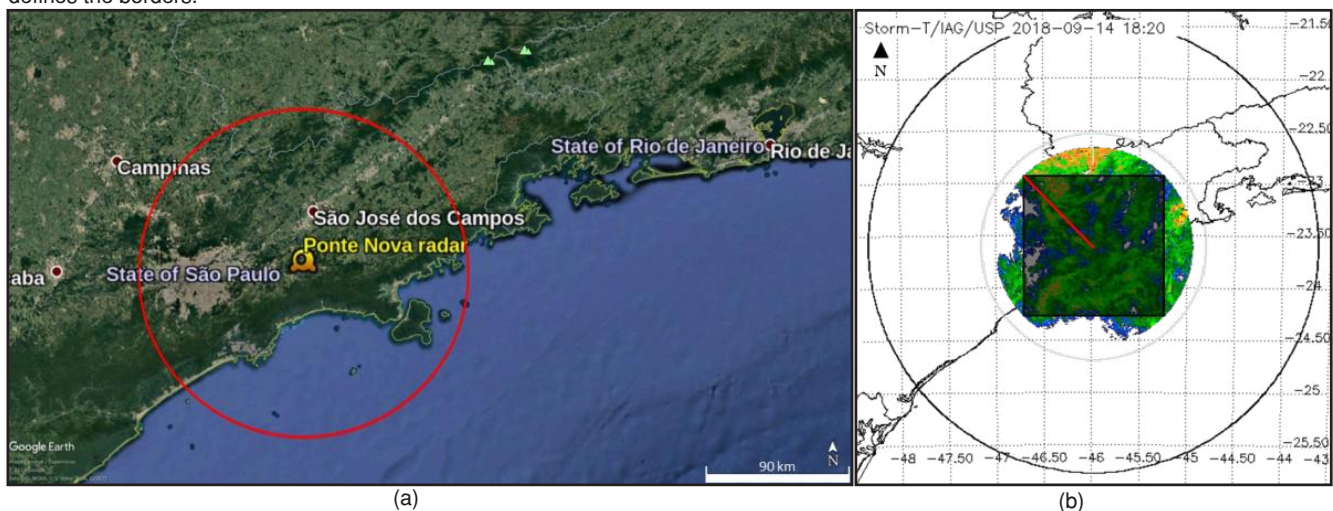
of the refractive index in the atmosphere, for example, the beam at an elevation angle of 0.5° rises to approximately 1 km about 100 km far from the radar [37].

In this study, we have used a total of 254,270 PPIs of the radar reflectivity factor. These radar measurements represent sweeps at 0.5° of elevation restricted to 100 km of range (Figure 1b) for the period of March 2015 to December 2019 with a time interval of 5 min. Each PPI has been quality controlled to avoid ground clutter and anomalous propagations by means of the coincident polarimetric measurements of this radar [38]. Based on these data, the following pre-processing steps were performed:

1. Transformation from polar to Cartesian coordinates: with the objective of obtaining images on a regular grid, with a horizontal grid resolution of 4 km per pixel (the matrix had 40×40 pixels). Thus, each new image represents a matrix of Cartesian coordinates with 4×4 km² resolution;
2. Defining the boundaries: To utilize a regular square grid and eliminate the area without data as measured by radar, the images were cut into a square inscribed in a circle of 100 km (Figure 1);
3. Normalization of the reflectivity values: Reflectivity values range typically from 0 to 60 dBZ. To obtain values of reflectivity in the interval (0,1), the data were divided by 60.
4. Organization of datasets with a time interval of 15 min: train (2016, 2017 and 2019), validation (from March 2015 to December 2015) and test (2018).

Pre-processed dataset used in this study is available at https://doi.org/10.7910/DVN/ZADDNQ.

Figure 1: (a) Location of the weather radar. The red circle marks 100-km of range; **(b)** Reflectivity image from the Plan Position Indicator (PPI) radar at 0.5 , with a map of the surrounding area in the background. The red line marks the radius of 100 km and the darker-colored square defines the borders.

2.2 Models

2.2.1 ENCAST

Ensemble NowCASTing (ENCAST) [16] is the nowcasting algorithm available at SELEX weather radar and it is used operationally by SPOL-FCTH radar. The model identifies, tracks, and extrapolates rain cells by using the differences between pairs of consecutive derived images from the weather radar. The tracking algorithm is based on the cross-correlation procedure that derives one movement vector for each area of precipitation analyzed and performs cross-correlation over this area. Moreover, ENCAST converts pseudo radar reflectivity factor CAPPIs (Constant Altitude PPI, a horizontal cross-section of PPIs obtained from radar scans at different elevation angles) to the rainfall rate by using a fixed Z-R relation ($Z = 300R^{1.4}$) and uses it to represent the closest surface rainfall as the image input. It uses a rain threshold in cell identification. Based on the cell's position in the present and previous scans a forecast is computed for a user-defined time interval.

For this study, FCTH provided the ENCAST outputs with 500-m × 500-m resolution. For each output, ENCAST forecast 7 time steps, ranging from 0 to 60 min lead time. Later, the rain fields were downscaled to a pixel of 4 km × 4 km.

2.2.2 PredRNN++

PredRNN++ is the model proposed by Wang et al. (2018) [35,39] as an improvement of PredRNN [28]. To increase the temporal and spatial long-term memory, the model utilizes two structures: "causal LSTM", to capture complex dependencies and variations, and "gradient highway unit" (GHU), to keep the gradients during training. The Causal LSTM adopts a cascaded mechanism [40,41], where spatial memory is a function of temporal memory. Inspired by LSTM [42,43], GHU facilitates the training of deep neural networks. It uses adaptive units to regulate information flow inside the model, preventing the gradient backpropagated from quickly vanishing [35,43]. Figure 2 illustrates the PredRNN++ information flow.

Figure 2: PredRNN++ architecture of the model. Blue parts indicate the gradient highway connecting the current time step directly with prior inputs, while the red parts show the deep transition pathway. Where t denotes time step, k denotes kth hidden layer in the stacked model, M_t^k is the spatial memory, C_t^k is the temporal memory, H_t^k is the final output (determined by the dual memory states) and Z_t is the hidden state, provided by "gradient highway unit" (GHU). Source: adapted from Wang et al. [35].

The PredRNN++ model predicts 10 future frames (target) given 10 previous inputs, so each register is a sequence of 20 images. The input was organized in such a way that, between one record and the next, there is one time-step forward in the dataset.

The model architecture and the hyperparameters established by the authors were maintained [35,39]: 4 layers of causal LSTM with 128, 64, 64, 64 units in each layer, respectively, one gradient highway layer with 128 units, convolution filter of size 5. The loss function was used with ADAM optimization algorithm with a starting learning rate of 10^{-3}, and a batch size of 8 records, also organized in sequence.

To train and test the PredRNN++ model, we considered the entire dataset, which means that we did not separate the days with and without reflectivity. Further, we considered all the reflectivity range, from 0 to 60 dBZ, but we scaled the data into the (0,1) interval. The period of data used for training includes the complete years of 2016, 2017 and 2019; the data from March 2015 to December 2015

were used as validation sets; the data from the complete year of 2018 were used as a blind test set. The time step used between images was 15 min instead of 5 min so that the training set comprises around 51,800 images, the validation set 15,800 images, and the test set 19,900 images.

The VPDL model was run on the Santos Dumont supercomputer, installed in the National Laboratory for Scientific Computing, LNCC (Portuguese acronym). The hardware used was two NVIDIA Tesla V100-16 GB with NVLink and 384 Gb of RAM.

The model was trained for 20 epochs and validated every 1 epoch (51,800 iterations). Each output comprises 10 time steps, ranging from 15 min to 150 min lead time. It should be mentioned that the training of the model is time-consuming (about 12 h/epoch) and requires computational resources to speed up the training (such as GPU) in addition to RAM and storage capacity. However, once the model is trained, the execution of the test set is fast (about 3 s/iteration).

3. EXPERIMENTAL SETUP

To evaluate the performance of the PredRNN++ model, we calculate standard categorical statistics, enumerated below, for the test set (the year of 2018), between the results of the VPDL model and the observed reflectivity images and between the results of the ENCAST precipitation nowcasting model and the observed reflectivity images.

Different precipitation nowcasting systems cannot be compared if they are designed for different purposes [10]. However, ENCAST works with both convective and stratiform precipitation [16] and PredRNN++ is also expected to work with both types of precipitation. It is worth mentioning that although the radar reflectivity images have been quality controlled, we observed random noise that could be attributed to anomalous propagation, especially over the metropolitan area of São Paulo, which changes the refractivity index. As an approximation, based on the Z-R relation ($Z = 300R^{1.4}$), to avoid such spurious contamination, we considered that pixels above the threshold of 20 dBZ represent rainy pixels in the radar images, which is equivalent to approximately 0.5 mm/h. This threshold will also be compared with the ENCAST precipitation forecast.

As ENCAST predicts precipitation rate and PredRNN++ predicts radar reflectivity, we used binary metrics to evaluate the results of the VPDL model against the ENCAST results. We converted the values of the pixels into a 0/1 (e.g., no/yes) matrix using a dBZ threshold (defined below) for the observed and predicted fields of the VPDL model, and a mm/h threshold for the ENCAST forecast, where values lower than or equal these thresholds were converted to 0, and values greater than the thresholds were set to 1. As shown in the results section, some analyses

of the reflectivity dataset and preliminary analysis of the results of the VPDL model reinforced the choice to evaluate the results in binary form.

We calculated the verification statistics up to 1-h lead time, using pairs of forecast and observation for second subsets and three rain cases (listed below). Pixel by pixel, the forecast hits and misses for each case or subset were accumulated in confusion matrix (Table 1), and then we calculate the statistics. The subsets are the complete test set (the year of 2018), named "All", and the summer season set, from January to March of 2018), called "Summer". The dates of the three rain cases are: 31 July 2018, 05 December 2018 and 22 December 2018.

The following are the forecast and observation pairs of the thresholds used to evaluate the model's performance:

- 1 dBZ for reflectivity predicted and observed;
- 10 dBZ for reflectivity predicted and 20 dBZ for reflectivity observed (the choice of the predicted threshold is explained in the results section). These values are compared with the ENCAST forecast;
- 1 mm/h for precipitation predicted from ENCAST, and 20 dBZ for reflectivity observed.

In the analyses of the results, we refer to pixels with and without reflectivity as wet and dry pixels, respectively. In Table 1, a positive event corresponds to a wet pixel (reflectivity greater than the threshold) and a negative event corresponds to a dry pixel (reflectivity lower than or equal to the threshold)."

Table 1: Confusion matrix (a type of contingency table).

		Observed	
		YES	NO
Predicted	YES	**TP**	**FP**
	NO	**FN**	**TN**

where:

TP: corresponds to the number of observed positive events (yes) that were correctly predicted;

FP: corresponds to the number of observed negative events (no) that were predicted incorrectly;

FN: corresponds to the number of observed positive events that were not predicted;

TN: corresponds to the number of observed negative events that were correctly predicted as negative.

Based on the confusion matrix, six standard categorical statistics were calculated:

1. The Probability Of Detection (*POD*) or Recall: the fraction of observed positive events that were correctly predicted. The range of possible values is 0 to 1, where the best possible *POD* is 1 and the worst is 0.

$$POD = \frac{TP}{TP+FN} \qquad (1)$$

2. The False Alarm Rate (*FAR*): the fraction of predicted positive events that did not occur. The range of possible values is 0 to 1, where the best possible *FAR* is 0 and the worst is 1.

$$FAR = \frac{FP}{TP+FP} \qquad (2)$$

3. The Probability Of False Detection (*POFD*) or the probability of false alarm: the fraction of observed negative events that were incorrectly predicted as positive. The range of possible values is 0 to 1, where the best possible *POFD* is 0 and the worst is 1.

$$POFD = \frac{FP}{FP+TN} \qquad (3)$$

4. The Bias score: the ratio between the number of predicted positive events and the number of observed positive events. This indicates how many times the number of predicted positive events exceeds the number of observed positive events [44]. *BIAS* = 1 indicates unbiased forecast, *BIAS* > 1 overforecast and *BIAS* < 1 underforecast.

$$BIAS = \frac{TP+FP}{TP+FN} \qquad (4)$$

5. The Critical Success Index (*CSI*), also known as the Threat Score: the ratio of correctly predicted observed positive events by the total number of positive events, predicted or needed. The *CSI* is an alternative to the *POD* when the positive event occurs substantially less than the negative event [44]. The *CSI* depends on the number of *TN*s compared to the total number of cases [45]. The range of possible values is 0 to 1, where the best possible *CSI* is 1 and the worst is 0. where:

$$CSI = \frac{TP}{TP+FP+FN} = \frac{TP}{Total-TN} \qquad (5)$$

where:

$$Total = TP+FP+FN+TN \qquad (6)$$

6. The Equitable Threat Score (*ETS*) or the Gilbert Threat Score: this is a skill score based on the *CSI* [44,45]. The *ETS* quantifies the improvement of the forecast compared to a random forecast. The range of possible values is −1/3 to 1, where the best possible *ETS* is 1 and 0 indicates no skill.

$$ETS = \frac{TP-R}{TP+FP+FN-R} \qquad (7)$$

$$R = \frac{(TP+FP)*(TP+FN)}{Total} \qquad (8)$$

Different from the *CSI*, the *ETS* depends directly on the *TN* due to the *R*. The frequency of observed positive events (*(TP + FN)/Total*) determines how close the *ETS* and *CSI* are; so, as the positive event becomes rarer, the *ETS* gets closer to the *CSI* [45].

The *CSI* and *ETS* are generally used in the assessment of quantitative precipitation forecasting [46–48]. A subjective analysis of the images must be made in order to visually certify the quality of the results.

4. RESULTS AND DISCUSSION

The training and test sets of PredRNN++ include both dry (without rain) and wet days (with rain). When considering wet days, all types of weather events (e.g., rain, hail) are included in the dataset and can occur anywhere in the image. We did not discriminate isolated storms from storms caused by frontal systems, for example. However, it is evident that all storms do not behave in the same way [16], and the formation of storms can be associated with diverse characteristics, such as development speed, variable intensity, atmospheric and terrain forcing (e.g., surface and ocean), and association with other weather systems.

Figure 3 illustrates the prediction for 8:25 on 31 July 2018 and Figure 4 illustrates the prediction for 16:50 on 22 December 2018. As in the examples of Figures 3 and 4, we observed that in general the PredRNN++ model smoothed the predicted reflectivity values; this was another reason why we chose to evaluate the results in binary form, by analyzing the occurrence and non-occurrence of reflectivity above the defined thresholds. We associate the model smoothing to a forecast error, instead of systematic bias, as shown in the scatter plot in Figure 5. As we can see by the red dashed line in the graphs of observed vs. predicted 30 min (Figure 5a) and 60 min (Figure 5b) forecasts, this behavior increases with the prediction horizon.

Figure 3: Prediction for 8:25 on 31 July 2018: **(a)** 10 input frames of PredRNN++; **(b)** 1-h prediction of PredRNN++; **(c)** observed reflectivity, ground truth of (b); **(d)** observed reflectivity greater than 20 dBZ, used as "truth" compared to (e); **(e)** 1-h prediction of Ensemble NowCASTing (ENCAST).
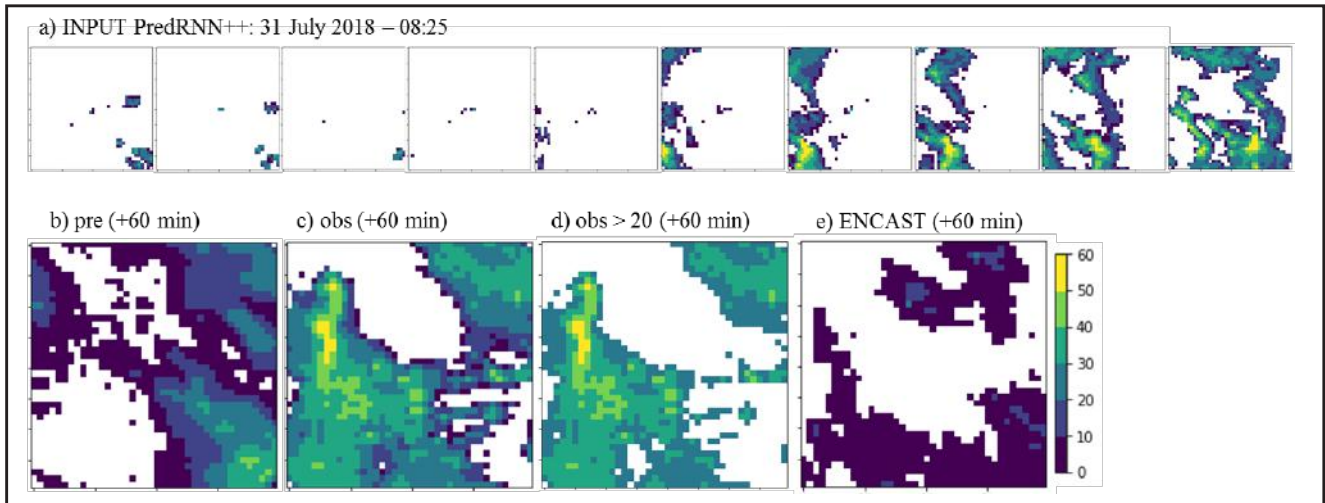

4.1 Evaluation of the Models

First, the performance of the PredRNN++ model was evaluated against the reflectivity image (ground truth) by calculating the following verification statistics: False Alarm Rate (FAR), Probability Of Detection (POD), Probability Of False Detection (POFD), BIAS, Critical Success Index (CSI), Equitable Threat Score (ETS). From Figure 6, we can quickly visualize the expected degradation of the forecast with increasing prediction period up to 150 min lead time. Table 2 shows these statistical values for the subsets "All" and "Summer" for 15, 30, 45 and 60-min lead times. Table 2 considers the 1 dBZ threshold for both observed and predicted reflectivity.

Figure 4: Prediction for 16:50 on 22 December 2018: (a) 10 input frames of PredRNN++; (b) 1-h prediction of PredRNN++; (c) observed reflectivity, ground truth of (b); (d) observed reflectivity greater than 20 dBZ, used as "truth" compared to (e); (e) 1-h prediction of ENCAST.
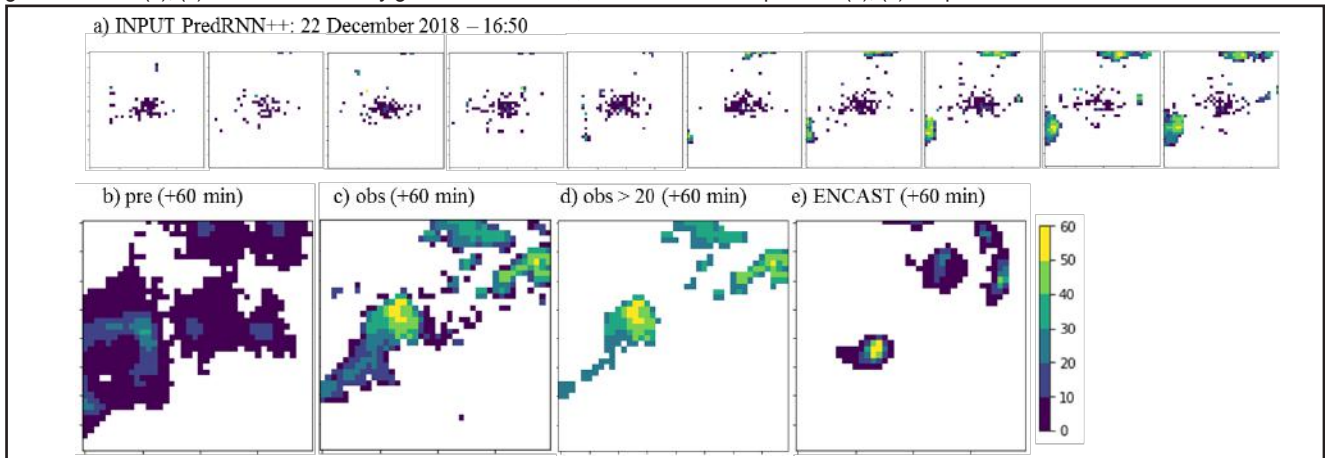
Figure 5: Scatter plot of results of PredRNN++for the test set (the year of 2018): (a) observed vs. predicted 30-min forecast; (b) observed vs. predicted 60-min forecast.
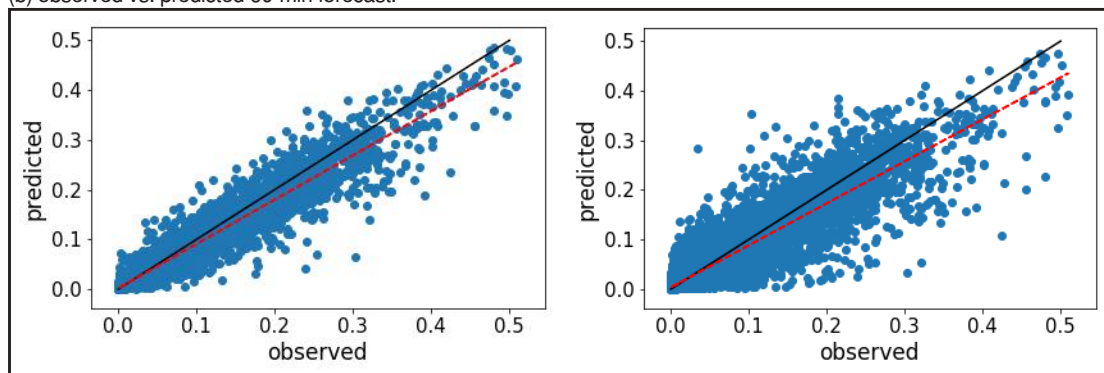
Figure 6: Verification statistics per prediction time (minutes) up to 150 min lead time, calculated over the subset minutes.
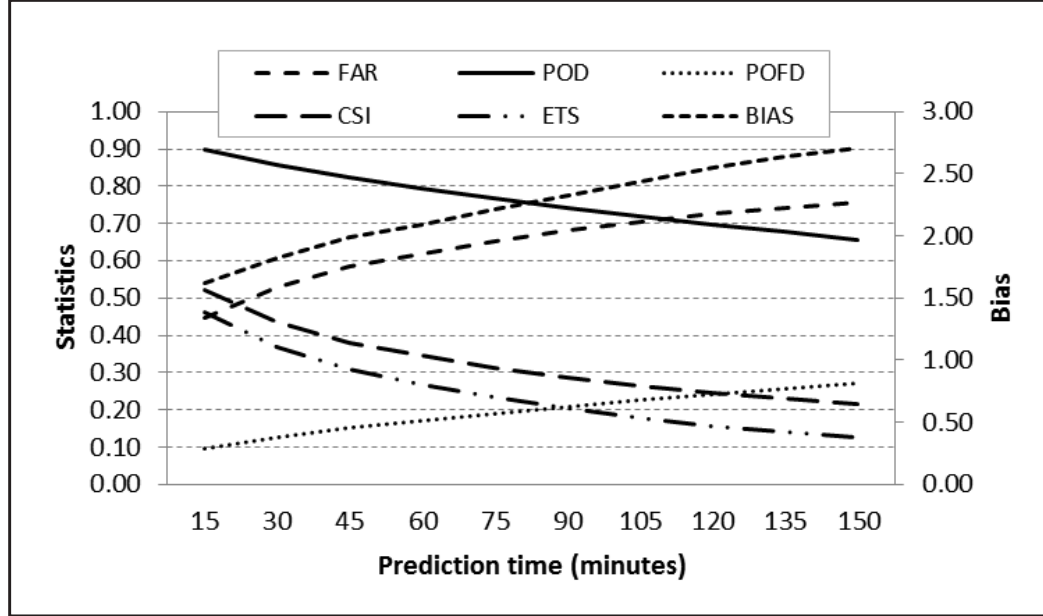
Table 2: Binary statistics from PredRNN++ model applied to all test data, for each lead time (in minutes): False Alarm Rate (FAR); Probability of Detection (POD); Probability of False Detection (POFD); the BIAS score; Critical Success Index (CSI), and Equitable Threat Score (ETS). All statistics were computed using thresholds of 1 dBZ for predicted and observed reflectivity.

Period	Lead time (min)	FAR ↓	POD ↑	POFD ↓	BIAS (~1)	CSI ↑	ETS ↑
All	15	0.45	0.90	0.10	1.62	0.52	0.46
	30	0.53	0.86	0.13	1.82	0.44	0.37
	45	0.59	0.83	0.15	1.99	0.38	0.31
	60	0.62	0.79	0.17	2.09	0.35	0.27
Summer	15	0.43	0.91	0.12	1.61	0.54	0.46
	30	0.51	0.87	0.16	1.80	0.45	0.36
	45	0.56	0.84	0.19	1.93	0.40	0.31
	60	0.59	0.81	0.21	1.99	0.37	0.27

The 15-min lead time, the first output, has the best statistics. In general (in the "All" subset) the model overforecasts by 1.6 times the number of predicted positive events (BIAS); 90% of the observed positive events were correctly predicted (POD); 45% of the predicted positive events did not occur (FAR); and 10% of the observed negative events were predicted as positive (POFD). The frequency of observed positive events was 12% of the total, and the CSI and ETS were 0.52 and 0.46, respectively. As observed in Figure 6, as time increases, the forecast skills decrease. The statistics for 60-min lead time are: BIAS of 2.09, POD of 79%, FAR of 62%, POFD of 17%, CSI of 0.35, and ETS of 0.27.

"All" considered all dry and wet weather events in a whole year. By including dry days in statistical computations, the number of TNs increased, and the number of TPs decreased. The presence of other echoes (ground clutter for example) throughout the dataset also had an influence as this can increase the number of FPs. As a note, the return from particulates in the atmosphere is usually very similar to the return from raindrops or cloud particles; the concentration and size of these particles can be enough to give a radar detectable echo [44]. In the summer, the percentage of wet days is expected to be greater than when considering an entire year. This difference can be seen in Table 2 when comparing "All" and "Summer". The frequency of observed positive events increased to 15% of the total.

"Summer" compared with "All" has a lower FAR (43% for 15-min, and 59% for 60-min lead time); and the number of correctly predicted positive events (POD) was also higher (91% for 15-min, and 81% for 60-min prediction). However, the number of events incorrectly predicted as positive increased to 12% for 15-min, and 21% for 60-min prediction. The BIAS, CSI and ETS showed similar values.

4.2 Case Studies

In this subsection, the results of the PredRNN++ model were compared with the precipitation nowcasting model ENCAST for three rain cases. As stated earlier, these cases were collected within the test set (the year of 2018). The cases were selected from the significant cases of the monthly bulletin published by the Center for Weather Forecasting and Climate Studies, part of the National Institute for Space Research (CPTEC/INPE, Portuguese acronym) [49]. The first case occurred on 31 July 2018, when a frontal system passed over São Paulo. The second case occurred on 5 December 2018, where the displacement of a frontal system by the ocean, associated with convection in the interior of the continent formed a moisture channel that extended over the state of São Paulo, among other regions, causing deep convection. The third case occurred on 22 December 2018, in which the passage of a frontal system, associated with high-level circulation, caused deep convection over São Paulo, among other regions. In the latter case, in addition to hail, a record number of trees were reported to have been blown down.

As stated earlier, the ENCAST model predicts precipitation and the output of the PredRNN++ model is reflectivity. To calculate the verification statistics, the outputs of the two models were compared to the observed reflectivity fields at the threshold of 20 dBZ. Additionally, from an analysis presented earlier, the PredRNN++ model smoothed the predicted reflectivity values. By evaluating the number of pixels per reflectivity range (as shown in Figure 7), we noted that the number of pixels above 10 dBZ in the predicted images is comparable to the number of pixels above 20 dBZ in the observed images. Thus, we established the threshold of 10 dBZ for predicted values and compared them to the observed values above 20 dBZ, in order to evaluate precipitation edges. Figures 3 and 4 illustrate examples of the cases of 31 July 2018 and 22 December 2018, respectively. We can observe the thresholds in the color bar.

Figure 7: Time series of the number of pixels per image according to the thresholds established in the legend (for 30-min prediction) and time lag (x 15 min) of TP events up to 60 min lead time forecast for each case study: (a) and (b) 31 July 2018, (c) and (d) 5 December 2018, (e) and (f) 22 December 2018. The arrows mark the delays between the observed (red) and predicted (blue) number of pixel peaks. The vertical red dashed lines mark the observed and predicted "rain start".
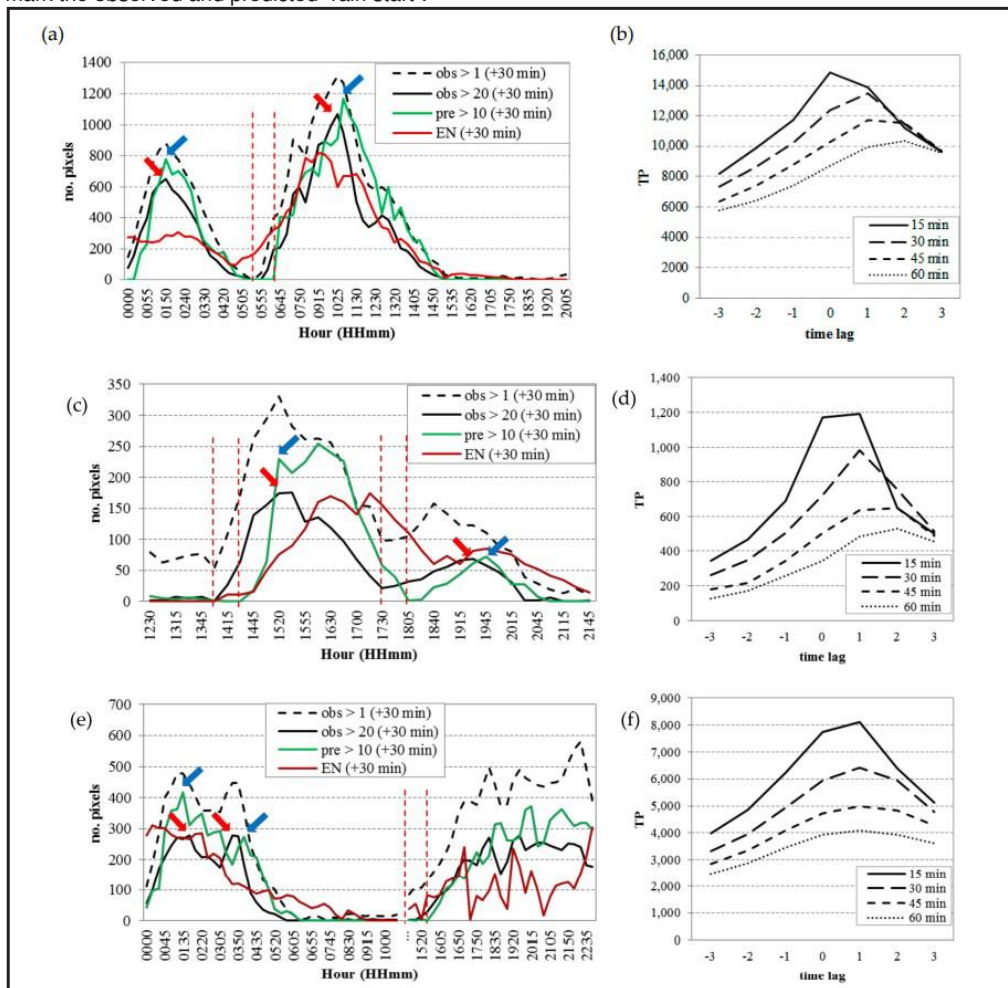
The statistics of the cases are presented in Table 3 and are organized into three blocks according to the reflectivity thresholds used in the observed (obs) and predicted (pre) data for 15, 30, 45 and 60-min lead times: Block 1 does not alter the thresholds used as input and output of the DL model, as presented in Table 2 (pre > 1 dBZ and obs > 1 dBZ); Block 2 is used to assess whether the model can generate precipitation pixels (pre > 10 dBZ and obs > 20 dBZ); Block 3 represents the statistics for comparison with Block 2, calculated on the ENCAST model (ENCAST > 1 mm/h and obs > 20 dBZ). The verification metrics are the same as shown in Table 2.

We highlight that two different variables, reflectivity and rain, were compared in Block 3. So, as shown before, we evaluated image patterns instead of numerical values. In these analyses, it is necessary to remember that not all echoes above 20 dBZ observed on the radar are equivalent to rain as predicted by ENCAST. The ENCAST model takes different radar fields when calculating precipitation.

In all cases, we can note the degradation of the forecast with an increasing prediction period, but in Block 3 this degradation is very subtle. Between Blocks 1 and 2, the degradation of certain statistics is noted, which can be explained by the decrease in the number of positive events predicted and observed (TP, FP and FN) and, consequently, the increase in TN due to the thresholds used in Block 2.

The observed variation between the cases in each Block is explained by the nature of the rainfall, which is different in each case. Figure 7a,c,e shows the time series of the number of pixels per image for 30-min lead time. We can observe the variations in the number of peaks and the number of pixels for each case, in the y-axis scale. In quantitative terms, ENCAST has fewer wet pixels compared with the other fields presented; this also has a negative effect on the calculation of verification statistics, as will be discussed below. Figure 7a,c,e also shows different delays between the time of occurrence and the forecast of the number of pixel peaks forecasted (shown by arrows); lags between the increase in the number of observed wet pixels, which can be seen as the start of the rain, and the increase in predicted wet pixels (vertical red dashed lines). Figure 7b,d,f specifically shows the time lag of TP events up to 60 min forecast for each case study. We can note that for the 30-min prediction, the lag is around 15 min, and for the 1-h prediction, between 15 and 30 min. We can also note the degradation of the results with an increasing prediction period.

Comparing the statistics obtained in Blocks 2 and 3 in Table 3, we note that within each Block the difference between cases is presented differently by the two models. Despite the thresholds used in Block 2, which reduced the observed and predicted positive areas, Block 2 performed better than ENCAST (Block 3). The fact that the verification statistics were calculated on small positive areas penalized the evaluation of the models. Although the pattern is similar between the images, if the centers are displaced and

Table 3: Binary statistics of PredRNN++ model (for 15, 30, 45 and 60-min prediction times) and ENCAST nowcasting model (for 10, 20, 30, 40, 50, 60-min prediction times) applied to selected cases: 31 July 2018, 05 December 2018 and 22 December 2018. The graphics and metrics are similar to those presented in Figure 5 and Table 2. The table is divided into three blocks according to the evaluated model and the thresholds: (Block 1) PredRNN++, pre > 1 dBZ and obs > 1 dBZ; (Block 2) PredRNN++, pre > 10 dBZ and obs > 20 dBZ; (Block 3) ENCAST, ENCAST > 1 mm/h and obs > 20 dBZ.
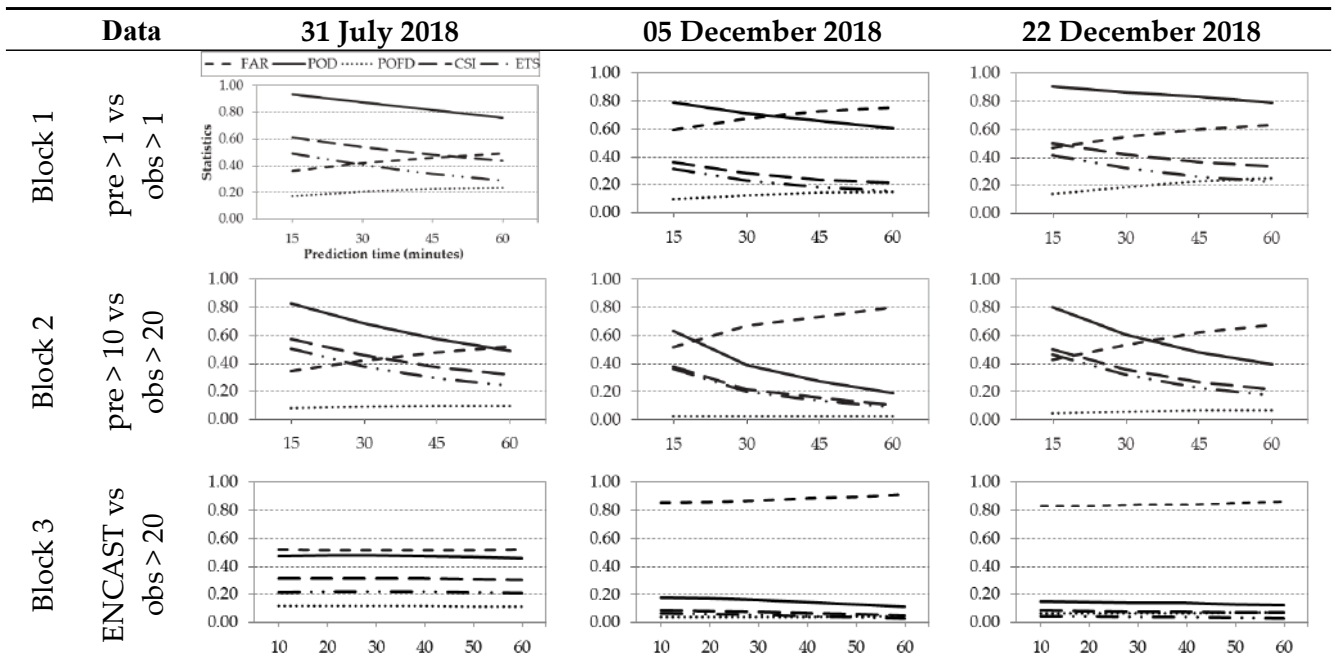
do not overlap, the forecast is given as wrong in the pixel by pixel confusion matrix [50]. Therefore, even though the number of hits (TP) was small in both models, TP of the PredRNN++ model was slightly higher than ENCAST, which improved its statistics when compared with ENCAST. The examples presented in the Figures 3 and 4 show the aspect of the lack of overlap in the positive areas predicted and observed, and also that the PredRNN++ model predicts a larger positive area compared with ENCAST. This can masquerade pixel by pixel statistics.

5. CONCLUSIONS

In this study, we evaluate the usability of a video prediction deep learning (VPDL) model to support nowcasting. We use the PredRNN++ model as a VPDL model to predict reflectivity images and precipitation edges from weather radar images for up to 1-h lead time and compare the results with an extrapolation-based model used for precipitation nowcasting, ENCAST. We also evaluate the feasibility of a VPDL model for continuous use in nowcasting, as this gives the meteorologist an indication or a trend of the occurrence of localized precipitation regardless of the type of weather event.

We evaluate the model results against the ground truth images in two subsets and compare the VPDL model statistics with ENCAST statistics in three case studies: the entire test set ("All", the entire year of 2018), the summer season set ("Summer"), and the days 31 July 2018, 5 December 2018, and 22 December 2018, as the case studies, respectively. By using pixel by pixel confusion matrix for the architecture used in the VPDL model, we find that: the VPDL model overforecasts the prediction of wet pixels; "Summer" (more homogeneous dataset) shows a better performance than "All"; and the VPDL model outperforms the ENCAST model in the three analyzed cases. We highlight that we only had access to three cases of ENCAST and to compute the ENCAST statistics we used the binary field of precipitation as prediction and the binary field of reflectivity greater than 20 dBZ as observation.

The forecast for precipitation is an important aspect of nowcasting. However, due to model architecture, the results are smoothed, which affects the analysis of predicted reflectivity instead of the analysis of pixels with rain and no rain. As a tool to assist nowcasting, this model should be used in parallel with other data and models. In fact, the model provides trends in the localization and development of rain edges of systems that can cause damage. We recommend that caution be taken in analyzing the range of predicted values since this can lead to a tendentious prediction of a strong system.

In general, the results obtained here agree with the most recent results published on the potential of the use of a VPDL model as an additional tool to assist nowcasting. We highlight certain advantages such as rapid execution (after training), 3 s/iteration, the use of a single input with little pre-processing, but a long history for training is necessary.

From other studies, we assume that training the model with events of the same type can improve the model's performance. However, another aim of the present study is to assess the viability of a continuous execution of the VPDL model in predicting reflectivity edges regardless of the meteorological phenomena. In this respect, the model shows some lags between the "rain start" in observed images and predicted images. We assume that the addition of other variables that give an indication of the state of the atmosphere before the sudden appearance of targets in the radar image adds extra information to the model training and improves the quality of the forecast in terms of the life cycle of the weather event and even the prediction of the event.

As expected, an issue that arises in not considering physical processes is that extrapolation models are conservative: the model considers that an element will remain in the image and may only change its position (rotation and translation). Taking a cloud as an example of an image element, these models cannot predict dissipation due to rain, or the formation of a new cloud where there was nothing before. This is observed in mathematical extrapolation models as well as VPDL models. Deep learning models can fit observations very well, but only by integrating knowledge of the physical processes to train and provide constraints can the model achieve physical consistency [26].

With the addition of topography information, the model will be able to distinguish the formation of clouds by an orographic barrier, for example. It is worth mentioning that the addition of more variables to the VPDL model increases the model's complexity, storage, processing time, among other limiting factors.

The next steps in this study, which are currently being developed, also include the evaluation of possible improvements in the architecture of the VPDL model and the running of other VPDL models.

Even though meteorological systems that trigger natural disasters vary by location, a general solution can contribute as a tool to assist decision-makers and consequently issue efficient alerts.

REFERENCES

Golnaraghi, M.; Etienne, C.; Guha-Sapir, D.; Below, R. *Atlas of Mortality and Economic Losses from Weather, Climate, and Water Extremes (1970–2012)*; World Meteorological Organization (WMO): Geneva, Switzerland, 2014.

UNISDR, U. Hyogo framework for action 2005–2015: Building the resilience of nations and communities to disasters. In *Proceedings of the Extract from the final report of the World Conference on Disaster Reduction (A/CONF. 206/6), Kobe, Hyogo, Japan, 18–22 January 2005*; The United Nations International Strategy for Disaster Reduction: Geneva, Switzerland, 2007.

CEPED, U. *Atlas Brasileiro de Desastres Naturais: 1991 a 2012*; Centro Universitário de Estudos e Pesquisas sobre Desastres, Federal University of Santa Catarina: Florianópolis, Brazil, 2013.

Asadieh, B.; Krakauer, N.Y. Global trends in extreme precipitation: Climate models vs. observations. *Hydrol. Earth Syst. Sci. Discuss.* **2014**, *11*, 11369–11393.

Zilli, M.T.; Carvalho, L.M.; Liebmann, B.; Silva Dias, M.A. A comprehensive analysis of trends in extreme precipitation over southeastern coast of Brazil. *Int. J. Climatol.* **2017**, *37*, 2269–2279.

WMO. Available online: http://www.wmo.int/pages/prog/amp/pwsp/Nowcasting.htm (accessed on 08 November 2017).

Atlas, D. *Radar in Meteorology*; American Meteorological Society: Boston, USA, 1990.

Büyükbas, E.; Sireci, O.; Hazer, A.; Temir, I.; Macit, A.; Gecer, C. *Training Materials on Weather Radar Systems. Instruments and Observing Methods, Technical Report no.88*; World Meteorological Organization (WMO): Geneva, Switzerland, 2006; p. 54.

Calheiros, A.J.P.; Enoré, D.P.; Mattos, E.V.; da Costa, I.C.; Machado, L.A.T. *Sistema De Previsão Imediata: Descrição dos Produtos*; Instituto Nacional de Pesquisas Espaciais (INPE): São José dos Campos, SP, Brazil, 2016.

Reyniers, M. *Quantitative Precipitation Forecasts Based on Radar Observations: Principles, Algorithms and Operational Systems*; Institut Royal Météorologique de Belgique: Brussel, Belgium, 2008.

Wilson, J.W.; Crook, N.A.; Mueller, C.K.; Sun, J.; Dixon, M. Nowcasting thunderstorms: A status report. *Bull. Am. Meteorol. Soc.* **1998**, *79*, 2079–2100.

Wilson, J.; Feng, Y.; Chen, M.; Roberts, R. Nowcasting Challenges during the Beijing Olympics: Successes, Failures, and Implications for Future Nowcasting Systems. *Weather Forecast.* **2010**, *25*, 1691–1714.

Met Office, Nowcasting. Available online: https://www.metoffice.gov.uk/weather/learn-about/how-forecasts-are-made/hours-ahead/nowcasting (accessed on 08 November 2017).

Held, G.; Gomes, J.L.; Nascimento, E. Forecasting a severe weather occurrence in the State of São Paulo, Brazil, on 24 May 2005: The Indaiatuba Tornado. In *Proceedings of the 8th International Conference on Southern Hemisphere Meteorology and Oceanography, Foz do Iguaçu, Brazil, 24–28 April 2006*; pp. 1799–1807.

Pierce, C.; Seed, A.; Ballard, S.; Simonin, D.; Li, Z. Nowcasting. In *Doppler Radar Observations-Weather Radar, Wind Profiler, Ionospheric Radar, and Other Advanced Applications*; InTech Open Access Publisher: 2012.

Instruction Manual Rainbow® 5; Selex Systems Integration GmbH: Backnang, Germany, 2017.

DIXON, M.; WIENER, G. TITAN: Thunderstorm identification, tracking, analysis, and nowcasting—A radar-based methodology. *J. Atmos. Ocean. Technol.* **1993**, *10*, 785–797.

World Meteorological Organization. *Guidelines for Nowcasting Techniques*; (WMO-No. 1198); WMO Publication: Geneva, Switzerland, 2017.

Luk, K.C.; Ball, J.E.; Sharma, A. An application of artificial neural networks for rainfall forecasting. *Math. Comput. Modeling* **2001**, *33*, 683–693.

Bushara, N.O.; Abraham, A. Computational intelligence in weather forecasting: A review. *J. Netw. Innov. Comput.* **2013**, *1*, 320–331.

McGovern, A.; Elmore, K.L.; Gagne, D.J.; Haupt, S.E.; Karstens, C.D.; Lagerquist, R.; Smith, T.; Williams, J.K. Using artificial intelligence to improve real-time decision-making for high-impact weather. *Bull. Am. Meteorol. Soc.* **2017**, *98*, 2073–2090.

Germann, U.; Zawadzki, I.; Turner, B. Predictability of precipitation from continental radar images. Part IV: Limits to prediction. *J. Atmos. Sci.* **2006**, *63*, 2092–2108.

Mueller, C.; Saxen, T.; Roberts, R.; Wilson, J.; Betancourt, T.; Dettling, S.; Oien, N.; Yee, J. NCAR auto-nowcast system. *Weather Forecast.* **2003**, *18*, 545–561.

AMS Glossary. Available online: http://glossary.ametsoc.org/wiki/Predictability (accessed on 27 February 2020).

Franch, G.; Nerini, D.; Pendesini, M.; Coviello, L.; Jurman, G.; Furlanello, C. Precipitation nowcasting with orographic enhanced stacked generalization: Improving deep learning predictions on extreme events. *Atmosphere* **2020**, *11*, 267.

Reichstein, M., Camps-Valls, G., Stevens, B., Jung, M., Denzler, J., Carvalhais, N. Deep learning and process understanding for data-driven Earth system science. *Nature* **2019**, *566*, 195–204.

Shi, X.; Chen, Z.; Wang, H.; Yeung, D.Y.; Wong, W.K.; Woo, W.C. Convolutional LSTM network: A machine learning approach for precipitation nowcasting. In Proceedings of the Advances in Neural Information Processing Systems 28 (NIPS 2015), Montreal, QC, Canada, 7–12 December 2015; pp. 802–810.

Wang, Y.; Long, M.; Wang, J.; Gao, Z.; Yu, P.S. PredRNN: Recurrent Neural Networks for Predictive Learning using Spatiotemporal LSTMs. In Proceedings of the Neural Information Processing Systems 30 (NIPS 2017), Long Beach, CA, USA, 4–9 December 2017; pp. 879–888.

Rew, J.; Park, S.; Cho, Y.; Jung, S.; Hwang, E. Animal Movement Prediction Based on Predictive Recurrent Neural Network. *Sensors* **2019**, *19*, 4411.

Shi, X.; Gao, Z.; Lausen, L.; Wang, H.; Yeung, D.Y.; Wong, W.K.; Woo, W.C. Deep learning for precipitation nowcasting: A benchmark and a new model. In Proceedings of the Neural Information Processing Systems 30 (NIPS 2017), Long Beach, CA, USA, 4–9 December 2017; pp. 5617–5627.

Tran, Q.K.; Song, S.K. Computer Vision in Precipitation Nowcasting: Applying Image Quality Assessment Metrics for Training Deep Neural Networks. *Atmosphere* **2019**, *10*, 244.

Klein, B.; Wolf, L.; Afek, Y. A dynamic convolutional layer for short range weather prediction. In Proceedings of the IEEE Conference on Computer Vision and Pattern Recognition, Boston, MA, USA, 7–12 June 2015; 2015, pp. 4840–4848.

Mathieu, M.; Couprie, C.; LeCun, Y. Deep multi-scale video prediction beyond mean square error. In Proceedings of the International Conference on Learning Representations (ICLR), San Juan, Puerto Rico, 2–4 May 2016.

Srivastava, N.; Mansimov, E.; Salakhudinov, R. Unsupervised learning of video representations using lstms. In Proceedings of the 32nd International Conference on International Conference on Machine learning (37), Lille, France, 7–9 July 2015; pp. 843–852.

Wang, Y.; Long, M.; Wang, J.; Gao, Z.; Yu, P.S. PredRNN++: Towards a resolution of the deep-in-time dilemma in spatiotemporal predictive learning. *PLMR* **2018**, *80*, 5123–5132.

Saisp Homepage. Available online: https://www.saisp.br/estaticos/sitenovo/produtos.xmlt (accessed on 26 December 2018).

Rinehart, R.E. *Radar for Meteorologists: Or You, too, can be a Radar Meteorologist, Part. III*, 5th ed.; Rinehart Publications: Nevada, Missouri, USA, 2010.

Straka, J.M.; Zrni , D.S.; Ryzhkov, A.V. Bulk Hydrometeor Classification and Quantification Using Polarimetric Radar Data: Synthesis of Relations. *J. Appl. Meteor.* **2000**, *39*, 1341–1372.

PredRNN++ Code. Available online: https://github.com/Yunbo426/predrnn-pp (accessed on 07 May 2019).

Xu, Z.; Wang, Y.; Long, M.; Wang, J.; KLiss, M.O.E. PredCNN: Predictive Learning with Cascade Convolutions. In Proceedings of the 27th International Joint Conference on Artificial Intelligence (IJCAI-18), Stockholm, Sweden, 13–19 July 2018; pp. 2940–2947.

Oord, A.V.D.; Dieleman, S.; Zen, H.; Simonyan, K.; Vinyals, O.; Graves, A.; Kalchbrenner, N.; Senior, A.; Kavukcuoglu, K. Wavenet: A generative model for raw audio. *arXiv* **2016**. arXiv:1609.03499.

LeCun, Y.; Bottou, L.; Bengio, Y.; Haffner, P. Gradient-based learning applied to document recognition. *Proc. IEEE* **1998**, *86*, 2278–2324.

Srivastava, R.K.; Greff, K.; Schmidhuber, J. Training very deep networks. In Proceedings of the 28th International Conference on Neural Information Processing Systems (NIPS 2015), Montreal, QC, Canada, 7–12 December 2015; Volume 2, pp. 2377–2385.

Wilks, D.S. *Statistical Methods in the Atmospheric Sciences*, 2nd ed.; Academic Press: New York, USA, 2006.

Schaefer, J.T. The critical success index as an indicator of warning skill. *Weather Forecast.* **1990**, *5*, 570–575.

Hamill, T.M. Hypothesis tests for evaluating numerical precipitation forecasts. *Weather Forecast.* **1999**, *14*, 155–167.

Sharifi, E.; Steinacker, R.; Saghafian, B. Assessment of GPM-IMERG and other precipitation products against gauge data under different topographic and climatic conditions in Iran: Preliminary results. *Remote Sens.* **2016**, *8*, 135.

Wang, C.C. On the calculation and correction of equitable threat score for model quantitative precipitation forecasts for small verification areas: The example of Taiwan. *Weather Forecast.* **2014**, *29*, 788–798.

CPTEC/INPE bulletin of "casos significativos do mês". Available online: https://www.cptec.inpe.br/noticias/quadro/143 (accessed on 07 January 2019).

Ebert, E. Fuzzy verification of high resolution gridded forecasts: A review and proposed framework. *Meteorol. Appl. A J. Forecast. Pract. Appl. Train. Tech. Modeling* **2008**, *15*, 51–64.

Long-term spatial-temporal characterization of cloud-to-ground lightning in the metropolitan region of Rio de Janeiro

Tales Bernardes Paulucci [1]

Gutemberg Borges França [2]

Renata Libonati [1,2,3]

Alexandre M. Ramos [3]

ABSTRACT

Remote-sensing techniques are currently the only means of collecting information to monitor the atmospheric dynamics of lightning from the regional to the national scales, allowing for the generation of homogeneous and long time series. Attempts to characterize the impacts of atmospheric discharge in Brazil presuppose an understanding of spatial and temporal lightning patterns. Despite the high frequency of lightning and significant disturbances caused in highly populated regions such as the metropolitan region of Rio de Janeiro (MRRJ), these phenomena are not well characterized when using a long-term contemporaneous dataset. Accordingly, this work focuses on the spatial and temporal variability of cloud-to-ground lightning in the metropolitan region of Rio de Janeiro, an area affected by a high level of atmospheric discharge every year. We performed a statistical analysis of lightning data taken from a Lightning Location System for the 16-year period of 2001 to 2016 and analysed characteristics such as polarity, peak currents, geographic distributions and diurnal, intra- and inter-annual variability. Extremely high levels of high activity were observed from 258,794 cloud-to-ground lightning events recorded over the analysed period and for 64.3% events occurring in summer, 20.5% events occurring in spring and 12.9%, and 2.3% events occurring in autumn and winter. The discharge events were predominantly negative (93.54% of the total). Peak levels of electrical activity were observed from roughly 18:00 to 19:00 local time, when there is more potential energy available for convection. The results of the spatial analysis reveal that most lightning observed over Rio de Janeiro derived from the orographic effect, which spurs the formation of convective storms along the southern part of the slope.

Keywords: Cloud to ground lightning, Thunderstorm, Flashes, Southeastern Brazil, Rio de Janeiro.

1. INTRODUCTION

The occurrence of electric discharge from the atmosphere is a result of complex physical interactions of the climate system associated with microphysical, dynamic and thermodynamic processes and which occur predominantly within clouds with intense convective activity. The activity of atmospheric electricity can be related to the anomalies of land and sea temperatures (Petersen and Rutledge 1998; Soriano and Pablo 2002), atmospheric aerosols of urban pollution, heat island effects or fire (Orville et al. 2001; Wierzchowski et al. 2002; Naccarato et al. 2003; Boian and Kirchhoff 2004; Farias 2009; Pinto et al. 2013, Russo et al. 2017). Storm events generated by convective clouds are responsible for the redistribution of heat and moisture into the atmosphere and are often accompanied by heavy rains; strong winds; hail; electric discharge; and

floods and landslides with various direct and indirect human and socio-economic impacts such as power grid collapses, aviation disorders and other disturbances (Wierzchowski et al. 2002). In particular, in terms of storm intensity levels, the associated lightning activity plays an important role.

Over the last decades the use of remote sensing systems has allowed for unprecedented advances in the monitoring of atmospheric dynamics of lightning and especially by tracking its occurrence in time and space. The first Lightning Location Systems (LLSs) introduced in the late 1970s (Krider et al. 1980) collected detailed information on the spatial distribution and temporal variations of lightning occurrence in specific regions, accurately showing the instant at which a flash reaches the ground and informing parameters such as polarity and peak discharge currents. LLSs have been operating around the world, providing data for atmospheric research in different countries and mainly in the United States of America (Lopez and Holle 1986; Orville 1991; Watson et al. 1994; Reap 1994; Orville and Silver 1997; Hodanish et al. 1997; Lyons et al. 1998; Huffines and Orville 1999, Romps et al. 2014), Japan (Hojo et al. 1989). More recently, many studies have emerged from Eurasia from Austria (Diendorfer et al. 1998; Schulz et al. 2005), Spain (Soriano et al. 2001; Soriano et al. 2005), Portugal (Rodrigues et al. 2010; Ramos et al. 2011; Russo et al. 2017), China (Chen et al. 2004), and Papua New Guinea (Orville et al. 1997) in particular. In South America, Brazil has been the focus of considerable lightning research (Pinto et al. 1996; Rocha et al. 1997; Pinto et al. 1999a; Pinto et al. 1999b; Naccarato et al. 2001; Pinto et al. 2003; Naccarato et al. 2003; Pinto et al. 2004; Fernandes et al. 2006; Pinto and Pinto 2008; Bourscheidt et al. 2009; Gin et al. 2012; Pinto et al. 2013; Santos et al. 2016, Santos et al. 2018) among many other countries.

Brazil, due to its large territorial coverage and predominant situation in a tropical region (particularly its southeastern region) is one of the regions experiencing the highest rates of lightning in the world (Pinto and Pinto 2003). Several studies have investigated lightning patterns over the southeastern region of Brazil (SRB) and mainly during the 1990s and early 2000s. For example, Pinto et al. (1996) used the Lightning Positioning and Tracking System (LPATS) for the first time to observe characteristics of lightning in the SRB during the summer season of 1992-1993. Rocha et al. (1997) conducted a similar study in the winter of 1993 in the SRB on polarity, multiplicity, and peak current patterns of the first stroke and compared their results to data for the same region for summer following Pinto et al. (1996). Pinto et al. (1999a, 1999b) presented information on 1.1

million cloud-to-ground lightning (CG) events detected by LPATS in the SRB in 1993, representing the first studies on the country to collect data for an entire year. One of the first long-term analyses of lightning patterns in Brazil was conducted by Pinto et al. (2006), showing a comparison between mean monthly distributions of lightning frequency and percentages of positive and peak currents of positive and negative CG for 1999 to 2004. The first climatological records of lightning in the SRB were presented by Pinto et al. (2003) for a 7-year period of negative CG running from 1989-1995 while Pinto et al. (2009) and Pinto et al. (2008) conducted studies based on data taken from BrazilDAT for 1999 to 2006 and Naccarato et al. (2005) addressed the 6-year period running from 1999-2004 for the SRB. More recently, Pinto et al. (2013) conducted a thorough overview of temporal and spatial distributions of lightning for the decade of 1999 to 2009 for Campinas, São Paulo and Rio de Janeiro, 3 important cities in the SRB, and found that variability in thunderstorm patterns may be related to variations in atmospheric circulation that modulate convective activity over large scales with two different mechanisms of urban activity found in the city of Rio de Janeiro: pollution and heat islands.

Although the footprint and process related to the occurrence of lightning are well known for various tropical regions around the world, analogous research is still needed for highly populated regions such as the Metropolitan Region of Rio de Janeiro (MRRJ), Brazil, which is a complex urban area of unequal socioeconomic relevance often hit by a large volume of atmospheric discharge every year. Despite the region's specific vulnerability to atmospheric discharge, to the best of our knowledge studies focusing on the characterization of lightning patterns and on the MRRJ in particular is still lacking. In this regard, this work aims to serve as a reference of the incidence of lightning in the MRRJ. Here we conduct a study on a 16-year period (2001-2016), which is much longer than periods usually used in studies of Southeastern Brazilian. Pinto et al. (2006), for example, studied CG patterns in the southeastern region and in some central-western and southern regions over a period of 6 years (1999-2004); Pinto and Pinto (2008) studied the city of São Paulo for a period of 8 years (1999-2006); Pinto et al. (2003) conducted a 7-year study of strictly negative CG patterns for 1989-1995, Naccarato et al. (2005) addressed a 6-year period (1999-2004), and Pinto et al. (2013) studied the 10-year period running from 1999-2009 for the southeastern region of Brazil. Therefore, we conduct a comprehensive analysis of long-term variations occurring over this region for the past 16-years.

2. DATA AND METHODS

The MRRJ was selected for this study due to its economic, political and cultural importance. According to the Brazilian Institute of Geography and Statistics (IBGE), it is the second most populous region in the country with a population estimated at 6,498,837, with a high population density (5,265.82 habitants/km²), with an area of approximately 1200 km², and with the second largest Gross Domestic Product (GDP). It is also the most popular international tourist destination in Brazil (IBGE, 2017).

Fig. 1: Topographical map of the state of Rio de Janeiro highlighted within the SRB (a). Map of the metropolitan region of Rio de Janeiro (black rectangle: 22.7-23.1oS and 43-44oW) highlighting principal counties within and close to the MRRJ (thin black lines) and the altitude (m) (b).
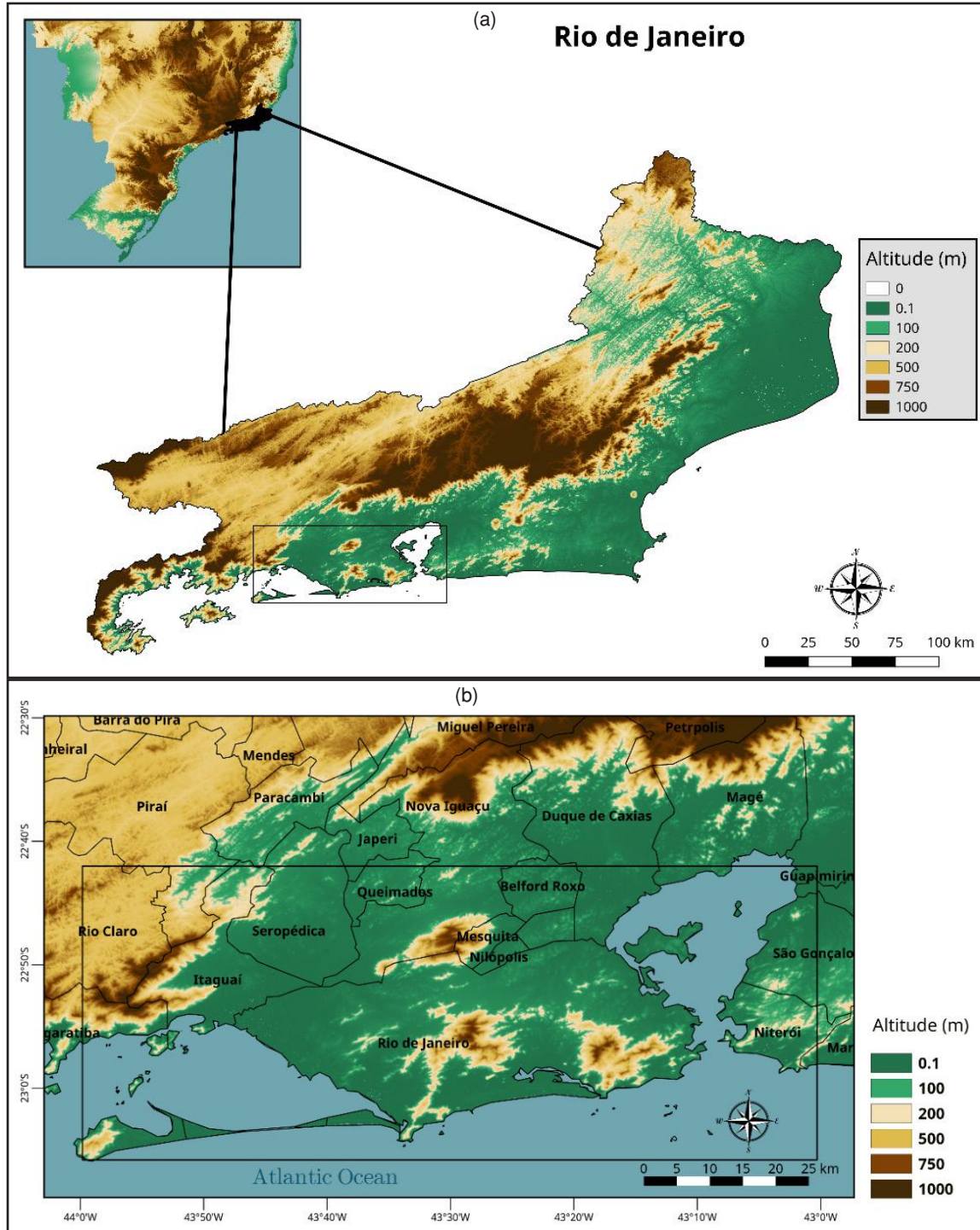
The term atmospheric electric discharge has often been used as a term equivalent to lightning. There are two fundamental types of lightning: (1) that occurring in the sky and (2) that reaching the ground (Naccarato 2005). Three types of lightning occurring in the sky can be identified: (1) intracloud (IC) lightning, which occurs within the same storm cloud; (2) cloud-to-cloud (CC) lightning occurring between different clouds; and (3) air (AIR) lightning forming from a cloud and traveling into the atmosphere itself without reaching another cloud or the ground. Cargo pockets that form in the atmosphere around storm clouds are responsible for this kind of lightning (Ogawa 1995). Lightning striking the ground, also known as lightning, is classified into two basic types: (1) cloud-to-ground (CG) lightning characterized by discharge starting from a cloud and reaching the surface of the Earth and (2) ground-to-cloud (GC) lightning moving from the ground to a cloud (Naccarato 2005).

Here we present an analysis to describe the main patterns of temporal and spatial distributions of atmospheric electrical discharge to study particular characteristics such as polarity and peak currents on hourly, monthly, seasonal and inter-annual time scales for a 16-year period (2001-2016) in the MRRJ. An exploratory data analysis was conducted on cloud-to-ground lightning (CG) occurring from 1 January 2001 to 31 December 2016 for a region delimited by coordinates 22.7°S to 23.1°S and 43.0°W to 44.0°W, which correspond to an area of 4,573 km² (Fig.1).

The dataset used here was provided by the Integrated National Network of Atmospheric Discharge Detection (RINDAT). The data cover geographic locations, times, peak currents, and polarity and multiplicity levels (which were not used here) of CG atmospheric discharge. Detection efficiency levels range between 70% and 90%; the average location accuracy level ranges from 0.5 km to 2 km; the average accuracy of peak current estimates of discharge range from 20% to 50% and discrimination capacities of CG and CC discharge are valued at approximately 80% to 90%. The system operates through a Global Positioning System (GPS), which provides lightning timing information at resolutions of up to 300 nanoseconds (additional information is available on http://www.rindat.com.br/).

First, spatial patterns of the observed CG incidents for the 16-year period were analysed using a density function, which is a spatial analysis tool used to calculate the density of point features (in this case, each incidence of cloud-to-ground lightning detected) per unit of area for each location within an area of interest. The result is a smoothed spatial grid of frequency for each grid point representing the number of points (CG) positioned within a pre-defined radius of influence. Here we used a regular grid of 600 m x 600 m.

All temporal analyses were carried out at the MRRJ scale considering all lightning occurring over the area. Lightning summary statistics were estimated from the averaged value for the 16-year period. For instance, daily cycles were computed by averaging the total number of lightning events (as well as other characteristics such as polarity and peak currents) occurring in each hour of the day over the 16-year period. The same procedure was applied for monthly, seasonal and annual cycles. Standardized anomalies (Z) were also used to compare normal years with years with above/below average lightning occurrence. Annual values of lightning occurrence are used to calculate long-term means ($\overline{X}$) and standard deviations (s) used to obtain standardized anomalies (Z) for each year:

$$Z = \frac{\left(X - \overline{X} \right)}{s} \tag{1}$$

3. RESULTS AND DISCUSSION

The mean spatial lightning density is equal to 3.54 flashes.km⁻².yr⁻¹ for the study area for the 16-year period (2001-2016). Fig. 2 shows a clear spatial density pattern of flashes occurring over the region and shows a higher frequency of GCL occurrence in the eastern area of the municipality of Piraí, northeast of Rio Claro, southeast and east of Nova Iguaçu, in Belford Roxo and southeast of Queimados. We find a density gradient oriented from south to north where oceanic and coastal areas present lower values for continental regions to the north and positioned further away from the coast, accordingly to Williams et al. (2003), some studies reveal a logical relationship between lightning activity and vertical ascension speed.

It is also worth mentioning two separate regions with high density values: one near the municipality of Nova Iguaçu and another close to the northwestern end of a rectangular region south of the municipality of Piraí. The distribution close to the municipality of Nova Iguaçu may be related to the presence of the Mendanha Massif in the region. In general, the highest values are predominantly found in the mountainous region (which includes a chain of mountains called the Órgãos and Mar Mountains) positioned in northern and northwestern areas of the study area. Such a spatial distribution may serve as evidence of the orographic effect, as the frequent passage of frontal systems and tropical heat sources combined with dynamics of winds close to the mountain chain would induce the formation of convective storms along the southern part of

the slope, increasing the occurrence of electric discharge in this region. Naccarato (2005) showed - in agreement with this work - that the spatial configuration of GC peaks in the southeastern area of the state of Minas Gerais south of the state of Rio de Janeiro and east of the state of São Paulo following from the elevation of terrain in the same region (Serra da Mantiqueira configuration), during warmer months of the year, which is used as a convection mechanism by the steep slope (orography) of Serra do Mar topography (reaching more than 1,000 meters in altitude in some areas) for formation of cumulonimbus clouds.

The distribution of atmospheric discharge peaks in the windward area and close to this slope and this may be attributed to the windward slope and to the distance between the windward and leeward faces of Serra do Mar formed by a mountain chain. Pinto et al. (2013) also presents spatial density levels in the SRB and shows high values in the northern area of the city of Rio de Janeiro. Similar results were found by Orville et al. (2002), Burrows et al. (2002) and Ramos et al. (2011) for regions characterized by complex terrain with orographic systems in the USA, Canada, and Portugal, respectively.

The study of inter- and intra-annual variability in the incidence of atmospheric discharge is an essential facet of this work, as it covers a study period of 16 years (2001-2016), which is much longer than periods usually used in studies of the Southeastern Brazilian region. Pinto et al. (2006), for example, studied CG in the southeast region and in parts of central-west and south regions for a period of 6 years (1999-2004) and Pinto and Pinto (2008) studied the city of São Paulo for a period of 8 years (1999-2006). Therefore, this part of the study allows for a comprehensive analysis of long-term variations observed in the region.

For instance, Fig. 3 shows inter-annual variations in the total levels of electric discharge for the MRRJ for the study period and the inter-annual percentage of positive CG events. The annual mean and standard deviation are equal to 16,175 and 7,121 flashes, respectively. With lightning density defined as the annual rate of flashes occurring per area, the study region presents a relatively strong average lightning density level of equal to 3.54 ± 1.56 flashes.km^{-2}.yr^{-1}. The most and fewest flashes occurred in 2001 (31,853 flashes) and 2011 (2,984 flashes). Although inter-annual variations in CG are dependent on local factors, a 2001 peak was also found by Naccarato (2005), Pinto and Pinto (2008), Pinto et al. (2013) and dos Santos et al. (2016) for the SRB, which includes our study region. Naccarato (2005) suggested that this peak may be related to a La Niña phenomena of moderate intensity as discussed by Horizonte (2005) and Pinto et al. (2004b). We also find an interesting pattern in lightning events occurring from 2004 involving an approximately cyclical pattern of growth occurring in from 2004 to 2006, from 2007 to 2009 and from 2011 to 2013 and with declining trends observed from 2006 to 2007, for 2009 to 2011 and for 2013 to 2014, denoting the possibility of periodicity in the annual variation of the number of flashes occurring over the MRRJ. While the atmospheric mechanisms that explain the inter-annual variability of lightning in the tropics are complex and still not fully understood, they may be associated with processes that spur variability in convective activity such as El Niño/La

Fig. 2: Spatial pattern of CG density (flashes/km) in the study region from 2001 to 2016 showing each municipality encompassing the MRRJ.
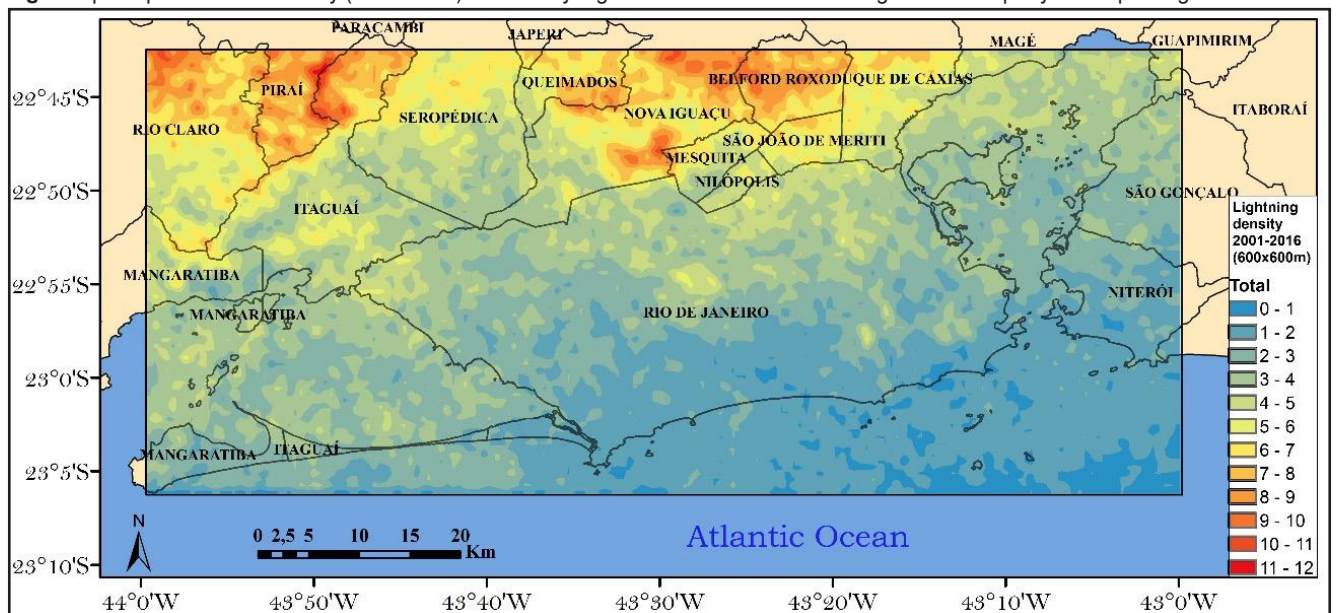
Niña phenomena (Sátori et al. 2009). Variations in atmospheric circulation due to frontal systems, the South Atlantic Convergence Zone (SACZ) and El Niño/La Niña phenomena are the main mechanisms that modulate convective activity at a large scale in the SRB (Pinto et al. 2003).

According to studies conducted by Chaves and Nobre (2004), warm and cool SST anomalies observed in the South Atlantic intensify and weaken the SACZ, respectively. The aforementioned work shows a positive anomaly for the SST running from November 2000 to February 2001 and thus perhaps the cause of peak flashes occurring in 2001 as shown in Fig. 3. It is also important to note that during the austral summer rainfall in the SRB is modulated by the SACZ with a northwest-southeast-oriented cloud cover band generated from moisture from the Amazon region and transported by the South American Low-Level Jet (SALLJ) (Herdies et al. 2002). The advection of moisture over the SRB by the SACZ is shaped by interactions occurring between frontal systems originating from the extra-tropics and from tropical convection. Almost 65% of all extreme precipitation events occurring in the region are associated with broad and intense patterns of convective activity in the SACZ (Carvalho et al. 2002). During 2014 the SRB experienced an extreme and prolonged drought event with a complete absence of SACZ episodes occurring during the austral summer due to a persistent pattern of mid-level anticyclone circulation (Coelho et al. 2015) offsetting convection over the region and inhibiting lightning occurrence as observed in Fig. 3. On the other hand, anthropogenic climate modification at the local level in the MRRJ was identified by Lucena et al. (2011), Lucena et al. (2013) and Peres et al. (2018) and has characterized the region as an urban heat island over the past decades. Accordingly to several studies there is evidence of a thermal and pollution effect on CG activity over urban areas and relationships with inter-annual variations in lightning (Steiger et al. 2002; Naccarato et. al. 2003, Pinto et al. 2004).

Fig. 4a presents a histogram of peak current (in kA) distributions of positive and negative GC flashes observed at kA intervals of $[0,20[$, $[20,40[$, $[40,60[$, $[60,80[$ and $[80,\infty[$ in the MRRJ from 20 April 2000 to 31 December 2016. Mean values of peak currents of negative and positive flashes are equal to 20.6 and 21.3 kA, respectively, and their maximum values are 360 and 222 kA, respectively. It is important to emphasize that the mean peak current of negative flashes differs significantly from values obtained by Pinto et al. (1996) for Southeastern Brazil (42 kA), by Orville (1990) for Florida (40-45 kA) and by Petersen et al. (1992) for Australia (39 kA). However, the mean peak current generated from positive flashes is very similar to that obtained by Pinto et al. (1999) (22 kA for the SRB).

Fig. 3: Inter-annual variability of total CG within the MRRJ during the study period. Open (closed) circles indicate years with above (below) 1 (-1) standard deviations from the mean values of the total number of CG, i.e., of high (low) lighting activity considering the 16-year period.
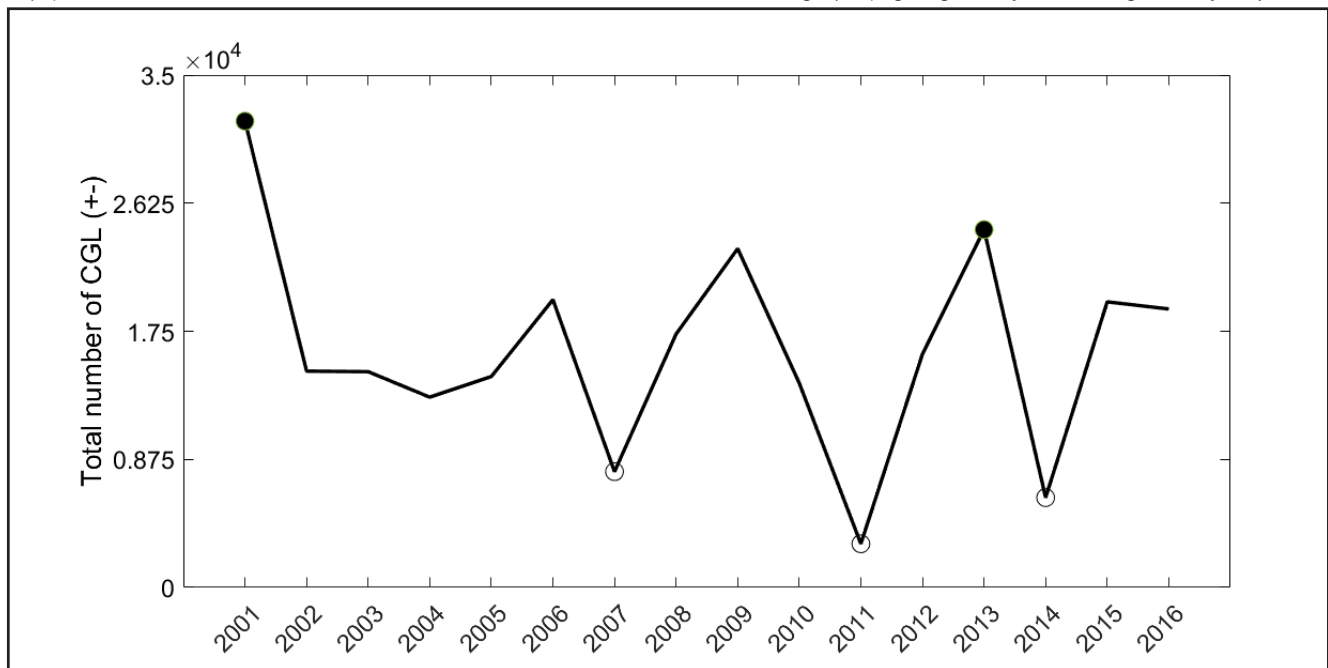
Annual variation in peak currents of GC atmospheric discharge is illustrated in Fig. 4b. The observed patterns of current peaks differ from those observed in the SRB (Naccarato 2005), in the USA (Orville and Huffines 2001) and in Austria (Schulz et al. 2005), which show only minor variations and less pronounced negative flashes while positive patterns show stronger variations and higher values. Variations in the peak currents of negative flashes do not show statistically significant values in the MRRJ whereas

positive patterns show a tendency of decline at a rate of 0.77 kA.year-1 (1% significance test ANOVA). Mean values of the peak currents of positive flashes are relatively higher than negative values for most of the period although from 2011 lower values and a tendency toward both polarities were observed. The years 2003, 2004, 2008 and 2016 were the only years for which differences in mean values of positive and negative current peaks were higher than 5 kA. Thus, in most years both polarities present close values.

Fig. 4: (a) Distribution of the peak current of positive and negative CG at kA intervals of [0, 20[, [20, 40[, [40, 60[, [60, 80[and [80, [; (b) Inter-annual variability of the peak current of positive and negative CG.
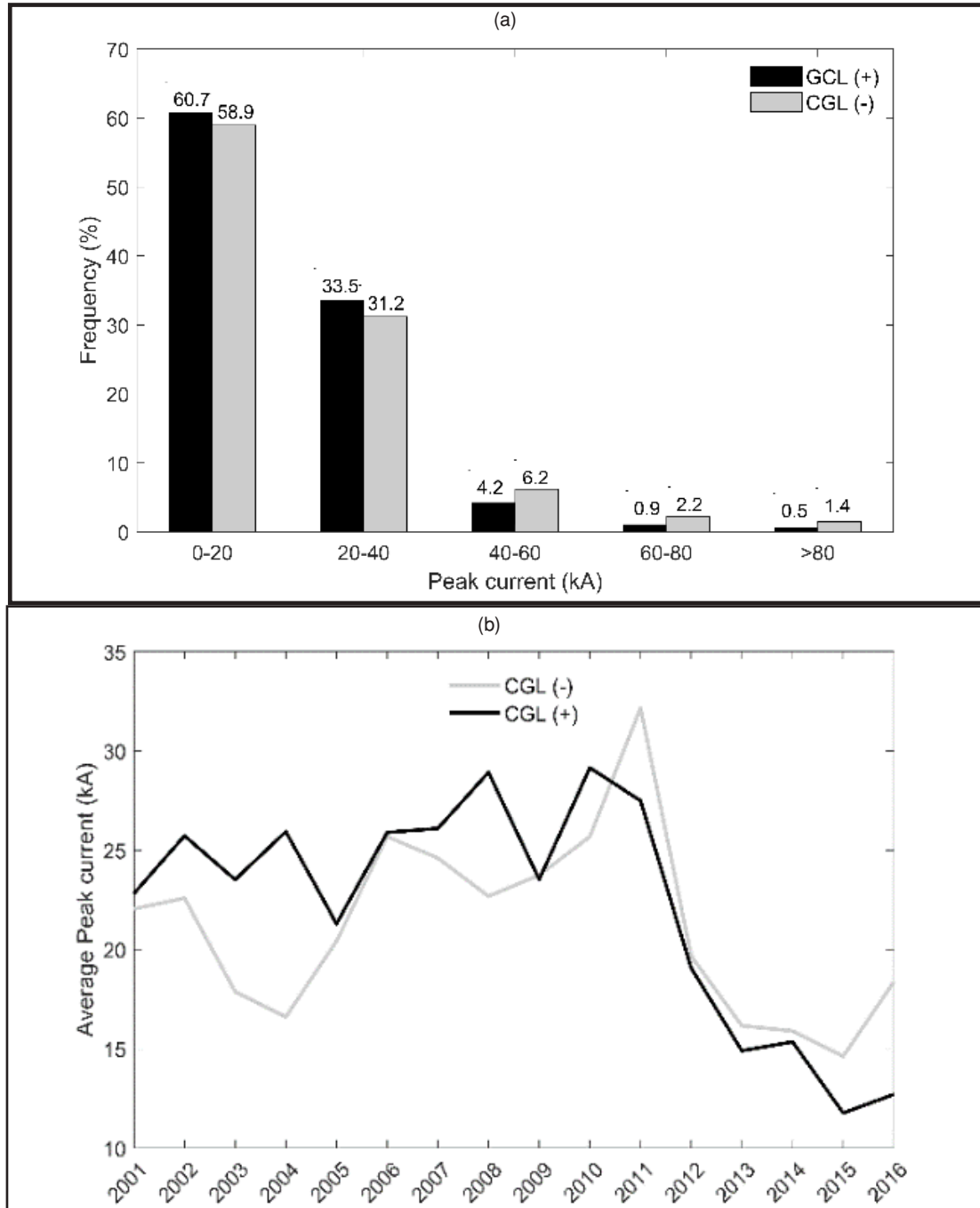
Fig. 5 shows the seasonal distribution of CG flashes [+-] and CG flashes [+] for the MRRJ and the total number of CG flashes [+-] occurring in each season of the study period. As expected, most discharge events occurred in summer, corresponding to 64.3% of all discharge for the period, followed by those occurring in spring at 20.5%. Winter is the season with the lowest average frequency of flashes in the period with only 2.3% of the total number. This distribution differs from that observed by Pinto et al. (1999b) for Southeastern Brazil for 1993, showing maximum levels of electric activity in spring attributed to differences in the sizes and locations of both study areas.

It is found that MRRJ discharge is characterized as predominantly negative (93.54% of all 258,794 flashes detected). Stratiform regions of mesoscale convective systems (MCSs) tend to produce more lightning with positive polarity due to a significant reduction in cloud depth. On the other hand, regions with intense convection such as the SRB, which consequently leads to the formation of clouds of great depth, produce more lightning with negative polarity (Rakov and Uman 2003). Changes in the height and depth of the negative charge centre near the base and in the positive charge centre overtop of clouds may be caused by high concentrations of aerosols in the atmosphere (so-called cloud condensation nuclei or CCN), which affect the relationship between positive and negative lightning (Lyons et al. 1998; Naccarato et al. 2003). This effect is more common in regions with high rates of air pollution taking the form of particulate matter such as in large urban centres and nearby burning areas. The percentage of positive flashes in the region is small with little variation during spring, summer and autumn. On the other hand, in winter, this percentage almost doubles in relation to other seasons of the year, which may be attributed to the higher vertical shear of wind (Orville and Huffines 2001) due to the passage of cold fronts and due to an enormous increase in aerosol concentrations in this period, which is usually dry (Naccarato et al. 2003). The vertical gradient of winds with height is directly related to weather and seasonal patterns. The higher the gradient with height, the stronger the displacement of positive versus negative charges (cloud shear), exposing a positive charge centre on the surface and making it easier for positive lightning to reach the ground. This behaviour has often been observed in winter storms in Japan (MacGorman and Rust 1998; Rakov and Uman 2003).

These results are compatible with those obtained by Orville et al. (1997) for Papua New Guinea. Orville et al. (1987) analysed results for the northeastern USA where polarity reverses abruptly, accounting for 80% of positive flashes occurring in winter and for less than 5% occurring in summer. Pinto et al. (1999.b) found values of approximately 35% for summer and winter in Southeastern Brazil, little variation in polarity levels throughout the year for tropical areas and higher percentages of positive flashes during winter storms than in summer at higher latitudes, supporting the results observed here.

Fig. 6 shows the monthly variation in the average rate of flashes (and not the total number) for data time series and the monthly variation in the average peak current for negative and positive discharge. It should be noted that the months with the highest

Fig. 5: Percentage of CG flashes [+-] (grey – left axis) and positive CG flashes [+] (black outline– right axis) occurring in the MRRJ in each season of the study period. Values shown above grey bars indicate the total number of CG [+-] events occurring per season.
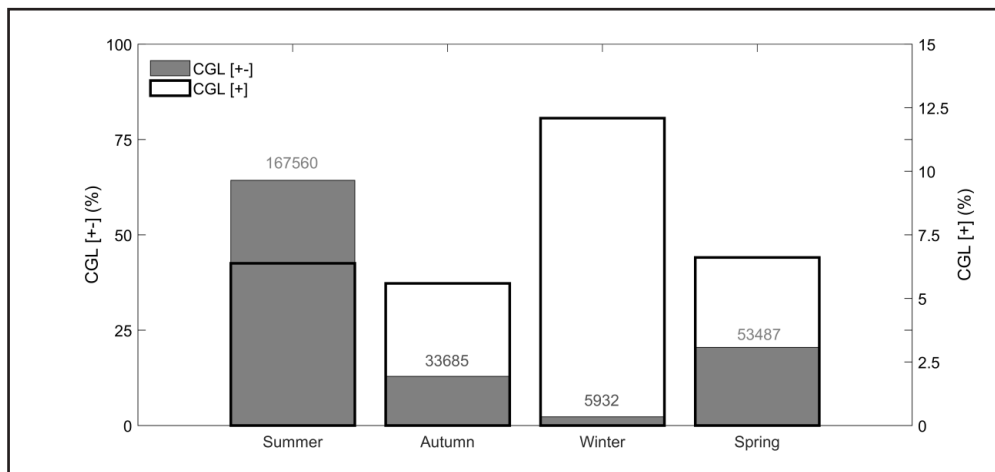
frequency of discharge run from December to March with a rate exceeding 2500 flashes.month^{-1}, corresponding to more than 80% of all lightning detected by the RINDAT in the period and agreeing with the results of Pinto et al. (1999.b); Naccarato et al. (2001); Naccarato (2005) and Pinto et al. (2003) in their work on flash data for Southeastern Brazil. These results also complement results for the USA presented by Orville and Huffines (2001), patterns for Europe given by Soriano et al. (2001) and Schulz et al. (2005) and trends for Oceania given by Orville et al. (1997) who observe monthly/ seasonal distributions of electric discharge across the globe with more significant activity observed in the hottest months of the year. This characterises widely recognised seasonal and climatic lightning patterns resulting from higher potential levels of energy available for convection in summer in each hemisphere, which promotes the formation of convective clouds and thunderstorms across all continents but mainly in tropical regions (Christian et al. 2003). The highest average flash rate is equal to 4041 flashes.month^{-1} (25% of the total) observed in February while months running from May to August present average rates of less than 130 flashes.month^{-1} (corresponding of roughly 3% of the total data population). The work of Pinto et al. (2013) in particular shows variations in monthly thunderstorm data for the city of Rio de Janeiro for 1997-2009 and presents the same intra-annual behaviours except that the month with the most significant day of thunderstorms occurs in January. We find no significant differences in atmospheric discharge levels across polarities of monthly variations.

It also should be noted that Fig. 6 illustrates that variations between discharge levels of both polarities present approximately similar seasonal variations. This diverges from the results of Naccarato (2005) who observed more considerable differences in monthly polarity variations from data for the SRB. The mean peak currents of negative flashes tend to be higher from January to March and lower than positive ones from April to December, which results in the formation of average annual peak currents for positive and negative values of 23.8 kA and 20.5 kA, respectively. In summer and early autumn, mean peak positive and negative currents are more similar in value. However, the positive mean is higher in the colder months (from May to November), which may suggest that positive discharge behaves differently in the colder seasons as also noted by Naccarato (2005). This differentiation may be associated with the fire period and consequently an increase in aerosol concentrations in the atmosphere (observed mainly in the Brazilian Cerrado and predominantly in the states of Mato Grosso and Mato Grosso do Sul) transported to study area (Boian and Kirchhoff 2004). Fernandes et al. (2006) revealed an association between the reduction of currents of negative flashes and fire periods. On the other hand, Naccarato (2005) observed a recovery of peak current values as summer approaches and as the rainy season begins in the SRB.

Fig. 7a depicts hourly variations in the percentage of total CG levels from both polarities in the MRRJ for the data time series. It is important to note

Fig. 6: Intra-annual variability of CG (bars, right axis) and positive and negative CG peak current (black curves, left axis) for the 2001-2016 period.
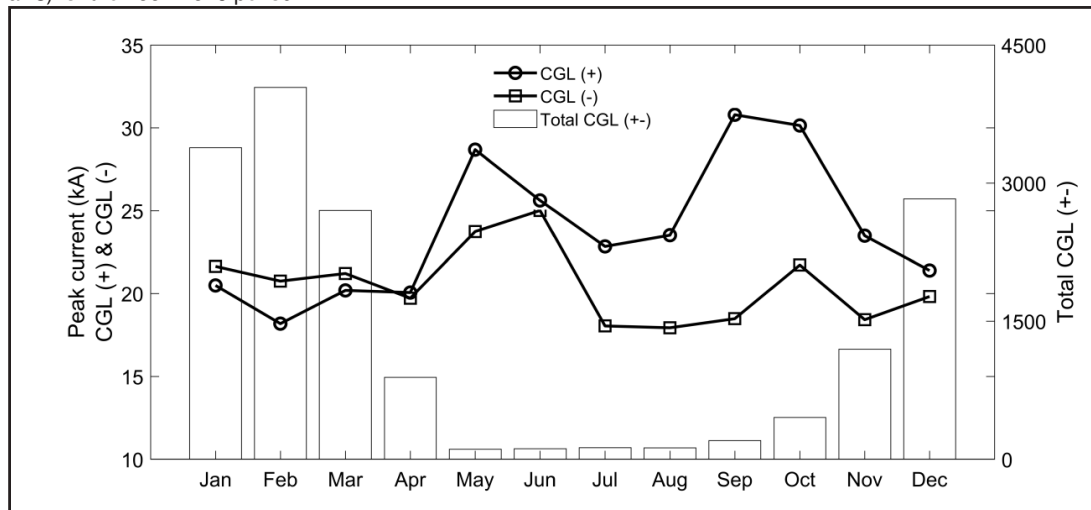
Fig. 7: (a) Average daily cycle of total numbers of positive (left axis) and negative (right axis) CG concerning the 16-year period. (b) The same as the upper panel but for average peak current (kA).
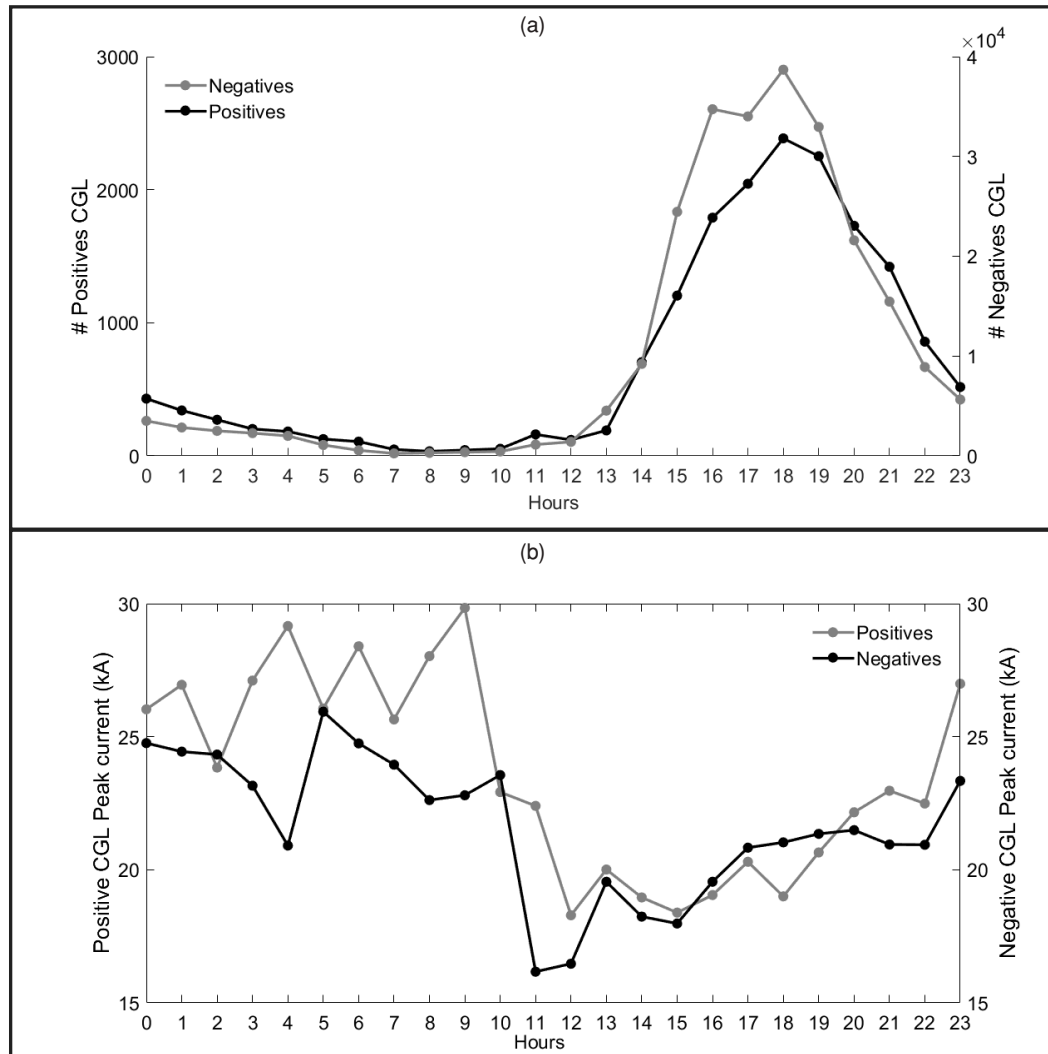
that the scale of the number of positive flashes is reduced and presented on the secondary vertical axis to facilitate a comparison with information on negative flashes. A typical daily variation is observed with higher values shown for the late afternoon and early evening and with lower values shown for the morning. In the period running between 16:00 and 20:00 local time, 56% of total discharge events are detected by the RINDAT and the period with the highest occurrence of atmospheric electrical activity occurs from 18:00 to 19:00 local time with 15.4% of total lightning events as observed by Pinto and Pinto (2008) and Pinto et al. (1999b) and Bourscheidt et al. (2009) for the city of São Paulo and for the SRB, respectively. Peak electrical activity is observed at approximately 18:00 local time and 2 hours from the occurrence of the maximum daily

temperature in the region (Naccarato 2005) when the atmosphere includes more potential energy available for convection conditions generating instability that leads to the formation of convective storms which generate atmospheric discharge. Orville and Huffines (2001) noted for the USA that peak activity schedules are influenced by regional factors. Fig. 7b shows that average hourly variations in the current peak between both polarities show similar patterns during daytime hours and that the average peak current value of positive flashes (23,56 kA) is higher than the negative average (21,63 kA) for a full day. We also find a significant decrease in mean current peaks at 10:00 and 12:00 local time following a gradual increase in values. According to Naccarato (2005), from 22:00 to 11:00 local time the atmosphere does not present thermodynamic characteristics necessary for the

formation of storms and its flash origins are more related to the passage of frontal systems. From 12:00 to 21:00 local time storms are caused predominantly by atmospheric instability caused by an increase in temperature and heat exchange across the surface.

It is important to note that the period of the day with the highest occurrence of lightning does not coincide with the period of higher peak currents, which suggests that storms caused by late-afternoon thermodynamic instability involve less intense discharge in terms of electric currents despite a higher frequency of lightning occurrence.

4. CONCLUSION

This study provides an updated overview of spatial and temporal variability in CG events recorded for the MRRJ over a 16-year period, revealing the main characteristics (geographic distribution, intra- and inter-annual variability, diurnal cycles, and peak currents) of atmospheric electricity for the region with 258,794 flashes detected over an area of 4,573 km^2 from 2001 to 2016.

Through an analysis of the temporal characteristics of lightning it was possible to detect behaviours already known by the scientific community and common to different regions of the globe: (1) a predominance of discharge with negative polarity; (2) seasonal variations in polarity with increases in the percentage of positive flashes occurring in winter; (3) seasonal variations in the number of flashes with the highest values occurring in summer and with the lowest values observed in winter; (4) seasonal variations in current intensity (positive values are more intense in winter/spring and negative values are more intense in summer); (5) relationships between polarity and current intensity (positive flashes are on average more intense than negative flashes); and (6) daytime cycles of electrical activity with the most frequent occurrence observed in the late afternoon and early evening.

The results of this study have demonstrated unique geographic and temporal characteristics of CG observed in the MRRJ over the past 16 years. In general, we observed declines in the peak currents of positive events over the years with a significant decrease observed in the period running from 2011 to 2016. The highest incidence levels are observed in the late afternoon (18:00-19:00 local time), and 93% of events occur in spring and summer (November to April), with February being the month with the highest incidence of lightning, followed by January and December. The intensity of the peak currents of positive and negative lightning is higher from 00:00-10:00 local time and during summer. On the other hand, in winter positive flashes are of a higher intensity than negative ones, and in September a difference of roughly 1/3 is observed in agreement with the work of Nacarato (2005). Our analysis of spatial density highlights the influence of the Atlantic Ocean (in the southern region) and of orographic effects of the Orgãos and Mar mountain chains (along the north side) on lightning distribution, revealing an increasing gradient from southern to northern areas of the study region.

Climate model projections point to considerable alterations in atmospheric variables, such as air temperature and moisture, leading to changes in convection and stability, particularly in the tropics. Consequently, future patterns of lightning are also expected to change since all of these factors directly and indirectly drive them. However, considerable uncertainties remain regarding regional responses to lightning in a changing climate and partly due to the current lack of information on recent patterns occurring in specific regions. This study significantly extends earlier analyses of atmospheric electricity patterns in Southeastern Brazil by using a long-term and contemporaneous dataset and by specifically focusing on the representation of lightning processes occurring over the MRRJ. The findings reported here together with instability indices should be of great use for the development of early warning systems and prevention strategies mitigating the impacts of atmospheric discharge in an area that is especially prone to such phenomena. Given the observed interannual variability in lightning occurrence over the past 16 years, further long-term studies focusing on how climate variability and change affect SRB lightning are of paramount importance. Further research must also quantify urban heat island effects on lightning occurrence in the region.

ACKNOWLEDGEMENTS

REFERENCES

Boian, C., & Kirchhoff, V. W. J. H. (2004). Measurements of CO in an aircraft experiment and their correlation with biomass burning and air mass origin in South America. Atmospheric Environment, 38(37), 6337–6347.

Bourscheidt, V., Junior, O. P., Naccarato, K. P., & Pinto, I. R. C. A. (2009). The influence of topography on the cloud-to-ground lightning density in South Brazil. Atmospheric Research, 91(2–4), 508–513.

Burrows, W. R., King, P., Lewis, P. J., Kochtubajda, B., Snyder, B., & Turcotte, V. (2002). Lightning occurrence patterns over Canada and adjacent United States from lightning detection network observations. Atmosphere-Ocean, 40(1), 59–80.

Carvalho, L. M., Jones, C., & Liebmann, B. (2002). Extreme precipitation events in southeastern South America and largescale convective patterns in the South Atlantic convergence zone. Journal of Climate, 15(17), 2377–2394.

Chaves, R. R., & Nobre, P. (2004). Interactions between sea surface temperature over the South Atlantic Ocean and the South Atlantic Convergence Zone. Geophysical Research Letters, 31(3), L03204. https://doi.org/10.1029/2003GL018647

Chen, S. M., Du, Y., & Fan, L. M. (2004). Lightning data observed with lightning location system in Guang-Dong province, China. IEEE Transactions on Power Delivery, 19(3), 1148–1153.

Christian, H. J., Blakeslee, R. J., Boccippio, D. J., Boeck, W. L., Buechler, D. E., Driscoll, K. T., et al. (2003). Global frequency and distribution of lightning as observed from space by the Optical Transient Detector. Journal of Geophysical Research: Atmospheres, 108(D1), ACL-4.

Coelho, C. A., de Oliveira, C. P., Ambrizzi, T., Reboita, M. S., Carpenedo, C. B., Campos, J. L. P. S., et al. (2016). The 2014 southeast Brazil austral summer drought: regional scale mechanisms and teleconnections. Climate Dynamics, 46(11–12), 3737–3752.

Diendorfer, G., Schulz, W., & Rakov, V. A. (1998). Lightning characteristics based on data from the Austrian lightning locating system. IEEE Transactions on Electromagnetic Compatibility, 40(4), 452–464.

Farias, W. R. G., Pinto, O., Jr., Naccarato, K. P., & Pinto, I. R. C. A. (2009). Anomalous lightning activity over the Metropolitan Region of São Paulo due to urban effects. Atmospheric Research, 91(2–4), 485–490.

Fernandes, W. A., Pinto, I. R., Pinto, O., Longo, K. M., & Freitas, S. R. (2006). New findings about the influence of smoke from fires on the cloud-to-ground lightning characteristics in the Amazon region. Geophysical research letters, 33(20), L20810. https://doi.org/10.1029/2006GL027744.

Gin, R. B. B., Pereira Filho, A. J., Beneti, C. A. A., & Guedes, R. L. (2012). Estudo das descargas elétricas atmosféricas no Sul e Sudeste do Brasil: Análise preliminar. XI Congresso Brasileiro de Meteorologia.

Herdies, D. L., da Silva, A., Silva Dias, M. A., & Nieto Ferreira, R. (2002). Moisture budget of the bimodal pattern of the summer circulation over South America. Journal of Geophysical Research: Atmospheres, 107(D20), LBA-42.

Hodanish, S., Sharp, D., Collins, W., Paxton, C., & Orville, R. E. (1997). A 10-year monthly lightning climatology of Florida: 1986–1995. Weather and Forecasting, 12(3), 439–448.

Hojo, J., Ishii, M., Kawamura, T., Suzuki, F., Komuro, H., & Shiogama, M. (1989). Seasonal variation of cloud-to-ground lightning flash characteristics in the coastal area of the Sea of Japan. Journal of Geophysical Research: Atmospheres, 94(D11), 13207–13212.

Horizonte, B. (2005). Mapeando a climatologia das descargas atmosféricas em Minas Gerais, utilizando dados de 1989 a 2002-uma analise exploratória. Doctoral dissertation, Pontifícia Universidade Católica de Minas Gerais. Huffines, G. R., & Orville, R. E. (1999). Lightning ground flash density and thunderstorm duration in the continental United States: 1989–1996. Journal of Applied Meteorology, 38(7), 1013–1019.

Krider, E. P., Noggle, R. C., Pifer, A. E., & Vance, D. L. (1980). Lightning direction-finding systems for forest fire detection. Bulletin of the American Meteorological Society, 61(9), 980–986.

Lopez, R. E., & Holle, R. L. (1986). Diurnal and spatial variability of lightning activity in northeastern Colorado and central Florida during the summer. Monthly Weather Review, 114(7), 1288–1312.

Lucena, A. J., E. B. Correa, O. C. Rotunno Filho, L. F. Peres, J. R. A. Franc¸a, and M. G. A. da Silva Justi (2011), Heat island and precipitation events in the metropolitan area of Rio de Janeiro (RMRJ). Proceedings of the XIV World Water Congress (in Portuguese).

Lucena, A. J., Rotunno Filho, O. C., Franc¸a, J. R., Peres, L., & Xavier, L. N. R. (2013). Urban climate and clues of heat island events in the metropolitan area of Rio de Janeiro. Theoretical and Applied Climatology, 111(3–4), 497–511. Lyons, W. A., Nelson, T. E., Williams, E. R., Cramer, J. A., & Turner, T. R. (1998). Enhanced positive cloud-to-ground lightning in thunderstorms ingesting smoke from fires. Science, 282(5386), 77–80.

MacGorman, D. R., & Rust, W. D. (1998). The electrical nature of storms. Oxford University Press on Demand. Naccarato, K. P. (2005). Análise das características dos relâmpagos na região sudeste do Brasil. PhD thesis, INPE, São Jose´ dos Campos, INPE-8380-TDI/770.

Naccarato, K. P., Pinto, O., & Pinto, I. R. C. A. (2003). Evidence of thermal and aerosol effects on the cloud-to-ground lightning density and polarity over large urban areas of Southeastern Brazil. Geophysical Research Letters, 30(13), 1674. https://doi. org/10.1029/2003GL017496

Naccarato, K. P., Pinto, O., Pinto, I. R. C. A., Cazetta Filho, A., & Amorim, G. E. (2001, October). Lightning characteristics in the southeastern region of Brazil: 1999–2000. 7th International Congress of the Brazilian Geophysical Society. Ogawa, T. (1995). Lightning currents. In H. Volland (Ed.), Handbook of atmospheric electrodynamics (Vol. 1, pp. 93–136). Boca Raton: CRC Press.

Orville, R. E. (1990). Peak-current variations of lightning return strokes as a function of latitude. Nature, 343(6254), 149.

Orville, R. E. (1991). Lightning ground flash density in the contiguous United States-1989. Monthly Weather Review, 119(2), 573–577.

Orville, R. E., & Huffines, G. R. (2001). Cloud-to-ground lightning in the United States: NLDN results in the first decade, 1989–98. Monthly Weather Review, 129(5), 1179–1193.

Orville, R. E., Huffines, G. R., Burrows, W. R., Holle, R. L., & Cummins, K. L. (2002). The North American lightning detection network (NALDN)—First results: 1998–2000. Monthly Weather Review, 130(8), 2098–2109.

Orville, R. E., Huffines, G., Nielsen-Gammon, J., Zhang, R., Ely, B., Steiger, S., et al. (2001). Enhancement of cloud-to-ground lightning over Houston, Texas. Geophysical Research Letters, 28(13), 2597–2600.

Orville, R. E., & Silver, A. C. (1997). Lighting ground flash density in the contiguous United States: 1992–95. Monthly Weather Review, 125(4), 631–638.

Orville, R. E., Weisman, R. A., Pyle, R. B., & Henderson, R. W. (1987). Cloud-to-ground lightning flash characteristics from June 1984 through May 1985. Journal of Geophysical Research: Atmospheres, 92(D5), 5640–5644.

Orville, R. E., Zipser, E. J., Brook, M., Weidman, C., Aulich, G., Krider, E. P., et al. (1997). Lightning

in the region of the TOGA COARE. Bulletin of the American Meteorological Society, 78(6), 1055–1067.

Peres, L., de Lucena, A. J., Rotunno Filho, O. C., & de Almeida Franc¸a, J. R. (2018). The urban heat island in Rio de Janeiro, Brazil, in the last 30 years using remote sensing data. International Journal of Applied Earth Observation and Geoinformation, 64, 104–116.

Petersen, W. A., & Rutledge, S. A. (1992). Some characteristics of cloud-to-ground lightning in tropical northern Australia. Journal of Geophysical Research: Atmospheres, 97(D11), 11553–11560.

Petersen, W. A., & Rutledge, S. A. (1998). On the relationship between cloud-to-ground lightning and convective rainfall. Journal of Geophysical Research: Atmospheres, 103(D12), 14025–14040.

Pinto, O., Gin, R. B. B., Pinto, I. R. C. A., Mendes, O., Diniz, J. H., & Carvalho, A. M. (1996). Cloud-to-ground lightning flash characteristics in southeastern Brazil for the 1992–1993 summer season. Journal of Geophysical Research: Atmospheres, 101(D23), 29627–29635.

Pinto, O., Naccarato, K. P., Pinto, I. R. C. A., Fernandes, W. A., & Neto, O. P. (2006). Monthly distribution of cloud-to-ground lightning flashes as observed by lightning location systems. Geophysical Research Letters, 33, L09811. https://doi.org/10. 1029/2006GL026081.

Pinto, I. R. C. A., & Pinto, O., Jr. (2003). Cloud-to-ground lightning distribution in Brazil. Journal of Atmospheric and SolarTerrestrial Physics, 65(6), 733–737.

Pinto, O., & Pinto, I. R. C. A. (2008). On the sensitivity of cloudto-ground lightning activity to surface air temperature changes at different timescales in São Paulo. Brazil. Journal of Geophysical Research: Atmospheres, 113, D20123. https://doi.org/10.1029/ 2008JD009841.

Pinto, O., Pinto, I. R. C. A., de Campos, D. R., & Naccarato, K. P. (2009). Climatology of large peak current cloud-to-ground lightning flashes in southeastern Brazil. Journal of Geophysical Research: Atmospheres, 114, D16105. https://doi. org/10.1029/ 2009JD012029.

Pinto, O., Jr., Pinto, I. R. C., Diniz, J. H., Cazetta Filho, A., Cherchiglia, L. C., & Carvalho, A. M. (2003). A seven-year study about the negative cloud-to-ground lightning flash characteristics in Southeastern Brazil. Journal of Atmospheric and Solar-Terrestrial Physics, 65(6), 739–748.

Pinto, O., Pinto, I. R. C. A., & Ferro, M. A. S. (2013). A study of the long-term variability of thunderstorm

days in southeast Brazil. Journal of Geophysical Research: Atmospheres, 118(11), 5231–5246.

Pinto, I. R. C. A.; Pinto Jr., O; Pinto Neto, O (2004) The impact of the El Niño on the lightning distribution in South America. International Conference on Lightning Detection, 18., 2004, Helsinki, Finlandia. Proceedings Helsinki: Vaisala Inc., CDROM.

Pinto, I. R. C. A., Pinto, O., Jr., Gomes, M. A. S. S., & Ferreira, N. J. (2004). Urban effect on the characteristics of cloud-to-ground lightning over Belo Horizonte-Brazil. Annales Geophysics, 22(2), 697–700. https://doi.org/10.5194/angeo-22-697-2004.

Pinto, O., Pinto, I. R. C. A., Gomes, M. A. S. S., Vitorello, I., Padilha, A. L., Diniz, J. H., et al. (1999a). Cloud-to-ground lightning in southeastern Brazil in 1993: 1. Geographical distribution. Journal of Geophysical Research: Atmospheres, 104(D24), 31369–31379.

Pinto, I. R. C. A., Pinto, O., Rocha, R. M. L., Diniz, J. H., & Carvalho, A. M. (1999b). Cloud-to-ground lightning in southeastern Brazil in 1993: 2. Time variations and flash characteristics. Journal of Geophysical Research: Atmospheres, 104(D24), 31381–31387.

Rakov, V. A., & Uman, M. A. (2003). Lightning: physics and effects. Cambridge: Cambridge University Press. Ramos, A. M., Ramos, R., Sousa, P., Trigo, R. M., Janeira, M., & Prior, V. (2011). Cloud to ground lightning activity over Portugal and its association with circulation weather types. Atmospheric Research, 101(1–2), 84–101. Reap, R. M. (1994). Analysis and prediction of lightning strike distributions associated with synoptic map types over Florida. Monthly Weather Review, 122(8), 1698–1715.

Rocha, R. M. L., Pinto, I. R. C. A., & Pinto Jr, O. (1997, November). Cloud-to ground lightning flash characteristics in Southeastern Brazil in the Winter Season. 5th International Congress of the Brazilian Geophysical Society.

Rodrigues, R. B., Mendes, V. M. F., & Catalão, J. P. D. S. (2010). Lightning data observed with lightning location system in Portugal. IEEE Transactions on Power Delivery, 25(2), 870–875.

Romps, D. M., Seeley, J. T., Vollaro, D., & Molinari, J. (2014). Projected increase in lightning strikes in the United States due to global warming. Science, 346(6211), 851–854.

Russo, A., Ramos, A. M., Benali, A., & Trigo, R. M. (2017, April). Forest fires caused by lightning activity in Portugal. EGU General Assembly Conference Abstracts (Vol. 19, p. 17613). Santos, A. P. P., Coelho, C. A., Pinto Ju´nior, O., dos Santos, S. R. Q., de Lima, F. J. L., & de Souza, E. B. (2018). Climatic diagnostics associated with anomalous lightning incidence during the summer 2012/2013 in Southeast Brazil. International Journal of Climatology, 38(2), 996–1009.

Santos, A. P. P., Júnior, O. P., de Souza, E. B., Azambuja, R., & dos Santos, S. R. Q. (2016). Spatiotemporal variability and identify Extreme Events of Lightning in the State of São Paulo during the Summer. Revista Brasileira de Geografia Física, 9(2), 346–352.

Santos, A. P. P., Pinto Junior, O., Santos, S. R. Q., Lima, F. J. L., Souza, E. B., Morais, A. A. R., et al. (2017). Climatic Projections of Lightning in Southeastern Brazil Using CMIP5 Models in RCP's Scenarios 4.5 and 8.5. American Journal of Climate Change, 6, 539–553.

Satori, G., Williams, E., & Lemperger, I. (2009). Variability of global lightning activity on the ENSO time scale. Atmospheric Research, 91(2–4), 500–507. Schulz, W., Cummins, K., Diendorfer, G., & Dorninger, M. (2005). Cloud-to-ground lightning in Austria: A 10-year study using data from a lightning location system. Journal of Geophysical Research: Atmospheres, 110, D09101. https://doi.org/10.1029/ 2004JD005332.

Soriano, L. R., & de Pablo, F. (2002). Maritime cloud-to-ground lightning: The western Mediterranean Sea. Journal of Geophysical Research: Atmospheres, 107(D21), 4597. https://doi.org/10. 1029/2002JD002211.

Soriano, L. R., De Pablo, F., & Tomas, C. (2005). Ten-year study of cloud-to-ground lightning activity in the Iberian Peninsula. Journal of Atmospheric and Solar-Terrestrial Physics, 67(16), 1632–1639.

Soriano, L. R., Pablo, F., & Diez, E. G. (2001). Cloud-to-ground lightning activity in the Iberian Peninsula: 1992–1994. Journal of Geophysical Research: Atmospheres, 106(D11), 11891–11901. Steiger, S. M., Orville, R. E., & Huffines, G. (2002). Cloud-toground lightning characteristics over Houston, Texas: 1989–2000. Journal of Geophysical Research: Atmospheres, 107(D11), 4117. https://doi.org/10.1029/2001JD001142.

Watson, A. I., Lo´pez, R. E., & Holle, R. L. (1994). Diurnal cloud-to-ground lightning patterns in Arizona during the southwest monsoon. Monthly Weather Review, 122(8), 1716–1725.

Wierzchowski, J., Heathcott, M., & Flannigan, M. D. (2002). Lightning and lightning fire, central cordillera. Canada. International Journal of Wildland Fire, 11(1), 41–51.

Williams, E. R., Mushtak, V. C., & Boccippio, D. J. (2003). Another look at the dependence of lightning flash rate on the temperature of boundary layer air in the present climate. Proceedings 12th International Conference on Atmospheric Electricity (pp. 9–13).

An Automated Nowcasting Model of Significant Instability Events in the Flight Terminal Area of Rio de Janeiro - Brazil

Gutemberg Borges França[I]

Manoel Valdonel de Almeida[I]

Alessana C. Rosette[I]

ABSTRACT

This paper presents anovel model, based on neural network techniques, to produce short-term and locally specific forecasts of significant instability for flight in the terminal area of Rio de Janeiro, Brazil. Twelve years of data were used for neural network training/validation and test. Data are originally from four sources: 1) hourly meteorological observations from surface meteorological stations at five airports distributed around the study area; 2) atmospheric profiles collected twice a day at the meteorological station at Galeão Airport; 3) rain rate data collected from a network of twenty-nine rain gauges in the study area; and 4) lightning data regularly collected by national detection networks. An investigation was undertaken regarding the capability of a neural network to produce early warning signs—or as a nowcasting tool—for significant instability events in the study area. The automated nowcasting model was tested using results from five categorical statistics, indicated in parentheses in forecasts of the first, second, and third hours, respectively—namely: proportion correct (0.99, 0.97, and 0.94), BIAS (1.10, 1.42, and 2.31), the probability of detection (0.79, 0.78, and 0.67), false-alarm ratio (0.28, 0.45, and 0.73), and threat score (0.61, 0.47, and 0.25). Possible sources of error related to the test procedure are presented and discussed. The test showed that the proposed model (or neural network) can grab the physical content inside the dataset, and its performance is quite encouraging for the first and second hours to nowcast significant instability events in the study area.

Keywords: neural networks; nowcasting; significant instability event.

1. INTRODUCTION

Aviation is negatively or positively influenced by the atmospheric conditions at any place and time (Ahrens, 2008). In particular, the Terminal Area (TA) of an airport is the area where the aircraft are waiting for landing or take-off and, thus, is quite sensitive to weather conditions. The air traffic controllers and pilots require precise information about the weather conditions at the TA to make short-term decisions that fall into the time scale of nowcasting, which ranges from the interval of a few minutes up to 6 h. During the few last decades, various works associated with nowcasting—for example, Wilson (1966), Wilk and Gray (1970) and others—have initially proposed nowcasting approaches based on extrapolations of radar data to generate nowcasting of thunderstorms. To follow up this idea, the convective tracking approaches were improved by including the cell evolution in time and intensity using radar data (Dixon and Wiener 1993). Wilson et al. (1998) presented a review of the nowcasting techniques developed during the 1960s and 1970s. The advancement of parallel computing and data availability allowed a numerical weather model to assimilate via rapid update cycle (and, more recently, via rapid refresh method) mesoscale data such as satellite and/or radar data to nowcast convective systems. Several authors have addressed the latter in the last two decades or so—e.g., Xue et al. (2003), Sun and Wilson (2003), Schroeder et at. (2006), Liu et al. (2008) and others. Mueller

I. *Federal University of Rio de Janeiro (UFRJ), Rio de Janeiro, Brazil. Correspondence to:* gutemberg@lma.ufrj.br.

et al. (2003) proposed a sophisticated system to nowcast (up to 1 h) thunderstorm locations based on a combination of surface meteorological, radar, satellite data and numerical modelling, which considers the storm stages. Mass (2012) provided a comprehensive review of nowcasting including current developments and future challenges. Considering the aviation application, Isaac et al. (2006), Isaac et al. (2011) and Isaac et al. (2012) presented a sequence of works that resulted in a refined nowcasting system for aviation that uses data from numerical models, surface observations, radar, satellite and a microwave radiometer to generate nowcasts for principal airports in Canada up to approximately 6 h. In contrast, in Brazil, a meteorologist currently uses his experience to integrate different in situ meteorological observations and/or atmospheric model outputs using conceptual models on how the atmosphere works to generate nowcast at principal airports. In particular, the TA of Rio de Janeiro, the focus of this study, has five airports (see Fig. 1) whose flights are significantly affected (by delays and trajectory changes), especially during the approximations for landing or take-off, by Significant Instability Events (SIE), which are normally associated with convective weather. Groisman et al. (2005)

presented evidence that the incidence of convective weather has increased approximately 58 % per year in south-eastern Brazil—where the Rio de Janeiro TA is located—since the 1940s. Therefore, the objective here is to present an Automated Nowcast Model (ANM) to generate short-term and local-specific predictions of SIEs, based on neural network techniques, for the fight TA of Rio de Janeiro, Brazil.

2. METEOROLOGICAL DATASETS AND STUDY AREA

This study used four datasets from 1 January 1997 to 31 December 2008, as follows:

- TEMP is the meteorological code used to report profiles of atmospheric variables and is normally generated daily at 00:00 UTC and 12:00 UTC on all radiosonde stations, one of which, in this work, is located at Galeão´s Airport, whose international aviation code is SBGL, where SB and GL denote Brazil and Galeão, respectively (see Fig. 1). The TEMP-coded dataset was obtained online from http://weather.uwyo.edu/upperair/sounding.html;

Figure 1: Satellite image of Rio de Janeiro´s metropolitan area. Yellow triangles [red squares] indicate location of the twenty-nine rain gauges from Alerta Rio's System that belongs the City Hall of Rio de Janeiro [five airport meteorological stations].

Source: Adapted from www.google.com.br/maps.

- METAR and SPECI are meteorological codes employed to report hourly surface meteorological conditions and significant change (decline or improvement) in the weather condition, at any time from the full hour. Figure 1 shows the locations of five surface meteorological stations (represented by red icons) in the Rio de Janeiro metropolitan area. The SPECI data were used only for the model test. The stations (or airports) are Galeão (SBGL), Santa Cruz (SBSC), Santos Dumont (SBRJ), Jacarepaguá (SBJR), and Afonsos (SBAF). The data were obtained at the URL address mentioned above;

- rain rate (RR) is obtained from twenty-nine rain gauges (represented by yellow triangles in Fig. 1) distributed over the Rio de Janeiro metropolitan area. The data were obtained from http://www.rio.rj.gov.br/alertario/ and collected by Alerta Rio's System, which belongs the City Hall of Rio de Janeiro; and

- lightning reports, regularly collected by the National Integrated Lightning Detection Network (RINDAT), characterize each occurrence by indicating location (latitude, longitude), intensity polarity (cloud to ground or ground to the cloud), and time (UTC with accuracy in milliseconds). ELETROBRAS FURNAS Company kindly made the data available.

Table 1 summarizes all information on the datasets used for ANM training, test and validation in this study. Figure 1 shows the study region and the flight terminal area of Rio de Janeiro.

Table 1: Datasets and meteorological variables used in the distinct stages of development of the neural network-based automated nowcasting model. It covers a period from 1 January of 1997 to 31 December 2009.

Time series	Frequency and data period	Input: Primary variables Total number: 8	Input: Derived variables Total number: 4	Data percentage used for SNM training/ validation	Data percentage used for SNM test	Validation variables	Output variable
		Predictors purpose: characterization of atmospheric conditions					
METAR (data are from SBGL, SBSC, SBJR, SBAF and SBRJ)	Hourly from 1 January 1997 to 31 December 2008	Dew point at surface	Julian day			Class 1 as in Table 2	
TEMP (data are from SBGL)	Daily at 0000 and 1200 UTC from 1 January 1997 to 31 December 2008	Humidity at 850 and 500 hPa. Pression at 1000, 850, 700, and 500 hPa	K, Vapour pressure at 1000, and 850 hPa,	70 %	30 %	---	Yes = class 1 or No = class 0
Rain rate (RR) per hour (data are from the 29 rain gauges)	Every 15 minutes from 1 January 1997 to 31 December 2008	RR for 1 hour	---			---	
Lightning inside a radius of 50 km centred at SBGL	Varies	---	---	---	100%	1 (lightning) or 0 (no lightning)	

## 3. METHODOLOGY AND ALGORITHM DESCRIPTION

Meteorologists have limited windows of time in which to integrate all available data and generate a nowcast, as stated by Mueller et al. (2003). Therefore, the idea is to create an automated nowcast model in which a neural network algorithm is used for data fusion, similar to the work performed by Cornman et al. (1998) for detecting and extrapolating weather fronts. At present, one may find applications of neural network in numerous fields of science, such as modelling, time series investigations, and image pattern recognition, owing to their capability to learn from input data (Haykin, 1999). Normally, stages of neural networks are denoted by a global function (Equation 1), as described by Bishop (2006)—for example:

$$y_k \left(X, W \right) = \sigma \left(\sum_{j=0}^{M} w_{kj}^{(2)} h \left(\sum_{i=0}^{D} w_{ji}^{(1)} x_i \right) \right) \qquad (1)$$

where x_i and y_k are the input and output, respectively; (1), (2) and w_{ji}, w_{kj} represent the input layer, hidden layer and the connection weights (that should be determinated) between input and hidden layers and hidden and output layers, respectively; **D** and **M** are the number of inputs and number of neurons in the internal layer, respectively; and **σ** and **h** are linear and no linear transfer functions between the neural network layers, respectively. Thus, determination of the output via Eq. (1) crucially depends on the values of the weights that are worked out, similarly as in a multiple linear regression using a set of inputs and outputs; however, instead, to minimize the distance as in nonlinear regression, the neural networks attempt to minimize the cost function. Given that the SIE forecast problem requires a categorical output, it was decided to use probabilistic neural networks, initially proposed by Specht (1990, 1991), which is based on radial-basis function (RBF), A RBF network consists of three layers: the input layer; the second layer (or hidden), apply a non-linear transformation, denoted as **h** that, here, is Gaussian function, of the input space to the hidden space. The third layer, the outgoing, is linear (**σ**), providing the network response. Further details about neural networks and their applications may be found in Pasini et al. (2001), Haykin (1999), Pasero and Moniaci (2004), Bremnes and Michaelide (2005), Bishop (2006), Haupt et al. (2009) and Hsieh (2009).

Figure 3 depicts a general flowchart for the proposed automated nowcasting model. It has four major steps: (1) data processing; (2) definitions of input and output variables; (3) training and validation; and (4) test. These steps are described below.

Figure 3: Automated Nowcast Model flowchart.
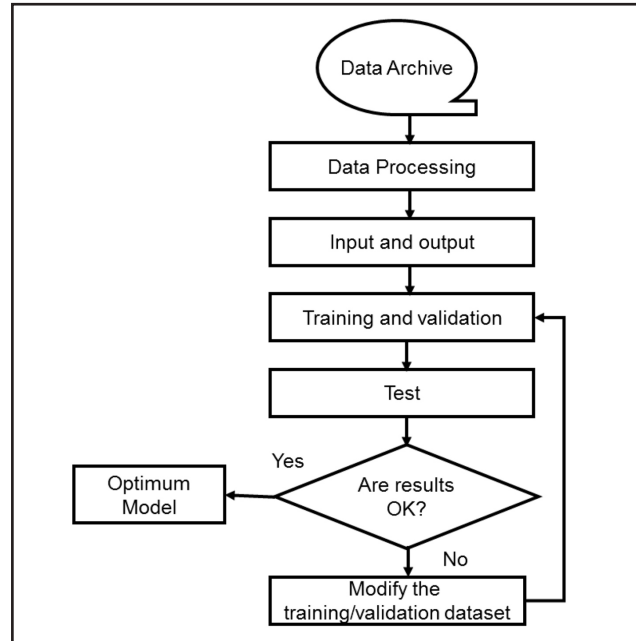
3.1 Step 1—Data processing:

All datasets were sorted chronologically, and their statistical consistency was observed, resulting in 63,320 hours of meteorological records. Based on weather conditions reported by METAR, each meteorological record was classified into two classes — "0" and "1", representing nonexistence of important weather conditions (low impact to flight flow) and the existence of significant atmospheric instability (or SIE, as previously defined) for flights in the TA of Rio de Janeiro, respectively. Table 1 shows all weather conditions reported in terms of METAR code and their classification per class.

3.2 Step 2—Input and output definition:

ANM data fusion is based on a neural network, which must be sequentially trained, validated and subsequently tested to forecast the presence or absence of SIEs. The latter corresponds to the learning process of a neural network. The input and

output variables play an important role in ANM data fusion and should be previously defined.

3.2.1 Input variables

These variables are the predictors of ANM and indicate the atmospheric stages of SIEs in the study area that are used by the ANM during its learning process. A meteorological record is composed of primary and derived variables that are extracted from METAR, TEMP, and RR and calculated using primary variables. The purpose of ANM is to nowcast SIEs and other weather conditions; therefore, all inputs (or predictors) should thermodynamically represent the presence or absence of SIE, which are embedded in the meteorological records utilized to train/validate and test the ANM. The latter should be able to classify or forecast weather conditions of classes numbered as "0" and "1", and its performance is evaluated by cross-test with observations as presented later. The criterion to select input (primary and derived) variables is based on a conceptual model of how the atmosphere works—particularly during SIE occurrence, which have typical atmospheric patterns. Several input variables are used—for example, atmospheric instability indices, i.e., K-index (K) $= (T_{850} - T_{500}) + Td_{850} - (T_{700} - Td_{500})$, where T_z and Td_z represent temperature and dew point, respectively, in Celsius degrees, and z is the given atmospheric pressure in hPa; Total Totals (TT) $= T_{850} + Td_{850} - 2T_{500}$; Lapse Rate (LR), represented by $LR = 1000(T_{500} - T_{700})/ (GPH_{500} - GPH_{700})$, where

GPH denotes the geopotential height; and others defined in columns three and four of Table 1. At the beginning, many inputs were generated. However, with regard to the neural network training, it is necessary to adopt a method to prune collinear inputs that bring no new information and, thus, could reduce the network performance. Pasini and Ameli (2003) have investigated heuristic pruning methods. Here, autocorrelation was selected and enforced to remove collinearity of the input. Twelve variables then remained, divided into eight primary and four derived variables as listed in columns three and four of Table 1, respectively.

3.2.2 Output variables

The output is defined as weather conditions reported in METAR codes and divided into two classes, "0" and "1", which represent the absence and presence of SIEs, respectively, as shown in Table 2. In other words, classes 0 and 1 indicate nonexistence of significant instability and existence of significant instability (i.e., weather condition of METAR code as T, TL, TRW-, TRW, TRW+) in the TA of Rio de Janeiro, respectively.

Following Pasini (2015) and aiming to avoid the overfitting problem during the learning process of the neural network, which is represented by step 3, the meteorological records were divided into three subsets: training, validation and test. Figure 4(a) shows the initial training and validation datasets representing 70 % of the original records (or 44,324) with 30 % (or 18,996) for testing, as shown in Fig. 4(b).

Table 2: Weather condition classification in METAR and attributed ANM classes.

| Class	METAR code	Weather condition	Class	METAR code	Weather condition
	H	Haze		R	Moderate rain
	K	Smog		RF	Moderate rain with fog
	F	Fog	0	R+	Heavy rain
	L-	Light drizzle		R+ F	Heavy rain with fog
	L- F	Light drizzle with fog		RW	Showers
0	L	Moderate drizzle		RW+	Heavy showers
	LF	Moderate drizzle with fog		T	Thunderstorms
	L	Heavy drizzle		TL	Thunderstorms with light drizzle
	R-	Light rain	1	TRW-	Thunderstorms with showers
	R- H	Light rain with haze		TRW	Thunderstorms with moderate showers
	R- F	Light rain with fog		TRW+	Thunderstorms with heavy showers

Figure 4: Histograms of frequency accordingly to two classes "0" and "1" that represent no SIE and SIE, respectively: (a) and (b) show initial class distribution of training/validation and test datasets that correspond to 70% (or 44,324) and 30% (or 18.996) of meteorological records, respectively. (c) similarly presents class distribution of meteorological recordings for optimal training.
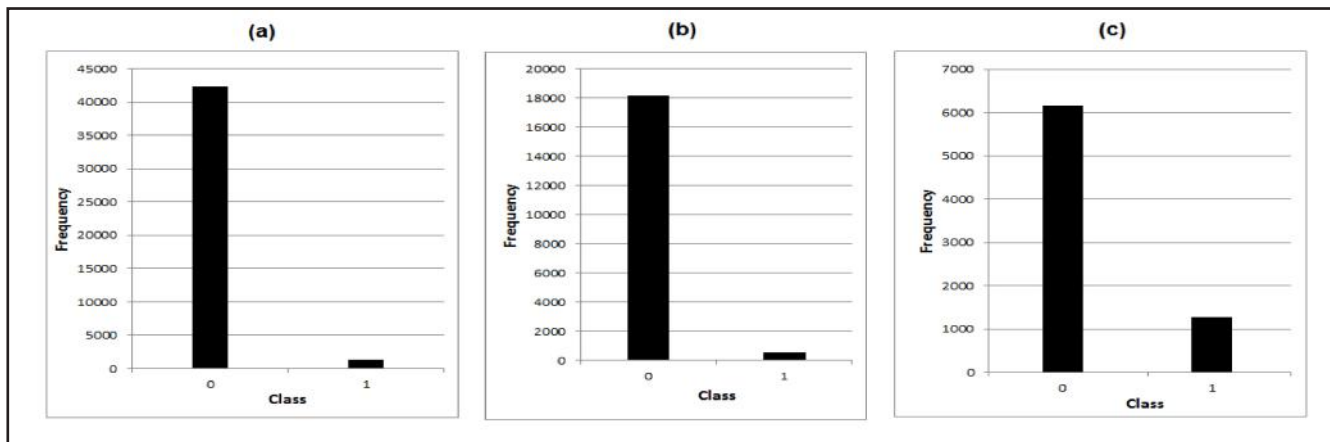
3.3 Step 3—Neural Network Training and Validation

The internal number of neurons (previously defined as **M**) of probabilistic neural networks is here determined based on cascade-correlation algorithm suggested by Fahman and Lebiere (1990). Figure 2 shows generally an example of a cascade forward network for five inputs and one output. The training and validation are performed in an iterative cycle composed of a looping of two phases, which are executed using a specific dataset (initially the one in Fig. 4(a), which could be artificially modified until the optimal dataset is reached, as described in step 4), and a constant number of inputs (defined as **D** is equal to twelve). The two phases are described as follows:

Figure 2: A schematic view of a cascade forward network with five inputs.
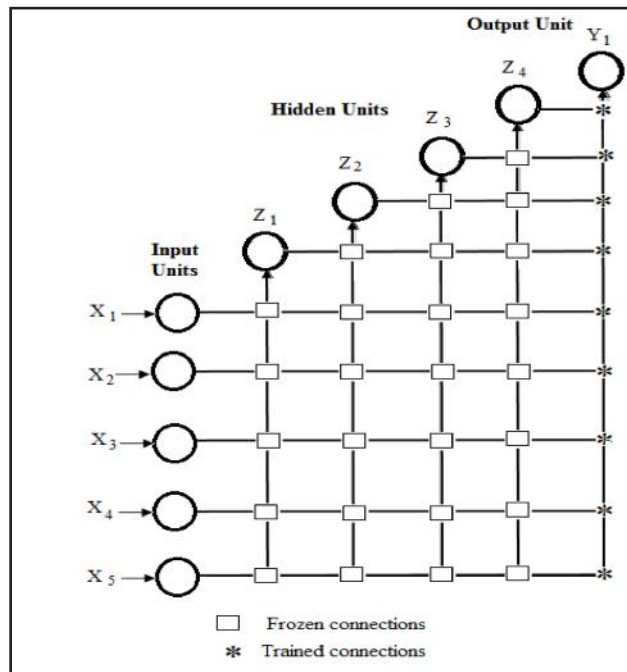
1. It starts with a minimal (only one neuron) internal layer of the neural network (represented generally by Eq. (1)) and automatically adds new hidden neurons one at a time, in each round, finally resulting in a multilayer structure with the input connection frozen (represented by squares in Fig. 2); and

2. The follow-on neural network is applied to the validation dataset, and the error is calculated. There are then two options: first, return to (i) if the test error has not increased from the previous round and the number of neurons in the internal layers is less than 150; or second, to go step 4, which means that the final (or that could be an optimum) neural network configuration (or ANM) has been obtained.

3.4 Step 4—Test:

This step compares the SIE forecasts (output) of ANM with the true observations, which are assumed to have at least one of two conditions:

a) weather conditions (class 1 of Table 2) reported by METAR or SPECI (corresponding the test dataset in Fig. 4(b)); and/or

b) lightning reported inside a 50-km radius centred at Galeão airport during a 1-h period. The lighting data are included in the test because the weather conditions reported in METAR or SPECI represent an observation by the meteorologist at an instant of time; therefore, sometimes it does not correctly represent an entire one-hour period, which is the minimum time interval for an ANM forecast, and the lightning data will be continuously generated during the entire ANM forecast time and beyond the METAR observation, which

depends on the meteorologist's observation skills. The lightning data allow the ANM forecast verification to be spread out to encompass the entire flight terminal area of Rio de Janeiro. Moreover, it is assumed in this work that the presence of lighting is related with SIE. Therefore, these two conditions will certainly permit a better ANM test, which is accomplished via a two-dimensional contingency table. The calculation of five categorical statistics used to verify the frequency of correct and incorrect forecasted values is performed as follows: 1) proportion correct (PC), which shows the frequency of the ANM forecasts that were correct (a perfect score equals one); 2) BIAS, which represents the ratio between the frequency of ANM estimated events and the frequency of ANM observed events (a perfect score equals one); 3) probability of detection (POD), which represents the probability of the occasions when the forecast event actually occurred (hits), and the scale varies from zero to one, where one indicates a perfect forecast; 4) false-alarm ratio (FAR), which indicates the fraction of ANM-predicted SIEs that did not occur (a perfect score equals zero); and 5) threat score (TS), which indicates how the ANM forecasts correspond to the observed SIEs (a perfect score equals one). In particular, the TS is relatively sensitive to the climatology of the studied event, tending to produce poorer scores for rare events, such as an SIE. Therefore, the model is considered to be optimal when it creates SIE nowcasting with scores as near perfect as possible for the five statistics described (Wilks, 2006).

Finally, if the test results of the ANM do not indicate satisfactory performance, a normal procedure is to rearrange the representativeness of the target class one in the training data (i.e., modifying the training/testing dataset) and then go to step 3 and repeat step 4 in Fig. 3. Otherwise, the optimal model is reached. The ANM training strategy and results are discussed in the next section.

4. ANALYSIS AND RESULTS

To assess the performance of the nowcasting system proposed for the TA of Rio de Janeiro, the ANM output variables were divided into two classes as previously defined—namely: class zero (no SIE) and class one (SIE). Figure 4(a) and Fig. 4(b) depict the frequency of the classes in the initial (1st) training/validation and test datasets, respectively, corresponding to 70 % and 30 % of the total number of meteorological records. It is observed in Fig. 4(a), that class frequencies are not proportionally distributed. In particular, class one (defined as SIE) is poorly represented, accounting for approximately two percent of all meteorological

records. This increases the difficulty of the neural network learning process; for phenomenon knowledge, a better representation of target class one is needed in the training dataset—i.e., class one should have a higher weight than the other classes or at least a similar weight to another class in the training dataset—to facilitate better neural network training. The following paragraphs summarize the strategy to overcome the low frequency of SIEs in the sequence of training/validation executed in this work in the procedure to achieve the optimal model, as illustrated in Fig. 3.

4.1 Neural network training

Neural network training is a time-consuming activity, and to overcome the mentioned problem, a common strategy is to alter the training dataset—for example, by taking the original data as a reference to artificially create another new training dataset by modifying the representation of the classes in the data population and testing the model performance to make an optimum and/or gradually reducing the input variables by evaluating a particular variable relevance (or contribution) for the output results. The latter was not performed in this work, and the input number was held constant and equal as previously explained in §3.2. In fact, there is no straightforward set of calculations to accomplish this goal. It is significant to observe that the test dataset shown in Fig. 4(b) has similar class frequencies to the original dataset, shown in Fig. 4(a). The idea is to provide real scenarios of rare events during the test process. Table 3 presents the training scheme (or strategy) and attempts to convey the concept of successive training used in the present work. The training strategy is based on decreasing records of class 0 and keeping class 1 fixed in each training/testing executed by following the steps in Fig. 3. The optimal ANM was obtained in the nth training corresponding to the dataset in Fig. 4(c). The resulting test statistics were achieved by two options: first, by considering items a); and second, by considering items a) and b) of §3.4. The latter item (item b)—lightning reported inside a 50-km radius centred at SBGL airport during a 1-h period—represents an SIE. Table 3 shows categorical statistical verifications of the optimal model results. The ANM forecast performance slowly declines from the first to the second hour and declines more rapidly from the second to the third hour. By including the lightning data in the test, the ANM results were improved, as shown by the first [L], second [L], and third [L] hours. The comparison between the two test datasets (with and without lightning data) shows that BIAS, POD, and FAR values improved by 14 %, 11 %, and 12 % (for the first, second, and third hours); 3 %, 3 %, and 6 % (for the first, second, and third hours); and 13

%, 13 %, and 5 % (for the first, second, and third hours), respectively. In particular, the BIAS values improved more than the other statistics because of the inclusion of the lightning data in the test. In addition, although TS normally tends to produce poorer scores for rare events, its results have also improved here with the inclusion of lightning data in the test of optimal training as shown in Table 3, column thirteen.

The best ANM result corresponds to the first hour. The BIAS is the lowest, equal to 1.10 (which means that the results slightly overestimated the observations for the considered forecasts); even so, the readings for PC, POD, FAR, and TS are quite respectable, equal to 0.99, 0.79, 0.28, and 0.61, respectively. The effects of the ANM for the second hour are slightly less useful than those for the first hour forecast but are nonetheless satisfactory. However, the statistical values for the third hour forecast are poorer than those for the second hour. One cause of the ANM's overall performance degeneration is that a neural network is a statistical model rather than a physical one, which means that the physical aspects are not included. In summary, it is possible to state that an optimal ANM should be able to forecast SIEs in the study area for up to 2 h.

4.2. Possible sources of error in the ANM test

The ANM optimal model output is considered a hit when it corresponds to event observations, if at least one of two weather conditions in §3.4 is satisfied. In particular, the weather condition reported in the METAR or SPECI is obtained from a human observer and may have some inconsistencies. The latter is common in meteorological observations; thus, consciousness of such matters is important when interpreting results from METAR at a specific time. The ANM results are slightly biased as previously presented for first hour forecast; therefore, in an attempt to explain that BIAS, the study pursued an investigation of possible sources of error in the meteorological observations used to verify the model forecasts. First of all, with regard to the learning process, the training dataset was composed only of meteorological records with a unique true association between their output (as class 1) and input variables (represented somehow in the thermodynamic atmospheric pattern during the development of an SIE from the METAR records). In other words, the training used only meteorological records whose output was characterized as a true SIE and none. However, in the test dataset, there are many meteorological records in which such a unique association (one-to-one relationship between input and output) is not always true; i.e., some meteorological records have a typical thermodynamic pattern of SIE (input), but the weather condition (output) does not correspond to an SIE (or prevailing actual weather situation). These records were used in the present study to verify ANM forecasts and have consequently produced the results in Table 3. A possible reason for false alarms and consequently biased ANM results is that hourly METAR records represent quasi-instantaneous meteorological

Table 3: Strategy condition and final test statistics of the optimal ANM. The ANM output equal to class one represents a true SIE (or yes) and class zero represents a false SIE (or no) forecast. The statistic values associated with the first [(L)], second [(L)], and third [(L)] are hours in which the ANM test using the lightning data was included.

| Training Strategy			Output class	Test data	Neural network configuration (Number of hidden neurons)	Statistics for SIE and no SIE					
Training (from 1st to n^{th})	Training dataset and strategy	Number of Inputs				Hour	PC	BIAS	POD	FAR	TS
n^{th} Optimum training	Gradually modifies for each looping in Figure 3 by decreasing classes 0 and keeping class 1 fixed	12	Yes, or No (Yes= class 1) or (No= class 0)	Yes, or No means classes one (including lighting existence in the period of 1 h) or zero in Table 2, respectively	123	1st	0.98	1,28	0.76	0.41	0.50
						$1^{st\,(L)}$	0.99	1.10	0.79	0.28	0.6
					138	2nd	0.97	1.59	0.75	0.52	0.41
						$2^{nd\,(L)}$	0.97	1.42	0.78	0.45	0.47
					134	3rd	0.94	2.64	0.61	0.77	0.20
						$3^{rd(L)}$	0.94	2.31	0.67	0.73	0.25

observations (which take approximately 10 min to generate and may carry inconsistencies); therefore, the weather condition (output) may be affected by a certain amount of subjectivity on the part of the meteorologist (see discussion below). These results have provided plenty of evidence that the validation parameters (i.e., weather condition report just mentioned in the METAR or SPECI in Table 2) are not totally appropriate for ANM validation because the METAR or SPECI are quasi-instantaneous observations and thus do not cover the entire ANM forecast time. The lightning data permit the ANM forecast verification to be spread out to encompass the entire TA of Rio de Janeiro. The comparisons between ANM forecasts and lightning detection have improved all statistical values.

4.3 Case Study

To elucidate the foregoing discussion, this section shows the ANM results for an SIE that occurred from 15:00 to 23:00 LT on 18 March 2009. Figure 5 depicts a synoptic weather situation through an enhanced GOES-10 (channel 4) satellite image at 1800 (local time), in which a cloud (or cloud complex) is classified, by an automatic stretch process, as a convective cell (which could certainly be associated with an SIE) if its top temperature is lower than minus 30° C.

The red box roughly represents the TA of Rio de Janeiro, which is influenced by SIEs (located approximately at the centre of the red box) and where a complex convective cloud (with cloud top temperature equal to minus 70° C) is clearly observed in the east. On this day, the K, TT, and LR index values, calculated from the SBGL atmospheric profile, were equal to 33.64, 44.97, and 5.5, respectively, indicating that a typical atmospheric instability pattern was dominating the area. Table 4 presents a comparison between ANM forecasts (column four) and the weather observations made by the meteorologist and registered in the METAR (columns two and three) for the considered period. From this result, it seems that the ANM overestimated the possibility of an SIE (compare columns three and four). However, the problem of verification of the output of the ANM is difficult because the meteorologist's observation does not always give a more appropriate weather condition (or a prevailing condition) for comparison; therefore, biased results may be obtained from the ANM. Lightning has been coincidently detected (column five) for all ANM forecasts of SIEs during the time of this particular case study, which indicates an unstable atmospheric pattern (meaning true SIE) in the flight area of the airport influenced by the event. In summary, the ANM forecasts usually capture the signs of an atmospheric instability pattern.

Figure 5: GOES-10 (channel 4)extracted and adapted from www.cptec.inpe.br that represents the synoptic weather situation at 1800 (local time) on 18 March 2009, where the top convective cloud temperatures are categorized by a temperature range from -30 C to -80 C. The red box roughly represents the study region.
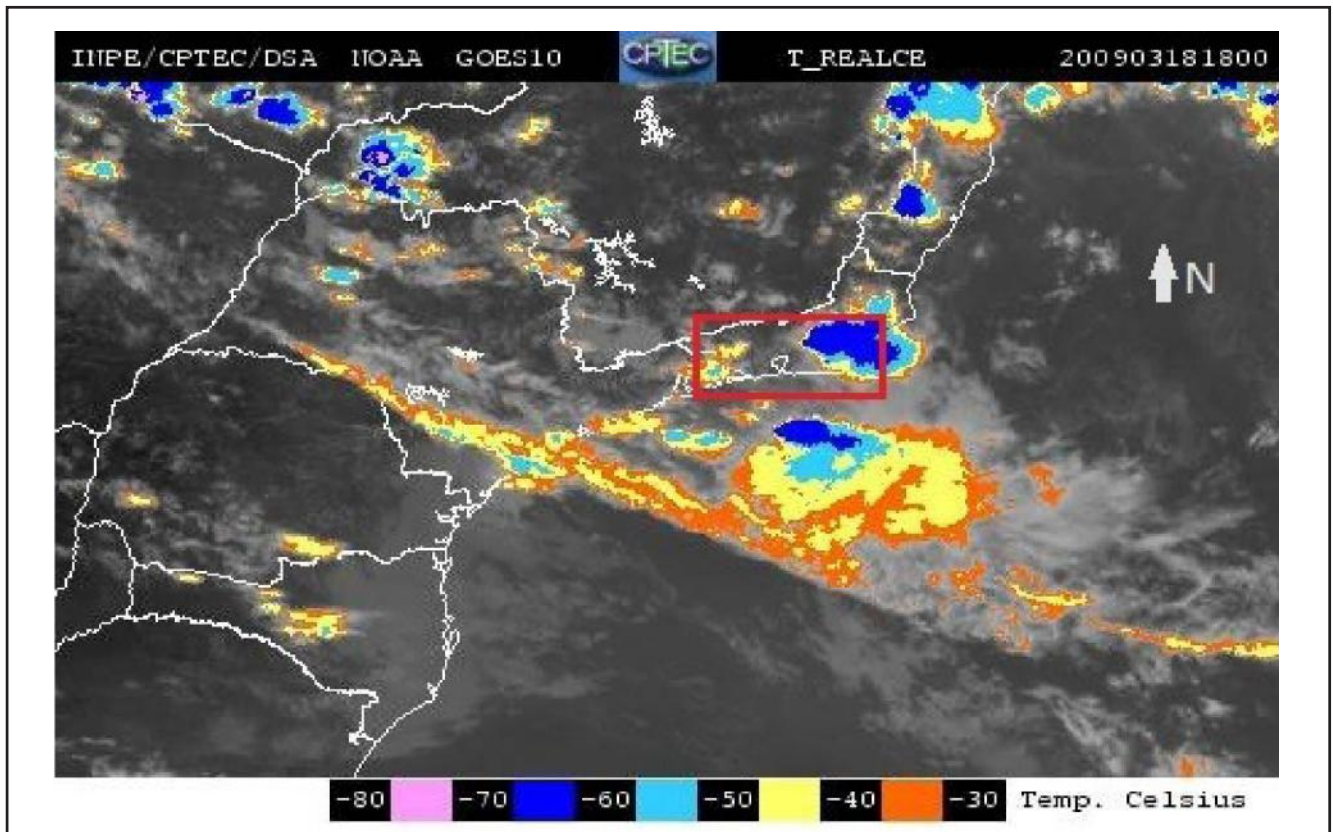
Table 4: ANM forecasts versus meteorological observations on March 18, 2009.

Local time	Weather condition (METAR)	Observed class	SNM class forecasts	Lightning detection
15	H	0	0	no
16	TRW-	1	1	yes
17	R	0	1	yes
18	R-	0	1	yes
19	H	0	1	yes
20	TRW-	1	1	yes
21	R+	0	1	yes
22	T	1	1	yes
23	TRW+	1	1	yes

5. CONCLUSIONS

In Brazil, the numerical prediction models have presently demonstrated certain difficulties in attempting to forecast local or short-term heavy rain, strong wind, and turbulence events that are normally associated with SIE occurrences. Hence, this work shows an automated nowcasting model for short-term and local-specific forecasting of SIEs based on a neural network technique for the flight terminal area of Rio de Janeiro. The main findings of this study are as follows:

a) the optimal ANM results of SIE forecasts for the first and second hours are encouraging because the categorical statistical values are quite acceptable. The proposed model has a very low computational cost, and it is possible to say that the ANM could alternatively forecast short-term strong atmospheric instability;

b) the third hour ANM forecast has the highest BIAS; perhaps the main reason for the ANM performance degeneration in time is that the neural network model is purely statistical rather than physical, and its use should therefore be limited to short-term nowcasting, possibly up to a 2-h timeframe;

c) there is visible evidence that the test data contain a certain amount of uncertainty. A key consideration regarding the ANM results versus test data and possible sources of error should be addressed; i.e., the use of METAR or SPECI weather conditions is affected by subjectivity on the part of the meteorologist and sometimes does not represent prevailing weather conditions. The results and case study showed that ANM forecasts might falsely be classified as hits;

d) the inclusion of lightning data in the test significantly improved the ANM statistic results and also provided evidence that weather conditions discussed in the previous item are not totally appropriate for ANM test; and

e) finally, the study may conclude that the optimal ANM developed here is clearly capable of predicting signs of a local atmospheric instability pattern in the TA of Rio de Janeiro.

Future studies are planned to include other data sources in the learning process, such as numerical models, meteorological satellites, RADAR, and/or SODAR wind profiles.

ACKNOWLEDGEMENTS

REFERENCES

Ahrens, C. D.: Meteorology Today - Introduction to Weather Climate and Environment. 9th Edition, Brooks/Cole, CA, USA, 2008.

Bishop, C. M.: Pattern Recognition and Machine Learning, Springer, New York, NY, USA, 430 227–229, 2006.

Bremnes, J. B. and Michaelides, S. C.: Probabilistic visibility forecasting using neural networks, Pure Appl. Geophys., 164, 1365–1381, 2007.

Cornman, L. B., Goodrich, R. K., Morse, C. S., and Ecklund, W. L.: A fuzzy logic method for improved moment estimation from Doppler spectra, J. Atmos. Ocean. Tech., 15, 1287–1305, 1998.

Dixon, M.J. and Wiener, G.M.: TITAN: Thunderstorm identification, tracking, analysis, and nowcasting--a radar-based methodology, J. Atmos. Ocean. Tech., 10, 785-797, 1993.

Groisman, P. Y., Knight, R. W., Easterling, D. R., Karl, T. R., Hegerl, G. C., and Razuvaev, V. N.: Trends in intense precipitation in the climate record, J. Climate, 18, 1326–1350, 2005.

Haupt, S.E., Pasini, A., Marzban. C.: Artificial Intelligence Methods in the Environmental Sciences, Springer, 424 pp, 2009.

Hsieh, W. W.: Machine Learning Methods in the Environmental Sciences: Neural Networks and kernels, Cambridge University Press, 349 pp, 2009.

Isaac, G. A., Bailey, M., Cober, S. G., Donaldson, N., Driedger, N., Glazer, A., Gultepe, I., Hudak, D., Korolev, A., Reid, J., Rodriguez, P., Strapp, J. W. and Fabry, F.: Airport Vicinity Icing and Snow Advisor, in: AIAA 44th Aerospace Sci. Meeting and Exhibit, Reno Nevada, AIAA-2006-1219, 2006.

Isaac, G. A., Bailey, M., Boudala, F., Cober, S.G, Crawford, R., Donaldson, N., Gultepe, I., Hansen, B., Heckman, I., Huang, L., Ling, A., Reid, J., Fournier, M.: Decision Making Regarding Aircraft De-Icing and In-Flight Icing Using the Canadian Airport Nowcasting System (CAN-Now), in: SAE 2011 International Conference on Aircraft and Engine Icing and Ground Deicing, 13-17 June 2011, Paper Number: 2011-38-0029; DOI: 10.4271/2011-38-0029.

Isaac, G.A., Bailey, M., Boudala, F.S., Cober, S.G., Crawford, R.W., Donaldson, N., Gultepe, I., Hansen, B., Heckman, I., Huang, L.X., Ling, A., Mailhot, J., Milbrandt, J.A., Reid, J. and Fournier, M.: The Canadian airport nowcasting system (CAN-Now). Accepted to Meteorol. Appl., 2012.

Haykin, S.: Neural Networks: A Comprehensive Foundation, Prentice Hall New Jersey, New Jersey, USA, 1999.

Liu, Y., Warner, T. T., Bowers, J. F., Carson, L. P., Chen, F., Clough, C. A., Christopher, A. D., Craig, H. E, C. h., Halvorson, S. F., Terrence, W. H. Jr., Lachapelle, L., Malone, R. E., Daran, L. R., Sheu, R-S., Swerdlin, S. P. and Weingarten, D.S.: The operational mesogamma-scale analysis and forecast system of the US Army Test and Evaluation Command. Part I: Overview of the modeling system, the forecast products, and how the products are used, J. Appl. Meteorol. Clim., 47(4), 1077-1092, 2008.

Mass, C.: Nowcasting the promise of new technologies of communication, modelling, and observation, Bulletin of the American Meteorological Society, 93(6): 797-809, 2012.

Mueller, C., Saxen, T., Roberts, R., Wilson, J., Betancourt, T., Dettling, S., Oien, N., and Yee, J.: NCAR auto-nowcast system, Weather Forecast, 18, 545–561, 2003.

Pasero, E. and Moniaci, W.: Artificial neural networks for meteorological nowcast, in: Computational Intelligence for Measurement Systems and Applications, CIMSA, IEEE International Conference on, Boston, MA, USA, 14–16 July 2004, IEEE, 36–39, 2004.

Pasini, A., 2015: Artificial neural networks for small dataset analysis, J. Thorac. Dis., 7(5): 953–960, doi: 10.3978/j.issn.2072-1439.2015.04.61, 2015.

Pasini, A., Pelino, V., and Potestà, S.: A neural network model for visibility nowcasting from surface observations: Results and sensitivity to physical input variables, J. Geophys. Res. Atmos., 106, 14951–14959, 2001.

Pasini, A. and Ameli, F.: Radon short range forecasting through time series preprocessing and neural network modelling, Geophys. Res. Lett., 30, doi: 10.1029/2002GL016726, 2003.

Schroeder, A., Stauffer, D. R., Seaman, N. L., Deng, Gibbs, A., Hunter, G. K. and Young, G. S.: An automated high-resolution, rapidly relocatable meteorological nowcasting and prediction system, Mon. Weather Rev., 134, 1237–1265, 2006.

Specht, D. F.: Probabilistic neural networks, in: IEEE T. Neural Networ., 3, 109–118, 1990.

Specht, D. F.: The general regression neural network, in: IEEE T. Neural Networ., 2(6): 568– 576, 1991.

Sun J., and Wilson, J. W.: The assimilation of radar data for weather prediction, in: Radar and atmospheric science: a collection of essays in honor of David Atlas, Wakimoto, R. and Srivastava, R. (Editors), American Meteorological Society, 175-198, 2003.

Xue, M., Wang, D., Gao, J., Brewster, K. and Droegemeier, K. K.: The Advanced Regional Prediction System (ARPS), storm-scale numerical weather prediction and data assimilation, Meteorol. Atmos. Phys., 82(1), 139-170, 2003.

Wilk, K. E. and Gray, K. C.: Processing and analysis techniques used with the NSSL weather radar system. In Preprints, 14th Conf. on Radar Meteorology, Tucson, AZ, 520 American Meteorological Society (pp. 369-374), 1970.

Wilks, D. S.: Statistical Methods in the Atmospheric Sciences: An Introduction, vol. 59 of International Geophysics Series, Academic Press, London, UK, 255–269, 2006.

Wilson, J. W.: Movement and predictability of radar echoes, Tech. Memo.: ERTM-NSSI-28, National Severe Storms Laboratory, Springfield, VA, 30 pp, 1966.

Ceiling and Visibility

Visibility and ceiling now casting using machine learning analysis for aviation applications

Fabricio Cordeiro[1]

Gutemberg França[2]

Francisco Albuquerque Neto[2]

Ismail Gultepe[3]

ABSTRACT

This work presents a novel approach for simulating visibility (V_{is}) and ceiling base height (H_c) in up to 1 hour using several machine learning (ML) algorithms.Ten years of meteorological data at 15 min intervals for Santos Dumont airport(SDA), Rio de Janeiro, Brazil were used in the ML method training and testing process. In the investigation, several categorical and regressive algorithms were trained and tested, and theresults were verified. The forecast results reveal that the categorical methods produced satisfactory results only up to 15-min for visibility prediction with the probability of detection greater than 85%. On the other hand, the regressive methods are found to be more capable of generating an accurate prediction of V_{is} and H_c compared to categorical methods simulations at least up to 60 minutes. The forecast evaluation metrics for V_{is} and H_c had correlation coefficients of 0.99 0.00 and 0.96 0.00 with mean absolute errors of 324±77 m, and 167±21 m, respectively. Results suggested that the ML methods can improve the prediction of V_{is} and H_c up to 1 h.

Keywords: Aviation meteorology, aeronautical meteorology; weather prediction; Nowcasting, Visibility, and Ceiling.

1. INTRODUCTION

Visibility and low ceiling parameters are often a matter of concern in aircraft landing operations because of their obstruction in the pilot's view over the airports. The Instrument Landing System (ILS), an accurate vertical and lateral landing guiding technology, permits airplanes to land with significantly reduced visibility and ceiling. Despite the fact that many airports have been certified to operate in accordance with instrument flight rules (IFR), some of them lack ILS and must rely on often inaccurate weather forecasts to avoid an unexpected landing impossibility due to visibility or ceiling limitations. According to the Brazilian Aeronautical Information Service (www.aisweb.decea.mil.br), there are 141 airports in Brazil that are approved for IFR operations, although only 47 of them presently have an ILS. Although rain and drizzle may impact the visibility (V_{is}) and ceiling height (H_c) significantly, mist and fog are the most restrictive events affecting the mentioned parameters in Brazilian airports [1]. Although rain and drizzle may impact the V_{is} and H_c significantly, mist and fog are the most restrictive events affecting the mentioned parameters in Brazilian airports [1].

[1] Integrated Center of Aeronautical Meteorology; fabricio@lma.ufrj.br

[2] Applied Meteorology Laboratory, Federal University of Rio de Janeiro; gutemberg@lma.ufrj.br; albuqueque@lma.ufrj.br

[3] Ontario Tech. University, Engineering and Applied Science; ismail.gultepe@ontariotechu.ca

Recently, a review of aviation meteorological issues presented all types of weather events that are critical for aviation operations [2]. It stated that the aviation accidents related to V_{is} and H_c can reach up to about 30% and comes after the wind impact.

The genesis of the fog/mist in the forecast models is usually a significant problem due to poor representation of the microphysical and aerosol properties [2]. For example, an objective 12-hour fog prediction model was developed based on the curve adjustment analysis via the least-squares technique of the observational data for Porto Alegre airport [3]; a numerical weather forecasting model for the regional scales was utilized to investigate the evolution of local mesoscale circulation and its impact on the occurrence of night fog formation in São Paulo [4]; and an alternative stochastic model for fog forecasting was established for the Guarulhos International Airport [5]. A visibility forecasting model developed in the early 1980s for fog events at the airports of Curitiba and Porto Alegre concludes that detailed observations and improved physical algorithms are required for accurate V_{is} predictions [6]. In addition to these studies, investigations [7, 8] were conducted on the physical and synoptic processes of fog and formation of stratus clouds and concluded that they are related to a wave disturbance field in trade wind in northern Brazilian cost and a high-pressure displacement along the east coast of South America in conjunction with a low hot core barotropic occurrence in northern Argentina and [9, 10] emphasized how difficult to predict the life cycle of marine and coastal fog.

Later in the 2000s, machine learning was limited to a single ML algorithm for visibility and ceiling predictions [11]. A neural network was tested to diagnose V_{is} using the Met Office's unified model prediction [12]. This study concludes that the performance of the parameterization is determined by the quality of the meteorological input parameters and the structure of the parameterization. Because of the changing weather conditions over short time periods, weather parameters are critical to improving aviation operations. Then, a pioneering method for very short-term forecasting [13] was developed based on neural network algorithms to predict the V_{is} and H_c at Guarulhos Airport, São Paulo. Similarly, a fog prediction method based on ML algorithm was developed for the Brazilian Air Force aerodrome at Pirassununga using meteorological observation data collected from 1989 to 2008, and it was concluded that the suggested neural network algorithm predictions are 95 percent equivalent to observations [14]. A series of works, [15], [16], and [17], explored the use of ML algorithms for short-term forecasting of convective events for the Rio de Janeiro metropolitan region. The current results of the ML algorithms show that they are capable of nowcasting convective events with high probability and low false alarm ratio. Recently, a fog forecasting method based on the ML algorithm was developed for the Afonso Pena International Airport in Paraná, Brazil [18]. The algorithm diagnoses V_{is} based on 15-min observed and predicted meteorological data, from the automatic surface meteorological station and simulated data using the numerical model of Weather Research and Forecast, respectively. The correlation coefficient of the 24-hour forecast, at 15-min intervals, and the observations is close to 90%. The fog predictions are slightly biased, i.e., a delayed onset and anticipated demise in 30 minutes or less.

On the other hand, numerical weather prediction (NWP) models perform poorly for low visibility and ceiling predictions [19]. In 2015, an investigation was conducted on the impact of the horizontal resolution of a regional climate model (RCM) on the reproduction of local weather characteristics related to fog in the metropolitan region of São Paulo [20]. RCM simulations showed the ability to characterize fog events with horizontal resolutions of 50 km and 20 km using data from June to September for 2003 and 2004 and stated that increased resolution resulted in prediction improvement of the fog occurrence.

The landing procedure in adverse weather conditions at the SDA in Rio de Janeiro is usually difficult for three reasons: 1) its runways are short, 2) there is no ILS to be used, and 3) its location is very close to the Rio Janeiro-Niterói bridge and Sugarloaf Mountain, as seen in Figure 1a and b. According to the INFRAERO (Airport Management Company) yearbook [21] approximately 100,144 aircraft landed during 2018, and 9,206,059 passengers traveled through the SDA and it was ranked as the third airport in Brazil that was most impacted by visibility restrictions. The Rio-São Paulo air bridge runs between Santos Dumont and Congonhas Airports, connecting the two largest cities in Brazil and representing 58% of SDA movements, with an average duration of 45 minutes.

The focus of this research is to use machine learning-based regressive and categorical algorithms to develop new short-term V_{is} and H_c forecasts for SDA, with potential general application to other Brazilian airports. In this work, section 2 provides the location of the project and observations. Section 3 presents the methods and characteristics of the ML algorithms used in the work. Section 4 is for the results. Section 5 is given for the conclusions driven from the work.

2. PROJECT SITE AND OBSERVATIONS

The SDA is located at 22.9103°S and 43.1631°W, near the center of Rio de Janeiro. Figure 1 shows the airport views from the northern and southern points. The Sugarloaf Mountain (pique at 407 meters) 4000 m away from the two airport runways is shown in Fig. 1c. The main runway identified as 20L/02R is 1323 meters long and only 63 meters longer than the secondary runway (20R/02L).

Considering the aircraft landing restrictions imposed by the obstacles, the Airspace Control Department established the visibility and ceiling limits for landing on the runways. Table 1 presents the operational limits for visibility (m) and ceiling height (feet) for the three main landing procedures at SDA. These procedures are 1) Area Navigation/ Global Navigation Satellite Systems (RNAV/ GNSS), 2) Non-Directional Beacon (NDB), and 3) Area Navigation/Required Navigation Performance (RNAV/RNP).

Table 1: Shows the operational limits for Vis and ceiling representing the three landing procedures on the runways of the SDA.

Landing procedure	RUNWAY	
	20	2
(1) RNAV/GNSS	4,500 meters /1,000 feet	5,000 meters/ 1,000 feet
(2) NDB	3,700 meters / 1,200 feet	4,800 meters / 1,500 feet
(3) RNAV/RNP	1,600 meters / 300 feet	1,600 meters / 300 feet

Observations for this work came from three sources: 1) SOnic Detection And Ranging (SODAR) as atmospheric profiler, 2) Automatic Surface Weather Station (ASWS), and 3) human observer. Table 2 shows details about the data sources and the 253 meteorological variables labeled as primary (collected directly from the meteorological instruments) and derived (determined using the primary) ones. The parameters used are the predominant visibility (Vis_p), the Ceiling (H_c), cloud cover (C_c), or cloud quantity (C_q), low cloud cover in okta (C_{lcc}), backscatter intensity (β), surface horizontal wind direction in degrees (θ_{dir}) and horizontal wind speed (U_h),

Figure 1: Views from the north (a) and south (b) directions for the SDA runways (02and 20), and SODAR and the automatic surface weather station (ASWS) are shown in (c).
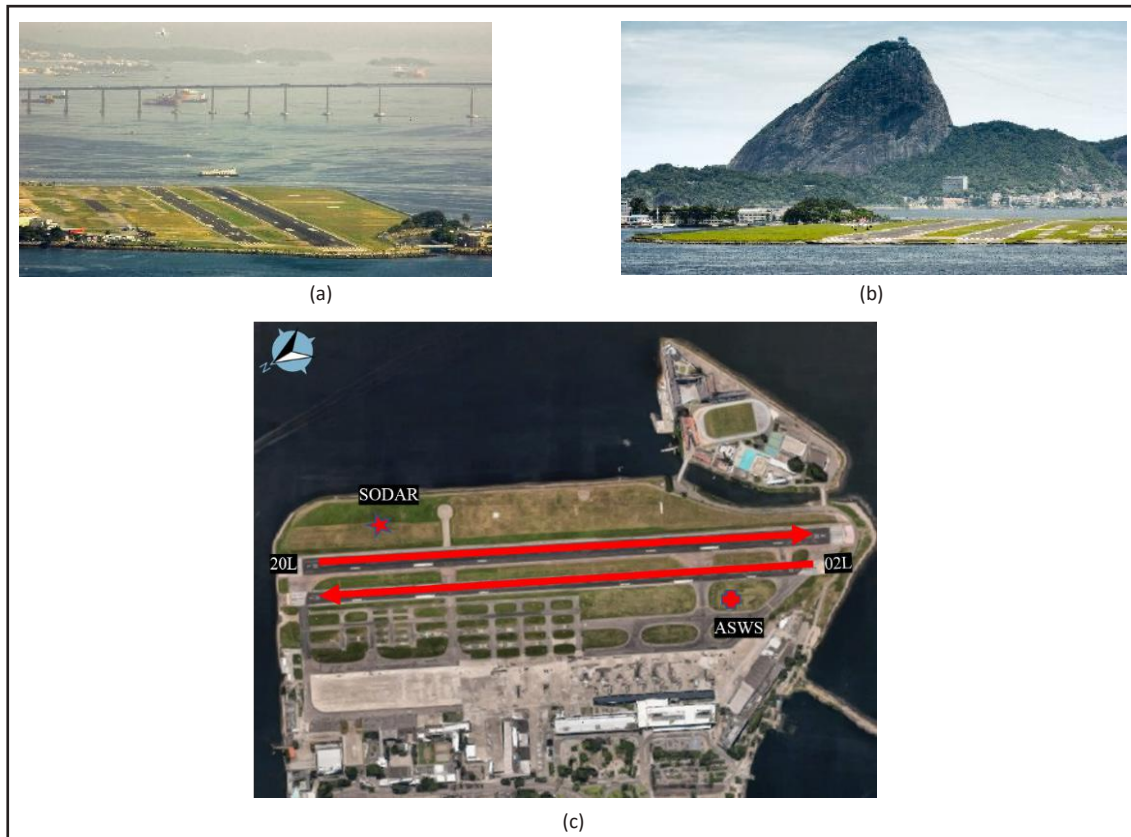
(a)

(b)

(c)

zonal wind component (u), meridional wind component (v), vertical air velocity (w_a), turbulent kinetic energy in (TKE), energy dissipation rate (EDR), relative humidity to water in % (RH_w), surface atmospheric pressure(P_s), dew point temperature (T_d), and air temperature (T_a). The red star and cross in Figure 1c represent the locations of SODAR and ASWS at SDA, respectively.

3. METHOD

In this work, the machine learning analysis with categorical or regressive algorithms are used to evaluate V_{is} and H_c predictions at the SDA because they are commonly used to recognize physical patterns in a specific data set. They are based on the principle that it is possible to learn from a set of training data and consequently be able to correctly classify new standards [22]. This research is part of a sequence of short-term prediction studies based on machine learning algorithms that have been carried out by the Applied Meteorology Laboratory at the Federal University of Rio de Janeiro and can be found in the work of [13, 15, 16, 17, 18, 23 and 24]. So, in the present study, the WEKA software

package [25] developed by the University of Waikato in New Zealand is used, with and without the Auto-WEKA subsystem [26, 27]. WEKA was chosen because it has a series of machine-learning-based algorithms that can be used to classify thermodynamic atmospheric patterns in the data set related with Vis and H_c limits at the SDA.

3.1. Detailed analysis

Knowing that meteorological observations represent the variation in time and space of the local atmospheric thermodynamic behavior, local atmospheric patterns with restricted V_{is} and H_c thresholds for the landing procedures are obtained at the above-mentioned airport. Analysis steps taken are followed up as:

i. Taking the 15-min ASWS data as a reference, the other data were chronologically disposed, and then their statistical consistency was verified. Data are represented at 15, 30, 45 minutes for each hour, and all the observations are interpolated to the same time intervals (Table 2). Overall, the number of observations at 15 min intervals reached 350,400 data;

Table 2: Observation characteristics and meteorological variables used in the machine learning algorithms during training and testing. A total of 253 meteorological variables are used in the analysis.

Source Freq. (min)	(Input) variable		Variable qty.	Record qty.	Data Period	Output
	Primary	Derived				
1) 15	β (h,-t), where h and t are equal to 30, 40, 50, 60 e 70 meters and 00, 15, 30, 45, 60 and 120 minutes, respectively	u(h,-t), v(h, -t), w_a(h,-t), EDR (h,-t) and TKE(h,t), where h and t are equal to 30, 40, 50, 60 e 70 meters and 0, 15, 30, 45, 60 and 120 minutes, respectively	150	70,080	2017 to 2018	Visibility-range-t (where range is equal to 4,500, 3,700, 1,600 m) and/or Ceiling-range-t (being equal to 1,000 ft)/cloud$_{quant}$ (okta) for forecast periods (where t is equal to 15, 30, 45 and 60 minutes.
2) 15*	Month, Julian day, year, hour, Ta(h,t), θ_{dir} (h,-t), U_h (h,-t), RH_w (h,-t), T_d (h,-t), P_s (h,t) and RH_w (h,t), H_c (t)*, where h and t is equal 2 and 0,15, 30, 45, 60 and 120 minutes), respectively	----------	73	350,400	2009 to 2018	
3) 60**	-----	Vis_P (-t), Ceiling(-t), C_q (-t), C_c (-t), C_{lcc} (-t), where t is equal to 0,15, 30, 45, 60 and 120 minutes	30	87,600	2009 to 2018	

* The ceiling height is registered automatically by a ceilometer which is part of the ASWS instrument set.
**For when restriction has occurred.

ii. Examine the history of event occurrences that were limited by the airport operating V_{is} and H_c threshold values;

iii. The inputs (the meteorological variables, primary and derived) are selected by measuring the cross-correlation between a given variable and the class (output), and then the redundant ones are eliminated;

iv. Data sets are generated in order to train and test categorical and regression algorithms. **For categorical data sets**, the vector input represented by variables (in columns 2 and 3 of Table 2), that meet the intervals of $V_{is}(t) \leq 4,500, 3,700, 1,600$ m, are connected to respective outputs associated with the advanced values of $V_{isp}(+t)$ for each leading time of 15, 30, 45, and 60 minutes. These inputs are then connected to a binary output (target) of YES or NO, depending on whether the V_{is} intervals are satisfied. **For regressive data sets**, the vector inputs (variables) are directly coupled to the advanced values $V_{isp}(+t)$ or $H_c(+t)/C_q(+t)$ values of each leading time of 15, 30, 45, and 60 minutes (**because of the uncertainty in the observation of ceiling data, only regressive algorithms were used for ceiling prediction**);

v. The data sets (categorical and regressive) are then randomly divided into 60% for training and 40% for testing the categorical and regressive algorithms, respectively. It is a frequent practice to avoid overfitting, which occurs when a statistical model fits previously observed data very well but fails to predict new results.

vi. The YES and NO records of the **categorical algorithms** training dataset, defined in step v, are balanced through the WEKA ClassBalancer option in four configurations: (1) unmodified data set, (2) 50% YES, and 50% NO, (3) 60% YES and 40% NO, (4) 65% YES and 35% NO for the lead times using operational thresholds. **For regressive algorithms**, the training test data sets are as defined as given step iv without any artificial adjustment;

vii. Cross-validation approach (this includes dividing the complete data set into k mutually exclusive subsets of the same size, one for testing and the remaining k-1 for parameter estimation and assessing the algorithm's accuracy, [28]) is used to train **all categorical algorithms available in WEKA**, with the four training dataset configurations defined in step vi. Similarly, regressive algorithms are trained. The forecast preliminary findings are examined, and the algorithms with the highest performance (here referred to as selected ones) are chosen for future examination.

viii. Using the proper test dataset to run the algorithm tests. Sections 4.3, 4.4, 4.5, and 4.6 discuss the results of the highest performing category and regressive selected algorithms with WEKA´s default configuration.

ix. Training-test experiments for each lead time are carried out using the categorical or regressive original data set with Auto-WEKA (version 2.0) [27]. In this tool all available algorithms are tested and their hyperparameters optimized, which employs the unmodified dataset partitioned into 70% training and 30% testing (thus the step iv is ignored in here)[26]. Each experiment yields a ranking of the top-performing algorithms from best to worst.

3.2. Algorithm evaluation

The WEKA software with several classical statistics is used to evaluate the performance of categorical and regressive algorithms. The categorical algorithms have their forecasts versus the observed values by using a two-dimensional contingency table that makes it possible to determine the following categorical statistics [29]: (1) probability of detection (POD) that is a measured fraction of observed events that were correctly predicted. A perfect score is 1; (2) False alarm ratio (FAR), is a measure of the fraction of YES predictions in which the event did not occur. A perfect score is 0; (3) BIAS, measures the proportion of the event frequency prediction by the frequency of the observed events. The perfect score is 1; (4) F-measure (F-M), is a measure of the accuracy of a test. The perfect score is 1; and (5) KAPPA, is a way of measuring the performance of the binary classification algorithms where the perfect agreement is 1 ([30]).

The WEKA software evaluates regressive algorithms that have their performances mainly evaluated by the four following statistics [29]: (1) correlation coefficient (CC) that represents a measure of linear correlation between the forecasts and observations. It varies from +1 and 1, where here values near 1 are desired; (2) mean absolute error (MAE), which is a measure of error between paired observation and forecasts. The perfect score is zero; and (3) Relative absolute error (RAE), is expressed as a ratio, comparing a mean residual error to errors produced by a trivial method. The result of a practical method (or its predictions are better than a trivial method) generates a ratio of less than one.

3.3. Characteristics of the selected ML algorithms

The statistical evaluation of All WEKA's algorithms with default configuration given in step vii indicated that the following five algorithms performed better than the others and given as follows:

1) Bayes Net (BN) is a classifier based on the construction of a Bayesian network, using various research algorithms and quality measures, provides data

structures, network structures, and conditional probability distributions, and can classify binary, class values absent, and nominal class. [25]; 2) Multilayer Perceptron (MP) consists of standard perceptron with a defined number of hidden units using the activation function (for example, ReLu or sigmoid) and optimization based on minimizing the loss of quadratic error function [25]; 3) Random Forest (RF) is a classifier that consists of a collection of tree classifiers and is trained in different subsets of input resources and the one with the best performance is chosen [31]; 4) REPTree (RT) is a quick decision tree, which uses the logic of the decision and regression tree and creates several trees in different iterations, selecting the best of all trees generated through the mean square error [25]; and 5) Hoeffding Tree (HT) consists of a decision tree induction algorithm capable of learning from large data streams, assuming that the distribution generation examples do not change over time, as well as exploring the fact that a small sample may be sufficient to choose an ideal division attribute [25].

4. RESULTS

In this section, results are presented for V_{is} and H_c predictions using the five algorithms explained in the method section.

4.1. Visibility thresholds

The data set had the occurrence of 11,070, 3,996, and 728 low visibility events at 15-min intervals with $V_{isp} \leq 4,500, 3,700,$ and 1,600 meters, respectively. Figure 2 illustrates the hourly (a) and monthly (b) distributions of these events. This reveals that the three main aircraft landing procedures, (1) RNAV / GNSS, (2) NDB and (3) RNAV / RNP (Table 1) in some ways are compromised by the visibility restriction in every hour of the day, being a critical period just before sunrise until close to noon (approximately from 06 am to 11 am), throughout all months and the critical period is between May and July.

Figure 2: Represent the hourly (a) and monthly (b) distribution of 15-min meteorological records whose visibility are below or equal to the limits of 4,500 (bar and line in gray), 3,700 (bar and line in blue), and 1,600 (bar and line in orange) meters, respectively.
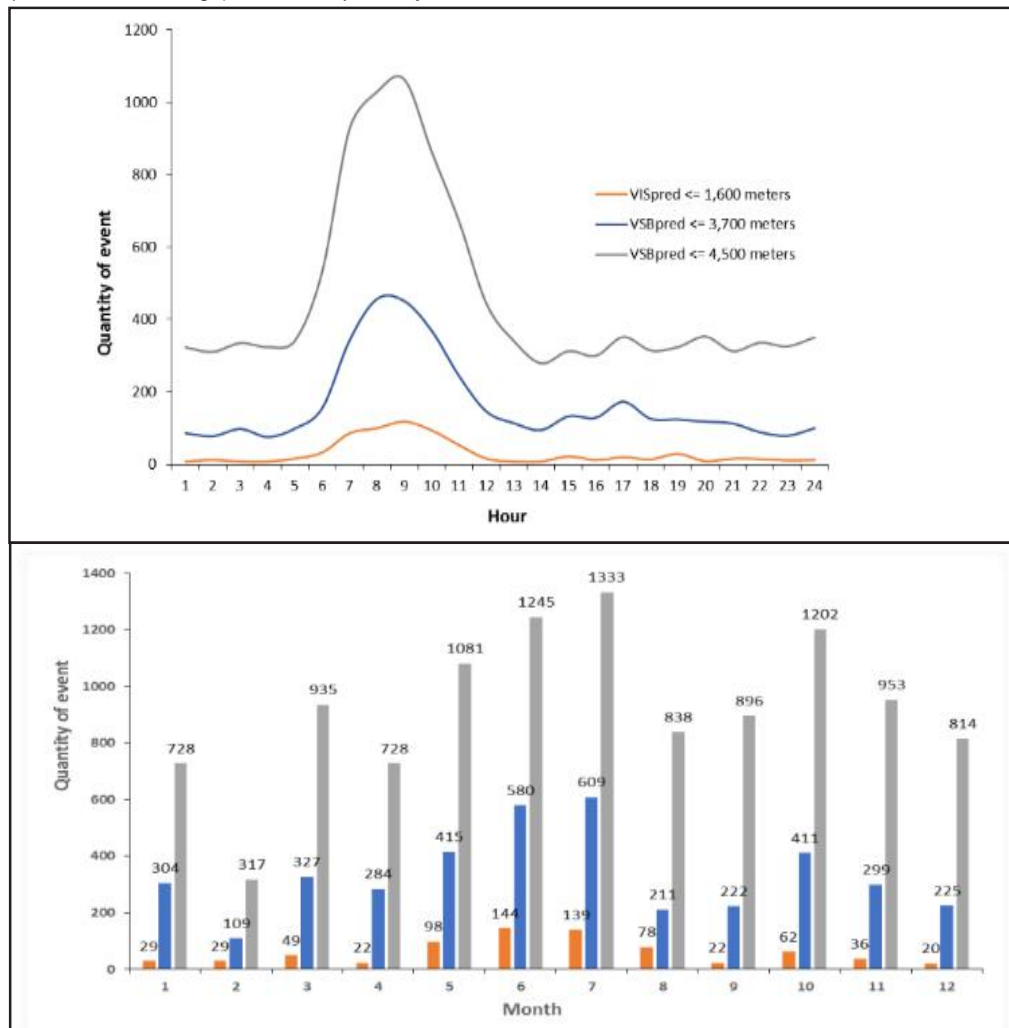
4.2. Ceiling thresholds

Similar to V_{is} analysis, using ceiling-related threshold, Figure 3 illustrates the hourly (a) and monthly (b) distributions of 4,736 events with $H_c \le 1,000$ ft from May to July, which is the most critical period. Figure 3b reveals that the RNAV / GNSS (1) landing procedure is affected somehow for the entire day. The critical period was usually occurring before sunrise until close to noon (06 am-11 am).

4.3. Algorithm Training and Results

The task of training and testing machine learning algorithms is time-consuming, and success depends directly on the choice of variables (input) that characterizes weather hazard conditions such as the local thermodynamic state of the atmosphere that precedes the occurrence of restrictions on the operational thresholds of V_{is} and H_c. Table 2 shows the 253 meteorological variables called primary and derived ones that are possible predictors. Thus, disregarding the 150 variables generated by SODAR (data source 1) in method´s step vi the cross-correlation of the remaining 103 variables were analyzed and the redundant ones were eliminated, resulting in an input data set consisting of 20 components, namely: month, Julian day, hour, θ_{dir} (2,0), U_h (2,0), U_h (2,-15), U_h (2,-30), cl(0), C_{lcc} (0), T_a (2,0), T_d (2,0), RH_w (2,0), P_s (2,0), V_{isp}(0), V_{isp}(-15), V_{isp}(-30), V_{isp}(-45), V_{isp}(-60), and V_{isp}(-120). These were the inputs used in the various training procedures for the V_{is} and H_c prediction algorithms. For experiments of training algorithms that included data from SODAR, the cross-correlation of the variables was also analyzed.

Figure 3: Represent the hourly (a) and monthly (b) distribution of 4,736 15-min meteorological records whose ceiling was $\le$ 1,000 ft.

(a)

(b)
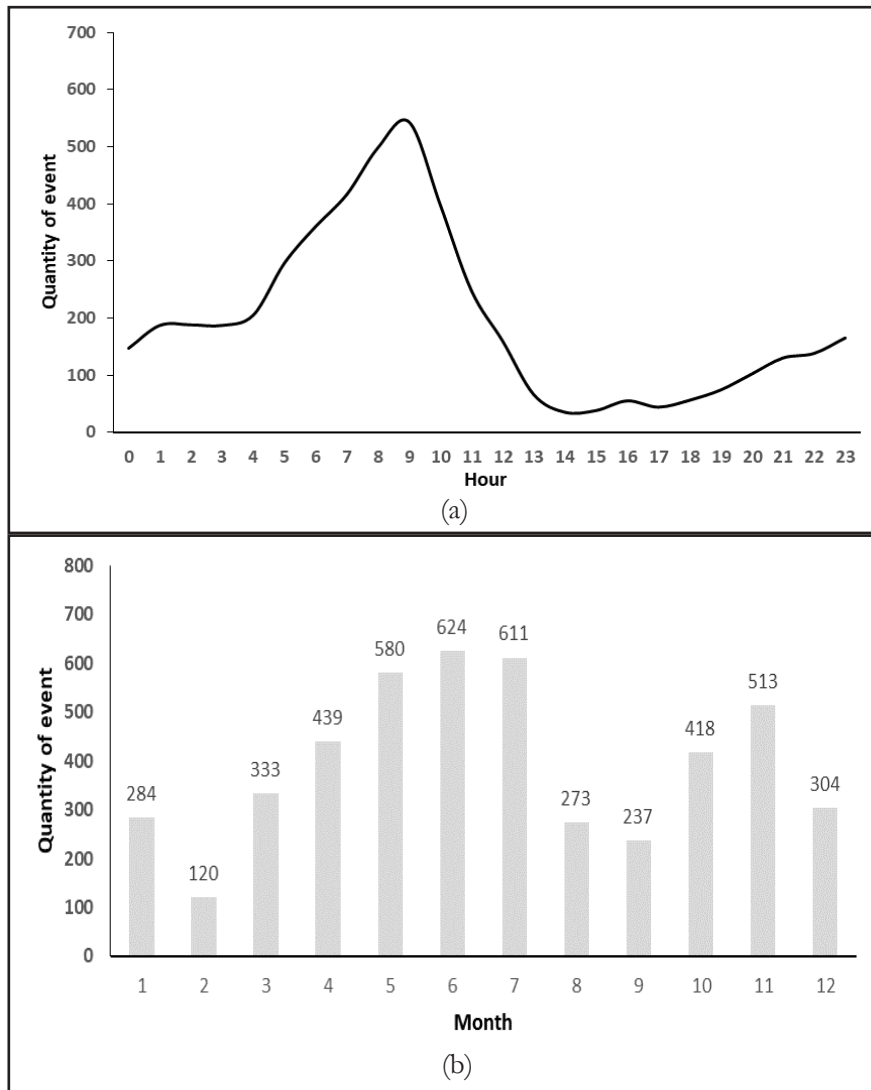
Several experiments of training and testing via cross-validation for 15-min forecasting of $V_{isp} \leq 4,500$ meters and $H_c \leq 1,000$ feet were carried out using all available WEKA's algorithms with the goal of selecting ML WEKA's algorithms for future investigation (step vii). Following an evaluation of the performance results of the algorithms, the five algorithms in Section 3.2 were selected and discussed further below.

4.4. Visibility categorical nowcasting

Experiments were carried out in order to assess visibility forecasts, and the following requirements were satisfied, namely: 1) the five categorical WEKA

algorithms selected (step viii in the method section), 2) the three visibility thresholds are used as $V_{isp} \leq 4,500$, $\leq 3,700$, and $\leq 1,600$; 3) the four lead times having at 15 min intervals up to 60 min, and 4) data set configuration based on using SODAR data or not, and using the Auto-WEKA support (namely Auto-WEKA default).

Tables 3 and 4 show the best test results of the 15- and 30-min predictions for the three defined visibility thresholds for the five selected algorithms (here called optimal). It is observed that the performance of the forecast decreases as the lead time increases and the visibility limit decreases. Just so that all statistics have the unit's ideal value, 1-FAR is adopted. Here it is defined whether a given method (the latter are defined

Table 3: Statistical test results of 15-minute VIS forecasts ≤ 4,500 (a), 3,700 (b), and 1,600 (c) meters for the five algorithms selected with input from ASWS (source 2) and observer (source 3), and the results highlighted in gray are those that also included data from SODAR (source 1).

Algorithm	Input data	POD (YES)	1-FAR (YES)	F-M (YES)	BIAS (YES)	POD (NO)	1-FAR (NO)	F-M (NO)	BIAS (NO)	KAPPA	Data set configuration
					(a) 15-min forecast for VIS ≤4,500 meters						
BN	2 and 3	0.83	0.99	0.72	0.77	0.99	0.83	0.99	0.99	0.71	4
MP	2 and 3	0.88	1.00	0.91	1.04	1.00	0.88	1.00	1.00	0.90	1
RF	2 and 3	0.91	1.00	0.91	0.99	1.00	0.91	1.00	1.00	0.91	Auto-WEKA
HT	2 and 3	0.91	1.00	0.91	1.00	1.00	0.91	1.00	1.00	0.91	1
RT	2 and 3	0.89	1.00	0.90	1.03	1.00	0.89	1.00	1.00	0.90	1
RF	1, 2 and 3	0.89	1.00	0.89	1.00	1.00	0.89	1.00	1.00	0.89	Auto-WEKA
					(b) 15-min forecast for VIS ≤3,700 meters						
BN	2 and 3	0.89	0.97	0.37	0.26	0.97	0.89	0.98	0.97	0.36	1
MP	2 and 3	0.84	1.00	0.88	1.10	1.00	0.84	1.00	1.00	0.88	1
RF	2 and 3	0.88	1.00	0.89	1.01	1.00	0.88	1.00	1.00	0.88	3
HT	2 and 3	0.82	1.00	0.86	1.12	1.00	0.82	1.00	1.00	0.86	1
RT	2 and 3	0.85	1.00	0.89	1.09	1.00	0.85	1.00	1.00	0.88	1
RF	1, 2 and 3	0.85	1.00	0.85	1.00	1.00	0.85	1.00	1.00	0.89	Auto-WEKA
					(c) 15-min forecast for VIS ≤1,600 meters						
BN	2 and 3	0.88	0.99	0.43	0.32	0.99	0.88	1.00	0.99	0.42	1
MP	2 and 3	0.68	1.00	0.78	1.34	1.00	0.68	1.00	1.00	0.78	1
RF	2 and 3	0.88	1.00	0.89	1.02	1.00	0.88	1.00	1.00	0.89	Auto-WEKA
HT	2 and 3	0.56	1.00	0.67	1.50	1.00	0.56	1.00	1.00	0.67	1
RT	2 and 3	0.89	1.00	0.89	1.00	1.00	0.89	1.00	1.00	0.89	1
RF	1, 2 and 3	0.89	1.00	0.89	1.00	1.00	0.89	1.00	1.00	0.89	Auto-WEKA

as the trained and tested algorithms) has the satisfactory performance to predict visibility for a given lead time when their POD and 1-FAR values are ≥ 0.8. Table 3 highlights the statistical results of the 15-minute forecast (and those satisfactory algorithms in bold) for visibility thresholds and they reveal that eleven algorithms performed coherently since the averages of the categorical statistics are almost close to the perfect score (value in parentheses), which are: POD (Y, N) (0.884 ± 0.012, 0.999±0.000), 1-FAR (Y,N) (0.996 ± 0.005, 0.884 ±0.012), F-M (Y, N) (0.891 ± 0.011, 0.998± 0.001), BIAS (Y,N) (1.016 ± 0.022, 1.000 ± 0.000), KAPPA (0.89 ± 0.008).

As previously analyzed, Table 4 also shows the best performance algorithms (and those satisfactory algorithms in bold), by visibility limit, 30-minute forecast. It is observed that no algorithm obtained POD (V) greater than 80% for the limit of VIS ≤ 3,700 meters and there are only three algorithms, i.e., one and two for VIS ≤ 4,500 and VIS ≤1,600, respectively, with satisfactory performance. The evaluation statistics suffered a percentage reduction (in parentheses) in relation to the 15-min predictions, as follows: POD(S,N) (7.53%, 0.08%), 1-FAR(S,N) (0.08%, 7.53%), F-M(S,N) (5.28%, 0.14%), BIAS(S,N) (5.06%, 0.06%), KAPPA(S, N) (10.89%, 0.008%). The results of the 45- and 60-min forecasts have deteriorated significantly and are therefore not discussed.

Table 4: Statistical test results of 30-minute VIS forecasts ≤ 4,500 (a), 3,700 (b), and 1,600 (c) meters for the five algorithms selected with input from ASWS (source 2) and observer (source 3), and the results highlighted in gray are those that also included data from SODAR (source 1).

Algorithm	Input data	POD (YES)	1-FAR (YES)	F-M (YES)	BIAS (YES)	POD (NO)	1-FAR (NO)	F-M (NO)	BIAS (NO)	KAPPA	Data set configuration
(a) 30-min forecast for VIS ≤4,500 meters											
BN	2 and 3	0.84	0.95	0.49	0.42	0.95	0.84	0.97	0.96	0.47	1
MP	2 and 3	0.75	1.00	0.80	1.15	1.00	0.75	0.99	1.00	0.79	1
RF	**2 and 3**	**0.82**	**0.99**	**0.81**	**1.00**	**0.99**	**0.82**	**0.99**	**1.00**	**0.81**	**Auto-WEKA**
HT	2 and 3	0.77	0.99	0.79	1.05	0.99	0.77	0.99	1.00	0.78	1
RT	2 and 3	0.74	1.00	0.78	1.12	1.00	0.74	0.99	1.00	0.78	1
RF	**1, 2 and 3**	**0.82**	**1.00**	**0.87**	**1.13**	**1.00**	**0.82**	**1.00**	**1.00**	**0.87**	**Auto-WEKA**
(b) 30-min forecast for VIS ≤ 3,700 meters											
BN	2 and 3	0.84	0.96	0.30	0.21	0.96	0.84	0.98	0.96	0.28	1
MP	2 and 3	0.61	1.00	0.70	1.39	1.00	0.61	1.00	1.00	0.70	1
RF	2 and 3	0.75	1.00	0.77	1.05	1.00	0.75	1.00	1.00	0.76	4
HT	2 and 3	0.67	0.99	0.61	0.83	0.99	0.67	1.00	1.00	0.60	1
RT	2 and 3	0.64	1.00	0.72	1.27	1.00	0.64	1.00	1.00	0.72	1
RF	1, 2 and 3	0.71	1.00	0.71	1.00	1.00	0.71	1.00	1.00	0.78	Auto-WEKA
(c) 30-min forecast for VIS ≤ 1,600 meters											
BN	2 and 3	0.81	0.99	0.32	0.24	0.99	0.81	1.00	0.99	0.31	1
MP	2 and 3	0.41	1.00	0.56	2.17	1.00	0.41	1.00	1.00	0.55	1
RF	2 and 3	0.73	1.00	0.76	1.11	1.00	0.73	1.00	1.00	0.76	3
HT	2 and 3	0.17	0.94	0.02	0.05	0.94	0.17	0.97	0.94	0.01	3
RT	2 and 3	0.66	0.34	0.76	1.39	1.00	1.00	1.00	1.00	0.76	1
RF	**1, 2 and 3**	**0.88**	**1.00**	**0.92**	**1.10**	**1.00**	**0.88**	**1.00**	**1.00**	**0.71**	**Auto-WEKA**

4.5. Visibility regressive nowcasting

Similarly, in the previous case, the experiments were run out employing regressive algorithms while considering conditions, which are as follows: 1) the five WEKA regressive algorithms selected, 2) the three visibility thresholds are used as V_{isp} = 4,500, = 3,700, and = 1,600 the four lead times of 15 min intervals up to 60 min, 3) for the data set of four delivery times, and 4) two data sets including SODAR data or not and using the Auto-WEKA support. Table 5 shows the summary of the best statistical results for the test experiments with regressive algorithms for all lead time and it is noted that RF is the algorithm with the best performance regardless of the input data set or the lead time considered. All predictions are almost perfectly correlated (column 4), which means that the trends of the predicted values follow the behavior of the observations almost perfectly. Figure 4 shows the three thresholds (± MAE) of visibility represented by the black lines and their respective minimum (cross) and maximum (black triangle) errors for better 15-, 30-, 45-, 60-min predictions. It is also noted that the results are quite reliable because the variations in meters of the visibility forecasts, regardless

the lead time, for 4,500, 3,700 and 1,600, vary within the following ranges of [4,148; 4,852], [3,348; 4,052], and [1,248; 1,952], representing maximum percentage changes for each respective visibility limit equal to 7.8%, 9.5%], and 22%, respectively. In short, assuming here that the absolute maximum percentage acceptable error of forecasting the visibility of a given method is equal to 20%, the results of the predictions with the regressive algorithms are more expressive than with the categorical ones since these remain consistent and close to the observations for the entire forecast time.

Table 5: Better statistical results of short-term visibility forecast using regressive algorithms and whose training was performed using the data set with the configuration (5) whose records are divided as Auto-WEKA default.

Algorithm	Lead time (minute)	Input data source	CC	MAE (meter)	RAE
RF	15	1, 2 and 3	0.99	198.58	0.04
RF	15	2 and 3	0.99	189.85	0.04
RF	30	1, 2 and 3	0.99	304.86	0.06
RF	30	2 and 3	0.99	291.38	0.06
RF	45	1, 2 and 3	0.99	378.70	0.08
RF	45	2 and 3	0.99	351.85	0.07
RF	60	1, 2 and 3	0.99	409.32	0.08
RF	60	2 and 3	0.99	343.88	0.07

Figure 4: Minimum (cross) and maximum (black triangle) errors for each visibility thresholds (± mean absolute error), represented by the horizontal black lines at 4,500, 3,700, and 1,600 meters of the best regressive forecasts of 15, 30, 45, 60 minutes in Table 5.

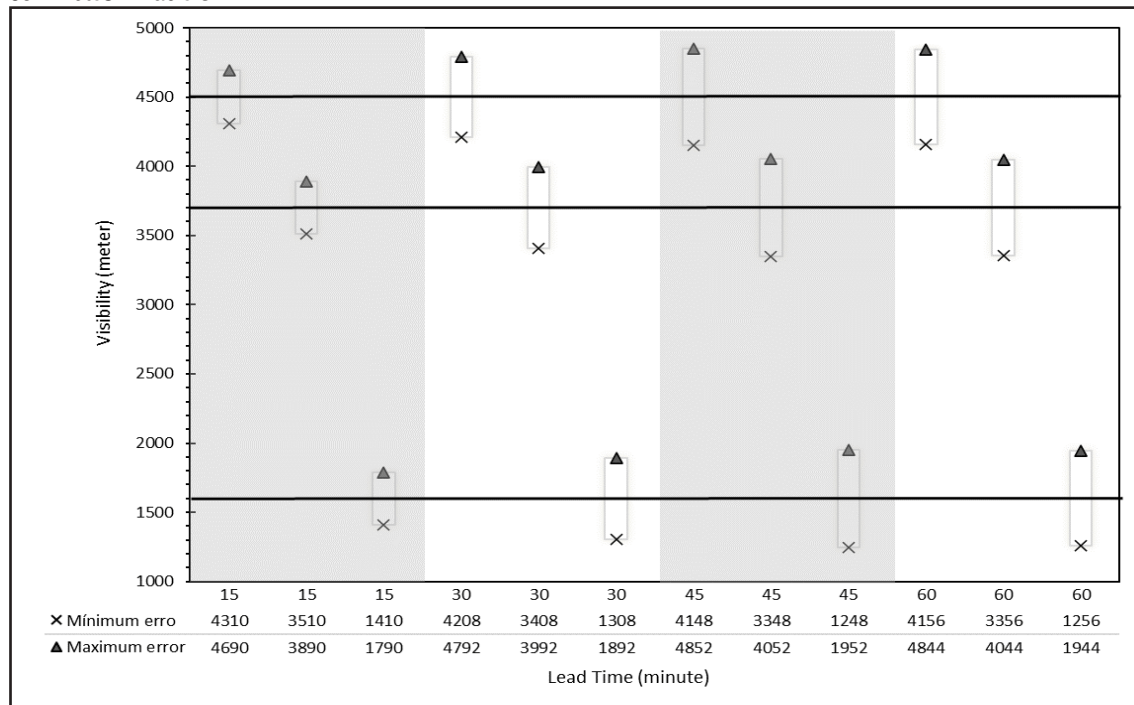|	15	15	15	30	30	30	45	45	45	60	60	60
✕ Mínimum erro	4310	3510	1410	4208	3408	1308	4148	3348	1248	4156	3356	1256
▲ Maximum error	4690	3890	1790	4792	3992	1892	4852	4052	1952	4844	4044	1944

Lead Time (minute)

Figure 5 exemplifies the performance of the set of predictions and the observations for a low-visibility event that occurred between 5 am and 1 pm on June 23, 2009. Regardless of the forecast time, it is noted that the 15-, 30-, 45- and 60-min visibility forecasts followed the behavior of the observation (black line in Fig. 5) with all correlation coefficients > 0.95 and their mean absolute errors are ≤ 321 meters. This can be verified through the behavior of the predicted visibilities, as they followed the observations almost perfectly, that is, they decreased at 5:45 am, remained relatively stable after 8:00 am - when the observed visibility oscillated close to 1,000 meters -, and increased with the increase in observations from 11:45 am. Furthermore, the 15-, 30-, 45-, and 60-min forecasts slightly overestimated the observations (based on the mean error of forecast-observation values for each leading time) by about 146.4, 121.9, 224.2, and 292.1 meter, respectively.

4.6. Ceiling nowcasting

Before presenting the results of the algorithms for forecasting the ceiling and the quantity of clouds, it is important to mention that the SODAR data was collected in the period 2017-2018 and during this period the ceilometer, part of the ASWS instrument panel, was inoperative. Thus, the training of the algorithms for the ceiling is limited to the period 2009-2016 and that is why the results in Table 6 are missing data from SODAR. Table 6 shows a summary of the best results for the ceiling test experiments with regressive algorithms for all lead times. Similarly, to the visibility results, the RF algorithm also resulted in the best performance of ceiling forecasts, regardless of the input data set or the lead time considered. It is also observed that the predicted values of H_c/C_q of 15-, 30-, 45- and 60-min are highly correlated with the observations with their values varying in the range of [0.96;0.97]/[0.77;0.86], respectively (column 4, Table 6) and the observations are close to the predictions since the MAE and the RAE, specifically for ceiling, vary in the ranges of [126.13;195.19] and [0.10;0.16], respectively. The results of the three ceiling thresholds (i.e., 1,200, 1,000, and 300 feet) can be considered encouraging since they vary approximately within the following ranges of H_c [1,005; 1,395], [805; 1,195] and [105; 495], respectively.

Figure 5: Regressive forecasts of visibilities and observations in the period from 5 am to 1 pm on June 23, 2009.
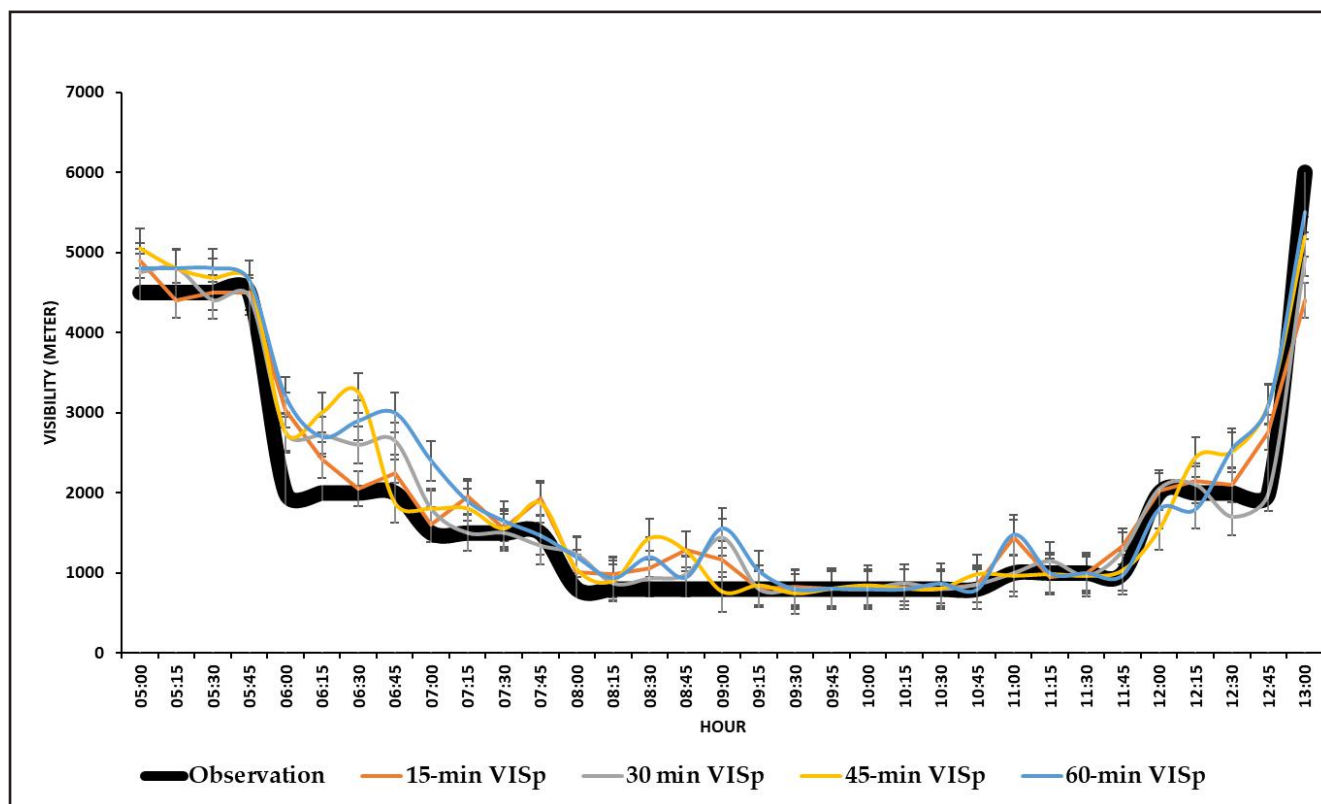
Table 6: Better statistical results of short-term Hc/Cq forecast using regressive algorithms and whose training was performed using the data set with the configuration 5) whose records are divided as Auto-WEKA default.

Algorithm	Lead time (minute)	Input data source	CC	MAE (feet/okta)	RAE
RF	15	2 and 3	0.97	126.13 feet	0.1
RF	15	2 and 3	0.86	0.55 okta	0.32
RF	30	2 and 3	0.97	166.02 feet	0.14
RF	30	2 and 3	0.81	0.69 okta	0.4
RF	45	2 and 3	0.96	182.95 feet	0.15
RF	45	2 and 3	0.83	0.63 okta	0.37
RF	60	2 and 3	0.96	195.19 feet	0.16
RF	60	2 and 3	0.77	0.77 okta	0.44

5. CONCLUSION

This study proposes a set of objective methods based on ML (the latter are defined as the trained and tested algorithms), with an extremely low computational cost but capable of making short-term forecasts up to 60 min for the operational thresholds related to the visibility and ceiling reporting periods for the airport operations.

Analysis of historical meteorological data suggested that the weather conditions at any airport can be more impacted by the restriction of visibility than the ceiling, and the critical period of the day is just before sunrise until close to noon during May, June, and July. The results with optimal categorical methods of the visibility predictions are satisfactory in 15 minutes and have not been successful in any forecast for the ceiling. On the other hand, the ceiling and visibility predictions, based on regressive methods, up to 60 min are encouraging since the values of the metrics are quite acceptable.

In summary following conclusions can be drawn from the present work:

- ML algorithms resulted in up to 20% better prediction in V_{is} when regressive techniques were used with a significant amount of reliable data;

- Training data sets need to be improved accurately in temporal and space resolutions and use of data from sensors (visibility meters, ceilometer, etc.) instead of human observations. When sensor's observations were used in training, ML algorithms resulted more accurate V_{is} and H_c predictions;

- The 1-h V_{is} and H_c data obtained by observers may not follow the dynamics of some meteorological phenomena, impairing the assertiveness of the method. Furthermore, observations provide a spatial resolution for V_{is}, which may reduce the efficacy of the algorithm's training compared to a continuous sensor V_{is} collection. It is obvious that the lack of lengthier history series for the SODAR data profiles, the absence of visibility sensor usage, and the ceilometer's inoperability since 2016 were all factors that led to the trained algorithm's performance decline; and

- Based on the results, it is concluded that the ML methods proposed here can identify the visibility and ceiling restrictions accurately and, thus, can improve short term forecast up to 1 hr. Thus, the new ML based methods can be considered as an alternative for operational forecasts based on NWP models.

In the future, it intends to use a numerical weather forecasting model to simulate the atmospheric conditions of visibility and ceiling limits, followed by training-testing ML algorithms with simulated numerical and observations - including a long series of high-frequency data sampling from sources such as SODAR, ceilometer, and automatic weather station - to extend the prediction time beyond one hour.

REFERENCES

A DECEA (2018) Relatório de Performance do Sistema de Controle do Espaço Aéreo Brasileiro (SISCEAB), http://especiais.decea.gov.br/performance/wp-content/uploads/2020/08/Rela_SISCEAB_ESTUDO-2_compressed.pdf, Accessed 04 January 2021.

Gultepe, I., Sharman R., Williams, P. D., & Shou, B. et al. (2019) A review of high impact weather for aviation meteorology. Pure and Applied Geophysic, https://doi.org/10.1007/s00024-019-02168-6.

Lima, J. S. (1982) Previsão de ocorrências de nevoeiros em Porto Alegre: método objetivo, São José dos Campos: Instituto de Proteção ao Voo do Ministério da Aeronáutica, Technical report, 18pages.

Silva Dias, M. A. F., & Jaschke Machado, A. (1997) The role of local circulations in summertime convective development and nocturnal fog in São Paulo, Brazil. Boundary-Layer Meteorology, https://doi.org/10.1023/A:1000241602661.

Oliveira, G. A. (2002). Método estatístico no auxílio à previsão de nevoeiro para o aeroporto de Guarulhos. Master Thesis. Federal University of Santa Catarina. https://repositorio.ufsc.br/xmlui/bitstream/handle/123456789/83415/188292.pdf?sequence=1&isAllowed=y. Accessed 04 January 2021.

França, V. D. J., (2008) Avaliação da metodologia de previsão de nevoeiro e visibilidade horizontal do modelo ETA. Master thesis. National Institute for Space Research.172p.

Fedorova, N., Levit, V., & Fedorov. D., (2008) Fog and stratus formation on the coast of Brazil. Atmospheric Research, https://doi.org/10.1016/j.atmosres.2007.11.008.

Fedorova, N., Levit, V., Silva, A. O., & Santos, D. M. B. (2013) Low Visibility formation and forecasting on the northern coast of Brazil. Pure and Applied Geophysics, https://doi.org/10.1007/s00024-012-0565-6.

Gultepe, I., Tardif, R., Michaelides, S. C., Cermak, J., Bott, A., Bendix, J., et al. (2007a). Fog research: A review of past achievements and future perspectives. Journal of Pure and Applied Geophysics, 164, 1121–1159. Special issue on fog, edited by I. Gultepe.

Gultepe, I., Pagowski, M., & Reid, J. (2007b). Using surface data to validate a satellite based fog detection scheme. Journal of Weather and Forecasting, 22, 444–456.

Hansen, B. (2007). A fuzzy logic-based analog forecasting system for ceiling and visibility. Weather and Forecasting, 22, 1319–1330.

Claxton, B. M. (2008). Using a neural network to benchmark a diagnostic parameterization: The Met Office's visibility scheme. Quarterly Journal of the Royal Meteorological Society, 134, 1527–1537.

Almeida, M. V. (2009). Aplicação de técnicas de redes neurais artificiais na previsão de curtíssimo prazo da visibilidade e teto para o aeroporto de Guarulhos – SP. Doutoral thesis. Federal University of Rio de Janeiro. http://www.coc.ufrj.br/pt/teses-de-doutorado/153-2009/1186-manoel-valdonel-de-almeida. Accessed 04 January 2021.

Colabone, R. O., Ferrari. A. L., Vecchia. F. A. S., & Tech. A. R. B., (2015) Application of artificial neural networks for fog forecast. Journal of Aerospace Technology and Management, http://dx.doi.org/10.5028/jatm.v7i2.446.

França, G. B., Almeida, M. V., Bonnet, S. M., & Albuquerque Neto, F. L. (2018) Nowcasting model of low wind profile based on neural network using SODAR data at Guarulhos airport. International Journal of Remote Sensing, https://doi.org/10.1080/01431161.2018.1425562.

Freitas, J. H. V., França, G. B., & Menezes, W. F., (2018) Convection forecasting using decision tree in Rio de Janeiro metropolitan area. Anuário IGEO, https://doi.org/10.11137/2019_1_127_134.

Almeida, V. A., França, G. B., & Velho, H. F. C., (2020a) Short-range forecasting system for meteorological convective events in Rio de Janeiro using remote sensing of atmospheric discharges. International Journal of Remote Sensing, https://doi.org/10.1080/01431161.2020.1717669.

Platenik, J. E. G., França, G. B., Pereira Neto, A. V., SILVA, R. M., (2020) Previsão de Nevoeiro Utilizando Multicritérios Baseados em Simulações do Modelo WRF para o Aeroporto Internacional Afonso Pena. Anuário IGEO, https://doi.org/10.11137/2020_4_376_383.

Zhou, B., Du, J., Gultepe, I. et al. Forecast of Low Visibility and Fog from NCEP: Current Status and Efforts. Pure Appl. Geophys. 169, 895–909 (2012). https://doi.org/10.1007/s00024-011-0327-x.

Da Rocha, R. P., Gonçalves. F. L.T., & Segalin. B. (2015) Fog Events and local atmospheric features simulated by regional climate model for the metropolitan area of São Paulo, Brazil. Atmospheric Research, https://doi.org/10.1016/j.atmosres.2014.06.010.

Perini, A. B., Paulo Filho, D. P., Rodrigues, E. S., Amaral, F. S., & Reichert, R. F. L. (2019). Anuário Estatístico Operacional 2018. INFRAERO. https://www4.infraero.gov.br/media/677124/anuario_2018.pdf. Accessed 04 January 2021.

Bishop, C. M. (2006). Pattern Recognition and Machine Learning. Springer-Verlag, Berlin, Heidelberg. ISBN: 978-0-387-31073-2.

Silva, W. L., Albuquerque Neto. F. L., França, G. B., & Matschinske, M. R. (2016) Conceptual model for runway change procedure in Guarulhos International Airport based on SODAR data. The Aeronautical Journal, https://doi.org/10.1017/aer.2016.33.

Almeida, V. A., França, G. B., & Velho, H. F. C., (2020b) Data assimilation for nowcasting in the terminal area of Rio de Janeiro. Ciência e Natura, https://doi.org/10.5902/2179460X53224.

Witten, I. H., Frank, E., Hall, M. A., & Pal, C. J. (2016). Data Mining: Practical Machine Learning Tools and Techniques. Fourth ed. Morgan Kaufmann. ISBN 978-0-12-804291-5.

Thornton, C., Hutter, F., Hoos, H. H., & Leyton-Brown, K. (2013) Auto-WEKA: Combined selection and hyperparameter optimization of classification algorithms, KDD '13: Proceedings of the 19th ACM SIGKDD international conference on Knowledge discovery and data mining, https://doi.org/10.1145/2487575.2487629

Kotthof, L., Thornton, C., Hoos, H. H., Hutter, & F., Leyton-Brown, K. (2016). Auto-WEKA 2.0: Automatic model selection and hyperparameter optimization in WEKA. Journal of Machine Learning Research, 17, 1-5.Holmes, G., Donkin, A. and Witten, I.

H., "WEKA: a machine learning workbench," *Proceedings of ANZIIS '94 - Australian New Zealnd Intelligent Information Systems Conference,* 1994, pp. 357-361, doi: 10.1109/ANZIIS.1994.396988.

Wilks, D.S. (2006) Statistical Methods in the Atmospheric Sciences. 2nd Edition, Academic Press, London.

Landis, J. Richard, and Gary G. Koch. "The Measurement of Observer Agreement for Categorical Data." Biometrics, vol. 33, no. 1, [Wiley, International Biometric Society], 1977, pp. 159–74, https://doi.org/10.2307/2529310.

Breiman, L. (2001) Random Forests. Machine Language, https://doi.org/10.1023/A:1010933404324.

Multi-criteria fog forecast based on WRF simulations for Afonso Pena International Airport

José Eduardo Gonçalves Platenik[1]

Gutemberg Borges França[2]

Antonio Vicente Pereira Neto[1]

Ricardo Marcelo da Silva[2]

Vinícius Albuquerque de Almeida[2]

ABSTRACT

It provides a method for 24-hour fog forecasting at Curitiba's Afonso Pena International Airport, Brazil. Eighty-one fog events from May to July 2019 were utilized to develop, test, and train the multi-criteria approach (decision tree), and their 15-minute reconstructions and records were made by the Weather Research and Forecasting (WRF) model and an automatic weather station, respectively. The correlation for the predicted and observed temperature, relative humidity, and wind speed data are equal to 0.93, 0.89, and 0.74, respectively. The application of the four established multi-criteria indicates that the probability of detection by criteria I, II, III, and IV of the fog events forecast for the onset (demise in parentheses) are, respectively, 93.22% (91.53%), 93.22% (93.75%), 88.14% (88.75%) and 90% (87.5%). The fog forecasts are slightly biased, i.e., a delayed onset and anticipated demise in 30 minutes or less.

Keywords: fog; multi-criteria; forecast.

1. INTRODUCTION

In general, visibility-restricting meteorological events like fog, precipitation, and others have a significant impact on airport landing and takeoff operations. Data presented by Gultepe et al. (2007) show that the monetary losses—and occasionally the human losses—caused by low visibility in various societal sectors are comparable to the losses brought on by severe weather events like tornadoes and hurricanes.

Fog is defined by the World Meteorological Organization (WMO) as the suspension in the atmosphere of water droplets or ice crystals that reduces horizontal visibility to less than 1,000 meters (WMO, 1992), and this phenomenon has a significant impact on some Brazilian airports' landing and take-off operations (INFRAERO, 2019). Fog is frequently categorized as either radiation (caused by radiative loss cooling the Earth's surface, typically on cloudless nights) or advection (caused by warm, humid air moving over a cooler surface). The mechanisms of fog formation and classification are described in detail in the works of Oke (1988), Varejão-Silva (2005), and França et al. (2018), among others.

Meteorological phenomena are thought to be critical for the organization, execution, and management of air navigation and airflow management, with a focus not only on flight safety but also on resource and logistics optimization. Due to the enormous losses associated with fog's effect on air travel, the aeronautical industry must plan and take specific safety precautions to avoid accidents, delays, or flight cancellations. The fog forecast is critical to the logistics of flight planning and the safety of air operations (Gultepe et al., 2019).

The numerical models of weather forecasting (Richardson, 1922), or simply atmospheric models, which

are based on partial differential equations and initialized from initial conditions obtained from various sources of observed and estimated data, are one of the operational tools currently used in meteorological forecasting services. These models produce forecasts for basic and parametric meteorological quantities. Despite advances in the development of atmospheric models, these must still be improved in order to overcome the challenge of confidently and accurately forecasting fog formation conditions, as well as its onset and end, as required by aviation (Gultepe, 2006; Croft & Ward, 2015).

Pereira (2014) pioneered fog forecasting work based on artificial neural networks for Curitiba airport, which is the focus of this paper. The results show a significant false alarm rate of about six times the frequency of the phenomenon.Payra and Mohan (2014) developed a procedure that provides very confident fog forecast results 24 hours in advance using surface meteorological data from New Delhi, India, and forecast data generated by the Weather Research and Forecasting atmospheric model (WRF, Skamarock et al., 2008). The results of fog and non-fog occurrences indicate a hit rate of around 94% and an accuracy of event onset ranging from 30 to 90 minutes. France et al. (2018) investigated two fog events at Guarulhos International Airport in So Paulo, Brazil, using data collected at high frequency (15 minutes) from automatic surface stations and the vertical wind profile of the lower troposphere extracted by Sound Detection And Ranging (SODAR) and radiosounding every 12 hours from Marte Airport in São Paulo, Brazil, demonstrating that the processes associated with low visibility phenomena (beginning, duration, and end) are similar (e.g. height of the layer, turbulent kinetic energy, wind intensity, among others).

In their review of the meteorology knowledge that is currently available for aeronautical operations, Gultepe et al. (2019) examined the variables produced by a regional atmospheric model to describe the boundary layer's favorable environment for the occurrence of fog.

In Brazil, the Department of Air Space Control (DECEA) is the sector in charge of providing the necessary means (systems and equipment) for the safe and efficient management, control, and security of the air navigation service, as established in national standards and international agreements and treaties established by the International Civil Aviation Organization (ICAO), to which Brazil is a signatory (Federal Decree No. 21,713/1946). In order to comply with ICAO standards, DECEA maintains an aeronautical meteorology service, issuing routine meteorological forecasts that include the forecast of reduced horizontal visibility, whether with a focus on flight safety or on airflow management. air traffic,

which is regarded as critical information for optimizing resources and contributing to flight safety and efficiency.

Fog influences airport operations, particularly takeoffs and landings, to varying degrees depending on the airport infrastructure. According to the 2018 operational statistical yearbook (INFRAERO, 2019), the Afonso Pena international airport is the sixth largest in the country in terms of aircraft movement, and fourth in passenger movement, with approximately 210 (two hundred and ten) landings and takeoffs daily and has its landing and takeoff operations impacted by approximately 300 (three hundred) hours per year due to low visibility restrictions (Oliveira, 2019).Given the limitations imposed by fog on Curitiba airport, as well as the current degree of subjectivity used by meteorologists to prepare fog forecasts for this location, more assertive prognostic models are required.

The goal of this work is to develop a 24h-predictive fog model for the Afonso Pena International Airport (Curitiba) using a multiple criteria approach (decision tree) and observational data from the Curitiba airfield surface meteorological station, as well as forecasts generated by the WRF atmospheric model, as developed by Payra and Mohan (2014).

2. STUDY AREA AND DATA

Figure 1 depicts the domain used in the WRF simulations, as described in section 4, with nested grids of 9, 3, and 1 km spatial resolution, centered on Afonso Pena International Airport, São José dos Pinhais (black dot), which is located at latitude 25° 32' S and longitude 49°10' W.

Figure 1: Computational domain for WRF simulations, with nested grids of 9, 3, and 1 km. The black dot represents the approximate location of Afonso Pena International Airport.
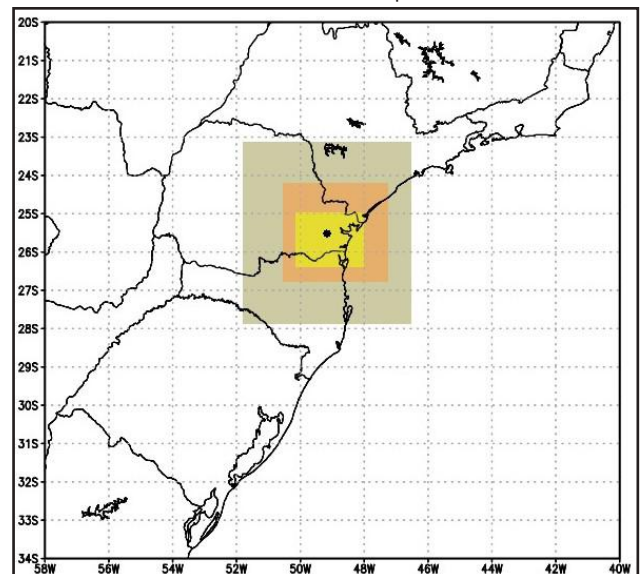
Table 1 displays the specifics (source, frequency, and meteorological variables) of the data used to examine the behavior of visibility in the study area and establish here multi-criteria fog forecasting.

3. METHOD

Figure 2 depicts the steps of the method, which are as follows:

Step 1: Collect data as shown in Table 1;

Step 2: Select fog events based on the visibility of the runway visual range;

Step 3: The WRF model is used to simulate atmospheric conditions, with outputs every 15 minutes beginning at 00Z on the day before the events (selected in Step 2), removing the initial 12 hours of model spin-up. Simulations are run with the GFS model's initial and boundary conditions (as described in Table 1). Skamarock et al. (2019) provide a detailed description of the WRF model, which is used as a simulation tool. Several authors, including Goswami and Tyagi (2007), Mohan and Bhati (2011), Goswami and Sarkar (2017), Naira et al. (2017), and Pithani et al. (2018), have studied different configurations of the WRF model for simulating physical processes within the boundary layer (e.g., fog). This work used the same WRF configuration as Payra and Mohan (2014), which is based on the sensitivity tests performed by Mohan and Bhati (2011), in this work:

a) Three computational domains covering the area between 20°S-34°S and 40°W-58°W were established, roughly centered on the Afonso Pena International Airport (Figure 1). In the three domains, the horizontal resolutions are 9 km (60 x 60 grid points), 3 km (112 x 97 points), and 1 km (214 x 160 points) (Figure 1);

b) According to Payra and Mohan (2014), a vertical discretization with 33 levels is used, with 10 levels below 2,500 meters; and

c) The parameterizations of physical processes were selected: Kessler Scheme (Kessler, 1969) for microphysics, Kain-Fritsch Scheme (Kain, 2004) for cumulus; Rapid Radiative Transfer Model- RRTMG (Iacono et al., 2008) for long and short wave radiation; Mellor-Yamada-Janjic Scheme (MYJ) (Janjic, 1994) for planetary boundary layer; and Noah-MP Land Surface Model (Niu et al., 2011; Yang et al., 2011) for surface processes; Eta Similarity Scheme (Janjic, 1994) for surface layer.

Step 4: The behavior of a sample of observational data (temperature, relative humidity, and wind speed and direction) from the events is compared to data simulated by the WRF (for the grid point closest to the airport), using the fog formation principle described, for example, in Oke (1988), Varejão-Silva (2005), and Payra and Mohan (2014). Thus, multi-criteria (intervals of meteorological variable behavior) are established for detecting fog formation and dissipation conditions; and

Step 5: Performance is statistically assessed after multi-criteria are applied to an independent test sample of fog events.

Table 1: Data used.

Source	Period	Frequency	Variables
Automatic Surface Weather Station (EMS)[1]	2019	15-minute	atmospheric pressure (hPa), air temperature (°C); Wet bulb temperature (°C), relative humidity (%); precipitation (mm); solar radiation (W/m²); Runway Visual Range (RVR – Runway Visual Range) (m); wind direction (°) and wind speed (m/s).
Meteorological Aerodrome Report (METAR) e Special Report (SPECI) [1]	2019	METAR, hourly; SPECI, varies, can be registered at any time except the full hour.	atmospheric pressure (hPa), air temperature (°C); Wet bulb temperature (°C), relative humidity (%); wind direction (°) and wind speed (m/s); cloud coverage; horizontal visibility (unit of length); weather present.
Global Forecast System (GFS) / National Centers for Environmental Prediction (NCEP) [1]	2015-present	3-hour	Initialization and contour variables for simulations with the WRF2 model[2]

[1] https://www.redemet.aer.mil.br/

[2] https://rda.ucar.edu/datasets/ds084.1/

[3] https://rda.ucar.edu/datasets/ds084.1/#metadata/grib2_levels.html?_do=y

Figure 2: Block diagram of method steps.
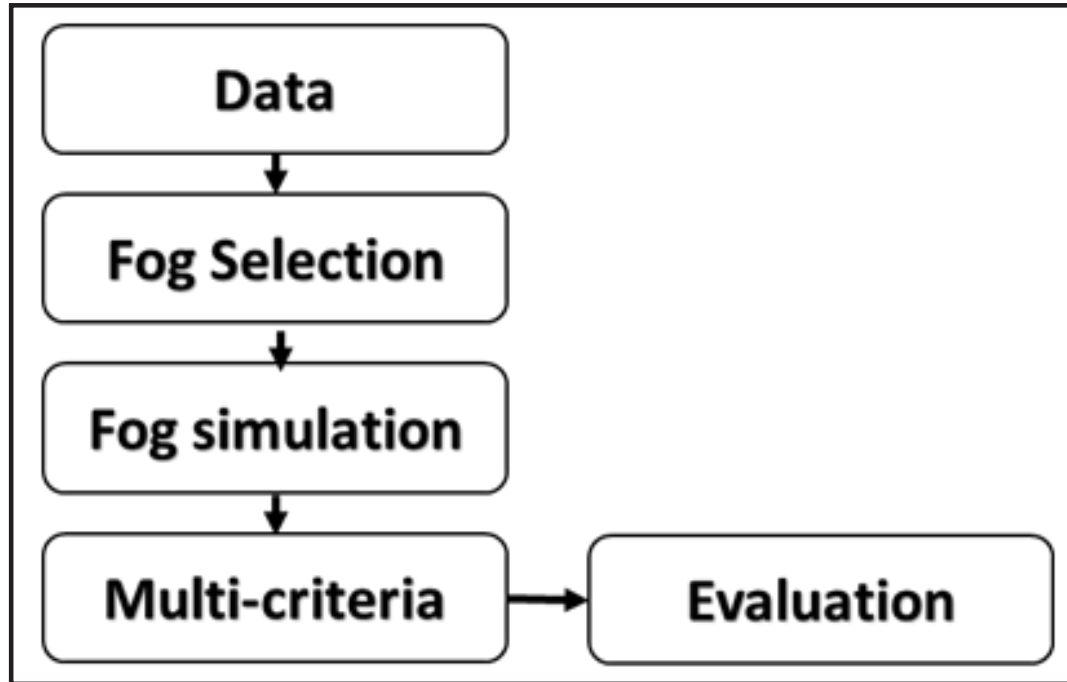
4. RESULTS

4.1 Fog Selection

Eighty-one fog events that took place over a period of thirty days between May and July 2019 were chosen for this study. Twenty-two events were used to create the multi-criteria, and fifty-nine events were used to assess them, as shown in Table 2.

4.2 WRF simulation and multi-criteria establishment

All events in Table 2 were simulated using the WRF atmospheric model in accordance with the setup described in step 3 of the method, and both the observed and jointly modeled data were examined. Observing the behavior of variable temperature, relative humidity, and wind speed in 15-minute intervals, the observed correlations are 0.93, 0.89, and 0.74, respectively. Figures 3a, 3b, 3c, 3d, and 3e show the behaviors of observations and WRF simulations of temperature at 2 m, relative humidity, wind speed, wind direction, and wind speed for the twenty and two fog events used to establish the multicriteria, respectively.

In most cases, criteria must be established through a process of trial and error, which takes time, until an ideal balance between false alarm reduction and event detection is found. The following criteria were established based on the behavior of the observed and predicted meteorological variables:

I)   relative air humidity greater than 95% and wind speed between 0.5 m/s and 3 m/s;

II)   relative air humidity greater than 95% and air temperature at a height of 2 m, between 8° C and 16° C;

III) relative air humidity greater than 95%; wind speed between 0.5 m/s and 3 m/s; air temperature at 2 m height between 8° C and 16° C; and

IV)   relative air humidity greater than 95%;

4.3 Application of multicriteria and evaluation

The 15-minute results of applying the four criteria as specified in step 4 of the method and established in item 5.2 are shown in Table 3. Each line shows the date, the start and end of the period during which the fog events occurred (column 4), the overall length of the events during the period, and the other columns show the application of the four criteria—that is, whether the event meets the requirements for beginning or ending (columns 6 to 9) and termination (columns 10 to 13), respectively.

Table 2: Fog events selected for establishment and evaluation of the multi-criteria.

Day	Date	Onset (h)	Demise (h)	Number of fog event (Visibility<1.000 meters)	Used for
1	26/05/19	04:30	12:30	3	
2	27/05/19	01:45	10:45	4	
3	04/06/19	00:00	10:00	4	
4	07/06/19	03:45	11:40	2	Establishment of
5	11/06/19	01:45	23:00	3	Multi-criteria
6	12/06/19	03:30	10:45	2	
7	25/07/19	04:30	04:45	1	
8	26/07/19	06:30	10:30	3	
9	03/05/19	00:45	11:30	3	
10	04/05/19	07:30	10:45	4	
11	05/05/19	08:15	08:30	1	
12	21/05/19	00:00	12:30	3	
13	22/05/19	03:30	10:00	5	
14	08/06/19	05:45	09:45	3	
15	09/06/19	05:15	12:45	2	
16	10/06/19	09:00	10:45	2	
17	13/06/19	04:45	10:45	6	
18	18/06/19	04:15	07:15	1	
19	19/06/19	05:30	09:45	2	Evaluation
20	22/06/19	04:00	04:15	1	
21	23/06/19	04:00	13:00	2	
22	24/06/19	08:15	08:30	1	
23	09/07/19	00:45	13:15	2	
24	10/07/19	01:30	03:15	1	
25	11/07/19	04:00	09:45	2	
26	12/07/19	04:00	11:00	5	
27	20/07/19	10:15	12:30	1	
28	24/07/19	08:00	10:30	3	
29	27/07/19	07:00	07:30	1	
30	31/07/19	02:45	00:00	8	

Results indicate that criteria I and II slightly outperform criteria III and IV when applied separately. It has been found that criteria I (related to relative humidity and wind speed), II (related to relative humidity and temperature at 2 m), III (related to relative humidity, wind speed, and temperature at 2 m), and IV (related to relative humidity, wind speed, wind direction, and temperature at 2 m) are able to predict the start (end in parentheses) with respective hit rates of 93.22% (91.53%), 93.22% (93.75%), 88.14% (88.75%), and 90% (87.5%). The criteria typically cause events to begin 15 to 30 minutes later and end 15 to 30 minutes earlier. In short, the findings show that the forecasting power is reduced by the addition of meteorological variables, such as in criteria III and IV.

Figure 3: Observed (dash line) and simulated (continuous line) behavior of: a. temperature at 2 m, b. relative humidity at 2 m, c. wind speed for the period between May 3 and 5, 2019. Figures 3d and 3e represent the observed and simulated wind speed and direction, respectively, for the 8 days of fog events used to establish the multi-criteria.
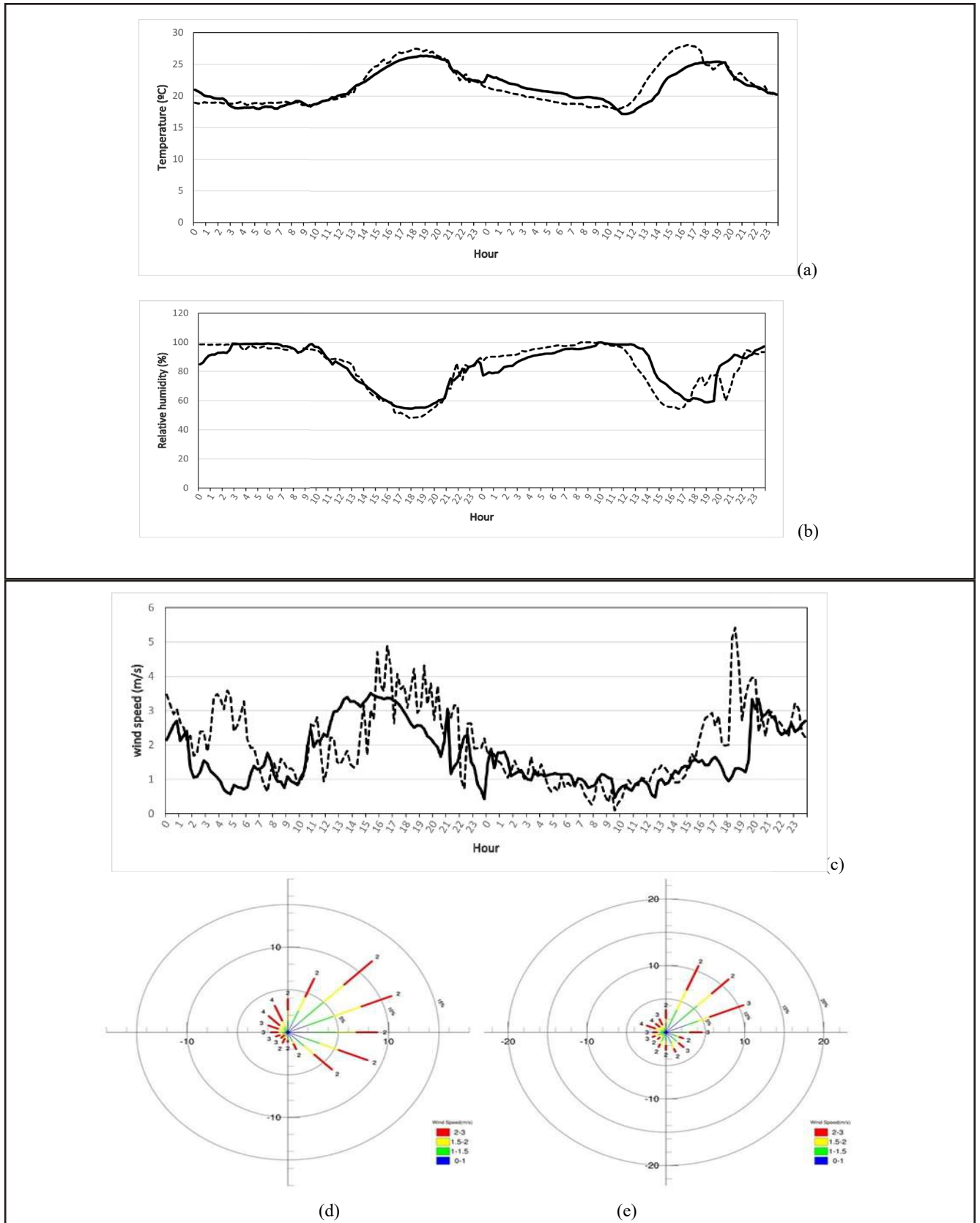
Table 3: List of days where fog occurred that was used to assess the four established criteria.

Day	Onset (h)	End (h)	Event	Duration (h)	Forecast Criterion (onset)				Forecast Criterion (End)			
					I	II	III	IV	I	II	III	IV
03/05/19	00:45	11:30	3	04:30	yes	yes	no	no	yes	yes	no	no
04/05/19	07:30	10:45	4	01:15	no	no	no	no	yes	yes	no	no
05/05/19	08:15	08:30	1	00:15	yes	yes	no	no	yes	yes	no	no
21/05/19	00:00	12:30	3	12:00	yes	yes	yes	yes	yes	yes	yes	yes
22/05/19	03:30	10:00	5	00:45	yes	yes	yes	yes	yes	yes	yes	yes
08/06/19	05:45	09:45	3	02:00	yes	yes	yes	yes	yes	yes	no	no
09/06/19	05:15	12:45	2	06:00	no	no	no	no	no	no	no	no
10/06/19	09:00	10:45	2	01:30	yes	yes	yes	yes	yes	yes	yes	yes
13/06/19	04:45	10:45	6	13:00	yes	yes	yes	yes	yes	yes	yes	yes
18/06/19	04:15	07:15	1	03:00	yes	yes	yes	yes	yes	yes	yes	yes
19/06/19	05:30	09:45	2	02:30	yes	yes	yes	no	yes	yes	yes	yes
22/06/19	04:00	04:15	1	00:15	no	no	no	no	no	no	no	no
23/06/19	04:00	13:00	2	08:45	yes	yes	yes	yes	no	no	no	no
24/06/19	08:15	08:30	1	00:15	yes	yes	yes	yes	yes	yes	yes	yes
09/07/19	00:45	13:15	2	12:00	yes	yes	no	no	no	no	no	no
10/07/19	01:30	03:15	1	01:45	yes	yes	yes	yes	yes	yes	yes	yes
11/07/19	04:00	09:45	2	00:30	no	no	no	no	yes	yes	no	no
12/07/19	04:00	11:00	5	04:00	yes	yes	yes	yes	no	no	no	no
20/07/19	10:15	12:30	1	02:15	yes	yes	yes	yes	yes	yes	yes	no
24/07/19	08:00	10:30	3	00:45	yes	yes	yes	yes	yes	yes	yes	yes
27/07/19	07:00	07:30	1	00:30	yes	yes	yes	yes	yes	yes	yes	yes
31/07/19	02:45	00:00	8	05:00	yes	yes	yes	yes	yes	yes	yes	yes
				Hitting rate	93%	93%	88%	90%	91%	93%	88%	87%

5. CONCLUSION

In this work, multiple criteria are established for forecasting the beginning and end of fog events, with a lead time of 24 hours, for Afonso Pena International Airport, Paraná - Brazil. These criteria are based on data modeled by the WRF atmospheric model and observed data. The results show that the multi-criteria can forecast when a fog event will start and end, but it is noted that the established criteria have a slight tendency to postpone the fog's beginning and anticipate its end. To ensure statistical consistency of the results, it is planned to expand the sample of data that has been analyzed. Additionally, computational intelligence (such as neural networks and decision trees) will be used to operationalize the developed model in the future.

REFERENCES

Croft, P. J., Ward B., 2015. Clouds and Fog: *Encyclopedia of Atmospheric Sciences.*Cambridge, Academic Press, 2998p.

França, G. B., Carmo, L. F. R., Almeida, M. V., Neto, F. L. A. 2018. Fog at the Guarulhos International Airport from 1951 to 2015. *Journal of Pure and Applied Geophysics.*

Goswami, P., & Sarkar, S. 2017. An analogue dynamical model for forecasting fog-induced visibility: validation over Delhi. *Meteorological Applications*, 24, 360–375.

Goswami, P., & Tyagi, A. 2007. "Advance forecasting of onset, duration and hourly fog intensity over Delhi", Research Report RR CM 0714. Bangalore, India: Centre for Mathematical Modelling and Computer Simulation.

Gultepe, I. 2006. A New Visibility Parameterization for Warm-Fog Applications in Numerical Weather Prediction Models, *Journal of Applied Meteorological and Climatological, 45(11)*: 1469–1480.

Gultepe, I.; Tardif, R.; Michaelides, S. C.; Cermak, J.; Bott, A.; Bendix, J.; *et al.* 2007. Fog research: A review of past achievements and future perspectives. *Journal of Pure and Applied Geophysics*, *164*: 1121–1159.

Gultepe, I.; Sharman, R.; Williams, P.; Zhou, B.; França, G. & Almeida. 2019. A Review of High Impact Weather for Aviation Meteorology. *Journal of Pure and Applied Geophysics, 176*: 1869–1921.

Iacono, M. J.; Delamere J. S.; Mlawer, E. J.; Shepard, M. W.; Clough, S. A. & Collins, W. 2008. Radiative forcing by long-lived greenhouse gases: Calculations with the AER Radiative transfer models. *Journal of Geophysical Research, 113(13)*: D13103.

INFRAERO. 2019. Anuário Estatístico Operacional da INFRAERO de 2018. Disponível em <http://www4.infraero.gov.br/media/677124/ANUARIO_2018.PDF>. Acesso em 23 de fevereiro de 2020.

Janjic, Z. I. 1994. The step-mountain eta coordinate model: further developments of the convection, viscous sublayer, and turbulence closure schemes. *Monthly Weather Review 122(5)*: 927-945.

Kain, J. S. 2004. The Kain–Fritsch Convective Parameterization: An Update. *Journal of Applied Meteorology, 43(1)*: 170–181.

Kessler, E. 1969. On the distribution and continuity of water substance in atmospheric circulation. *Meteorological Monographs, 10(32)*, 1-84.

Mohan, M, Bhati, S. 2011. Analysis of WRF model performance over subtropical region of Delhi, India," *Advances in Meteorology*.

Naira, Chaouch, Marouane, Temimi, Michael, Weston, & Hosni, Ghedira. 2017. Sensitivity of the meteorological model WRF/ARW to planetary boundary layer schemes during fog conditions in a coastal arid region. *Atmosheric Research*, 187(2017), 106–127.

Niu, G.-Y., Yang, Z.-L., Mitchell, K.E., Chen, F., Ek, M.B., Barlage, M., Kumar, A., Manning, K., Niyogi, D., Rosero, E., et al., 2011. The community noah land surface model with multiparameterization options (noah-mp): 1. model description and evaluation with local-scale measurements. *J. Geophys. Res.*

Oliveira, M. V., 2019: Caracterização e Previsão dos Nevoeiros no Aeródromo SBCT utilizando Inteligência Artificial. *Departamento de Meteorologia do Instituto de Geociências, Universidade Federal do Rio de Janeiro, Dissertação de Mestrado,* 173p.

Oke, T. R., 1988: The urban energy balance. *Progress in Physical Geography*, Volume 12, pp. 471-508.

Payra, S., Mohan, M. 2014. Multirule Based Diagnostic Approach for the Fog Predictions Using WRF Modelling Tool. *Hindawi Publishing Corporation: Advances in Meteorology*, ID456065, 11p.

Pereira, M. C. M. 2014. *Emprego de Redes Neurais Artificiais RBF na Previsão de Nevoeiro no Aeroporto Internacional Afonso Pena*. Programa de Pós-graduação em Métodos Numéricos em Engenharia, Universidade Federal do Paraná, Dissertação de Mestrado, 109p.

Pithani, P., Ghude, S. D., Prabhakaran, T., et al., 2018. WRF model sensitivity to choice of PBL and microphysics parameterization for an advection fog event at Barkachha, rural site in the Indo-Gangetic basin. India: *Theoretical and Applied Climatology*.

Skamarock, W.C; Klemp, J. B.; Dudhia, J.; Gill, D. O.; Barker, D. M.; Duda, M.; Huang, X. Y.; Wang, W.; Powers, J. G. 2008. A description of the advanced research WRF Version 3. *Technical Notes.* National Center for Atmospheric Research. Boulder, Colorado. 125p.

Skamarock, W. C., J. B. Klemp, J. Dudhia, D. O. Gill, Z. Liu, J. Berner, W. Wang, J. G. Powers, M. G. Duda, D. M. Barker, and X.-Y. Huang, 2019. A Description of the Advanced Research WRF Version 4. NCAR Tech. Note NCAR/TN-556+STR, 145 pp. doi:10.5065/1dfh-6p97

Varejão-Silva, M. A. 2005. Meteorologia e Climatologia. Versão digital. Recife. PE. Brasil.

WMO. 1992. *Vocabulário Meteorológico Internacional.* Organização Meteorológica Mundial. Genebra. 802p.

Yang, Y.-J., Shi, T., Tang, W.-A., et al., 2011. Study of observational environment of meteorological station based on remote sensing: cases in six stations of Anhui province. Remote Sens. Technol. Appl. 26 (6), 791e797.

Fog at the Guarulhos International Airport from 1951 to 2015

Gutemberg Borges França[I]

Luiz Felipe Rodrigues do Carmo[I]

Manoel Valdonel de Almeida[I]

Francisco Leite de Albuquerque Neto[I]

Abstract

This paper presents and discusses the fog occurrences before and after the construction of the Guarulhos International Airport, using data from 1951 to 2015. The analysis showed the following: 1) A total of 19,816 hours of fog were registered. 2) The minimum average, mean and maximum average of the fog temperature had significantly increased after the airport was constructed from 1.2 C to 6.9 C, 12.1 C to 14.5 C and 20.2 C to 20.7 C, respectively, due to the urban development around the airport during the study period. 3) The average fog hours per year decreased by approximately 73.1%, i.e., from 492 84.45 to 132 54.51 hours per year. 4) Most of the fog events occurred due to longwave cooling on clear nights with relatively low wind speeds (characterizing radiation fog), with over 65% having duration of 2 hours and occurring in the early hours of the day during March-September period. 5) The maximum probability of fog occurrence dropped about 10% from before to after the construction of the airport. Finally, two fog events are investigated using data collected during the fog evolution using atmospheric sounding profiles (from an acoustic sounder) and automatic meteorological stations and preliminary results showed that the values of cooling rate and turbulent kinetic energy play key roles in the onset and growth-dissipation phases of the fog, respectively.

1. INTRODUCTION

Fog is the major restrictive physical phenomenon that influences the landing and take-off operations at Guarulhos International Airport, São Paulo, Brazil. Restricted visibility for take-off and landing means that flights will be diverted or delayed, thereby causing substantial financial losses in the aviation and related sectors. According WMO (1966), fog is defined as microscopic water droplets or ice crystals suspended in air that reduce horizontal visibility to less than 1,000 meters. It is usual to classify fog event based on its geneses as radiation fog (caused by cooling thermal radiation at the land surface, predominantly cloud-free atmosphere) and advection fog (caused by the blowing of warm-humid air on a cooler land/water surface). Studies about fog formation and forecasting have been conducted over time, for example, Emmons and Montgomery (1947) described the process of fog formation; Kunkel (1984) studied the parameterization for extinction coefficients and mean terminal velocities based on 11 fogs drop size measurements; Bott et al. (1990) and Bott (1991) had invetigated the microphysics and physico-chemical properties of aerosols of radiation fog; Bergot and Guedalia (1994), Teixeira (1999) and Bergot et al. (2005) carried out studies on fog prediction using deterministic models; Tardif (2007) studied radiation

I. Federal University of Rio de Janeiro (UFRJ), Rio de Janeiro, Brazil. Correspondence to: gutemberg@lma.ufrj.br.

fog and the impacts on vertical resolution in the numerical prediction model; Gultepe and Milbrandt (2007) and Gultepe et al. (2009) had been carried out studies about fog forecasting based on field campaigns, which had been investigated marine and continental fog conditions. In particular, Silva Dias and Jaschke Machado (1997) used a regional-scale numerical model to investigate the local circulation evolution and its impacts on convection and nocturnal fog occurrence in São Paulo. Oliveira (2002) proposed an alternative stochastic model for fog forecasting for the Guarulhos International Airport. Fedorova et al. (2008) investigated the physical and synoptic processes of fog and stratus cloud formation over the northern and southern coasts of Brazil, and Fedorova et al. (2013) investigated the visibility and its forecasting at the Maceio International Airport in the Brazilian Northeast. Da Rocha et al. (2015) evaluated the impact of the horizontal resolution of a regional climate model on reproducing local climate features caused by foggy conditionsat the Metropolitan Area of São Paulo. Colabone et al. (2015) proposed a neural network-based fog nowcastingmodel for the Brazilian Air Force airfield, called Campo Fontenelle, in Pirassununga city in the State of São Paulo, Brazil. Silva et al. (2016) proposed a conceptual model for runway changes based on acoustic sound data for the Guarulhos International Airport. The latter is the largest airport in Brazil based on the number of passengers served and is also the hub for most national/international aviation companies operating in Brazil. The airport is often affected by fog eventsevery year bringing major problems to landing and take-off operations and thus was recently equipped with an acoustic sounder, or SODAR, aiming to study fog evolution by observing the top fog layer. Therefore, the objective of this work is to present an unique diagnostic of the variations and daily probability fog occurrences before and after construction ofthe Guarulhos International Airport, São Paulo, Brazil, based on data collection from 1951 to 2015 and, also, show the preliminary results of the characterizations of fog events using high temporal resolution data from a SODAR and automatic meteorological stations.

2. STUDY REGION AND DATA

The Guarulhos International Airport was inaugurated on 20 January 1985 and originatedas a Brazilian Air Force airfield called Cumbica, which, in the Tupi-Guarani indigenous language, means low cloud or fog. In fact, the Guarulhos airport location favors the formation of fog since its runways are located near the Forest of Cantareira Mountain and permanent marsh region due to waters from the Baquirivu-Guaçu River. Figure 1 gives an overview of the study area. Over time, the data collection facilities at the Guarulhos International Airport havebeen improved. Table 1 provides details about the dataset used to characterize the fog events in this work. Most of the fog data used herewere generated from human observations, except for the period starting in 2006 when an Automatic Meteorological Station (AMS) was installed. In addition, the visibilitieson the two runways were automatically registered by Runway Visual Range (RVR – MITRAS Transmissometer-Vaisala) starting in 2005. Table 1 specifies the meteorological variables used, which are represented by W, u, v w, BLH, TKE, PRP and RH, which correspond to surface wind (i.e., direction in degrees and speed in $m.s^{-1}$ or knots), zonal wind component, meridional wind component, vertical wind component, boundary layer height (km), turbulent kinetic energy (m^2/s^2), precipitation (mm) and relative humidity (%), respectively. To standardize the differences between the automatically collected information, including the instantaneous visibility

Table 1 : Meteorological variables usedand their data sources.

Data Source	Meterological Variable	Sampling frequency	Period
SODAR	u, v, w, BLH and TKE	15-minute	2011-2015
Conventional meteorological station	W, Tair, RH, PRP and AP.	1-hour	1951-2006
Automated meteorological station	W, Tair, RH, PRP and Atmospheric pressure.	1-minute	2006-2015
VAISALA - RVR	Visibility	1-second	2005-2015

Figure 1 : Characteristics of the region of the Guarulhos International Airport.

registered by the RVR, and that collected by human beings, only the fog events that lasted a full hour (i.e., one hour, two hours, etc.) were included in the study; therefore, the fog climatology presented in the results sections may be slightly less than that observed.

3. DISCUSSION OF RESULTS

Figure 2 (a) shows the average of T_{air} and the variations of fog hours per year during the period from 1951 to 2015 corresponding to the total of 19,816 hours of fog. There are three distinct periods of numbers of fog hours, i.e., (1) from 1951 to 1979, during which the fog hours (FH) per year and STandard Deviation (STD) are equal to 491.47 and 84.45, respectively; (2) from 1980 to 1985 (FH=266.2 and STD =118.37); and (3) from 1986 to 2015 (FH=132 and STD =54.51). Overall, the average T_{air} and FH have oppositebehaviors, i.e., when T_{air} was gradually growing, the FH declined. Period (2) coincides with the building period of the Guarulhos International Airport. It is also noted that between period (1) and period (3) there were a significant increase of the mean$T_{air}$of 1.4 °C, from 18.4 °Cto 19.8 °C, anddecrease of the average of number of fog hours of approximately 73.1%, from 491.47 to 132 hours. The latter may be attributed to the development of the area surrounding the Guarulhos International Airport caused by the construction of new roads, houses, buildings and population increase.Figure 2 (b) shows the variation minimum average (dotted line), mean (solid line) and maximum average (dashed line) of the fog T_{air} per year during the data period and the gray rectangle represents data recorded in period (2), as in Figure 2 (a). And it can be observed that there were significant increases in the mean values of minimum average, mean and maximum average of the fog T_{air}, between period (1) and period (3), from 1.2°C to 6.9°C (this is one more expressive of 5.65 times), 12.1°C to 14.5°C and 20.2°C to 20.7°C, respectively.

Figure 3 shows the percentage variations of FH versus the hour of the day (local time) corresponding to 19.816 events (or hours) with visibilities of less than 1 km at the Guarulhos International Airportduring the period from 1951 to 2015. The highest frequencies of fog occurrence (representing 91.1% of fog population) are distributed in early hours of the day, i.e., from 00 to 09h (local time), with peak frequency of 15.6% at the time of sunrise at 06h, and the main reason is that the most fog events in the study area are generated due to longwave cooling on predominantly cloud-free atmosphere with relatively low wind speeds (which typifies a radiation fog), as discussed here in section 4.

Figure 2: (a) Variations of fog hours and average Tair in the degree Celsius per year and where (1), (2) and (3) represent, in the data set, the periods before, during and after the installation of the Guarulhos International Airport, respectively. (b) The maximum average (dashed line), mean (solid line) and minimum average (dotted line) values of the fog temperature per year during the study period.
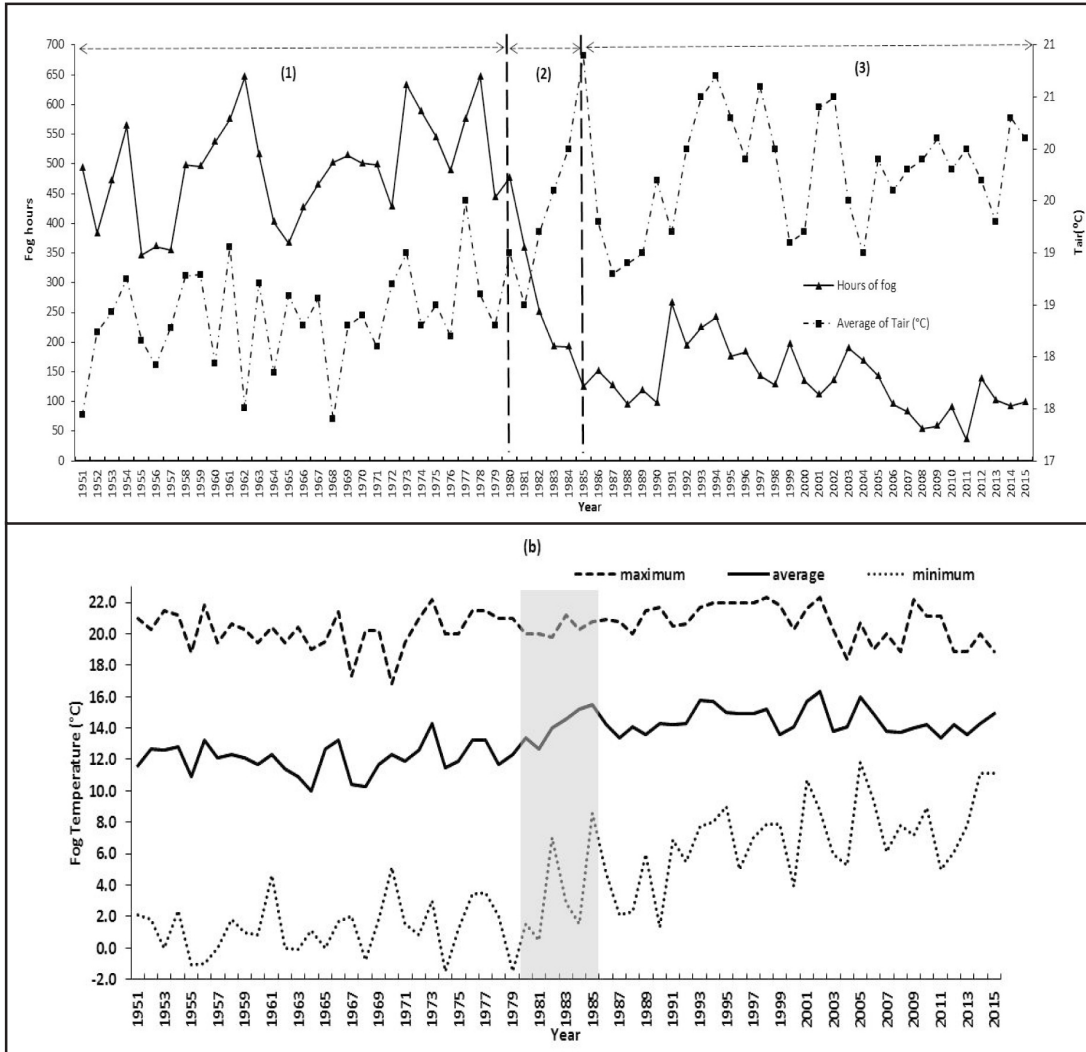
Figure 3 : Percentage of fog occurrence versus local time during the period from 1951 to 2015.
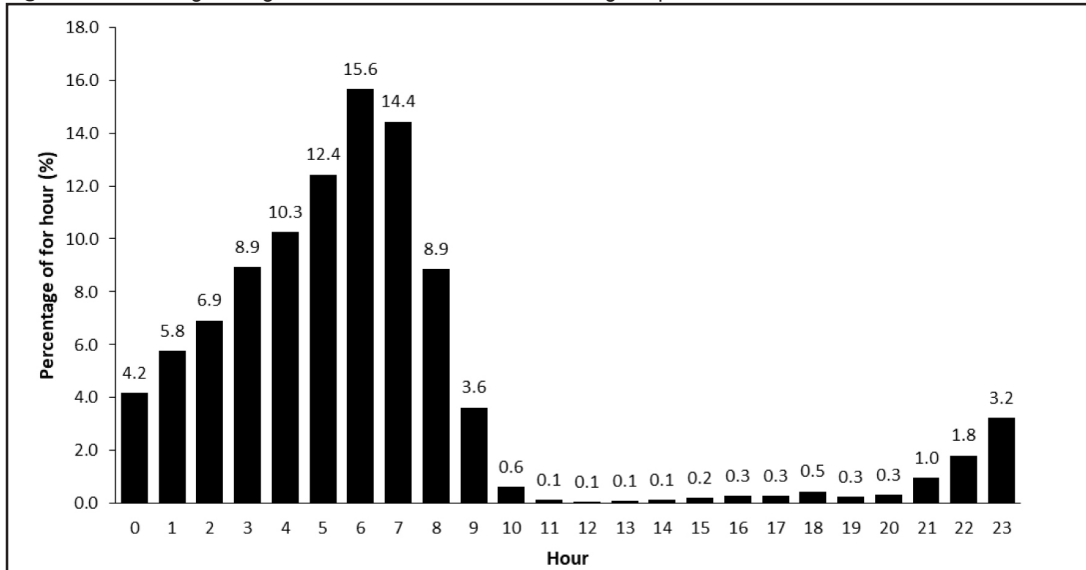
Figure 4 (a) depicts the monthly frequency of FH. The highest fog frequencies occurredfrom March to September that is the coldest period of the year— corresponding to approximately 80.6% of fog events — with peaks of 16.3% and 16.0% in May and June, respectively.Figure 4 (b) shows the percentage of fog occurrences in relation to fog duration in hours, which shows that the highest occurrence was two hours, corresponding to 66.9% of the population. The longest recorded fogswere twelve hours long. The fog periods and their percentages of occurrence are, respectively, written and specified in parentheses, i.e., one hour (47.40%), two hours (18.50%), three hours (9.25%), four hours (7.51%), five hours (5.78%), six

hours (3.47%), seven hours (2.31%), eight hours (2.31%), nine hours (1.73%), ten hours (1.16%), eleven hours (1.16%) and twelve hours (0.58%).The data set reveals that, during fog events, the mean values of visibility, the mean fogT_{air}, RH versus fog duration up to 1-h; greater than 1-h and less than or equal to 3-h and greater than 3-h are approximately equal to 798 ± 128 meters, 16.6 ± 0.6 °C; 89.6 ± 8%; 592 ± 324 meters; 16.3 ± 2.0°C, 99.0 ± 1.0%; and 322 ± 173 meters, 15.1 ± 1.8 °C, 99.1 ± 0.8%, respectively. As expected, the latter shows that longer fog events, i.e., lasting more than 3 hours, have their average visibility and temperature lower than the shorter fog events.

Figure 4: (a) and (b) represent the monthly variations of fog hours and percentages of fog occurrence versus its duration (hour) during the period from 1951 to 2015, respectively.
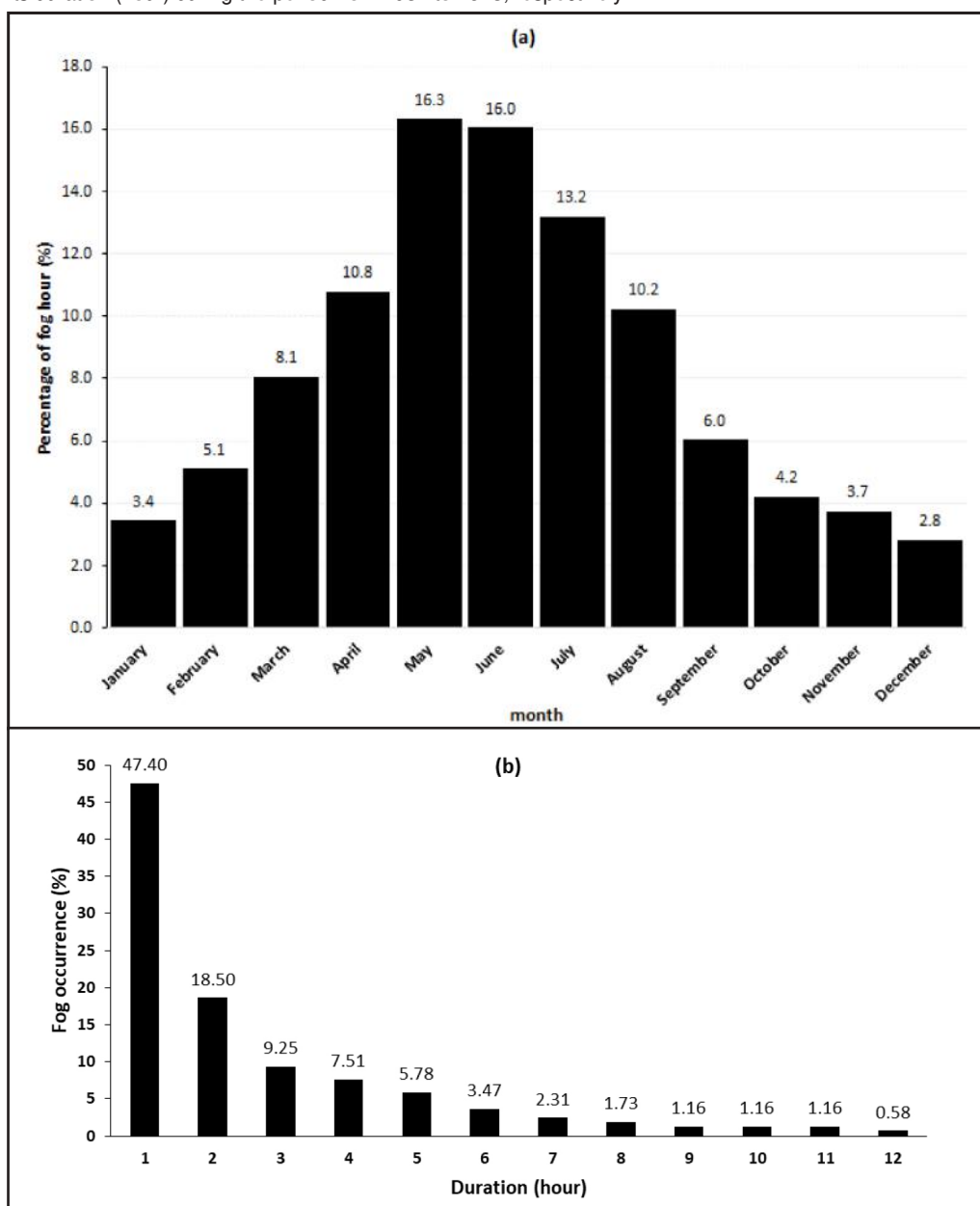
With the aim of studying foggy conditions beforeand after the construction of the Guarulhos International Airport, the data set was subdivided into two subsets, corresponding to 1961-1990 and 1991-2015, and referred to herein as A and B. The period A is classified as the fog climatology, following the World Meteorological Organization (WMO, 2011) definition (when fog conditions were recorded over a period of 30 years). On the other hand, although the B period is an incomplete climatology spanning 25-year, this period is used here to analyze the post-construction airport period. Figure 5 (a) shows the variation fog hours versus the month of each period A and B represented by the dotted and solid lines, respectively. The peaks of the curves occurred in different months, i.e., in May for period A and in June for period B. In addition, a significant decrease in the amplitude variation of fog hours per month was observed during the B period. Possiblyit can affirm that the decrease in fog hours, as previouslydiscussed, is due to the increase in mean T_{air} that occurred between 70s and 80s (related to the development of the area surrounding the airport), as observed clearly in Figure 2 (a). In summary, the data set revealed that there were significant changes, indicated in parentheses, of the physics quantities between period A and B, respectively, i.e., RH (from 82.9% to 81.7%), mean fog Tair (from 12.8°C to 14.6°C), mean minimum fog T_{air} (from 2.2°C to 7.7°C), mean maximum fog T_{air} (from 20.3°C to 20.7°C) and fog hours (from 298 hours to 152 hours).

The Figure 6 shows the percentage of fog occurrence versus fog duration in hours for period A and B andobserves that the occurrence of fog persists with the same durations of the period before the construction of the airport. However, fogs lasting 1 and 2 hours increased, respectively, their occurrence frequencies of approximately 6.9% and 0.4% between period A and B, while the longer fogs decreased their frequencies.

Additionally, Figures 7(a) and 7(b) show the probabilities of fog occurrences per month and hour of the day, i.e., when the horizontal visibility is less than 1 km, for periods A and B, respectively. Generally, the maximum probability of fog occurrences drops from over 50%, in Figure7 (a) in period A to less than 40%, in Figure 7 (b), in period B, which is likely due to the increase of T_{air} during period B.

Figure 5 : the average, minimum, maximum monthly fog hours for the periods corresponding to 1961-1990 (dash line) and 1991-2015 (solid line).
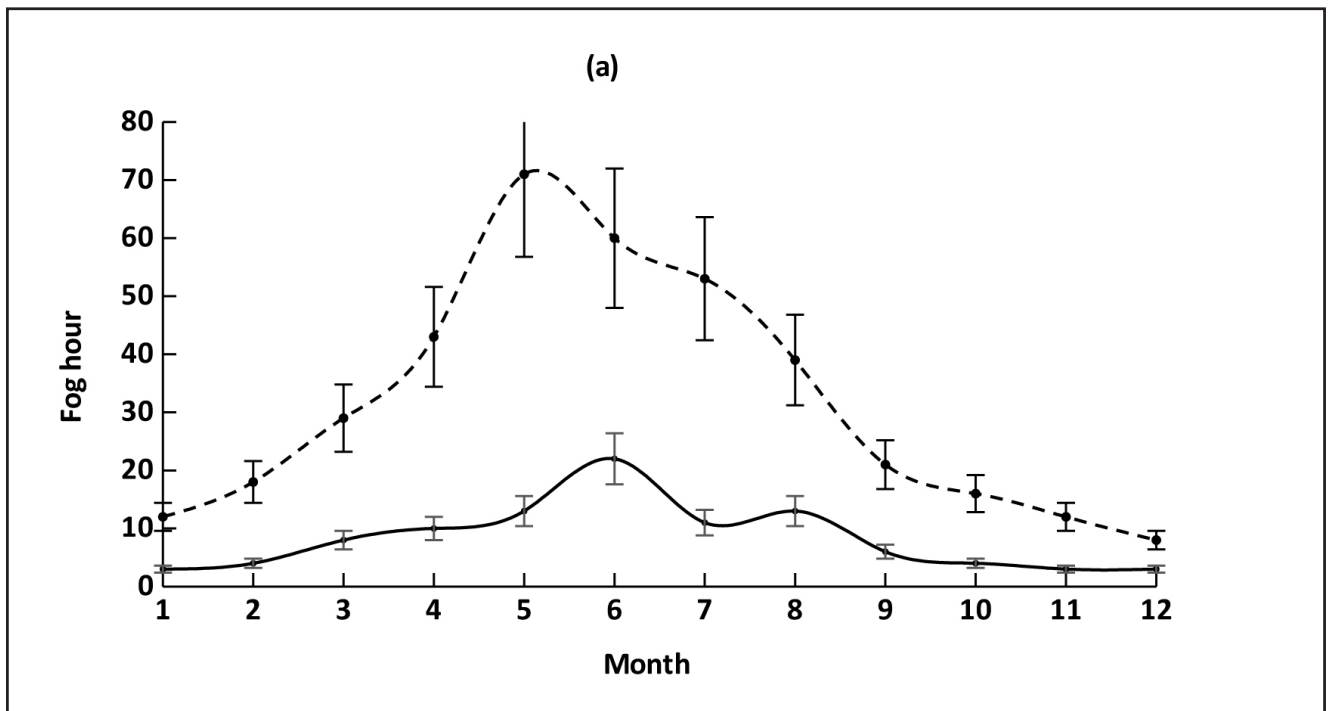
Figure 6 : Percentages of fog versus its duration (hour) during from 1951 to 1980 (gray bar) and 199 to 1991 to 2015 (black bar), respectively.
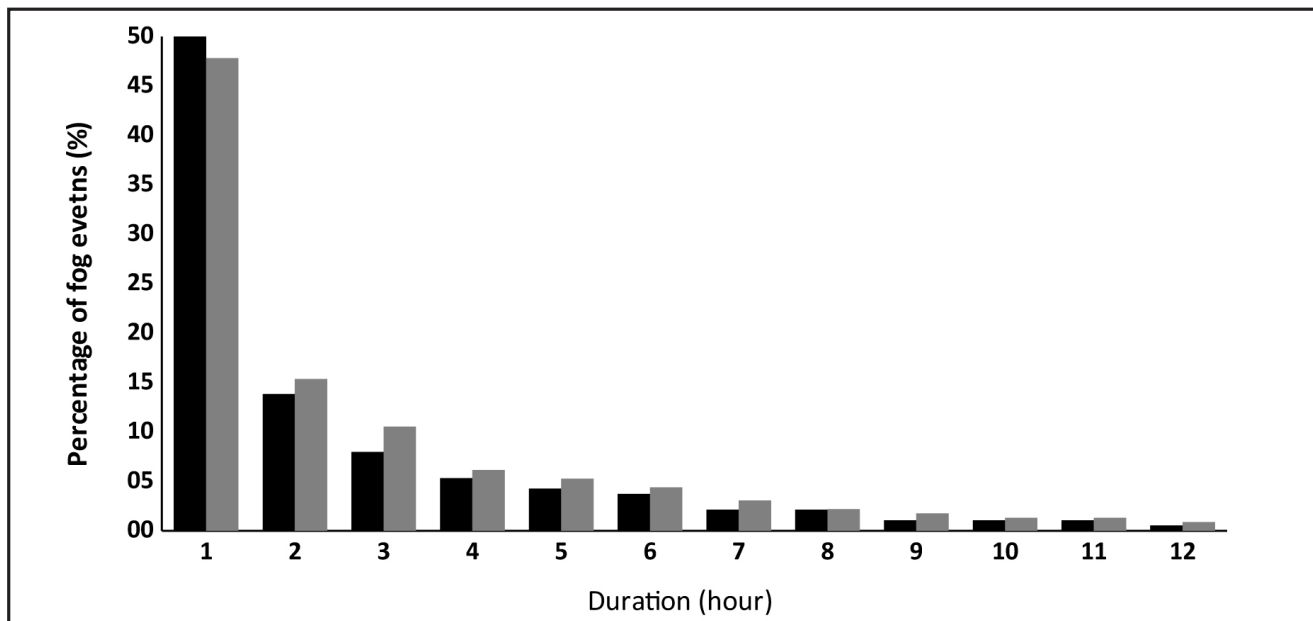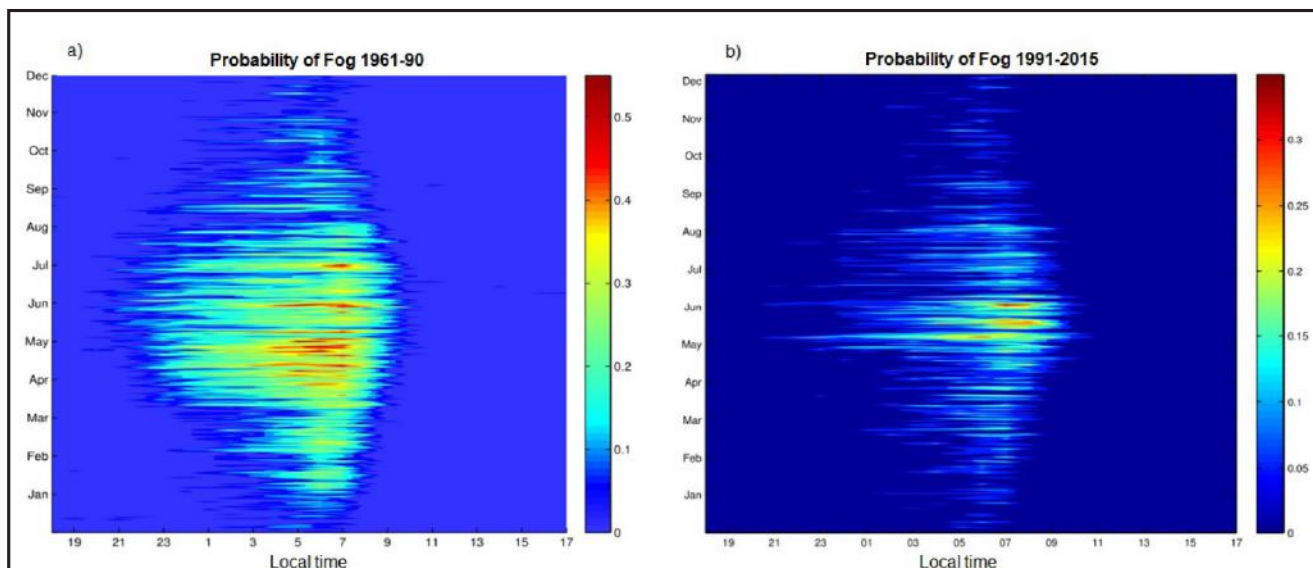

Figure 7 : Percentages of fog versus its duration (hour) during from 1951 to 1980 (gray bar) and 199 to 1991 to 2015 (black bar), respectively.

4. SYNOPTIC ANALYSIS AND THE USEOF SODAR AND AMS DURING TWO FOG EVENTS

In the study of this airport, the fog typically occurs because of longwave cooling, which reduces T_{air} to the dew point temperature (Td), on clear nights with low wind speeds. After the fog onset, the liquid water in the fog increases due to the cooling rate, which will be higher with a dryer atmosphere (Teixeira and Miranda, 2001). After sunrise, T_{air} begins to gradually increase at the surface, working in conjunction with the longwave cooling rate at the top layer of the fog, which causes an increase in the turbulent kinetic energy (TKE), and thus, the fog

is intensified for some time until the fog dissipates. To analyze the importance of each measured and calculated physical quantity in the fog evolution (i.e., its onset, growth, and dissipation), two typical radiation fog events of 3:45 hours that occurred on 08 September 2011 and 05 April 2012 (referred to herein as events 1 and 2) and are here characterized and discussed.

Figures 8 (a)-(c) and (b)-(d) depict images of brightness temperature of channel 4 registered by GOES-12 satellite at 1000 (GMT)and 0900 (GMT), which roughly represents the onset times of events 1 and 2 (as in Figure 9 (a) and (c)), and synoptic charts of 0000 (GMT) on 08 September 2011 and 05 April 2012, respectively, which

are regularly made available by the National Institute for Space Research (INPE) on http://satelite.cptec.inpe.br.

The synoptic surface analysis event 1, represented by Figure 8 (a-b), shows that the study area, represented roughly by the black rectangle, had been influenced by the proximity of South Atlantic Subtropical High, whose point core of 1027 hPa is approximately located at 26ºS,27ºW, which brought divergence and clear sky and, thus, conditions for formation of radiation fog.

It noted also that there was a very low intensity trough positioned over the area with NW-SE orientation. Similarly to event 1, the synoptic surface analysis for event 2 (Figures 8 (c) - (d)) shows the positioning of South Atlantic Subtropical High, whose point core of 1026 hPa is approximately located at 38ºS,30ºW influencing also the circulation in the study area bringing typical conditions, as aforementioned, for formation of radiation fog.

Figure 8: (a)-(b) and (b)-(d) are GOES 12 brightness temperature images of Channel 4 (spectral band centered at 11 m) collected at 1000 (GMT) and 0900 (GMT) and synoptic analysis charts of 0000 (GMT) on 08 September 2011 and 05 April 2012, respectively. The black rectangle represents the study regions.
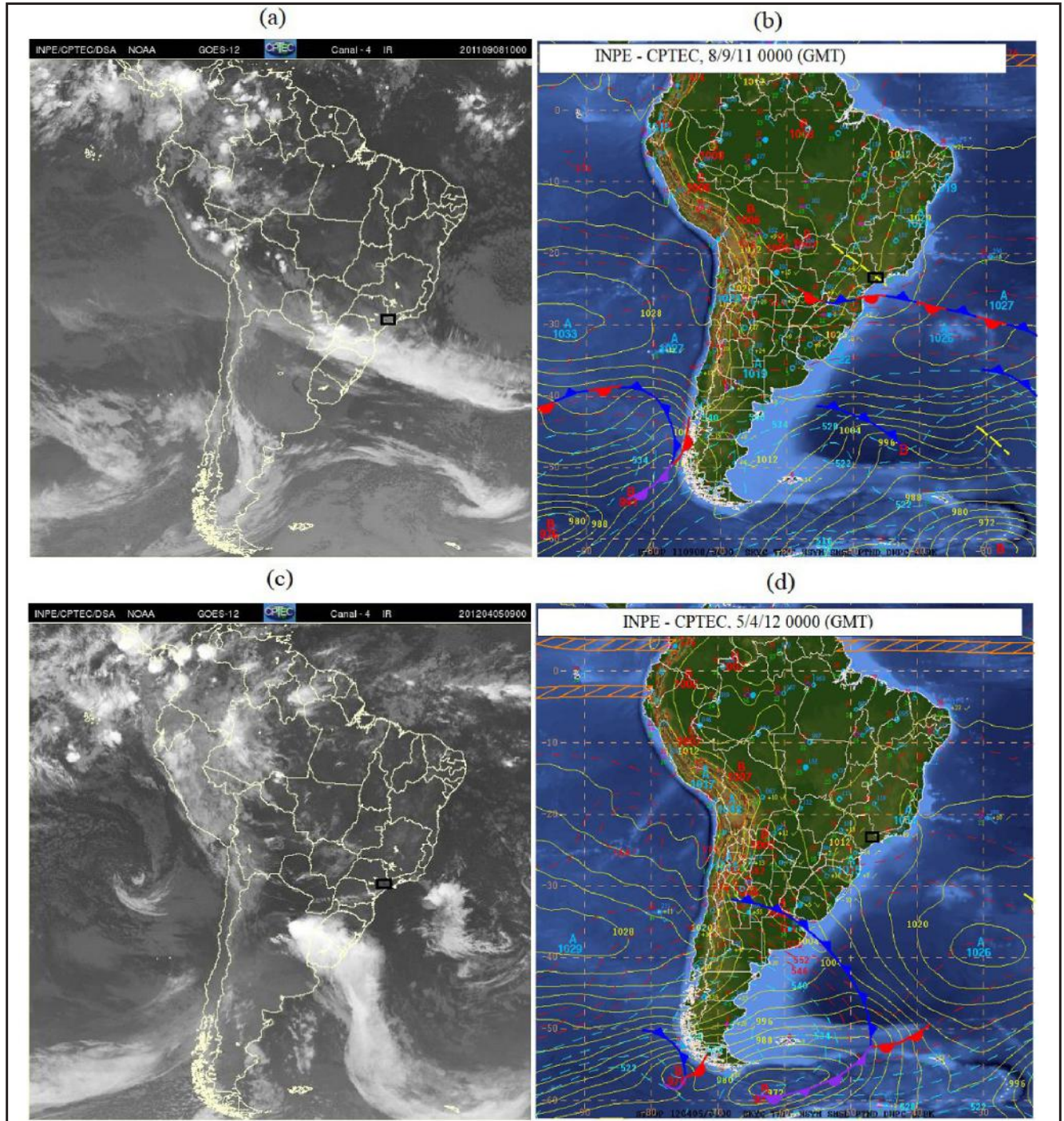
Figures 9 (a) and 9 (b) show the variations of TKE, BLH and visibility at 15-minute intervals during fog events that occurred at the International Guarulhos Airport on 08 September 2011 and 05 April 2012. The two vertical lines limit the periods of the fog in the aforementioned figures, i.e., the lines delineate the period when the visibility is less than 1 km. Figures 9 (c) and 9 (d) show the Skew-T profile plots of T_{air} (solid black line on the right) and Td (solid black line on the left), collected viaa sounding launched at Marte receiving station, located approximately 18 km from the airport, at 09:00 (local time) during fog events 1 and 2, respectively. Table 2 presents the averages and variations of the atmospheric pressure, T_{air}, cooling rate (CR), TKE and wind registered during the seven hours before (columns 2 and 3) and during (columns 4 and 5) the fog evolution registered for event 1 and 2, respectively. The investigation shows the following:

a) The thickness of the fog represented by the BLH of event 1 is approximately twice that ofevent 2; a reasonable reason for this is the atmospheric conditions during event 1, which was much drier than event 2, as shown by the differencesT_{air} –Td (i.e., the drier the atmosphere), as seenin Figures 9 (b) and 9 (d), respectively. As a consequence, the CR of the event 1 is approximately twice as high -due to the lower atmospheric absorption –as that of event 2, as seen in Table 2, columns 2 and 3, respectively. In addition, the CR value seems to be fundamental in the onset process of the radiation fog, as event 1 and 2;

b) Despite a T_{air} difference of approximately 5 °C between events 1 and 2, T_{air} had no apparent impact on the duration of the fog;

c) The wind blew from the northeast influenced by the proximity of South Atlantic Subtropical High, with wind speeds varying between approximately 1.5 and 4.0 m.s^{-1}. The average speed is approximately three times greater in event 1 than in event 2 before the fog onset and is almost the same magnitude during the event maturations;

d) As far as the fog dissipation is concerned, the TKE seems – as shown in Figure 9 (a) and 9 (c)– to play a pivotal role in fog dissipation, givinga clear advance signal of the dissipation. In both figures, TKE (dashed line with dot) and BLH (dashed line) are positively correlated since their values tend to follow each otherdue to the turbulence process noted above, which is responsible for the intensification of the fog and, a few minutes later, triggers the fog dissipation, in concordance with the results presented by Dabas et al. (2011), which also used SODAR data to study fog evolution. On the other hand, the trigger for fog onset is not so clear, and thus, further investigations will be needed. In summary, the preliminary results presented show that SODAR is able to identify the BLH or the thickness of a fog layer; therefore, its data will be important for the future parameterization of fog onset, growth, and dissipation.

Figure 9: (a)-(c) are the two time series of visibility (solid line), turbulent kinetic energy (dashed line with dot) and boundary layer height (dashed line with dot) at 15-minute sampling intervals, and (b)-(d) show the Skew-T plots from the Marte soundings launched at 0900 hours (local time) on 08 September 2011 and 05 April 2012, respectively.
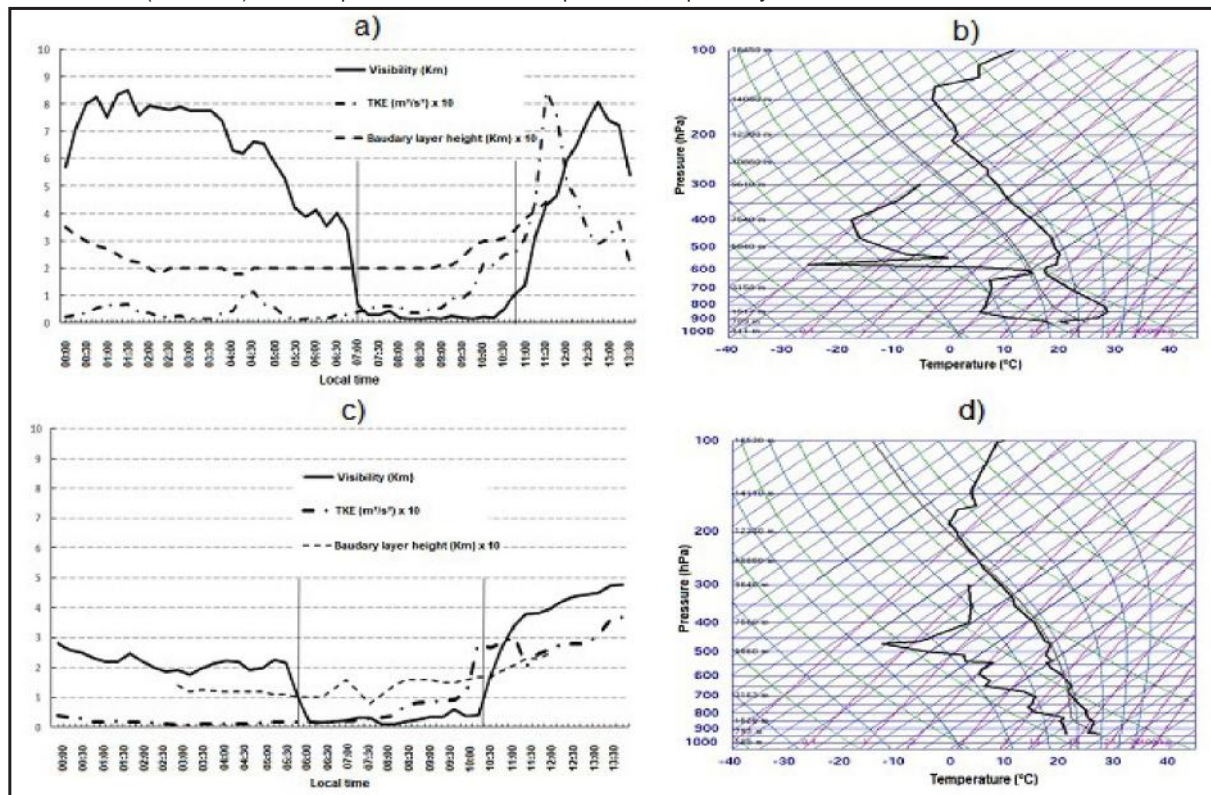
Table 2: Averages and variations of atmospheric pressure, T_{air}, cooling rate, TKE and the wind before and during the two fog events registered on 8 September 2011 and 5 April 2012.

Physical quantity	7 hours before fog onset		Fog period: 3:45 hours	
	08-SET-2011	05-APR-2012	08-SET-11	05-APR-2012
Pressure (hPa)	1017.0 ± 1.1	1017.0 ± 1.1	1016.0 ± 0.5	1017.2± 0.8
Boundary layer height (m)	220 ± 1	140 ± 2	211 ± 1	134 ± 2
T_{air} (ºC)	15.3 ± 0.8	22.7 ± 2.3	14.2 ± 0.3	19.5 ± 0.9
Cooling rate °C per hour	-0.41 ± 0.01	-0.26 ± 0.78	-0.25 ± 0.01	-1.01 ± 0.21
TKE (m²/s²)	0.56 ± 0.22	0.031 ± 0.024	0.65 ± 0.31	0.039 ± 0.021
Wind speed (m.s⁻¹)	2.9 ± 1.0	1.17 ± 0.48	2.1 ± 0.6	1.69 ± 0.35
Wind direction (º)	58.9 ± 15	68.5 ± 30.5	69.8 ± 41	60.89 ± 13

5. CONCLUSION

This paper mainly presents the climatological study of the fog occurrences before and after the construction of the International Guarulhos Airport for the period from 1951 to 2016. In addition, fog events were characterized using acoustic sounder and automatic meteorological station data with 15-minute sampling intervals. The principal conclusions of this work are given below.

- The construction of the studied airport and local urban development promoted a significant increase in the fog temperature, which caused a significant decrease of fog hours (to approximately one fifth the initial value), which has lowered the restrictions on the landing and take-off operations at the airport.
- More fog events occur in the early hours of the day, with over 72% of them occurring during the fall-spring period. The majority of fog events (over 65% of fog events) had durations about two hours.
- Most fogs were caused bylongwave cooling on clear nights with low wind speedsand the values of the cooling rate and TKE play important roles their onset and growth-dissipation phases, respectively;

- The maximum probability of fog occurrence fell significantly from before to after the construction of the International Guarulhos Airport;
- The SODAR provided reliable measurements of the thickness of the fog,in concordance with the results obtained by Dabas et al. (2011). The preliminary results have revealed that the fog evolution is positively correlated with turbulent kinetic energy and is potentially an important physical quantity for the parameterization offogonset,growth and dissipation.

Currently, researchers from the Applied Meteorological Laboratory of the Federal University of Rio de Janeiro and the operational community are involved in testing and validating models based on computational intelligence or deterministic modeling for short-term fog forecasting; the results will be published in future works.

ACKNOWLEDGMENTS

REFERÊNCIAS

Bergot, T., Carrer, D.J. Noilhan, P. Bougeault (2005): Improved site-specific numerical prediction of fog and low clouds: A feasibility study. Wea. Forecasting, 20, 627–646.

Bergot, T.,Guedalia, D. (1994): Numerical forecasting of radiation fog. Part I: numerical model and sensitivity tests. Monthly Weather Review, 122, 1218–1230.

Bott, A., Sievers, U., &Zdunkowski, W. (1990): A radiation fog model with a detailed treatment of the interaction between radiative transfer and fog microphysics. Journal of the Atmospheric Sciences, 47, 2153–2166.

Bott, A. (1991): On the influence of the physico-chemical properties of aerosols on the life cycle of radiation fogs. Bound.-Layer Meteor., 56, 1–31.

Colabone, R. O., Ferrari, A. L., Vecchia, F. A. S. Tech, A. R. B., (2015): Application of Artificial Neural Networks for Fog Forecast, Journal of Aerospace Technology and Management, 7 -2. http://dx.doi.org/10.5028/jatm.v7i2.446

Dabas, J., Chauhan, A., Kumar, M., (2011): Existence of the Mild Solutions for Impulsive Fractional Equations with Infinite Delay, International Journal of Differential Equations, 2011.

Da Rocha, R. P., Gonçalves, F. L. T., Segalin, B. (2015): Fog events and local atmospheric features simulated by regional climate model for the metropolitan area of São Paulo, Brazil. Atmospheric Research, 151: 176-188. doi.org/10.1016/j.atmosres.2014.06.010

Emmons, G., Montgomery, R. B. (1947): Note on the Physics of Fog Formation. Journal of Meteorology, 4, 206.

Fedorova, N., Levit, V., Fedorov, D., (2008): Fog and stratus formation on the coast of Brazil. Atmospheric Research, 87, 268-287. doi.org/10.1016/j.atmosres.2007.11.008

Fedorova, N., Levit, V., Silva A. O., Santos D. M. B., (2013): Low Visibility Formation and Forecasting on the Northern Coast of Brazil. Pure and Applied Geophysics, 170(4), 689–709. DOI: 10.1007/s00024-012-0565-6

Gultepe, I., Milbrandt, J. A. (2007): Microphysical observations and mesoscale model simulation of a warm fog case during FRAM project. J. Pure Appl. Geophys., 164, 1161–1178.

Gultepe, I., Pearson, G., Milbrandt, J. A., Hansen, B., Platnick, S., Taylor, P., et al. (2009): The fog remote sensing and modeling (FRAM) field project. Bulletin of the American Meteorological Society, 90, 341–359

Kunkel, B. A. (1984): Parameterization of droplet terminal velocity and extinction coefficient in fog models. J. ClimateAppl. Meteor., 23, 34–41.

Oliveira, G. A. (2002): Método estatístico no auxílio à previsão de nevoeiro para o aeroporto de Guarulhos, Master Thesis, Federal Universityof Santa Catarina, 104p. https://repositorio.ufsc.br/xmlui/bitstream/handle/123456789/83415/188292.pdf?sequence=1&isAllowed=y

Silva, W. L., Neto, F. A., França, G. B., Matschinske, M. R. (2016): Conceptual model for runway change procedure in Guarulhos International Airport based on SODAR data. The Aeronautical Journal, 120(1227), 725-734.

Silva Dias, M.A.F., Jaschke Machado, A. (1997): The role of local circulations in summertime convective development and nocturnal fog in São Paulo, Brazil. Boundary-Layer Meteorology, 82: 135-157. doi:10.1023/A:1000241602661

Tardif, R. (2007): The impact of vertical resolution in the explicit numerical forecasting of radiation fog: A case study. J. Pure Appl. Geophys., 164 (Special issue), 1221–1240.

Teixeira, J., 1999: Simulation of fog with the ECMWF prognostic cloud scheme. Quart. J. Roy. Meteor. Soc., 125, 529–553.

Teixeira, J., Miranda, P. M. A. (2001): Fog prediction at Lisbon Airport using a one-dimensional boundary layer model. Met. Apps, 8, 497–505.

WMO (1966): International Meteorological Vocabulary, World Meteorological Organization, (WMO-No 1182) Geneva, 276 pp. DOI: 10.1002/qj.49709339524.

WMO (2011). Guide to Climatological Practices, World Meteorological Organization, (WMO-No 100), Geneva.

Clear Air Turbulence

Clear Air Turbulence in Southeast Brazil: Case Studies

Francisco Pinheiro Gomes[1]

Gutemberg Borges França[1]

Antonio Vicente Pereira Neto[1]

ABSTRACT

This analyzes the classic indexes that are modelled numerically to predict turbulence in the southern region of Brazil. Historical clear sky turbulence (CAT) events were reconstructed by using 25.465 AIREP messages, from 2015 to 2019, and 12.959 CAT records by aircraft from February 2018 to December 2019. The observations have shown that CAT events are proportionally distributed (in parentheses, its severity) in 94 % (light), 4 % (moderate), and 1 % (severe). Synoptic analyses of five cases studied reveal that turbulence records occurred during clear sky conditions in the presence of jet stream. Three joint analysis of the compositions of the variables modeled by GFS0.25 and WRF (18, 6 and 2 km grid), defined as, (1) wind profile, potential temperature (Θ), turbulent kinetic energy (TKE); and (2) Richardson (Ri) and vertical speed (W), and (3) separately the CAT indicator indices called Ri, Brown, Ellrod-Endlich, and Ellrod-Knap, and Ellroad-Knox, showed that the improvement of spatial resolution data plays an important role in CAT forecasting. The result of the initial attempt to adjust the predictive indexes, using modeled WRF data (18, 6, and 2 km grid) is encouraging since the adjusted indexes were able to detect over 96% of CAT events.

**Keywords:** Clear air turbulence, CAT Index, WRF Model Simulations, AIREP.

1. INTRODUÇÃO

Depending on its intensity, turbulence during a flight can be uncomfortable for the crew and passengers, cause physical harm, or result in serious accidents. Although knowledge of the causes and characteristics of turbulence has grown substantially in recent decades (Endlich, 1964; Dutton and Panofsky, 1970; Lilly, 1971; Brown, 1973; Lee et al. 1984; Mc Lean, 1986, Ellrod and Knapp, 1992 ; Clark, 1997; Marroquin,1998; Kaplan et al., 2000; Ellrod et al., 2010; and Sharman et al., 2017), this phenomenon continues to be a risk for aviation. Turbulence is a property of most fluids (liquid and gas) found in nature. Perhaps the best example of turbulent flow is found in the atmosphere where those flying can experience extreme swaying that affects the safety of the aircraft. Fortunately, flights in a turbulent atmosphere are still less frequent at a rate of 1 in 20, according to Lester (1990). The latter defines turbulence as the fluid state where the velocity is chaotic and apparently random. In aviation, the concept of turbulence is related to the response of the aircraft (or bumps suffered). According to the International Civil Aviation Organization (ICAO) global air navigation plan, the number of flights has been doubling since 1977 at 15-year intervals (ICAO, 2016) and in a recent study carried out by Gultepe et al. (2019). it is concluded that clear sky turbulence (CAT) was responsible for more than 70% of global air incidents in the period from 2000 to 2011. The main airports in the country, with the exception of Brasilia airport, are located in the flight region that is controlled by the Curitiba air navigation control center, known as Curitiba FIR, as shown in Fig. 1. According to the Department of Airspace Control, there were 488,743 flights in 2018 (with a monthly average of 40,000 flights) in this region (DECEA, 2018). According to Lyra et al. (2007), the airspace of the Curitiba FIR is one of those regions influenced by the subtropical jet that is probably the shear formation mechanism for the CAT records.

[1] Laboratório de Meteorologia Aplicada, Universidade Federal do Rio de Janeiro, Rio de Janeiro, RJ, Brasil.
Autor de correspondência: Francisco Pinheiro Gomes, franpg66@gmail.com

Figure 1: The region in emphasis represents the Curitiba FIR and the circles are the occurrences of turbulence records by the A320 aircraft of the airline LATAM in the period from 2018 to 2019.
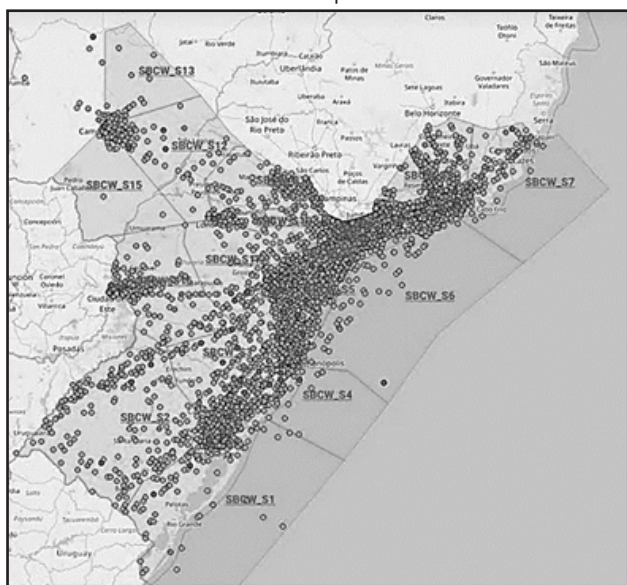
Thus, the purpose of this research is to compare clear-sky turbulence indicator variables simulated by a numerical model to in situ turbulence recorded by aircraft in the Curitiba FIR.

2. MATERIAL AND METHOD

Table 1 presents details of the modeled and collected data used in this work.

Figure 1 depicts the spatial representation of the 12,959 vertical variations of gravitational acceleration (VRTG) events (also known as anomalies of gravitational acceleration [g] or CAT) recorded by the LATAM Company's A320 aircraft in 2018. (LATAM, 2019). Table 2 shows the limits of g intervals for VRTG records that classify turbulent events as (1) mild, (2) moderate, and (3) severe. The VRTG is recorded, on an hourly basis, and represents only the highest absolute value of this time interval, and this ensures that only one event is recorded in conditions of long turbulence (LATAM, 2019).

Table 1: Data Summary.

Source	Freq.	Information	Quant.	Period
1. VRTG (LATAM company)	variable	record of vertical acceleration in flight (g).	12,959	01/12/2018 to 31/12/2019
2. AIREP (www.redemet.aer.mil.br)	variable	coded position message from an aircraft in flight, containing operational and/or meteorological information, including location (latitude, longitude, and altitude) of the occurrence of CAT.	25,465	02/10/2015 to 04/06/2019
3. GFS 0.25 (http://www.wxmaps.org/pix/sa.vv)	3h	analysis and forecast with grid (latitude; longitude) of 0.25° by 0.25°	---	selected cases
4. WRF	3h	forecast with grids of 18, 6, and 2 km with 87 levels (according to Kim et al., 2018)	3,840	selected cases
5. TEMP (www.redemet.aer.mil.br)	12h	coded message from altitude meteorological stations. It represents the temperature, relative humidity and wind profiles for the locations of Bueno Aires, Porto Alegre, Curitiba, São Paulo and Rio de Janeiro.	---	selected cases
6. Surface charts (www.redemet.aer.mil.br)	6h	meteorological information from surface meteorological stations.	---	selected cases
7. GOES-16 Image	15 min	thermal images (13.3 μm).	---	selected cases
8. METAR (Meteorological Aerodrome Report)	1 h	meteorological codes containing present weather, wind, air temperature and atmospheric pressure observations generated by surface meteorological stations located at aerodromes.	---	selected cases

Table 2: Values of the g variation intervals in the VRTG records that classify the classes of turbulence events defined as 1 (light), 2 (moderate), and 3 (severe) for aircraft of the type A320 LATAM.

Class 1		Class 2		Class 3	
-g	+g	-g	+g	-g	+g
0.6g≤	≥1.4g	0.4g≤	≥1.6g	0.2g≤	≥1.8g

Source: Adapted from LATAM(2019).

AIREP messages report the operational conditions of the flight and may also include CAT detection. Here, the AIREP was used to observe the space-time distribution of turbulence occurrences in the Curitiba FIR from 10/02/2015 to 06/04/2019. The images from the GOES-16 satellite (Geostationary Operational Environmental Satellite), atmospheric profiles, and surface charts were jointly analyzed to diagnose the synoptic conditions acting (verify possible mechanisms of formation of CAT, presence of convective cells, wind shear, and atmospheric circulation) during VRTG recordings by aircraft for selected and studied events.

The numerically modeled atmospheric data has two sources, namely: 1) analysis and forecast from the GFS0.25 model (Global Forecast System), and 2) forecast data generated by the atmospheric model Weather Research and Forecasting (WRF). The simulations were carried out using the dynamic solution ARW (Advanced Research WRF). Shared memory parallel computing support was used. For the 24 h simulations, with a 12 h spinoff, three computational domains centered at 27°S 49°W were created, covering the area between 20°S-33°S and 40°W-58°W. The horizontal resolutions applied in the three domains are 18 km (90 x 90 points), 6 km (151 x 151 points), and 2 km (253 x 253 points). The number of vertical levels is equal to 87 with the pressure at the top of the atmosphere being 50 hPa, according to Kim et al. (2010). The parameterization schemes of the physical processes used in this work were, according to Table 3:

The sequence of steps of the idealized method to identify the turbulent or non-turbulent atmospheric environment, in the forecasts generated by the GFS0.25° and WRF, is described below. The steps consider the behavior of the values of 9 (nine) variables that are defined as follows: (1) wind profile (PV), (2) vertical wind speed (W), (3) potential temperature (Θ), (4) turbulent kinetic energy (TKE), (5), and turbulence indices, as briefly described Table 4, called (6) Richardson number (Ri), (7) Brown (B), (6) Ellrod-Endlich (E-1), (8) Ellrod-Knap (E-2), and (9) Ellroad Knox (E-3).

The steps are:

i. Data processing - analysis of the spatiotemporal distribution of historical data from CAT records considering AIREP messages and VRTG records;

ii. Selection of events - cases with and without CAT records are collected and synoptic conditions are analyzed using the atmospheric profile, surface map, GOES-16 satellite image and METAR data, as described in Table 1;

iii. Simulation of events - the atmospheric conditions of the cases selected in item ii are reproduced using the WRF with grid resolutions of 18, 6, and 2 km with 87 levels;

iv. Analysis of meteorological compounds - two meteorological Compounds (C) were defined with the following variables, that is,
C1: PV, Θ, TKE and
C2: Ri, W
using the GFS0.25° and WRF outputs for the selected cases and, thus considering the selected events, the behavior of these compounds C1 and C2 is analyzed as a function of the VRTG observations;

v. Adjustment of the CAT indexes with the observations - The distribution of the statistics of the values of each index (Ri, B, E-1, E-2, E-3) is analyzed versus the observations of the

Table 3: Parameterizations used in simulations with WRF.

Physical Process	Reference
For deep convection	Kain-Fritsch (Kain, 2004)
For explicit convection	Kessler (Kessler, 1969)
For long and shortwave radiation	*Rapid Radiative Transfer Model*- RRTMG (Iacono *et al.*, 2008)
For planetary boundary layer	Mellor-Yamada Janjic (Janjic, 1994)
For surface processes	Noah Land Surface Model- Noah LSM (Chen e Dudhia, 2001)

VRTG and, thus, it is done adjustment, via trial and error, the classifying LIMITE value, of each index i (LIMITEClas(i)), of CAT testing, for n-intervals of values of index i, considering the following routine:

a) use the expression LIMITEclas(i) ≥ [Average of Index(i) – factor(DEVPAD(i)], where factor varies in the range of [0+ΔX; n] in ΔX =0 to n, increment of 0.1; and

b) test each LIMITEclas(i) with an independent sample and statistically evaluate the results versus the VRTG observations until the optimal LIMITEclas(i) is obtained.

3. RESULTADOS E DISCUSSÕES

Fig. 2 presents the spatial density variation (where light colors represent higher values) of CAT occurrences considering 25,465 AIREP records that occurred between October 2, 2015, and June 4, 2019, in the Curitiba FIR. It is observed that there are CAT records throughout the FIR area, which may indicate that the reason for this distribution is associated with the presence, for most of the year, of the jet stream (which causes wind shear). Note, as the lighter colors in Fig. 2, that the higher frequency of CAT corresponds approximately to the São Paulo-Porto Alegre route

Table 4: Summary of CAT indexes.

Índice	Descrição	Referência
1. Richardson (Ri)	$Ri = \dfrac{\left(\frac{g}{\theta_m}\right)\left(\frac{\partial\theta}{\partial z}\right)}{\left(\frac{(\Delta u^2+\Delta v^2)^{1/2}}{\Delta z}\right)^2}$, where $\left(\frac{g}{\theta_m}\right)\left(\frac{\partial\theta}{\partial z}\right)$ is the static stability with g representing the acceleration of gravity (9.8 m. s^{-2}), θ is the potential temperature and θ_m represents the potential temperature at the middle level of the layer, and $\left(\frac{\partial u}{\partial z}\right)^2 = \left(\frac{(\Delta u^2+\Delta v^2)^{1/2}}{\partial z}\right)^2$ is the vertical shear. If $Ri < 0.25$ there is a higher probability of turbulence occurring, and *u* and *v* are the zonal and meridional components of the wind, respectively.	Miles Howard (1964)
2. Brown (B)	$\Phi_m = \sqrt{0.3 \times \left(\frac{\partial v}{\partial x} - \frac{\partial u}{\partial y} + f\right)^2 + \left(\frac{\partial v}{\partial x} + \frac{\partial u}{\partial y}\right)^2 + \left(\frac{\partial u}{\partial x} - \frac{\partial v}{\partial y}\right)^2}$, where $0.3 \times \left(\frac{\partial v}{\partial x} - \frac{\partial u}{\partial y} + f\right)^2$ is the absolute vorticity; $\left(\frac{\partial v}{\partial x} + \frac{\partial u}{\partial y}\right)^2$ is the shear deformation, $\left(\frac{\partial u}{\partial x} - \frac{\partial v}{\partial y}\right)^2$ is the elongation deformation and *f* is the Coriolis parameter.	Roach (1970)
3. Ellrod-Endlich (E-1)	$\dfrac{(\Delta u^2+\Delta v^2)^{\frac{1}{2}}}{\Delta z}$ x $\left[\left(\frac{\partial v}{\partial x} + \frac{\partial u}{\partial y}\right)^2 + \left(\frac{\partial u}{\partial x} - \frac{\partial v}{\partial y}\right)^2\right]^{1/2}$	Mancuso Endlich (1966)
4. Ellrod-Knap (E-2)	$\dfrac{(\Delta u^2+\Delta v^2)^{\frac{1}{2}}}{\Delta z}$ $\left(\left[\left(\frac{\partial v}{\partial x} + \frac{\partial u}{\partial y}\right)^2 + \left(\frac{\partial u}{\partial x} - \frac{\partial v}{\partial y}\right)^2\right]^{1/2} - \left(\frac{\partial u}{\partial x} + \frac{\partial v}{\partial y}\right)\right)$	Ellrod (1985)

where there is a higher frequency of flights in relation to the other routes of the FIR Curitiba. Fig. 3a shows the distribution of 12,959 occurrences of CAT by VRTG class and it is observed that 12,189, 638 and 132 occurrences are respectively of class 1, class 2, and class 3 corresponding to 94% (light), 4% (moderate) and 1% (severe) of records. Fig. 3b shows the hourly distribution of the amount of turbulence detected by LATAM flights, via VRTG(G), for classes 2 and 3, and it can be seen that there are turbulence records throughout all times, with the highest CAT frequency in daytime when flights are most frequent.

Figure 2: Density of CAT records considering 25,465 AIREP records that occurred in the South FIR between October 2, 2015, and June 4, 2019.

3.1 Seleção e ANÁLISE do evento de cat

Using the 132 class 3 VRTG records that occurred over the Curitiba FIR for the data period, a synoptic analysis was carried out, considering meteorological information within the 12-hour interval that preceded the VRTG record, using data from sources 5, 6, 7 and 8 (atmospheric profiles, surface chart, GOES-16 and METAR satellite images) described in Table 1.

Table 5 shows the details of the VRTG hourly records of September 29, 2018, the classes, geographic position, and flight level of the VRTG events detected by the aircraft. It is observed that the atmosphere was turbulent throughout the day, given the temporal distribution of the VRTG records. In Figs. 4a, 4b, and 4c are, respectively, shown GOES-16 images (thermal band, centered at 13.0 μm), part of the surface synoptic map and vertical section of the atmospheric profile between Porto Alegre (SBPA) and Galeão (SBGL), which includes the profiles of Curitiba (SBCT) and São Paulo (SBMT), corresponding to 12 UTC. The two red dots in Fig. 4a approximately represent the geographic positions of the class 3 VRTG records that occurred for the case studied, as shown in column 3 of Table 5. The surface synoptic chart (Fig. 4b) reveals that there was a high-pressure center of 1,023 hPa over the Atlantic Ocean near the coast of the state of Rio Grande do Sul. The METAR at Porto Alegre airport during the first hours of that day registered a clear sky condition with excellent visibility.

In Fig. 4c shows the longitudinal section of the wind profiles (in barbels) versus the positions of Porto Alegre (SBPA), Curitiba (SBCT), São Paulo (SBMT), and Galeão (SBGL), where it is possible to identify the location of the jet (J), between the gray lines, which is above the pressure level of 290 hPa over Porto Alegre. Wind speed varies between 50-80 knots and between 65-80 knots over Curitiba (SBCT) corresponding respectively to flight levels of 30,000 (FL300) and 32,000 feet (FL320).

Figure 3: (a) Distribution of 12,959 VRTG records by class. (b) hourly distribution of the joint records of VRTG classes 2 and 3 in the Curitiba FIR in the period from December 1, 2018, to December 31, 2019.
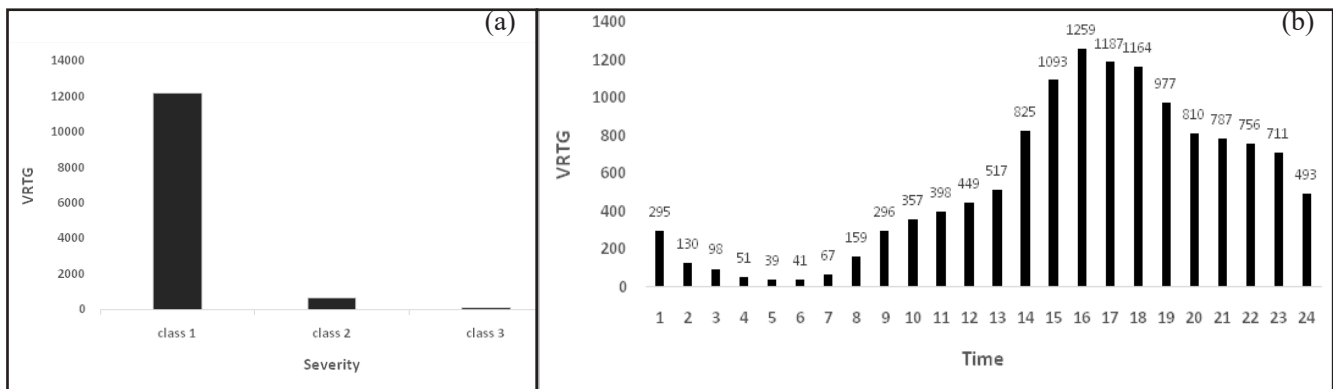
Figure 4: (a) GOES-16 image (thermal band, centered at 13.0 m) with black dots representing the locations of the VRTG recorded on September 29, 2018 (according to Table 5). (b) Surface map clipping at 12 UTC and (c) Vertical section between Porto Alegre (SBPA) and Galeão (SBGL), which includes the profiles of Curitiba (SBCT) and São Paulo (SBMT) at 12 UTC.

(a)

(b)

(c)
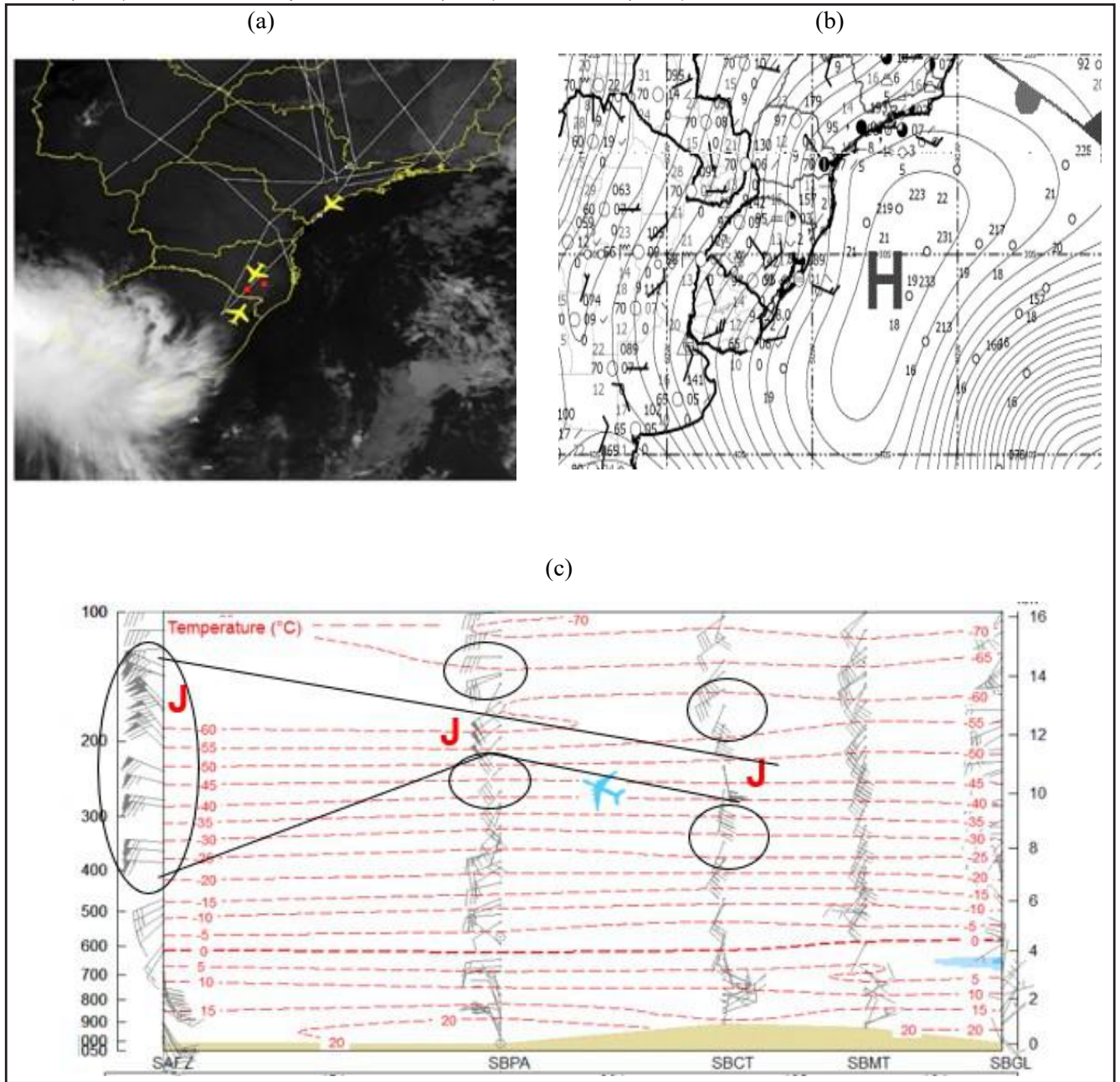
**Table 5:** VRTG records and their severity during the day 29/09/18.

Date	Time (UTC)	Class	Latitude (S)	Longitude(W)	Flight Level (ft)
	2	1	29.98	51.37	3,192
	4	3	27.16	50.31	33,568
	4	3	27.60	50.82	33,568
29/set/2018	5	1	22.93	43.78	8,796
	14	2	25.39	49.30	3,152
	15	1	23.59	46.72	2,044
	20	1	22.53	46.40	18,500
	23	1	30.11	56.02	31,828

Source: LATAM(2019).

Considering the meteorological compounds defined in the method of this work, Figs. 5a-5b respectively show the variable fields of compounds C1 and C2 in the longitudinal vertical section at 50°W, where the ordinates represent the atmospheric pressure in hPa versus the latitudinal interval between 30°S to 22°S, determined with GFS 0.25° to 3 UTC-29/09/2018 (closest time of recorded VRTG observation from 3:01(UTC) to 4 UTC). The black dot approximately represents the position of the occurrence of one of the class 3 VRTG, on the variable fields of the defined meteorological compounds, that is, C1 (Fig. 5a): wind profile (black barbels), Θ (values represented by the white lines approximately arranged along the profile), TKE, whose values in the field represented by the colors of the lower legend vary in the interval [100;900] m².s⁻², and C2 (Fig. 5b): Ri (values in field represented by the colors of the lower legend) and W (white curve with negative and positive values). Bearing in mind that the model results are hardly synchronized with the observations, the analysis area of the fields generated by the models was adopted in a rectangular area - dashed red line in Figs. 5, 6, and 7, wherein the vertical it was limited to pressure levels from 200 to 400 hPa, and in the horizontal, the approximate course of 1 hour of flight of the mentioned aircraft type, 400 km, or the interval 24-29S, corresponding to the VRTG recording time. The wind direction of C1 (from bottom to top, as shown in Figure 5a) generated by GFS 0.25° is quite similar to

the observations of radiosonde profiles (Fig. 4c), however, it differs significantly in magnitude. On the other hand, it clearly shows the present shear and consequently the indication of a turbulent flow of the atmosphere in the region where the VRTG recording took place. TKE values vary approximately in the observation area in the range of [200; 800] m².s⁻² which corroborates with the CAT indicator. The behaviors of Θ, W did not appear, in this case, as CAT indicators, since the lines of Θ hardly suffer variations when there is turbulence; W presented values close to zero and Ri with values between 0 and 1. The latter, according to Miles and Howard (1964), is an indicator of CAT when Ri ≤ 0.25. Similarly, Figs. 6-7 respectively illustrate the composites C1 and C2 closest to the VRTG record generated by the WRF for resolution of 18, 6 and 2 km, and considering conditions of the simulation described in advance of 12 h. As in the previous analysis, in the observation area, the simulated wind profiles showed a more pronounced shear and positioned the jet similarly to the observations, as shown in Fig. 4(c); the TKE varies in range greater than the previous [200; 900] m².s⁻²; Ri with values less than 1 and W ranging from negative to positive values. Thus, the results with increased spatial resolution using the WRF data (Figs. 6-7), like the results obtained by Kim et al. (2010), reproduced atmospheric conditions similar to those generated with GFS 0.25° data (Fig. 5), but slightly superior in identifying CAT conditions.

Figure 5: (a) represents the C1 composite: wind profile (barbs), Θ (white lines arranged along the profile), TKE (values in the field represented by the colors of the lower legend in m².s⁻². (b) represents the compound C2: Ri (values in the field represented by the colors of the lower legend) and W (white curves with negative and positive values), determined with GFS0.25 data from the 03Z of September 29, 2018.
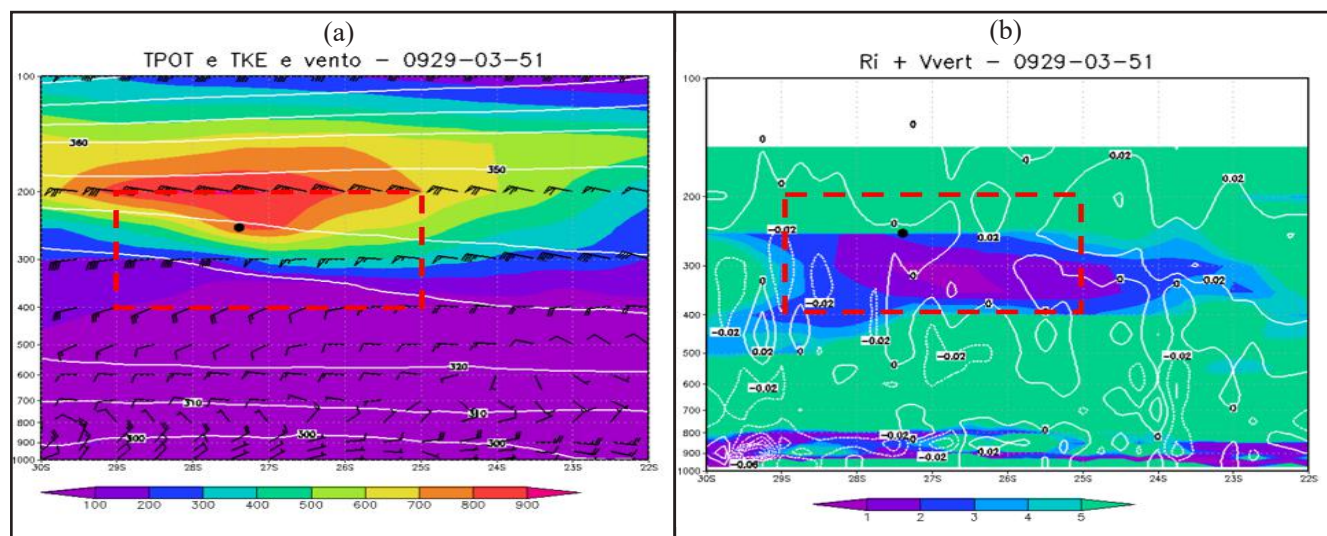
Figure 6: (a), (b) and (c) represent the C1 composite with WRF data, respectively for 18 km, 6 km and 2 km at 04Z on September 29, 2018. The wind profile is represented by barbs, ϴ by white lines arranged along the profile and TKE by the lower legend colors in m².s⁻².
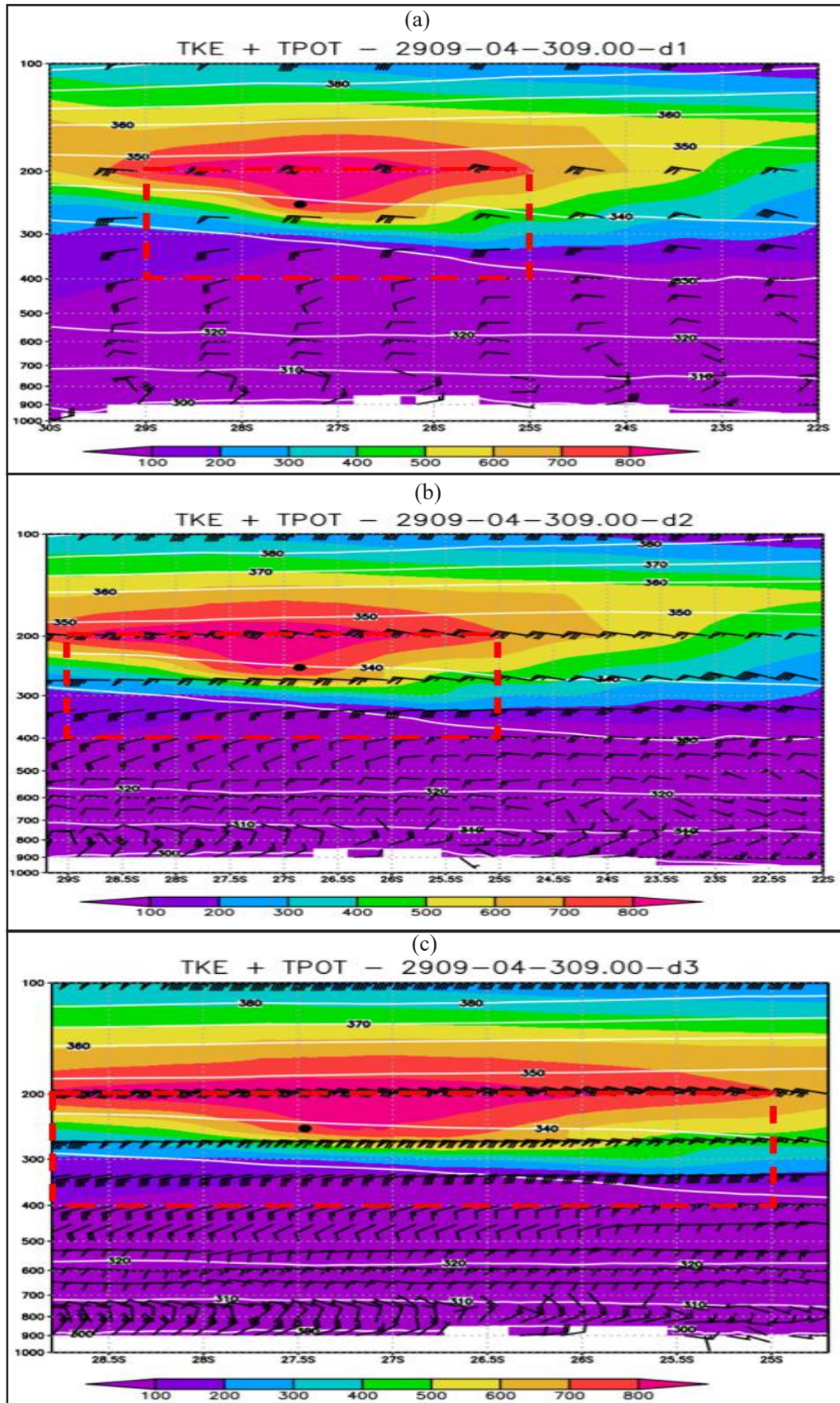
Figure 7: (a), (b) and (c) represent the C2 composite with WRF data, respectively for 18 km, 6 km and 2 km at 04Z on September 29, 2018. W is represented by the white curves with negative and positive values, Ri by the colors of the lower legend.
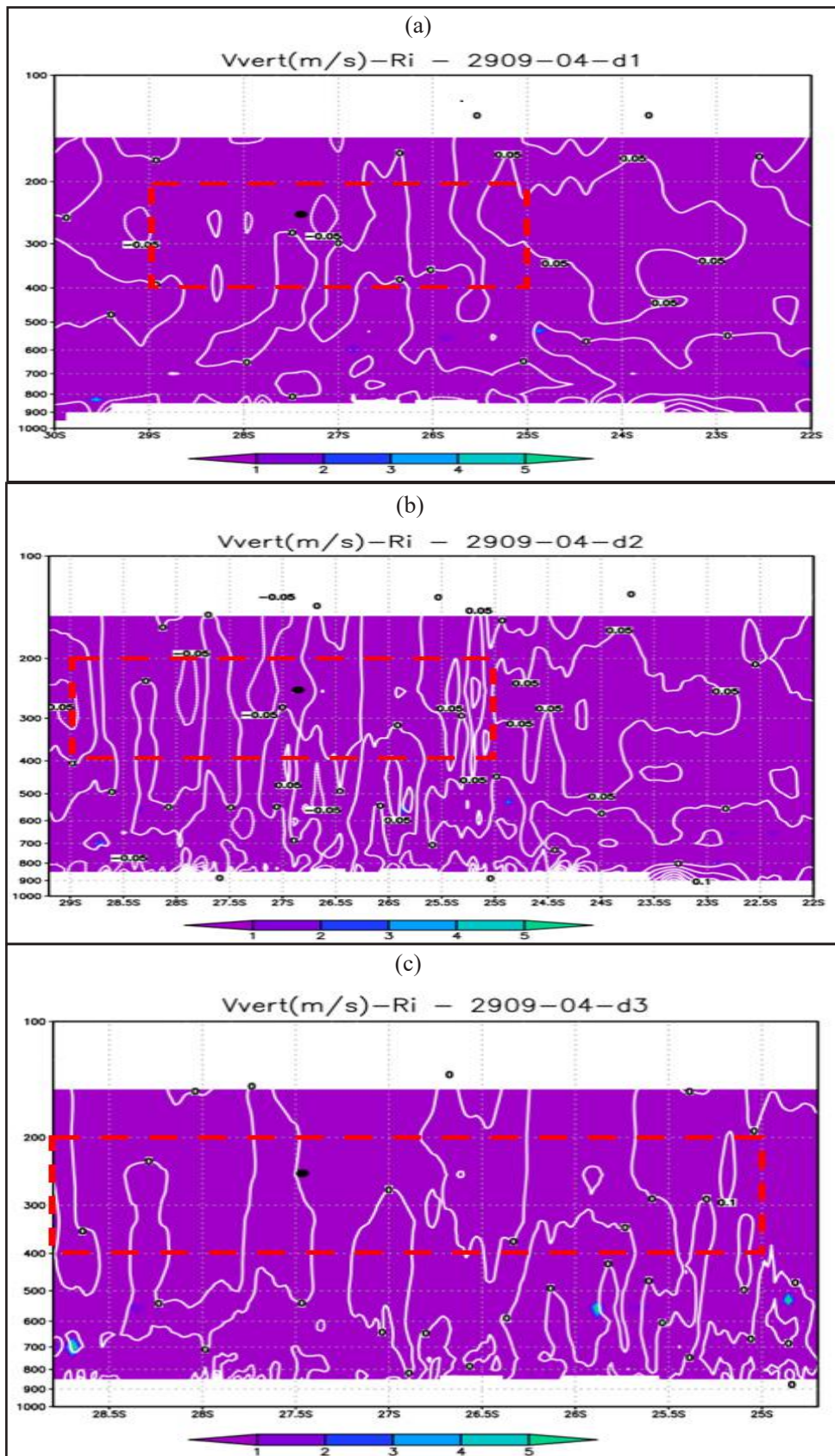
Table 6 shows the results of the analysis of the indices that represent the conditions of a turbulent atmosphere in the vicinity of the VRTG records, that is, where the indices vary within the following intervals Ri =[0; 0.25] (Miles and Howard, 1964), Brown =[4.0.10-6;12.10-6]m/s (Roach, 1970) E-1=[4.0.10-6; 12.10-6]m/s, E-2 =[4.0.10-6; 12.10-6]m/s, E-3=[4.0.10-6; 12.10-6]m/s (Knox, 2010 and Williams, 2016). It is observed that the Brown index was able to identify turbulent atmospheric conditions in line with all VRTG events, regardless of the model and/or spatial resolution used. The increase in resolution with the use of WRF caused the Ri number to increase its VRTG detection efficiency from 66%, with GFS 0.25°, to 100%. The E-1, E-2 and E-3 indices determined by the GFS 0.25° and WRF have, respectively, joint averages of VRTG hits similar and equal to 73% and 74%. In short, increasing the resolution in the simulations using WRF improved the efficiency of the detection rates for turbulent atmosphere conditions from 78% (with GFS) to 84% (with WRF), considering 22 VRTG events out of the five analyzed cases.

3.2 Adjustment of indices with observations

The adjustment of the indices with the observations aims to obtain the optimal classification limit per index (LIMITEClas(i)). For example, the Brown index, E-1 and E-2, which are calculated from the WRF outputs (18, 6 and 2km) for T-1h to T+1h (T time of VRTG recording) and in levels between the VRTG record (in hPa) with a spacing of ±50 hPa from the altitude, it allows analyzing the volume of the atmosphere around the records of each VRTG (day, time, latitude, longitude, time and altitude). In this way, the index values determined with WRF data, according to the mentioned conditions, were associated with the VRTG data for 04/23/2018, 05/18/2018, 05/21/2018 and 03/27/2019, resulting in 1,681 events. The optimal LIMITEclas(i) for the indices were determined via steps vi and vii of the method, and using data referring to 05/18/2018 and 03/27/2019, that is:

a) The mean and standard deviation were calculated for each index for the three mentioned grids of the modeled data;

b) The value of n was randomly assigned, and the percentage of correct answers was observed, according to each increment defined in step vi of the method. It is assumed that the optimal LIMITEclas(i) value is the one that correctly classifies 80% or more of the VRTG events until the optimal classifying threshold value per index is obtained. The values of the optimal LIMITEclas(B), LIMITEclas(E-1), and LIMITEclas(E-2) obtained from step vi of the method are equal to 3.82, 1.37, and 1.91, corresponding to the n factors of 2.5, 1.2 and 1.2, respectively, considering the VRTG events on 03/27/19 and 05/18/2018.

c) Finally, all three optimal limits calculated from the WRF data of all grades (18, 6, and 2 km) on 23/04/2018 and 21/05/2018 obtained previously were tested separately versus the events of VRTG. Preliminary results showed that the adjusted indices of B, E-,1 and E-2 were able to classify 0.96, 0.9,6 and 0.99% of VRTG events.

Table 6: Percentage of correct answers for the Ri, Brown, E-1, E-2 and E-3 indexes (GFS0.25 and WRF) versus the VRTG records of the five cases studied.

Case	Date	Flight level (ft)	Model Quant. VRTG	GFS Ri	B	E-1	E-2	E-3	WRF Ri	B	E-1	E-2	E-3
I	23/04/2018	32,000	4	20%	100%	100%	80%	100%	100%	100%	80%	100%	100%
II	29/09/2018	33,000	8	100%	100%	100%	100%	100%	100%	100%	88%	100%	100%
III	18/05/2018	15,000	4	75%	100%	100%	100%	100%	100%	100%	100%	100%	100%
IV	21/05/2018	38,000	3	33%	100%	0%	33%	0%	100%	100%	0%	0%	0%
V	27/03/2019	38.000	3	100%	100%	100%	100%	0%	100%	100%	100%	100%	33%
			Average score	66%	100%	80%	83%	60%	100%	100%	74%	80%	67%

4. CONCLUSION

This work proposes an analysis of clear sky turbulence indicator indices, obtained with numerical simulations via GFS 0.25° and WRF, versus data from turbulence event records by aircraft, for the prediction of CAT events in the Curitiba FIR. In summary, the main conclusions of this work are:

- In the studied area, the formation mechanism of turbulence events is associated only with the presence of the jet stream and not with convection;
- Considering the analysis of compounds C1 (wind profile, Θ, TKE) and C2 (Ri and W profile) for the presented case study, it was observed that the intensities of the wind profiles are underestimated in comparison to the observations but identified almost perfectly the jet stream (hence the shear) for both the data modeled by the 0.25° GFS as well as the one generated by the WRF. The values of TKE and Ri are more reliable in the presence of CAT the greater the resolution of the modeled data. The Θ and W values did not clearly indicate the turbulent atmosphere where the CAT in-situ recordings were observed;

- Analysis of the indices in representing the conditions of a turbulent atmosphere in the vicinity of the VRTG records (Table 5), demonstrated that the Brown index is the most efficient and that Ri becomes more efficient as the resolution of the modeled data increases. The E-1, E-2 and E-3 indices have similar efficiency regardless of the resolution or model used.
- Preliminary testing of the adjusted B, E-1 and E-2 indices determined with WRF data (18, 6 and 2 km) were able to predict the volume of the atmosphere with CAT twelve hours in advance for two days of VRTG records.

As a future goal, it is intended to extend the sample of analyzed events, considering only data modeled by WFR, aiming to establish a CAT forecast mechanism for operational use by organizations in the aeronautical sectors.

ACKNOWLEDGMENT

REFERENCES

BITAR, I. **Climatologia e Estudo de Caso da Turbulência de Céu Claro a partir de Registros de Aeronaves: Análise de Dados Observacionais e de Modelagem**. https://Sid.inpe.br/mtc-m21b/2015/03.13.04.06-TDI, 2015.

BROWN, R. New indices to locate clear air turbulence. **The Meteorological Magazine**, v. 102, n. 3, p. 347-361, 1973.

DECEA, Departamento de Controle do Espaço Aéreo. **Publicações de Informações Aeronáuticas. AIC-N**. Rio de Janeiro: DECEA, 2018.

DUTTON, J.A.; PANOFSKY H.A. Clear air turbulence: A mystery may be unfolding. **Science**, v. 167, n. 7, p. 937-944, 1970.

ELLROD, G.P.; LESTER P.F.; EHERNBERG J. Clear Air Turbulence. **Encyclopedia of the Atmospheric Sciences**, Academic Press, v. 1, n. 38, p. 393-403, 2002.

ELLROD, G.P. Detection of high level turbulence using satellite imagery and upper air data. **NOAA Tech. Memo. NESDIS**, p. 10-30, 1985.

ELLROD, G.P.; KNAPP, D.I. An objective Clear Air Turbulence Forecasting Technique: Verification and operational use. **Weather and Forecasting**, v. 7, n. 1, p. 150-165, 992.

ELLOD, G.P.; KONX, J.A. Improvements to an operational clear-air turbulence diagnostic index by addition of a divergence trend term. **Weather and Forecasting**, v. 25, n. 2, p. 789-798, 2010.

ENDLICH, R.M. The mesoescale structure of some regions of clear air turbulence. **J. Appl. Meteor.**, v. 3, n. 3 p. 261-276, 1964.

FRITTS, D.C.; ALEXANDER, M.J. Gravity dynamics and effects in the middle atmosphere, **Rev. Geophys.**, v. 41, n. 1, p. 1003, 2003. doi

GILL, P.G.; BUCHANAN, P. An ensemble based turbulence forecasting system. **Meteorological Applications**, v. 21, n. 1, p. 12-19, 2014.

GULTEPE, I. A review of high impact weather for aviation meteorology. **Pure Appl. Geophys**. v. 176, n. 9, p. 1869-192, 2019.

HOLTON, J.R. The role of gravity wave induced drag and diffusion in the momentum budget of the mesosphere, **J. Atmos. Sci.**, v. 39, n. 8, p. 791-799.

HOPKINS, R.H. Forecasting techniques of clear-air turbulence including that associated with mountain waves, **Secretariat of the World Meteorological Organization (WMO)**, v. 4, n. 482, p. 155, 1977.

INTERNATIONAL CIVIL AVIATION ORGANIZATION ENVIRONMENTAL (ICAO), **Aviation and Climate Change**, p. 40-19, 2016.

KIM J.-H.; CHUN, H.-Y.A. Numerical Study of Clear-Air Turbulence (CAT) Encounters over South Korea on 2 April 2007, **Journal of Applied Meteorology and Climatology**, v. 49, n. 12, p. 2381-2403, 2010.

KAPLAN, M.L.; LIN Y.L.; RIORDAN A.J.; LUX K.M.; HUFFMAN A. Observational and numerical simulation-derived factors that characterize turbulence accident environments preprints. **In 9th AMS Conference on Aerospace Range and Aeronautical Meteorology, 2000**.

KELLER, J.L. Clear air turbulence as a response to meso- and synoptic-escale dynamic processes. **Mon. Wea. Rev.**, v. 118, n. 12, p. 2228-2242, 1990.

KNOX, J.A. Possible mechanisms of clear-air turbulence instrongly anticyclonic flow. **Mon. Wea. Rev.**, v. 125, n. 4, p. 1251-1259, 1997.

Vertical Acceleration High in Flight, manual A320, **LATAM**, v. 1, n. 1, p. 485-486, 2019.

LYRA, CHAN, PEREIRA, Indicadores de Turbulência a partir de previsões do modelo regional ETA. **Revista Brasileira de Meteorologia**, v. 22, n. 2, p. 161-182, 2004.

LEE, D.R.; STULL R.S.; IRVINE W.S. Clear air turbulence forecasting techniques. Air Weather Service Tech. Note AFGWC/TN-79/001, **Air Force Global Weather Central**, Offutt AFB, NE, p. 16, 1984.

LESTER, P.F. **Turbulence: A New Perspective for Pilots**. Colorado: Jeppesen Sanderson, 1994.

LILLY, D.K. Turbulence in troposphere and stratosphere, **Symposium on Turbulence**, 1978.

MANCUSO R.L.; ENDLICH, R.M. Clear air turbulence frequency as a function of wind shear and deformation. **Mon. Wea. Rev.**, v. 95, n. 3, p. 581-585, 1966.

MILES, J.W.; HORWARD L.N. Note on a heterogeneous shear flow. **J. Fluid Mech.**, v. 20, n. 7, p. 331-336, 1964.

MARROQUIN, A. An advanced algorithm to diagnose atmospheric turbulence using numerical model output. Preprints. In: **16th Conf. on Weather Analysis and Forecasting**, Phoenix, AZ, Amer. Meteor. Soc., p. 79-81, 1988.

MCLEAN, J.C. Comments on the problem of turbulence in aviation. **Proc. Of Workshop on Atmospheric Turbulence Relative to Aviation, Missile and Space Programs**, NASA Langley Research Center, NASA Conf. Publication 2468, p. 53, 1986.

MEDEIROS, A.F. **Observações de Ondas de Gravidade Através do Imageamento da Aeroluminescência.** (INPE10478-TDI/932). Tese de Doutorado em Geofísica Espa cial, Instituto Nacional de Pesquisas Espaciais, São José dos Campos, 187 p., 2001.

Organização da Aviação Civil Internacional (OACI), **Plano de Navegação Aérea Global**, disponível em https://sirius. decea.mil.br/base-normativa/ganp-plano-global-de-navegação, 1990.

PANTLEY, K.C.; P.F. LESTER. Observations of severe turbulence near Thunderstorm tops. **J. Appl. Meteor.**, v. 29, p. 1171-1179, 1993.

ROACH, W.T. On the influence of synoptic development on the production of high level turbulence. **Quart. J. Roy. Meteor. Soc.** v. 96, p. 413-429, 1970.

SHARMAN R.D.; PEARSON. M. Prediction of Energy Dissipation Rates for Aviation Turbulence. Part I: Forecasting Nonconvective Turbulence. **National Center for Atmospheric Research**, 2016.

TRIER, S.B.; SHARMAN, R.D. Mechanisms influencing cirrus banding and aviation turbulence near a convectively enhanced upper-level jet stream. **Mon. Wea. Rev.**, v. 144, p. 3003-3027, 2016. doi

STORER, L.N.; GILL, P.G.; WILLIANS, P.D. Multi-model ensemble predictions of atmospheric turbulence. **Meteorological Applications**, v.26, n. 3, p. 416-428, 2019. doi

SHARMAN, R.D.; PEARSON, J.M. Prediction of energy dissipation rates for aviation turbulence. **Journal of Applied Meteorology and Climatology**, v. 56, n. 7, p. 317-337, 2017.

Internet Resources

REDEMET, www.redemet.aer.mil.br

NCEP, http://www.wxmaps.org/pix/sa.vv

In-flight turbulence forecast model based on machine learning for the Santiago (Chile) - Mendoza (Argentina) Air Route

Filipe Menegardo-Souza[1,2]

Gutemberg Borges França[1]

Wallace Figueiredo Menezes[1]

Vinícius Albuquerque de Almeida[1]

ABSTRACT

This article evaluates the traditional in-flight turbulence forecast tool for mountainous regions known as Harrison's Abacus and proposes a set of models based on machine learning (ML) techniques to generate 24-hour moderate-or-greater (MOG) turbulence predictions using post-processed data numerically modeled. The analyses are performed using measurements of automated *in situ* turbulence observations of the vertical acceleration in flight (VRTG) of LATAM aircrafts that occurred at the Andes crossing, on the Santiago (Chile) – Mendoza (Argentina)air route. The VRTG database contains 1300 records in 22 months from March 2018 to December 2019. Training and testing of several categorical ML algorithms were carried out and different thresholds applied to Harrison's Abacus were evaluated. The results of the MOG turbulence forecast demonstrate that the Harrison's Abacus based method has limited performance with true skill statistic (TSS) below 0.25, while those appropriately trained and balanced ML models can achieve TSS values greater than or equal to 0.60. The proposed MOG turbulence forecasting models based on ML presented ability to make successful predictions using new data (generalization capacity), showing promising tools for operational use, allowing for more reliable forecasts aiming at the safety of air navigation.

Keywords: CAT; Andes; machine learning; aviation weather.

1. INTRODUCTION

In-flight turbulence is a major concern for aviation as it can sometimes cause serious flight instability(Sharman, Trier, Lane, & Doyle, 2012; Storer, Williams, & Gill, 2019; Gultepe et al., 2019). The sudden fluctuations in speed and altitude that occur in this type of environment may lead to structural damage to aircraft and, more commonly, to incidents with passengers and crew(Sharman, Tebaldi, Wiener, & Wolff, 2006; Wolff & Sharman, 2008; Sharman, Cornman, Meymaris, & Pearson, 2014). These occurrences, in addition to the human cost, incur expenses for air carriers through paid indemnities and days of absence from work for the crew(Sharman & Lane, 2016; Storer et al., 2019). Several atmospheric mechanisms are associated with in-flight turbulence such as strong vertical and horizontal shear that occurs in the vicinity of jet streams(Dutton & Panofsky, 1970; Wolff & Sharman, 2008; Kim & Chun, 2010), gravity waves in strongly anticyclonic flows(Knox, 1997; Ellrod & Knox, 2010; Kim, Chun, Sharman, & Trier, 2014), breaking mountain waves(Smith, 1989; Nastrom & Fritts, 1992; Dörnbrack, Gerz, & Schumann, 1995; Wolff & Sharman, 2008; Smith, 2019), and breaking gravity waves induced by intense convection(Lane, Sharman, Trier, Fovell, & Williams, 2012; Kim et al., 2014; Sharman & Trier, 2019). It is important to note that in-flight turbulence generally

occurs at upper-level sand can last for several hours over the same region, especially when associated with synoptic scale meteorological events, such as those that occur in the vicinity of jet streams and in mountainous regions (Kim & Chun, 2010; Kim et al., 2018).

Although atmospheric disturbances occur at different scales, only the turbulent eddies encountered with size comparable to the aircraft(approximately 100 m) affect aviation(Sharman et al., 2006). For this dimension, it is not possible to directly and routinely predict atmospheric movement, but most of the energy associated with turbulent events at smaller scales comes from large-scale events (Dutton & Panofsky, 1970). As larger dimensions can be solved by numerical weather prediction (NWP) models, the problem of turbulence prediction is to identify the large-scale characteristics that lead to turbulent scale motions that affect aircraft (Storer et al., 2019). Thus, post-processing algorithms applied to the output of NWP models are commonly used to infer regions of significant turbulence. These inferences are based on diagnoses typically derived from spatial gradients of model variables (Gultepe et al., 2019).

Over the years, many post-processing diagnoses have been proposed, and some are used operationally. For example, Ellrod & Knapp (1992) developed an algorithm that uses velocity field outputs to derive a diagnosis based on horizontal strain and vertical wind shear. As each diagnosis is unable to predict all turbulence events, Sharman et al., (2006) generated the Graphical Turbulence Guidance (GTG). The product uses an ensemble of many diagnoses, which according to the authors, seems to improve the statistical performance of the predictions. However, as the diagnoses are empirical or are based on assumptions that cover physical aspects of the atmosphere, which are treated in part or are simplified, they are therefore subject to natural deficiencies of the technique used(Hon, Ng, & Chan, 2020).

Another technique used in forecasting is the application of objective methods based on observational data analysis. A well-known method used for mountainous regions is Harrison's Abacus. Developed by Harrison (1957 as cited in WMO, 1973), the model is a diagram that uses only two predictors, as follows: a) the pressure difference between windward and leeward (DP), and b) the normal wind speed about the mountain at 18000 ft flight level (FL180) (Vn).Originally, Harrison's Abacus was developed for mountain wave turbulence (MWT) prediction in the Rocky Mountain region of the United States of America (USA), but it is widely used by air carriers for flight planning across the Andes(Menegardo-Souza, 2018; Menegardo-Souza, França, Menezes, &

Almeida, 2021). For this purpose, Vn is used as the normal wind about the mountain range in FL180 to windward, and DP is the reduced pressure difference at mean sea level (QNH) extracted from the METAR code between Santiago (SCEL) and Mendoza (SAME) airports. According to Harrison's Abacus, for turbulence to occur, Vn must be at least 20 kt and DP greater than or equal to 0 hPa.

The application of machine learning(ML) techniques in in-flight turbulence studies is relatively recent. Williams (2014)produced a Convectively Induced Turbulence(CIT) now casting prediction, based on several data sources using the ML algorithm called random forest. Muñoz-Esparza, Sharman, & Deierling (2020) explored the use of regression trees in the combination of physics-based turbulence diagnostics derived from NWP model output within GTG to predict turbulence above 20000 ft. In both studies, the authors used Eddy Dissipation Rate(EDR) data for the USA. Hon et al. (2020)developed turbulence predictions for the Asia-Pacific region with ML techniques by combining a collection of turbulence diagnoses produced with post-processing of the NWP model. According to the authors, performance gains of 3% to 17% were obtained compared to turbulence indices when considered individually.

There are few studies on in-flight turbulence over South America, and in particular, the Andes. Many of them are related to the processes of generation, and forecasting of the zonda wind (regional term for the foehn wind) or relating it to mountain waves (Silva, 2004; Norte, 2015; Vásquez & Falcón, 2015). Lyra, Chan, & Dereczynski (2007)used post-processing algorithms applied to the NWP output to infer regions of significant turbulence in Brazil. Menegardo-Souza et al. (2021) carried out, based on measurements of automated *in situ* turbulence observations of the vertical acceleration in flight (VRTG) data, a study of synoptic patterns associated with unusual events of severe turbulence in the region of the Santiago (Chile) - Mendoza (Argentina) air route in summer in the southern hemisphere.

The objective of this study isto evaluate Harrison's Abacus as a turbulence prediction tool for the Andes and to present a set of categorical ML techniques to generate moderate or greater (MOG) turbulence24-hour predictions. This effort is part of aeronautical meteorology studies that have been carried out by the Laboratory of Applied Meteorology at the Federal University of Rio de Janeiro including França, Almeida, & Rosette (2016), França, Almeida, Bonnet, & Neto (2018), Paulucci, França, Libonati, & Ramos (2019), Almeida, França, & Velho (2020)and Menegardo-Souza et al. (2021). There are some internal papers (written not

in English) in the references, but all of them have at least English abstract.

2. OBSERVATION AND FORECAST DATA

This section describes the aviation turbulence observations used in this study, namely the vertical acceleration in flight, as well as weather station observations and the NWP model from which turbulence forecasts are generated.

2.1 Vertical acceleration in flight (VRTG) data

Aircraft record vertical accelerations in terms of anomalous gravitational acceleration, which can be used as an indicator of turbulent areas(LATAM, 2019). They are automated observations from vertical acceleration in flight (VRTG), with records of latitude, longitude, flight level, time and intensity event based on gravitational force (g). Although they are measurements dependent on the aircraft (Sharman et al., 2014), the VRTG data used here in this article was collected from similar size aircraft, which means that the "g" variation recorded via VRTG normalizes the turbulence events (i.e., light, moderate, and severe). These data have the advantage of reducing the known problems related to PIREP/AIREP(Sharman et al., 2006)as they are direct measures without human intervention. The aircraft-independent metric (Eddy Dissipation Rate - EDR), which is another way to infer regions with in-flight turbulence, although being implemented in some commercial airlines (Sharman et al., 2014), is not yet available in any of the Brazilian air carriers. It is important to note that VRTG data is not collected systematically, which is also the case with PIREP / AIREP messages, and its absence does not necessarily mean that there is no turbulence. According to Wandishin, Pettegrew, Petty, & Mahoney (2011), the spatial uncertainty of each in-flight turbulence record is around 150 km³, that is, each in-flight turbulence point represents a volume of the atmosphere.

In an undisturbed flight, the VRTG is equal to the unit g. If the aircraft experiences a sudden rise or fall, the VRTG values will be higher (positive g) or lower (negative g), respectively. Table 1 presents the VRTG thresholds used for turbulent events classification. VRTG measurements are carried out in the so-called monitoring window, which starts 10 s after takeoff and ends 4 s before landing. The turbulent event is considered when the VRTG values are within the limits established in Table 1, however only the highest maximum or lowest minimum will be recorded. This ensures that only one event is generated in long turbulent conditions. After 300 s of normal acceleration a new event can be generated (LATAM, 2019).

Table 1 - The severity of VRTG as a function of variation in vertical acceleration in flight (g).

Class 1		Class 2		Class 3	
-g	+g	-g	+g	-g	+g
0.6g<=	>=1.4g	0.4g<=	>=1.6g	0.2g<=	>=1.8g

Source: Authors adapted from (LATAM, 2019).

Here, it is assumed as MOG turbulence when the values of VRTG correspond to those of class 2 or 3 that are less than or equal to 0.4g or greater than or equal to 1.6g (changes in accelerometer >=0.6g), values that are in accordance with the established by the International Civil Aviation Organization (ICAO) for turbulence based on vertical accelerations in flight (Eick, 2014; ICAO, 2016). As air carriers operate with many limitations, despite being structurally prepared for much larger loads, the components of VRTG when the aircraft maneuvers in flight as in a turn, are small, hardly exceeding 1.13g or less than 0.87g, thus being far from the limits for registration (LATAM, 2019).

The study area is chosen to be (32.5°S-34.5°S, 068°W-071°W). A 22-months study period covering March 2018 to December 2019 is used. During this period, originally a total of 1300 VRTG records were collected by LATAM aircraft in the domain above the FL100 (3048 m), 1190 of which are Class 1, 91 of Class 2, and 19 of Class 3. The spatial distribution of these data with the distinction between the intensities can be seen in Figure 1. It is observed that there is a concentration of records in certain areas due to the alignment of aircraft on the region's airway. Turbulent events occurred in all sectors of the mountain range crossing, with no preferential region, affecting aircraft both to the west, east and above the Andes. It is noted that for the same time (minutes and seconds are not used), more than one VRTG record can occur, and with various intensity values. This is because there is more than one aircraft in flight and in different locations in the study area. Furthermore, the same aircraft can record more than one VRTG for the same hour, and of various intensities, following the measurement criteria.

In the 22 months of research, 16039 hours were analyzed to identify the existence of turbulence in the study area, regardless of the flight level that it has occurred. It should be noted that each hour may not contain VRTG data, or have one or more VRTG data, even at different intensities. If a given hour has at least one VRTG class 2 or 3 record, regardless of its spatial position in the domain, that hour is considered "YES" for MOG turbulence. A given hour with only VRTG class 1, or no data is considered "NO" for MOG turbulence. For the development of the

models proposed here, each observation of turbulence was considered valid for a period of 3-h before and after recording. In this way, the uncertainty in the data is reduced since the VRTG is dependent on the realization of the flight, and some hours could not have turbulence observation due to air traffic and flight planning reasons. Thus, of the 16039 hourly data analyzed, 662 were identified as "YES" for MOG turbulence and 15377 as "NO". To carry out case studies, the records of March 2nd, 2018, May 6th, 2018, and September 28th, 2018, were separated from the data set (leaving 15967 hourly data). With this, it was possible to evaluate the performance of the proposed models simulating the operating environment.

2.2 Weather station observations

Observational data from weather stations were collected from March 2018 to December 2019, for the implementation of the MOG turbulence prediction model based on Harrison's Abacus.

Data retrieved from the altitude weather station at Santo Domingo airport (SCSN) is used to obtain wind direction and speed at FL180. As usually only two meteorological balloon launches are performed per day, it was necessary to consider that the wind profiles obtained in 12Z and 00Z are constant in the periods between 07Z and 18Z and between 19Z and 06Z, respectively. QNH hourly pressure data from SCEL and SAME airports are taken from the METAR weather report code.

2.3 Numeric weather prediction (NWP) model

The spatial-temporal prediction fields of meteorological variables were generated using output data from the Global Forecast System (GFS), which is an NWP model produced by the National Center for Environmental Prediction (NCEP) with 3-h intervals analysis and prediction, on a global latitude-longitude grid of 0.25° by 0.25°. On all days analyzed, GFS data from 00Z were used with a forecast for up to 21Z of each day.

The NWP model outputs are defined for the so-called interest rectangle (Figure 2), which is a vertical section at 33.5°S, between 068°W - 071°W and vertical levels from 700 hPa to 200 hPa, to represent the atmosphere state in the study region. The interest rectangle is exactly at the mid-latitude of the domain, covering all flight levels that can be used to cross the Andes and the entire region between SCEL and SAME airports.

The Richardson number(Kronebach, 1964) (equation 01) and some atmospheric data extracted from the interest rectangle are shows in Table 2.

$$Ri = \frac{N^2}{(\partial U/\partial z)^2} = \frac{(g/\theta)\cdot(\partial\theta/\partial z)}{(\partial u/\partial z)^2+(\partial v/\partial z)^2}, \tag{01}$$

where N^2 is the Brunt-Vaisala frequency squared, U is horizontal wind speed, z is altitude, g is gravitational acceleration, and θ potential temperature.

Figure 1 - Spatial distribution of the 1,300 VRTG records above the FL100, from March 2018 to December 2019 in the study area, indicated according to their intensities. VRTG Class 1 (green), Class 2 (yellow), Class 3 (red). In black circles the airports of Santo Domingo (SCSN), Santiago (Arturo Merino Benítez International Airport - SCEL) and Mendoza (Governor Francisco Gabrielli International Airport - SAME).
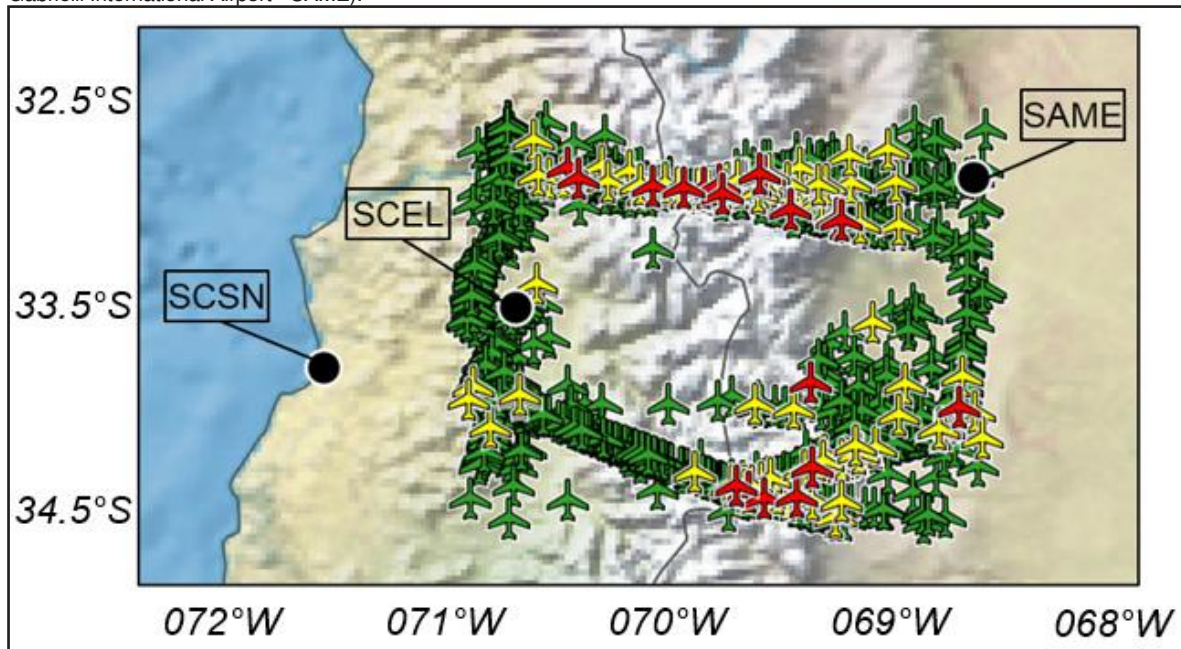
Source: Authors.

Figure 2 - Delimitation of the interest rectangle (red rectangle) at 33.5° S, between 068° W - 071° W and vertical levels of 700 hPa and 200 hPa, representing the atmosphere state in the study area.
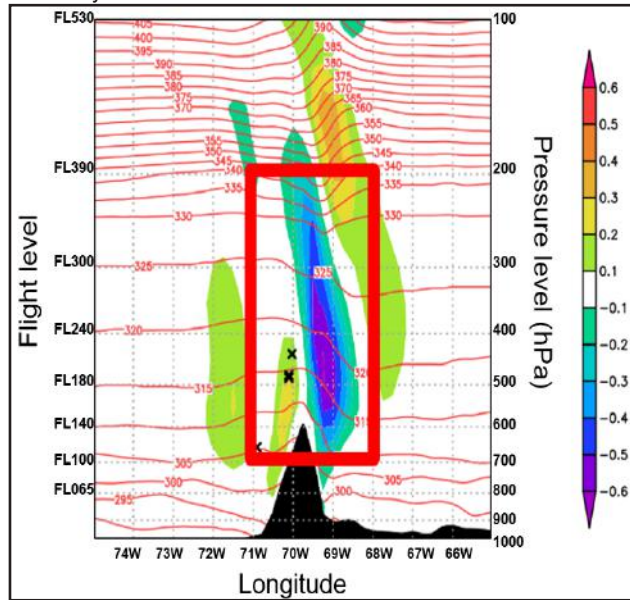
Source: Authors.

Table 2 - Atmospheric parameters extracted from the interest rectangle.

Parameter	Description
u	Zonal windspeed
w	Vertical speed
θ	Potential temperature
$\partial\theta/\partial x$	Zonal variation of the potential temperature
$\partial w/\partial x$	Zonal variation of the vertical speed
vws	Vertical windshear
Ri	Richardson number
w max	Maximum vertical speed
w min	Minimum vertical speed
w ave	Average vertical speed
w std	Standart deviation vertical speed
∂w	Difference between the highest and lowest vertical speed
Ri min	Minimum Richardson number
Ri ave	Average Richardson number
Ri max	Maximum Richardson number
ΣRi	Sum of Richardson number
vws max	Maximum vertical windshear
vws min	Minimum vertical windshear
vwsave	Average vertical windshear
Σvws	Sum of vertical windshear

Source: Authors.

The zonal wind speed (u), vertical speed (w), potential temperature (θ), zonal variation of the potential temperature ($\partial\theta/\partial x$), zonal variation of the vertical speed ($\partial w/\partial x$), vertical windshear (vws) and the Richardson number (Ri) are extracted for each of the twenty-four points within the interest rectangle(each longitude degree and every 100 hPa).

In addition to the parameters in table 2, the Brunt-Vaisala frequency (N), the Froude number(Stull, 1988) (equation 02) and the maximum zonal wind speed between the levels of 1000 hPa and 500 hPa at longitude 071°W (u max 1000 − 500 hPa)were calculated and added to the data set, totaling 184 selected attributes for each modeled time.

$$Fr = \frac{U}{NH},\qquad(02)$$

where U is the mean flow speed perpendicular to the mountain, N is the Brunt-Vaisala frequency and H the height of the mountain.

3. MODEL DEVELOPMENT METHODOLOGY

This section describes the methodological steps to carry out the evaluation of different thresholds applied to Harrison's Abacus and the training and testing of several categorical ML algorithms.

3.1 MOG turbulence prediction models

With the 15967 hourly data analyzed defined as "YES" or "NO" for MOG turbulence, as described in Section 2.1, along with the corresponding Vn and DP data (seen in Section 2.2), the model calibration based on Harrison's Abacus was performed, defining different thresholds for the predictors pair. The hourly dataset is randomly partitioned into 70% for calibration and 30% for testing.

For the development of the ML-based model using NWP model post-processing, the algorithms available in WEKA (Waikato Environment for Knowledge Analysis)software(Hall et al., 2009)were used. Of the fifty-six algorithms available on the platform, thirteen were selected during training and testing so they could be used with all the established methods aiming at the subsequent performance comparison and selection of the optimal model. These algorithms are described in Table 3. In all algorithms, the default WEKA software configuration was used. All models (trained algorithms) are evaluated by 10-fold cross-validation.

Table 3 - Algorithms used in the article.

Classifier	Description
BayesNet	classifier based on the construction of a Bayesian network, using various research algorithms and quality measures, provides data structures, network structures, and conditional probability distributions, and can classify binary, class values absent, and nominal class(Witten, Frank, Hall, & Pal, 2016).
NaiveBayes	it is a simple probabilistic classifier based on Bayes' theorem of posterior probability that calculates a set of probabilities by counting the frequency and combinations of values in a given data set (Patil & Sherekar, 2013).
Logistic	builds and uses a multinomial logistic regression model with a ridge estimator (Cessie & Houwelingen, 1992).
Multi-layer Perceptron	consists of standard perceptron with a defined number of hidden units using the activation function (for example, ReLu or sigmoid) and optimization based on minimizing the loss of quadratic error function(Witten et al., 2016).
Simple Logistic	builds linear logistic regression models. LogitBoost with simple regression functions as base learners is used for fitting the logistic models(Landwehr, Hall, & Frank, 2005).
Decision Table	decision table with a default rule mapping for the majority class. Searches for exact matches in the decision table using only the features included in the table(Kohavi, 1995)
JRip	bottom–up method learns rules by treating particular judgment of the examples in the training data as a class and finding the set of rules covering all the members of the class (Sonawani & Mukhopadhyay, 2013)
PART	generates ordered set of rules called decision lists. New data is compared with each rule in the list and the data is assigned the category of the rule to which it is best matching (Sonawani & Mukhopadhyay, 2013)
Hoeffding Tree	decision tree induction algorithm capable of learning from large data streams, assuming that the distribution generation examples do not change over time, as well as exploring the fact that a small sample may be sufficient to choose an ideal division attribute(Witten et al., 2016).
J48	generates a classification-decision tree for the given dataset by recursive partitioning of data. The basic algorithm recursively classifies until each leaf is pure that is the data has been categorized perfectly as possible ensuring maximum accuracy on the training data(Salzberg, 1994)
Random Forest	a collection of tree classifiers that are trained on different subsets of input features and the one with the best performance is chosen(Breiman, 2001).
RandomTree	constructs a tree that considers K randomly chosen attributes at each node. Performs no pruning. Also has an option to allow estimation of class probabilities (or target mean in the regression case) based on a hold-out set (backfitting)(Sonawani & Mukhopadhyay, 2013)
REPTree	quick decision tree, which uses the logic of the decision and regression tree and creates several trees in different iterations, selecting the best of all trees generated through the mean square error(Witten et al., 2016).

Source: Authors.

As the NWP model outputs are at 3-hour intervals, the turbulence observational dataset (15967 hourly data) needed to be paired to the model instances. In this case, 5344data (3-h interval) were now totaled in the study period, with 267 identified as "YES" for MOG turbulence and 5077 as "NO". For each of these times, the 184 attributes extracted from the interest rectangle (seen in Section 2.3) are determined to characterize the atmosphere state.

The dataset is unbalanced, so it is necessary to correct the prevalence, statistically balancing the occurrence of classes. The methods that implement this correction strategy are: 1) CostMatrix, attributing a weight to the error associated with the record whose class is less

numerous; 2) ClassBalancer, evaluates the instances in the data by adjusting the weight of each class in relation to the total set; 3) Replication or random removal of records so that the new set is representative of the original data. Thus, the following procedures were performed:

a) CostMatrix: it is modified the weights assigned to False Negative (Table 4) with the following multiples: 10, 20, 30, 50, 100, 200, and 380;

b) ClassBalancer: the weights of "YES" and "NO" of the dataset are varied by 50/50, 60/40, 70/30, 80/20, 90/10, and 96/4;

c) Majority class data removal: randomly remove data "NO";

d) Minority class data replication: "YES" data is replicated randomly in three ways: mode 1) considering values between the mean and one standard deviation for each of the 184attributes; mode2) considering values between the mean and two standard deviations for each of the 184 attributes, and mode 3) considering values between the median and quartiles for each of the 184 attributes.

Attributes are selected for each of the five dataset configurations (one unbalanced, one balanced by random removal of majority class data, and three balanced by random replication of minority class data) by the Correlation-based feature selection (CFS) method and Best First-Search heuristic with stopping criterion of five consecutive subsets that do not improve the method.

3.2 Model evaluation metrics

Quantitative evaluation of the effectiveness in predicting aviation turbulence events is performed using the relative operating characteristics (ROC) diagram. The ROC analysis is a well-established methodology for verifying binary forecasts of high-impact aviation weather phenomena such as turbulence(Sharman & Lane, 2016). The contingency table can be seen in Table 4.

Table 4 - Contingency table for the relative operating characteristics (ROC) analysis used in this study for performance evaluation. True Positive (TP), True Negative (TN), False Positive (FP) and False Negative (FN).

		FORECAST	
		YES	NO
OBSERVATION	YES	TP	FN
	NO	FP	TN

Source: Authors.

Using Table 4, the probability of detection(PODy), the probability of false detection(PODn) and the true skill statistic (TSS) are calculated as follows:

$$PODy = \frac{TP}{TP+FN}, \qquad (03)$$

$$PODn = \frac{TN}{TN+FP}, \qquad (04)$$

$$TSS = PODy + PODn - 1, \qquad (05)$$

PODy and PODn are not considered true probabilities, but the proportion of the observed data set correctly categorized by predictions(Kay et al., 2006). Together, PODy and PODn form the vertical and horizontal axes of the ROC diagram. A ROC curve is generated from a data set in space (PODy, PODn). In this way, the ROC curve reflects the skill of the prediction method as a whole, instead of focusing on particular realizations or configurations. Positive skill is indicated by proximity to the top left corner of the ROC diagram (i.e., high hit rate with few false alarms) while the diagonal represents "no skill" or a skill level equivalent to blind guess. To quantify the skill level, TSS is calculated, which is a measure of the ability of a model to discriminate between "YES" and "NO" predictions(Ellrod & Knox, 2010), ranging from -1 to +1, where +1 indicates perfect agreement and values of zero or less indicate performance no better than random(Allouche, Tsoar, & Kadmon, 2006).

4. RESULTS AND DISCUSSIONS

Following the method´s phases, the MOG turbulence forecast models with the Harrison's Abacus calibration and the training/testing of the ML algorithms are presented.

4.1 Performance of the Harrison's Abacus based MOG turbulence forecast

Several combinations of Vn and DP pair values were performed during the calibration phase, of which eight were selected as representative of all for illustration in the ROC curve, totaling sixteen experiments performed between calibration and test. The results of these experiments are seen in Figure 3. In it, each index shown refers to a pair of Vn and DP values. Index 1 is the original Harrison's Abacus parameters that are operationally used.

Figure 3 - Results of calibration experiments with Harrison's Abacus. ROC curve of PODy versus 1-PODn. Each index is a pair with different values of Vn and DP.
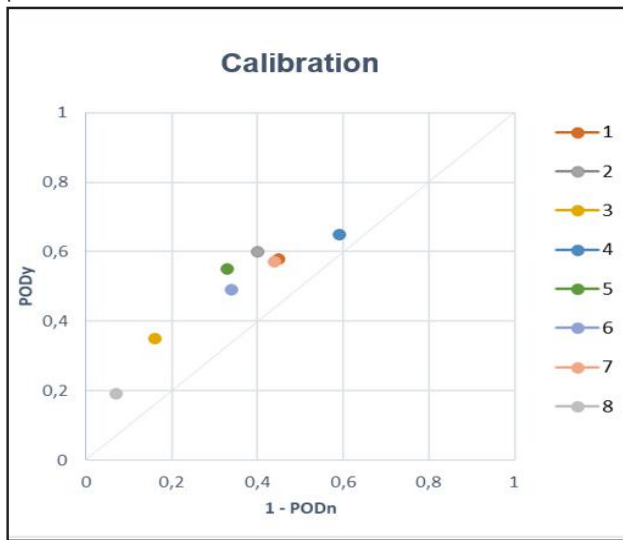
Source: Authors.

It is verified that the objective method considering only the parameters Vn and DP as predictors has an operational limitation in the predicting of MOG turbulence, with a TSS performance of less than 0.25. Index 1 reached PODy 0.58, PODn 0.55 and TSS 0.13. The best model was index 5, reaching PODy 0.55, PODn 0.67, and TSS of 0.22, showing an 9% gain compared to the original parameters of Harrison's Abacus. Table 5 shows the Vn and DP values used in each index and the results obtained in the calibration. The calibration results are practically the same as those obtained in the test.

Table 5 - Model calibration results based on Harrison's Abacus and Vn and DP values used for each index. VN in kt and DP in hPa.

Index	Vn>=	DP>=	PODy	PODn	TSS
1	20	0	0.58	0.55	0.13
2	0	3	0.60	0.60	0.20
3	40	0	0.35	0.84	0.19
4	20	-5	0.65	0.41	0.06
5	0	4	0.55	0.67	0.22
6	30	-2	0.49	0.66	0.15
7	26	-3	0.57	0.56	0.13
8	0	10	0.19	0.93	0.12

Source: Authors.

The reason for the low performance shown by the model may be related to the great variability of turbulence possibilities, when only Vn and DP are used as predictors. During Harrison's Abacus calibration, it was found that there is no possible combination of DP/Vn values that allows a TSS above 0.22. Thus, other methods that use other predictors and/or greater number of variables need to be applied to obtain an acceptable level of predictability.

4.2 Performance of the ML based MOG turbulence forecast

Considering the thirteen selected algorithms, the five dataset configurations (seen in Section 3.1), and the thirteen prevalence corrections (applied to the unbalanced dataset with CostMatrix and ClassBalancer), a total of two hundred and thirty-four experiments were performed.

Even with the great variability of selected attributes for each configuration of the data sets (more than 40), it is identified by CFS method and Best First-Search heuristic (seen in Section 3.1) that the atmospheric parameters most related to the predictability of MOG turbulence were the horizontal variations in potential temperature and vertical velocity in all sectors of the mountain range, and zonal wind, vertical wind shear, and Bulk Richardson number immediately above the mountain. This may be related to wave disturbances caused by MWT, causing both the potential temperature and the vertical velocity to oscillate abruptly over short distances, as well as the presence of strong winds that cause intense vertical shears, generating Clear Air Turbulence (CAT).

Figure 4a shows the ROC curve with the results of the thirteen experiments of the training and testing of ML algorithms using the unbalanced original data. Due to the problem of unbalanced MOG turbulence records (5% "YES" and 95% "NO"), most models were biased towards the majority class, demonstrated by the concentration in the lower-left corner of the ROC curve, with a high rate of PODn (above 0.90) and reduced PODy (less than 0.30). The best result with this data configuration was obtained with BayesNet finding PODy, PODn and TSS of 0.543, 0.898 and 0.441, respectively.

Correction of data prevalence by modifying the weights(ClassBalancer) of the "YES" and "NO" records to the proportions of 50/50, 60/40, 70/30, 80/20, 90/10 and 96/04, seventy-eight experiments were performed. There was an improvement in the overall performance of the models concerning the results obtained in training and testing with the unbalanced original data (Figure 4b). As the weight attributed to the "YES" records increased (from 50/50 to 96/04), the models gradually began prioritizing this class, losing quality in detecting "NO", moving from the lower-left corner of the ROC curve to the upper-right corner. The best result found with this method was obtained using the "YES" / "NO" ratio of 96/04, in which the model with Random Forest

reached PODy, PODn and TSS of 0.824, 0.789 and 0.613, respectively.

Using the CostMatrix to correct the prevalence in the data, assigning weight to the false negative (FN) in the proportions of 10, 20, 30, 50, 100, 200 and 380, ninety-one experiments were performed. As the assigned weight increased, the models gradually began to show the same trend seen with the ClassBalancer, moving from the lower-left corner of the ROC curve to the upper-right corner. The best result of this method was obtained with a weight of 380 (Figure 4c), in which the model with Random Forest reached PODy, PODn and TSS of 0.820, 0.826 and 0.646, respectively.

Performing the random removal of data from the majority class aiming at the statistical balance of the classes, 4810 records of "NO" were removed, leaving a total of 534 data, divided equally between "YES" and "NO". All models presented PODy and PODn performance above 70%, with values very close to each other. The best result obtained with this method was with the model using Random Forest, reaching a PODy, PODn and TSS of 0.839, 0.787 and 0.626, respectively.

For the statistical balancing of occurrences replicating new data from the minority class, 4810 "YES" records were added, using the three procedures described in Section 3.1, totaling 10154 data, divided equally between "YES" and "NO". In this case, all configurations generated models concentrated close to the upper left corner of the ROC curve, with high rates of PODy, PODn and TSS (Figure 4d). The best results were obtained with Random Forest. Table 6 shows the TSS values of all the trained algorithms in Figure 4.

Figure 4 - ROC curve with PODy versus 1-PODn values of the training and testing results of the ML algorithms: a) unbalanced original data; b)ClassBalancer 50/50; c)CostMatrix 380FN; d) Random Replication "YES" - mode 1.
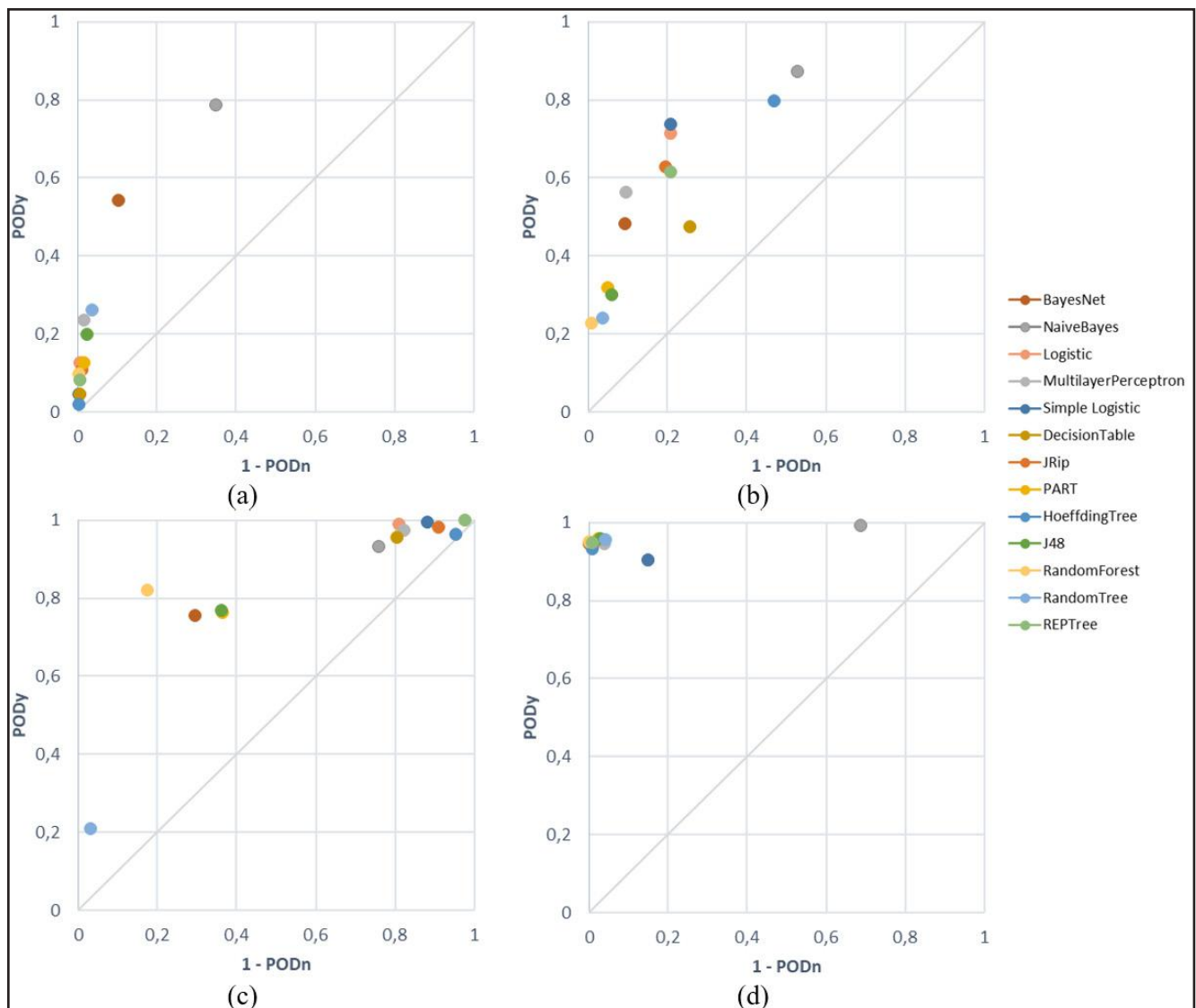
Table 6 - TSS of all models (trained algorithms) shown in Figure 4.

Algorithm	Fig.4a	Fig.4b	Fig.4c	Fig.4d
		TSS		
BayesNet	0.441	0.391	0.463	0.947
NaiveBayes	0.438	0.345	0.173	0.304
Logistic	0.121	0.508	0.178	0.755
Multilayer Perceptron	0.221	0.467	0.152	0.906
Simple Logistic	0.042	0.530	0.113	0.755
Decision Table	0.041	0.219	0.150	0.944
JRip	0.098	0.435	0.070	0.936
PART	0.112	0.269	0.401	0.936
Hoeffding Tree	0.017	0.328	0.010	0.927
J48	0.176	0.242	0.406	0.932
Random Forest	0.095	0.221	0.646	0.952
Random Tree	0.227	0.205	0.180	0.917
REPTress	0.077	0.406	0.022	0.941

Source: Authors.

In Table 7 there is a summary with the best TSS results obtained during the training and testing of the ML algorithms, identified for each of the different method configurations, number of samples, type of algorithm, PODy, PODn and TSS.

Among the methods that artificially manipulate the dataset, the best performance for each method was achieved using the CostMatrix 380FN, followed by ClassBalancer 96/04, and the worst with the unbalanced original data. By directly modifying the dataset, the best result was with the replication of data from the minority class "YES" based on the mean and one standard deviation, followed by the replication of "YES' based on the mean and two standard deviations, replication of " YES" based on the median and quartiles and the worst with the removal of data from the majority class "NO".

4.3 Case Studies

In this section, the case studies of the optimal predictive models in Table 7 (Unbalance Original Data, ClassBalancer 96/04, CostMatrix 380FN, Random Removal "NO", Random Replication "YES" - mode 1, Random Replication "YES" - mode 2, Random Replication "YES" - mode 3) is carried out, together with the index 5 model in Table 5, to evaluate their performance in predicting MOG turbulence, simulating the operating environment. Twenty-four data referring to March 2nd, 2018, May 6th, 2018, and September 28th, 2018 are analyzed.

Table 7 - Summary with the best TSS results obtained during the ML algorithms experiments.

Method	Samples	Algorithm	PODy	PODn	TSS
Unbalance Original Data	05344	BayesNet	0.543	0.898	0.441
ClassBalancer 50/50	05344	Simple Logistic	0.738	0.792	0.530
ClassBalancer 60/40	05344	Logistic	0.813	0.703	0.516
ClassBalancer 70/30	05344	Multilayer Perceptron	0.738	0.743	0.481
ClassBalancer 80/20	05344	BayesNet	0.610	0.829	0.439
ClassBalancer 90/10	05344	Random Forest	0.599	0.928	0.527
ClassBalancer 96/04	05344	Random Forest	0.824	0.789	0.613
CostMatrix 10FN	05344	Logistic	0.566	0.893	0.459
CostMatrix 20FN	05344	Simple Logistic	0.749	0.782	0.531
CostMatrix 30FN	05344	Multilayer Perceptron	0.640	0.877	0.517
CostMatrix 50FN	05344	Multilayer Perceptron	0.798	0.693	0.491
CostMatrix 100FN	05344	PART	0.581	0.866	0.447
CostMatrix 200FN	05344	Random Forest	0.618	0.910	0.528
CostMatrix380FN	05344	Random Forest	0.820	0.826	0.646
Random Removal "NO"	00534	Random Forest	0.839	0.787	0.626
Random Replication "YES" - mode1	10154	Random Forest	0.952	1.000	0.952
Random Replication "YES" - mode2	10154	Random Forest	0.951	0.999	0.950
Random Replication "YES" - mode3	10154	BayesNet	0.948	1.000	0.948
		Random Forest	0.950	0.998	0.948

Source: Authors.

The days were selected so that the models could be evaluated in three distinct situations of the atmosphere state: 1) day with all non-favorable times for turbulence; 2) day when there was a change in the atmosphere state, going from unfavorable to favorable to turbulence; and 3) day with all favorable times for turbulence. March 2nd, 2018 was selected as the non-favorable day as it was the median day of a total of three consecutive days characterized by the absence of VRTG data at all times. May 6th, 2018 was selected as the day on which there was a change in the atmosphere state, as in the two previous days no VRTG data were recorded at any time, and on the two following days yes. September 28th, 2018 was selected as a favorable day, as it was the median day of a total of three consecutive days characterized by the presence of VRTG data at most times.

To analyze the atmosphere state in those days, images from the GOES-16 satellite (channel 13 thermal band) and the NWP data from the GFS were used. In the interest rectangle (seen in Section 2.3) the wind, potential temperature, vertical velocity, and vertical wind shear were verified. In none of the tests was identified the presence of deep-convection in the satellite images, ruling out the possibility of CIT.

4.3.1 Case I: March 2nd, 2018

For March 2nd, 2018, no VRTG class 2 or 3 data were recorded. Analyzing the behavior of the atmosphere (Figure 5a), it appears that within the interest rectangle the wind has a speed less than or equal to 20 kt. The potential temperature isolines practically do not present disturbances and the vertical velocity is not significant, with values between +/- 0.1 m/s. This atmospheric pattern was maintained at all times of the day. The behavior of the vertical wind shear (Figure 5b), within the interest rectangle, was not significant, registering values smaller than 6 (10^{-3} s^{-1}), during all times of the day.

It is observed that the atmosphere state on March 2nd, 2018 did not present significant variations over the hours, indicating an unfavorable atmosphere for the formation of orographic waves and vertical wind shear.

Evaluating the optimal forecast models of MOG turbulence for March 2nd, 2018, Table 8 shows that all had the same performance, predicting that for this day there would be no possibility of turbulence at any time, agreeing with the observed data and the analysis of the atmosphere state.

Figure 5 - Representation of the atmosphere state on March 2nd, 2018 with data from the GFS model. The vertical section at 33.3 $^{\circ}$ S between 65 $^{\circ}$ W and 75 $^{\circ}$ W and from 1000 hPa to 100 hPa, with corresponding FL at 18Z: a) wind (kt), potential temperature (K) in red isolines and vertical speed (m/s) in colored hatching; b) wind (kt) and vertical wind shear (10-3 s-1) in colored hatching. Highlighted interest rectangle.
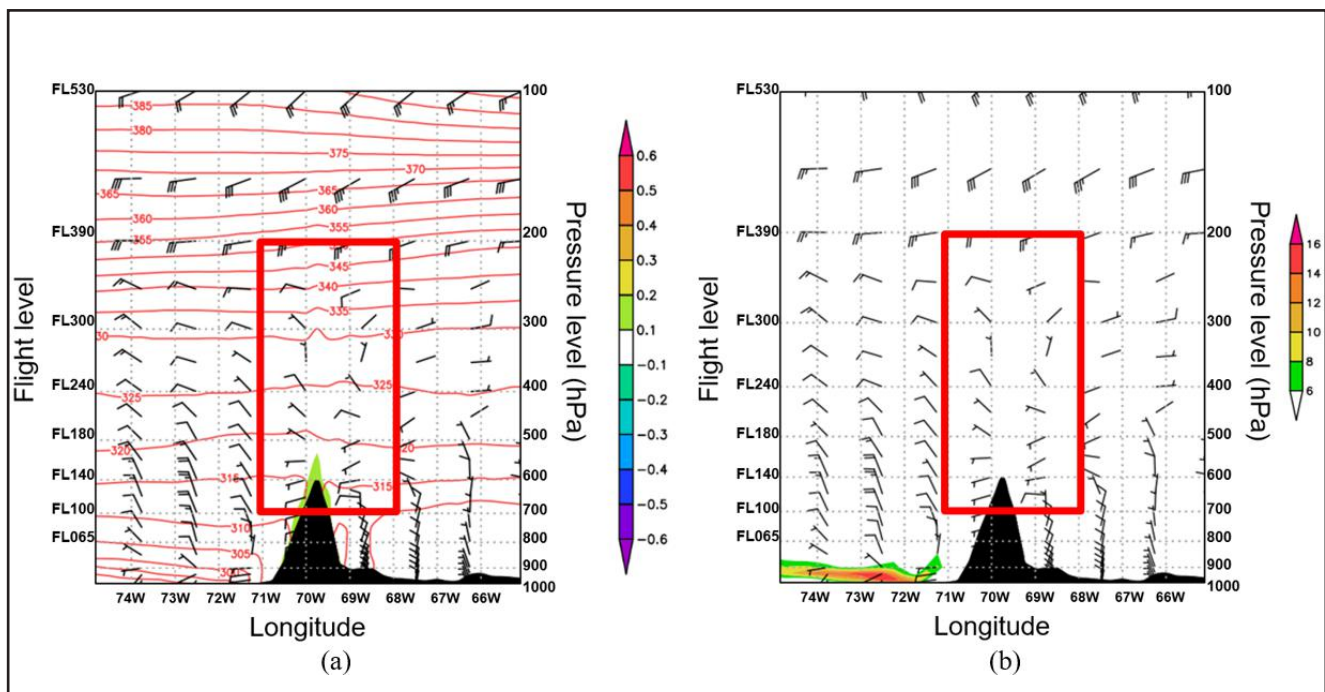
Source: Authors.

Table 8 - Results of optimal forecast MOG turbulence models for March 2nd, 2018 compared to observed data. In gray absence of turbulence, in red presence.

	0Z	3Z	6Z	9Z	12Z	15Z	18Z	21Z
OBSERVED								
Index 5								
Unbalance Original Data (BayesNet)								
ClassBalancer 96/04 (Random Forest)								
CostMatrix 380FN (Random Forest)								
RandomRemoval "NO" (Random Forest)								
Random Replication "YES" - mode 1 (Random Forest)								
Random Replication "YES" - mode2 (Random Forest)								
Random Replication "YES" - mode3 (BayesNet)								
Random Replication "YES" - mode3 (Random Forest)								

Source: Authors.

4.3.2 Case II: May 6th, 2018

For May 6th, 2018, only the hours of 18Z and 21Z were recorded VRTG class 2 and 3 data, indicating the possibility that the atmosphere was initially non-turbulent, changing to turbulent at the end of the period. Analyzing the behavior of the atmosphere (Figure 6a), within the interest rectangle the wind maintained a predominant northwesterly direction, increasing in intensity over time. Between FL100-180 the speed was up to 30 kt, while above this level it reached a peak of 90 kt at 21Z. Consequently, the zonal wind increased throughout the day, reaching its highest value at the end of the period, when it allowed the formation of orographic waves, which can be observed by disturbances in the potential temperature lines that gained amplitude from 12Z, and mainly at 18Z and 21Z. This fact was favored by the increase in vertical velocity alternating between rising and falling currents above and to the leeward of the Andes with maximum values of +0.2 m/s and - 0.3 m/s. The vertical wind shear behavior within the interest rectangle (Figure 6b) was more significant between FL140-240, with values greater than 8 (10^{-3} s^{-1}) at all hours. However, due to the intensification of the winds throughout the day, the vertical wind shear also increased, reaching over 12 (10^{-3} s^{-1}) at 12Z, and a peak above 14 (10^{-3} s^{-1}) at 18Z and 21Z.

Figure 6 - Representation of the atmosphere state on May 6th, 2018 with data from the GFS model. The vertical section at 33.3 ° S between 65 ° W and 75 ° W and from 1000 hPa to 100 hPa, with corresponding FL at 18Z: a) wind (kt), potential temperature (K) in red isolines and vertical speed (m/s) in colored hatching; b) wind (kt) and vertical wind shear (10-3 s-1) in colored hatching. Highlighted interest rectangle.
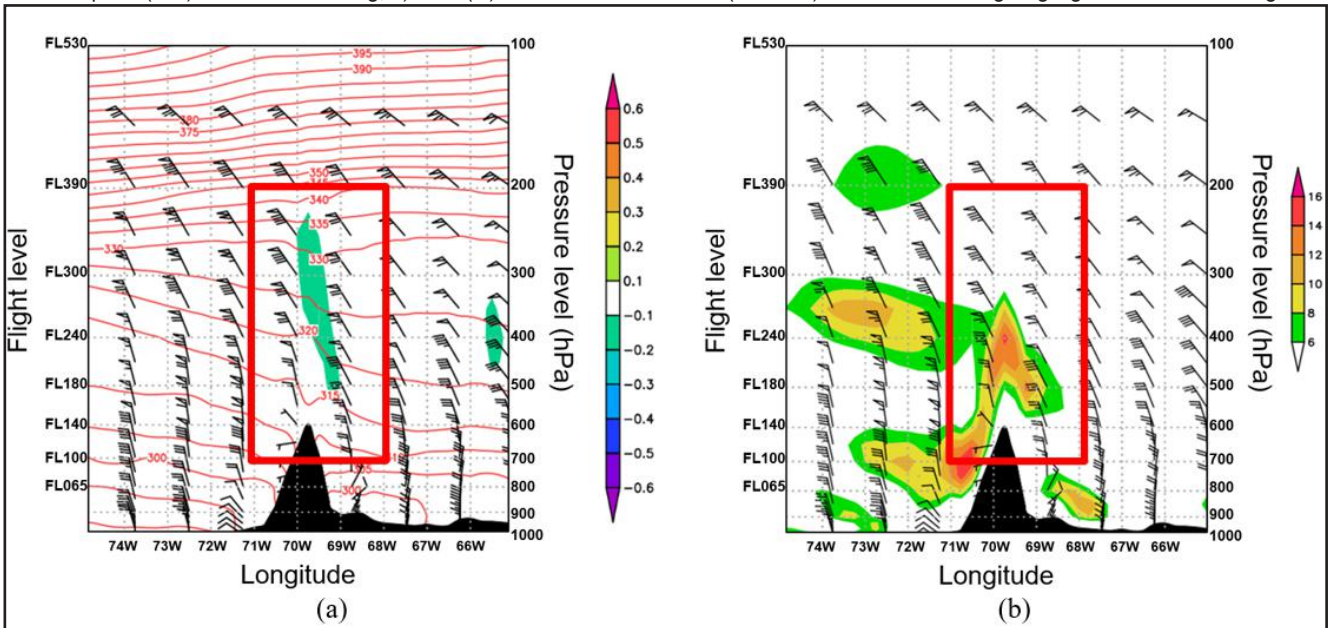
Source: Authors.

It is observed that the atmosphere state on May 6th, 2018 changed over the hours due to the intensification of the winds, which favored the formation of orographic waves and the increase in vertical wind shear, leaving a non-turbulent condition for turbulent.

Table 9 shows that the four predictive models based on the Random Replication of "YES" and the Index 5 model failed to identify the trend of variation in the state of the atmosphere, from non-turbulent to turbulent, not predicting the occurrence of MOG turbulence at any time of day. All other models were skilled in this indication but differing as to the start time of the MOG turbulence. The model based on the CostMatrix 380FN(Random Forest) predicted that the turbulence would start at 18Z, agreeing 100% with the observed data and with the atmosphere state. Models based on the Unbalanced Original Data (BayesNet), ClassBalancer 96/04 (Random Forest), and Random Removal of "NO" (Random Forest) anticipated the start time to 12Z, disagreeing with the observed data, but showing up possible, even if to a lesser degree, according to the analysis of the atmosphere state.

4.3.3 Case III: September 28 th, 2018

On September 28th, 2018, only at 06Z, 09Z and 12Z there were no VRTG class 2 or 3 data, which could indicate that it was a day with favorable conditions for the occurrence of MOG turbulence, however, interspersed with a period of attenuation of the phenomenon. Analyzing the behavior of the atmosphere (Figure 7a), it is verified that within the interest rectangle the wind above FL100 has a predominant west direction with a speed greater than or equal to 20 kt and peaks of more than 100 kt. These winds with a strong component perpendicular to the relief favor the formation of orographic waves, which can be observed along the vertical section by the large amplitude disturbances presented by the potential temperature lines, associated with intense ascending and descending currents in the upper and leeward Andes with extreme values greater than +/- 0.6 m/s. This atmospheric pattern was maintained at all times of the day. The vertical wind shear behavior within the interest rectangle (Figure 7b) was significant near FL390, ranging from 6 to 12 (10^{-3} s^{-1}) and mainly between FL100-240, where it presented values greater than 14 (10^{-3} s^{-1}) and highs above 16 (10^{-3} s^{-1}) during all times of the day.

It is observed that the atmosphere state on September 28, 2018, did not show significant variations over the hours, being influenced by orographic waves and by vertical wind shear, with both contributing to the generation of MOG turbulence. Thus, the absence of VRTG class 2 and 3 data in the period from 06Z to 12Z does not necessarily mean that there was no MOG turbulence, but that possibly it simply was not recorded, either because a flight was not performed at those times, or the flight was performed at a less favorable FL for the selected severity.

Table 9 - Results of optimal forecast MOG turbulence models for May 6th, 2018 compared to observed data. In gray absence of turbulence, in red presence.

	0Z	3Z	6Z	9Z	12Z	15Z	18Z	21Z
OBSERVED	⬜	⬜	⬜	⬜	⬜	⬜	🟥	🟥
Index 5	⬜	⬜	⬜	⬜	⬜	⬜	⬜	⬜
Unbalance Original Data (BayesNet)	⬜	⬜	⬜	⬜	🟥	🟥	🟥	🟥
ClassBalancer 96/04 (Random Forest)	⬜	⬜	⬜	⬜	🟥	🟥	🟥	🟥
CostMatrix 380FN (Random Forest)	⬜	⬜	⬜	⬜	⬜	⬜	🟥	🟥
RandomRemoval "NO" (Random Forest)	⬜	⬜	⬜	⬜	🟥	🟥	🟥	🟥
Random Replication "YES" - mode 1 (Random Forest)	⬜	⬜	⬜	⬜	⬜	⬜	⬜	⬜
Random Replication "YES" - mode2 (Random Forest)	⬜	⬜	⬜	⬜	⬜	⬜	⬜	⬜
Random Replication "YES" - mode3 (BayesNet)	⬜	⬜	⬜	⬜	⬜	⬜	⬜	⬜
Random Replication "YES" - mode3 (Random Forest)	⬜	⬜	⬜	⬜	⬜	⬜	⬜	⬜

Source: Authors.

Figure 7 - Representation of the atmosphere state on September 28th, 2018 with data from the GFS model. The vertical section at 33.3 ° S between 65 ° W and 75 ° W and from 1000 hPa to 100 hPa, with corresponding FL at 18Z: a) wind (kt), potential temperature (K) in red isolines and vertical speed (m/s) in colored hatching; b) wind (kt) and vertical wind shear (10-3 s-1) in colored hatching. Highlighted interest rectangle.
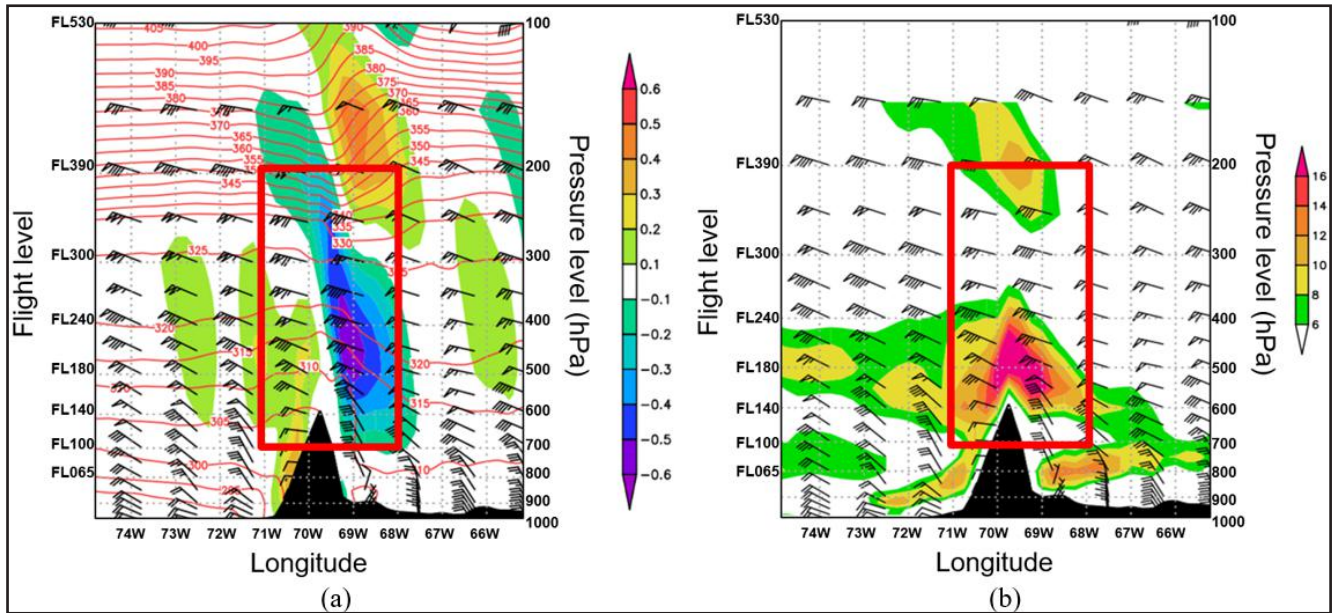
Source: Authors.

Table 10 shows that the four predictive models based on Random Replication of "YES" failed to identify the occurrence of MOG turbulence at any time. All other models were effective in predicting turbulence, differing in terms of the possibility of having some time for attenuation of the phenomenon. The Index 5 model predicted that there would be no turbulence from 3Z to 6Z and the model based on the Unbalanced Original Data(BayesNet) that there would be no turbulence only at 3Z. The models based on ClassBalancer 96/04 (RandomForest), CostMatrix 380FN (Random Forest), and Random Removal "NO" (Random Forest) predicted that MOG turbulence would occur throughout the day.

These models presenting the best performances, going accordingly with the analysis of the atmosphere state.

5. CONCLUSIONS

This article evaluates a traditional in-flight turbulence forecast tool for mountainous regions known as Harrison's Abacus and presents a set of machine learning (ML) techniques to generate MOG turbulence 24-hour predictions. The research covers the Santiago (Chile) – Mendoza (Argentina) route, over the 22 months, from March 2018 to December 2019, using LATAM aircraft VRTG records. The main conclusions are as follows.

Table 10 - Results of optimal forecast MOG turbulence models for September28th, 2018 compared to observed data. In gray absence of turbulence, in red presence.

	0Z	3Z	6Z	9Z	12Z	15Z	18Z	21Z
OBSERVED	red	red	gray	gray	gray	gray	red	red
Index 5	red	gray	gray	red	red	red	red	red
Unbalance Original Data (BayesNet)	red	gray	red	red	red	red	red	red
ClassBalancer 96/04 (Random Forest)	red	red	red	red	red	red	red	red
CostMatrix 380FN (Random Forest)	red	red	red	red	red	red	red	red
RandomRemoval "NO" (Random Forest)	red	red	red	red	red	red	red	red
Random Replication "YES" - mode 1 (Random Forest)	gray	gray	gray	gray	gray	gray	gray	gray
Random Replication "YES" - mode2 (Random Forest)	gray	gray	gray	gray	gray	gray	gray	gray
Random Replication "YES" - mode3 (BayesNet)	gray	gray	gray	gray	gray	gray	gray	gray
Random Replication "YES" - mode3 (Random Forest)	gray	gray	gray	gray	gray	gray	gray	gray

Source: Authors.

The use of an objective model based on Vn and DP (Harrison's Abacus) to predict MOG turbulence proved to be ineffective for operational use, because it was found impracticable to define a threshold of the pair of predictors with the acceptable performance of PODy, PODn and TSS. Its extreme simplicity, while conceptually appealing, makes it incompatible with the atmospheric complexity associated with MOG turbulence and with the necessary reliability of a forecast for flight planning and safety.

With ML techniques, it was possible to expand the dimensionality of the analyzed parameters, covering a greater number of variables necessary for good predictability of the phenomenon. The best results found with these techniques were obtained through the artificial manipulation of the dataset using weights (ClassBalancer and CostMatrix) and with the random removal of data from the majority class "NO", aiming at balancing classes. Such procedures responded with positive performances, both in training and testing and in the case studies, and these three models being skillful tools for operational use.

The prevalence correction technique with random replication of data from the minority class "YES", despite having generated models with the best performances during the training and testing phase, it was verified with the case studies that they were biased. The method ended up greatly altering the data, making the new dataset not representative of the original data. As a result, the model presented over fitting, failing to acquire the necessary generalizability. For this study, this data balancing technique proved to be inappropriate.

This research demonstrates the benefits and how promising is the application of ML techniques to the problem of in-flight turbulence forecasting, presenting generalization capacity and out performing traditional tools. For future works, it is suggested to use a longer study period and include EDR data, if available, aiming at the statistical consistency of the results. Analyze the effectiveness of applying the technique in areas that have little relief influence. It is also suggested to compare the prediction of the proposed models with other turbulence models that are operationally used.

Conflicts of interest/Competing interests

Not applicable.

Availability of data and material

Not applicable.

Code availability

Not applicable.

Authors' contributions

All authors contributed to the study conception and design. Material preparation, data collection and analysis were performed by Filipe Menegardo-Souza. The first draft of the manuscript was written by Filipe Menegardo-Souza and all authors commented on previous versions of the manuscript. All authors read and approved the final manuscript.

REFERENCES

Allouche, O., Tsoar, A., & Kadmon, R. (2006). Assessing the accuracy of species distribution models: Prevalence, kappa and the true skill statistic (TSS). *Journal of Applied Ecology*, 43(6), 1223–1232.https://doi.org/10.1111/j.1365-2664.2006.01214.x

Almeida, V. A. de, França, G. B., & Velho, H. C. (2020). Data assimilation for nowcasting in the terminal area of Rio de Janeiro. *Ciência e Natura*, *42*(0), 40. https://doi.org/10.5194/amt-9-2335-2016

Breiman, L. (2001). Random Forests. *Machine Learning*, *45*(1), 5–32.https://doi.org/10.1023/A:1010933404324

Cessie, S. le, & Houwelingen, J. C. van. (1992). Ridge Estimators in Logistic Regression. *Journal of the Royal Statistical Society: Series C (Applied Statistics)*, *41*(1), 191–201.https://doi.org/10.2307/2347628

Dörnbrack, A., Gerz, T., & Schumann, U. (1995). Turbulent breaking of overturning gravity waves below a critical level. *Applied Scientific Research*, *54*(3), 163–176. https://doi.org/10.1007/BF00849114

Dutton, J. A., & Panofsky, H. A. (1970). Clear air turbulence: A mystery may be unfolding. *Science (New York, N.Y.), 167*(3920), 937–944. https://doi.org/10.1126/science.167.3920.937

Eick, D. (2014). Turbulence Related Accidents and Incidents. Presented at the Turbulence Impact Mitigation Workshop 2, Washington, DC: NCAR. Retrieved September 9, 2020, from https://ral.ucar.edu/sites/default/files/public/events/2014/turbulence-impact-mitigation-workshop-2/docs/eick-turbulencerelatedaccidents.pdf

Ellrod, G. P., & Knapp, D. I. (1992). An Objective Clear-Air Turbulence Forecasting Technique: Verification and Operational Use. *Weather and Forecasting, 7*(1), 150–165. American Meteorological Society.https://doi.org/10.1175/1520-0434(1992)007<0150:AOCATF>2.0.CO;2

Ellrod, G. P., & Knox, J. A. (2010). Improvements to an Operational Clear-Air Turbulence Diagnostic Index by Addition of a Divergence Trend Term. *Weather and Forecasting, 25*(2), 789–798. American Meteorological Society. https://doi.org/10.1175/2009WAF2222290.1

França, G. B., Almeida, M. V. de, Bonnet, S. M., & Neto, F. L. A. (2018). Nowcasting model of low wind profile based on neural network using SODAR data at Guarulhos Airport, Brazil. *International Journal of Remote Sensing, 39*(8), 2506–2517. Taylor & Francis. https://doi.org/10.1080/01431161.2018.1425562

França, G. B., Almeida, M. V. de, & Rosette, A. C. (2016). An automated nowcasting model of significant instability events in the flight terminal area of Rio de Janeiro, Brazil. *Atmospheric Measurement Techniques, 9*(5), 2335–2344. Copernicus GmbH. https://doi.org/10.5194/amt-9-2335-2016

Gultepe, I., Sharman, R., Williams, P. D., Zhou, B., Ellrod, G., Minnis, P., Trier, S., et al. (2019). A Review of High Impact Weather for Aviation Meteorology. *Pure and Applied Geophysics*, *176*(5), 1869–1921. https://doi.org/10.1007/s00024-019-02168-6

Hall, M., Frank, E., Holmes, G., Pfahringer, B., Reutemann, P., & Witten, I. H. (2009). The WEKA data mining software: An update. *ACM SIGKDD Explorations Newsletter, 11*(1), 10–18.http://dx.doi.org/10.1145/1656274.1656278

Harrison, H. T. (1957). Forecasting the mountain wave at Denver, Colorado. *United Airlines Met. Circular*, (42).

Hon, K. K., Ng, C. W., & Chan, P. W. (2020). Machine learning based multi-index prediction of aviation turbulence over the Asia-Pacific. *Machine Learning with Applications, 2,* 100008.https://doi.org/10.1016/j.mlwa.2020.100008

ICAO. (2016). Doc 4444, Procedures for Air Navigation Services—Air Traffic Management.

Kay, M. P., Henderson, J. K., Stacey, A. K., Jennifer, L. M., Lacey, D. H., & Barbara, G. B. (2006). *Quality Assessment Product Development Team: Graphical Turbulence Guidance, Version 2.3.* Presented at the Aviation Weather Technology Transfer (AWTT) Technical Review Panel. Retrieved September 9, 2020, from https://esrl.noaa.gov/fiqas/publications.html

Kim, J.-H., & Chun, H.-Y. (2010). A Numerical Study of Clear-Air Turbulence (CAT) Encounters over South Korea on 2 April 2007. *Journal of Applied Meteorology and Climatology, 49*(12), 2381–2403. American Meteorological Society. https://doi.org/10.1175/2010JAMC2449.1

Kim, J.-H., Chun, H.-Y., Sharman, R. D., & Trier, S. B. (2014). The Role of Vertical Shear on Aviation Turbulence within Cirrus Bands of a Simulated Western Pacific Cyclone. *Monthly Weather Review, 142*(8), 2794–2813. American Meteorological Society. https://doi.org/10.1175/MWR-D-14-00008.1

Kim, J.-H., Sharman, R., Strahan, M., Scheck, J. W., Bartholomew, C., Cheung, J. C. H., Buchanan, P., et al. (2018). Improvements in nonconvective aviation turbulence prediction for the World Area Forecast System. *Bulletin of the American Meteorological Society,* 2295–2311.https://doi.org/10.1175/BAMS-D-17-0117.1

Knox, J. A. (1997). Possible Mechanisms of Clear-Air Turbulence in Strongly Anticyclonic Flows. *Monthly Weather Review, 125*(6), 1251–1259. American Meteorological Society. https://doi.org/10.1175/1520-0493(1997)125<1251:PMOCAT>2.0.CO;2

Kohavi, R. (1995). The power of decision tables. In N. Lavrac & S. Wrobel (Eds.), *Machine Learning: ECML-95*, Lecture Notes in Computer Science (pp. 174–189). Berlin, Heidelberg: Springer. Retrieved September 9, 2020, from http://citeseerx.ist.psu.edu/viewdoc/summary?doi=10.1.1.49.4576

Kronebach, G. W. (1964). An Automated Procedure for Forecasting Clear-Air Turbulence. *Journal of Applied Meteorology and Climatology, 3*(2), 119–125. American Meteorological Society. https://doi.org/10.1175/1520-0450(1964)003<0119:AAPFFC>2.0.CO;2

Landwehr, N., Hall, M., & Frank, E. (2005). Logistic Model Trees. *Machine Learning, 59*(1), 161–205. https://doi.org/10.1007/s10994-005-0466-3

Lane, T. P., Sharman, R. D., Trier, S. B., Fovell, R. G., & Williams, J. K. (2012). Recent Advances in the Understanding of Near-Cloud Turbulence. *Bulletin of the American Meteorological Society, 93*(4), 499–515. American Meteorological Society. https://doi.org/10.1175/BAMS-D-11-00062.1

LATAM. (2019). *Vertical Acceleration High in Flight* (pp. 485–486).

Lyra, A. de A., Chan, C. S., & Dereczynski, C. P. (2007). Indicadores de turbulência a partir de previsões do modelo regional ETA. *Revista Brasileira de Meteorologia, 22*(2), 161–182. https://doi.org/10.1590/S0102-77862007000200003

Menegardo-Souza, F. (2018). *Avaliação dos Resultados do Ábaco de Harrion no Diagnóstico de Turbulência no Cruzamento da Cordilheira dos Andes* (Specialization Course). Instituto de Controle do Espaço Aéreo (ICEA), São José dos Campos. Retrieved September 9, 2020, from https://www.anac.gov.br/assuntos/setor-regulado/profissionais-da-aviacao-civil/meteorologia-aeronautica/arquivos/MET001V_Final_RevisaoBanca_2TMENEGARDO.pdf

Menegardo-Souza, F., França, G. B., Menezes, W. F., & Almeida, V. A. (2021). Synoptic Patterns of Unusual Severe Turbulence Events in the Santiago (Chile)–Mendoza (Argentina) Route Region in Summer in the Southern Hemisphere. *Pure and Applied Geophysics*. https://doi.org/10.1007/s00024-021-02809-9

Muñoz-Esparza, D., Sharman, R. D., & Deierling, W. (2020). Aviation Turbulence Forecasting at Upper Levels with Machine Learning Techniques Based on Regression Trees. *Journal of Applied Meteorology and Climatology, 59*(11), 1883–1899. American Meteorological Society.https://doi.org/10.1175/JAMC-D-20-0116.1

Nastrom, G. D., & Fritts, D. C. (1992). Sources of Mesoscale Variability of Gravity Waves. Part I: Topographic Excitation. *Journal of the Atmospheric Sciences, 49*(2), 101–110. American Meteorological Society.https://doi.org/10.1175/1520-0469(1992)049<0101:SOMVOG>2.0.CO;2

Norte, F. A. (2015). Understanding and Forecasting Zonda Wind (Andean Foehn) in Argentina: A Review. *Atmospheric and Climate Sciences, 5*(3), 163–193. Scientific Research Publishing. http://dx.doi.org/10.4236/acs.2015.53012

Patil, T. R., & Sherekar, S. (2013). Performance Analysis of Naive Bayes and J48 Classification Algorithm for Data Classification. *Int. J. Comput. Sci. Appl., 6,* 256–261. Retrieved September 9, 2020, from https://researchpublications.org/IJCSA/NCAICN-13/189.pdf

Paulucci, T. B., França, G. B., Libonati, R., & Ramos, A. M. (2019). Long-Term Spatial–Temporal Characterization of Cloud-to-Ground Lightning in the Metropolitan Region of Rio de Janeiro. *Pure and Applied Geophysics, 176*(11), 5161–5175. https://doi.org/10.1007/s00024-019-02216-1

Salzberg, S. L. (1994). C4.5: Programs for Machine Learning by J. Ross Quinlan. Morgan Kaufmann Publishers, Inc., 1993. *Machine Learning, 16*(3), 235–240.https://doi.org/10.1007/BF00993309

Sharman, R., Cornman, L., Meymaris, G., & Pearson, J. (2014). Description and Derived Climatologies of Automated In Situ Eddy-Dissipation-Rate Reports of Atmospheric Turbulence. *Journal of Applied Meteorology and Climatology, 53*, 1416–1432.https://doi.org/10.1175/JAMC-D-13-0329.1

Sharman, R., & Lane, T. (Eds.). (2016). *Aviation Turbulence: Processes, Detection, Prediction.* Springer International Publishing.

Sharman, R., Tebaldi, C., Wiener, G., & Wolff, J. (2006). An Integrated Approach to Mid- and Upper-Level Turbulence Forecasting. *Weather and forecasting, 21*, 268–287. https://doi.org/10.1175/WAF924.1

Sharman, R., & Trier, S. B. (2019). Influences of Gravity Waves on Convectively Induced Turbulence (CIT): A Review. *Pure and Applied Geophysics, 176*(5), 1923–1958. https://doi.org/10.1007/s00024-018-1849-2

Sharman, R., Trier, S. B., Lane, T. P., & Doyle, J. D. (2012). Sources and dynamics of turbulence in the upper troposphere and lower stratosphere: A review. *Geophysical Research Letters, 39*(12). https://doi.org/10.1029/2012GL051996

Silva, A. R. (2004). *Ondas Orográficas Sobre a Cordilheira dos Andes em Latitudes Subtropicais: Estudo de caso* (M.Sc). Instituto Nacional de Pesquisas Espaciais (INPE), São José dos Campos, Retrieved September 9, 2020, from http://mtc-m16.sid.inpe.br/col/sid.inpe.br/jeferson/2004/05.27.09.45/doc/publicacao.pdf

Smith, R. B. (1989). Mountain-induced stagnation points in hydrostatic flow. *Tellus A, 41A*(3), 270–274. https://doi.org/10.1111/j.1600-0870.1989.tb00381.x

Smith, R. B. (2019). 100 Years of Progress on Mountain Meteorology Research. *Meteorological Monographs*, 59, 20.1-20.73. https://doi.org/10.1175/AMSMONOGRAPHS-D-18-0022.1

Sonawani, S., & Mukhopadhyay, D. (2013). A Decision Tree Approach to Classify Web Services using Quality Parameters. Presented at the International Conference on Web Engineering and Application (ICWA). Retrieved September 9, 2020, from https://arxiv.org/abs/1311.6240

Storer, L. N., Williams, P. D., & Gill, P. G. (2019). Aviation Turbulence: Dynamics, Forecasting, and Response to Climate Change. *Pure and Applied Geophysics, 176*(5), 2081–2095. https://doi.org/10.1007/s00024-018-1822-0

Stull, R. B. (1988). *An Introduction to Boundary Layer Meteorology*. Atmospheric and Oceanographic Sciences Library. Springer Netherlands.

Vásquez, H., & Falcón, N. (2015). ONDAS DE MONTAÑA EN LA CAPA LÍMITE PLANETARIA DE LA REGIÓN ANDINA VENEZOLANA. *Revista Brasileira de Meteorologia, 30*(3), 241–253. Revista Brasileira de Meteorologia. https://doi.org/10.1590/0102-778620130626

Wandishin, M. S., Pettegrew, B. P., Petty, M. A., & Mahoney, J. L. (2011). *Quality Assessment Report: Graphical Turbulence Guidance, Version 2.5. NOAA Technical Memorandum OAR GSD-39*. Retrieved September 6, 2020, from https://www.esrl.noaa.gov/fiqas/publications/articles/OAR-GSD-39-Tec-Memo.pdf

Williams, K. (2014). Using random forests to diagnose aviation turbulence. *Machine Learning*, 51–70. https://doi.org/10.1007/s10994-013-5346-7

Witten, I., Frank, E., Hall, M. A., & Pal, C. J. (2016). *Data Mining: Practical Machine Learning Tools and Techniques* (p. 621).

WMO. (1973). *The airflow over moutains.* WMO N° 355. Retrieved from Technical Note N° 127. Retrieved September 6, 2020, from https://library.wmo.int/doc_num.php?explnum_id=1814

Wolff, J. K., & Sharman, R. (2008). Climatology of Upper-Level Turbulence over the Contiguous United States. *Journal of Applied Meteorology and Climatology, 47*(8), 2198–2214. American Meteorological Society. https://doi.org/10.1175/2008JAMC1799.1

Synoptic patterns of unusual severe turbulence events on Santiago (Chile) – Mendoza (Argentina) route region insummer in Southern Hemisphere

Filipe Menegardo-Souza[1,2]

Gutemberg Borges França[1]

Wallace Figueiredo Menezes[1]

Vinícius Albuquerque de Almeida[1]

ABSTRACT

Statistical analyzes of the seasonal and temporal distributions of the turbulence events on the Santiago (Chile) – Mendoza (Argentina) route region are constructed using automated in situ turbulence observationsmeasurements of the vertical acceleration in flight (VRTG) fromLATAM airlines aircraft. The VRTG database contains 2,485 recordsover 22 months, from March 2018 to December 2019. Although in the winter inSouthern Hemisphere (SH) was the period with the greatest occurrence of turbulence in the Andes, the severe ones were more frequent in the summer and early autumn in SH. Throughon synoptic-scale analysis generated by the post-processing of Global Forecasting System,it was possible to identifythat the unusual severe turbulence events are not related to neither Convectively Induced Turbulence (CIT) nor Mountain Wave Turbulence (MWT), but withthe upper-levels atmospheric mechanismsthat caused severe Clear Air Turbulence (CAT) by an interaction tripodbetween the Bolivian High, Upper-level Jet Stream, and Topography.

Keywords: CAT; Bolivian High; aviation weather; Andes.

1. INTRODUCTION

In-flight turbulence can be dangerous, representing a major concern for aviation, as it can sometimes cause serious flight instability (Sharman, Trier, Lane, & Doyle, 2012);(Sharman & Pearson, 2017);(Storer, Williams, & Gill, 2019);(Gultepe et al., 2019). And so, the sudden fluctuations in speed and altitude that occur in this type of environment may lead to structural damage to aircraft and, more commonly, to incidents with passengers and crew (Sharman, Tebaldi, Wiener, & Wolff, 2006);(Wolff & Sharman, 2008);(Sharman, Cornman, Meymaris, & Pearson, 2014). There are three main sources of turbulence that impact aviation as follows (Marlton, 2016);(Kim et al., 2018): 1) shear instability, typically in regions without significant cloud coverage associated with the strong vertical and horizontal shear that occurs in the vicinity of jet streams (Dutton & Panofsky, 1970);(Wolff & Sharman, 2008);(Kim & Chun, 2010);(Storer et al., 2019). Gravity waves in strongly anticyclonic flows related to inertial instability and/or geostrophic adjustment have also been considered as an important mechanism (Knox, 1997); (Ellrod & Knox, 2010);(Kim, Chun, Sharman, & Trier, 2014)(Clear Air Turbulence – CAT); 2) breaking mountain waves, that occurs in the presence of

orography(Nastrom & Fritts, 1992); (Wolff & Sharman, 2008); (Kim & Chun, 2010)related to the upward propagation of the gravitational wave's energy in a stable environmentcarrying momentum to the upper troposphere, providing the breaking of the wave at cruise levels(Smith, 1989);(Turner, 1999). Additionally, these waves may overturn and break as they approach a critical level where the wave phase speed is equal to the wind component projected along the horizontal wave vector(Dörnbrack, Gerz, & Schumann, 1995);(Doyle, Shapiro, Jiang, & Bartels, 2005);(Sharman et al., 2012). When the energy does not propagate vertically, trapped lee waves are produced downstream and are normally restricted to low altitudes(Carney et al., 1995);(Smith, 2019)(Mountain Wave Turbulence – MWT); and 3) breaking gravity waves induced by intense convection, categorized into in-cloud and out-of-cloud, depending on its location (Convectively Induced Turbulence - CIT). Far away from convection, this event is defined as Near-Cloud Turbulence (NCT)(Lane, Sharman, Trier, Fovell, & Williams, 2012); (Kim et al., 2014);(Sharman & Trier, 2019).

In South America, the Andes acts as an obstacle to the flow of prevailing westerly winds on the subtropical and extratropical latitudes (Silva, 2004);(Menegardo-Souza, 2018). It is a continuous mountain range that extends in the North-South direction for more than 7000 km, with a width varying from 200 to 700 km and an average altitude of 4500 m (Norte, 2015). Airflow, often associated with jet stream, when interacting with the topography, cause disturbances that can reach the tropopause and reach thousands of kilometers downstream. For this reason, air carriers have specific operational procedures for crossing the Andes and the turbulence condition is vital for flight planning, influencing even the choice of the route to be used (Menegardo-Souza, 2018).

The validation of the in-flight turbulence prediction, and diagnosisis difficult, because the objective verification data sets are limited (Storer et al., 2019). Traditionally, the only routine observationsare those provided verbally by pilots, known as PIREP, in the United States of America (USA), and as AIREP internationally(Sharman et al., 2014). The use of flight reporting data has a limitation, as it can contain a substantial positioning and time error when the turbulence occurred, in addition to being dependent on the subjectivity of the crew and the type of aircraft (Sharman et al., 2006). To resolve these deficiencies, an in-situ turbulence notification algorithm based on the Eddy Dissipation Rate (EDR) has been implemented in some commercial airlines(Sharman et

al., 2014).Currently, none ofthe Brazilian air carriers has implemented the algorithm. However, automated turbulence observations fromthe vertical acceleration in flight (VRTG) have become available, with records of latitude, longitude, flight level, time, and intensity of the turbulence eventbased on gravitational force (g).These data have the advantage of reducing the aforementioned problems related to PIREP/AIREP as they are direct measures without human intervention. Regarding in-flight turbulence, it is known that its intensity is proportional to the aircraft type. However, the VRTG data used here was collected from the similar size LATAM aircrafts, which means that the "g" variation recorded via VRTG normalizes the turbulence events (i.e., light, moderate, and severe). Another important point is that VRTG data is not collected systematically, which is also the case with PIREP/AIREP messages, and its absence does not necessarily mean that there is no turbulence.

There arefew studies on in-flight turbulence over South America, and in particular, the Andes. The papersare related to the processes of generation, formation, and forecasting of the zonda wind (a regional term for the foehn wind) or relating it to the mountain waves, such asSilva (2004),Norte (2015) andVásquez & Falcón (2015). Climatological survey using AIREP data was made by Mello (2015) in Brazil, and other studies used post-processing algorithms applied to the output of the numerical weather prediction (NWP) to infer regions of significant turbulence such asLyra, Chan, & Dereczynski (2007) in Brazil, andSharman & Pearson (2017) in USA based on EDR data from American air carriers.No research has been found in the literature specifically related to atmospheric turbulence and the use of VRTG.

The objective of this study is to investigate and understand the atmospheric conditions favorable to the frequent reports of severe turbulence in the Santiago-Mendoza route region from December 2018 to April 2019, based on the post-processing of data recovered from Global Forecasting System analysis, considering the combined investigation of windshear, potential temperature, and other variables using synoptic-scale analysis. This technique is widely applied to identify atmospheric patterns as example Andrade & Cavalcanti (2018).This paper contributes to understand possible mechanisms for atmospheric turbulence events in South America. The application of synoptic-scale analysis helps to show the interaction between different atmospheric scales, including the importance of a seasonal synoptic system, such as Bolivian High, which can directly

influence the determination of a preferential region of severe turbulence, a smaller scale process, affecting an important air route.This effort is part of aeronautical meteorology studies that have been carried out by the Laboratory of Applied Meteorology at the Federal University of Rio de Janeiro includingFrança, Almeida, &Rosette(2016),França, Almeida, Bonnet, & Neto (2018),Paulucci, França, Libonati, & Ramos (2019) andAlmeida, França, & Velho (2020). There are some internal papers (written not in English) in the references, but some of them have at least English abstract.

2. STUDY AREA

The study area is the region delimited by the latitudes 28°S and 39°S and longitudes 64°W and 76°W (polygon highlighted in Figure 1),including the Andes region between the airports of Santo Domingo (SCSN), Santiago (Arturo Merino Benítez International Airport-SCEL), and Mendoza (Governor Francisco Gabrielli International Airport - SAME), which is the main airway for crossing the Andes.

The study area is characterized by different atmospheric systems throughout the year such as the Bolivian High (BH) and the Upper-Level Jet Streams (JS) (Reboita, Gan, Rocha, & Ambrizzi, 2010). The BH is an upper-level anticyclone that occurs in Southern Hemisphere (SH)summer over centralSouth America along with a trough in northeastern Brazil(Carvalho, 1989). Its origin and maintenance are related to the latent heat released in severe thunderstorms and to a lesser degree by the sensible heating of the atmosphere over the Bolivian plateau (Zhou &Lau, 1998);(Figueroa, Satyamurty, & Silva Dias, 1995);(Marengo, Soares, Saulo, & Nicolini, 2004). Its seasonal variability is directly related to the spatial and temporal distribution of precipitation in the Amazon basin (Lenters & Cook, 1997). In SH fall, the BH moves northward following the trend towards the end of the rainy season. In SH winter, the upper-level high practically disappears only returning in SH late spring with the intensification of convection over the continent. However, its maximum occurs in SH summer(Shi, Higgis, Yarosh, & Kousky, 2000);(Reboita et al., 2010).

Figure 1: Study area with an indication of Santo Domingo (SCSN), Santiago (SCEL), and Mendoza (SAME) airports.
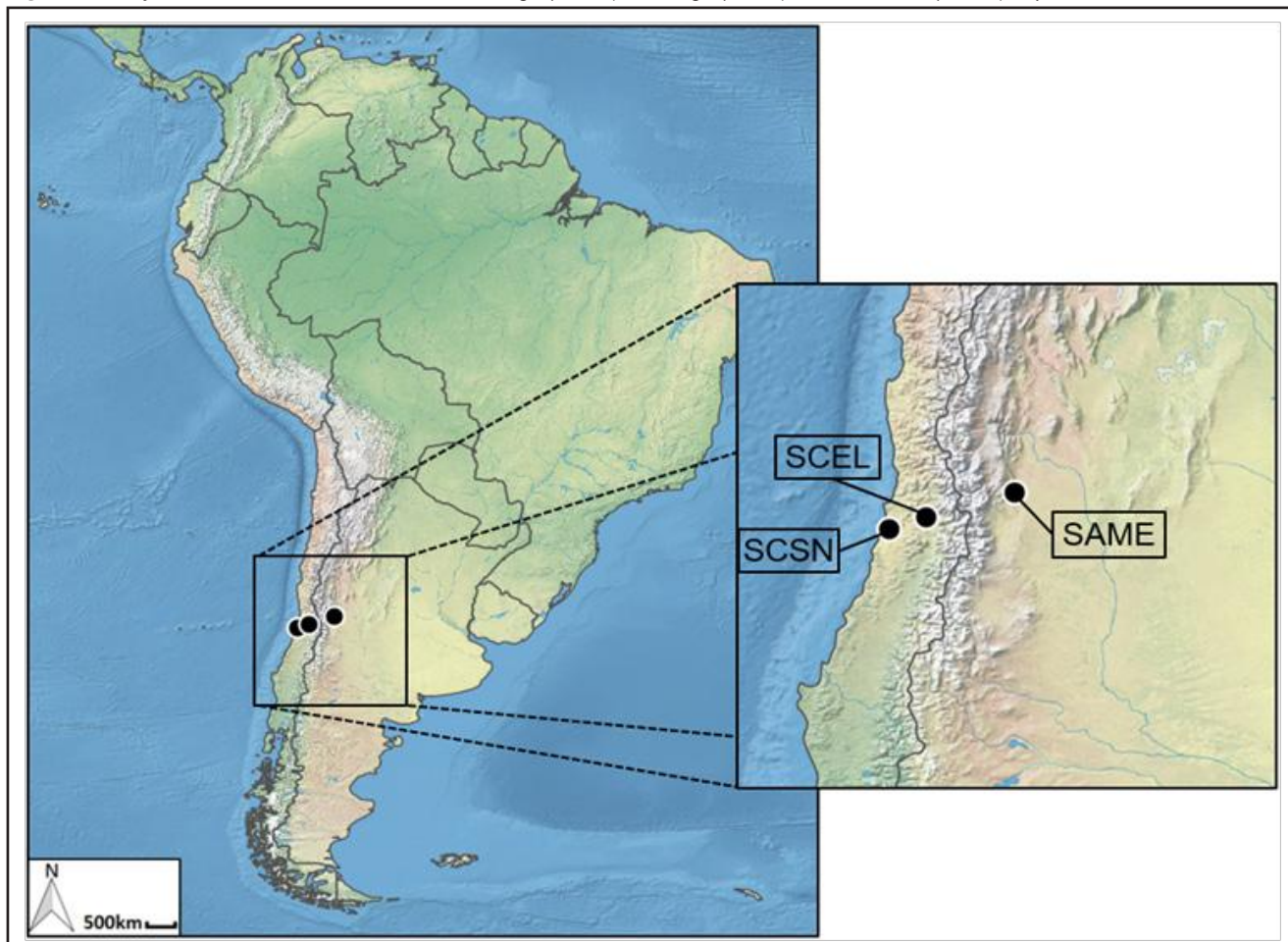
The JS forms a relatively narrow range of strong winds at the upper levels of the atmosphere (National Weather Service, 2020), close to the tropopause in a region where the zonal wind component, from the west, reaches maximum values (Zimmermann, 2017);(Pezzi, Rosa, & Batista, 2020). In the significant weather (SIGWX) charts it appears as a line of maximum speed with its surroundings showing strong horizontal and vertical shear. According to Reiter (1969) there are two distinct jet streams: the polar jet (PJ) and the subtropical jet (SJ). They flow around the globe, alternating in altitude and latitude, sometimes dividing and even disappearing completely to appear elsewhere (National Weather Service, 2020). Its average position moves towards the equator in the SH winter period and towards the poles in the SH summer (Cavalcanti, Ferreira, Dias, & Silva, 2009). During the SH summer, the SJ practically disappears,the PJ predominating. In some cases, the jets are coupled and even associated with the BH, located on the southern edge of this circulation (Pezzi et al., 2020). InSH fall, the gradual increase in the latitudinal temperature gradient favors the intensification of the JS. However, their maximum speed over South America is reached in SH winter(Pezzi et al., 2020). InSH spring, the jets begin to lose strength in comparisontoSH winter and acquire a slight anticyclonic curvature on their north side in response to the appearance of BH (Pezzi et al., 2020).

3. DATA AND METHOD

The research data and methodological steps are described in this section.

3.1 Data

Table 1 shows the details inherent to the data set used (that is, type, frequency, specific information, and source) for the period from March 2018 to December 2019.

Aircraft record vertical accelerations in terms of the anomalous gravitational acceleration (g), which can be used as an indicator of turbulent areas (LATAM, 2019). In an undisturbed flight, the VRTG is equal to the unit g. If the aircraft experiences a sudden rise or fall, the VRTG values will be higher (positive g) or lower (negative g), respectively. Table 2 presents theVRTGthresholds used for turbulent events classification. VRTG measurements are carried out in the so-called monitoring window, which starts 10 s after takeoff and ends 4 s before landing. The turbulent event is considered when the VRTG values are within the limits established in Table 2, however only the highest maximum or lowest minimum will be recorded. This ensures that only one event is generated in long turbulent conditions. After 300 s of normal acceleration a new event can be generated(LATAM, 2019).

Here, it is assumed as severe turbulence when the values of VRTG correspond to those of class 3 (column 3) that are less than or equal to 0.2g or greater than or equal to 1.8g, values similar to those used by International Civil Aviation Organization (ICAO) for vertical accelerations in flight according toEick (2014). As air carriers operate with many limitations, despite being structurally prepared for much larger loads, the components of VRTG when the aircraft maneuvers in flight as in a turn, are small, hardly exceeding 1.13g or less than 0.87g, thus being far from the limits for registration(LATAM, 2019).It is worth mentioning that 2,485 VRTG eventsof classes 1, 2 and 3 were recorded during the study period and although only LATAM has provided these data for the paper, it is the main air carrier to carry out flights in the Santiago-Mendoza route region, performing a monthly average in 2019 of 7,212 landings and takeoffs only in SCEL, with variations less than 10%.

Table 1: Data set used in the research.

Data	Frequency	Information	Source
VRTG	variable	Vertical acceleration in flight (g)	LATAM Airlines Brazil
TEMP	12h	Wind at FL180 (500hPa)	REDEMET (https://redemet.decea.gov.br)
GFS 0.25°	3h	Analysis and forecast grids on a 0.25 by 0.25 global latitude-longitude grid	NCAR (https://rda.ucar.edu/datasets/ds084.1/)
GOES-16	15min	Channel 13 thermal band	CPTEC (http://satelite.cptec.inpe.br/)

Table 2: The severity of VRTG as a function of variation in vertical acceleration in flight (g) (adapted from (LATAM, 2019).

Class 1		Class 2		Class 3	
-g	+g	-g	+g	-g	+g
0.6g<=	>=1.4g	0.4g<=	>=1.6g	0.2g<=	>=1.8g

Source: Adapted from (LATAM, 2019).

TEMP meteorological code is extensively used to report the atmospheric profile of temperature, humidity, and wind and is normally generated daily at 00Z and 12Z. Here, data retrieved from an upper-air station in SCSN (seen in Figure 1), is used. This weather station was chosen because it is located on the windward side of the Andes, close to the Pacific Ocean. It is assumed here that the wind profiles obtained in 12Z and 00Z are constant in the periods between 07Z to 18Z and 19Z to 06Z, respectively. In the absence of TEMP data, forecast data generated by World Area Forecast Center (WAFC) (available at Meteorological Portal of the Aeronautical Command–REDEMET) are used.

The data used to build the synoptic-scale analysis (in section 3.2) are 00Z analysis with 0.25° x 0.25° horizontal resolution from the Global Forecast System (GFS) / National Centers for Environmental Prediction (NCEP).

Images from the Geostationary Operational Environmental Satellite (GOES) 16 satellite channel 13 (thermal band centered at 10.3 μm) is used to identify the presence of convective cells and resolve doubts regarding the origin of the turbulence (available at Center for Weather Forecasting and Climate Studies– CPTEC).

3.2 Method

The investigation performed here is composed of two steps, as follows:

1. **Analysis of turbulence occurrence**: analysis of the VRTG records by class, according to Table 2, and its monthly occurrence for the data period; selection of VRTG value above flight level 100 (FL100) to avoid low VRTG oscillations during landing and take-off procedures; and calculation of zonal wind component at a flight level (FL) 180, its monthly average and standard deviation using data from the wind profile collected by radiosondes (TEMP code); and
2. **Atmospheric patterns related to turbulence events**: construction of synoptic-scale analysis based on the streamlines, wind speed, vertical windshear, and potential temperature from the GFS data, for FL300, FL340, and FL 390 when VRTG class 3 was recorded in the dataset; another analysis was constructed by performing a vertical section at 33.5°S (the average latitude of the study area), with data on wind, vertical speed, and potential temperature.

4. RESULTS AND DISCUSSIONS

Following the method´s phases, the results as presented and discussed.

4.1 VRTG Data Analysis

Over the 22 months of the study period 2,485 VRTG records were identified, resulting in an average of almost 4 encounters with in-flight turbulence per day. If only severe turbulence is considered, it would be at least 3 per month. Figure 2 displays the VRTG occurrence versus class intensity from March 2018 to December 2019. It may be noted that VRTG records are predominantly of class 1 (91.6% or 2277 occurrences) followed by VRTG classes 2 and 3 with 5.51%. (137 occurrences) and 2.85% (71 occurrences), respectively. These results are somewhat similar to those obtained from the CAT climatology carried out by Mello (2015), but in Brazil, using data from AIREP, when the author found that only 2.7% were severe turbulences. Therefore, the turbulence that most concerns aviation, the severe one, affects less than 3% of cases. According to Figure 2, generally there are more VRTG records in July with nearly 200 occurrences in 2018 and 2019. Besides, it is observed from May to November 2018, the monthly VRTG exceed the limit of 100 occurrences, while in 2019, four months (i.e., June, July, September, and October). There is an apparent seasonal behavior of total turbulence considering the monthly average, alternating between the months of greatest occurrence, typically from May to November with a peak in July (SH winter) and the lowest between December and April with a minimum in December (SH summer). The same variability in turbulence events was found in some studies, even though they deal with other regions such as Mello (2015), Wolff & Sharman (2008) and Jaeger & Sprenger (2007), the last performed a CAT climatology using reanalysis data with turbulence indicators.

Figure 2: The VRTG occurrence versus Class turbulence from March 2018 to December 2019. Class 1 (green), Class 2 (yellow) e Class 3 (red).
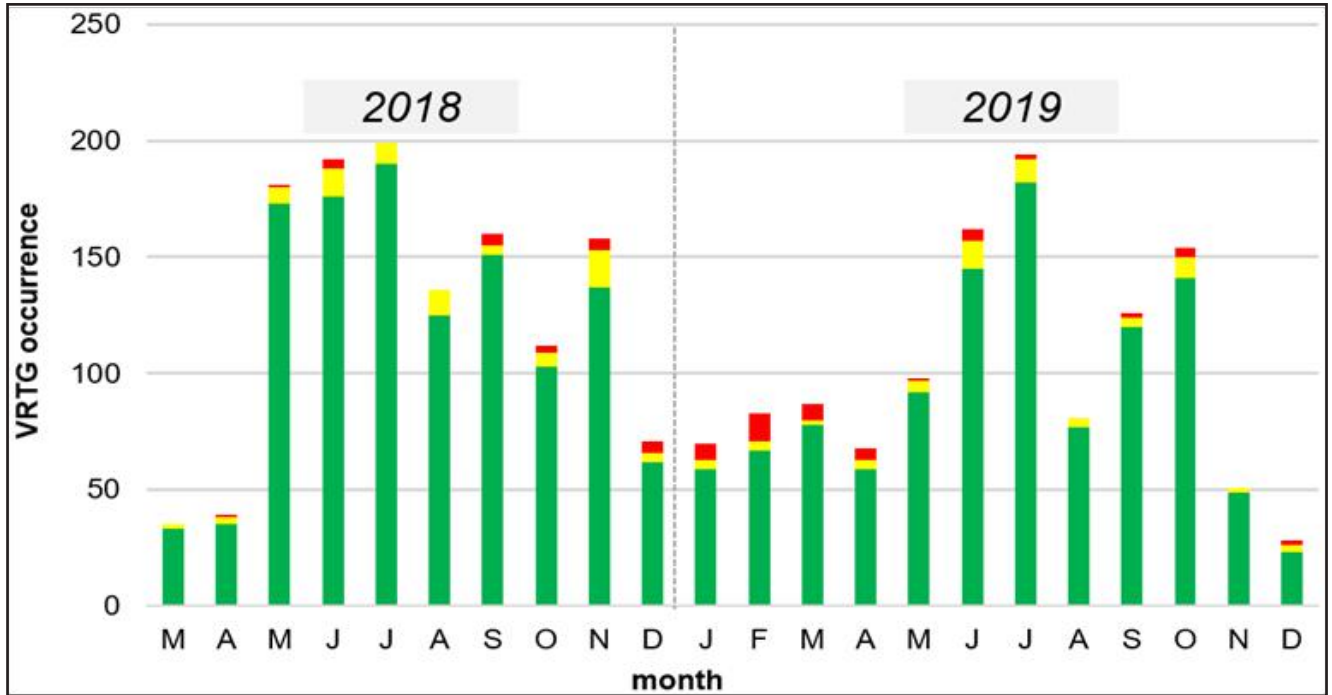

Many studies disregard light turbulence data, considering only those of moderate or greater intensity (MOG). Here, all turbulence intensities are considered. Comparing the turbulence of classes 1 and 2, there is a similarity in the seasonal variation. But an important fact to be highlighted is the specific behavior of severe turbulence (class 3). Although the total VRTG shows a minimum in the SH summer, the maximum of severe turbulence is observed in this period. More than half of the VRTG class 3, about 51% (corresponding to 36 events), are concentrated in just five months from December 2018 to April 2019, in contrast to only 14% (or 343 occurrences) of the total VRTG of classes 1 and 2. This characteristic was not found in any other research in the literature. One hypothesis for this increase in cases of severe turbulence could be CIT. This kind of turbulence event occur within convective clouds, as well as in the clear air above or around the cloud, and sometimes far from the cloud boundaries (Sharman & Trier, 2019). According to Kaplan et al. (2005), about 86% of the cases of severe turbulence examined in the USA were within 100 km of deep convection. But CIT frequency estimates vary, depending on the region and favorable season for a thunderstorm to form. All thirty-six cases of severe turbulence were studied and verified through satellite image data that there was no record of deep-convection. According to Shi et al. (2000) andReboita et al.(2010) the Andes study region has one of the least rainfall in South America, which indicates that the

unexpected increase of severe turbulence occurrences in the SH summer and early autumn is probably not related to turbulent mechanisms of CIT.

A very important questionis whether the air will flow over a mountain or not. The interaction between atmospheric stability, air flow and topography can generate a wide spectrum of different characteristics waves and this can be verified analyzing low-level winds(Stull, 1988); (Wolff & Sharman, 2008). Then, according to the constant cross-mountain wind speed (U) and stratification (CUS) theory(Smith, 1989); (Reinecke & Durran, 2008), the FL180 wind was chosen to estimate an effective constant wind speed across the mountain. Thisparameter is also commonly used in air carriers flight planning to predict MWT based on Harrison's Abaco (Harrison 1957 as cited in WMO, 1973); (Menegardo-Souza, 2018).Figure 3 shows that the monthly average of the zonal component of the wind speed in FL180 (Vn) experienced an intensification between SH late autumn to early spring, remaining in a large part of this period with an average speed above 30 kt, reaching a peak of almost 70 kt. The opposite occurred during SH summer and early autumn, when Vn was lower, with an average speed below 20 kt, even reaching negative values (close to minus 10 kt), which also indicates the presence of weak low easterly winds. The Vn has a high variability given the values of the standard deviations reaching values between 10 to 20 kt. This shows that in the study area it can occursincestrong westerly to weak easterly winds, but with the prevalence of the first.

**Figure 3:** Monthly average and standard deviation of the zonal wind speed at FL180 (Vn).
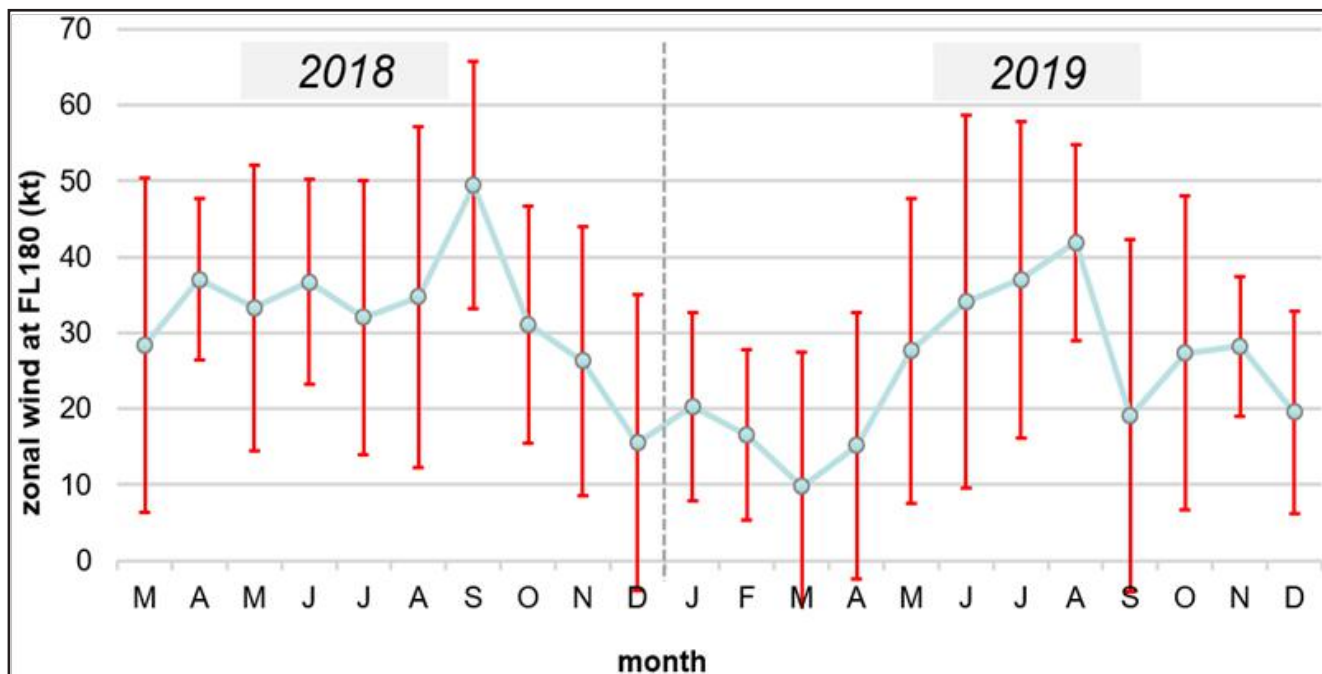
So, perhaps, the highest record of total cases of turbulence detected between May to November indicates that it may be related to the intensification of prevailing westerly winds in mid-latitudes during SH winter, as also identified in several studies (e.g. Jaeger & Sprenger (2007), Mello (2015)andWolff & Sharman (2008)). This mechanism is extremely important in the Andes region, since the specific positioning of the north-south oriented mountain range acts as an obstacle with average topographic heights of 4.5 km to the predominant westerly atmospheric flow, causing mountain waves that can break and generate MWT. A similar feature was seen by Wolff & Sharman (2008) for the Rocky Mountains in the USA and Vásquez & Falcón (2015) for the Venezuelan Andes. The first identified that in the western part of the USA the occurrences of MWT predominate due to the strong, westerly low-level wind, which are more common in the Northern Hemisphere (NH) winter months and over regions with topographic heights greater than or equal to 1.5 km. Another type of analysis was done by Silva (2004), studying the dynamics of the atmosphere in the Andes near SAME during the occurrence of the zonda winds (Andean Foehn), identified the importance of the interaction of the elevation with the atmospheric flow, finding high values of turbulent kinetic energy (TKE) at the top of the mountain and the presence of intense

and deep JS between the levels of 100 and 650 hPa. The zonda winds have a higher frequency in SH winter and spring seasons (Norte, 2015). However, lower values of Vn from December 2018 to April 2019, indicate that the unexpected increase of severe turbulence occurrences in the SH summer and early autumn is probably also not related to thetrapped lee waves.

Regarding flight levels versus VRTG records in the study area, it isobserved, as shown in Figure 4, that all VRTG classes are detected at all flight levels below FL400. Considering the total VRTG data, 21% (523 occurrences) were between FL300-400, and the rest below FL300 (1962 occurrences). However, it is noted an increase of VRTG class 3 at higher altitude with 54% (38 events) of these cases above the FL300. The comparison of these results with other studies is not so simple, since the flight levels used by the aircraft may differ for each region based on aspects such as topography, type of aircraft, flight phase and flight time. Another point to be considered is that the aircraft are usually at cruise levels, which would cause a bias in the records, as well as proximity to JS.Mello (2015) identified that the largest occurrences of CAT in Brazil are between FL300-400, with about 82.2% of the cases, not categorizing between the intensities of the turbulences.Mello's results differ greatly from those found here.

Figure 4: Flight levels versus VRTG records in the study area. Class 1 (green), Class 2 (yellow) e Class 3 (red).
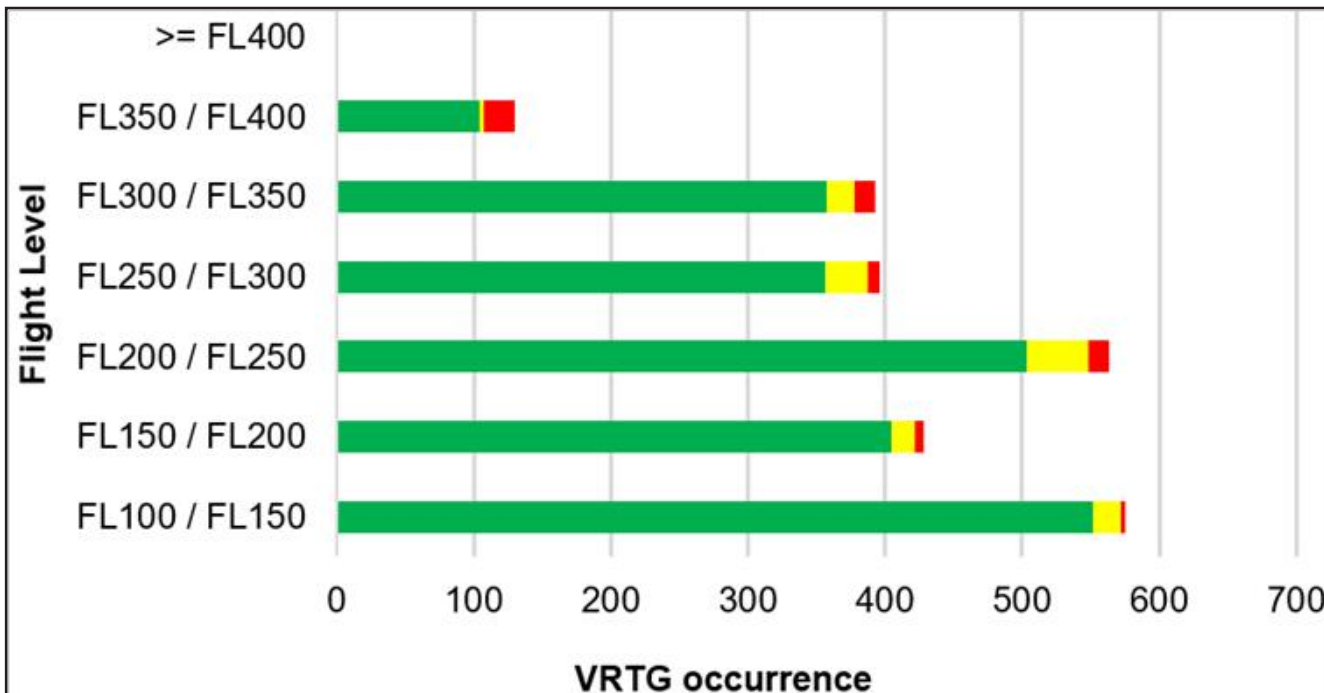

As the aircraft in the study area are close to the landing or takeoff from Santiago airport (SCEL), the main airport in the region, this influences the preferred flight level to be used and, subsequently, in the VRTG records. As the flight levels most used in the study area are below FL300, this indicates that the reason for the increase in VRTG class 3 numbers with altitude, has a predominant relationship with the atmospheric mechanisms of the upper levels. Thus, it can perhaps be said that the increase of severe turbulence events in the SH summer and early autumn, as shown in Figure 2, in addition to the origin in vertically propagating mountain waves (MWT), could also be CAT. Therefore, a synoptic-scale analysisis discussed in the next section.

4.2 Synoptic-scale analysis

As presented and discussed in the previous section, the turbulence that most impacts the flight, the severe one, was most significant from December 2018 to April 2019 (SH summer and early autumn), precisely in a period already known for lower incidence of turbulence given the results found in other studies and also in this paper, when considering the total VRTG records. This unusual result was investigated with the generation of synoptic-scale analysisabove FL300, which represents here the average of the atmospheric variablesconsidering the thirty-six events of severeturbulence.

Figure 5 a-c represent the synoptic-scale analysis of FL300, FL340, and FL390 for streamlines (blue lines), wind speed (kt) (black dotted line), and vertical wind shear (10-3s-1) (hatched area in color), for only severe events, from December 2018 to April 2019. There is a presence of a wide anticyclonic circulation (BH) dominating central South America, acting between the FL300 and FL390 with an Upper Tropospheric Cyclonic Vortex(UTCV) downstream northeastern coast of Brazil. This is a typical atmospheric configuration for the season according toCarvalho (1989),Shi et al. (2000) andReboita et al. (2010). The maximum wind speeds (greater than or equal to 50 kt),are predominantly restricted to high and middle latitudes, according to Cavalcanti et al. (2009) andPezzi et al. (2020), reaching up to 25°S and over 60 kt in part of the study area. It isimportant to note that the streamlines associated to BH spread along its southern border over the central-north of Chile and Argentina, which favors a narrowing of the atmospheric flow, causing vertical windshear. Over the central region of Argentina, there is also an area of strong shear that occurs together with maximum wind speeds, which may indicate the coupling of PJ with SJ. In general, the shear values are less than 5 (10-3s-1), which may be the result of the attenuation of the values due to the analysis being an average of the parameters.

Figure 5: The synoptic-scale analysis from December 2018 to April 2019 for only VRTG Class 3 events above FL300. In the black rectangle, the study area of this research. Streamlines(blue lines), wind speed (kt) in the black dotted line and vertical wind shear (10-3s-1) in the hatched area in color to a) FL300; b) FL340; c) FL390.

(a)

(b)

(c)
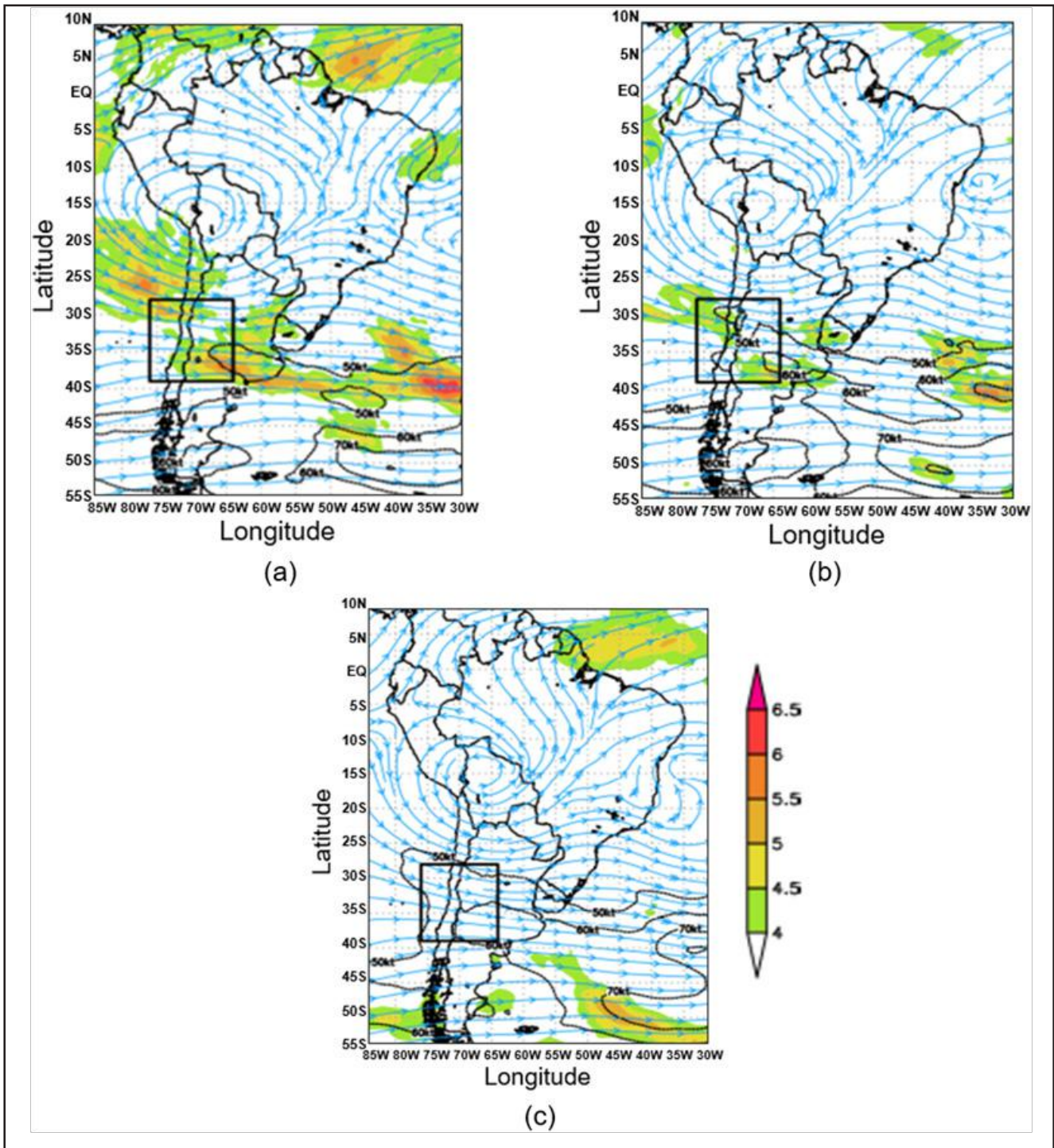
For more details on atmospheric patterns, Figure 6 represents the vertical section at 33.5°S from 1000 to 100 hPa with corresponding flight level, between longitudes 64°W to 70°W of the wind (kt), potential temperature (K) (red line), and vertical speed (m/s) (hatched area in color) of synoptic-scale analysis from December 2018 to April 2019. Note that above the FL300 the wind has a predominant west direction with a speed greater than or equal to 50 kt and the wind below the FL180 is normally lower than 20kt, which confirms the results found in Figure 3. These low-level weak winds do not favor the formation of mountain waves, which can be seen along the vertical section, by the potential temperature lines that show almost no disturbances, which, in other words, indicates almost no vertical speed. Another

important fact is that approximately 67% (24 events) of the VRTG class 3 records from December 2018 to April 2019 occurred to the windward side of the mountain range. Thus, perhaps mountain waves were not so significant for the occurrences of severe turbulence from December 2018 to April 2019, since MWT normally occurs above and leeward of the mountain (Carney et al., 1995).

This specific form of data processing has not been seen in any other survey of known turbulence, especially in the summer and early autumn months. Normally, attention to the hazard of the turbulence is restricted to winter, which has not proved an absolute truth for the Andes region.

4.2.1 Case Study

Although the use of synoptic-scale analysis is a classic tool to study patterns in the occurrence of atmospheric phenomena, these are averaged values of the parameters and, therefore, can smooth or mask some specific characteristics. For this reason, the VRTG class 3 record that occurred at FL300 at 71.8°W 31.5°S, on 03Z January 21st, 2019, was selected as a case study aimed at further detailing the conditions for the generation of severe turbulence, and to be a counterpoint to the previous analysis. Figure 7 a-c represent the atmospheric patterns on 03Z January 21st,

2019, combining GOES-16 satellite channel 13 thermal band, synoptic characteristics, and vertical section. It can be seen in Figure 7a that there are no convective clouds in the study area, showing only a few medium and high clouds. There is also an apparent anticyclonic pattern of cloudiness centered in northern Argentina. Thus, the absence of thunderstorms again eliminates the possibility a CIT event.
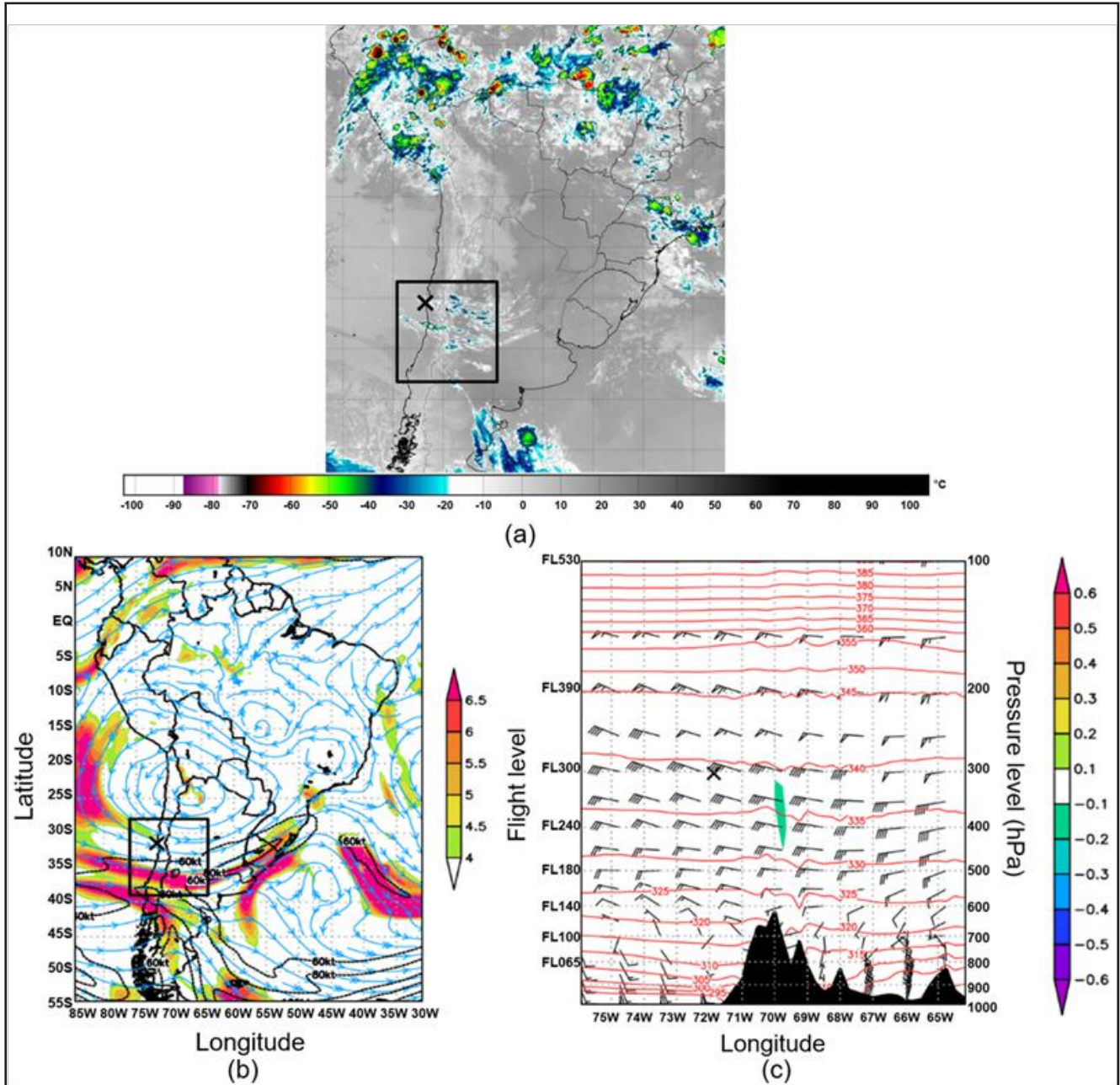
In the analysis of the atmospheric flow at FL300 (Figure 7b), one can observe the BH centered in the north of Argentina, with its southern edge spreading down to 35°S. Below this latitude, PJ and SJ are coupled, with slightly anticyclonic curvature, acting on the study region and diverging towards eastern Argentina. The interaction between these systems causes the formation of a strong vertical wind shear area with values above 6 (10-3s-1). In the vertical section at latitude 31.5°S (Figure 7c), the wind is predominant from the west with a speed greater than or equal to 50 kt above the FL300 and less intense winds below this level. From the surface to the top of the mountain, the wind is weak, reaching only the intensity of 20 kt in FL180. The potential temperature lines indicate a slight wave of small amplitude over the mountain range, where the vertical speed was minimal. However, the aircraft experienced severe turbulence in the windward Andes, so MWT did not contribute to the origin of the phenomenon.

Figure 6: The synoptic-scale analysis from December 2018 to April 2019 for only VRTG Class 3 events above FL300. The vertical section at 33.5 S from 1000 to 100hPa between 64 W to 70 W displays wind (kt) on the dewlap, potential temperature (k) on the red lines, and vertical speed (m/s) in the hatched area in color.
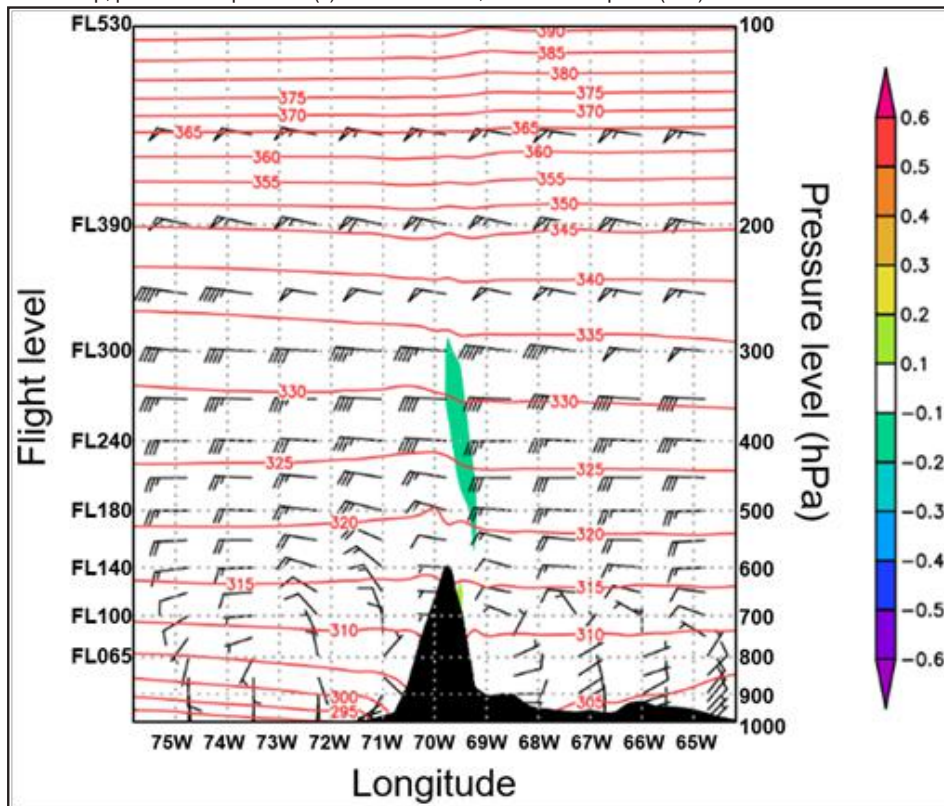
Figure 7: The atmospheric patterns on 03Z January 21st, 2019: a) GOES-16 satellite channel 13 thermal band with a temperature range in °C. Source: adapted from CPTEC (http://satelite.cptec.inpe.br/); b) streamlines (blue lines), wind speed (kt) (black dotted line), and vertical wind shear (10-3s-1) (hatched area in color) for the FL300; c) vertical section at 31.5°S from 1000 to 100hPa between 64°W to 70°W of the wind (kt) on dewlap, potential temperature (k) (red lines), and vertical speed (m/s) (hatched area in color). Highlighted in the rectangle, the study area, and in "x" the positioning of the aircraft that registered the VRTG Class 3.

(a)

(b)

(c)

The synoptic patterns found in the case study were therefore like those found in the synoptic-scale analysis. Once again, BH acts as a flagship, dominating the atmospheric flow, modulating, and favoring the coupling of SJ with PJ, causing strong vertical wind shear in a thin atmospheric layer already due to the Andes. These mechanisms favor the formation of severe CAT with vertical windshear values higher than those shown in the compounds because they did not suffer the attenuation of the technique. Maximum windshear valuespeak above

6 $(10^{-3}s^{-1})$ in a wide area, showing a more adequate value for the generation of severe turbulences, serving as a parameter to be observed by researchers and forecasters.

5. CONCLUSIONS

The mechanisms of severe turbulence formations are investigated, based on modeled data and VRTG records by LATAM aircraft from December 2018 to April 2019 in the Andes region. The main conclusions are as follows.

When analyzing the VRTG, it appears that although SH winter was the period of greatest occurrence of turbulence in the Andes, a result similar to that found for others regions byMello (2015), Wolff & Sharman (2008) and Jaeger & Sprenger (2007), it was in the SH summer and early autumn that the greatest records of severe turbulence were found. Thisfact, which was unknown and had no similar result in other studies, proved to have origins at the upper levels that caused severe CAT.

The synoptic-scale analysis showed the presence of a wide anticyclonic circulation that is characteristic mainly in SH summer, the Bolivian High. It can be observed that the spread of its southern edge modulates the flow of winds at high levels to higher latitudes, providing an anticyclonic curvature of the JS over the region.This narrowing of the atmospheric flow together with the topography, favors the coupling of PJ with SJ, channeling an area of maximum wind.

As verified by Wolff & Sharman (2008), MWT is favored by strong westerly winds perpendicular to the mountain, with turbulence occurring to the leeward. However, in this research, low-level winds are of weak intensity and, besides, many of the VRTG class 3 occurred windward of the mountain range. Convective clouds are not so significant in the study area, see the low rainfall indexes presented by Shi et al. (2000) andReboita et al. (2010), and the case study carried out. Thus, mountain waves and convective formations were of little significance for the genesis of the severe turbulence cases analyzed.

The BH spreading its southern edge to mid-latitudes, the coupling of PJ with SJ, and the presence of topography with an average altitude of 4500 m favored the occurrence of strong vertical wind shear at upper levels and, consequently, a greater number of severe CAT recorded in the summer and early autumn.

It is expected that this knowledge may contribute to reduce the gap of atmospheric turbulence studies in South America and help the researchers and forecasters to identify the phenomenon risk situations, enabling better diagnostics and issuing more easily alerts aiming at the safety of air navigation.For future studies, it is suggested to use a longer study period and include the EDR data, if available, to confirm the conditionsof severe CAT in the SH summer and early autumn here identified. Also, we suggest the development of CAT forecast models using GFS post-processing and machine learning to verify if there is an improvementcompared to existing methods.

ACKNOWLEDGMENTS

REFERENCES

Almeida, V. A. de, França, G. B., & Velho, H. C. (2020). Data assimilation for nowcasting in the terminal area of Rio de Janeiro. *Ciência e Natura, 42*(0), 40. https://doi.org/10.5194/amt-9-2335-2016

Andrade, K. M., & Cavalcanti, I. F. A. (2018). Atmospheric characteristics that induce extreme precipitation in frontal systems over Southeastern Brazil during summer: Observations and atmospheric model simulation. *International Journal of Climatology, 38*(14), 5368–5385.https://doi.org/10.1002/joc.5744

Carney, T. Q., Bedard, A. J., Brown, J. M., McGinley, J., Lindholm, T., & Kraus, M. J. (1995).

Hazardous Mountain Winds and Their Visual Indicators. *Advisory Circular*, 00–57(FAA), Retrieved September 9, 2020, from https://www.researchgate.net/project/Aviation-Hazards

Carvalho, A. M. G. (1989). *Conexões entre a circulação em altitude e a convecção sobre a América do Sul* (M.Sc). Instituto Nacional de Pesquisas Espaciais (INPE), São José dos Campos.

Cavalcanti, I. F. de A., Ferreira, N. J., Dias, M. A. F. da S., & Silva, M. G. A. J. da. (2009). *Tempo e clima no Brasil*. São Paulo: Oficina de Textos.

Dörnbrack, A., Gerz, T., & Schumann, U. (1995). Turbulent breaking of overturning gravity waves

below a critical level. *Applied Scientific Research, 54*(3), 163–176. https://doi.org/10.1007/BF00849114

Doyle, J. D., Shapiro, M. A., Jiang, Q., & Bartels, D. L. (2005). Large-Amplitude Mountain Wave Breaking over Greenland. *Journal of the Atmospheric Sciences, 62*(9), 3106–3126. American Meteorological Society. https://doi.org/10.1175/JAS3528.1

Dutton, J. A., & Panofsky, H. A. (1970). Clear air turbulence: A mystery may be unfolding. *Science (New York, N.Y.), 167*(3920), 937–944. https://doi.org/10.1126/science.167.3920.937

Eick, D. (2014). Turbulence Related Accidents and Incidents. Presented at the Turbulence Impact Mitigation Workshop 2, Washington, DC: NCAR, Retrieved September 9, 2020, from https://ral.ucar.edu/sites/default/files/public/events/2014/turbulence-impact-mitigation-workshop-2/docs/eick-turbulencerelatedaccidents.pdf

Ellrod, G. P., & Knox, J. A. (2010). Improvements to an Operational Clear-Air Turbulence Diagnostic Index by Addition of a Divergence Trend Term. *Weather and Forecasting, 25*(2), 789–798. American Meteorological Society. https://doi.org/10.1175/2009WAF2222290.1

Figueroa, S. N., Satyamurty, P., & Silva Dias, P. L. (1995). Simulations of the summer circulation over the South American region with an eta coordinate model. *Journal of the Atmospheric Sciences, 52,* 1573–1584. https://doi.org/10.1175/1520-0469(1995)052<1573:SOTSCO>2.0.CO;2

França, G. B., Almeida, M. V. de, Bonnet, S. M., & Neto, F. L. A. (2018). Nowcasting model of low wind profile based on neural network using SODAR data at Guarulhos Airport, Brazil. *International Journal of Remote Sensing, 39*(8), 2506–2517. Taylor & Francis. https://doi.org/10.1080/01431161.2018.1425562

França, G. B., Almeida, M. V. de, & Rosette, A. C. (2016). An automated nowcasting model of significant instability events in the flight terminal area of Rio de Janeiro, Brazil. *Atmospheric Measurement Techniques, 9*(5), 2335–2344. Copernicus GmbH. https://doi.org/10.5194/amt-9-2335-2016

Gultepe, I., Sharman, R., Williams, P. D., Zhou, B., Ellrod, G., Minnis, P., Trier, S., et al. (2019). A Review of High Impact Weather for Aviation Meteorology. *Pure and Applied Geophysics, 176*(5), 1869–1921. https://doi.org/10.1007/s00024-019-02168-6

Jaeger, E. B., & Sprenger, M. (2007). A Northern Hemispheric climatology of indices for clear air turbulence in the tropopause region derived from ERA40 reanalysis data. *Journal of Geophysical Research: Atmospheres, 112*(D20). https://doi.org/10.1029/2006JD008189

Kaplan, M. L., Huffman, A. W., Lux, K. M., Cetola, J. D., Charney, J. J., Riordan, A. J., Lin, Y.-L., et al. (2005). Characterizing the severe turbulence environments associated with commercial aviation accidents. Part 2: Hydrostatic mesoscale numerical simulations of supergradient wind flow and streamwise ageostrophic frontogenesis. *Meteorology and Atmospheric Physics, 88*(3), 153–173. https://doi.org/10.1007/s00703-004-0079-6

Kim, J.-H., & Chun, H.-Y. (2010). A Numerical Study of Clear-Air Turbulence (CAT) Encounters over South Korea on 2 April 2007. *Journal of Applied Meteorology and Climatology, 49*(12), 2381–2403. American Meteorological Society. https://doi.org/10.1175/2010JAMC2449.1

Kim, J.-H., Chun, H.-Y., Sharman, R. D., & Trier, S. B. (2014). The Role of Vertical Shear on Aviation Turbulence within Cirrus Bands of a Simulated Western Pacific Cyclone. *Monthly Weather Review, 142*(8), 2794–2813. American Meteorological Society. https://doi.org/10.1175/MWR-D-14-00008.1

Kim, J.-H., Sharman, R., Strahan, M., Scheck, J. W., Bartholomew, C., Cheung, J. C. H., Buchanan, P., et al. (2018). Improvements in nonconvective aviation turbulence prediction for the World Area Forecast System. *Bulletin of the American Meteorological Society*, 2295–2311. https://doi.org/10.1175/BAMS-D-17-0117.1

Knox, J. A. (1997). Possible Mechanisms of Clear-Air Turbulence in Strongly Anticyclonic Flows. *Monthly Weather Review, 125*(6), 1251–1259. American Meteorological Society. https://doi.org/10.1175/1520-0493(1997)125<1251:PMOCAT>2.0.CO;2

Lane, T. P., Sharman, R. D., Trier, S. B., Fovell, R. G., & Williams, J. K. (2012). Recent Advances in the Understanding of Near-Cloud Turbulence. *Bulletin of the American Meteorological Society, 93*(4), 499–515. American Meteorological Society. https://doi.org/10.1175/BAMS-D-11-00062.1

LATAM. (2019). *Vertical Acceleration High in Flight* (pp. 485–486).

Lenters, J. D., & Cook, K. H. (1997). On the Origin of the Bolivian High and Related Circulation Features of the South American Climate. *Journal of the*

Atmospheric Sciences, 54(5), 656–678. American Meteorological Society. https://doi.org/10.1175/1520-0469(1997)054<0656:OTOOTB>2.0.CO;2

Lyra, A. de A., Chan, C. S., & Dereczynski, C. P. (2007). Indicadores de turbulência a partir de previsões do modelo regional ETA. *Revista Brasileira de Meteorologia, 22*(2), 161–182. https://doi.org/10.1590/S0102-77862007000200003

Marengo, J. A., Soares, W. R., Saulo, C., & Nicolini, M. (2004). Climatology of the Low-Level Jet East of the Andes as Derived from the NCEP–NCAR Reanalyses: Characteristics and Temporal Variability. *Journal of Climate, 17*(12), 2261–2280. American Meteorological Society. https://doi.org/10.1175/1520-0442(2004)017<2261:COTLJE>2.0.CO;2

Marlton, G. J. (2016). *On the development, characterisation and applications of a balloon-borne atmospheric turbulence sensor* (PhD). University of Reading. Retrieved September 9, 2020, from http://centaur.reading.ac.uk/68910/

Mello, I. B. F. de. (2015). *Climatologia e Estudo de Caso da Turbulência de Céu Claro a Partir de Registro de Aeronaves: Análise de dados observacionais e de modelagem* (M.Sc). Instituto Nacional de Pesquisas Espaciais (INPE), São José dos Campos. Retrieved September 9, 2020, from http://mtc-m21b.sid.inpe.br/col/sid.inpe.br/mtc-m21b/2015/03.13.04.06/doc/publicacao.pdf

Menegardo-Souza, F. (2018). *Avaliação dos Resultados do Ábaco de Harrion no Diagnóstico de Turbulência no Cruzamento da Cordilheira dos Andes* (Specialization Course). Instituto de Controle do Espaço Aéreo (ICEA), São José dos Campos, Retrieved September 9, 2020,from https://www.anac.gov.br/assuntos/setor-regulado/profissionais-da-aviacao-civil/meteorologia-aeronautica/arquivos/MET001V_Final_RevisaoBanca_2TMENEGARDO.pdf

Nastrom, G. D., & Fritts, D. C. (1992). Sources of Mesoscale Variability of Gravity Waves. Part I: Topographic Excitation. *Journal of the Atmospheric Sciences, 49*(2), 101–110. American Meteorological Society. https://doi.org/10.1175/1520-0469(1992)049<0101:SOMVOG>2.0.CO;2

National Weather Service. (2020). The Jet Stream. Retrieved September 6, 2020, from https://www.weather.gov/jetstream/jet

Norte, F. A. (2015). Understanding and Forecasting Zonda Wind (Andean Foehn) in Argentina: A Review. *Atmospheric and Climate Sciences, 5*(3),

163–193. Scientific Research Publishing. http://dx.doi.org/10.4236/acs.2015.53012

Paulucci, T. B., França, G. B., Libonati, R., & Ramos, A. M. (2019). Long-Term Spatial–Temporal Characterization of Cloud-to-Ground Lightning in the Metropolitan Region of Rio de Janeiro. *Pure and Applied Geophysics, 176*(11), 5161–5175. https://doi.org/10.1007/s00024-019-02216-1

Pezzi, L. P. P., Rosa, M. B., & Batista, N. N. M. (2020). A Corrente de Jato sobre a América do Sul. *CPTEC*. Retrieved September 11, 2020, from http://climanalise.cptec.inpe.br/~rclimanl/boletim/cliesp10a/jatclim.html

Reboita, M. S., Gan, M. A., Rocha, R. P. da, & Ambrizzi, T. (2010). Regimes de precipitação na América do Sul: Uma revisão bibliográfica. *Revista Brasileira de Meteorologia, 25*(2), 185–204. https://doi.org/10.1590/S0102-77862010000200004

Reinecke, P. A., & Durran, D. R. (2008). Estimating Topographic Blocking Using a Froude Number When the Static Stability Is Nonuniform. *Journal of Atmospheric Sciences, 65*, 1035. https://doi.org/10.1175/2007JAS2100.1

Reiter, E. R. (1969). *Jet-Stream Meteorology*. Chicago: University of Chicago Press.

Sharman, R., Cornman, L., Meymaris, G., & Pearson, J. (2014). Description and Derived Climatologies of Automated In Situ Eddy-Dissipation-Rate Reports of Atmospheric Turbulence. *Journal of Applied Meteorology and Climatology, 53*, 1416–1432. https://doi.org/10.1175/JAMC-D-13-0329.1

Sharman, R., & Pearson, J. M. (2017). Prediction of Energy Dissipation Rates for Aviation Turbulence. Part I: Forecasting Nonconvective Turbulence | Journal of Applied Meteorology and Climatology | American Meteorological Society. *Journal of Applied Meteorology and Climatology, 56*, 317–377. https://doi.org/10.1175/JAMC-D-16-0205.1

Sharman, R., Tebaldi, C., Wiener, G., & Wolff, J. (2006). An Integrated Approach to Mid- and Upper-Level Turbulence Forecasting. *Weather and forecasting, 21*, 268–287. https://doi.org/10.1175/WAF924.1

Sharman, R., & Trier, S. B. (2019). Influences of Gravity Waves on Convectively Induced Turbulence (CIT): A Review. *Pure and Applied Geophysics, 176*(5), 1923–1958. https://doi.org/10.1007/s00024-018-1849-2

Sharman, R., Trier, S. B., Lane, T. P., & Doyle, J. D. (2012). Sources and dynamics of turbulence in the upper troposphere and lower stratosphere: A review. *Geophysical Research Letters, 39*(12). https://doi.org/10.1029/2012GL051996

Shi, W., Higgis, R. W., Yarosh, E., & Kousky, V. E. (2000). The Annual Cycle and Variability of Precipitation in Brazil. *NCEP/Climate Prediction Center Atlas, 9.* Retrieved September 6, 2020, from https://www.cpc.ncep.noaa.gov/research_papers/ncep_cpc_atlas/9/atlas9.htm

Silva, A. R. (2004). *Ondas Orográficas Sobre a Cordilheira dos Andes em Latitudes Subtropicais: Estudo de caso* (M.Sc). Instituto Nacional de Pesquisas Espaciais (INPE), São José dos Campos, Retrieved September 9, 2020, from http://mtc-m16.sid.inpe.br/col/sid.inpe.br/jeferson/2004/05.27.09.45/doc/publicacao.pdf

Smith, R. B. (1989). Mountain-induced stagnation points in hydrostatic flow. *Tellus A, 41A*(3), 270–274. https://doi.org/10.1111/j.1600-0870.1989.tb00381.x

Smith, R. B. (2019). 100 Years of Progress on Mountain Meteorology Research. *Meteorological Monographs, 59*, 20.1-20.73. https://doi.org/10.1175/AMSMONOGRAPHS-D-18-0022.1

Storer, L. N., Williams, P. D., & Gill, P. G. (2019). Aviation Turbulence: Dynamics, Forecasting, and Response to Climate Change. *Pure and Applied Geophysics, 176*(5), 2081–2095. https://doi.org/10.1007/s00024-018-1822-0

Stull, R. B. (1988). *An Introduction to Boundary Layer Meteorology*. Atmospheric and Oceanographic Sciences Library. Springer Netherlands.

Turner, J. (1999). Development of a mountain wave turbulence prediction scheme for civil aviation. *Met Office Forecasting Research Technical Report, 265*.

Vásquez, H., & Falcón, N. (2015). ONDAS DE MONTAÑA EN LA CAPA LÍMITE PLANETARIA DE LA REGIÓN ANDINA VENEZOLANA. *Revista Brasileira de Meteorologia, 30*(3), 241–253. Revista Brasileira de Meteorologia. https://doi.org/10.1590/0102-778620130626

WMO. (1973). *The airflow over moutains*. WMO N 355, Retrieved September 6, 2020, from https://library.wmo.int/doc_num.php?explnum_id=1814

Wolff, J. K., & Sharman, R. (2008). Climatology of Upper-Level Turbulence over the Contiguous United States. *Journal of Applied Meteorology and Climatology, 47*(8), 2198–2214. American Meteorological Society. https://doi.org/10.1175/2008JAMC1799.1

Zhou, J., & Lau, K.-M. (1998). Does a Monsoon Climate Exist over South America? *Journal of Climate, 11*(5), 1020–1040. American Meteorological Society. https://doi.org/10.1175/1520-0442(1998)011<1020:DAMCEO>2.0.CO;2

Zimmermann, D. F. R. (2017). *Climatologia do jato subtropical na América do Sul* (M.Sc). Universidade de São Paulo (USP), São Paulo, Retrieved September 9, 2020, from https://www.iag.usp.br/pos/sites/default/files/d_diego_f_r_zimmermann_corrigida.pdf
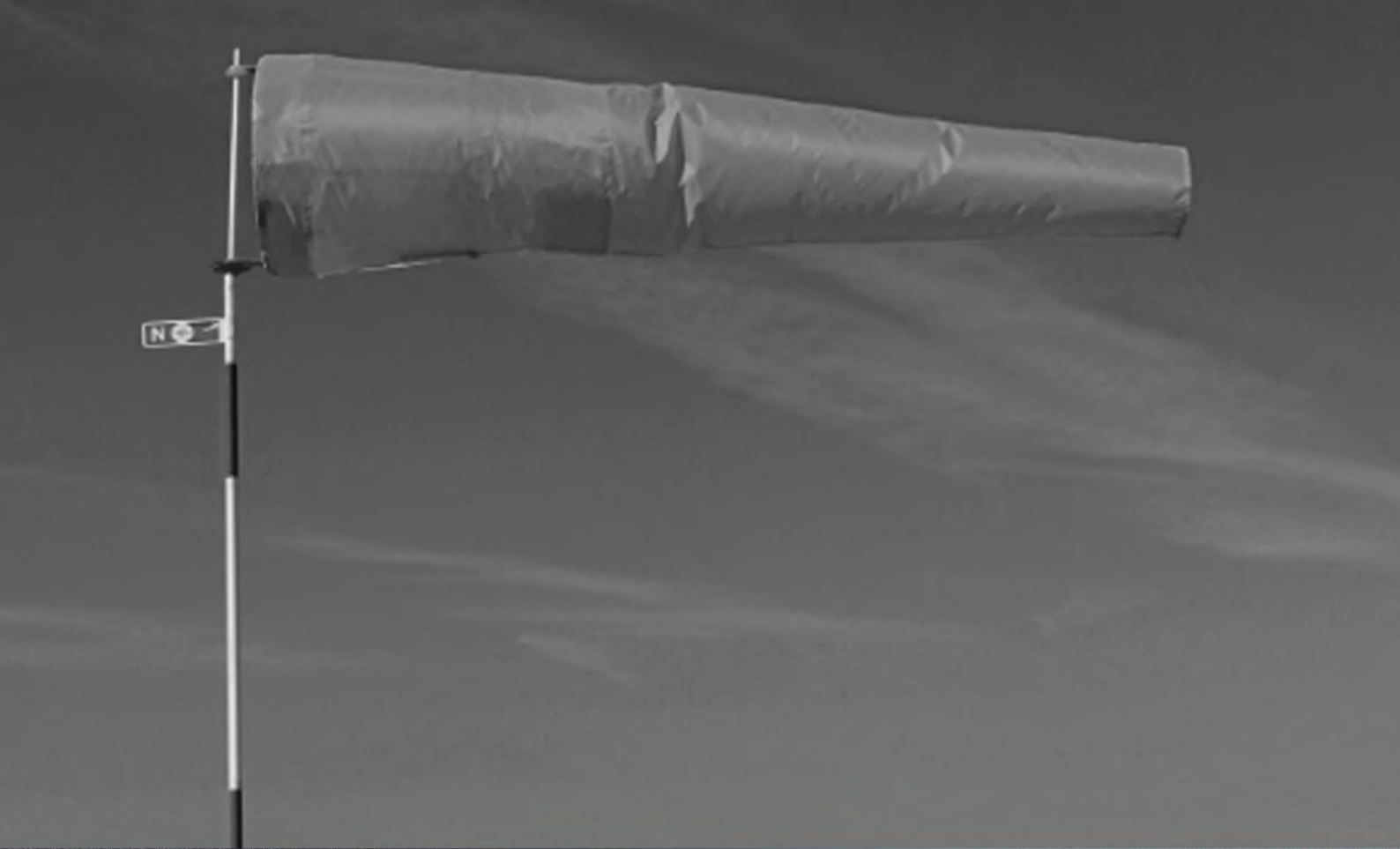
Wind

Nowcasting model of low wind profile based on neural network using SODAR data at Guarulhos Airport, Brazil

Gutemberg Borges França [1]

Manoel Valdonel de Almeida [1]

Suzanna Maria Bonnet [1]

Francisco Leite Albuquerque Neto [1]

ABSTRACT

A generalized regression neural network model was tested—as a nowcasting tool—to forecast the low wind profiles up to 45 minutes (i.e., at heights of 10, 100, 200 and 300 m) at the Guarulhos International Airport, São Paulo, Brazil. A dataset representing over four years was generated from sonic detection and ranging and surface meteorological station, which registered vertical wind profiles with intervals from 10 m to approximately 500 m in height every 15 minutes, and surface meteorological variables were collected each minute, respectively. These data were simultaneously used to train, validate and test the proposed model. The u and v forecasts generated at 300, 200 and 100 m were better than at 10 m, which could certainly be attributable to the surface roughness. In addition, the results also revealed that the performance of the model is time-dependent—decreasing over time —and that this may be correlated with the fact that the neural network is a statistical rather than physical model. The forecasts of wind components u and v are slightly biased (or closely matched to observations) at all heights, and forecast intervals with maximum values have median and average errors equal to 0.070 ms-1 and -0.017 ms-1 , respectively. The forecast model's results were evaluated using the values of four categorical statistics: probability of detection; probability for non-events; bias; and false-alarm ratio, with respectable minimum and maximum values for u wind principal components equal to 0.841, 0.833, 0.159, 0.981 at 10 m for 45 minutes forecasts and 0.989, 0.987, 0.011, 0.999 at 300 m for 15 minutes forecasts, respectively.

1. INTRODUCTION

Landing could be considered the most dangerous phase of a flight, since the aircraft has lower speed and more limited control due to the use of flaps, spoilers and landing gear. In addition, the aforementioned danger may increase if it coexists with meteorological phenomena such as wind gusts, downdrafts or wind shear, which could quickly alter the wind profile and influence the trajectory of the approach for landing.

The traffic pattern of aircraft landing and taking-off in any airport depends mainly on the behaviour of the wind direction profile near the surface. In fact, the runway should have a preferable surface wind blowing in opposite directions for landing and take-off procedures. Therefore, the air traffic controller requires precise short-term wind forecasts in order to make rapid and correct decisions on whether or not the runway-in-use will be changed, considering air traffic flux optimization and safety requirements. At present, the majority of Brazilian airports are lacking sensors capable of generating a precise diagnostic of vertical

[1.] Centro de Ciências Matemáticas e da Natureza (CCMN) - IGEO/Meteorologia, Universidade Federal do Rio de Janeiro (UFRJ), Rio de Janeiro, Brazil

wind profiles at high frequency and detecting changes in the wind direction. Furthermore, the current numerical weather prediction models used in Brazil are not yet able to produce short-term and locally specific predictions of the aforementioned phenomena.

The SOnic Detection And Ranging (SODAR) equipment is an atmospheric profiler with a high frequency of data collection that has been used to investigate the turbulence of the atmospheric boundary layer for the last three decades. Motta *et al.* (2005), Sumner and Masson (2006), Gottschall and Peinke (2008) and Van den Berg (2008) have studied atmospheric stability, wind shear impact and intensity of turbulence in wind energy production using SODAR data. Gerz *et al.* (2009) used SODAR data for diagnosing and nowcasting fog and wind shear at the Frankfurt International Airport. Chan (2014) found efficient uses of SODAR data in detecting turbulence and wind shear at the Hong Kong International Airport. Silva *et al.* (2016) developed a conceptual model for wind profile behaviour based on an investigation of 234 runway-in-use changes using SODAR and surface meteorological station data for the Guarulhos International Airport (Brazil) from 1 September 2011 to 31 December 2013. The results showed that a change of wind direction at 10 m occurs after an interval period of 30 to 60 minutes past the change of wind direction at 300 m. Therefore, the main purpose of this study is to develop a Wind

Profile Forecast Model (WPFM) to generate short-term forecasts of wind profiles at 10, 100, 200 and 300 m for the Guarulhos international airport based on neural network techniques and using SODAR and Surface Meteorological Station (SMS) data.

The present paper is part of a sequence of studies related to nowcasting that has been successfully executed by our group at the Applied Meteorological Laboratory at the Federal University of Rio de Janeiro, as described in Almeida (2009), Silva *et al.* (2016), and França *et al.* (2016).

2. STUDY AREA AND DATA

The Guarulhos International Airport is located in the city of Guarulhos-SP, approximately 25 km from downtown São Paulo. It has two parallel runways aligned in magnetic orientation, i.e., runway 09 (270° magnetic) and 27 (90° magnetic). It is situated at an altitude of 750 m. As in Figure 1, runway 09R has a length of 3000 m and runway 27R 3700 m, while both are 45 m wide. The cross and star, both in red, represent the locations of SODAR and SMS, respectively. [Figure 1 near here] The time period for the data used in this work was from 1 September 2011 to 15 September 2015. Runway 09R is considered the main runway since it is aligned to the prevailing easterly wind, and most take-offs/landings are realized in that direction. Table 1 describes the meteorological variables extracted from each data source.

Figure 1: Runways (yellow arrows) and location of SODAR (red cross) and SMS (red star) at Guarulhos Airport.

Table 1: Data sources, input (primary and derived, corresponding to 58 inputs), and output used for training-validation and testing of all wind profile forecast models.

| Source | Frequency | Inputs | | Output |
		Primary	Derived	
SODAR	15 min.	**v** and **u** wind components at heights of: 30, 60, 90, 120, 150, 180, 210, 240, 270 and 300 m (collected for a given time (T)); TKE*, SigW* and EDR* (at heights: 30, 60, 90, 120, 150 and 180 m).	**v** and **u** wind components at heights: 100, 200, and 300 m (collected for a given T-15 minutes);	Wind profile (**v** and **u** at heights of 10, 100, 200 and 300 m) for 15, 30 and 45 minutes
SMS	15 min.	Temperature in 2 m, atmospheric pressure and dewpoint temperature in 2 m.	**v** and **u** averages of the last two minutes	

TKE*, SigW*and EDR* represent turbulence kinetic energy, standard deviation of vertical wind component and energy dissipation rate, respectively.training-validation and testing of all wind profile forecast models.

3. METHOD

The neural network model is a well-known technique used to classify and recognize patterns. Its principle is to learn patterns from a set of training data and thus develop the ability to correctly classify new standards (Bishop, 2006). The main problem in using neural networks is deducing the proper size of the network to carry out a certain task; here, that task is to forecast a wind profile. According to Haykin (1994), it is not possible to design a high-performance neural network model using its minimum network size. Generally, a neural network is represented by a function, such as:

$$y_k(x,w) = \sigma\left[\sum_{j=0}^{M} w_{kj}^{(2)} h\left(\sum_{i=0}^{D} w_{ji}^{(1)} x_i\right)\right] \qquad (1)$$

where w_{ji} and w_{kj} are the connection weights between input and hidden layers and hidden and output layers, respectively, x_i is the vector of inputs with length D, M is the number of neurons in the hidden layer and y_k is the output vector. The superscripts (1) and (2) of the Equation (1) are references to input and hidden layers, respectively, σ and h are linear and nonlinear transfer functions between neural network model layers, respectively.

Considering the objective previously defined, the neural network model output (y_k) corresponds to forecasts of the wind profile at heights of 10, 100, 200 and 300 m for time periods of 15, 30 and 45 minutes (Table 1, output column). To obtain the optimum WPFM, three steps were followed:

Step 1- data processing: here, the input and output of WPFM were defined. The SMS and SODAR datasets were sorted, and their relevance was statistically analysed from the correlation significance among variables and targets. All selected variables were normalized to a range of [-1, 1]. The wind direction forecast can show some difficulties regarding number sequence discontinuity in a northerly direction, as (for example) when the wind direction changes from 355° to 5° (or vice-versa). To avoid this scenario, the wind vector was decomposed into u and v components and used as WPFM input/output. Initially, 82 variables were selected, but after removing collinear inputs from correlation/autocorrelation analysis (Pasini and Ameli, 2003), 58 variables remained. The time series was divided in three subsets: train (80.0%), validation (10.0%) and test (10.0%). Table 2 shows the total number of meteorological recordings used for each developed model. For a same level and forecast period, the same input dataset in the models WPFM-u and WPFM-v (or WPFM-u-v) were used to predict u and v wind components, respectively.

Table 2: Number of meteorological recordings used for training-validation and testing of WPFM at 10, 100, 200, and 300 m for interval times in the forecasting of 15, 30, and 45 min, respectively.

Level in height (metros)	Forecast period	Number of meteorological recordings			Optimum Number of neurons
		Training and Validation	Test	Total	
	15	9269	2595	11864	131
10	30	9348	2455	11803	128
	45	8347	2087	10434	134
	15	10306	2601	12907	128
100	30	7323	1831	9154	121
	45	7219	1852	9071	120
	15	8448	2113	10561	122
200	30	10141	2468	12609	123
	45	9101	2277	11378	122
	15	8302	2075	10377	124
300	30	7945	1987	9932	126
	45				123

Step 2 – Train-validation of WPFM: This step corresponds to obtaining the optimal topology for each WPFM via the use of a cascade-correlation algorithm (Fahman and Lebiere, 1990) by defining the number of neurons at the hidden layer:

a) This algorithm starts WPFM with only one neuron in the hidden layer. For each interaction, a new hidden unit neuron is added, one by one, resulting in final multi-layer; and

b) Validation corresponds to evaluate the Mean Square Error (MSE) (observation – forecast) by considering the observation as the validation subset. It then returns to (a) if the MSE has not increased from previous interaction or the number of neurons in the hidden layer is less than or equal to 150 (the defined limit). Otherwise, the final WPFM configuration is obtained and thus goes to step 3;

Step 3 – The test of WPFM: The algorithm creates a simple comparison between WPFM results and observations—represented by test subset—by investigating the MSE (observation – forecast). The optimum WPFM is reached when the MSE for the test dataset is acceptable, which here means that a WPFM is able to satisfactorily generate nowcasting of wind profile for specific height and forecast periods. Otherwise, the usual procedure is to try (for example) to introduce eventually new inputs or rearrange/combine them and repeat step 2.

4. RESULTS AND DISCUSSION

The training-test of the neural network is a pivotal phase for the effective model and is usually a trial and error task in order to obtain an optimum model as, for example, discussed by França et al. 2016, Pasini (2015), Pasini (2003) and Pasini et al., (2001). Table 1 and lines 2 and 3 of column 3 present the resulting inputs used for validating all optimum neural networks models to forecast the wind profile at the Guarulhos International Airport. It is observed that the optimal WPFM was obtained by minimizing the MSE rather than by reaching the defined limit of neurons (equal to 150) in the hidden layer, as in Table 2, column 6. Columns 4 and 5 in Table 2 present the number of meteorological recordings used for the training-test and validation of all WPFMs. Column 6 shows the number of neurons for each optimum WPFM obtained.

4.1 WPFM results versus wind observations

To evaluate the potential wind forecast profile model proposed here, the u and v wind observations collected at heights of 10 m from the SMS and at 100, 200, and 300 m from the SMS and SODAR (as in Table 2, column 5) are used for validation of the forecast results generated by WPFM-*u-v* at the wind heights for forecast intervals. Figure 2 shows error histograms (observation–WPFM) for u and v components at

Figure 2: (a–c) and (d–f) are the histogram of errors (observation – WPFM) of u and v wind components at 10 m in height for 15, 30, and 45 min.
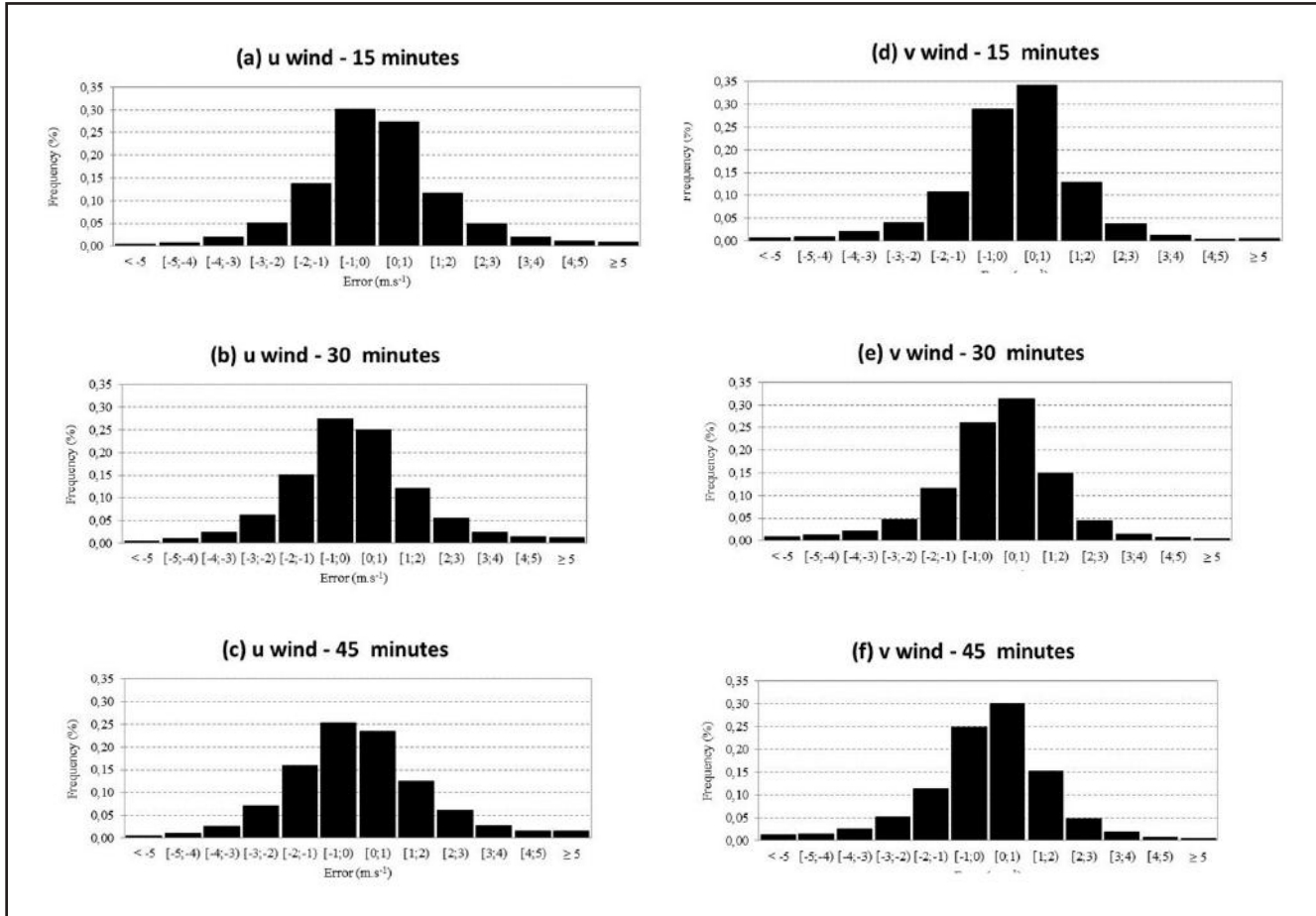
10 m of height for 15, 30 and 45 minutes forecasts. It is evident that the majority of the errors are quite small, and most of the density (more than 90.0%) falls within the interval between [-3, 3] ms^{-1}, independent of wind component. As seen in Table 3, the average (AE) and median (ME) errors are also small, which means that all WPFMs tend to forecast with a slight bias (in some of the models negative and in others positive) compared to the observed data.

**Table 3:** Median and average and errors (observation – forecast) of u and v winds for nowcasting of 15, 30 and 45 minutes.

Wind component	Time (minute)	Statistics	Height (m)			
			10	100	200	300
u	15	MD	0.07	-0.01	-0.02	-0.009
		AE	-0.004	-0.014	-0.003	0.004
	30	MD	0.1	-0.03	-0.01	0.02
		AE	-0.006	-0.017	-0.012	0.026
	45	MD	0.1	-0.03	-0.008	0.011
		AE	-0.02	-0.01	-0.01	0.004
v	15	MD	-0.06	0.004	0.005	0.02
		AE	-0.003	0.004	0.012	0.016
	30	MD	-0.04	-0.01	-0.01	0.007
		AE	0.035	-0.011	-0.007	0.027
	45	MD	-0.09	-0.01	-0.02	-0.02
		AE	-0.006	-0.002	0.001	0.006

Aiming to investigate for which intervals the forecasts of WPFM-*u-v* are more or less accurate, plots of forecasts versus observations were generated, showing 1:1 plots represented by Figure 3 of 10 m in height at 15, 30 and 45 minutes forecasts. This type of plot contrasts the similarities between the model results and observations (Dhar et al., 2014). In general, all WPFMs tend to systematically overestimate at the lower end and underestimate at the higher end. This can be observed for both wind components at all heights and forecast times. Additionally, these differences in the extremes increase over time. The tendency is greatest at 10 m because of surface roughness, which induces higher variance of *u* and

v components than at 100, 200 and 300 m. This means that forecast products are better generated at 300, 200 and 100 m than at 10 m and that all nowcasting undergoes deterioration over time.

Figure 4 displays the hourly frequency of wind direction at 10 m from the meteorological station of the Guarulhos International Airport, excluding calm wind occurrences corresponding to 4.5% of 132,014 events. It is observed that the major frequencies are zonal (East to West) rather than meridional (North to South) from 10° to 200°, directions which correspond to approximately 80.4% of the occurrences. The latter defines that *u* is the domain wind component.

Figure 3: (a–c) and (d–f) are plots of predictions versus observations of u and v wind components at 10 m in height for 15, 30, and 45 mins, respectively.and 45 min.
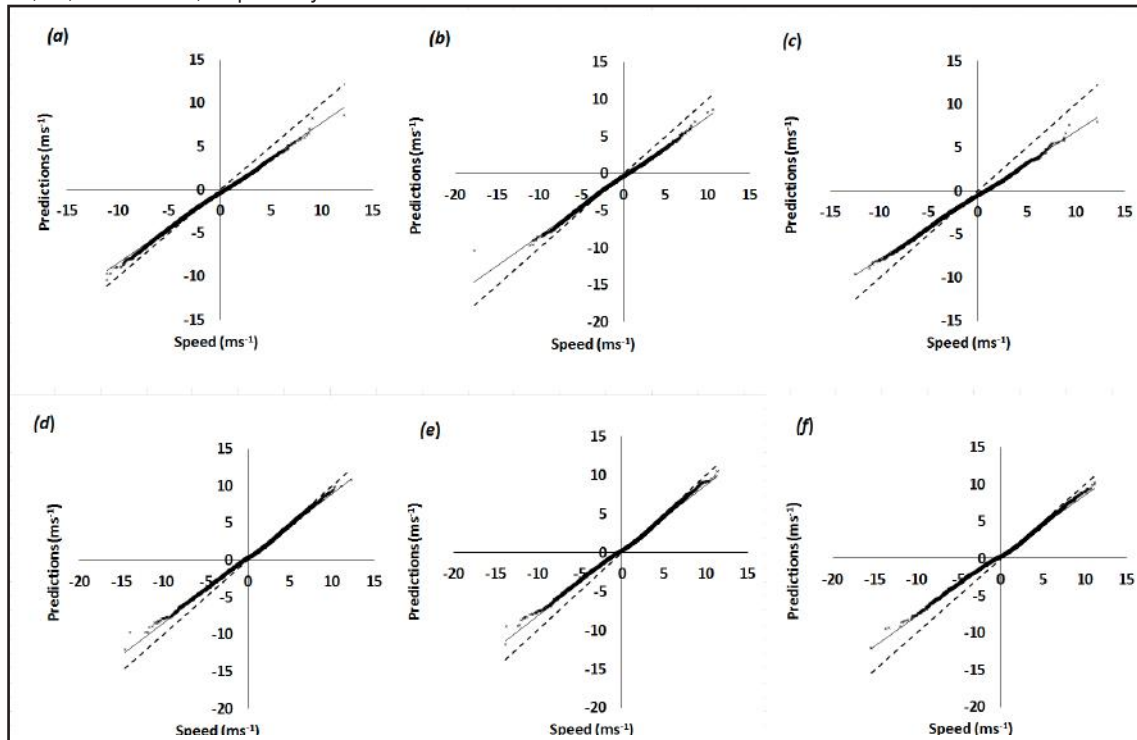
Figure 4: Hourly wind direction at 10 m; climatology of Guarulhos Airport at 10 m in height from 1 January 1987 to 31 December 2006, corresponding to 126,074 samples.
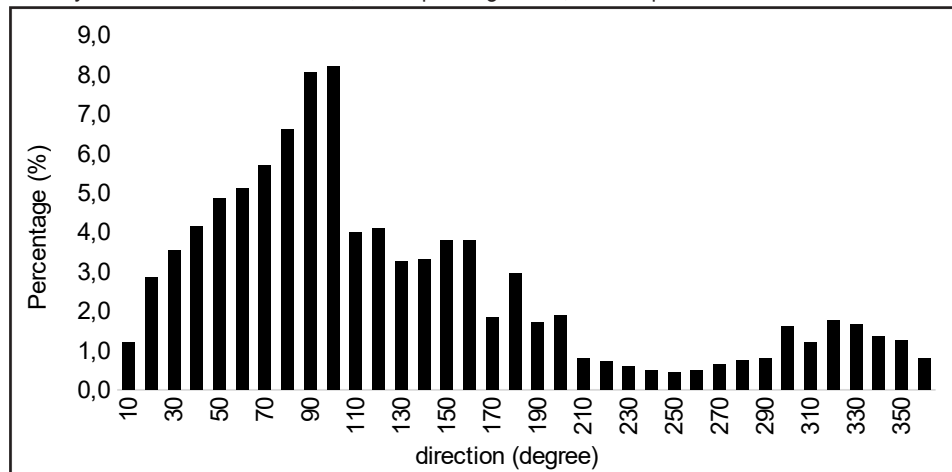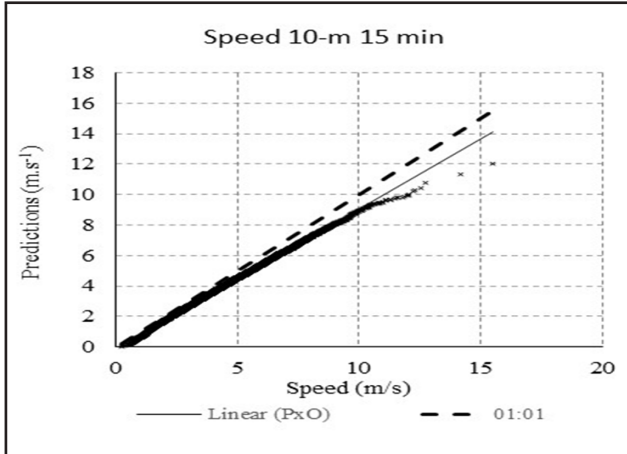
Figure 5 shows the WPFM results for wind speed specifically at 10 m for the 15 minutes forecast period. It reveals that the WPFM results tend to underestimate the high-speed wind (approximately 91.0% of the wind speed observed are below 10 ms^{-1}).

Figure 5: Wind speed observed versus forecasted at 10 m in height for forecast intervals of 15 min.

4.2 Results for aeronautical applications

The runways of Guarulhos International Airport are oriented in magnetic coordinates based on the preferential wind direction Northeast–Southwest, as shown in Figure 4. At this airport, the frequency of high-speed winds is quite negligible. However, since the wind direction should preferably occur in opposition to the wind direction at 10 m, that preferential wind direction plays an important role whether or not the air traffic controller decides to reassess the traffic pattern for landing/take-off procedures. Once the u component is aligned with the runways and, as previously verified, the dominant wind direction at the Guarulhos airport, a high-quality nowcasting of the u component is required to make the decision to change the runway-in-use. Based on ICAO Air Navigation Services Procedures (2007), which are followed by the Brazilian Aeronautics Command (see ICA 100-37, 2016), the criteria to change the runway-in-use is based on whether or not the signal of $u_{t+\Delta t}$ (forecast for Δt minutes) is in opposition to u_t (observation at time t), i.e., from negative to positive direction (or vice-versa), when $\left| u_{t+\Delta t} \right| \geq$ 3 ms^{-1}. Then, in order to evaluate the performance of the WPFM-u-v results, results are cross-verified based on a two-dimensional contingency table. The cross-verification is done while considering two conditions: 1) using all pairs of u and v; and 2) using only samples of u where $\left| u_{t+\Delta t} \right| \geq 3$ ms^{-1}. The latter condition represents typical aeronautical purposes. From this contingency table, certain statistical tests are computed (Wilks, 1995): 1) Probability Of Detection (POD); 2) Probability for non-events (Podno); 3) Bias (the ratio between the frequency of forecasted events and the frequency of observed events) and 4) False-Alarm Ratio (FAR). The aforementioned statistics are determined based a standard contingency table as Table 4.

Table 4: Contingency table for validation statistics representing the sums of each WPFM and observation pair.

	Wind Direction	
	Observation	
Forecast	+	-
+	++	+ -
-	- +	--

The comparisons between u and v statistics (i.e., columns 3, 5, 7 and 9, 10, 11 of Table 5, respectively) show that all v statistics are relatively better, with the exception of Podno at 10 m. Considering the aeronautical purposes (condition 2), the statistics (columns 4, 6 and 8) show that all WPFM-u have good ability to predict u and signal changes with POD, Bias, and FAR. Podno values are highly regarded, and their minimum and maximum values are equal to 0.841, 0.833, 0.159, and 0.981 at 10 m for a 45 minutes forecast and equal to 0.989, 0.987, 0.011, and 0.999 at 300 m for a 15 minutes forecast, respectively. The forecast performance is better at upper levels (300 m) and declines near the surface (10 m). This can be seen for the forecast period too, as the prediction accuracy declines slightly as the forecast period increases. One reason for the WPFM performance degeneration is that a neural network is a data model, which means that the physical aspects are not included.

4. CONCLUSIONS

This study used cascade-correlation training of a generation regression neural network model to nowcast the wind profiles up to 300 m in height at Guarulhos International Airport, and its performance was evaluated using a cross-verification approach. The results indicate that the model has enough skill to perform wind profile forecasts at a specific location for short-term use, as aviation requires. The findings are as follows:

Table 5: Test statistics of cross-verification of u and v wind directions (positive and negative) for forecast intervals of 15, 30, and 45 min, respectively. Columns 4, 6, and 8 are the statistical results for u (or +) greater than or equal to 3 ms 1 for forecast intervals of 15, 30, and 45 min (for 5819 events), respectively.

Wind component		U						V		
		15 min.		30 min.		45 min.		15 min.	30 min.	45 min.
Level (m)	Statistics	all **u**	u≥3m/s	all **u**	u≥3m/s	all u	u≥3m/s	all **v**	all **v**	all **v**
10	POD	0.721	**0.875**	0.713	**0.857**	0.715	**0.841**	0.909	0.904	0.899
	Bias	0.805	**0.926**	0.755	**0.862**	0.713	**0.833**	1.041	1.039	1.044
	FAR	0.279	**0.125**	0.287	**0.143**	0.285	**0.159**	0.091	0.096	0.101
	Podno	0.940	**0.985**	0.941	**0.983**	0.943	**0.981**	0.596	0.572	0.569
	Statistics	all **u**	u≥3m/s	all **u**	u≥3m/s	all u	u≥3m/s	all **v**	all **v**	all **v**
100	POD	0.837	**0.984**	0.797	**0.973**	0.797	**0.955**	0.932	0.915	0.902
	Bias	0.931	**0.975**	0.899	**0.970**	0.899	**0.957**	1.013	1.009	1.010
	FAR	0.163	**0.016**	0.203	**0.027**	0.203	**0.045**	0.068	0.085	0.098
	Podno	0.968	**0.999**	0.962	**0.998**	0.962	**0.996**	0.891	0.865	0.846
	Statistics	all **u**	u≥3m/s	all **u**	u≥3m/s	all u	u≥3m/s	all **v**	all **v**	all **v**
200	POD	0.858	**0.973**	0.825	**0.959**	0.809	**0.956**	0.939	0.925	0.917
	Bias	0.914	**0.995**	0.890	**0.971**	0.859	**0.941**	1.010	1.017	1.009
	FAR	0.142	**0.027**	0.175	**0.041**	0.191	**0.044**	0.061	0.075	0.083
	Podno	0.973	**0.998**	0.967	**0.997**	0.964	**0.996**	0.906	0.886	0.872
	Statistics	all **u**	u≥3m/s	all **u**	u≥3m/s	all u	u≥3m/s	all **v**	all **v**	all **v**
300	POD	0.862	**0.989**	0.844	**0.971**	0.817	**0.929**	0.939	0.928	0.917
	Bias	0.933	**0.987**	0.865	**0.941**	0.826	**0.956**	1.009	1.003	1.004
	FAR	0.138	**0.011**	0.156	**0.029**	0.183	**0.071**	0.061	0.072	0.083
	Podno	0.980	**0.999**	0.978	**0.998**	0.974	**0.995**	0.930	0.917	0.906

The u and v forecasts for 15, 30 and 45 minutes are closely matched to observations at all levels, as indicated by the small average and median errors, which represent that all WPFM forecasts tend towards some minor bias. Considering the absolute value wind speed at 10 m for a 15 minutes forecast period, the WPFM results tend to underestimate the high-speed wind (approximately 91.0% of the wind speed occurrences are below than limit of 10 ms^{-1}).

The u and v forecasts are better generated at 300, 200 and 100 m than at 10 m, which could certainly be blamed on the surface roughness. In addition, the results also revealed that the performance of the model is time-dependent—decreasing over time—and that this may be correlated with the neural network's nature as a statistical rather than physical model.

Regarding the use of the model for possible utilization in decision-making for the runway in use, it is observed that all statistical values are close to ideal; thus, it has potential use as an operational tool to corroborate with the aircraft controller's judgement in making decisions in the future.

ACKNOWLEDGEMENTS

REFERENCES

Almeida, M.V., 2009, *Aplicação de Técnicas de Redes Neurais Artificiais na Previsão de curtíssimo prazo da Visibilidade e Teto para o Aeroporto de Guarulhos* – SP (Doctoral dissertation, COPPE/UFRJ, Federal University of Rio de Janeiro, Brazil).

Bishop, C. M., 2006, *Pattern Recognition and Machine Learning* (Springer, New York, NY, USA, 430 227–229).

Chan, P. W., 2014, Performance and aviation applications of minisodars at Hong Kong International Airport. *Meteorological Applications*, **21**: 62–73. doi:10.1002/met.1388.

Dhar, S. S., Chakraborty, B. and Chaudhuri, P., 2014, Comparison of multivariate distributions using quantile-quantile plots and related tests. *Bernoulli Society for Mathematical Statistics and Probability* Vol. 20, No. **3**, 1484-1506.

Fahlman, S. E. and Lebiere, C., 1990, The cascade-correlation learning architecture. *Advances in Neural Information Processing Systems II*, D. S. Touretzky, ed., Morgan Kaufmann, San Mateo, California, 524 – 532.

França, G. B., Almeida, M. V., Rossete, A. C., 2016, An automated nowcasting model of significant instability events in the flight terminal area of Rio de Janeiro, Brazil. *Atmospheric Measurement Techniques*, v. **9**, p. 2335-2344, 2016.

Gerz, T., Holzäpfel, F., Gerling, W., Scharnweber, A., Frech, M., Wiegele, A., Kober, K., Dengler, K., Rahm, S., 2009, The Wake Vortex Prediction and Monitoring System WSVBS Part II: Performance and ATC Integration at Frankfurt *Airport, Air Traffic Control Quarterly*, Vol. **17**, No. 4, 2009, pp. 323-346.

Gottschall, J. and Peinke, J., 2008, How to improve the estimation of power curves for wind turbines. *Environmental Research Letters* 3.1: 015005.

Haykin, S., 1999, *Neural Networks: A Comprehensive Foundation*, Prentice Hall New Jersey, New Jersey, USA.

Motta, M., Barthelmie, R. J. and Vølund, P., 2005, The influence of non-logarithmic wind speed profiles on potential power output at Danish offshore sites*. Wind Energy* **8** 219–36.

Pasini, A., 2003, *I Cambiamenti Climatici. Meteorologia e Clima Simulato*. Pearson, Italia Spa.

Pasini, A. and Ameli, F., 2003, Radon short range forecasting through time series preprocessing and neural network modelling. *Geophysical Research Letter*, **30**, doi: 10.1029/2002GL016726.

Pasini, A., 2015, Artificial Neural Networks for Small Dataset Analysis. *Journal of Thoracic Disease*, 7(5), 953.

Silva, W. L., Albuquerque Neto, F. A., França, G. B. and Matschinske, M., 2016, Conceptual model for runway change procedure in Guarulhos International Airport based on SODAR data. *The Aeronautical Journal*, 120(1227), 725-734. doi:10.1017/aer.2016.33.

Sumner, J. and Masson, C., 2006, Influence of Atmospheric Stability on Wind Turbine Power Performance Curves. *ASME Journal of Solar Energy Engineering*, 128(4):531-538. doi:10.1115/1.2347714.

Van den Berg, G. P., 2008, Wind Turbine Power and Sound in Relation to Atmospheric Stability. *Wind Energy* 11.2 (2008): 151-169.

Wilks, D. S., 2006, *Statistical Methods in the Atmospheric Sciences: An Introduction*, vol. 59 of International Geophysics Series, Academic Press, London, UK, 255–269.

ICAO, Air Navigation Services Procedures (2007) Brazil, Command of the Air Force, Airspace control Department. *ICA 100-37: Air Traffic Services*. DECEA, 2016.

Conceptual Model for Runway Change Procedure in Guarulhos International Airport based on SODAR Data

Wanderson Luiz Silva[1]

Francisco Leite Albuquerque Neto[1]

Gutemberg Borges França[1]

Martim Roberto Matschinske[2]

ABSTRACT

In this work, we qualify and quantify the advantages of using SODAR (sonic detection and ranging) from current scenarios of Aeronautical Meteorology, with the goal of establishing a conceptual model for runway change procedures at Guarulhos International Airport (São Paulo, Brazil). The methods consist of the analysis of data from DECEA and INFRAERO about the reports of the runway changes in Guarulhos, besides the SODAR data between September 2011 and December 2013. It is noted that in 234 analyzed cases of runway change, there were significant periods of weak intensity wind on the surface as well as the anticipated modification wind direction at altitude detected by SODAR, indicating a future change in levels closer to the surface. Checking the intersection of both scenarios, it is possible to observe that there is time enough so that the air traffic controller could anticipate the needed runway change minimizing the impact on the aircraftflow, and this period has an average duration of 1 hour and 24 minutes. Therefore, it confirms that the preliminary analysis of the information provided by SODAR can help predict alterations in wind direction, requiring redirection and bringing advantages in economic and security terms.

Keywords: Aeronautical Meteorology; Guarulhos Airport; Runway Usage; SODAR.

Nomenclature

AIP = Airport Improvement Program

COPPETEC = Project, Research and Technology Studies Coordination

CTCEA = Brazilian Organization for Scientific and Technological Development of Airspace Control

DECEA = Department of Airspace Control

GMT = Greenwich Mean Time

ICAO = International Civil Aviation Organization

INFRAERO = Brazilian Airport Infrastructure Company

LMA = Laboratory of Applied Meteorology

NREL = National Renewable Energy Laboratory

SBGR = Guarulhos International Airport

SODAR = Sonic Detection and Ranging

UFRJ = Federal University of Rio de Janeiro

WCA = Wind Change in Altitude

Wd = Wind Direction

Wr = Aligned Wind

Wt = Total Wind

[1] Laboratory of Applied Meteorology, Federal University of Rio de Janeiro, Brazil.

[2] Implementation Commission of theAirspace Control System, Brazil. wanderson@igeo.ufrj.br.

1. INTRODUCTION

The atmospheric conditions have positive or negative influences on aviation in any time and place[1]. Meteorological products for aviation are chosen according to the user's knowledge of their applications, need and operational significance, ease of access and available technology. The Aeronautical Meteorology marks conditions through observations with continuous and integrated monitoring of the meteorological variables on the surface and at altitude, serving as raw material for the most appropriate operating procedures for safe, efficient and economical air traffic flow.

The first 500 meters of the atmosphere, starting from the surface, is most critical especially for the initial and final stages of flight operations due to possible presence of turbulence, wind shear, sudden changes in wind direction and formation of fog[2]. These unsteady low-altitude atmospheric phenomena have negative impacts on safety of flight during take-off, final approach and landing phases at which aircraft have relatively lower airspeed and compromised maneuverability by extension of flaps, spoilers and exposed landing gear. However, the surface meteorological stations installed in airports are incapable of detecting most of the mentioned phenomena. Altitude meteorological stations would be able to detect such phenomena, but their temporal resolution of 12 hours (published at 00 GMT and 12 GMT) makes this capacity incompatible with the frequency and the time of occurrence of the reported phenomena.

The staff of Applied Meteorology Laboratory at the Federal University of Rio de Janeiro (LMA – UFRJ) has been conducting studies and experiments with two SODAR (Sonic Detection and Ranging) equipments installed in Guarulhos International Airport (SBGR, São Paulo, Brazil) since 2011. This equipment is a low-cost, easily installed

Figure 1: SODAR (Sonic Detection and Ranging) equipment.

acoustic wind profiler (Fig. 1) that uses the reflection of acoustic pulses in the atmospheric inhomogeneities to estimate the wind direction and speed in three dimensions at 15-minute intervals[3]. These activities have been allowing the development of methods for detection and prediction of phenomena in question, with a potential of sequencing arrival and departures optimally, as well as an increase in flight safety.

A monitoring and short-term forecasting ("nowcasting") study of local weather was developed at Frankfurt International Airport in Germany using SODAR and other instruments[4]. The analysis showed a fairly stable system and the time of separation between aircraft could be reduced by about 75% when compared to the stipulated time by the International Civil Aviation Organization (ICAO)[5]. The National Renewable Energy Laboratory (NREL[6]) compared wind direction and speed data for 120 days coming from a meteorological tower, 70 meters high with measurements made by a SODAR instrument in Hebei (China). The data measured by SODAR showed excellent agreement with the meteorological tower data, with correlation coefficients equal to or greater than 0.96.

Chan examined the application and the performance of two minisodars at the Hong Kong International Airport (China)[7]. The available data measurements in various heights show that minisodars grant, in general, reliable information for aviation. They provide useful indications of windshear at low levels, mechanical turbulence associated with markedly rough terrain, and downburst related to thunderstorms. Through these case studies, it was found that minisodars are very fruitful in monitoring wind direction change at low levels, since these events may compromise aircraft performance and safety.

The goal of this study is the qualification and quantification of the existing gains in the use of wind profiler information (SODAR) at Guarulhos International Airport (São Paulo, Brazil) to serve as the scope for establishing a conceptual model for changing in runway-in-use procedure, aiming to enhance air traffic safety and save aircraft fuel, allowing planning the change of runway in use driven by the shift in wind direction, in order to minimize delays in landing and take-off procedures on these cases.

2. DATA AND METHODOLOGY

According to the Airport Improvement Program (AIP), São Paulo/Guarulhos International Airport (SBGR) has two parallel runways which are identified as 09R/27L and 09L/27R (Figure 2). The length of runway 09R/27L and 09L/27R are 3000 m (9842 ft) and 3700 m (12139 ft), respectively[8]. Runways cannot be used simultaneously since the lateral spacing between their centerlines is less than the minimum safe wake turbulence separation of 760 m (2500 ft).

Figure 2: Schematic illustration of the runways from Guarulhos International Airport.

In situations with a low volume of air traffic, runway 09L/27R is used because this runway is longer and is closer to the airport apron. At times of heavy air traffic volume, runway 09L/27R is used for take-off and runway 09R/27L is used for landing, because the latter runway has high-speed exits and its threshold begins 500m before the threshold of the runway 09L/27R, preventing the turbulence wake of landing aircraft from interfering with aircraft operating on runway 09L/27R. Runway 09 is aligned to the prevailing east wind, so it is considered the standard airport runway. Therefore, in the presence of west winds, the direction of landings and take-offs must be changed to the Runway 27, as explained below.

The methodology is based on an evaluation of data from SBGR, where there are two SODAR installations next to its runways. Therefore, the methods consist in collecting data from the Department of Airspace Control (DECEA) and on the Brazilian Airport Infrastructure Company (Infraero) about the change in runway-in-use reports at SBGR, along with the SODAR data at the airport. This study analyzes change in runway-in-use cases with SODAR data from September 2011 to December 2013 (234 cases) following the conceptual model described hereafter.

a) Firstly, cases with Runway 09 changed to Runway 27 at the airport between September 2011 and December 2013 (available total time) are identified

via movement data in SBGR. Analyses are based on dates and times (GMT) when the changes in runway-in-use took place.

b) From the cases identified in the item a, those cases that wind actually changed at the surface are selected, that is, when there really was a need for runway change (with or without change in runway-in-use from air traffic control tower). Wind changes at altitude occur earlier than on the surface since the increased viscous friction near the ground delays the propagation of these changes in the wind field. Thus, only those that SODAR detected in relative advance of wind alteration at 300 m above the runway surface are considered. Moreover, the main objective of this study is focused on the gain that the instrument can provide, so it is selected to work only the cases which it is observed. This refers to about 92% of the total.

c) Considering the wind profile change described in item b, these wind direction change patterns at the surface are identified via SODAR data. In Figure 3, as an example, it is shown the wind vector measured by SODAR on 09/05/2011 in several vertical levels. It is noted that around 11 a.m., the wind modified its direction on the surface (from NE to NW), and at 300 m it had already changed around 10 a.m., as highlighted in the black box.

Figure 3: 05th September 2011.
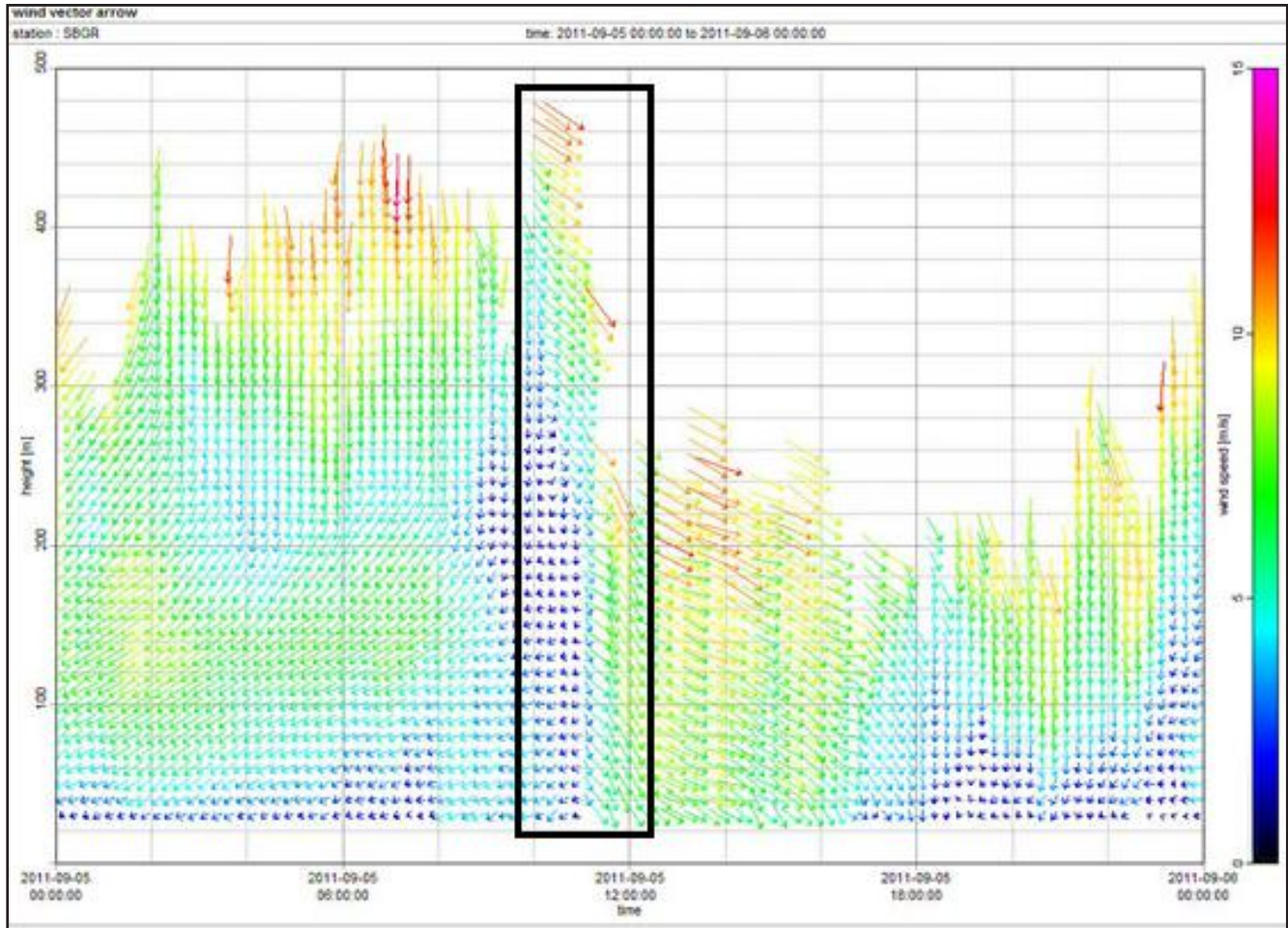
d) Then, the resultant speed components aligned with the runway direction on the aircraft are calculated. This is made with wind direction and speed data on surface (minute by minute), considering operations on the Runway 09, in accordance with Equation 1:

$$Wr = Wt.\cos\left(Wd - \varphi\right) \qquad (1)$$

where **Wr** is the wind component aligned with the runway (the wind component in the direction of landing or take-off) in *knots*, **Wt** is the total wind in *knots*, **Wd** is the wind direction in *degrees* and φ is the magnetic North correction. The 9 and 27 runways of Guarulhos airport are oriented to the magnetic north, that is, with a difference of around 20° to the true north. Since the runways are oriented east to west, there is a slight inclination, as seen in Fig. 2. This explains the reason for the difference between the wind direction Wd and the angle of $\emptyset = 70°$ in the cosine of Equation (1). Thus, winds direction between 340° and 160°, passing by 0° (360°), mean normal operation on the 09 runway, while wind direction between 160° and 340° indicates the need to use the 27 runway.

The Department of Airspace Control (DECEA)[9], which regulates the choice of runway, provides a selection of the most advantageous runway to air traffic control when the total wind Wt is less than 6Kn. In this work, the definition of calm period relates to an aligned wind speed Wr that does not cause any inconvenience to air traffic (<1-6Kn).

e) From the aligned wind **Wr**, wind intensity values between 0 and 6 knots are filtered to check the calm period in each value selected with the aim of future comparisons, in order to define which one is the best to adopt.

f) Finally, the start time of the calm period via minute-by-minute surface data is identified. As the main goal is to identify the time between the calm period (with wind change in altitude in order to indicate future need of change in runway-in-use) and the time when the wind finally changes its direction on the surface, these conditions are evaluated with the aim of quantifying this period.

Figure 4 shows a schematic diagram representing briefly the applied methodology in this study. Once SODAR detects the wind direction change at altitude, it must be observed when the air is calm at the surface. Thereafter, it becomes possible to arrange for a runway change before the wind direction change at the surface, so that the aircraft flow doesn't suffer significant disruption.

Figure 4: Schematic flowchart representing shortly the methodology of this research.
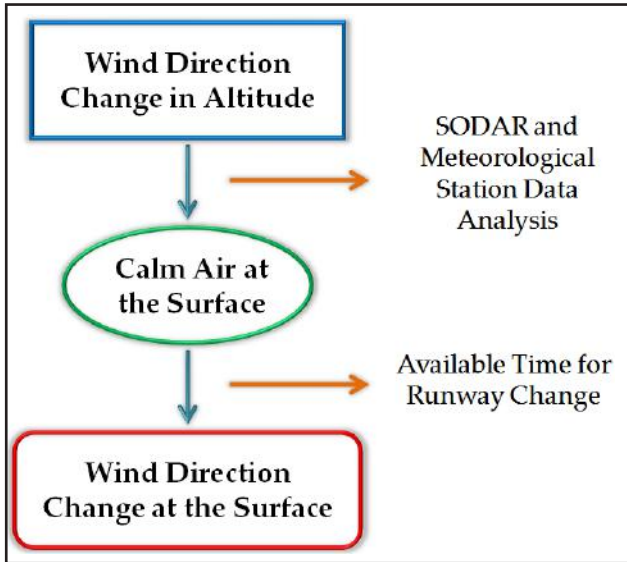

3. RESULTS AND DISCUSSIONS

In Table 1, as an initial demonstrative example, it is presented the values for the aligned wind **Wr** module up to 4 knots, that is, the analysis considering possible change in runway-in-use in SBGR with **Wr** module less than 4 knots and wind at 300 m with indicative of changing its direction between September and November 2011. The first two columns indicate the date and the time, respectively, when there was change in runway-in-use ordered by the air traffic controller. Then, it is shown the begin (outset) of the calm periods around the change in runway-in-use time, so the period during which the aircraft from SBGR remained under aligned wind **Wr** less than 4 knots.

Soon after the start times of calm periods in Table 1, there are the times when the wind began to change its direction at 300 m to indicate future change in runway-in-use (that is, out of the range between 340° and 160°) and the times when it changed on the surface, that is, the moment when it went from headwind to tailwind on the Runway 09 (even that below the maximum value of calm period). This is verified more intuitively knowing that positive values of Equation 1 indicate a headwind (09 runway, winds between 340° and 160°), while negative values indicate a tailwind (need to switch to Runway 27, winds between 160° and 340°), as the wind rose shown in Figure 5.

Table 1: Analysis for the ligned wind Wr module up to 4 knots.

Date	Time (Runway Change)	Outset	Time - Wind Change (Altitude)	Time - Wind Change (Surface)	Total Time
9/5/11	16:04	15:59	13:30	14:05	00:00:00
9/6/11	07:33	07:19	05:00	05:54	00:00:00
9/8/11	15:16	15:12	13:45	14:43	00:00:00
9/9/11	08:49	-	06:45	07:39	-
9/9/11	17:43	-	15:15	17:05	-
9/20/11	14:26	14:05	12:30	13:56	00:00:00
9/21/11	11:02	04:26	10:00	11:09	01:09:00
9/23/11	15:50	13:44	15:00	15:50	00:50:00
10/1/11	15:12	-	14:00	14:38	-
10/2/11	14:28	07:10	12:00	14:27	02:27:00
10/8/11	20:18	-	19:00	19:45	-
10/14/11	09:39	05:50	08:00	09:18	01:18:00
10/25/11	14:30	14:17	13:45	14:27	00:10:00
10/26/11	07:24	00:00	02:00	07:25	05:25:00
10/27/11	11:34	01:35	06:15	11:30	05:15:00
10/29/11	17:07	14:21	16:00	16:54	00:54:00

Figure 5: Finally, the start time of the calm period via minute-by-minute surface data is identified. As the main goal is to identify the time between the calm period (with wind change in altitude in order to indicate future need of change in runway-in-use) and the time when the wind finally changes its direction on the surface, these conditions are evaluated with the aim of quantifying this period.
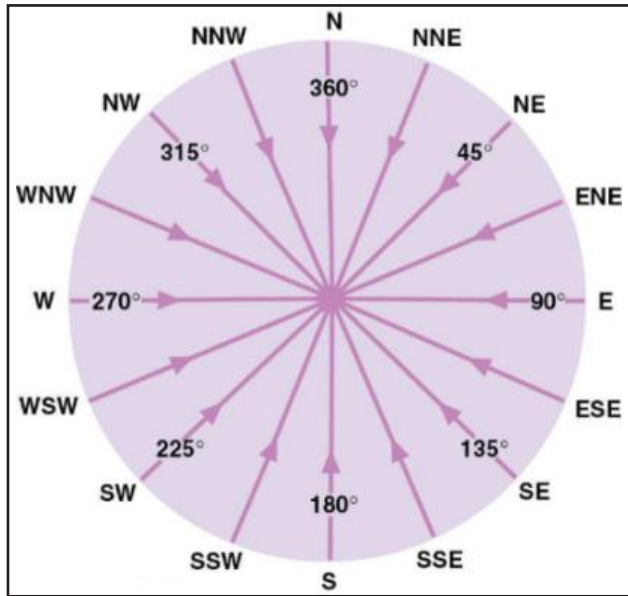
In this way, it was possible to make a calculation of the available total time to change in runway-in-use by programmed way (last column), meeting economy and safety criteria, considering that for the runway modification, it is necessary the coincidence of calm period on surface with wind direction alteration at 300 m. Between September 2011 and December 2013 were analyzed 234 cases of change in runway-in-use, as described previously. Table 2 summarizes the available average time in each calm period (according to **Wr** values) for that change in runway-in-use could be carried out in order to contribute to greater efficiency in air traffic flow.

In all cases evaluated, there were significant calm periods on the surface, as well as the anticipated modification of the direction of the wind at altitude, indicating a later change at the surface. Checking the intersection of both scenarios, it was observed that there is adequate time for the air traffic controller to perform the change in runway-in-use, minimizing the impact on the aircraft flow. This period has an average duration of 1 hour and 24 minutes considering calm period with **Wr** less than 4 knots and 1 hour and 42 minutes to calm period with **Wr** less than 5 knots.

It is important to note that the available periods to change in runway-in-use vary by method of evaluating the calm period. For example, considering calm period with **Wr** less than 3 knots, there is a period for changing in runway-in-use about 1 hour and 12 minutes while for calm period with **Wr** less than 6 knots, this time settles around 1 hour and 56 minutes.

Figure 6 shows the statistics associated with the changes in runway-in-use at Guarulhos airport taking into account wind and time (chronological) conditions sufficiently reasonable for the air traffic. From 234 cases with change in runway-in-use, in 196 of them (84%) there was an indication, more than 20 minutes in advance of wind direction change by SODAR at higher levels (about 300 meters), before it changes on surface, regardless of the calm period. This information is already significantly valuable for operational organization purposes of landings and take-offs at an airport, since the indication that in the future the wind at surface will change is essential for the proper precautions.

If we evaluate the cases in which this wind direction change anticipation was followed by calm period on surface, it is observed that in 41% of cases there was enough time (more than 20 minutes) for air traffic redirection under calm conditions with **Wr** less than 4 knots and 58% for 5 knots. Obviously, the higher the level considered to calm period, the longer available time the air traffic controller will have to perform the change in runway-in-use. Therefore, it confirms that the preliminary analysis of information provided by SODAR can help to predict these changes, enabling a flow redirection and bringing advantages in economic and security terms.

Table 2: Mean time available for changing in runway-in-use related to calm periods of aligned wind **Wr**.

Calm Period	Time
Wr < 1 knots	00h07min
1 < Wr < 2 knots	00h32min
2 < Wr < 3 knots	01h12min
3 < Wr < 4 knots	01h24min
4 < Wr < 5 knots	01h42min
5 < Wr < 6 knots	01h56min

Figure 6: Percentage of cases in which there was a time of 20 minutes or more to perform the change in runway-in-use for safety reasons within 234 analysed occurrences. We consider cases where SODAR detected wind change in altitude (WCA), regardless of the calm period on surface, in addition to the occurrences where such changes were accompanied by calm periods with Wr less than 1, 2, 3, 4, 5 and 6 Kn, and calm period for Wt less than 6Kn.
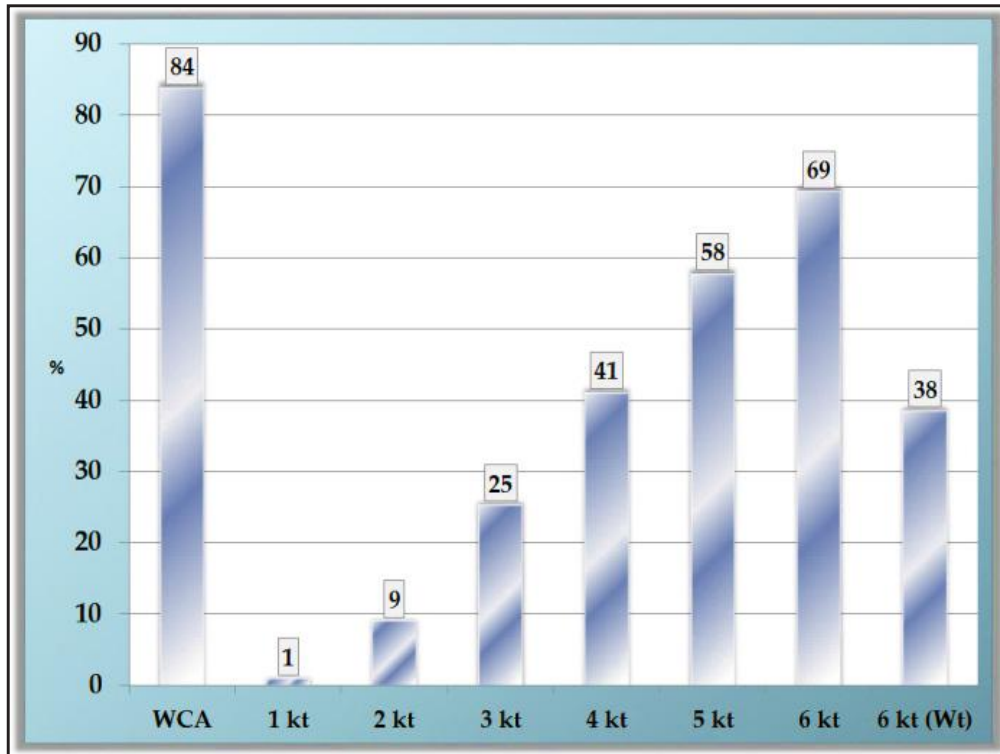
4. CONCLUSIONS

The creation and description of a conceptual model for changing in runway-in-use procedure in Guarulhos International Airport recognises that air traffic control centres depend dramatically on knowledge of weather conditions for their operations.

In the event of wind direction change, the runway for landings and take-offs must be changed so that aircraft always land or take off in the opposite direction to the wind at the surface and in the first metres of height above the airport. It was observed that there is enough time for the air traffic controller to plan and perform the change in runway-in-use minimizing the impact on the aircraft flow with the support of SODAR, and this period has an average duration of 1 hour and 24 minutes considering calm period **Wr** less than 4 knots. In addition, it was found that in 58% of cases there was time (more than 20 minutes) for air traffic redirection under conditions of calm period on surface with **Wr** below 5 knots, preceded by wind change in altitude detected by SODAR.

With this in mind, and knowing that the wind direction change associated with breezes and frontal systems primarily occurs first a few hundred meters above the surface, mainly due to friction, the preliminary analysis of information provided by SODAR can help predict these changes enabling a redirection of traffic flow and bringing advantages in economic and security terms, as shown. Currently, the LMA-UFRJ is developing predictive models based on artificial neural networks to perform nowcasting up to an hour at intervals of 15 minutes of the wind direction and speed in Guarulhos airport.

ACKNOWLEDGMENTS

REFERENCES

1. AHRENS, C. D. Meteorology Today - Introduction to Weather Climate and Environment, **9**th Edition, *Brooks/Cole*, CA, USA, 2008.

2. WALLACE, J. M. and HOBBS, P. V. Atmospheric Science - An Introductory Survey, **2**nd Edition, *Academic Press*, 2006.

3. SODAR Manual. Scintec Flat Array Sodars - Software Manual APRun, Version **1.22**, *Scintec AG*, Rottenburg, Germany, 2010.

4. GERZ, T., HOLZÄPFEL, F., GERLING, W., SCHARNWEBER, A., FRECH, M., KOBER, K., DENGLER, K. and RAHM, S. The Wake Vortex Prediction and Monitoring System WSVBS Part II: Performance and ATC Integration at Frankfurt Airport, *Air Traffic Control Quart*, **17**, (4), pp. 323-346, 2009.

5. ICAO – INTERNATIONAL CIVIL AVIATION ORGANIZATION. Air Traffic Management – Procedures for Air Navigation Services, *Doc 4444, ATM/501*, **15**th Edition, pp. 180, 2007.

6. NREL – NATIONAL RENEWABLE ENERGY LABORATORY. Comparison of Triton SODAR Data to Meteorological Tower Wind Measurement Data in Hebei Province, China, *NREL/TP-5000-52709,* **38**, 2012.

7. CHAN, P. W. Performance and Aviation Applications of Minisodars at Hong Kong International Airport, *Meteorological Applications*, **21**, pp. 62-73, 2014.

8. DECEA – Department of Airspace Control. ROTAER – Publicação Auxiliar de Rotas Aéreas, *Comando da Aeronáutica*, **5**th Edition, pp. 778, 2014.

9. DECEA – Department of Airspace Control. ICA – Instrução do Comando da Aeronáutica **100-12** / Regras do Ar, Ministério da Defesa, pp. 77, 2013.
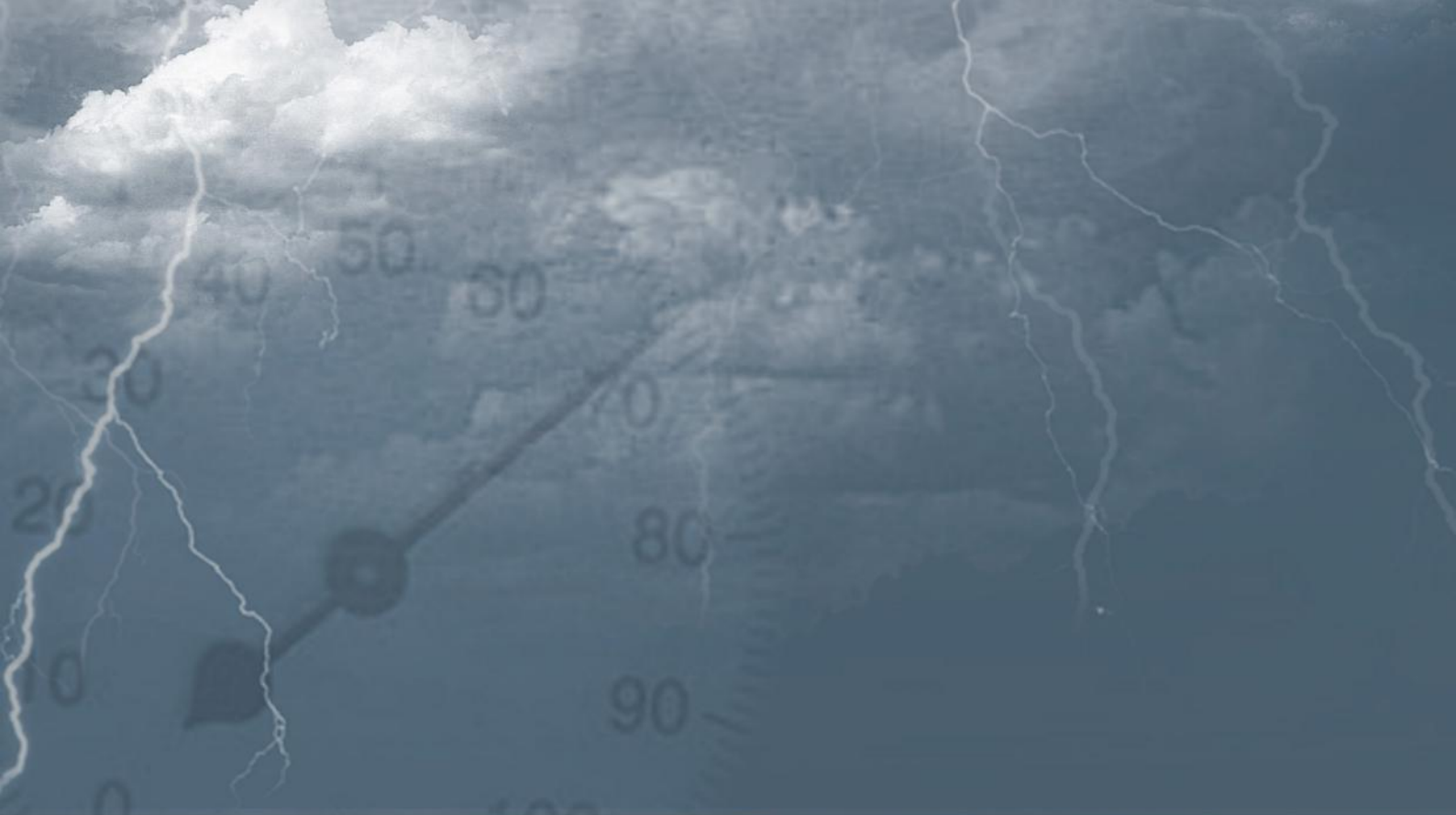
Review

A Review Of High Impact Weather For Aviation Meteorology

I. Gultepe [1,2,3]

[1]Ismail Gultepe, MRD, ECCC, Toronto, Ontario, Canada. Ismail.gultepe@canada.ca
[2]Adj. Prof., Appl. Sci. and Engineering Faculty, University of Ontario Institute of Technology, Oshawa, ON, Canada

R. Sharman;sharman@ucar.edu;
National Center for Atmospheric Research, Research Applications Laboratory
P.O. Box 3000, Boulder, Colorado 80307

Paul D.Williams;p.d.williams@reading.ac.uk
Department of Meteorology, University of Reading, Earley Gate, Reading RG6 6BB, UK

Binbin Zhou;Binbin.Zhou@noaa.gov
IMSG and EMC/NCEP/NOAA, College Park, MD, USA

G. Ellrod;gary.ellrod@gmail.com
EWxC, LLC, Granby, CT, USA

P.Minnis; p.minnis@nasa.gov
Science Systems and Applications, Inc.One Enterprise Parkway, Suite 200, Hampton, VA 23666

Stan Trier, trier@ucar.edu
National Center for Atmospheric Research, Research Applications Laboratory
P.O. Box 3000, Boulder, Colorado 80307

S.Griffin,sarah.griffin@ssec.wisc.edu
Space Science and Engineering Center, Cooperative Institute for Meteorological Satellite Studies (CIMSS)
1225 W. Dayton, University of Wisconsin – Madison, Wisconsin 53706

Seong.S.Yum,seongsooyum@gmail.com
Dept. of Atmospheric Sciences, Yonsei Univeristy,Seoul 03722, Korea

B. Gharabaghi;bgharaba@uoguelph.ca
Water Resources Engineering, School of Engineering, University of Guelph,
50 Stone Road East, Guelph, Ontario, N1G 2W1, Canada

W. Feltz;wayne.feltz@ssec.wisc.edu
Space Science and Engineering Center,Cooperative Institute for Meteorological Satellite Studies (CIMSS)
1225 W. Dayton, University of Wisconsin – Madison, Wisconsin 53706

M.Temimi; marouane.temimi@ku.ac.ae
Water & Environ. Eng. Program, Masdar Institute, Khalifa University of Science and Technology, Abu Dhabi, UAE

Z. Pu;zhaoxia.pu@utah.edu
Department of Atmospheric Sciences, University of Utah, Salt Lake City, Utah, USA

L.N.Storer;luke.storer@pgr.reading.ac.uk
Department of Meteorology, University of Reading, Earley Gate, Reading RG6 6BB, UK

P.Kneringer, philipp.kneringer@uibk.ac.at
University Innsbruck ,Innsbruck, Tirol Austria

M.J. Weston,mjweston@masdar.ac.ae
Masdar Institute of Science and Technology, Abu Dhabi, UAE
Hui-ya Chuang, hui-ya.chuang@noaa.gov
NCEP Environmental Modeling Center, 5830 University Research Court, College Park, MD 20740, USA

L. Thobois, lthobois@leosphere.com
Leosphere Inc., 3 Rue Jean Rostand 91400 Orsay, France

[3] Corresponding Author: Ismail Gultepe, MRD, ECCC, Toronto, Ontario, Canada. Ismail.gultepe@canada.ca

A.P. Dimri, apdimri@hotmail.com
School of Environmental Sciences, Jawaharlal Nehru University, New Delhi, India

S.J. Dietz, Sebastian.Dietz@uibk.ac.at
University of Innsbruck, Innsbruck, Austria

Gutemberg B. França, gutemberg@lma.ufrj.br
M.V. Almeida,valdonel@lma.ufrj.br
F.L. Albquerque Neto, albuquerque@lma.ufrj.br
Department of Meteorology Federal University of Rio de JaneiroAs. Athos da Silveria Ramos, 274 Cidade Universitária 22941-616, Rio de Janeiro, Brazil

Abstract

This review paper summarizes current knowledge available for aviation operations related to meteorology and provides suggestions for necessary improvements in the measurement and prediction of weather-related parameters, new physical methods for numerical weather predictions (NWP), and next-generation integrated systems. Severe weather can disrupt aviation operations on the ground or in-flight. The most important parameters related to aviation meteorology are wind and turbulence, fog visibility (Vis) and ceiling, rain and snow amount and rates, icing, ice microphysical parameters, convection and precipitation intensity, microbursts, hail, and lightning. Measurements of these parameters are functions of sensor response times and measurement thresholds in extreme weather conditions. In addition to these, airport environments can also play an important role leading to intensification of extreme weather conditions or high impact weather events, e.g., anthropogenic ice fog. To observe meteorological parameters, new remote sensing platforms, namely wind LIDAR, sodars, radars, and geostationary satellites, and in-situ instruments at the surface and in the atmosphere, as well as aircraft and Unmanned Aerial Vehicles (UAV) mounted sensors, are becoming more common. At smaller time and space scales (e.g., <1 km), meteorological forecasts from NWP models need to be continuously improved for accurate physical parameterizations. Aviation weather forecasts also need to be developed to provide detailed information that represents both deterministic and statistical approaches. In this review, we present available resources and issues for aviation meteorology and evaluate them for required improvements related to measurements, nowcasting, forecasting, and climate change, and emphasize future challenges.

Keywords: Fog and precipitation visibility, Aviation Meteorology, Ice microphysics, Wind shear and Gust, Nowcasting and Forecasting.

1. INTRODUCTION

Numerous studies have shown that weather severely impacts both civilian and defense aviation operations (e.g., Cook et al. 2009, Rudra et al., 2015, Gultepe et al. 2014; 2017a). The impact of atmospheric processes on aviation has been recognized since the 1900s. For example, Dines (1917) stated that

> "thus it appears that the demand of the airman on the meteorologist is that he shall be able to forecast wind and fog, and to less extent clouds, on the route, the airman is proposing to follow."

Presently, his comments on aviation-related parameters such as wind speed (U_h) and visibility (V_{is}) are still valid.

Weather conditions that cause or contribute to the aviation accidents include wind, visibility/ceiling, high density altitude, turbulence, carburetor icing, updrafts/downdrafts, precipitation, icing, thunderstorms, wind shear, thermal lift, temperature (T) extremes, and lightning (NTBS 2010). Figure 1a shows a bar plot of the statistics of weather-related conditions from 1994 to 2003 that affect near-surface aviation operations; they are mostly wind and visibility (NTSB 2010). In Figure 1a, Vis, ceiling height (hc), and precipitation related conditions occurred 485 times, wind and turbulence 1381 times, and icing and engine icing 150 times. This work suggested that from 2003 through 2007, there were 8,657 aviation related accidents and weather was a factor in 1,740 of these accidents. Figure 1b shows these parameters in percentiles also for 1994-2003 period; wind and visibility are still the most critical parameters. For small, non-commercial aircraft (Part 91 class) the primary cause of weather-related accidents from 2000-2011 was adverse winds, followed by low ceilings (hc) (Figure 1c). At cruising levels of commercial jet aircraft (Part 121 class), this picture is different, with over 70% of weather-related accidents from 2000-2011 being related to turbulence (Figure 1d) (e.g., Sharman and Lane 2016).

Figure 1: Statistics for 2223 aircraft related accidents related to meteorological parameters during 2003-2017 time period; (a) actual numbers of accidents, and (b) probabilistic distributions (NTSB aviation accident and incident data base; NTSB 2007).
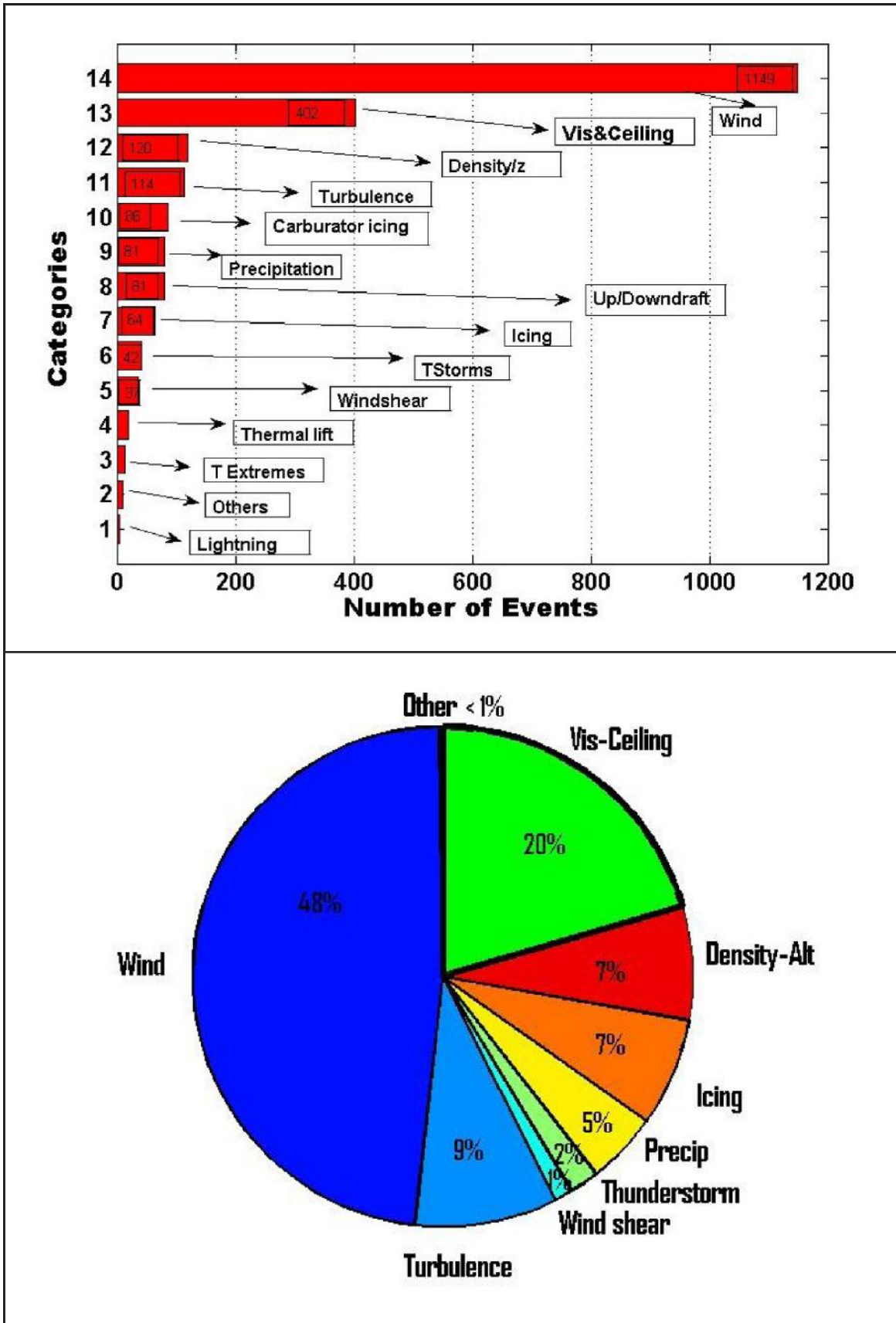
Continued; (c) Part 91-Weather as cause/factor during all accidents for the period of 2000-2011. The NTSB (national Transportation Safety Board) based statistics which resulted in 19441 accidents and 29% of these accidents was related to weather conditions (Eick, 2017). (d) Part 121-air carrier weather related cause/factors for 2000-2011.
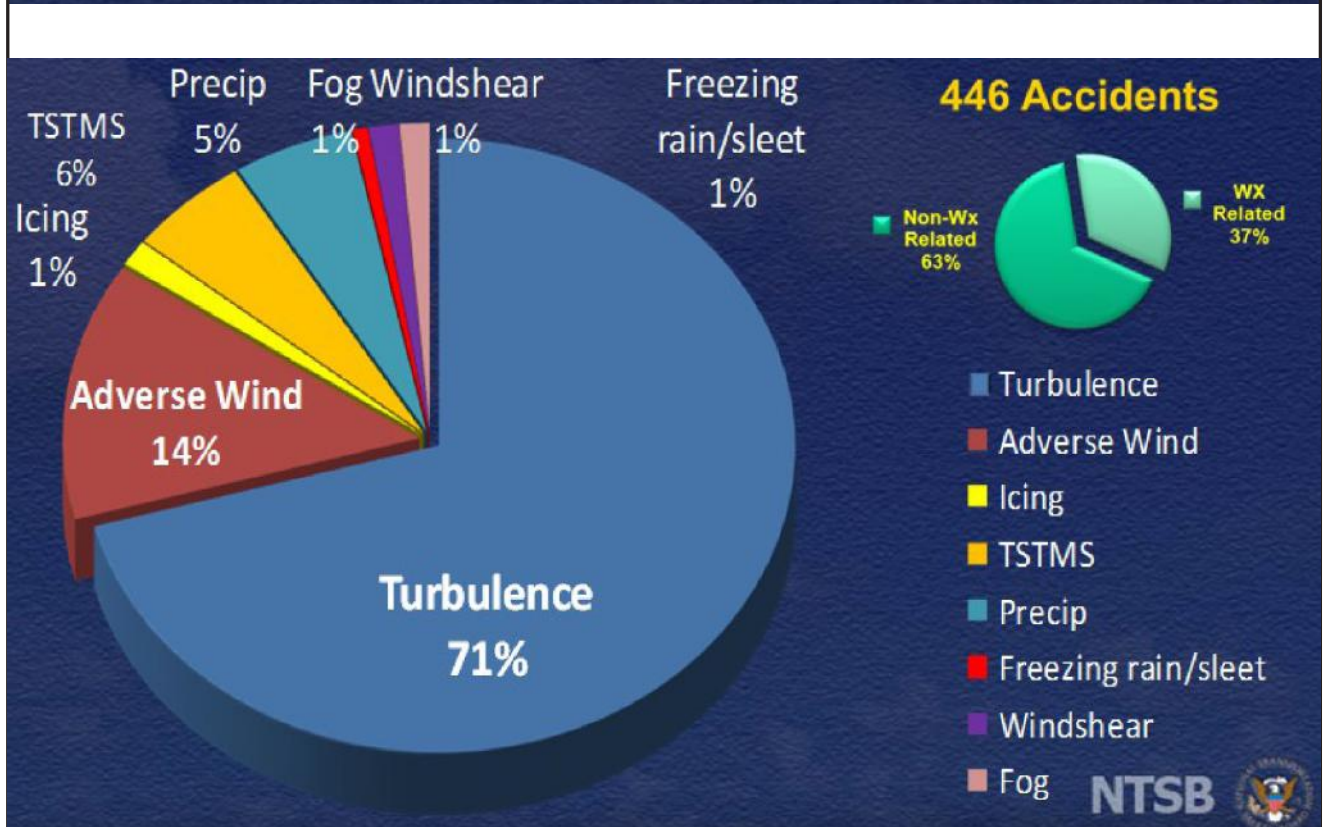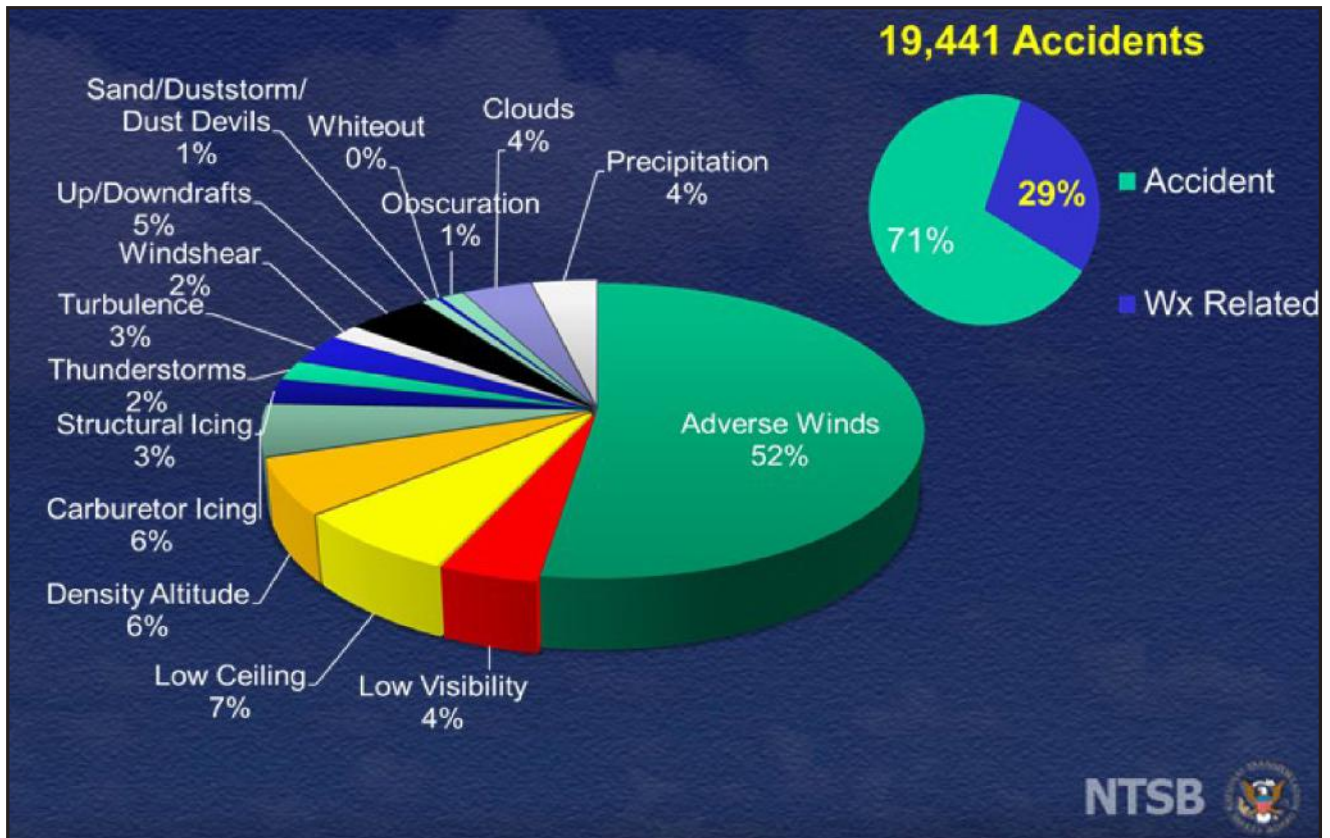
Delays and damage to aircraft during landing, taking off and high-level cruise due to hazardous weather can often occur. Gultepe et al. (2007) stated that a three-days freezing fog event in the UK resulted in about 50M US$ in financial losses for businesses. Kessinger et al. (2006) also stated that aviation hazards for oceanic flights could impact both safety, economic efficiency, and productivity that lead to a total cost of about 62.7M US$ per year. Cook et al. (2009) quantified the impact of weather factors on flight delays and find the contributing factors are highly airport dependent. Because of its importance to aviation, the National Oceanic and Atmospheric Administration (NOAA) National Weather Service (NWS) operationally provides forecasts of cloud-top height, turbulence, lightning detection, precipitation, icing, low clouds and fog, and volcanic ash. These forecasts are available to the public through their website (https://www.aviationweather.gov/).

Figure 2: Various weather conditions representing visibilities related to warm fog, moisture, rain, freezing fog, ice fog, snow, blowing snow, and ashes (from top left to the right boxes).
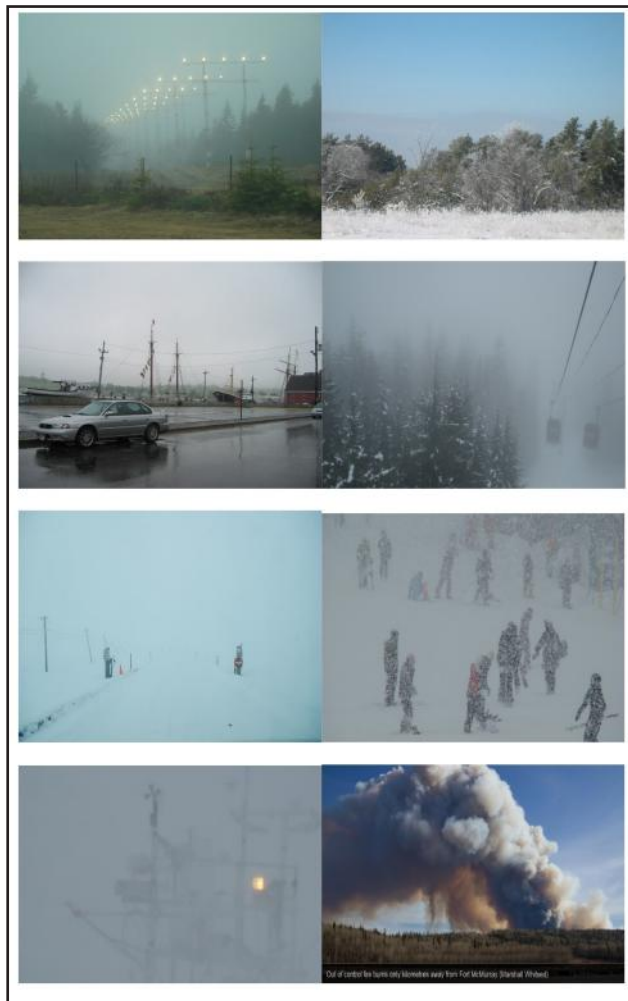
Strong wind regions within jet streams called jet streaks (JS) can also affect aircraft operations (Uccellini and Johnson 1979; Uccellini 1980). They studied transverse circulations in the left exit and right entrance regions of jet streaks (which are the divergence regions) using Numerical Weather Prediction (NWP) models. Rose et al. (2004) detailed the interactions between upper and lower level jets, and the development of severe convective system. They stated that

> "in the (jet) exit region, the geometry of this adjustment, combined with warm, moist, lower tropospheric air to the right and ahead of the jet streak and cool, dry air at the jet streak level, produced the differential advections that convectively destabilized the atmosphere."

Results of their work suggest that development of severe convective storms can be influenced by mass and momentum fluxes along the propagation of an upper tropospheric jet streak. The development of a low-level jet (LLJ) usually was not considered for convection development in regard to synoptic-scale processes (Uccellini 1980). He stated that a systematic upper level flow pattern led to leeside cyclogenesis or a leeside trough, and that produced the strong pressure gradient forces needed for the development of LLJs. These studies suggested that improved knowledge of the relationships between JS and LLJ are important for understanding aviation weather hazards. Clear-air turbulence (CAT) and eddies related to jet streams can also be extremely important for mountainous and high-level flights near jet streams (e.g., Ellrod and Knapp 1992; Gultepe et al 1995).

Reduced Vis, commonly caused by fog and precipitation (Tardiff and Rasmussen 2007; Gultepe et al. 2009), is also caused by dust and ash (Fig. 2). The transport of fine-grained dust by strong winds can occur over a broad range of time and spatial scales (Hadley et al. 2004) and impact not only Vis but have also been associated with engine failure.

Another critical hazard for aviation is aircraft icing (Isaac and Schemenauer, 1979; Guttman and Jeck 1987; Politovich 1989; Tafferner et al., 2003; Vivekanandan et al. 2001). Prediction of icing and deicing conditions (at the airports) is important for flight safety (Rasmussen et al. 2001; Black and Mote 2015). The accumulation of ice on aircraft before takeoff has long been recognized as one of the most significant safety hazards affecting the aviation industry. As little as 0.1 mm of clear ice over 2 minutes on a wing surface can increase drag and reduce airplane lift by 25-30% and reduce critical angle of attack by 8 degrees (https://aircrafticing.grc.nasa.gov/1_1_3_2.html; TC 2004).

Recently it has been realized that prevention of aircraft engine power losses due to high ice water content (HIWC) at higher elevations is essential for safe aviation operations (Leroy et al. 2016; 2017). The HIWC conditions, typically associated with deep convection, can cause engine power loss and air data events (affecting altitude and airspeed measurements) on commercial aircraft and need to be better characterized (Mason et al., 2006).

Improvements in aviation nowcasts and forecasts require better measurements and predictions of atmospheric parameters such as T, RH, wind and turbulence, icing, and Vis. These parameters are also related to climatic change over various scales. Therefore, for future research, the impact of climate change on meteorological parameters needs to be evaluated. For example, state-of-the-art research done by Goodman and Griswold (2017) suggest that temperature and pressure are important for aviation applications because they can impact aircraft drag and lift. Their work suggested suggests that aviation related impacts due to climate change need to be evaluated.

State-of-the-art global climate models were used in the Coupled Model Inter-comparison Project Phase 5 (CMIP5) simulating climate extreme indices described by the Expert Team on Climate Change Detection and Indices (ETCCDI) (Sillmann et al. 2001; 2013). In their work, the climatic indices based on daily T and precipitation amounts and rates were calculated using multi-model simulations. They found that the duration of cold and warm spells changed significantly since the 1950s. These works also suggest that climate change issues related to aviation operations are needed be evaluated in depth.

Global and regional weather prediction systems are needed to characterize the atmospheric state in details required to diagnose aviation related hazards. Accurate predictions of the most dangerous processes related to Vis, wind and turbulence, icing, and convection are essential to reduce in-flight injuries, structural damage, ground preparations for flights, and flight delays (e.g., Mecikalski et al. 2007, Sharman et al. 2012; Sharman and Lane 2016; Karstens et al 2018). Therefore, forecasting and nowcasting of aviation related meteorological parameters require a better understanding of the underlying meteorological processes. In this respect, knowledge of dynamics of upper-level and low-level jets, gusts, eddies, large-amplitude gravity waves, wind shear (including low level wind shear (LLWS) as well as physics and thermodynamics of cloud, fog, and precipitation can be very important for aviation mission planning and reducing financial losses (Uccelini and Johnson 1979; Zhou et al., 2004; NWSPD 2004; FAA 1988 Thobois et al 2018).

The goal of this review is to provide a summary of meteorological parameters, processes, and their prediction issues that are critical for aviation operations and that create challenges for forecasters. The critical parameters, processes, and analysis techniques of importance for aviation meteorology over various scales can be listed as

- Weather physics
1. Clouds and fog
2. Ice and droplet microphysics
3. Precipitation type and rate
4. Freezing precipitation
5. Icing, and ground deicing
6. Frost
7. Visibility and ceiling
8. Blowing snow
9. Convective activities and high ice water content
10. Lightning
11. Ash and dust
12. Physical parameterizations

- Weather Dynamics
1. Turbulence
2. Wind gusts
3. Waves
4. Jet streak intensity
5. Low Level Wind Shear (LLWS)
6. Microburst and tornados
7. Temperature and RH (relative humidity)

- Weather Forecasting (Multi-scale)
1. NWP time and space scale issues
2. Data integration
3. Artificial intelligence
4. Deterministic versus probabilistic methods for nowcasting
5. Integrated systems
6. Climate change modeling for aviation applications
7. Contrails and climate change
8. Reporting systems for aviation meteorological applications

Considering the above items, NWP and climate change models play an important role on their own or integrated with observations to improve nowcasting and long-term forecasting of high impact weather events. Weather-related events such as fog, precipitation, clear-air and in-cloud turbulence, wind shear, gust, or icing may be related to changing climate conditions; if this is the case, for the next 50 years and beyond, aircraft flying conditions need to be considered to improve future aviation operations in response to extreme weather conditions.

In this overview, observations will first be summarized in the next sections and followed by discussions of NWP issues. Then, integrated methods will be introduced for aviation operation applications. In the final section, future issues and possible challenges related to observations, NWP, and climate change will be provided.

2. OBSERVATIONS

Observations are needed to discern and monitor meteorological parameters required for safe and efficient aviation operations. These are clearly needed in the terminal area of major airports and at cruise levels along flight routes, but also over wide areas to support a range of operational activities at smaller airfields and other remote locations. Helicopter air ambulance operation in remote areas, for example, represents a particular aviation weather need that creates significant forecasting challenges. Observations are important since some parameters are poorly diagnosed by NWP models at the scales needed by the aviation community and they are also used for model initializations. Clearly, observations are critical for providing monitoring and nowcasting related to aviation meteorological parameters for operations, and that cannot be predicted accurately with NWPs alone for lead times less than a few hours.

2.1 Ground based in-situ observations

The Aviation Automated Weather Observation System (AV-AWOS) originally suggested by Mandel (1975) provides meteorological parameters critical for aviation operations. Their proposed AWOS included additional parameters such as Vis and sky conditions. Later, Wade (2003) used the ASOS (Automated Surface Observing Systems) with a the light-emitting diode weather identifier (LEDWI) sensor to discriminate drizzle from other particles because precipitation rate from drizzle is usually less than 0.25 mm hr^{-1}. AWOS and ASOS were designed for unattended locations and use multi-sensor based algorithms (Ramsay et al 1999). Presently, these types of systems are continuously being improved by adding ultrasonic 3D wind systems, fog and precipitation sensors, as well as a portable ceilometer and a microwave radiometer (Ware et al., 2010; Gultepe et al., 2018). In addition to individual ground based in-situ sensors, compact meteorological platforms were also developed for visibility, icing, fog, and precipitation type studies and applications such as ones developed by Landolt et al. (2010), Rasmussen and Landolt (2008), and Gultepe et al. (2018). Sims et al. (2000) used an integrated

icing diagnostic algorithm (IIDA) that extensively utilized ground based in-situ systems with other observational and prediction systems. Similarly, supersites having various high-resolution ground based in-situ sensors (see next subsection) were also designed and used for operations.

2.2 Meteorological Supersites

Meteorological supersites with various sensors can be designed for specific goals related to atmospheric-hydrologic-oceanographic applications. Presently, these supersites with extensive ground based in-situ and remote sensing platforms have been used by researchers (Rasmussen et al. 2012, Gultepe et al. 2018, 2015; Ralph et al. 2014; Song et al., 2018). They were designed for aviation and forecasting validations/operations and included mainly observations representing Vis, U_h, turbulence, fog (FG), precipitation amount (PA) and intensity (PR), h_c, and cloud base height (h_b), and atmospheric profiling of meteorological parameters. Although supersites usually are located at a single point, representing a small area around it, Gultepe et al. (2018) used their supersites with satellite sites (e.g., smaller weather observing station) located within a 1 km perimeter radius. These observations provided statistical advantages to evaluate the scale issues related to measurements (Gultepe et al. 2018). The fact that most accidents occur around airports emphasizes that high resolution observations and areal representation of observations as done in above work are needed to improve aviation operations/NWP simulations.

2.3 Aviation Weather reports

Detailed airport observations can be used for making flight decisions by pilots and airport authorities, and for verifying forecasts. These observations usually are reported at 30-min or 60-min intervals as METARs (Meteorological Aviation Routine Weather Reports). At some airports, observations are also performed by using weather sensors autonomously (Gultepe et al. 2017). Weather forecasts for aviation operations are provided 2 hrs in advance based on trend-type forecasts (TRENDs) and over 2 hrs as terminal aerodrome forecasts (TAFs) (Jacobs and Maat 2004). Both TAFs and TRENDs contain information on horizontal wind (Uh), Vis, cloud amount (C_a), h_b, and PR in the vicinity of the airport (Lynn 1997). The TAF can be issued as often as 12 times a day, including eight short TAFs with lead times from 1 to 10 h, and four long TAFs with lead times from 8 to 26 h (Jacobs and Maat 2004). In fact, most aircraft landing and takeoff decisions are made based on Vis and hb, as well as wind conditions at the airports (Thobias et al 2018).

PIREPS (voice-transmitted pilot reports) are commonly used to report icing and turbulence conditions and they are easily available but the PIREP reporting system was not proposed to be used for research or forecasting applications (Schultz and Politovich 1992a, 1992b; Kelsch and Wharton 1996; Schwartz 1996). These studies stated that inspection of PIREPS on turbulence and icing conditions reveal serious shortcomings that limit their usefulness. Lately, Bernstein et al. (2004) also stated that icing algorithms developed by many others overestimated icing amounts compared to PIREPS. These works suggested that the PIREP reporting systems need to be improved. Shultz and Politovich (1992a; 1992b) suggested that the FAA should consider creating a standard PIREPS system similar to the standard airways report made by surface weather reporting stations.

The TAFs and TRENDs are a good source of meteorological short time predictions and provide important support for forecasters. The TAF and TREND guidance and the AUTOTAF encoding software have been developed and implemented in close cooperation with the German company Meteo Service Weather Research (Knüppfer 1997; Jacobs and Maat 2004). Automated TAFs (Lynn 1997; Kilpinen 1994) use both direct NWP model outputs and model observation soundings (MOS; Glahn and Lowry 1972; Hart et al. 2004). The MOS-based methods usually use local data as in Jacobs and Matt (2004). In their work, an approach using observations from upstream locations and local data were used. Recently, using PIREPS, blended algorithms for aviation operations have been suggested for improving short term forecasts (Bailey et al. 2016). A combined physical–statistical approach is often applied to low clouds and Vis predictions because of NWP short-term unreliable prediction issues. Lately, Herzegh et al. (2015) developed an expert system for Vis and cloud base (h_b) forecasts based on blended numerical model and observational data. In their work, current and historical METARs, GOES observations, NWP output from the Rapid Update Cycle (RUC), NCEP (National Center for Environment Prediction), and GFS (global forecasting system) runs, MOS forecasts, as well as observational based rule methods for short term predictions were used. These works indicated importance of airport and pilot reports to be used for aviation operations.

2.4 Aircraft in-situ observations for icing

Research aircraft observations have been used for meteorological research extensively and here we only provided icing related research that generated significant improvements for icing measurements and predictions (Politovich 1989; Cooper et al. 1984; Sand et al. 1984; Isaac et al. and Schemenauer 1979; Isaac et al. 2005; Reehorst et al. 2005). For example, icing research using aircraft platforms has been done by NASA Glenn, Canadian NRC (National Research Council) and EC (Environment Canada), NCAR, and University of Wyoming (Politovich 1989, 1996; Isaac et al. 2005; Serke et al. 2008; Reehorst et al. 2005). Bernstein et al. (2005) developed a Current Icing Algorithm (CIP) that utilized satellite, radar, surface, lightning and PIREPS observations together with 3D model hourly diagnostics to retrieve icing and SLD potentials. Figure 3a shows the conceptual diagram of their CIP algorithm that was adapted by FAA to be used operationally. Figure 3b shows an example of the splintering mechanism which generated many small droplets which then quickly froze during a wet snow case at T=-3ºC on March 15 2013 during SAAWSO (Satellite Applications for Arctic Weather and SAR (Search And Rescue) Operations) project took place over St. Johns' area, NL, Canada (Gultepe et al. 2018).

Based on aircraft in-situ observations of cloud microphysical parameters, super cooled large droplets (SLD) impact on aviation certification issues was emphasized by Politovich (1989), Isaac et al. (2005), and Bernstein et al. (2005). Politovich (1989) noted that substantial loss in rate of climb capability occurs in less than 10 mins when droplet number concentration, $Nd < 0.1-1$ cm^{-3} and mean volume diameter (MVD) at about 30-400 μm. Various icing types occurring at the surface of aircraft (Politovich 1996; Levis 1947; 1978) can significantly impact aircraft lift and drag forces that can lead to aircraft accidents. Lately, high ice water content is also found to be an important factor for aircraft engine icing (Leroy et al. 2016; Haggerty et al. 2018) and that needs to be further researched for operational applications.

2.5 Satellite Observations

Observations from passive radiometric imagers (e.g. the Advanced Baseline Imager, ABI) mounted on operational satellites, such as the Geostationary Operational Environmental Satellites (GOES), are used extensively for evaluation of meteorological events e.g., fog and convection, as well as for nowcasting and data assimilation algorithms used in the NWP modeling systems. Both imager and sounder spectral radiances and relevant parameters derived from radiances have been used extensively for these purposes. Examples of these products and potential applications are discussed below and in following sections.

Figure 3: CIP (Current Icing Potential) project conceptual diagram (**a**). Precipitation types: snow (asterisks), rain (large open circles), and freezing drizzle (small gray circles). (Adapted from Bernstein et al. 2005) American Meteorological Society. Used with permission. (**b**) shows a picture of splintering mechanism, which generated many small droplets and then quickly froze occurred during a wet snow case at T = - 3 C on March 15 2013 during SAAWSO project (Gultepe et al. 2017a, b) took place over St. Johns' area, NL, Canada.
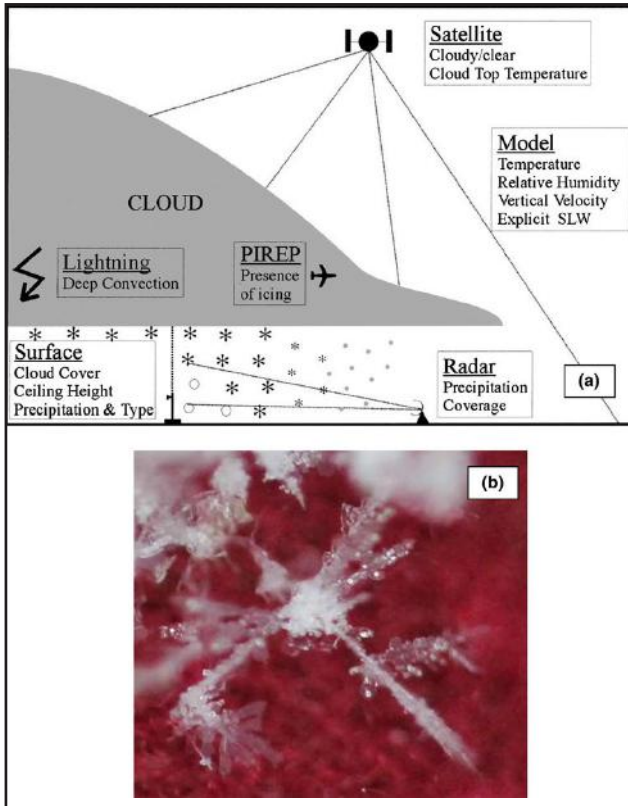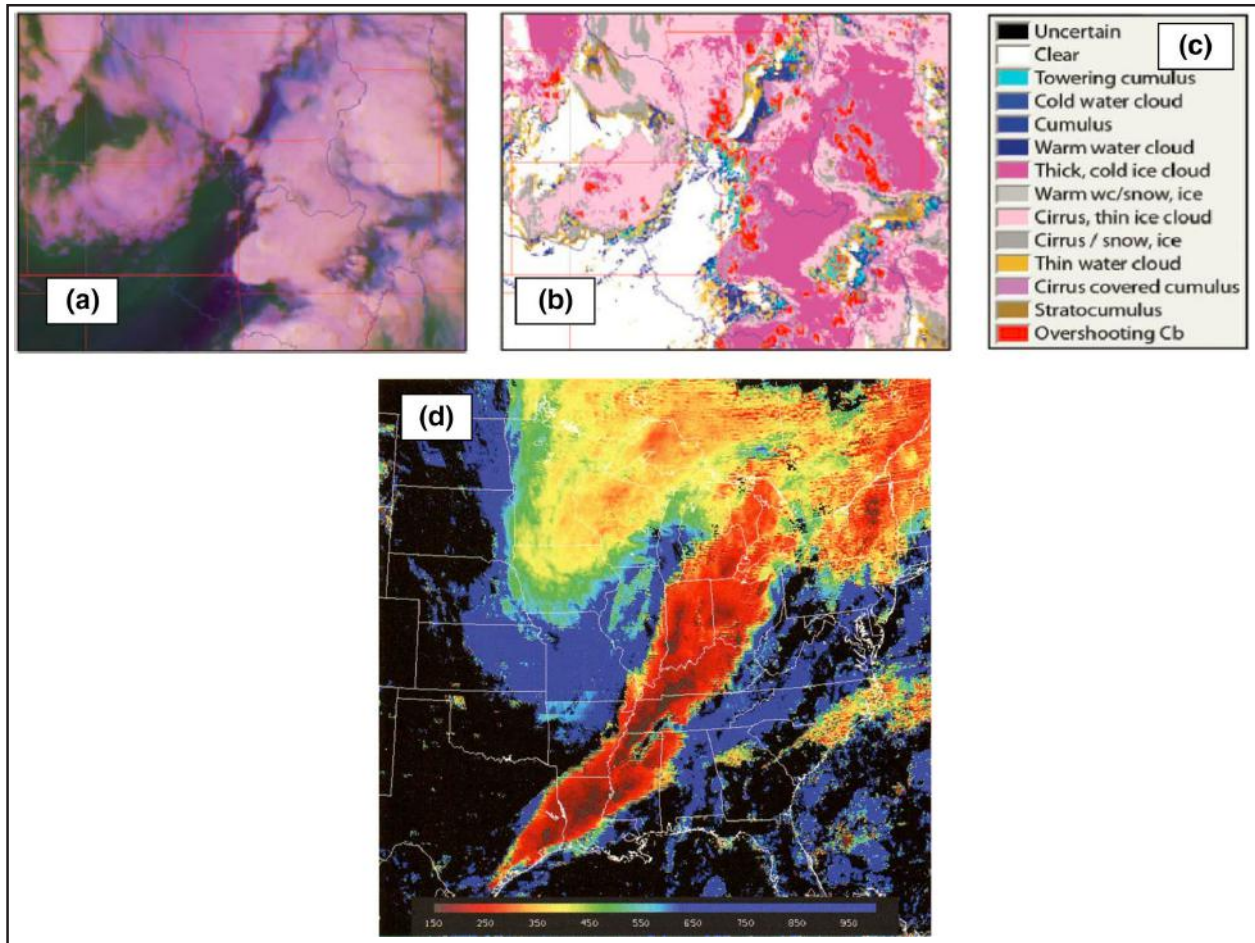

In addition to passive radiometric imagers on satellites, active remote sensing platforms are also starting to be used on the satellites such as Cloudsat (Sun-Mack 2017; Deng et al. 2010) and CALIPSO (Smith 2014). The EarthCARE satellite mission is planned for 3D weather predictions by blending data from satellite based active sensors together with simulations from a 3D NWP model (Miller et al. 2014; Illingworth et al. 2015; Barker et al. 2011). The use of active sensors on these satellite platforms can provide insight information on cloud vertical structure, cloud top properties, and both microphysics and precipitation that can be blended with NWP simulations and ground based remote sensing platform data to be used for aviation applications.

A variety of cloud properties are retrieved in near-real time using the Satellite Clouds and Radiation Property retrieval System (SatCORPS; https://satcorps.larc.nasa.gov) applied to global geostationary and polar orbiting satellite imager data (Minnis et al. 2008; Minnis

et al. 2016) using adaptations of the algorithms of Minnis et al. (2011). The parameters retrieved include, among others, the scene identification of the pixel as either cloudy or clear, cloud top phase, cloud top and height temperatures and altitudes, cloud optical depth, and cloud particle effective radius. Recent additions include multi-layered cloud detection and properties, aerosol concentration over ocean, and convective cloud overshooting top identification (e.g., Bedka et al., 2017). These products are currently used for a number of aviation applications such as aircraft icing (Bernstein et al. 2006; Smith et al. 2012), engine icing (Yost et al. 2018), and cloud ceiling, and aviation and severe weather NWP model data assimilation (Benjamin et al. 2016; Jones et al. 2016). Satellite observations retain significant potential for additional use by aviation systems. Improvements and enhancements in the satellite based retrieved products l can expand that potential. For example, determining the separation between multilayer clouds (Sun-Mack et al. 2018) will likely improve chances of flying in clear air in multilayered conditions.Knowing the thickness of an icing layer and a thick ice cloud location above the supercooled droplets segment (e.g., Smith 2014) can further provide more choices for pilots faced with a hazard and few options.

Another source of cloud information is the algorithm developed by Sieglaff et al. (2011), which classifies each GOES pixel into groups of clear, liquid water, supercooled liquid water, mixed phase, opaque ice, non-opaque ice, and multilayered ice cloud (ice cloud is the highest cloud layer). These groups are described in the work of Pavolonis and Heidinger (2004) and Pavolonis et al. (2005). Details of the algorithm can be found in Pavolonis (2010a,b) and Heidinger (2010). Similarly, Liu et al. (2009) also defined cloud types based on China's FY-2C multichannel images and a neural network method. The satellite cloud analyses utilize clear-sky background correction, satellite zenith angle, and sensor spectral response functions. These were then used for the cloud mask and type algorithms to be portable to many sensors. The cloud-type algorithm relies on an upfront cloud mask algorithm to determine which pixels contain cloud (Heidinger 2010). The satellite observations can usually lead to detection of cloud phase, fog, icing, and turbulence from spectral radiance measurements (Minnis et al. 2011; Pavolonis et al. 2010a, 2010b, Pavolonis and Heidinger 2004; Smith et al. 2012, Gultepe et al. 2007; Ellrod and Pryor 2018). Integrated systems based on in-situ observations, NWP model output, as well as GOES satellite products can improve monitoring fog conditions that include fog area and its intensity (defined by optical depth).

A number of efforts have focused on detecting and analyzing overshooting tops (indicating convective activity) using GOES products from VIS (Visible) and IR (Infrared) imagery (Nair et al. 1998; Mecikalski et al. 2007; Bedka et al. 2010). In addition to garnering information directly from the VIS reflectance and IR brightness temperatures, and their differences with other channels were used to detect overshooting tops. Texture analyses have allowed the discrimination of convective cloud features within a shield of stratus-like clouds that often cover a convective complex. Figure 4a-c show the texture-based clustering analysis results based on Mecikalski et al. (2007). In this figure, large-scale convective structures are visible, along with smaller cumulus and stratiform clouds. Figure 4d shows a cloud-top pressure product developed through the combination of height estimates from the CO_2 ratio technique for the upper clouds and from the older "IR window" technique for lower clouds (Schreiner et al. 1993; Donovan et al. 2007). The IR window technique uses the 11μm thermal IR temperature to estimate T at cloud top, and combines it with an atmospheric sounding to get T to a corresponding pressure and height. The isolated overshooting cumulus tops were also detected as in red. Improvements on this technique have been reported by Bedka and Khlopenkov (2016).

The reasons for recent advances in aviation safety due to meteorological satellites are their ability to provide critical information of weather conditions, the enhanced speeds of data transmission and computer analysis, better calibrated high-resolution satellites, algorithm maturity, and more reliable validations using observations. Therefore, hazards, such as turbulence, in-flight icing, convective storms, and volcanic ash, can be diagnosed from satellite-based observations, and are used extensively in national aviation forecasting systems (Mecikalski et al. 2007). The algorithms are always subject to improvement based on validation studies using in-situ observations, passive (e.g., microwave) and active (radar and lidar) remote sensing retrievals, and integrated observations.

The aviation products in NOAA NWS operations include volcanic ash, cloud-top height, turbulence, lightning detection, precipitation, icing, and low clouds and fog (Schmit et al. 2017; Goodman et al. 2012). Recently, with the

introduction of GOES-16 (16th Geostationary Operational and Environmental Satellite) products, lightning detection for aviation applications became possible. New sensors available on GOES-16 include total lightning detection and mapping of in-cloud and cloud-to-ground flashes (from the Geostationary Lightning Mapper (GLM; Goodman et al. 2012; Goodman et al. 2013). It is expected that the use of GLM data for severe weather research will improve aviation weather forecasts related to convection and storm physics.

Airborne ash from volcanic eruptions can also be a major threat to aviation safety (Casadevall 1994; Miller and Casadevall 2000; Hufford et al. 2000; Simpson et al. 2000). VIS satellite imagery can be used to detect ash clouds, but not to discriminate ash particles from natural water and ice clouds. Ash detection and discrimination is accomplished via multispectral infrared image analysis. The multispectral technique uses a strong 12-μm absorption signature (e.g., Prata 1989; Hufford et al. 2000; Mecikalski et al. 2007), leading to a negative value of the 11-12 μm brightness temperature difference. As discussed by Ellrod et al. (2003), this technique is often termed as the reverse-absorption method. Volcanic eruptions usually release high concentrations of SO_2 having strong absorption bands at 7.3 and 8.6 μm that can aid the ash detection algorithms. SO_2 absorption channels are presently available on the high-resolution Moderate Resolution Imaging Spectroradiometer (MODIS) imager and the Atmospheric Infrared Sounder (AIRS) sounding instrument in polar orbit on NASA's Earth Observing System (EOS) satellites, and with the next-generation operational geostationary satellites (e.g., Himawari-8, GOES-16) (Goodman et al. 2010; Hutchison et al. 2008; Mecikalski et al. 2007; Schmit et al. 2005).

The National Aeronautics and Space Administration (NASA) developed an Advanced Satellite Aviation-Weather Products (ASAP) system that transfers new satellite-observing products into operational use based on a collaborative effort with the FAA's existing Aviation Weather Research Program (AWRP) (Mecikalski et al. 2002; 2007). The ASAP ash detection algorithms are currently being developed at UW-CIMSS. The standard reverse absorption technique (Prata 1989) that uses channel differencing between 11-12 μm BBT (Black Body Temperature), is supplemented with VIS at 0.65 μm and near-IR at 3.75 μm channels for volcanic ash detection (Pavolonis et al. 2006). This new algorithm does not depend on a negative value of 11-12 μm brightness temperature difference because this difference is often absent in tropical eruptions and it is used globally.

Hadley et al. (2004) studied the rare resuspension of volcanic ash and dust from the Katmai area volcanic eruption by strong winds on 20–21 September 2003 and found that the ash/dust cloud created severe disruptions to aviation operations while aircraft were attempting to avoid dust/ash clouds. Another volcanic ash event occurred from Mount Cleveland, Alaska when it erupted on 19 February 2009

and led to several severe disruptions of commercial aircraft traffic. The use of satellites for ash detection has recently become very common but issues with data analysis are still important, and more work needs to be done. Simpson et al. (2000) also suggested that detailed volcanic ash PIREPs are needed to improve real-time awareness for aviation routing.

Two major regions of dust originate from Asia (Gobi and Mongolian deserts) and Africa (Sahara Desert). Dust events usually occur when surface winds exceeding 5 m s^{-1} (Hadley et al. 2004) loft the dust particles into the atmosphere where they can travel across either the North Pacific or the tropical Atlantic Oceans, respectively (Gillette 1978). Dust can also affect radiative forcing and world climate (Myhre and Stordal 2001), as well as aviation safety (Simpson et al. 2003).

Satellite-based wind vectors can be used to infer wind shear, turbulence, and convective activity (Hubert and Whitney 1971; Mecikalski et al. 2007; Perrier et al 2008; Bedka et al 2009). In the northern latitudes, polar winds are needed for better aviation flight planning because of lack of other observations and issues with NWPs through assimilation of observations (Key et al. 2003). Polar winds from satellite based retrievals (Turner and Warren 1989; Herman 1993) can be highly effective for aviation management because of the lack of airport availability after long flight times over Arctic regions. Santek et al. (2010), using the National Centers for Environmental Prediction (NCEP) Global Forecast System (GFS), ran an experiment during August and September 2004, with and without the Terra satellite based MODIS (Moderate Resolution Imaging Spectroradiometer) Polar winds. From the five cases examined, it was determined that the addition of the polar winds modifies the mass balance in synoptic-scale waves near the polar jet streams that can affect flight planning.

2.6 LIDAR observations

LIDAR-based observations are used to obtain Doppler wind speed (Vd) based on motion of air particles and backscattering ratio as well as depolarization rate. Excluding deep and heavy in-cloud water content conditions, they can provide 3D wind components from combination of LIDARS and based on various scanning modes. At low elevation angles, they can also provide horizontal wind profiles to analyze turbulence and gust, and aerosol loading at higher levels.

LIDAR-based wind retrievals using the Doppler concept became important in the 1980s. Bilbro and Vaughan (1978) and Bilbro et al. (1984) used a coherent Doppler system to obtain 2-D wind components from an installation onboard the NASA Convair 990. For a recent overview of the use of LIDARs in atmospheric research see Reitebuch (2012). Recently, LIDARs have been used for aviation research and operations (Gultepe et al 2017; Fuertes et al 2014; Tucker et al 2009, and Sathe et al. 2011). Tucker et al. (2009) used

a High Resolution Dial LIDAR (HRDL) at 2.022 μm to study mixing height, turbulence, shear, and aerosol profiles. The HRDL velocity and backscattered signal measurements collected during a ship-based field campaign were used in wind analysis. In their work, wind air velocity variance profiles were used for mixing height estimation. This was a significant development of LIDAR use in the aviation research. Their results are shown in Figure 5 which shows time-height cross sections of σ_w^2 (vertical air velocity variance) and boundary layer height (ho) (a), horizontal wind shear height (hspd) (b), and multiple products related to shear and mixing height (c). Their work also suggested that a motion-stabilized scanning coherent Doppler LIDAR can perform azimuth scans, elevation scans, and zenith stares to obtain the velocity field in three dimensions from a moving platform and that can improve aviation forecasts over the coastal regions.

Figure 5 : The time-height cross sections of HRDL (lidar) vertical air velocity variance (σw^2) (a), horizontal mean wind speed shear height (h_{spb}) (b), and composite velocity variance (σv_2) (c) for a 24-h period on 11 Aug 2006 during TexAQS 2006 project (Adapted from Tucker et al. 2009).
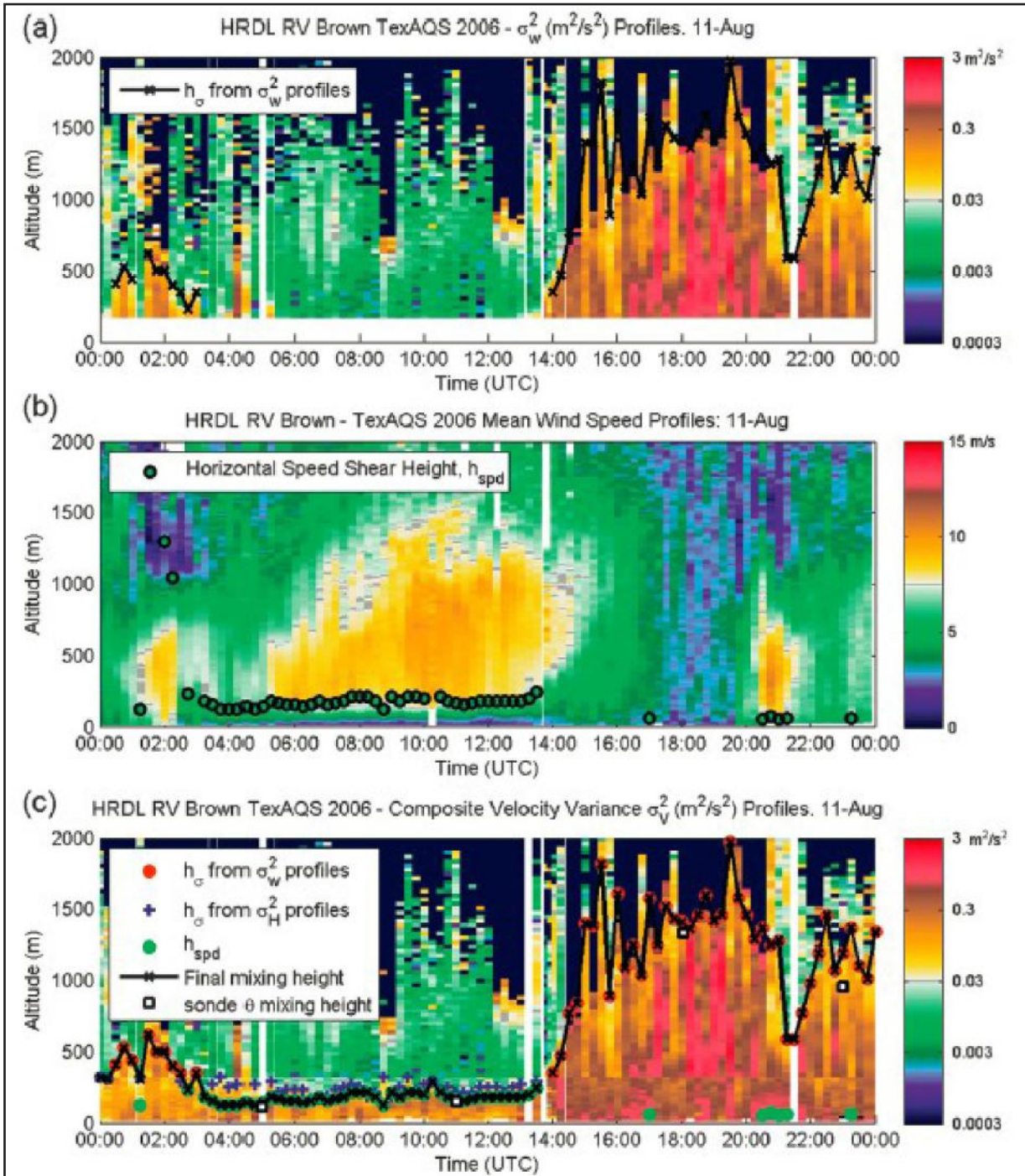
Lately, Doppler Lidar wind measurements have been used for aircraft operations at airports (Thobois et al. 2018; Chan and Shao 2007; Chan et al. 2006) to diagnose wind shear, gust, microburst, and aerosol loading, which can be serious issues for aviation operations (Sharman et al., 2012, Kessinger et al. 2006, Wong et al. 2013, Kim et al. 2015, 2016, and Gultepe et al. 2018). But, presently Doppler lidars are used mostly in an experimental mode at the airports. Among Doppler LIDARs commercially available are 1) Halo LIDAR (Gultepe et al 2016), 2) Leosphere Cube LIDAR (Thobois et al 2018), and 3) Lockheed Martin Coherent Technologies (LMCT) LIDAR (http://www.lockheedmartin.com). These LIDARS provide Doppler wind measurements in various scanning modes. The Halo LIDAR observations were used to obtain backscatter ratio and VAD winds, and compared to CL51 ceilometer backscatter ratio observations during an ice

fog event occurred nearby Heber City, UT, are shown in Figs. 6a and 6b, respectively. The Cube Doppler LIDAR from Leosphere Inc is designed specifically for aviation applications and provides related aviation wind and turbulence parameters continuously (Tobia et al., 2018). Examples of turbulence estimation from LIDARs can be found in e.g., Frehlich and Cornman (2002), Hill et al. (2010), Chan (2016), and Vrancken (2016).

LMCT LIDAR at 2 μm (latest one at 1.6 μm) uses pulsed laser light to detect particles and varying weather conditions in the atmosphere (Bluestein et al 2010; De Wekker et al. 2012; Bluestein et al 2014). The company has developed a pulsed coherent 2 limiting diode-pumped solid-state LIDAR receiver on an injection-seeded, Q-switched, 2 micron laser that meets Navy requirements for remote sensing, moderate range, high spatial resolution wind field measurements around air stations and aircraft carriers.

Figure 6: The 16 January 2015 mountain ice fog event during MATERNHORN project occurred over the Utah Mountains; a) Halo backscatter ratio and 3D winds based on Doppler velocities and VAD technique, and b) CL-31 Backscatter ratio (β).
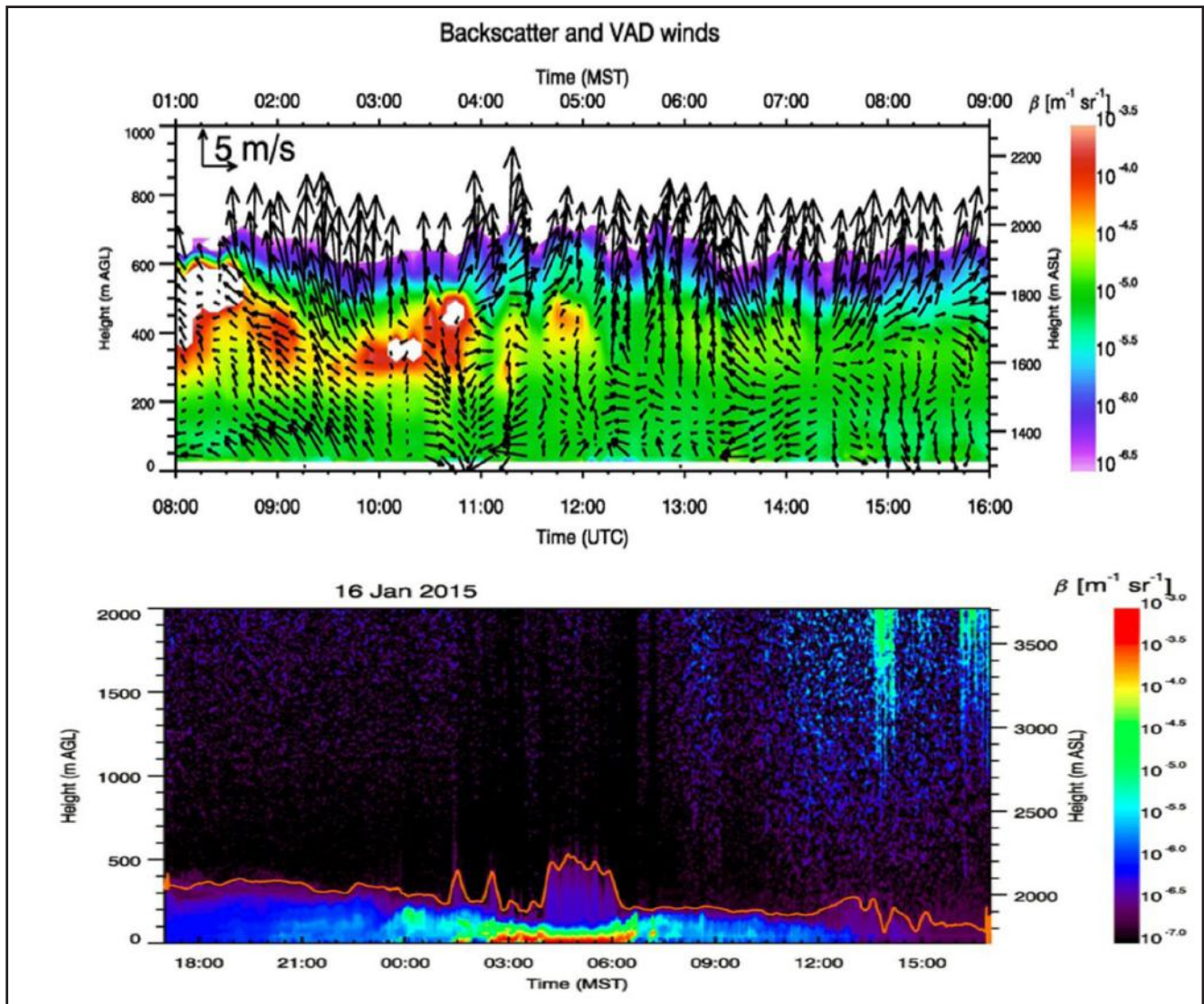
2.7 Sodar observations

The SOnic Detection And Ranging (SODAR) is often used for atmospheric profiling. SODAR uses the Doppler concept to estimate 3D wind profiles from the propagation characteristics of high frequency sound waves to investigate the atmospheric boundary layer and has been used since 1980s. For example, SODAR data were used to investigate the boundary layer dynamics in detail by Motta, et al. (2005), Sumner and Masson (2006), Gottschall and Peinke (2008), and Van den Berg (2008). In these works, atmospheric stability, wind shear, and turbulence intensity were analyzed for wind energy production. Gerz et al. (2009) and Chan (2014) used SODAR observations specifically for nowcasting applications to investigate aviation related meteorological events, such as fog, gust, and wind shear, at the Frankfurt International Airport and at the Hong Kong International Airport, respectively. Silva et al. (2016) developed a conceptual model to investigate wind profile changes using 234 runway cases that utilized a SODAR and surface meteorological station data from the Guarulhos International Airport (GIA) São Paulo, Brazil. França et al. (2018) also used SODAR data for training a neural network model for nowcasting the low level wind profiles at the lead times of 45 mins for the GIA Airport.
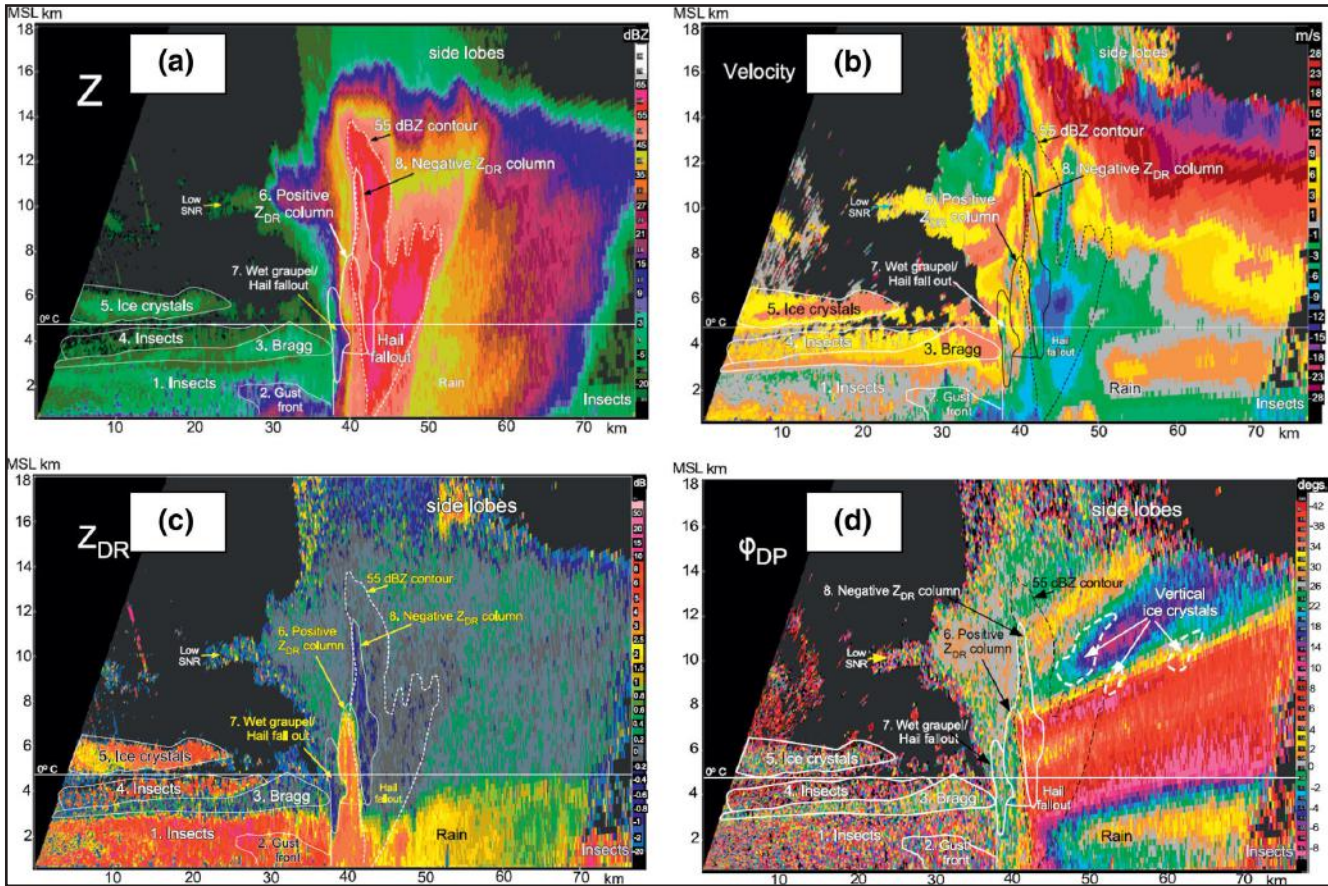
2.8 Radar observations

Doppler and dual-polarized radars (and conventional ones) such as X (8-12GHz), C(4-8 GHz), and S (2-4GHz) band radars have been used to detect storm convective activity and intensity, as well as icing conditions within clouds to identify particle microphysical characteristics (Merritt, 1969; Rasmussen et al 1992; Ryzhkov et al. 2002; Schuur et al. 2012; Smith et al 2016; Hubbert et al 2018). Storm precipitation type and intensity are related to Vis, icing levels, and convective intensity, and these are all important for aviation operations. Smith et al. (2016) developed the Multi-Radar Multi-Sensor (MRMS) system that is operational at the National Centers for Environmental Prediction (NCEP). The MRMS system consists of the Warning Decision Support System–Integrated Information (WDSS-II; Lakshmana et al. 2007) suite. The severe weather and aviation products, as well as the quantitative precipitation estimation (QPE) products, are created by the National Mosaic and Multi-Sensor QPE (NMQ; Zhang et al. 2011) system.

Dual polarized Doppler radars such as the Weather Surveillance Radar-1988 (WSR-88D) radar and radars with dual polarization capabilities such as S-band radars (S-Pol) can improve rainfall estimates, discriminate ice and rain, identify hail cores and updraft regions, and as a result in general increase data quality (Hubbert et al. 2017, 2018; Chandrasekar et al. 2013; Kumjian 2012 and 2013a,b). Hubbert et al stated that the Weather Surveillance Radar-1988 Doppler polarimetric (WSR-88DP) is not able to scan along vertical planes (RHIs), and although this may be acceptable for operational purposes, it does limit research objectives. The S-Pol has increased range resolution using 1-µs transmit pulse length that corresponds to 150-m compared to WSR-88DP's 250-m resolution. The result is that S-Pol is able to obtain high-resolution, high-data-quality measurements related to storm structure and microphysics. In the end, improved storm physics and dynamical information can further be used for aviation operations that concern with wind and turbulence, gust, icing, high IWC, and low visibilities, as well as lightning and particle type and phase.

Dual polarized radars can effectively be used for melting layer and particle phase and type detection (Schuur et al. 2012; Ryzhkov et al. 2002, 2013; Van Den Broeke 2016; Hubbert et al 2018). The sensitivity of this radar decreases with reducing particle size but retrieval of particle phase and 3D wind structure can improve forecasting and nowcasting algorithms related to gust and low Vis. Van Den Broeke et al. (2016) stated that quasi-vertical profiles of the polarimetric radar variables could improve short term forecasts in winter. Hubbert et al. (1018) summarized polarimetric variables used in S-Pol data interpretation. Figure 7 shows range-height plots of reflectivity (Z), and V_D, differential reflectivity (Z_{DR}), and differential phase (φ_{DP}) parameters from a convective storm. Using Z (indicates core of storms), Z_{DR} (reflectivity weighted particle mean axis ratio of particle distribution), V_D (particle motion), and φ_{DP} (particle microphysics), LDR defined as linear depolarization ratio (particle shape), KDP defined as specific differential phase (particle type and shape), ϱ_{hv} defined as co-polar correlation coefficient (particle type and phase), and ϱco-x defined as co- to cross-channel correlation coefficient (canted crystals and cloud electrification). A combination of these variables can be used for evaluating storm physics and dynamics (Hubbert et al., 1998, 2018; Ryzhkov et al. 2002, 2013; Van Den Broeke 2016) that can further be used for operation applications.

Figure 7: A reflectivity RHI of a large convective cell gathered at 0005:23 UTC 26 Jun 2015. Reflectivity field (Z) is shown in **a** where the dashed line marks the 55-dBZ contour; 60 dBZ is seen up to 13 km MSL, indicating the likely presence of large hail, Doppler velocities in **b**, the various regions based on S-Pol radar Z_{DR} marked with white contour lines ìn (**c**), and differential phase e $\emptyset_{DP}$ is shown in **d**; starting offset is set at about 0 °C and over marked regions of vertical ice crystals, $\emptyset_{DP}$ is decreasing in range (d) Adapted from Hubbert et al. (2018), © American Meteorological Society (AMS). Used with permission.

Doppler radar applications for fog and Vis work can be used to provide accurate nowcasting products for aviation weather. Hamazu et al. (2003) used a 35-GHz scanning Doppler radar (Ka band, 27-40 GHz) for fog observations and prediction. They used the three-dimensional structure of reflectivity and velocity field in a fog event for short term predictions. The characteristics and performance of an 8.6-mm-wavelength Doppler radar were described in observing sea fog. The Doppler radar measurements were also used for eddy dissipation rate predictions. Aircraft based turbulence measurements with well-coordinated Doppler radar spectral width measurements were used to estimate energy dissipation rates within thunderstorms anvils (Meischner et al. 2001; Cohn 1995). The lower limit detectable dissipation rate with the C-band Doppler radar is found to be about 10^{-3} m^2 s^{-3}. Techniques for deriving Doppler radar estimates of energy dissipation rate were also described by Williams and Meymaris (2016), and comparisons to in situ aircraft measurements were provided in Dehghan et al. (2014). Doppler spectrum width as measured by operational weather radars was used for both turbulence and wind shear estimation and could also possibly be used for severe weather warnings (e.g., Hocking and Hocking 2018).

The K-band radars (Ku (12-18GHz), K(18-27 GHz), Ka (27-40 GHz) (Matrosov 1995; Loffler-Mang et al. 1999), and W-band radars (40-300 GHz, Gossard et al. 1997; Mead et al., 1989) have been used for cloud microphysical structure but usually they are not used operationally for Aviation operations. When large water mass content exists within clouds, these radar beams can be attenuated significantly. Presently, Ku and Ka band radars are part of active sensors used on GPM satellite that focuses on precipitation from the space (Skofronic-Jackson et al. 2017). These cloud radars can provide specific information for cloud and fog properties, as well as precipitation information but they are operationally expensive and mostly they are used for experimental research.

2.9 Atmospheric thermodynamic profiling

2.9.1 Water vapor and temperature profiling

Water vapor profiling is critical for weather forecasting because of the detail it can provide about cloud formation, nucleation processes, and storm development. Ferrare et al. (1995) provided a summary of water vapor measurements that included satellite-based retrievals (Soden et al. 1994), microwave (Han et al. 1994), differential absorption LIDAR (DIAL) (Ismail and Browell 1994), and Raman LIDAR (Ansman et al. 1997; Whiteman et al. 1992). The difference between the Raman LIDAR and DIAL LIDAR is that the former measures only vapor mixing ratio (q_v) and the latter measures both q_v and T. The work of Wulfmeyer (1998) used a DIAL system developed at the MaxPlanck Institute (MPI) in Hamburg for the measurement of absolute humidity profiles and this has been improved through the work of many others (Wulfmeyer et al. 1995, Wulfmeyer and Bosenberg 1996; Wulfmeyer 1998', and Wulfmeyer and Bosenberg 1998). Eichinger et al. (1999) used a Raman LIDAR to study ABL vapor profiles. The DIAL systems have some inherent advantages over Raman LIDARs profiles. The DIAL systems are generally smaller, lighter, and use considerably less energy than Raman LIDAR systems. They can be used for aircraft based research because atmospheric backscatter increases with a range in a downward-looking system, and thus partially compensates the decrease in signal strength with range. Because of the strong atmospheric attenuation of both UV and near-UV light channels, DIAL systems in the near-IR are better suited for deep atmospheric water vapor sounding profiles. Recent overviews of the DIAL can be found in Wirth (2012), and Fix (2012).

The radar–RASS system (Radio Acoustic Sounding System) was developed at the University of Hamburg for measuring wind profiles in the lower troposphere and virtual temperature profiles in the boundary layer (Peters et al. 1988; Peters 1990). The turbulent variables measured with the DIAL system and the radar–RASS include vertical profiles of water vapor and vertical wind variance and latent heat flux that uses the eddy correlation technique. Neely and Thayer (2011) also used a similar method to study high level moisture profiles over Greenland, which can be used to detect thermal and dynamical instabilities leading to particle formation and eventually cloud formation.

The Profiling microwave radiometers (PMWRs) have been also used for measuring q_v and T, as well as Liquid Water Content (LWC) which can be important for supercooled droplet detection and icing conditions (Solheim et al. 1998; Gultepe et al. 2014). The Radiometrics Inc. MP-3000A profiling radiometer is used to retrieve the profiles of T, RH with respect to water (RHw), and LWC over Whistler Mountain (Ware et al., 2013; Gultepe et al 2014). The MP-3000A observes 21 K-band (22–30 GHz) and 14 V-band (51–59 GHz) microwave channels at multiple elevation angles, one zenith infrared (9.6–11.5 µm) channel, and surface temperature, humidity and pressure sensors. The atmosphere is semi-transparent in the K-band and lower V-band channels during non-precipitating conditions, receiving emission from the atmosphere in addition to cosmic background radiation. The PMWR provides T, qv, RHw, and LWC in the vertical (Bianco et al., 2005) but it needs to be validated using in-situ observations; this may be a challenge for stratiform clouds because of a weak signal from cloud water content compared to convective clouds' water content. Integrated liquid water retrieval from microwave radiometer observations near the 22.2 GHz water vapor molecular resonance is well established (Westwater, 1978; Turner et al., 2007). Integration of above remote sensing platforms can cover atmospheric thermodynamic conditions over the airports, and when they are combined with LIDAR and Radar observations, as well as with surface in-situ observations, both clear air and cloud regions nearby airports can be analyzed for evaluating aviation hazards.

Atmospheric thermodynamic profiling for operational icing research is important to prevent aviation accidents. Serke et al (2008; 2014) developed a compact small platform attachable to a radiosonde balloon that is similar to the radiosonde unit. With this system they were able to measure liquid water content profile within the clouds. This state-of-the-art icing platform promises to develop future balloon based systems to be used for icing and thermodynamic profiling.

In Arctic regions, profiles of water vapor can be important for aviation nowcasting applications, such as fog and low clouds, and storm development. The Arctic LIDAR Technology (ARCLITE) facility, having a Rayleigh/Mie/Raman LIDAR system, has been in operational use since 1993 at the Sondrestrom Upper Atmospheric Research Facility, Kangerlussuaq, Greenland (Neely and Thayer 2011). In their research, molecular and aerosol backscatter is measured at 532 nm to retrieve T profiles, and a Raman channel for molecular nitrogen (608 nm) to determine aerosol extinction values. A Raman water vapor channel at 661 nm was used to measure water vapor mixing ratio profiles into the upper troposphere. They suggested that use of Raman LIDAR technology for ABL water vapor soundings is available and is comparable with balloon based profiles.

Because measurements of water vapor profiles in Arctic environments are rare, DIAL and Raman LIDAR based methods for water vapor profiling can improve fog, cloud, and Vis for short term predictions.

2.9.2 UAVs thermodynamic profiling

Unmanned aerial vehicles (UAVs) are becoming very popular for meteorological and environmental applications (e.g., Bottyan et al. 2013; 2016; Gultepe et al. 2018). UAVs can be accurately controlled by ground based pilots to move the UAVs in certain flight paths that represent constant altitude flights and profiling models. Measurements from the UAVs include various meteorological parameters similar to a radiosonde sounding. In addition to T, RHw, pressure (P), altitude (z), Vis, U_h and direction (Gultepe et al 2018; Bates et al 2013). They may also be used for air quality monitioring of trace gases such as O_3, CO_2, CO, and PM2.5, and earth surface morphology, including snow coverage, water accumulation, and surface temperature. Measurements from UAVs have also been used to estimate temperature and velocity turbulence levels (e.g., Lawrence and Balsley 2013).

For aviation operations, UAVs can be used near airports to gather weather information that can help to improve the NWP's initial conditions and monitor weather conditions in real time. Although they have limitations on flying time (e.g., quadcopter UAVs), measuring 3D windcomponents, and flying into the clouds and fog, UAVs are being developed for extreme weather conditions (especially with fixed wing UAVs, Griffin and Velden., 2018).I In the future, UAVs can fly into the cloud systems (Wick et al. 2018; Wurman et al. 2012), and may provide continuous and accurate weather measurements. Uncertainty in UAV measurements can be significant for wind related parameters because of the impact of the rotors or body of the UAV on airflow. Therefore, additional work is needed to improve wind measurements from UAVs (Reineman et al. 2013; Gultepe et al. 2018). Various meteorological parameters from the UAVs are also being used by Jonassen et al. (2012) for boundary layer (BL) research. These parameters include aerosol number concentrations (N_a), fog droplet number concentration (N_d), Vis, particle spectra, and air quality parameters (Boer et al. 2017; Gultepe et al. 2017).

The UAVs can be used to improve NWP predictions for meteorological applications that include wind speed, Vis, RH and T. Jonassen et al. (2012) work also stated the importance of UAVs observations to improve NWP simulations, and this area of research is needed for further development of aviation products.

2.9.3 Aircraft based in-situ systems

Commercial aircraft flights can provide additional observations of meteorological parameters related to aviation operations. Automated meteorological reports from on board sensors mounted on major commercial air carriers are generally referred to internationally as Aircraft Meteorological Data Relay (AMDAR) reports. In the USA, they are called Aircraft Communication Addressing and Reporting System (ACARS) reports, and the meteorological data is referred to as Meteorological Data Collection and Reporting System (MDCRS) (Moninger et al. 2003). The MDCRS reports are essential for NWP model initializations, especially for rapidly updated models such as the NOAA's WRF-RAP model (Benjamin et al. 2016). Also, the commercially available Tropospheric Airborne Meteorological Data Reporting system (TAMDAR), utilizing commercial flight data collection systems, provides a data base for aviation parameters such as wind, turbulence, temperature, etc. (Moosakhanian et al. 2006). The TAMDAR data (Moninger et al. 2010; Benjamin et al. 2006a,b; Fournier 2006) used with the RUC model over three year period revealed that TAMDAR data significantly improved RUC forecasts. The meteorological parameters obtained from AMDAR and TAMDAR are similar to radiosonde measurements. TAMDAR also provides EDR (defined as energy dissipation rate to the 1/3 power) estimates and icing detection amount. Moninger et al. (2010) over two 10-day periods provided results on meteorological parameters such as T, RHw, and wind representing winter and summer conditions. Their assessment showed that TAMDAR's impacts on 3-h RUC forecasts of temperature, relative humidity, and wind are found to be positive and, for temperature and relative humidity, the improvements were substantial.

Estimates of turbulence are also available from selected AMDAR flights as either derived equivalent gust velocity (DEVG), or EDR. Both of these turbulence estimation algorithms are summarized in Sharman (2016); for more detailed discussions see Sharman et al. (2014), Cornman (2016), Cornman et al (1995), and Kim et al. (2017). Stickland (1998) reevaluated DEVG and EDR estimations for aviation applications. Even thoughboth parameters are dependent on aircraft type, he recommended the use of EDR for aviation operations. This recommendation has been followed up by requiring EDR to be the international standard for aircraft turbulence intensity reporting (ICAO 2001). EDR can also be estimated from second-order structure functions of the AMDAR winds (Frehlich and Sharman 2010), and possibly through Mode-S and ADS-B (Automatic Dependent Surveillance-Broadcast) messages (Kopec et al. 2016). So far though, these techniques have not been implemented operationally.

Another experimental commercial aircraft on-board system is the Backscatter Cloud Probe (BCP) that provides information about the concentration and size of ice crystals in clouds. The probe has been tested as part of the European Research Infrastructure program, IAGOS (In-service Aircraft for a Global Observing System). Bestwick et al. (2015) demonstrated that the BCP measurements could be used to diagnose HIWC conditions, providing pilots with an onboard warning of an HIWC hazard. The sensor output could also be broadcast as part of other systems such as TAMDAR. Additional research is needed for use of the BCP operationally.

A number of experiments for evaluating high ice water content regions (HIWC), including the EU High Altitude Ice Crystals (http://www.haic.eu) and North American HIWC Projects (Strapp et al. 2016), were developed and executed using remote sensing and airborne in situ probes. Leroy et al. (2016; 2017). Leroy et al studies characterized the ice particle size distributions in HIWC regions in the atmoshere using in situ measurements while Protat et al. (2014) used airborne C-band polarimetric radar data to profile the cloud IWC. Yost et al. (2017) developed a prototype method for detecting HIWC conditions using geostationary satellite data coupled with in-situ total water content (TWC) observations obtained during aircraft-related icing projects. They developed three satellite-derived parameters that were used for determining high HIWC probability conditions. These include 1) the overshooting convective updraft or textured anvil cloud, 2) tropopause-relative infrared brightness T, and 3) daytime-only cloud optical depth. Their results are consistent with aircraft flight reports obtained near deep convective storms and cirrus anvils (Lawson et al. 1998; Mason et al. 2006; Bravin et al., 2015). Prediction of HIWC conditions needs to be improved by combining NWP model simulations and remote sensing results. Both require more in-situ observations to establish reliable statistics (Gultepe and Heymsfield 2016; Haggerty et al., 2018).

Overall, observations from various observational platforms summarized above can contribute to improvements of aviation nowcasts, weather reports, and NWP predictions extensively, and they may eventually lead to improvements in aviation operations, but their limitations should also be considered.

3. NWP MODELS

NWP models are important for improving aviation related nowcasts (defined here as lead times < 3 hrs) and forecasts over medium and large lead times (>3 hrs). Their short-term success in nowcasting is strongly related to the incorporation of observations. An NWP model's ability to accurately simulate atmospheric dynamical and physical processes depends critically on several initialization parameters and PBL characteristics (Jonassen et al. 2012). The spatial grid resolution and the parameterization schemes used to represent processes related to clouds, radiation, precipitation, and turbulence are most crucial ones (Pleim and Xiu 1995; Alapaty et al. 2001; Teixeira et al. 2008; Lin et al 1983; Tomita 2008; Khairoutdinov and Kogan, 2000; Ferrier et al. 1994; Herrington et al. 2013; Pu et al. 2018).

The quality of the data used to initialize and force the model for predictions is also essential for the success of numerical model simulations. Many models are initialized from global atmospheric analyses or forecasts (e.g., from the Global Forecast System (GFS) or the European Centre for Medium-Range Weather Forecasts (ECMWF)) with low resolutions, typically being 15–50 km in the horizontal and 3–6 h in time. Therefore, scale issues play an important role for predictions over short times scales. These atmospheric data may not be accurate enough for high-resolution simulations of local features such as fog or turbulence, and these can be sensitive to small errors in the large-scale flow (Nance and Durran 1997; Belair et al. 1998; Khairoutdinov and Randall 2006; Kucken et al. 2012; Selz and Craig, 2014). Because of these errors, data assimilation techniques using detailed and accurate observations are necessary for generating more accurate initial conditions for NWP models for all scales. The quality of the analysis data for model initialization depends mainly on the data assimilation techniques and quality of observations, which compile the short-range forecasts (from a model to generate the first guess), observations, and their error statistics (Kalnay 2003; 1996). The quality and coverage of the observations used to create the analysis have also influence on the accuracy of the analysis (e.g., Langlandet al. 1999). Observations can be particularly sparse over areas such as the world's oceans, Arctic, and Antarctic, and that can likely lead to large uncertainties in predictions.

3.1 downscaling

Because of scale resolution issues, numerical model simulations can include large uncertainties in the predicted parameters. The winds can be to some extent reproduced by numerical downscaling of a state-of-the-art ECMWF operational analysis using the WRF model (Jonassen et al. 2012). By assimilating profile data obtained from the UAS (Unmanned Airplane Systems) at Eyrarbakki in southwest Iceland into a NWP model,substantial improvements of wind, T, and RH

predictions in the region were achieved. Using automatic nonlinear/linear methods that use NWP MOS (Model Output Statistics) data, Vislocky and Fritsch (1995) also developed a statistical model to predict meteorological sounding parameters that are important for aviation. Their method was time consuming but, with increasing computer resources, their method could improve integrated predictive systems over various scales.

3.2 Initial conditions

Initialization of NWP forecasts requires assimilation of various observations for regional models as well as short-range NWP model outputs (Kalnay 2003; 1996, Warner 2011). For instance, inputs into the operational MRMS-Severe/Aviation system (Smith et al. 2016; Wen et al. 2017; Benjamin et al. 2009) include radar data from the U.S. WSR-88D network, GOES radiances and cloud properties (Minnis et al. 2008), surface terrain elevation information, the National Lightning Detection Network (Orville 2008; Smith et al. 2016), and hourly surface and upper-air analyses from the Rapid Refresh model (Benjamin et al. 2009). Several individual and automated algorithms have been developed using the MRMS system to obtain an integrated forecasting and analysis system that provides real-time products applicable to severe weather and aviation nowcasting. In this system, automated algorithms based on data from multiple radars provided better information with greater temporal resolution and spatial coverage than a single-radar.

3.3 Turbulence

Since operational NWP models are too coarse to even begin to resolve turbulence scales relevant for aircraft, post-processing algorithms applied to NWP model output are commonly used to infer regions of significant turbulence. These inferences are based on "diagnostics" of turbulence derived typically from spatial gradients of various NWP model output variables. In the past, various post-processing turbulence diagnostics have been proposed, and some are used operationally. For example, the TI (Turbulence Index) diagnostic developed by Ellrod and Knapp (1992) uses NWP model output velocity fields to derive a diagnostic based on the product of horizontal wind deformation and vertical wind shear. The TI has been used by the Aviation Weather Center (NOAA/AWC) (Behne 2008), the Air Force Weather Agency (Brooks and Oder 2004), the Met Office in the United Kingdom (Turp and Gill 2008), and the Canadian Meteorological Centre (Turcotte and Verret 1999). The physical basis of TI was considered initially

due to frontogenesis through the process of dynamical deformation (Mancuso and Endlich 1966; Ellrod and Knapp 1992). The hypothesis suggested that stronger horizontal thermal gradients caused by frontogenesis can lead to an increase in the vertical shear of the horizontal wind through the thermal wind relation, and indicates that a higher potential for clear air turbulence (CAT) occurs via the local reduction in Richardson number (Ri) and consequent production of Kelvin–Helmholtz instability). Commercial aircraft encounter severe or greater turbulence about 5000 times each year. These incidents resulted in tens of millions of dollars in injury claims per year (Sharman et al. 2006). In fact, these statistics were obtained only for the US airspace and are not a global representation. A significant limitation for the forecasting of all aviation turbulence types is to identify the source of gravity waves (McCann 2001; McCann et al 2012; Knox et al 2008). Observations from early field projects (Sorenson 1964) indicated that two flow regimes associated with CAT are possible: strongly cyclonic and strongly anticyclonic flows. Because the TI neglects anticyclonic shear or curvature in its derivation, Ellrod and Knox (2010) suggested that a new methods should be taken into account for the anticyclonic shear.

The Graphical Turbulence Guidance (GTG) product uses an ensemble mean of many different diagnostics, which seems to improve the statistical performance of the turbulence forecasts (Sharman et al. 2006, Kim et al. 2011, Sharman and Pearson 2016, Kim et al. 2018). Example turbulence diagnostics typically used for clear-air and mountain wave sources include vertical and horizontal wind shears, static stability, wind speed, horizontal deformation, frontogenesis, ageostrophic indicators, turbulent kinetic energy (TKE), and Richardson number (Ri) (e.g., Knox et al. 2016). These diagnostics are designed to capture grid-scale processes (10–100 km) that may lead to sub-grid scale turbulence.

The GTG product does provide short-term forecasts, but its usage is limited by a 1-h update cycle, because of the latency in receiving the underlying NWP-model data and the time required to compute the turbulence diagnostics. Therefore, forecasts are usually not available until at least 2h beyond the valid time. Pinto et al. (2015) and Sharman and Pearson (2016) also stated that because of the highly transient and small spatial scales of turbulence associated with convective storms, neither the NWP model nor the turbulence-forecasting post-processing algorithms are particularly skillful at forecasting turbulence associated with convection. To address these issues, Pearson and Sharman et al. (2016) developed a turbulence nowcast system (GTGN) which merges turbulence observations with short-term

GTG forecasts to produce more timely and accurate information for tactical turbulence avoidance. Their results suggested that turbulence nowcasts integrated with observations considerably outperforms the corresponding turbulence forecasts.

3.4 Low level wind shear (LLWS)

Low level wind shear (LLWS) at airports can occur due to fronts, thunderstorms, inversions, and surface obstructions (FAA-P-8740-40, 2008). Traditionally, surface in-situ wind sensors are used to identify LLWS cases, but recently, remote sensing platforms and aircraft based measurements are also used for detection. The surface sensors are located at the certain distances along the flight paths (Thobois et al. 2018; Oude et al. 2018), but do not cover higher levels; therefore, Doppler lidar (for cloud free conditions) and radars (cloudy air conditions) can be used for LLWS detection (Chan et al. 2007). Low level wind shear prediction using NWP models depends on model time and space resolutions (especially within the PBL), model physics, and large scale forcing conditions, and initial conditions. Using a NWP model output, and both QuikSCAT space borne scatterometer (QSCAT) and Buoy observations (Kara et al. 2007, 2008) stated that wind speed errors near ocean boundaries can be up to 5 m s^{-1}. For high resolution NWP forecasts, root mean square error (RMSE) in wind speed is estimated as high as 4 m s^{-1}. Banta et al. (2017) suggested that wind speed error in NWPs were larger than the required accuracy overhigh resolution areas and suggested the use of LIDAR observations to improve forecasts (McCarty et al 2017). Gao et al. (2012) and Moninger et al. (2010) stated that errors in AMDAR measurements can be as high as 4-6 m s^{-1}, and suggested some corrections. Wind speed directional errors can be up to 35 degrees for AMDAR measurements and usually increase toward to the surface (Gao et al. 2012). Therefore, accuracy of wind speed and direction measurements as well as their simulation from NWP models need to be improved since these parameters are directly used in the LLWS calculations (Chun et al. 2017).

3.5 Physical processes for aviation nowcasts

The production of aviation meteorological forecasts is based mainly on forecasters using numerical weather prediction (NWP) model data in combination with available observations (e.g., Jacobs and Matt 2004, Fahey et al. 2016, Bright et al. 2016). Their work suggests that NWP modeling has not yet reached a state where physical processes such as clouds and precipitation can be resolved at the spatial and temporal resolutions necessary for reliable aviation weather forecasts. Jacobs and Maat (2004) also emphasized that various physical processes associated with fog and low stratus clouds are not adequately described in NWP models due to the complexity of the underlying physical processes and the lack of sufficient vertical resolution in the atmospheric BL. Because of this, sudden weather changes on small time and spatial scales can only be evaluated and predicted if the forecaster has access to detailed observations concerning current weather changes. The results of their work strongly emphasized that quality of short-term forecasts, up to 6 h, depends mainly on the availability of local and upstream observations.

3.6 Icing

Most if not all, current icing algorithms include empirical relations (e.g., temperature dependency) as described in Thompson et al. (1997). In their work, inflight icing potential was predicted using algorithms developed by the National Center for Atmospheric Research (NCAR), the National Weather Service's National Aviation Weather Advisory Unit, and the Air Force Global Weather Center. The numerical model data from the Eta, MAPS, and MM5 models were used in their research. As part of the WISP94 field program (Thompson et al. 1997), detailed evaluations of icing algorithms were conducted. Most of the icing algorithms used in NWPs are only functions of T (Noh et al. 2013; Tan and Storelvmo 2016; Odegaard 1997). Thompson et al. (1997) stated that they all predict a flat or increasing frequency of icing at decreasing temperatures.

Statistical studies of pilot-reported icing (Rasmussen et al. 1992) suggested that the number of icing reports decreases with decreasing T. Note that saturation vapor pressure also diminishes with decreasing T. The decreases usually occurs at lower temperatures (<-15°C) because of increasing ice nucleation processes at cold T and less available vapor content. In the Thompson et al. work (1997), all algorithms predicted increasing or stable icing at lower temperatures as expected because of nature of the parameterizations used in the models. These models simply diagnose icing conditions empirically where clouds can occur as a function of RH and T interval between 0°C and -20°C. In fact, the large uncertainty in RH, as high as 10-15% (Gultepe et al. 2016), may lead to substantial differences in icing rates. Similar issues also exist for airport ground operations where de-icing calculations are strongly related to T and Vis (Thompson et al. 1997, Brown et al. 1997). Traditionally, the need for ground de-icing was assessed based on horizontal Vis, but research by Rasmussen

et al. (2001, 2003) showed that the icing hazard was more dependent on the liquid equivalent of snowfall rate and particle shape. This discovery led to the development of NCAR's Weather Support to De–Icing Decision Making System (WSDDM, Rasmussen, et al. 2001).

The above studies signify that icing research is presently immature and need to be improved for NWP model simulations for aviation operations.

3.7 Visibility Reduction due to Fog and Precipitation

Visibility reduction due to fog and precipitation is critical for aircraft operations. In fact, fog after wind represents one of the most hazardous weather events affecting aviation activities. Over last decade, progress has been made in the study of fog processes (e.g., MATERHORN-fog, Gultepe et al. 2016) and climatology (Hodgess and Pu 2016; Albers 1977; Tardif and Rasmussen, 2007; Dorman et al. 2017). NWP models were also used for simulating various types of fog events (e.g., Bergot et al. 2007; Guedalia and Bergot 1994; Bott et al. 1990; Pu et al. 2016; Lin et al. 2017; Chachare and Pu 2018; Pithani et al., 2018) and indicated that numerical simulation of fog is sensitive to various physical parameterization schemes (Gultepe et al 2006; Stolinga and Warner 1999), initial model conditions (Jones 1965; Anderson 1996), and land surface processes (Guedalia and Bergot 1994). Specifically, numerical prediction of the fog presents one of the challenges in NWP due to uncertainties in model physics and Vis algorithms (Gultepe et al. 2009, Guedalia and Bergot 1994, Lin et al. 2017). Also, significant errors in near-surface atmospheric variables prevent accurate prediction of fog and precipitation (especially snow) in NWPs (e.g., Pu et al. 2016; Pu 2017). These errors, therefore, need to be reduced when using NWP models for Vis predictions.

3.8 Satellite data assimilations

Satellite-based wind vectors can be used to infer wind shear, turbulence, and convective activity. Convective clouds identified by the CCM (convective cloud mask, Mecikalski et al. 2007) were supported by the work of Velden et al. (1997, 1998, 2005) that developed the atmospheric motion vector (AMV) algorithm. In this way, GOES-based wind products can be utilized for wind-related event analysis and in data assimilation that can be used for NWP initial conditions and nowcasting applications. Short-term (0 to 1 hr) convective storm nowcasting remains a problem for operational weather forecasting and poses a significant financial risk for the aviation industry (Sieglaff et al. 2011). The output from NWP models and meteorological observations, including

these from radars, are extensively used for short-term convective forecasting but all these have shortcomings. Geostationary imagers data can help reduce some uncertainty, and that can be valuable for convective initiation predictions. The University of Wisconsin Convective Initiation (UWCI) nowcasting algorithm provides an objective, satellite-based decision support tool (Mecikalski et al. 2007). Lately, winds are being obtained from satellites (e.g., Aeolus satellite, Baker et al., 2014) based active platforms such as Doppler LIDARs that can also be used for data assimilations techniques but currently they are used in research method and their data can be used cautiously for aviation operations. Folger and Weissmann (2014) investigated pressure height corrections operational atmospheric motion vectors (AMVs) from the geostationary satellites Meteosat-9 and -10 with cloud-top heights retrieved from LIDAR observations by the polar orbiting Cloud–Aerosol Lidar and Infrared Pathfinder Satellite Observations (CALIPSO) satellite. They found out that 700 mb pressure errors were reduced up to 20%.

3.9 Cloud base height

Cloud base height (h_c) is an important parameter for aviation operations (Table 1), but without proper prediction of cloud microphysical parameters, h_c cannot be estimated accurately. Its estimation is related to cloud total water content (CTWC) and relative humidity (as well as dew point temperature depression (Guttman and Jeck 1987). The formation of cloud at low levels is also related to Planetary Boundary Layer (PBL) physical and dynamical conditions. Unfortunately, cloud TWC from NWPs can be subject to large uncertainties in the PBL because of issues related to model resolution at low levels and turbulence/physical processes interactions. For example, a warm bias of about 3.3 °C in sea surface temperature (SST) can lead to a q_v bias of 1.2 g kg^{-1} that was simulated by ECMWF (Sun et al., 2003). Therefore, improved NWP prediction of RH and T in the PBL can lead to more accurate TWC prediction and that can be used for improving forecasting of h_c levels.

Table 1: FAA based flight classification that is based on cloud ceiling height and horizontal visibility (Adapted from Verlinden and Bright 2017).

Flight classification	Cloud ceiling (ft)	Horizontal Visibility (miles)
IFR	<1000	<3
MVFR	>=1000 and <=3000	>=3 and <=5
VFR	>3000	>5

3.10 Microphysical schemes for fog, cloud, and precipitation

NWPs need better physically-based algorithms to improve fog, cloud and precipitation processes. Detailedand accurate microphysical algorithms are required at various scales to obtain reliable precipitation amount and types, Vis, wind, and turbulence, and cloud radiative properties. Recently, new microphysical algorithms based on improving the single particle growth history were developed (Harrington et al 2013a; 2013b) rather than assumed size distributions for each particle phase (Gultepe et al. 2018; Ferrier 1994, Lin et al. 1983) improved predictions. Pu et al. (2018) found that the simulation of clouds within mesoscale convective systems is sensitive to the various microphysical schemes. They commented that ice hydrometeors play an important role in the accurate numerical prediction of clouds and precipitation. Lately, there has been a shift in the way ice-phase hydrometeors are represented in microphysics schemes, moving from predefined hydrometeor categories with prescribed physical characteristics (e.g., bulk density) and focusing on the prediction of the particle physical evolution instead (Harrington et al. 2013a,b; Morrison and Milbrandt 2015). This has led to the smoother evolution of ice crystals during growth and avoids the artificial process of "conversion" between ice categories and auto-conversion processes. These results suggest that further improvements of the microphysical algorithms can lead to the development of better weather warning and decision making systems.

The NCEP and UKMet Office are working together to create World Area Forecast (WAF) guidance for the aviation weather community worldwide. NCEP has a plan to upgrade its GFS to a Finite Volume – Version 3 model in 2019 (FV3: see https://www.gfdl.noaa.gov/fv3/fv3-documentation-and-references), which will employ an advanced cloud-allowed microphysical scheme, so that better cloud-related predictions of Vis, ceiling, and reflectivity can be provided to the global aviation weather community.

As stated on the various challenging topics described above, NWP predictions for nowcasting applications related to aviation operations may include large uncertainties; therefore, integrated methods should be considered for short term forecasts (e.g., lead time <6 hours), and these are described in next section.

4. INTEGRATED SYSTEMS

4.1 Numerical guidance systems for aviation

A numerical guidance system (NGS) for aviation applications that includes post-processing NWP model output, and local and upstream observations representing high-resolution topography can be used to provide information on changing weather conditions at airports (Hansen et al. 2008). The NGS, supported by detailed predictions of Vis, ceiling, wind, and precipitation observations as well as TAF and TREND type weather forecasts, can be used more efficiently for aviation weather nowcasts.

The NGS can be supplied with high-resolution remote sensing observations such as radar, LIDAR, and wind profilers. For example, Nakamura et al. (2009) and Luce et al. (2010) used both LIDAR and radar to study CAT conditions below a cirrus cloud system. A statistical approach, known as the Graphical Turbulence Guidance (Sharman et al. 2006, Sharman and Pearson 2017), was developed to predict turbulence using a weighted regression of multiple turbulence diagnostics. This product and others such as convection, icing, ceiling and visibility, and surface wind gusts are available operationally on NOAA's Aviation Digital Data Service website (https://www.aviationweather.gov/).

4.2 Integrated systems for nowcasting and test bed sites (supersites)

Integrated weather nowcast systems rely on both in-situ and remote sensing observations, as well as NWP model forecasts. Test bed sites (also called supersites) are an integral part of meteorological research and operations. Ralph et al. (2013) emphasized that they (supersites) can foster new forecast innovations and their transition into operations. The supersites present new opportunities for businesses and agencies to improve their products and services. Their work extensively studied the importance of test beds for research and operations. They also stated that: "Test beds tend to be "outsiders" relative to either the core mission of forecasting or the core mission of research. In spite of this, they enable more rapid improvements in forecast services and demonstrate tangible relevance of research centers to forecast services in the future." A supersite, planned by NWS as the "Operations Proving Ground (OPG)" in Kansas City, MO, will provide full integration testing of new tools and methods in an operational environment. These OPGs require a well-established research community focused on

performing exploratory research and development. They also suggested that transformational research can provide breakthrough advances for forecast/operation services in the future. The objectives of test beds can accelerate the translation of research and development into operations, services, and decision making for short lead time periods. Overall, a test bed site can be used for operational systems, and provide better use of data in forecasts and applications to improve economic/public safety benefits (Ralph et al., 2013).

A new integrated system for aviation operations called The Short-Term Prediction Research and Transition (SPoRT) program using NASA, NOAA, and DoD satellite data and research capabilities is available to the operational weather community to improve short term weather forecasts on regional and local scales (Ralph et al. 2013; Stano et al. 2010; Ellrod and Gultepe 2007). The SPoRT focuses on weather and aviation related problems that include the timing and location of severe weather, changing weather conditions influenced by topography, visibility, land-ocean boundaries, and the monitoring weather in remote areas. The SPoRT involves forecasters in the entire process who help develop product training materials and help assess the utility of the products.

The NOAA NWS Advanced Weather Interactive Processing System (AWIPS, Argyle et al. 2017; Raytheon, 2016) program is a complex network of systems that ingest and integrate meteorological, hydrological, satellite, and radar data for display at Weather Forecast and River Forecast Centers. Weather forecasters then use the data to provide accurate weather, water, and climate predictions and highly reliable warnings and advisories (Kelly and Ghirardelli 1998). As stated in their work, the AWIPS results are extensively used in aviation operations and nowcasting, including time-sensitive, high-impact warnings to protect life and property (Ghirardelli and Glahn 2010). Their work emphasized that the Localized Aviation MOS (Model Observed Sounding) Program (LAMP) consisting of analyzing observations, advective models, and statistical methods can improve the longer-range MOS forecasts based on the GFS model.

One of the earlier integrated systems developed was the CAN-Now project, and its primary objective was to provide a four-season Forecasting/nowcasting system at the major Canadian airports with detailed nowcasts and forecasts (Isaac et al. 2014). The CAN-Now output allows airport related decision makers, including pilots, dispatchers, de-icing crews, ground operators, and air traffic controllers to make accurate decisions to improve safety and efficiency. The prototype nowcasts rely on existing routinely available weather information including NWP model output, site climatologies, remote sensing and lightning network observations, and in-situ measurements of wind, precipitation, visibility, ceiling, and temperature. The integrated nowcast system called The Adaptive Blending of Observations and Models (ABOM) system was developed by Bailey et al. (2009) to be included in the CAN-Now system. The prototype system was used in a nowcasting mode for detecting weather hazards and providing forecasts out to about 3–6 h for most phenomena, and out to 36 h for some subsets of phenomena.

There are several other types of integrated systems that are being used in Europe. The integrated nowcasting through comprehensive analysis (INCA) (Haiden et al. 2011) and AROME-NWC (Auger et al. 2015; Seity et al. 2011) are common ones. These systems include downscale processes and updates NWP predictions using the latest observations from surface in-situ observations and high-resolution (1 km) orography data. A verification of INCA simulations of T, RH, and wind analyses was performed against high-resolution network observations in Austria by Kann et al. (2011) and Haiden et al. (2011). The AROME was developed in France that uses a non-hydrostatic mesoscale model version simulated for the forecast time range of 0–30 h (Auger et al. 2011; Seity et al., 2011). This model is initialized by using a 3-D variational data assimilation scheme (3DVar), and that provides the initial fields relevant for an accurate nowcast; The AROME system was related to the ALADIN–France model (Fischer et al., 2005). Integrated turbulence nowcasts have also been developed to be used for short-term NWP forecasts nudged by in situ and radar observations of turbulence (Pearson and Sharman 2016).

Another example of the use of integrated systems to detect and nowcast hazardous weather is provided by the low-level wind shear (LLWS) alert systems (Thobois et al 2018). It is well-known that thunderstorms can be accompanied by intense updrafts and downdrafts. The strong downdrafts or downbursts below cloud base on or near the ground can force low flying aircraft downward. Then, strong divergent flow, producing low-level (horizontal) wind shear, can lead to unexpected rapid changes in aircraft airspeed and heading. The outflow winds associated with downbursts have horizontal extents > 4 km and can typically persist from 5-30 min. During the Joint Airport Weather Studies project (McCarthy et al. 1982), Doppler radar examination of numerous thunderstorm downdrafts and outflows indicated that wind shear particularly hazardous to aircraft occurred on much smaller temporal and spatial scales, and Fujita (1981, see also McCarthy and Serafin 1984, Wilson and

Wakimoto, 2001) termed this smaller scale, but more hazardous downdrafts/outflows as "microbursts". The damaging outflow winds associated with microbursts have horizontal extents of ≤ 4 km and can persist from 2-10 min, typically (Wilson et al. 1984).

The scale and suddenness of microbursts make them particularly hazardous to aircraft departing or approaching an airport. Thunderstorm outflow or microburst wind shear is known to have caused 21 aircraft accidents with 438 fatalities in the United States between 1975 and 1994 (Wolfson et al. 1994). In response to these accidents, the Federal Aviation Agency (FAA) developed and deployed three ground-based low altitude wind-shear detection systems: the Low Altitude Wind Shear Alert System (LLWAS) (e.g., Linden and Simpson 1985, Wilson and Gramzow 1991), Terminal Doppler Weather Radar (TDWR) (e.g., Wilson et al. 1984, Michelson et al. 1990), and Airport Surveillance Radar Weather Systems Processor (ASR-9 WSP) (Weber and Stone 1995, Cho 2015). The FAA-sponsored Integrated Terminal Weather System (ITWS) uses TDWR reflectivity data with short-term NWP model nowcasts to predict microburst intensity and location (Wolfson et al. 1994). Since the deployment of these systems, along with enhanced pilot training, commercial aircraft LLWS accidents have dropped to nearly zero in the U.S. The dramatic decrease in these accidents testifies to the safety benefits provided by these detection systems.

Enhanced physical understanding of the microburst phenomenon has been provided by high-resolution simulations (e.g., Proctor 1988, 1989, Orf et al. 1996, Orf and Anderson 1999, Nicholls et al. 1993), and laboratory studies (e.g., Ferrero et al. 2014). Because of its importance to aviation, LLWS is routinely forecasted using the vector wind difference of wind between 2000 ft AGL (619.5 m) and the surface (e.g., NOAA NWS Instruction 10-813, 2016), although these forecasts are mainly driven by resolvable non-convective sources, e.g., frontal passages, low-level jets, lee side mountain effects, sea breeze fronts, etc. As NWP model resolution increases to become convection-resolving, routine microburst nowcasts using both observations and NWP forecasts can become routine.

4.3 Artificial Intelligence

As done for other scientific research involving large data sets, increasing data volume and resolution of observations, as well as model simulation output for weather forecasting, led to the application of artificial intelligence for aviation (AIA) research and guidance. Because current NWP models runs have increased time

and space resolutions (McGovern et al. 2017; Weygandt et al. 2009), as well as new observing systems, including in-situ platforms, weather radars, LIDARs, and GOES-16 also generate data at high time and space scale resolutions (Stano et al. 2010; Goodman et al. 2012). Forecasters and users do not have usually time to make rapid decisions if data are not somehow prepared for easy evaluation in advance (Karstens et al. 2015). These data sets are called *"big data."* Artificial intelligence (AI) methods (Pasini and Marzban 2008) use various techniques to process big data sets and then apply the results to weather forecasting issues, which are crucial for creating timely weather reports (McGovern et al. 2017). They stated that AI techniques based on physical understanding of the environment could improve prediction skill of high-impact weather situations. The AI approach expands information available over MOS techniques (Glahn and Lowry 1972) for deriving probabilistic, categorical, and deterministic forecasts available from NWP models.

McGovern et al. (2017) provided an extensive summary of AI techniques used in the meteorological applications. Haupt et al. (2008) also provided an overview of AI techniques applicable to artificial neural networks (ANNs), including decision tree algorithms, genetic algorithms (Allen et al. 2007), fuzzy logic, and principal component analysis (Elmore and Richman 2001). In this area, using a decision tree technique, Burrow et al. (2005) developed lightning detection algorithms for mid-latitudes. Williams (2014) used a random forest approach to diagnose convectively-induced turbulence. These works suggest that AI methods are starting to be used extensively in post-processing of NWP output and in-situ observations.

The AI systems and statistical based neural network systems can help transfer knowledge related to aviation forecasts into the aviation operations when fast computer systems become easily available in the future. But, basic understanding of physical and dynamical processes still need to be developed for the atmosphere that includes cloud, fog, aerosols, as well as wind and turbulence.

5. FUTURE CHALLENGES AND ISSUES

There are various challenging topics related to aviation meteorology that can significantly impact aviation operations, and these are summarized below.

5.1 Visibility and Ceiling Issues

Jacobs and Maat (2005) show that for lead times greater than 4 h, the TAF guidance provides more accurate cloud h_c and Vis forecasts than those derived

manually by forecasters. For shorter lead times (<3 hr), their work suggested that the differences in the comparisons of aviation related parameters are found to be small. For aviation applications, the economic value of reliable weather forecasts is very high (Hansen et al 2009; Gultepe et al 2016). For this reason, large occurrence of high impact weather related to hc and Vis at an airport can reduce airport capacity that can leadi to enormous economic costs. The cloud ceiling (defined in meters for cloud cover >=6/10 of the sky) predictions can be performed based on NWP predictions using the lowest level of cloud total condensed water content (TCWC). The fuzzy logic-based analog forecasting systems (Hansen 2007; Bankert et al. 2004) can also be used for this purpose. A terminal aerodrome forecast (TAF) provides weather conditions and their most probable time of occurrence at the airports. The C_h and Vis (defined by Glickman 2000) are the two variables that together determine flight category [e.g., instrumented flight rules (IFR where Ch<1000 ft or Vis<3 miles) or visual flight rules (VFR) (see Table 1 for flight condition definitions).

The meteorological and aviation scientific communities recently studied meteorological parameters important for aviation operations that are related to ceiling height and Vis forecasts (Rudack and Ghirardelli 2010). These forecasts are valuable for making economical decisions and societal context (e.g. the loss of life). Gultepe et al. (2007) suggested that reductions in Vis can be caused by several hydrometeor types including fog, haze, mist, rain, snow, and blowing snow. Figure 2 shows the meteorological events that contribute to the integrated Vis estimations. Because of Vis complexity and difficulty in measurements especially in cold climates, its use in NWPs can still be difficult and includes large uncertainties (Gultepe et al. 2006, 2018).

5.2 Contrails and Frost

Contrail formation, development, and dissipation are important for aviation and climate sciences but studies on these are limited. Contrails form when water vapor condenses on IN (ice nuclei) and then freeze on aerosols from the exhaust of aircraft engines at T less than typically -40°C (Schumann et al. 2012 for an overview). Although contrails at -40°C occur at high levels in mid-latitudes and tropical weather, they can also occur near the surface during Arctic winter (Gultepe et al. 2015). Heymsfield et al. (2010; 2011; 2005) also stated the importance of contrail microphysical conditions for better understanding of ice cloud nucleation processes. Contrails can indicate higher values of moisture at the cold temperatures that may cause frost and light snow precipitation at high northern latitudes (Gultepe et al. 2016; 2017). Figure 8 shows heavy frost conditions occurred on an ice particle counter during an Arctic project (Gultepe et al., 2015; 2018). Frost formation on aircraft surfaces is also a condition for deicing at the airports which is a required by the FAA (2017).

Figure 8: Frost formation on ice particle counter sensor which occurred during the FRAM ice fog project in Barrow, AL, on April 16 2008.
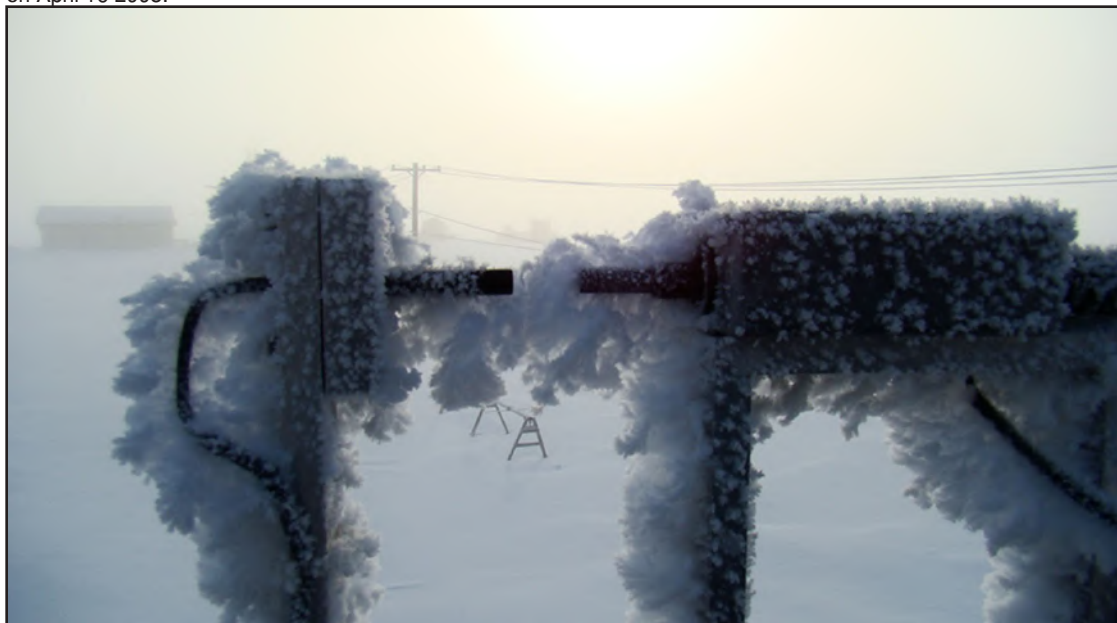
Over the northern latitudes, contrails, including aircraft-produced ice particles (APIPs), can be visible within the ABL over the airports (Gultepe and Heymsfield 2016; Heymsfield et al. 2011; Schumann and Heymsfield 2017; Gultepe et al. 2014; 2015, Woodley et al. 1991; Langmuir et al. 1948; Ludlam 1956). Contrails may modify the atmospheric environment in several ways. For example, Heymsfield et al. (2011) stated that holes in clouds are also due to inadvertent seeding of clouds with IN particles generated by aircraft and these are produced through spontaneous freezing of cloud droplets in air (Heymsfield and Sabin 1993; Heymsfield and Sabin 1989) and that is cooled as it flows around aircraft propeller tips or jet aircraft wings. Their work also suggested that polar clouds are particularly susceptible to the APIPs effects through modifications in radiative processes. This may also suggest that ice crystals sampled by aircraft probes over the Arctic environment may include APIPs and these need to be researched. Contrails are considered as prototype cirrus which impacts the energy budget of the atmosphere by reflecting incoming SW radiation and trapping outgoing IR radiation (Markowicz and Witek 2011, Schumann et al. 2012; Spangenberg et al. 2013; Minnis et al. 2013). How contrails from an aircraft can contribute to global climate change was studied in detail by Minnis et al. (1998, 1999), Schumann et al. (2012), Schumann and Heymsfield (2017). Whether or not contrails would contribute to global warming or cooling is still not clear, and probably cannot be ascertained without resort to high-resolution climate models (Schumann and Mayer 2017).

5.3 Climate change impact on aviation

Future research on the combined impacts of climate change and climate variability on aviation operations can help airlines and other aircraft operators for long term planning. For example, Goodman and Griswold (2017) investigated future density-altitude (DA) trend evaluations. Their work stressed the importance of future investigations on the impacts of ENSO and Atlantic Oscillations (AO) on DA to be used in seasonal-scale planning of aviation operations. The weight restriction is an important factor in planning future flight operations, therefore, needs to be evaluated. For this reason, airlines may need to be rescheduled out of the hottest parts of the day. Other potential impacts include anticipated jet stream changes with consequent impacts to CAT (e.g., Williams and Joshi 2013; Williams 2017; Storer et al. 2017), and changes to convection (e.g., Del Genio et al. 2007) and other extreme events (Puempel and Williams 2016). Both Irvine et al.

(2016) and Williams (2016) suggested that the effect of wind changes as a potential impact of climate change on aviation can be important for future aviation operations. This is of particular interest for trans-Atlantic flights, where the pattern of upper-level winds over the north Atlantic, in particular the location and strength of the jet stream, strongly influences both the optimal flight route and the resulting flight time. Some of these effects may be mitigated by "climate optimized routing" procedures (e.g., Matthes et al. 2012).

Figure 9 shows the time series of cold spell T and warm spell T indexes obtained from CMIPS models (Sillmann et al. 2013a,b) where increasing warm days and slightly decreasing cold days are seen from 1948 to 2005. Therefore, increasing convective activities are likely expected and that can be related to shear, turbulence, and heating processes and these can play an important role for planning procedures of the aviation applications.

5.4 Operational satellites

Lately, geostationary satellites with more than the traditional five imaging channels are being used for weather analysis and operations, and these satellites carry additional channels in the IR windows. A review paper on geostationary satellites is given this special issue by Ellrod and Pryor (2018); therefore, limited information is provided in this sub-section. The ABI is used on the Geostationary Operational Environmental Satellite-R Series (GOES-16) and that views Earth with 16 spectral bands (compared to five on previous GOES), including two visible channels, four near-infrared channels, and ten infrared channels. Himawari 8 is a Japanese weather satellite and carries an Advanced Himawari Imager (AHI) with also a 16 channel multispectral imager to capture visible and infrared images of the Asia-Pacific region (Berndt et al 2018). The instrument was designed and built by Exelis Geospatial Systems (now Harris Space & Intelligence Systems). The FY-4 (FengYun-4) is the China Meteorological Administration (CMA) second-generation three-axis stabilized, geostationary meteorological satellite developed by CAST (China Academy of Space Technology) (Yang et al 2017). Two variants of spacecraft of the FY-4, with one carrying optical sensors and the other carrying microwave sensors were developed. FV-4 carries an AGRI (Advanced Geosynchronous Radiation Imager) with 14 channels, VISSR (Visible and Infrared Spin-Scan Radiometer) 5 channels, GIIRS (Geostationary Interferometric Infrared Sounder), LMI (Lightning Mapping Imager, Goodman et al. 2013), and a SEP (Space Environment Package). All these satellites can improve global aviation products in more detail.

Figure 9: Time series of percentile indices from 1948 to 2005 of the ensemble mean (solid) and median (dashed) of 31 CMIP5 models (black) and 18 CMIP3 models (green). The shading indicates the interquartile ensemble spread (range between the 25th and 75th quantiles). Note that the percentile indices from the reanalysis ERA40 (blue) from 1958 to 2001 and NCEP1 (red) from 1948 to 2005 are calculated with a different base period (1961 to 1990) than those from ERA-Interim (cyan) and NCEP2 (orange) with a base period from 1979 to 2008. Displayed are global averages over all land for CSDI (a) and for WSDI (b). Grey shading along the horizontal x-axis indicates the evolution of globally averaged volcanic forcing according to Sato et al. (1993) (Adapted from Sillmann 2013a, b). American Meteorological Society. Used with permission.
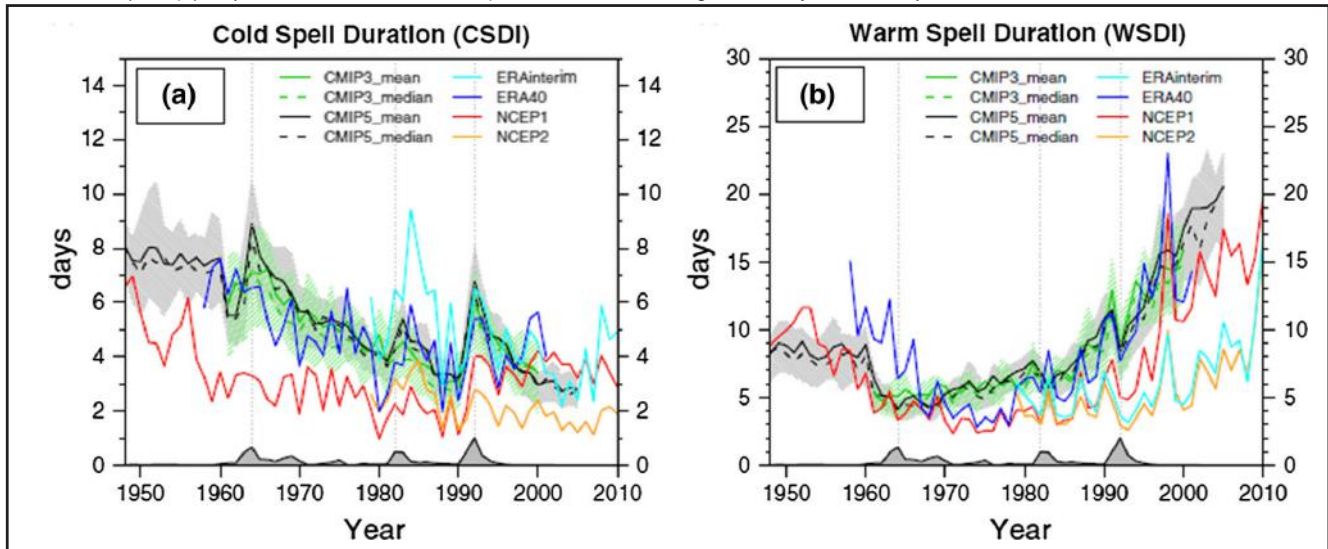
New generation imagers are also being deployed on polar-orbiting satellites, which provide aviation information over high-latitude regions, which are only partially observed by geostationary orbiters. These new imagers, such as the Visible Infrared Imaging Radiometer Suite (VIIRS) on the Suomi National Polar-orbiting Partnership (NPP) satellite and NOAA-20+ series, provide a large number of channels that are similar to or more expansive than their geostationary satellite counterparts (Menzel et al. 2018). These imagers will greatly enhance the satellite information useful for aviation over Polar Regions. Inclusion of spectral IR capability for geostationary satellites such as Chinese GIIRS (Menzel et al. 2018) can improve knowledge obtained for atmospheric stability, providing information on convective weather warnings and forecasts (Chiodi and Harrison 2010). Spectral IR capability has been used in polar orbiting satellites e.g., AIRS (the Atmospheric Infrared Sounder), CrIS (Cross-Track Infrared Sounder; Zhang et al. 2016, Wang et al., 2012) and IASI (the Infrared Atmosphere Sounding Instrument) on Aqua, Suomi-NPP, NOAA-20, and METOP (Meteorological Operation) satellites (Mittaz and Harris 2011; Blumstein et al. 2007; Wang and Cao 2008) to obtain T, RH, and wind vertical structure in the region with no clouds and above the cloud tops. More extensive development of spectral IR techniques can revolutionize technology related to aviation weather forecasts.

To improve nowcasting techniques for detecting, tracking, and monitoring the early development of small convective clouds, convective initiation forecasts over the CONUS and possibly over marine environments were studied in detail using satellite observations (Mecikalski et al. 2007). Historically, most of the convective weather predictions used weather radars (e.g., Mueller et al. 2003). However, radars usually do not see the early stages of convective cloud development prior to precipitation development. Since the 1990s, NCAR began to incorporate satellite information into convective storm nowcasting system (the Auto-Nowcaster). Satellite feature detection algorithms (e.g., Bankert 1994; Bankert et al 2009; Roberts et al. 1999; Tag et al. 2000, and Roberts and Rutledge 2003) were usually used to classify cloud types, identify surface convergence boundaries, and monitor the cloud growth based on the changes in their IR cloud-top T. These developments were positive for nowcasting systems but additional data sets from GOES-16 channels can further provide information related to cloud types and related physics and dynamical processes, and need to be researched.

5.5 Measurement uncertainties

5.5.1 T and RH: A better understanding of the uncertainties in observations can be important for decision making systems, and that can be used for obtaining better physical parameterizations for NWP simulations and improvements in data assimilation techniques (e.g. 4-D Var). Both T and RH uncertainties in NWP predictions can be very large

and that affect the prediction of cloud formation, visibility, and convective intensity, and surface-air interactions through turbulent fluxes using NWPs (Feingold 1999). Figure 10 shows RHw measurements obtained during the FRAM project (Gultepe et al. 2014; Gultepe 2015). This plot shows that Vis is strongly related to RHw; increasing RHw results in decreasing Vis. A small change in RHw at about 4-5% can lead to Vis changes from 50 km down to few meters. This means the possible errors in RHw from NWP predictions can lead to significant issues for aviation forecasts, e.g. Vis and cloud types and that can affect operations significantly.

Figure 10: Vis versus RH_w from a severe fog case event at the FRAM site during in Snow-V10 project.
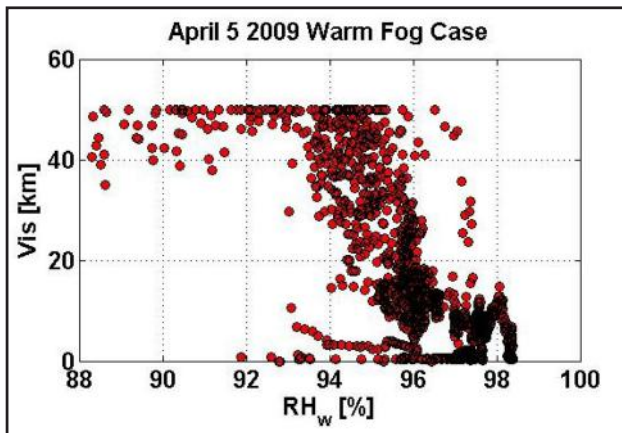

5.5.2 **Visibility and Ceiling height:** The present challenges of Vis and h_c measurements are related to precipitation/fog hydrometeors types and scale issues (Gultepe and Isaac 2004; 2006). They suggested that discrimination of droplets from precipitation and its usage in Vis parameterizations are critical for NWP Vis predictions. Figure 11a shows a scatter plot of Vis measurements from the most commonly used sensors (Vaisala FD12p and Sentry sensors), and ice fog crystals (Fig. 11b) occurring over Yellowknife International Airport (CYK) during the FRAM ice fog project (2010-2011 winter, Gultepe et al., 2016).I Ice fog crystal sizes were found to be usually <300 µm. The concentration of the Vis observations (along green line) in Fig. 11a is seen above the 1:1 line (red line), indicating that FD12p instrument Vis values were usually larger than Sentry Vis by about 50%. For this reason, in automated observing systems, a double Vis sensor approach should be used for model validations and comparisons with METAR observations. Especially, this needs to be improved for cold climate applications where warming trend can cause severe cold fog events (Figure 12).

Figure 11: Vis from FD12P sensor against Sentry Vis **(a)** for all precipitation types and ice fog, and ice fog crystals **(b)** collected during FRAMIF project took place over Yellowknife International Airport (2010–2011 Winter).
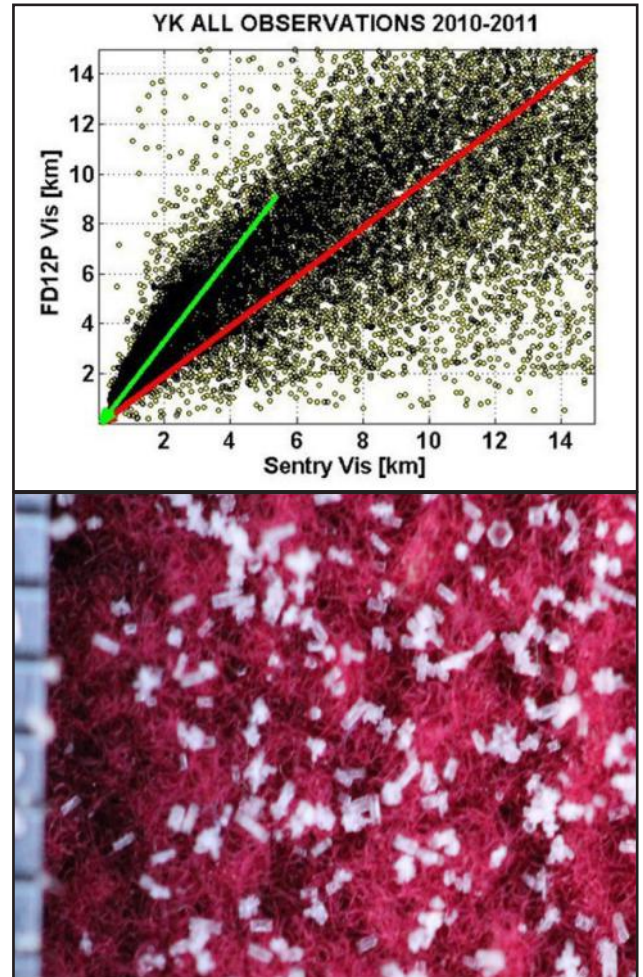
Based on fog occurrence, forecasting Vis over short time intervals (0-6 hrs) is challenging and most NWP models do not explicitly predict Vis (Chmielecki and Raftery 2011); therefore, Vis forecasts must first be derived from other meteorological parameters such as cloud water content (CWC), RHw, and precipitation. Roquelaure and Bergot (2008, 2009) were the first to use Bayesian model averaging (BMA) analysis in Vis forecasting. Zhou et al. (2009) also described the use of a short-range ensemble forecast system to generate probabilistic visibility forecasts. The UK Met Office Global and Regional Ensemble Prediction System (MOGREPS) and NOAA NCEP Ensemble Prediction Model (Zhou et al. 2009; Zhou and Du 2010) have already been used for probabilistic aviation weather predictions (Gill and Buchanan 2014; Chun et al. 2017; Kim et al., 2015).

Figure 12: Ice fog occurrence over the Arctic Ocean on Aug 24 2010 (Permission by G. Toth).
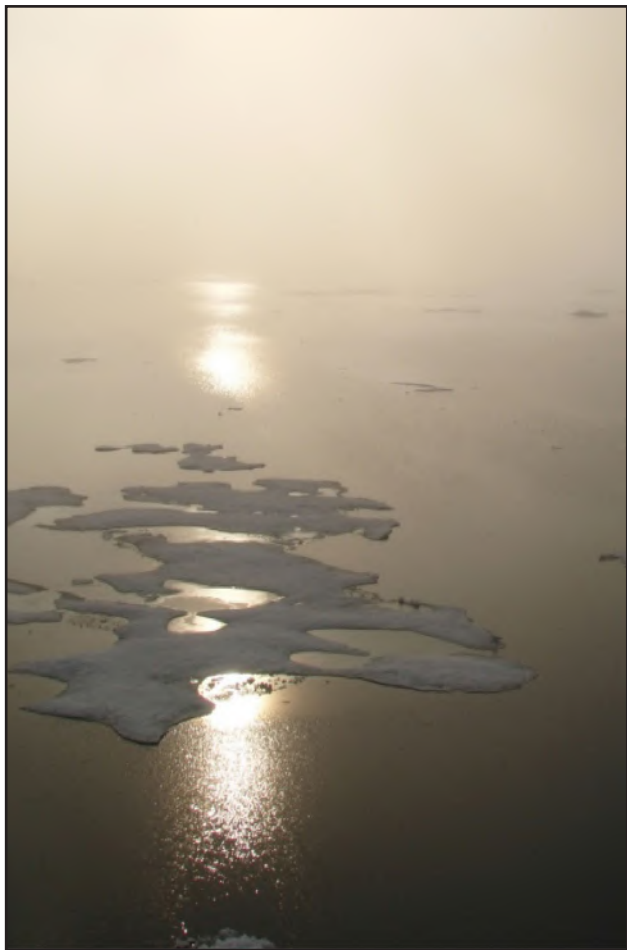
Operationally, aviation-related interests in the US typically use two types of ceiling and Vis forecasts provided by the NWS Global Forecast System (GFS) model: 1) GFS MOS forecasts and 2) GFS Localized Aviation Model Output Statistics Program (LAMP) forecasts. Both the GFS MOS and GFSLAMP produce probabilistic forecasts for seven ranges of Vis and return to the user a categorical forecast corresponding to the most likely range of values. These existing methods do not provide a general framework for generating a full predictive probability density function (PDF) for Vis (Chmielecki and Raftery 2011). They stated that predictive PDFs are attractive for Vis forecasts because both thresholds of ceiling height and Vis correspond directly to the conditions governing flight rules. A predictive PDF allows the user to determine the probability of Vis falling below any threshold of interest rather than a single pre-specified threshold. Therefore, PDF based approaches for ensemble prediction of Vis and ceiling height need more research.

Cloud ceiling measurements are usually performed by ceilometers or are based on manual observations of sky conditions at airports. It is defined as the height of the lowest layer of clouds above the surface that is either broken or overcast, but not thin. The broken and overcast conditions are measured by the "octals", which are 8 equal segments of the sky (NOAA 2012; Free and Sun 2013). The ceilometers measurements usually provide cloud conditions at 3 levels e.g. low clouds, middle clouds, and high level clouds, but they may not have the same meaning as man-made observations. Therefore, these measurements should be properly compared and integrated for aviation applications.

5.5.3 Turbulence and EDR

Measurements of 3D wind components and prediction of EDR and gust conditions are also critical to aviation operations (Sharman et al. 2018, Gultepe et al. 2018, current issue). Although gust values usually are presented based on the horizontal wind components, the vertical component also plays a significant role in gust and EDR estimation. These can be obtained using in-situ ultrasonic sensors (Gultepe et al. 2018) or from AMDAR or TAMDAR EDR reports obtained from commercial flights, and also likely from remote sensing platforms such as LIDAR and radar, and inferences for satellite features (Benjamin et al. 2007). In all events, EDR is an estimated quantity that is not actually "measured", so it is particularly difficult to determine the uncertainty in the estimate. Pearson and Sharman (2017) studied EDR from onboard aircraft estimates versus nearby METARs wind speed and wind gust measurements (Figures 13a and 13b, respectively). The fits for each represent large variability in data. The scatter around the mean curves was very large. This is not surprising since turbulence is a microscale phenomenon with large spatial and temporal variability. But this implies that uncertainties in the use of dynamical parameterizations for EDR versus gust can be large and NWPs need probabilistic approaches or better diagnostic approaches.

Figure 13: Plots of (left) 117 069 wind speed and (right) 15 382 wind gust observations (kt) matched with in situ EDR reports within 5 km, 5 min, and 1000 ft of each other. Median speed and gust values within each 1-kt bin are shown as black dots. Fit lines to the median values are shown in black (linear) and purple (square root). Adapted from Pearson and Sharman 2017).
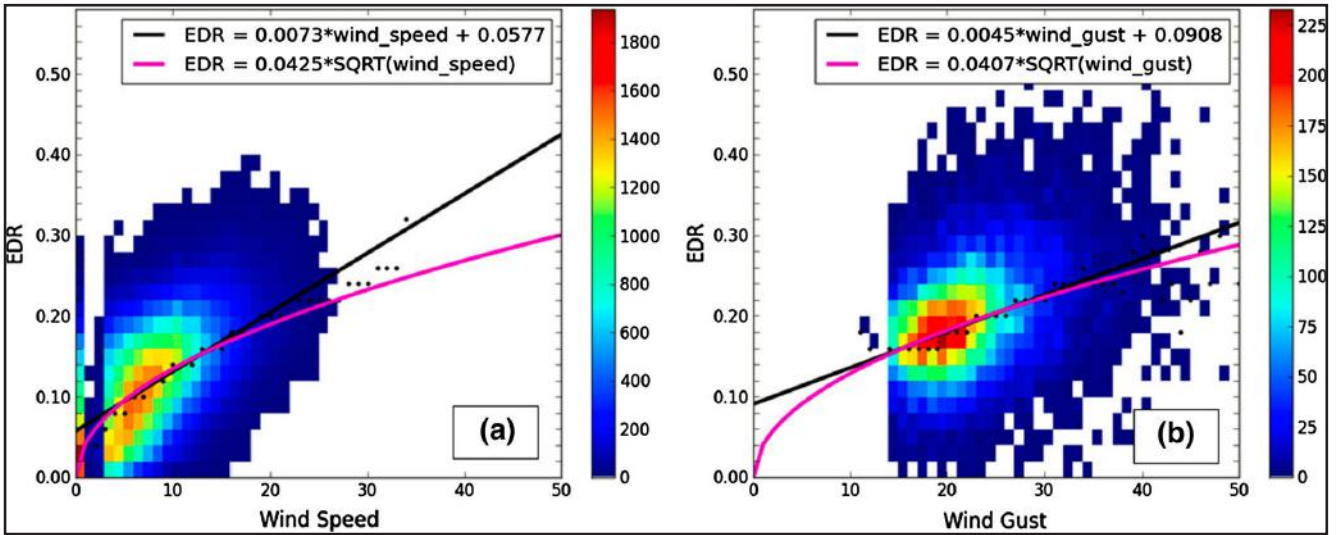
5.5.4 Low Level Wind Shear (LLWS) measurements

As provided previously low level wind shear measurements can have large uncertainties based on measurement field designs and instrument type. For example, ultrasonic wind sensors (2D or 3D) can have issues when icing or precipitation occur (Gultepe et al. 2018). If they are heated for icing conditions, additional issues may arise due to heating the tips of sensing units. On the other hand, icing may also affect conventional wind measurements using regular anemometers. Use of Doppler LIDAR based techniques may work nicely to obtain good results for clear air and light cloud conditions but under the heavy precipitation and large optical thickness conditions they cannot penetrate in-cloud conditions and will fail for wind measurement retrievals (Thobois et al. 2018). Table 2 (ICAO 2005) provides criteria for low LLWS definitions that indicates the accuracy wind speed and direction measurements should have.

Table 2: Synthesis of the ICAO guidelines for observing low level wind shears (ICAO, 2005). TDWR: Terminal Doppler Weather Radar, LLWAS: Low level wind shear, PPI: Plan Position Indicator. HKO: Hong Kong Observatory.

Features	Alerts	Warnings
Coverage	3 NM extension to runways is commonly used whatever the wind shear equipment (LLWAS, Lidars, TDWR/Radars)	Up to 9.55 km for a glide slope of 3Deg in order to monitor up to the altitude of 500 m.
Update Frequency	• LLWAS: update every 30 sec • Radar/lidar: update between 1 to 6 mins	Typically 5 minutes are used for radars and lidars
Resolution	• LLWAS: 1 NM between 2 anemometers • RADAR: 100-250 m • Lidar: 100-200 m	Same as alerts
Scanning patterns	One horizontal scan (PPI) at 3 deg scans per approach are used	Several products can be used from 2 to 5 PPI scans
Methods for computing alerts	• Wind shear alerts: Headwind/tailwind changes over 1 NM or along the runway superior to 15 Knots. • Microburst alerts: Headwind/tailwind changes over 1 NM or along the runway superior to 40 Knots. • LLWAS: NCAR Algorithm • RADAR: Runway-oriented wind shears algorithms like the ones developed by MIT-Lincoln Lab for TDWR, HKO algorithm, products of commercial software like RAINBOW5 developed by Selex and IRIS developed by Vaisala.	Additional products can be computed from radial radar or lidar data according to local needs like shear products, gust front detection, wind reconstruction

5.6 Convection parameterization and prediction

Convection parameterizations developed based on the data obtained from NWP models, observations, and integrated methods can play an important role for aviation operations (Wang and Seeman1997; Megenhardt et al., 2000; Grell and Deveny 2002; Dupree et al., 2009; Yang et al., 2012). Wang and Seeman (1997) used four cumulus parameterization schemes (CPSs) representing the Anthes–Kuo, Betts–Miller, Grell, and Kain–Fritsch schemes based on The Pennsylvania State University–National Center for Atmospheric Research mesoscale model. The model's precipitation forecast skill is found to be better in rainfall amount compared to the areal coverage or the peak amount. They also stated that CPSs in warm-season cases with moist downdrafts were able to predict the surface features, such as pressure centers and gust front, more accurately but improving mesoscale quantitative precipitation forecasts overall remain a very challenging problem, even when a model is equipped with a sophisticated subgrid-scale convective scheme. This suggests that use of forecaster contributions for providing convective outlooks, mesoscale concepts, and severe weather warnings such as heavy precipitation, hail, and tornado watches can improve short term predictions for aviation operations. Usually, aviation forecasts need a forecast warning time of less than a 1 hr time-period. The Storm Prediction Center (SPC) of NOAA NWS has also a human component for severe weather prediction (Karstens et al. 2018; Cohen et al. 2017). The human component needs to be considered because accumulated errors of NWP model physical components for predictions can be significant when simulation times are less than 1 hr. In fact, synoptic scale environments associated with severe weather conditions can complicate short term predictions but human based knowledge can help to improve short term predictions.

Convection-allowing numerical model (CAM) ensembles can provide extensive information related to storm intensity, location, and evolution but do not forecast accurately maximum hail size at the surface (McGovern et al. 2017). Based on the large variability related to meteorological observations and NWP scale issues, and deterministic parameterizations, probabilistic analysis of the aviation meteorological parameters predictions are needed. For example, Figure 14 shows the observed frequency of hail amount for sizes >25 mm versus forecast probability using the CAM Analysis and Prediction of Storms (CAPS) ensemble predictions(McGovern et al., 2017). Verification results and a single forecast case in Fig. 14 are given for the machine-learning hail forecasts and other storm surrogate probability forecasts, including HAILCAST (1-D Hail Forecasting model, Jewell and Brimelow 2009), column total graupel, and updraft helicity (McGovern et al. 2017). The Random Forest (RF) analysis (Ahijevych et al. 2016)

used for this experiment was trained using CAPS ensemble forecasts during May-June 2014, and evaluated based on CAPS ensemble forecasts. The performance diagram in Fig. 14a shows that for a given probability threshold, the machine-learning models tend to have fewer false alarms, a lower frequency bias, and higher overall accuracy than other methods. The attributes diagram in Fig. 14b indicates that the probabilities from the machine-learning models and updraft helicity are generally reliable, while other methods tend to produce probabilities that are overconfident. These results suggest that probabilistic approaches for convection prediction need to be developed in the future that are based on RF or other AI methods.

The demand for accurate nowcasts of convective precipitation that includes heavy precipitation and hail has led to development of the high-resolution data assimilation and rapid cycling numerical weather prediction system (e.g., Sun et al. 2013). In their work, they reviewed the recent progress on the use of NWP for nowcasting convective precipitation and provided future expected challenges and opportunities. They emphasized that NWP models generally produce larger quantitative precipitation forecasts (QPFs) than nowcasting systems beyond a few forecast hours. Therefore, they suggest blending radar echo extrapolation with a numerical model run to generate a seamless 0–6-h forecast. Nowcasting and Initialization for Modeling Using Regional Observation Data System (NIMROD; Golding 1998) was the first system that used blended radar echo extrapolation with a NWP output. For the first hour nowcast, the extrapolation of the observed precipitation field was given full weight, and it was gradually relaxed with increasing lead time to where the model eventually received full weight. This method was better than earlier radar echo tracking systems. The blending of the corrected model forecasts with extrapolation forecasts allows for a smooth transition from the extrapolation to model forecasts (Sun et al. 2013). Similar results have been shown over the years starting with Browning (1980), Doswell (1986), and Austin et al. (1987).

A recent paper by Sokol and Zacharov (2012) described a new blending method that assimilates the extrapolated radar reflectivity with a nudging technique. The decrease in skill by extrapolation related to the size and organization of the precipitation were also emphasized by Wilson (1966) and Wilson et al. (1998). Based on a large set of predictor fields, and inserting the location of boundary layer convergence lines in NCAR's AutoNowcaster (ANC) (Mueller et al. 1993), Wilson et al. (2004) predicted storm initiation up to one hour in advance that shows the importance of BL processes. The ANC system uses fuzzy logic to combine predictor fields that reflect the atmospheric environmental conditions and boundary layer forcing based on observations and numerical model runs.

To meet the needs of nowcasting, numerical models have to be run at resolutions less than a few kilometers. Wilson and Roberts (2006) stated that the 10-km Rapid Update Cycle (RUC10) 3-h forecasts issued every 3 hr were correct at predicting areas of convective initiation only 13% of the time. Sun et al. (2013) stated that possible factors limiting the model's ability to predict precipitation initiation was likely insufficient model resolution in addition to many other factors. Models with high resolutions can enable the explicit representation of convective processes without cumulus parameterization schemes. These models are called as "convection-permitting" or "convection-allowing" NWP (e.g., Sun et al. 2013). Many other studies show that forecasts from the convection-permitting models produced more skillful guidance than those from a coarser-resolution model employing convective parameterization (e.g., Done et al. 2004; Kain et al. 2006; Weisman et al. 2008; Clark et al. 2009). Verification of convection forecasts is challenging, and innovative methods are needed to account for small errors in model derived location and timing (e.g., Pinto et al. 2015).

Overall, various algorithms and systems have been used in storm convection prediction. The FAA Aviation Weather Research Program (AWRP) has led to very successful development of forecasts of both convective systems and winter storms, using heuristic and numerical models for aviation applications (Wolfson et al 2008; Wolfson and Clark 2006). The FAA effort consolidating the storm prediction systems led to the establishment of collaboration between MIT Lincoln Laboratory (MIT LL), the National Center for Atmospheric Research (NCAR) Research Applications Laboratory (RAL), the NOAA Earth Systems Research Laboratory (ESRL) Global Systems Division (GSD) and NASA, called the Consolidated Storm Prediction for Aviation (CoSPA; Wolfson et al. 2008). The CoSPA is funded under the FAA's Aviation Weather Research Program (AWRP) (Dupree et al 2009). One of the goals of the Next Generation Air Transportation System (NextGen) project (Stobie et al 2008) is to consolidate the redundant and sometimes conflicting forecast systems into a Single Authoritative Source (SAS) for aviation uses (Dupree et al 2009). The current CoSPA prototype for 0-6 hour forecasts is part of the NextGen Initial Operational Capability (IOC) in 2013.

5.7 Observational methods

The accurate testing of nowcasting products is strongly related to observations and their analysis. Golding (1998) suggested that products should be assessed against both point observations and analyses. Nowcasting systems usually integrate observations with Numerical Weather Prediction (NWP) model products for short term predictions up to six hours ahead. In Golding et al. (1998), precipitation, cloud, and visibility were the main conditions to be considered in the analysis. The precipitation rate in the analysis used a combination of the processed radar and satellite data, surface reports, and NWP simulation output. The precipitation type was also diagnosed in their work using NWP fields. Improving nowcasts is a strong function of the integrated systems that are used in the observations and model outputs (Bailey et al. 2009). Developments of these nowcasting systems in the near future will likely be improved by artificial intelligence (AI) methods and using new observational platforms such as S-Pol radars and LIDARs.

Generally, NWP prediction assessments against point observations are only reported for analyses because the representativeness errors of meteorological parameters are of similar magnitude to the forecast errors. In general, assessments of predictions against analyses performed over restricted geographical areas are considered good because of observational coverage. If not considered, then the verification statistics can be very uncertain. Because of possible natural variability in observations, use of supersites with satellite stations (Gultepe et al. 2018; Ralph et al. 2013) should to be further researched for data assimilation and model output validations. Verifications performed by (Vislocky and Fritsch 1997) showed that the observations-based methods were not only far superior to persistence climatology at all lead times (5%–20% improvement) but also outperformed the MOS-based technique at the 1- and 3-hr lead time projections with skill increases averaging four percentage points. This suggests that for nowcasting applications, observations should be weighted more than MOS techniques.

In the future, although expanded computational techniques can be expected to reduce the uncertainty in the predicted parameters related to aviation meteorology, improvements in individual models and physical parameterizations and their careful verification is paramount (e.g., Yano et al. 2018 and references therein). Physical parameterizations related to aviation meteorology forecasting are not well-represented at NWP scales presently in use; therefore, new scale-dependent physical parameterizations will be needed to improve the NWPs predictions in deterministic or probabilistic approaches.

Forecasting accuracy of high impact weather parameters are strongly dependent on availability of integrated data sets (both observations and predictions) and should take advantage of probabilistic forecast methods (Benjamin et al. 2010; Zhou et al. 2009). Unfortunately, errors related to components of the NWP ensemble simulations do not usually cancel out each other but tend to accumulate. As shown in this review, both measurements and statistical approaches, as well as newly developed scale-dependent physical (e.g. Vis) and dynamical parameterizations (e.g.

Figure 14: Performance diagram comparing different hail forecasting methods (a). Attributes diagram indicating the reliability of different forecasting methods (b) (Adapted from McGovern et al. 2017). American Meteorological Society. Used with permission.
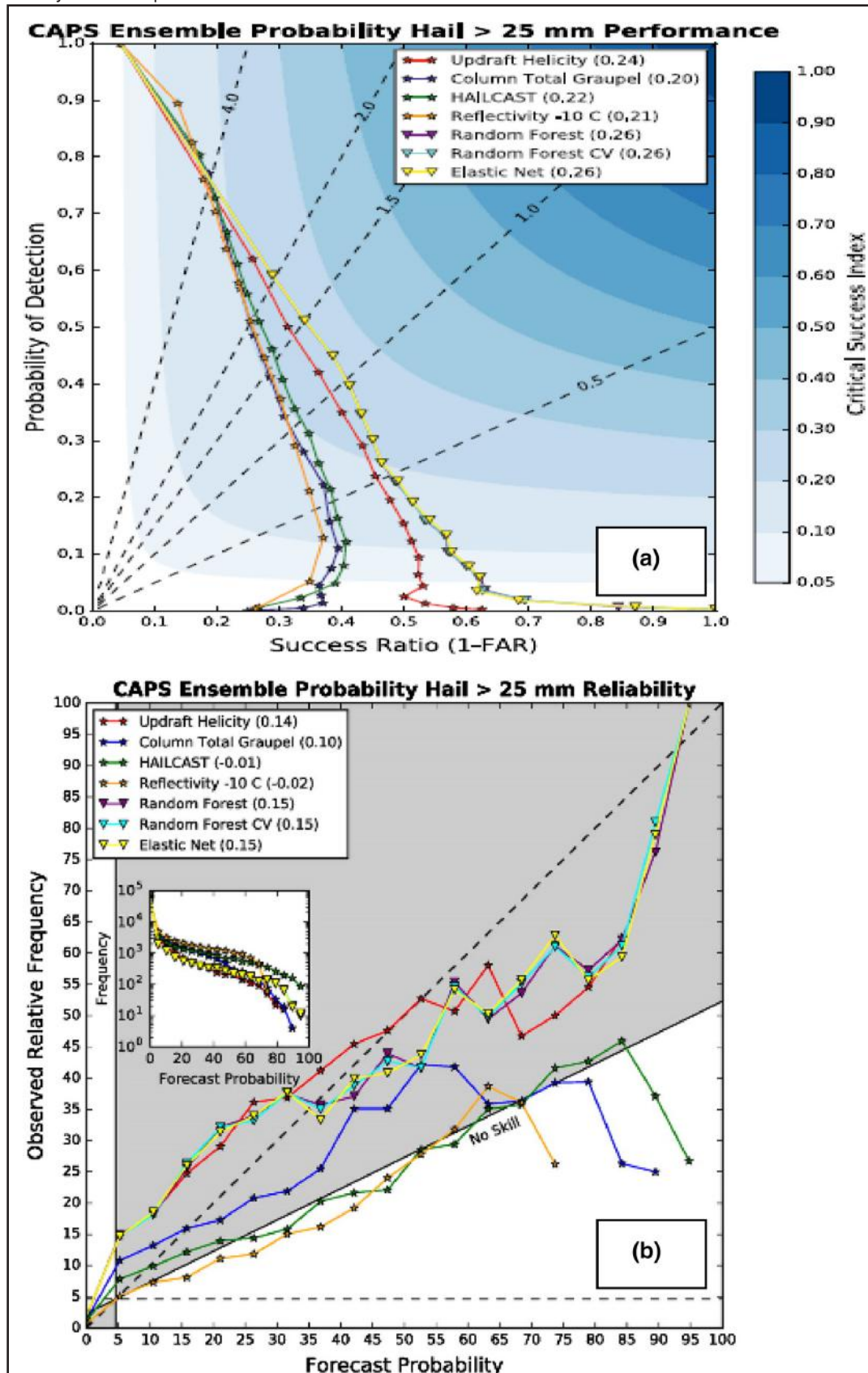
EDR, CAT) parameterization are needed to improve the accuracy of the NWP model predictions that are related to core physical and dynamic processes.

Overall, the issues with predictions of gusts and EDR, Vis, precipitation amount and rate, fog, icing/deicing, and lightning as well as convective intensity require more advanced designs for the meteorological supersites and physically-based approaches for parameterizations of severe weather parameters under various climatic environments. In this respect, in-situ observations at the surface and within the atmospheric layer in both cloud and cloud-free regions are required to improve the aviation nowcasting and also for improving the accuracy of the long-range forecasts.

In response for the needs of global aviation community, NCEP and UK Met Office are currently assigned by ICAO (International Civil Aviation Organization) to create World Area Forecast (WAF) guidance for the aviation weather community worldwide. Both centers are now providing operational global icing and turbulence forecasts based on their global forecast systems. NCAR's fuzzy logic icing and GTG turbulence algorithms have already been implemented into NCEP's Unified Post Processor (UPP) to generate both icing and turbulence forecasts (Chuang et al. 2018). Results of this collaboration indicated that aviation meteorology issues are not only locally recognized but also globally, and need to be evaluated and integrated.

ACKNOWLEDGMENT:

REFERENCES

Ahijevych, D., J. O. Pinto, J. K. Williams, and M. Steiner, 2016: Probabilistic forecasts of mesoscale convective system initiation using the random forest data mining technique. *Wea. Forecasting*, 31, 581–599, doi:10.1175/WAF-D-15-0113.1.

Alapaty, K., N. L. Seaman, D.S. Niyogi, and A.F. Hanna, 2001: Assimilating Surface Data to Improve the Accuracy of Atmospheric Boundary Layer Simulations. *J. Appl. Meteor.*, 40, 2068–2082.

Albers, H.W., 1977: ICAS items. *Bull. Amer. Meteor. Soc.*, 58, 342–343.

Allen, C. T., S. E. Haupt, and G. S. Young, 2007: Source characterization with a genetic algorithm–coupled dispersion–backward model incorporating SCIPUFF. *J. Appl. Meteor. Climatol.*,46, 273–287.

Anderson, J. L., 1996: Selection of Initial Conditions for Ensemble Forecasts in a Simple Perfect Model Framework. *J. Atmos. Sci.*, 53, 22–36.

Ansmann, A., I. Mattis, U. Wandinger, F. Wagner, J. Reichardt, and T. Deshler, 1997: Evolution of the Pinatubo Aerosol: Raman Lidar Observations of Particle Optical Depth, Effective Radius, Mass, and Surface Area over Central Europe at 53.4 N. J. Atmos. Sci., 54, 2630–2641. Appleman, H., 1953: The formation of exhaust condensation trails by jet aircraft. *Bull. Amer. Meteor. Soc.*, 34, 14–20.

Auger, L., O. Dupont, S. Hagelin, P. Brousseau and P. Brovelli, 2015: AROME–NWC: a new nowcasting tool based on an operational mesoscale forecasting system. *Q. J. R. Meteorol. Soc*. 141: 1603–1611.

Austin, G. L., P. Dionne, and M. Roch, 1987: On the interaction between radar and satellite image nowcasting systems and mesoscale numerical models. Proceedings.. Mesoscale Analysis and Forecasting, Vancouver, BC, Canada, European Space Agency, 225–228.

Bailey M. E., Isaac G. A., Driedger N., Reid J. 2009: Comparison of nowcasting methods in the context of high-impact weather events for the Canadian Airport Nowcasting Project. *International Symposium on Nowcasting and Very Short Range Forecasting*, 30 August – 4 September 2009, Whistler, British Columbia.

Bailey, M. E., G.A. Isaac, I. Gultepe, I. Heckman and J. Reid, 2014: Adaptive Blending of Model and Observations for Automated Short-Range Forecasting: Examples from the Vancouver 2010 Olympic and Paralympic Winter Games. J. *of Pure and Applied Geophysics*. DOI 10.1007/s00024-012-0553-x. 171, 257-276.

Baker, W.E., R. Atlas, C. Cardinali, A. Clement, G.D. Emmitt, B.M. Gentry, R.M. Hardesty, E. Källén, M.J. Kavaya, R. Langland, Z. Ma, M. Masutani, W. McCarty, R.B. Pierce, Z. Pu, L.P. Riishojgaard, J. Ryan, S. Tucker, M. Weissmann, and J.G. Yoe, 2014: Lidar-Measured Wind Profiles: The Missing Link in the Global Observing System. *Bull. Amer. Meteor. Soc.,95,* 543–564.

Bankert, R.L., 1994: Cloud Classification of AVHRR Imagery in Maritime Regions Using a Probabilistic Neural Network. *J. Appl. Meteor.*, 33, 909–918.

Bankert, R. L., M. Hadjimichael, A.P. Kuciauskas, W.T. Thompson, and K. Richardson, 2004: Remote Cloud Ceiling Assessment Us,ing Data-Mining Methods. *J. Appl. Meteor.*, 43, 1929–1946.

Bankert, R. L., C. Mitrescu, S.D. Miller, and R.H. Wade, 2009: Comparison of GOES cloud classification algorithms employing explicit and implicit physics. *J. Appl. Meteor.* Climatol., 48, 1411–1421.

Banta, R., Y. Pichugina, A. Brewer, E. James, J. Olson, S. Benjamin, J. Carley, L. Bianco, I. Djalalova, J. Wilczak, M. Hardesty, J. Cline, and M. Marquis, 2017: Evaluating and Improving NWP Forecast Models for the Future: How the Needs Of Offshore Wind Energy Can Point the Way. *Bull. Amer. Meteor. Soc.* doi:10.1175/BAMS-D-16-0310.

Barker, H. W., Jerg, M. P., Wehr, T. , Kato, S. , Donovan, D. P. and Hogan, R. J. (2011), A 3D cloud construction algorithm for the EarthCARE satellite mission. *Q.J.R. Meteorol. Soc.*, 137: 1042-1058. doi:10.1002/qj.824.

Bates, T. S., P. K. Quinn, J. E. Johnson, A. Corless, F. J. Brechtel, S. E. Stalin, C. Meinig, and J. F. Burkhart, 2013: Measurements of atmospheric aerosol vertical distributions above Svalbard, Norway, using unmanned aerial systems (UAS). *Atmos. Meas. Tech.*, 6, 2115–2120.

Bedka, K. M., C. S. Velden, R. A. Petersen, W. F. Feltz, and J. R. Mecikalski, 2009: Comparisons of Satellite-Derived Atmospheric Motion Vectors, Rawinsondes, and NOAA Wind Profiler Observations. *J. Appl. Meteor. Climatol.*,48, 1542–15.

Bedka, K., J. Brunner, R. Dworak, W. Feltz, J. Otkin, and T. Greenwald, 2010: Objective Satellite-Based Detection of Overshooting Tops Using Infrared Window Channel Brightness Temperature Gradients. *J. Appl. Meteor. Climatol.*, 49, 181–202.

Bedka, K. M. and Khlopenkov, K., 2016: A probabilistic multispectral pattern recognition method for detection of overshooting cloud tops using passive satellite imager observations, *J. Appl. Meteorol. Clim.*, 55, 1983–2005, https://doi.org/10.1175/JAMC-D-15-0249.1.

Behne, D., 2008: NAM-WRF verification of subtropical jet turbulence. Electron. *J. Operational Meteor.*, Paper 2008-EJ3. [Available online at http://www.nwas.org/ej/pdf/2008-EJ3.pdf.].

Bélair, S., P. Lacarrère, J. Noilhan, V. Masson, and J. Stein, 1998: High-Resolution Simulation of Surface and Turbulent Fluxes during HAPEX-MOBILHY. *Mon. Wea. Rev.*, 126, 2234–2253.

Bernstein, B. C., F. McDonough, M. K. Politovich, B. G. Brown, T. P. Ratvasky, D. R. Miller, C. A. Wolff, and G. Cunning, 2005: Current Icing Potential: Algorithm Description and Comparison with Aircraft Observations. *J. Appl. Meteor.*,44, 969–986.

Benjamin, S., S. Weygandt, J. Brown, M. Hu, C. Alexander, T. Smirnova, J. Olson, E. James, D. Dowell, G. Grell, H. Lin, S. Peckham, T. Smith, W. Moninger, J. Kenyon, and G. Manikin, 2016: A North American Hourly Assimilation and Model Forecast Cycle: The Rapid Refresh. *Mon. Wea. Rev.*, 144(4), 1669-1694. doi:10.1175/MWRD-15-0242.1.

Benjamin, S. G., W. R. Moninger, T. L. Smith, B. D. Jamison, and B. E. Schwartz, 2006b: Impact of TAMDAR humidity, temperature, and wind observations in RUC parallel experiments. Preprints, *12th Conf. on Aviation, Range, and Aerospace Meteorology*, Atlanta, GA, Amer. Meteor. Soc., 4.5.

Benjamin, S. G., W. R. Moninger, T. L. Smith, B. D. Jamison, and B. E. Schwartz, 2006a: TAMDAR aircraft impact experiments with the Rapid Update Cycle. Preprints, *10th Symp. on Integrated Observing and Assimilation Systems for atmosphere, Oceans, and Land Surface*, Atlanta, GA, Amer. Meteor. Soc., 9.8. Available online at http://ams.confex.com/ams/pdfpapers/.

Benjamin, S. G., W. R. Moninger, T. L. Smith, B. D. Jamison, E. J. Szoke, and T. W. Schlatter, 2007: 2006 TAMDAR impact experiment results for RUC humidity, temperature, and wind forecasts. Preprints, 11th Symp. on Integrated Observing and Assimilation Systems for the Atmosphere, Oceans, and Land Surface, San Antonio, TX, *Amer. Meteor. Soc.*, 9.2.Available at http://ams.confex.com/ams/pdfpapers/119903.pdf.

Benjamin, S. G., B. D. Jamison, W. R. Moninger, S. R. Sahm, B. E. Schwartz, and T. W. Schlatter, 2010: Relative short-range forecast impact from aircraft, profiler, radiosonde, VAD, GPS-PW, METAR, and mesonet observations via the RUC hourly assimilation cycle. *Mon. Wea. Rev.*, 138, 1319–1343.

Benjamin, S. G., and Coauthors, 2009: *Rapid Refresh/RUC project technical review.* NOAA/ESRL/GSD Internal Review. [Available online at http://ruc.noaa.gov/pdf/RR-RUC-TR_11_3_2009.pdf.].

Benjamin, S. G., and Coauthors, 2004: An hourly assimilation–forecast cycle: The RUC. *Mon. Wea. Rev.*, 132, 495–518.

Berndt, E., N. Elmer, L. Schultz, and A. Molthan, 2018: A Methodology to Determine Recipe

Adjustments for Multispectral Composites Derived from Next-Generation Advanced Satellite Imagers. J. Atmos. Oceanic Technol., 0, https://doi.org/10.1175/JTECH-D-17-0047.1.

Bergot, T., E. Terradellas, J. Cuxart, A. Mira, O. Liechti, M. Mueller, and N.W. Nielsen, 2007: Intercomparison of Single-Column Numerical Models for the Prediction of Radiation Fog. *J. Appl. Meteor. Climatol.*, 46, 504–521.

Bernstein, B. C., C. A. Wolff, and P. Minnis, 2006: Practical application of NASA-Langley advanced satellite products to in-flight icing nowcasts. Proc. *44th AIAA Aerospace Sci. Mtg. & Exhibit,* Reno, NV, January 9-12, AIAA-2006-1220, 18 pp.

Bianco, L., Cimini, D., Marzano, F.S., & Ware, R. (2005). Combining microwave Radiometer and Wind Profiler Radar measurements for High-Resolution Atmospheric Humidity Profiling. *Journal of Atmospheric and Oceanic Technology.* 22, 7, 949-965.

Bilbro, J.W. and W.W. Vaughan, 1978: Wind Field Measurement in the Nonprecipitous Regions Surrounding Severe Storms by an Airborne Pulsed Doppler Lidar System. *Bull. Amer. Meteor. Soc.*, 59, 1095–1100.

Bilbro, J., G. Fichtl, D. Fitzjarrald, M. Krause, and R. Lee, 1984: Airborne Doppler Lidar Wind Field Measurements. *Bull. Amer. Meteor. Soc.*, 65, 348–359.

Black, A.W. and T.L. Mote, 2015: Characteristics of Winter-Precipitation-Related Transportation Fatalities in the United States. *Wea. Climate Soc.*, 7, 133–145.

Blumstein, D., B. Tournier, F. R. Cayla, R. F. T. Phupin, C. Bull, and G. Ponce, 2007: In-flight performance of the infrared atmospheric sounding interferometer (IASI) on MetOp-A. Atmospheric and Environmental Remote Sensing Data Processing and Utilization III: Readiness for GEOSS, M. D. Goldberg et al., Eds., *International Society for Optical Engineering (SPIE Proceedings*, Vol. 6684), 66840, doi:10.117/ 12.560907.

Bluestein, H. B., M. M. French, I. PopStefanija, R. T. Bluth, and J. B. Knorr, 2010: A mobile, phased-array Doppler radar for the study of severe convective storms: The MWR-05XP. *Bull. Amer. Meteor. Soc.*, 91, 579–600.

Bluestein, H. B., J. B. Houser, M.M. French, J.C. Snyder, G.D. Emmitt, I. PopStefanija, C. Baldi, and R.T. Bluth, 2014: Observations of the Boundary Layer near Tornadoes and in Supercells Using a Mobile, Collocated, Pulsed Doppler Lidar and Radar. *J. Atmos. Oceanic Technol.*, 31, 302–325.

Boer G. D., S. Palo, B. Argrow, G. LoDolce, J. Mack, R.-S. Gao, H. Telg, C. Trussel, J. Fromm, C. N. Long, G. Bland, J. Maslanik, B. Schmid, and T. Hock, 2017:The pilatus unmanned aircraft system for lower atmospheric research. *Atmos. Meas. Tech. Discuss.*, 8, 11987–12023.

Bottyán, Z., Zoltán Tuba and A. Z. Gyöngyösi, 2016: Weather Forecasting System for the Unmanned Aircraft Systems (UAS) Missions with the Special Regard to Visibility Prediction, in Hungary. L. Nádai and J. Padányi (eds.), Critical Infrastructure Protection Research, *Topics in Intelligent Engineering and Informatics*, DOI 10.1007/978-3-319-28091-2_2.

Bottyán, Z., F. Wantuch, A. Z. Gyöngyösi, Z. Tuba, K. Hadobács, P. Kardos, and R. Kurunczi, 2013: Development of a Complex Meteorological Support System for UAVs. World Academy of Science, Engineering and Technology *Inter. J.of Geo. and Environ. Eng.*,Vol:7, No:4.

Bott, A., U. Sievers, and W. Zdunkowski, 1990: A Radiation Fog Model with a Detailed Treatment of the Interaction between Radiative Transfer and Fog Microphysics. *J. Atmos. Sci.*, 47, 2153–2166.

Bravin, M., Strapp, J. W., and Mason, J., 2015: An investigation into location and convective lifecycle trends in an ice crystal icing engine database, Tech. rep., *SAE Technical Paper* 2015- 01-2130, SAE International, Warrendale, Pennsylvania, USA, doi:10.4271/2015-01-2130.

Bright, D. R., S. A. Lack, and J. A. Sparks, 2016: A Summary of Turbulence Forecasting Techniques Used by the National Weather Service. In: Aviation Turbulence: *Processes, Detection, Prediction*, R. Sharman and T. Lane, Eds., Springer, 213-226.

Brooks, G. R., and A. Oder, 2004: Low level turbulence algorithm testing at-or-below 10,000 ft. Preprints, *11th Conf. on Aviation, Range, and Aerospace Meteorology*, Hyannis, MA, Amer. Meteor.Soc., P4.16. [Available online at http://ams.confex.com/ams/pdfpapers/82122.pdf.].

Brown, R., 1973: New indices to locate clear-air turbulence. *Meteor. Mag.*, 102, 347–361.

Brown, B.G., G. Thompson, R.T. Bruintjes, R. Bullock, and T. Kane, 1997: Intercomparison of In-Flight Icing Algorithms. Part II: Statistical Verification Results. *Wea. Forecasting*, 12, 890–914.

Browning, K. A., 1980: Local weather forecasting. Proc. Roy. Soc. London, A371, 179–211.

Burrows, W. R., C. Price, and L.J. Wilson, 2005: Warm Season Lightning Probability Prediction for Canada and the Northern United States. *Wea. Forecasting*, 20, 971–988.

Casadevall, T. J., 1994: The 1989–90 eruption of Redoubt volcano. Alaska: Impacts on aircraft operations. J. Volcanol. *Geotherm.* Res., 62, 301–316.

Chachere, C. and Z. Pu, 2018: Numerical Simulations of an Inversion Fog Event in the Salt Lake Valley During the MATERHORN-Fog Field Campaign. *Pure and Applied Geophysics*, DOI: 0.1007/s00024-018-1770-8.

Chachere, C., and Z. Pu , 2016: Connection between cold air pools and mountain valley fog events in Salt Lake City, *Pure and App. Geo.* , doi:10.1007/s00024-016-1316-x.

Chan, P. W., 2016: LIDAR-based turbulence intensity for aviation applications. In: *Aviation Turbulence: Processes, Detection, and Prediction.* R. D. Sharman and T. P. Lane, Eds., Springer Publications. Chapter 9, 193-209.

Chan, P. W. 2014. "Performance and Aviation Applications of Minisodars at Hong Kong International Airport." *Meteorological Applications* 21: 62–73. doi:10.1002/met.1388.

Chan P. W, and Shao A. M., 2007: Depiction of complex airflow near Hong Kong International Airport using a Doppler LIDAR with a two-dimensional wind retrieval technique, *Meteorologische Zeitschrift.* 16, 491–504.

Chan, P. W., Shun, C. M., and Wu, K. C., 2006: Operational LIDARLIDAR-based System for Automatic Wind shear Alerting at the Hong Kong International Airport, *12th Conference on Aviation, Range, & Aerospace Meteorology*, American Meteorological Society, Atlanta, GA, USA, 29 January - 2 February 2006.

Chiodi, A.M. and D.E. Harrison, 2010: Characterizing Warm-ENSO Variability in the Equatorial Pacific: An OLR Perspective. *J. Climate*,23, 2428–2439, https://doi.org/10.1175/2009JCLI3030.1

Doswell, C.A. III*, 1980: Synoptic-scale Environments Associated with High Plains Severe Thunderstorms. *Bull. of Amer. Met. Soc..* 61, 1388-1400.

Chandrasekar, V., R. Keránen, S. Lim, and D. Moisseev, 2013: Recent advances in classification of observations from dual polarization weather radars. *Atmos. Res.*, 119, 97–111.

Chmielecki, R.M. and A.E. Raftery, 2011: Probabilistic Visibility Forecasting Using Bayesian Model Averaging. *Mon. Wea. Rev.*, 139, 1626–1636.

Cho, J. Y. N., 2015: "Enhanced Signal Processing Algorithms for the ASR-9 Weather Systems Processor", *Journal of Atmospheric and Oceanic Technology*, 32, 1847-1859.

Chun, H., J. Kim, D. Lee, S. Kim, M. Strahan, B. Pettegrew, P. Gill, P. D. Williams, U. Schumann, J. Tenenbaum, Y. Lee, H. Choi, I. Song, Y. Park, and R.D. Sharman, 2017: Research Collaborations for Better Predictions of Aviation Weather Hazards. *Bull. Amer. Meteor. Soc.*, 98, ES103–ES107, https://doi.org/10.1175/BAMS-D-17-0010.1

Clark, A. J., W. A. Gallus Jr., M. Xue, and F. Kong, 2009: A comparison of precipitation forecast skill between small convection-permitting and large convection-parameterizing ensembles. *Wea. & Forecasting*, 24, 1121–1140.

Cohen, A.E.*, S.M. Cavallo, M.C. Coniglio, and H.E. Brooks, 2017: Evaluation of Multiple Planetary Boundary Layer Parameterization Schemes in Southeastern U.S. Cold Season Severe Weather Environments. *Wea. & Forecasting*, 32, 1857-1884.

Cohn, S. A., 1995: Radar measurements of turbulent eddy dissipation rate in the troposphere: A comparison of techniques. *J. Atmos. Oceanic Technol.*, 12, 85–95.

Colson, D., and H. A. Panofsky, 1965: An index of clear-air turbulence. Quart. J. Roy. Meteor. Soc., 91, 507–513.

Cook, L., B. Wood, A. Klein, R. Lee, and B. Memarzadeh, 2009: "Analyzing the Share of Individual Weather Factors Affecting NAS Performance Using the Weather Impacted Traffic Index, *AIAA 2009-7017. 9th AIAA Aviation Technology, Integration, and Operations Conference (ATIO),* Hilton Head, SC, September 2009. Doi: 10.2514/6.2009-7017.

Cornman, L. B., 2016: Airborne in situ measurements of turbulence. *Aviation Turbulence: Processes, Detection, Prediction*, R. Sharman and T. Lane, Eds., Springer, 97-120.

Cornman, L. B., C. S. Morse, and J. Cunning, 1995: Real time estimation of atmospheric turbulence severity from in-situ aircraft measurements. *J. Aircraft*, 32,171–177.

Dehghan, A., W. K. Hocking, and R. Srinivasan, 2014: Comparisons between multiple in-situ aircraft measurements and radar in the troposphere. J. Atmos. Sol.-Terr. Phys., 118, 64-77.

Del Genio, A. D., M.-S. Yao, and J. Jonas, 2007: Will moist convection be stronger in a warmer environment? *Geophys. Res. Lett.*, 34, L16703, doi:10.1029/2007GL030525.

Deng, M., G. G. Mace, Z. Wang, and H. Okamoto, 2010: Tropical composition, cloud and climate coupling experiment validation for cirrus cloud profiling retrieval using CloudSat radar and CALIPSO lidar. *J. Geophys. Res.*, 115, D00J15,doi:10.1029/2009JD013104.

DeWekker, S. F. J., K. S.Godwin,G.D.Emmitt, and S.Greco, 2012: Airborne Doppler lidar measurements of valley flows in complex coastal terrain. *J. Appl. Meteor. Climatol.*, 51, 1558–1574.

Dines W. H., 1917: Meteorology and aviation. *Mon. Wea. Rev.*, 45, 401–401, https://doi.org/10.1175/1520-0493(1917)45<401b:MAA>2.0.CO;2

Donovan, M. F., E. R. Williams, C. Kessinger, G.Blackburn, P. H. Herzegh, R. L. Bankert, S. Miller, and F. R. Mosher, 2008: The identification and verification of hazardous convective cells over oceans using visible and infrared satellite observations. *J. Appl. Meteor. Climatol.*,47, 164-184.

Done, J., C. A. Davis, and M. L. Weisman, 2004: The next generation of NWP: Explicit forecasts of convection using the Weather Research and Forecasting (WRF) model. *Atmos. Sci. Lett.*, 5, 110–117.

Dorman, C. E., J.F. Mejia, D. Korocin, and D..J..McEvoy, 2017: Worldwide Marine Fog Occurrence and Climatology. A chapter in the book of *Marine Fog: Challenges and Advancements in Observations, Modeling, and Forecasting*. DOI:10.1007/978-3-319-45229-6_2.

Doswell, C. A., III, 1986: *Short-range forecasting. Mesoscale Meteorology and Forecasting*, P. Ray , Ed., Amer. Meteor. Soc., 689–719.

Dupree, W., D. Morse, M. Chan, X. Tao, H. Iskenderian, C. Reiche, M. Wolfson,J. Pinto, J. K. Williams, D. Albo, S. Dettling, and M. Steiner,S. Benjamin and S. Weygandt, 2009:The 2008 CoSPA Forecast demonstration (collaborative storm prediction for aviation). 89th AMS Annual MeetingARAM Special Symposium on Weather - Air TrafficPhoenix, AZ / 11-15 January 2009. P1.1. 19 pp.

Dutton, J. A., and H. A. Panofsky, 1970: Clear air turbulence: A mystery may be unfolding. *Science*, 167, 937–944.

Eichinger, W. E., D. I. Cooper, P. R. Forman, J. Griegos, M. A. Osborn, D. Richter, L. L. Tellier, and R. Thornton, 1999: The Development of a Scanning Raman Water Vapor Lidar for Boundary Layer and Tropospheric Observations. *J. Atmos. Oceanic Technol.*, 16, 1753–1766.

Eick D., 2014: Turbulence related accidents and incidents. Presentation at NCAR Turbulence Impact Mitigation Workshop 2, 3-4 Sep 2014. Available online at: https://ral.ucar.edu/sites/default/files/public/events/2014/turbulence-impact-mitigation-workshop-2/docs/eick-turbulencerelatedaccidents.pdf.

Ellrod, G. P. and J. A. Knox, 2010: Improvements to an Operational Clear-Air Turbulence Diagnostic Index by Addition of a Divergence Trend Term. *Wea. Forecasting*, 25, 789–798.

Ellrod, G. P., and I. Gultepe, 2007: Inferring low cloud base heights at night for aviation using satellite infrared and surface temperature data. *J. of Pure and Appl. Geophy*. Vol. 164, 1193-1205.

Ellrod, G. P., P. F. Lester, and J. Ehernberger, 2002: Clear air turbulence. *Encyclopedia of the Atmospheric Sciences*, J. R. Holton et al., Eds., Academic Press, 393–403.

Ellrod, G. P, B. H. Connell, and D. W. Hillger, 2003: Improved detection of airborne volcanic ash using multispectral infrared satellite data. *J. Geophys. Res.*, 108, 4356, doi:10.1029/2002JD002802.

Ellrod, G. P., and D. I. Knapp, 1992: An objective clear-air turbulence forecasting technique: Verification and operational use. *Wea. Forecasting*, 7, 150–165.

Ellrod, G. P., 1985: *Detection of high level turbulence using satellite imagery and upper air data*. NOAA Tech. Memo. NESDIS 10, 30 pp.

Elmore, K. L., and M. B. Richman, 2001: Euclidean distance as a similarity metric for principal component analysis. Mon. Wea. Rev., 129, 540–549.Endlich, R. M., 1964: The mesoscale structure of some regions of clear-air turbulence. *J. Appl. Meteor.*, 3, 261–276.

FAA, 1988: *Advisory Circular on Pilot wind shear guide*. AFS-200. AC No: 00-54, 56 pp.

FAA-P-8740-40, 2008: *Wind Shear*. HQ 101130. 8 pp.

FAA, 2017: *Continued Operational Safety (COS) Report. Special Category Light-Sport Aircraft*, July 2004-Sep 2017. 50 pp.Fahey, T., E. Wilson, R. O'Loughlin, M. Thomas, S. Klipfel, 2016: A History of Weather Reporting from Aircraft and Turbulence

Forecasting for Commercial Aviation. In: *Aviation Turbulence: Processes, Detection, Prediction*, R. Sharman and T. Lane, Eds., Springer, 31-58.

Feingold, G., W. R. Cotton, S.M. Kreidenweis, and J.T. Davis, 1999: The Impact of Giant Cloud Condensation Nuclei on Drizzle Formation in Stratocumulus: Implications for Cloud Radiative Properties. *J. Atmos. Sci.*, 56, 4100–4117.

Ferrare, R. A., S. H. Melfi, D. N. Whiteman, K. D. Evans, F. J. Schmidlin, and D. O. Starr, 1995: A Comparison of Water Vapor Measurements Made by Raman Lidar and Radiosondes. *J. Atmos. Oceanic Technol.*, 12, 1177–1195.

Ferrero, E., L. Mortarini, M. Manfrin, M. Solari, and R. Forza (2014), Physical simulation of atmospheric microbursts, *J. Geophys. Res. Atmos.*, 119, 6292–6305. doi:10.1002/2013JD021243.

Ferrier, B. S., W. K. Tao, and J. Simpson, 1995: A Double-Moment Multiple-Phase Four-Class Bulk Ice Scheme. Part II: Simulations of Convective Storms in Different Large-Scale Environments and Comparisons with other Bulk Parameterizations. *J. of Atmos. Sci.*, 52, 1001-1033.

Ferrier, B. S., 1994: A double-moment multiple-phase four-class bulk ice scheme. Part I: Description. *J. Atmos. Sci.*, 51, 249–280.

Fischer, A. S., P. Terray, E. Guilyardi, S. Gualdi, and P. Delecluse, 2005: Two Independent Triggers for the Indian Ocean Dipole/Zonal Mode in a Coupled GCM. *J. Climate*, 18, 3428–3449.

Fischer C, Montmerle T, Berre L, Auger L, Stefanescu S. 2005. Anover view of the variational assimilation in the ALADIN/France numerical weather-prediction system wave-driven circulation of the mesosphere. *Q. J. R. Meteorol. Soc*. 131: 3477–3492.

Fix, A., 2012: Tunable light sources for lidar applications. *Atmospheric Physics – Background, Methods, Trends, Prediction*, U. Schumann, Ed., Springer, 509-527.

Folger, K. and M. Weissmann, 2014: Height Correction of Atmospheric Motion Vectors Using Satellite Lidar Observations from CALIPSO. *J. Appl. Meteor. Climatol.*, 53, 1809–1819.

Fournier, G., 2006: Development of the Canadian aircraft meteorological data relay (AMDAR) program and plans for the future.*10th Symposium on Integrated Observing and Assimilation Systems for the Atmosphere, Oceans, and Land Surface*,

Atlanta, GA, Amer. Meteor. Soc. Annual Meeting. Available at https://ams.confex.com/ams/pdfpapers.

França, G. B., Almeida, M. V, Bonnet, S. M.and Albuquerque Neto, F. L. 2018. Nowcasting model of low wind profile based on neural network using SODAR data at Guarulhos Airport, Brazil. *International Journal of Remote Sensing*, 39:8, 2506-2517, DOI: 10.1080/01431161.2018.1425562.

Free, M., and B. Sun 2013: Time-Varying Biases in US total cloud cover data. *J. Atmos. Ocean., Tech.*, 30, 2838-2849.

Frehlich, R. G., and R. Sharman, 2010: Climatology of velocity and temperature turbulence statistics determined from rawinsonde and ACARS/AMDAR data. *J. Appl. Meteor. Climatol.*, 49, 1149–1169, doi:10.1175/2010JAMC2196.1.

Fuertes, F. C., G. V. Iungo, and F. Porté-Agel, 2014: 3D Turbulence Measurements Using Three Synchronous Wind Lidars: Validation against Sonic Anemometry. *J. Atmos. Oceanic Technol.*, 31, 1549–1556.

Grell, G. A., and D. Devenyi, 2002: A generalized approach to parameterizing convection combining ensemble and data assimilation techniques. Geophy. Res. Lett., 29, NO. 14, 1693, 10.1029/2002GL015311, 38-1 to 38-4.

Gerz, T., F. Holzäpfel, W. Gerling, A. Scharnweber, M. Frech, A. Wiegele, K.Kober, K. Dengler, and S. Rahm. 2009. "The Wake Vortex Prediction and Monitoring System WSVBS   Part II: Performance and ATC Integration at Frankfurt Airport." *Air Traffic Control Quarterly* 17 (4): 323–346. doi:10.2514/atcq.17.4.323.

Ghirardelli, J. E. and B. Glahn, 2010: The Meteorological Development Laboratory's Aviation Weather Prediction System. *Wea. Forecasting*, 25, 1027–1051.

Gill, P. G., 2012: Objective verification of World Area Forecast Centre clear air turbulence forecasts. *Meteor. Appl.*, 21, 3–11, doi:10.1002/met.1288.

Gill, and P. Buchanan, 2014: An ensemble based turbulence forecasting system. *Meteor. Appl.*, 21, 12–19, doi:10.1002/met.1373.

Gillette, D., 1978: A wind tunnel simulation of the erosion of soil: Effects of soil texture, sandblasting, wind speed, and soil consolidation on the dust production. *Atmos. Environ.*, 12, 1735–1743.

Glahn, H. R., and D. A. Lowry, 1972: The use of model output statistics (MOS) in objective weather forecasting. *J. Appl. Meteor.*, 11, 1203–1211.

Glahn, B., A. D. Schnapp, J. E. Ghirardelli, and J. Im, 2017: A LAMP–HRRR MELD for Improved Aviation Guidance. *Wea. Forecasting*, 32, 391–405.

Glickman, T. S., Ed., 2000: *Glossary of Meteorology*. 2d ed. Amer. Meteor. Soc., 855 pp.

Golding B. W., 1998. Nimrod: a system for generating automated very short range forecasts. *Meteorol. Appl.* 5: 1–16.

Goodman, S. J.,, R. J. Blakeslee, W. J. Koshak, D. Mach, J. Bailey, D. Buechler, L. Carey, C. Schultz, M. Bateman, E. McCaul Jr, and G. Stano ,2013: *The GOES-R Geostationary Lightning Mapper (GLM)*. V. 125-126, 34-49.

Goodman, S. J., J. Gurka, M. DeMaria, T. J. Schmit, A. Mostek, G. Jedlovec, C. Siewert, W. Feltz, J. Gerth, R. Brummer, S. Miller, B. Reed, and R.R. Reynolds, 2012: The GOES-R Proving Ground: Accelerating User Readiness for the Next-Generation Geostationary Environmental Satellite System. *Bull. Amer. Meteor. Soc.*, 93, 1029–1040.

Goodman, C., and J. Griswold, 2017: Climate Impacts on Density Altitude and Aviation Operations. *J. Appl. Meteor. Clim.* doi:10.1175/JAMC-D-17-0126.1, in press.

Gossard, E. E., J. B. Snider, E. E. Clothiaux, B. Martner, J. S. Gibson, R. A. Kropfli, and A. S. Frisch, 1997: The Potential of 8-mm Radars for Remotely Sensing Cloud Drop Size Distributions. *J. Atmos. Oceanic Technol.*,14, 76–87,

Griffin, S. M. & Velden, C. S., 2018: Hazard Avoidance Products for Convectively-Induced Turbulence in Support of High-Altitude Global Hawk Aircraft Missions. *Pure Appl. Geophys.* (2018). https://doi.org/10.1007/s00024-018-1772-6.

Guedalia, D. and T. Bergot, 1994: Numerical Forecasting of Radiation Fog. Part II: A Comparison of Model Simulation with Several Observed Fog Events. *Mon. Wea. Rev.*, 122, 1231–1246.

Guttman, N. B. and R. K. Jeck, 1987: Aircraft Icing Environment in Low Ceiling Conditions near Washington, D.C..*Wea. Forecasting*, 2, 114–126.

Gultepe, I., Agelin-Chaab, M., Komar, J., G. Elfstrom, F. Boudala, B. Zhou, 2018: A Meteorological Supersite for Aviation and Cold Weather Applications. *Pure Appl. Geophys*. https://doi.org/10.1007/s00024-018-1880-3.

Gultepe, I., A. J. Heymsfield, M. Gallagher, L. Ickes, and D. Baumgardner, 2017a: Ice Fog: The Current State of Knowledge and Future Challenges. *Meteorological Monographs*, 58, 4.1–4.24. https://doi.org/10.1175/AMSMONOGRAPHS-D-17-0002.1

Gultepe, I., A. J. Heymsfield, P. R. Field, and D. Axisa, 2017b: Ice-Phase Precipitation. *Meteorological Monographs*, 58, 6.1–6.36, https://doi.org/10.1175/AMSMONOGRAPHS-D-16-0013.1

Gultepe, I., and A. J. Heymsfield, 2016: Ice Fog, Ice Clouds, and Remote Sensing; Introduction. *Pure and Appl. Geophy.*, 173, N.9. DOI: 10.1007/s00024-016-1380-2. 2977-2982.

Gultepe, I., T. Kuhn, M. Pavolonis, C. Calvert, J. Gurka, G. A. Isaac, A. J. Heymsfield, P. S. K. Liu, B. Zhou, R. Ware, B. Ferrier, J. Milbrandt, B. Hansen, and B. Bernstein, 2014: Ice fog in Arctic during FRAM-IF project: Aviation and nowcasting applications. *Bulletin of Amer. Met. Soc.*, 95, 211–226.

Gultepe, I., B. Zhou, J. Milbrandt, A. Bott, Y. Li, A. J. Heymsfield, B. Ferrier, R. Ware, M. Pavolonis, T. Kuhn, J. Gurka, P. Liu, and J. Cermak, 2015: A review on Ice Fog Measurements and Modeling. *Atmospheric Research*. 151, 2-19.

Gultepe, I., G. A. Isaac, P. Joe, P. Kucera, J. Thériault, and T. Fisico, 2014: Roundhouse (RND) Mountain Top Research Site: Measurements and Uncertainties for Winter Alpine Weather Conditions. *J. of Pure and Applied Geophysics*. DOI: 10.1007/s00024-012-0582-5, 171, 59-85.

Gultepe, I., M. Pawgoski, and J. Reid. 2007: Using surface data to validate a satellite based fog detection scheme. *J. of Weather and Forecasting*, 22, 444-456.

Gultepe, I., R. Tardif, S. C. Michaelides, J. Cermak, A. Bott, J. Bendix, M. Müller, M. Pagowski, B. Hansen, G. Ellrod, W. Jacobs, G. Toth, S. G. Cober, 2007a: Fog research: a review of past achievements and future perspectives. *J. of Pure and Applied Geophy*. Special issue on fog, edited by I. Gultepe. Vol. 164, 1121-1159.

Gultepe, I., M. D. Müller, and Z. Boybeyi, 2006: A new warm fog parameterization scheme for numerical weather prediction models. *J. Appl. Meteor.*, 45, 1469-1480.

Gultepe, I., H. J. S. Fernando, E. R. Pardyjak, S. W. Hoch, Z. Silver, E. Creegan, L. S. Leo, Z. Pu, S. F. J. De Wekker, and C. Hang, 2016: An Overview of the MATERHORN Fog Project: Observations and Predictability. *Pure and Applied Geophysics*. 173, N.9. DOI: 10.1007/s00024-016-1374-0. 2983-3010.

Gultepe, I., 2015: Mountain Weather: Observations and Modeling. *Advances in Geophysics*. June Issue. Vol. 56. 229-312 pp.

Gultepe, I., and G. A. Isaac, 2004: An analysis of cloud droplet number concentration (Nd) for climate studies: Emphasis on constant Nd. *Q. J. Royal Met. Soc.*, 130, Part A, No. 602, 2377-2390.

Gultepe, I., Starr, D. O'C., Heymsfield, A. J., Uttal, T., Ackerman, T. P., and Westphal, D. L., 1995: Dynamical characteristics of cirrus clouds from aircraft and radar observations in micro and meso-gamma scales. *J. Atmos. Sci.*, 52, 4060-4078.

Gultepe, I., and Starr, D. O'C., 1995: Dynamical structure and turbulence in cirrus clouds: Aircraft observations during FIRE. *J. Atmos. Sci.*, 52, 4659-4182.

Gultepe, I., G. Pearson J. A. Milbrandt, B. Hansen, S. Platnick, P. Taylor, M. Gordon, J. P. Oakley, and S.G. Cober, 2009: The fog remote sensing and modeling (FRAM) field project. *Bull. Of Amer. Meteor. Soc.*, v.90, 341-359.

Hadley, D., G. L. Hufford, and J. J. Simpson, 2004: Resuspension of Relic Volcanic Ash and Dust from Katmai: Still an Aviation Hazard. *Wea. Forecasting*, 19, 829–840.

Haggerty, J., E. Defer, A. de Laat, K. Bedka, J.-M. Moisselin, R. Potts, J. Delanoë, F. Parol, A. Grandin, and S. DiVit. 2018: Detecting Clouds Associated with Jet Engine Ice Crystal Icing. *Bull. Amer. Meteor. Soc.*, Accepted.

Haiden, T., A. Kann, C. Wittmann, G. Pistotnik, B. Bica, and C. Gruber, 2011: The Integrated Nowcasting through Comprehensive Analysis (INCA) System and Its Validation over the Eastern Alpine Region. *Wea. Forecasting*, 26, 166–183.

Haiden, T., A. Kann, and G. Pistotnik, 2014: Nowcasting with INCA During SNOW-V10. *Pure and Appl. Geophy*. 171-1, 171-2, DOI. 10.1007/s00024-012-0547-8

Hamazu, K., H. Hashiguchi, T. Wakayama, T. Matsuda, R.J. Doviak, and S. Fukao, 2003: A 35-GHz Scanning Doppler Radar for Fog Observations. *J. Atmos. Oceanic Technol.*, 20, 972–986.

Han, Y., J. B. Snider, E. R. Westwater, S. H. Melfi, and R. A. Ferrare, 1994: Observations of water vapor by ground-based microwave radiometers and Raman lidar. *J. Geoph. Res.*, 99, D9, 18695-18702.

Hansen, B., Ismail Gultepe and Alister Ling, 2009: Update on WIND-3: An analog forecasting system for ceiling and visibility. *Joint session of the Sixth Conference on Artificial Intelligence Applications to Environmental Science and the 13th Conference on Aviation, Range and Aerospace Meteorology; 88th Annual Meeting of the American Meteorological Society*, New Orleans, LA, 20-24 January 2008. Oral presentation.

Hansen, B., 2007: A Fuzzy Logic–Based Analog Forecasting System for Ceiling and Visibility. Wea. Forecasting, 22, 1319–1330.

Harrington, J. Y., K. Sulia, and H. Morrison, 2013a: A method for adaptive habit prediction in bulk microphysical models. Part I: Theoretical development. *J. Atmos. Sci.*, 70, 349–364.

Harrington, J. Y., K. Sulia, and H. Morrison, 2013b: A method for adaptive habit prediction in bulk microphysical models. Part II: Parcel model corroboration. *J. Atmos. Sci.*, 70, 365–376, doi:10.1175/JAS-D-12-0152.1.

Hart, K. A., W. J. Steenburgh, D. J. Onton, and A. J. Siffert, 2004: An Evaluation of Mesoscale-Model-Based Model Output Statistics (MOS) during the 2002 Olympic and Paralympic Winter Games. *Wea. Forecasting*, 19, 200–218.

Haupt, S. E., and L. Delle Monache, 2014: *Understanding ensemble prediction: How probabilistic wind power prediction can help in optimizing operations*. WindTech International. Available at www.windtech-international.com/editorial-features/understanding-ensemble-prediction.

Heidinger, A. K., 2010: *ABI cloud mask algorithm theoretical basis document*. NOAA/NESDIS Center for Satellite Applications and Research, 67 pp.

Harrington, J. Y., K. Sulia, and H. Morrison, 2013: A Method for Adaptive Habit Prediction in Bulk Microphysical Models. Part I: Theoretical Development. *J. of Atmos. Sci.*, 70, 349-364.

Herman, L., 1993: High frequency satellite cloud motion at high latitudes. Preprints, Eighth Symp. on Meteorological Observations and Instrumentation, Anaheim, CA, *Amer. Meteor. Soc.*, 465–468.

Herzegh, P. H., E. R. Williams, T. A. Lindholm, F. R. Mosher, C. Kessinger, R. Sharman, J. D. Hawkins, and D. B. Johnson, 2002: Development of automated aviation weather products for oceanic/remote regions: Scientific and practical challenges, research strategies and first steps, Preprints, *10th Aviation, Range and Aerospace Meteorology Conference*, AMS, Portland, OR, 13-16 May 2002.

Herzegh, P., G. Wiener, R. Bateman, J. Cowie, and J. Black, 2015: Data Fusion Enables Better Recognition of Ceiling and Visibility Hazards in Aviation. *Bull. Amer. Meteor. Soc.*, 96, 526–532.

Heymsfield, A. J., G. Thompson, H. Morrison, A. Bansemer, RM Rasmussen, P. Minnis, Z. Wang, and D. Zhang, 2011: Formation and spread of aircraft-induced holes in clouds. *Science*, AAAS, 333, 77-81.

Heymsfield, A. J., and R. M. Sabin, 1989: Cirrus crystal nucleation by homogeneous freezing of solution drops. *J. Atmos. Sci.*, 46, 2252–2264.

Heymsfield, A. J., and R. M. Sabin, 1993: Homogeneous ice nucleation and supercooled liquid water in orographic wave clouds. *J. Atmos. Sci.*, 50, 2335–2353.

Heymsfield, A., D. Baumgardner, P. DeMott, P. Forster, K. Gierens, and B. Kärcher, 2010: Contrail Microphysics. *Bull. Amer. Meteor. Soc.*, 91, 465–472.

Heymsfield, A., J., C. Schmitt, A. Bansemer, C. Twohy, M. Poellot, A. Fridland, and H. Gerber, 2005: Homogeneous ice nucleation in subtropical and tropical convection and its influence on cirrus anvil microphysics. *J. Atmos. Sci.*, 62, 41–64.

Hill M., Calhoun R, Fernando H, Wieser A, Dörnbrack A, Weissmann M, Mayr G., and Newsom, R. 2010. Coplanar Doppler lidar retrieval of rotors from T-REX. *J. of Atmos. Sci.*, 67(3): 713–729.

Hocking, A., and Hocking, W. K., 2018: Tornado identification and forewarning with very high frequency windprofiler radars. *Atmos. Sci. Lett.*, 19:e795. Doi: 10.1002/asl.795

Hodges, D., and Z. Pu, 2015: The climatology, frequency, and distribution of cold season fog events in northern Utah. *Pure and Applied Geophysics*, doi:10.1007/s00024-015-1187-6.

Hubert, L. F. and L. F. Whitney, 1971: Wind estimation from wind estimation from geostationary –satellite pictures. *Mon. Wea. Rev.*, 99, 665–672.

Hubbert, J. C., 2017: Differential reflectivity calibra¬tion and antenna temperature. *J. Atmos. Oceanic Technol.*, 34, 1885–1906.

Hubbert, J. C., J. W. Wilson, T. M. Weckwerth, S. M. Ellis, M. Dixon, and E. Loew, 2018: S-Pol's Polarimetric Data Reveal Detailed Storm Features (and Insect Behavior). *Bull. Amer. Meteor. Soc.*,99, 2045–2060.

Hubbert, J. C., M. Dixon, S. M. Ellis, and G. Meymaris, 2009: Weather Radar Ground Clutter.

Part I: Identification, Modeling, and Simulation. *J. Atmos. Oceanic Technol.*,26, 1165–1180.

Hutchison, K. D., B. D. Iisager, T. J. Kopp, and J. M. Jackson, 2008: Distinguishing Aerosols from Clouds in Global, Multispectral Satellite Data with Automated Cloud Classification Algorithms. *J. Atmos. Oceanic Technol.*, 25, 501–518,

Hufford, G. L., L. S. Salinas, J. J. Simpson, E. G. Barske, and D.Pieri, 2000: Operational implications of airborne volcanic ash. *Bull. Amer. Meteor. Soc.*, 81, 745–755.

ICAO, 2005: *Manual On Low-Level Wind Shear And Turbulence First Edition* – 2005. Doc 9817, AN/449. . Publisher: International Civil Aviation Organization (ICAO). DOC-09817-001-01-E-P. 213 pp.

Illingworth, A. J., H. W. Barker, A. Beljaars, M. Ceccaldi, H. Chepfer, N. Clerbaux, J. Cole, J. Delanoë, C. Domenech, D. P. Donovan, S. Fukuda, M. Hirakata, R. J. Hogan, A. Huenerbein, P. Kollias, T. Kubota, T. Nakajima, T. Y. Nakajima, T. Nishizawa, Y. Ohno, H. Okamoto, R. Oki, K. Sato, M. Satoh, M. W. Shephard, A. Velázquez-Blázquez, U. Wandinger, T. Wehr, and G. van Zadelhoff, 2015: The EarthCARE Satellite: The Next Step Forward in Global Measurements of Clouds, Aerosols, Precipitation, and Radiation. *Bull. Amer. Meteor. Soc.*, 96, 1311–1332.

Irvine, E. A., Keith P. Shine, and Marc A. Stringer, 2016: What are the implications of climate change for trans-Atlantic aircraft routing and flight time? *Transportation Research*, Part D 47, 44–53.

Isaac, G. A., J. K. Ayers, M. Bailey, L. Bissonnette, B.C. Bernstein, S. G. Cober, N. Driedger, W. F. J. Evans, F. Fabry, A. Glazer, I. Gultepe, J. Hallett, D. Hudak, A. V. Korolev, D. Marcotte, P. Minnis, J. Murray, L. Nguyen, T. P. Ratvasky, A. Reehorst, J. Reid, P. Rodriguez, T. Schneider, B. E. Sheppard, J. W. Strapp, and M. Wolde, 2005: First Results from the Alliance Icing Research Study II. *43rd AIAA Aerospace Sciences Meeting and Exhibit 10 - 13 January 2005*, Reno, Nevada, AIAA 2005-252, 18 pp.

Isaac, G. A., M. Bailey, F. Boudala, W. Burrows, S. G. Cober, R. Crawford, N. Donaldson, I. Gultepe, B. Hansen, I. Heckman, L. Huang, A. Ling, J. Reid, and M. Fournier, 2014: The Canadian Airport Nowcasting System (CAN-Now), *QJRM Met. App.*, 21, 30-49.

Isaac, G. A. and R. S. Schemenauer, 1979: Large Particles in Supercooled Regions of Northern Canadian Cumulus Clouds. *J. Appl. Meteor.*, 18, 1056–1065.

Ismail, S. and E.V. Browell, 1994: Recent Lidar Technology Developments and Their Influence on Measurements of Tropospheric Water Vapor. *J. Atmos. Oceanic Technol.*, 11, 76–84.

Jacobs, A. J. and N. Maat, 2005: Numerical Guidance Methods for Decision Support in Aviation Meteorological Forecasting. *Wea. Forecasting*, 20, 82–100.

Jewell, R. and J. Brimelow, 2009: Evaluation of Alberta Hail Growth Model Using Severe Hail Proximity Soundings from the United States. *Wea. Forecasting*, 24, 1592–1609, https://doi.org/10.1175/2009WAF2222230.1.

Jonassen, M. O., H. Ólafsson, H. Ágústsson, Ó. Rögnvaldsson, and J. Reuder, 2012: Improving High-Resolution Numerical Weather Simulations by Assimilating Data from an Unmanned Aerial System. *Mon. Wea. Rev.*, 140, 3734–3756.

Jones, R. H., 1965: Optimal Estimation of Initial Conditions for Numerical Prediction. *J. Atmos. Sci.*, 22, 658–663.

Jones, T. A., K. Knopfmeier, D. Wheatley, G. Creager, P. Minnis, and R. Palikonda, 2016: Storm-scale data assimilation and ensemble forecasting with the NSSL Experimental Warn-on Forecast. Part 2: Combined radar and satellite data experiments. *Wea. Forecasting*, 31, 297-327, doi:10.1175/WAF-D-15-0107.1.

Kain, J. S., and Coauthors, 2010: Assessing advances in the assimilation of radar data within a collaborative forecasting-research environment. *Wea. Forecasting*, 25, 1510–1521.

Kalnay, E., et al. (1996), The NCEP/NCAR 40-year reanalysis project, *Bull. Am. Meteorol. Soc.*, 77, 437–471.

Kalnay, E., 2003: *Atmospheric Modeling, Data Assimilation and Predictability*. Cambridge University Press, 341 pp.

Kann, A., T. Schellander-Gorgas, and C. Wittmann, 2015: Enhanced short-range forecasting of sub-inversion cloudiness in complex terrain. *Atmos. Sci. Let.*, 16, 1–9.

Kaplan, M. L., A. W. Huffman, K. M. Lux, J. D. Cetola, J. J. Charney, A. J. Riordan, Y.-L. Lin, and K. T. Waight III, 2005a: Characterizing the severe turbulence environments associated with commercial aviation accidents. Part 1: A 44-case study synoptic observational analyses. *Meteor. Atmos. Phys.*, 88, 129–152.

Kaplan, M. L., A. W. Huffman, K. M. Lux, J. D. Cetola, J. J. Charney, A. J. Riordan, Y.-L. Lin, and K. T. Waight III, 2005b: Characterizing the severe turbulence environments associated with commercial aviation accidents. Part 2: Hydrostatic mesoscale numerical simulations of super gradient wind flow and streamwise ageostrophic frontogenesis. *Meteor. Atmos. Phys.*, 88, 153–173.

Kara, A. B., A. J. Wallcraft, and H. E. Hurlburt (2007a), A correction for land contamination of atmospheric variables near land-sea boundaries, *J. Phys. Oceanogr.*, 37, 803– 818.

Kara, A. B., A. J. Wallcraft, C. N. Barron, H. E. Hurlburt, M.A. Bourassa, 2008: Accuracy of 10 m winds from satellites and NWP products near land-sea boundaries. *J. Geoph. Res.*, 113, C10020, doi:10.1029/2007JC004516.

Karstens, C. D., and Coauthors, 2015: Evaluation of a probabilistic forecasting methodology for severe convective weather in the 2014 hazardous weather testbed. *Wea. Forecasting*, 30, 1551–1570.

Karstens, C. D., J. Correia Jr., D. S. LaDue, J. Wolfe, T. C. Meyer, D. R. Harrison, J. L. Cinteneo, K. M. Calhoun, T. M. Smith, A. E. Gerard, and L. P. Rothfusz, 2018: Development of a Human-Machine Mix for Forecasting Severe Convective Events. *Weather and Forecasting*, 33, 715-737.

Kelly, D. S., and J. E. Ghirardelli, 1998: A general overview of methodology and applications of the Local AWIPS MOS Program (LAMP), a short-range forecast guidance product. Preprints, *16th Conf. on Weather Analysis and Forecasting*, Phoenix, AZ, Amer. Meteor. Soc., 437–439.

Kelsch, M. and L. Wharton, 1996: Comparing PIREPs with NAWAU Turbulence and Icing Forecasts: Issues and Results. *Wea. Forecasting*, 11, 385–390.

Kessinger, C. , Paul Herzegh, Gary Blackburn, Robert Sharman, Gerry Wiener, Benjamin Hendrickson, Kay Levesque, Jason Craig, Ted Tsui, Jeffrey Hawkins, Richard Bankert, Earle Williams, Michael Donovan, Gary Ellrod, Robert Kistler, and David Fleming, 2006: The FAA AWRP oceanic weather program development team. Preprints, *AMS 12th Conf. on Aviation Range and Aerospace*. Poster 3.9/P1.19.

Kessinger, C. et al., 2006: The FAA AWRP Oceanic weather program development team. Preprints-CD, *12th Aviation, Range and Aerospace Meteorology Conference, AMS*, Atlanta, GA, 30 Jan. – 2 Feb. 2006.

Key, J. R., D. Santek, C. S. Velden, N. Bormann, J.-N. L. P. Riishojgaard, Y. Zhu, and W. P. Menzel, 2003: Cloud drift and water vapor winds in the polar regions from MODIS. IEEE Trans. *Geosci. Remote Sens.*, 41, 482–492.

Khairoutdinov, M., and Y. Kogan, 2000: A new cloud physics parameterization in a large-eddy simulation model of marine stratocumulus. *Mon. Wea. Rev.*, 128, 229–243.

Khairoutdinov, M. and D. Randall, 2006: High-Resolution Simulation of Shallow-to-Deep Convection Transition over Land. *J. Atmos. Sci.*, 63, 3421–3436.

Kilpinen, J., 1994: Computer-aided weather forecasting system set to enter operation in Scandinavia. *ICAO J.*, 49 (8), 17–18.

Kim, J.-H., Chun, H.-Y., R. D. Sharman and T. L. Keller, 2011: Evaluations of upper-level turbulence diagnostics performance using the Graphical Turbulence Guidance (GTG) system and pilot reports (PIREPs) over East Asia. *J. Appl. Meteor. Climatol.*, 50, 1936–1951; Corrigendum, 50, 2193.

Kim, S.-H., H.-Y. Chun, and P. W. Chan, 2017: Comparison of turbulence indicators obtained from in situ flight data. *J. Appl. Meteor. Climatol.*, 56, 1609-1623. doi: 10.1175/JAMC-D-16-0291.1.

Kim J. H, W. N. Chan, S. Banavar, and R. D. Sharman, 2015: Combined winds and turbulence prediction system for automated air-traffic management applications. *J. Appl. Meteor. Climatol.*, 54, 766–784, doi:10.1175/JAMC-D-14-0216.1.

Kim J. H., W. N. Chan, B. Sridhar, R. D. Sharman, P. D. Williams, and M. Strahan, 2016: Impact of the North Atlantic Oscillation on transatlantic flight routes and clear-air turbulence. *J. Appl. Meteor. Climatol.*, 55, 763–771, doi:10.1175/JAMC-D-15-0261.1.

Knox, J. A., 1997: Possible mechanisms of clear-air turbulence in strongly anticyclonic flow. Mon. Wea. Rev., 125, 1251–1259.

Knox, J. A., D. W. McCann, and P. D. Williams, 2008: Application of the Lighthill–Ford Theory of Spontaneous Imbalance to Clear-Air Turbulence Forecasting. *J. Atmos. Sci.*, 65, 3292–3304, https://doi.org/10.1175/2008JAS2477.1.

Knox, J. A. and Coauthors, 2016: Automated turbulence forecasting strategies. *Aviation Turbulence: Processes, Detection, Prediction*, R. Sharman and T. Lane, Eds., Springer, 243-260.

Knüppfer, K., 1997: Automation of aviation forecasts. The projects AUTOTAF and AUTOGAFOR. Preprints, *Seventh Conf. on Aviation, Range, and Aerospace Meteorology*, Long Beach, CA, Amer. Meteor. Soc., 444–449.

Kober, K., G. C. Craig, C. Keil, and A. Dörnbrack, 2012: Blending a probabilistic nowcasting method with a high resolution numerical weather prediction ensemble for convective precipitation forecasts, *Q. J. R. Meteorol. Soc.* 138: 755–768.

Koch, S. E., and F. Caracena, 2002: Predicting clear-air turbulence from diagnosis of unbalanced flow. Preprints, *10th Conf. on Aviation, Range, and Aerospace Meteorology*, Portland, OR, Amer. Meteor. Soc., 10.4. Available at http://ams.confex.com/ams/pdfpapers/39012.pdf.

Kope , J. M., Kwiatkowski, K., de Haan, S., and Malinowski, S. P., 2016: Retrieving atmospheric turbulence information from regular commercial aircraft using Mode-S and ADS-B, *Atmos. Meas. Tech.*, 9, 2253-2265, doi:10.5194/amt-9-2253-2016.

Kumjian, M. R., 2012: Freezing of raindrops in deep convective updrafts: A microphysical and polari¬metric model. *J. Atmos. Sci.*, 69, 3471–3490.

—, 2013a: Principles and applications of dual-polarization weather radar. Part I: Description of the polarimetric radar variables. *J. Oper. Meteor.*, 1, 226–242.

—, 2013b: Principles and applications of dual-polarization weather radar. Part II: Warm- and cold-season applications. *J. Oper. Meteor.*, 1, 243–264.

Kücken, M., D. Hauffe, and H. Österle, 2012: A High-Resolution Simulation of the Year 2003 for Germany Using the Regional Model COSMO. *J. Appl. Meteor. Climatol.*, 51, 1889–1903,

Lakshmanan, V., and T. Smith, 2009: Data mining storm attributes from spatial grids. *J. Atmos. Oceanic Technol.*, 26, 2353–2365.

Landolt, S., M. Politovich, R. Rasmussen, and A. Gaydos, 2010: A Comparison of an Automated Freezing Drizzle Algorithm to Human Observations. AMS Annual Meeting, Atlanta, Georgia, on 16-21 Jan 2010.,14th Conference on Aviation, Range, and Aerospace Meteorology 4 pp.Langland, R. H., and Coauthors, 1999: The North Pacific Experiment (NORPEX-98): Targeted observations for improved North American weather forecasts. *Bull. Amer. Meteor. Soc.*, 80, 1363–1384.

Langmuir, I., VJ Schaefer, B. Vonnegut, K. Maynard, R. Smith-Johannsen, D. Blanchard, and R.E. Falconer, 1948: *Final reports, Project Cirrus*, RL140. General Electric Res. Lab. Req 21190 with the Depart. Of the Army Project: 3-99-07-022, 119 pp.

Lawrence, D. A., and B. B. Balsley, 2013: High-resolution atmospheric sensing of multiple atmospheric variables using the DataHawk small airborne measurement system. *J. Atmos. Oceanic Technol.*, 30, 2352–2366. doi: 10.1175/JTECH-D-12-00089.1

Lawson, R. P., Angus, L. J., and Heymsfield, A. J. 1998: Cloud 5 particle measurements in thunderstorm anvils and possible weather threat to aviation, *J. Aircraft*, 35, 113–121.

Lee, D. R., R. S. Stull, and W. S. Irvine, 1984: *Clear air turbulence forecasting techniques. Air Weather Service Tech. Note* AFGWC/TN-79/001 (REV), Air Force Global Weather Central, Offutt AFB, NE, 16 pp.

Leroy, D., E. Fontaine, A. Schwarzenboeck, and J.W. Strapp, 2016: Ice Crystal Sizes in High Ice Water Content Clouds. Part I: On the Computation of Median Mass Diameter from In Situ Measurements. J. Atmos. Oceanic Technol., 33, 2461–2476.

Leroy, D., E. Fontaine, A. Schwarzenboeck, J.W. Strapp, A. Korolev, G. McFarquhar, R. Dupuy, C. Gourbeyre, L. Lilie, A. Protat, J. Delanoe, F. Dezitter, and A. Grandin, 2017: Ice Crystal Sizes in High Ice Water Content Clouds. Part II: Statistics of Mass Diameter Percentiles in Tropical Convection Observed during the HAIC/HIWC Project. *J. Atmos. Oceanic Technol.*, 34, 117–136.

Lewis, W. 1947: *A flight investigation of the meteorological conditions conducive to the formation of ice on airplanes.* NACA TN 1393.

Lin, C-Y, Z. Zhang, Z. Pu , F. Wang, 2017: Numerical Simulations of an Advection Fog Event over the Shanghai Pudong Airport with the WRF Model. *Journal of Meteorological Research*, 31 , 874-889.

Lin, Y. L., R. D. Farley, and H. D. Orville, 1983: Bulk Parameterization of the Snow Field in a Cloud Model. *J. Of Clim.and Appl. Meteor.*, 22, 1065-1092.

Linden, P. F., and J. E. Simpson (1985): Microbursts: a hazard to aviation. *Nature* 317 (17), 601-602.

Liu, Y., Xia, J., Shi, C. X., and Hong, Y., 2009: An improved cloud classification algorithm for China's FY-2C multi-channel images using artificial neural network, *Sensor*, 9, pp. 5558–5579.

Liu, YQ, YM Wang, L.LI, S. Han, and D. Infield, 2016: NWP wind correction methods and its impact on CFD based wind power forecasting. Journal of Renewable and Sustainable Energy 8, 033302 (20168, 033302 (2016); https://doi.org/10.1063/1.4950972Luce, H., T. Nakamura, M.K. Yamamoto, M. Yamamoto, and S. Fukao, 2010: MU Radar and Lidar Observations of Clear-Air Turbulence underneath Cirrus. *Mon. Wea. Rev.*, 138, 438–452.

Löffler-Mang, M., M. Kunz, and W. Schmid, 1999: On the Performance of a Low-Cost K-Band Doppler Radar for Quantitative Rain Measurements. *J. Atmos. Oceanic Technol.*,16, 379–387. Ludlam, F.H., 1956: Fall-streak holes, Weather, 11, 89-90.

Lynn, K. J., 1997: *International survey of TAF automation systems.* Forecasting systems, Met Office Internal Rep., 20 pp.

Mancuso, R. L., and R. M. Endlich, 1966: Clear air turbulence frequency as a function of wind shear and deformation. *Mon.Wea. Rev.*, 94, 581–585.

Mandel, E., 1975: An Early Look at the Development of an Unmanned Automated Surface Aviation Weather Observation System. *Bull. Amer. Meteor. Soc.*, 56, 979–982.

Markowicz, K.M. and M.L. Witek, 2011: Simulations of Contrail Optical Properties and Radiative Forcing for Various Crystal Shapes. *J. Appl. Meteor. Climatol.*, 50, 1740–1755.

Marroquin, A., 1998: An advanced algorithm to diagnose atmospheric turbulence using numerical model output. Preprints, *16th Conf. on Weather Analysis and Forecasting, Phoenix*, AZ,Amer. Meteor. Soc., 79–81.

Mason, J. G., Strapp, J. W., and Chow, P. 2006: The ice particle threat to engines in flight, in: *44th AIAA Aerospace Sciences Meeting*, Reno, Nevada, abstract number AIAA 2006-206, 9–12 January.

Matrosov, S.Y., 2005: Attenuation-Based Estimates of Rainfall Rates Aloft with Vertically Pointing Ka-Band Radars. *J. Atmos. Oceanic Technol.*, 22, 43–54.

Matthes, S., U. Schumann, V. Grewe, C. Frömming, K. Dahlmann, A. Koch, and H. Mannstein, 2012: *Climate optimized air transport. In Atmospheric Physics – Background, Methods, Trends, Prediction,* U. Schumann, Ed., Springer, 727-746.

McCann, D. W., 2001: Gravity waves, unbalanced flow, and clear air turbulence. *Natl. Wea. Dig.*, 25, 3–14.

McCann , D. W., J. A. Know, and P. D. Williams, 2012: An improvement in clear-air turbulence forecasting based on spontaneous imbalance theory: the ULTURB algorithm. *Meteorol. Appl.* 19: 71–78.

McCarthy, J., and Serafin, R. J., 1984: The microburst hazard to aircraft. *Weatherwise*, 37, 120-127.

McCarthy, J., J. W. Wilson, and T. T. Fujita, 1982: The Joint Airport Weather Studies (JAWS) Project. *Bull. Amer. Meteor. Soc.*, 63, 15-22.

McCarty, J., R. M. Banta, J. B. Olson, J. R. Carley, M. C. Marquis, W. A. Brewer, J. M. Wilczak, I. V. Djalalova, L. Bianco, E. P. James, S. G. Benjamin, and J. Cline, 2017: Assessment of NWP forecast models in simulating offshore winds through the lower boundary layer by measurements from a ship-based scanning Doppler lidar. *Mon Wea. Rev.*, Doi:10.1175/MWR-D-16-0442.1.

McGovern, A., K. L. Elmore, D. J. Gagne, S. E. Haupt, C. D. Karstens, R. Lagerquist, T. Smith, and J. K. Williams, 2017: Using Artificial Intelligence to Improve Real-Time Decision-Making for High-Impact Weather. *Bull. Amer. Meteor. Soc.*, 98, 2073–2090.

Mead, J. B., R. E. Mcintosh, D. Vandemark, and C. T. Swift, 1989: Remote Sensing of Clouds and Fog with a 1.4-mm Radar. *J. Atmos. Oceanic Technol.*,6, 1090–1097.

Meckalski, J. R., W. F. Feltz, J. J. Murray, D. B. Johnson, K. M. Bedka, S. T. Bedka, A. J. Wimmers, M. Pavolonis, T. A. Berendes, J. Haggerty, P. Minnis, B. Bernstein, and E. Williams, 2007: Aviation Applications for Satellite-Based Observations of Cloud Properties, Convection Initiation, In-Flight Icing, Turbulence, and Volcanic Ash. *Bull. Amer. Meteor. Soc.*, 88, 1589–1607.

Meckalski, J. R., and Coauthors, 2002: *NASA Advanced Satellite Aviation-weather Products (ASAP) Study Report*. NASA Tech. Rep., 65 pp.

Megenhardt, D., C. K. Mueller, N. Rehak, and G. Cunning, 2000: Evaluation of the National Convective Weather Forecast Product. Preprints. *9th Conf on Aviation, Range, and Aerospace Meteorology*, AMS, Orlando, FL 171-176.

Meischner, P., R. Baumann, H. Höller, and T. Jank, 2001: Eddy Dissipation Rates in Thunderstorms Estimated by Doppler Radar in Relation to Aircraft In Situ Measurements. *J. Atmos. Oceanic Technol.*, 18, 1609–1627.

Menzel, W. P., T. J. Schmit, P. Zhang, and J. Li, 2018: Satellite-Based Atmospheric Infrared Sounder Development and Applications. *Bull. Amer.* *Meteor. Soc.*,99, 583–603, https://doi.org/10.1175/BAMS-D-16-0293.1

Merritt, L. P., 1969: Comparison of Airborne and Ground Based Weather Radars. *J. Appl. Meteor.*, 8, 963–974.

Michelson, M., W. W. Shrader, and J. G. Wieler, 1990: Terminal Doppler Weather Radar. *Microwave J.*, 33, 139–148.

Miller, T. P., and T. J. Casadevall, 1999: *Volcanic ash hazards to aviation. Encyclopedia of Volcanoes*, H. Sigurdsson et al., Eds., Academic Press, 925–930.

Miller, Steven D., and Coauthors, 2014: Estimating Three-Dimensional Cloud Structure via Statistically Blended Satellite Observations. *J. Appl. Meteor. Climatol.*, 53, 437–455.

Minnis, P., K. Bedka, Q. Trepte, C. R. Yost, S. T. Bedka, B. Scarino, K. Khlopenkov, and M. M. Khaiyer, 2016: *A consistent long-term cloud and clear-sky radiation property dataset from the Advanced Very High Resolution Radiometer (AVHRR). Climate Algorithm* Theoretical Basis Document (C-ATBD), CDRP-ATBD-0826 Rev 1 AVHRR Cloud Properties - NASA, NOAA CDR Program, 19 September, 159 pp., DOI:10.789/V5HT2M8T.

Minnis, P., S. T. Bedka, D. P. Duda, K. M. Bedka, T. L. Chee, J. K. Ayers, R. Palikonda, D. A. Spangenberg, K. V. Khlopenkov, and R. Boeke, 2013: Linear contrails and contrail cirrus properties determined from satellite data. *Geophys. Res. Lett.*, 40, 3220-3226, doi:10.1002/grl.50569.

Minnis, P., L. Nguyen, R. Palikonda, P. W. Heck, D. A. Spangenberg, D. R. Doelling, J. K. Ayers, W. L. Smith, Jr., M. M. Khaiyer, Q. Z. Trepte, L. A. Avey, F.-L. Chang, C. R. Yost, T. L. Chee, and S. Sun-Mack, 2008: Near-real time cloud retrievals from operational and research meteorological satellites. Proc. SPIE 7108, *Remote Sens. Clouds Atmos.* XIII, Cardiff, Wales, UK, 15-18 September, 8 pp., doi: 10.1117/12.800344.

Minnis, P., U. Schumann, D. R. Doelling, K. M. Gierens, and D. W. Fahey, 1999: Global distribution of contrail radiative forcing. *Geophys. Res. Lett.*, 26, 1853-1856.

Minnis, P., S. Sun-Mack, D. F. Young, P. W. Heck, D. P. Garber, Y. Chen, D. A. Spangenberg, R. F. Arduini, Q. Z. Trepte, W. L. Smith, Jr., J. K. Ayers, S. C. Gibson, W. F. Miller, V. Chakrapani, Y. Takano, K.-N. Liou, Y. Xie, and P. Yang, 2011: CERES Edition-2 cloud property retrievals using TRMM VIRS and Terra and Aqua MODIS data, Part I: Algorithms.

IEEE Trans. Geosci. Remote Sens., 49, 11, 4374-4400, doi:10.1109/TGRS.2011.2144601.

Minnis, P., D. F. Young, L. Nguyen, D. P. Garber, W. L. Smith, Jr., and R. Palikonda, 1998: Transformation of contrails into cirrus during SUCCESS. *Geophys. Res. Lett.*, 25, 1157-1160.

Minnis, P., U. Schumann, D. R. Doelling, K. M. Gierens, and D. W. Fahey, 1999: Global distribution of contrail radiative forcing. *Geophys. Res. Lett.*, 26, 1853-1856.

Mittaz, J. and A. Harris, 2011: A Physical Method for the Calibration of the AVHRR/3 Thermal IR Channels. Part II: An In-Orbit Comparison of the AVHRR Longwave Thermal IR Channels on board MetOp-A with IASI. *J. Atmos. Oceanic Technol.*,28, 1072–1087, https://doi.org/10.1175/2011JTECHA1517.1

Moninger, W. R., R. D. Mamrosh, and P. M. Pauley, 2003: Automated Meteorological Reports from Commercial Aircraft. *Bull. Amer. Meteor. Soc.*, 84, 203–216.

Moninger, W. R., S. G. Benjamin, B. D. Jamison, T. W. Schlatter, T. L. Smith, and E. J. Szoke, 2010: Evaluation of Regional Aircraft Observations Using TAMDAR. *Wea. Forecasting*, 25, 627–645.

Moosakhanian, A., S. Schmidt, E. R. Dash, T.vS. Daniels, and P. Stough, 2006: FAA–NASA collaboration on automated aircraft weather observations—culminating in TAMDAR. *12th Conference on Aviation Range and Aerospace Meteorology*, Atlanta, GA, Amer. Meteor. Soc. Annual Meeting. Available at https://ams.confex.com/ams/pdfpapers/104168.pdf

Morrison, H. and J. Milbrandt, 2015: Parameterization of cloud microphysics based on the prediction of bulk ice particle properties. Part I: Scheme description and idealized tests. *J. Atmos. Sci.*, 72, 287–311.

Motta, M., R. J. Barthelmie, and P. Vølund. 2005. "The Influence of Non-Logarithmic Wind Speed Profiles on Potential Power Output at Danish Offshore Sites." *Wind Energy* 8: 219–236. doi:10.1002/(ISSN)1099-1824.

Mueller, C., T. Saxen, R. Roberts, J. Wilson, T. Betancourt, S. Dettling, N. Oien, and J. Yee, 2003: NCAR Auto-Nowcast System. *Wea. Forecasting*, 18, 545-561.

Mueller, C. K., J. W. Wilson, and N. A. Crook, 1993: The utility of sounding and mesonet data to nowcast thunderstorm initiation. *Wea. Forecasting,* 8, 132–146.

Myhre, G., and F. Stordal, 2001: Global sensitivity experiments of the radiative forcing due to mineral aerosols. *J. Geophys. Res.*, 106, 18 193–18 204.

Nair, U. S., R. C. Weger, K. S. Kuo, and R. M. Welch,1998: Clustering, randomness, and regularity in-cloud fields. The nature of regular cumulus cloud fields. *J. Geophys. Res.*, 103, 11 363–11 380.

Nance, L. B., and D. R. Durran, 1997: A modeling study of nonstationary trapped mountain lee waves. Part I: Mean-flow variability. *J. Atmos. Sci.*, 54, 2275–2291.

Neely, R. R. and J. P. Thayer, 2011: Raman Lidar Profiling of Tropospheric Water Vapor over Kangerlussuaq, Greenland. *J. Atmos. Oceanic Technol.*, 28, 1141–1148.

Newton, D. W. (1978). An integrated approach to the problem of aircraft icing. *Journal of Aircraft*, 15, 374–381.

Nicholls, M., R. Pielke, and R. Meroney (1993), Large eddy simulation of microburst winds flowing around a building, *J. Wind Eng. Ind. Aerodyn.*, 46-47, 229–237.

NOAA NWS, 2016: *Terminal aerodrome forecasts.*Instruction 10-813. (http://www.nws.noaa.gov/directives/).

NOAA, 2012: *NWSChat Live User Manual.* 12 pp.

Noh, Y., C. J. Seaman, T. H. Vonder Haar, and G. Liu, 2013: In Situ Aircraft Measurements of the Vertical Distribution of Liquid and Ice Water Content in Midlatitude Mixed-Phase Clouds. *J. Appl. Meteor. Climatol.*, 52, 269–279.

NTSB, 1996: *Aircraft accident report.* Vol. 1. National Transportation Safety Board NTSB/AAR–96/01–PB96–910401, 322 pp. [Available from NTSB, 490 L'Enfant Plaza, S.W., Washington, DC 20594.].

NTSB, 2010: *NASDAC Review of National Transportation Safety Board (NTSB) weather-related accidents (2003-2007)*. Available at http://www.asias.faagov/.

NWPSD, 2004: *Operations and Services, Aviation Weather Services, NWSPD*, 10-8, 2004, NWS Instruction 10-813,Terminal Aerodrome Forecasts, Feb. 1, 2004. 51 pp.

Ødegaard, V., 1997: Ice Phase Parameterization in a Numerical Weather Prediction Model. *Wea. Forecasting*, 12, 127–139.

Orf, L. G., and J. R. Anderson 1999): A numerical study of traveling microbursts, Mon. Weather *Rev., 127,* 1244–1257.

Orf, L. G., J. R. Anderson, and J. M. Straka, 1996: A three-dimensional numerical analysis of colliding microburst outflow dynamics, *J. Atmos. Sci.*, 53, 2490–2511.

Orville, R. E., 2008: Development of the National Lightning Detection Network. *Bull. Amer. Meteor. Soc.*, 89, 180–190.

Oude Nijhuis, A., L. Thobois, F. Barbaresco, S. De Haan, A. Dolfi-Bouteyre, D. Kovalev, O. Krasnov, D. Vanhoenacker-Janvier, R. Wilson, and A. Yarovoy, 0: Wind hazard and turbulence monitoring at airports with lidar, radar and Mode-S downlinks: The UFO Project. *Bull. Amer. Meteor. Soc.*,0, https://doi.org/10.1175/BAMS-D-15-00295.1.

Pasini, A., and C. Marzban, 2008: *Artificial Intelligence Methods in the Environmental Sciences*. Springer, 424 pp.

Pavolonis, M. J., 2010a: Advances in extracting cloud composition information from space borne infrared radiances: A robust alternative to brightness temperatures. Part I: Theory. *J. Appl. Meteor. Climatol.*, 49, 1992–2012.

Pavolonis, M. J, 2010b: *ABI cloud type/phase algorithm theoretical basis document*. NOAA/NESDIS/Center for Satellite Applications and Research (STAR), 60 pp.

Pavolonis, M. J., W. F. Feltz, A. K. Heidinger, and G. M. Gallina, 2006: A daytime complement to the reverse absorption technique for improved automated detection of volcanic ash. *Atmos. Oceanic Technol.*, 23, 1422-1444.

Pavolonis, M. J, and A. K. Heidinger and T. Uttal, 2005: Daytime global cloud typing from AVHRR and VIIRS: Algorithm description, validation, and comparisons. *J. Atmos. Oceanic Technol.*, 44, 804–826.

Pavolonis, M. J, and A. K. Heidinger, 2004: Daytime cloud overlap detection from AVHRR and VIIRS. *J. Appl. Meteor.*, 43, 762–778.

Pearson, J. M. and R. D. Sharman, 2017: Prediction of Energy Dissipation Rates for Aviation Turbulence. Part II: Nowcasting Convective and Nonconvective Turbulence. *J. Appl. Meteor. Climatol.*,56, 339–351, https://doi.org/10.1175/JAMC-D-16-0312.1

Perrie, W., W. Zhang, M. Bourassa, H. Shen, and P.W. Vachon, 2008: Impact of Satellite Winds on Marine Wind Simulations. *Wea. Forecasting*,23, 290–303.

Peters, G., D. Hasselmann, and S. Pang, 1988: Radio acoustic sounding using an FM CW radar. *Radio Sci.*, 23, 640–646.

Peters, G., 1990: Temperature and wind profiles from radar wind profilers equipped with acoustic sources. *Meteor. Rundsch.*, 42,152–154.

Pinto, J. O., J. A. Grim, and M. Steiner, 2015: Assessment of the High-Resolution Rapid Refresh Model's Ability to Predict Mesoscale Convective Systems Using Object-Based Evaluation. *Wea. Forecasting*, 30, 892–913

Pithani, P., Ghude, S., Naidu, C. V., Kulkarni, R. G., Steeneveld, G., Sharma, A., Prabhakaran, T., Chate, D.M., Gultepe, I.: WRF model Prediction of a dense fog event occurred during WInter Fog EXperiment (WIFEX). *Pure and Appl. Geophys. https://doi.org/10.1007/s00024-018-2053-0*

Pleim, J. E., and A. Xiu, 1995: Development and testing of a surface flux and planetary boundary layer model for application in mesoscale models. *J. Appl. Meteor.*, 34, 16–31.

Politovich, M. K., 1989: Aircraft Icing Caused by Large Supercooled Droplets. *J. Appl. Meteor.*, 28, 856–868.

Politovich, M. K., 1996. Response of a research aircraft to icing and evaluation of severity indices. *J. Aircraft 33*, 291–297.

Prata, A. J., 1989: Observations of volcanic ash clouds in the 10-12 micrometer window using AVHRR/2 data. Int. J. Remote Sens., 10, 751-761.

Proctor, F. H. (1988), Numerical simulations of an isolated microburst. Part I: Dynamics and structure, *J. Atmos. Sci.*, 45, 3137–3160.

Proctor, F. H. (1989), Numerical simulations of an isolated microburst. Part II: Sensitivity experiments, *J. Atmos. Sci.*, 46, 2143–2165.

Protat, A., S. Rauniyar, V.V. Kumar, and J.W. Strapp, 2014: Optimizing the Probability of Flying in High Ice Water Content Conditions in the Tropics Using a Regional-Scale Climatology of Convective Cell Properties. *J. Appl. Meteor. Clim.*, 53, 2438–2456.

Pu, Z., C. Lin, X. Dong, S. Krueger, 2018: Sensitivity of numerical simulations of a mesoscale convective system to ice hydrometeors in bulk microphysical parameterization. *Pure and Applied Geophysics*, DOI: 10.1007/s00024-018-1787-z

Pu, Z., 2017: Surface data assimilation and near-surface weather prediction over complex terrain. Book Chapter, *"Data Assimilation for Atmospheric, Oceanic and Hydrologic Applications (Vol. III)"*, Ed. By S.K. Park and L. Xu, Springer. pp.219-240. DOI 10.1007/978-3-319-43415-5_10.

Pu, Z. , C. Chachere*, S. Hoch, E. Pardyjak, and I. Gultepe, 2016: Numerical Prediction of Cold Season Fog Events Over Complex Terrain: The Performance of the WRF Model During MATERHORN-Fog and Early Evaluation, *Pure and Applied Geophysics*, doi:10.1007/s00024-016-1375-z.

Puempel, H. and P. D. Williams, 2016: *The impacts of climate change on aviation: Scientific challenges and adaptation pathways*. ICAO Environmental Report, pp 205-207. https://www.icao.int/ environmental-protection/Pages/env2016.aspx

Ralph, F. M., J. Intrieri, D. Andra, R. Atlas, S. Boukabara, D. Bright, P. Davidson, B. Entwistle, J. Gaynor, S. Goodman, J. Jiing, A. Harless, J. Huang, G. Jedlovec, J. Kain, S. Koch, B. Kuo, J. Levit, S. Murillo, L. P. Riishojgaard, T. Schneider, R. Schneider, T. Smith, and S. Weiss, 2013: The Emergence of Weather-Related Test Beds Linking Research and Forecasting Operations. *Bull. Amer. Meteor. Soc.*, 94, 1187–1211.

Ramsay, A. C., 1999: A multi-sensor freezing drizzle algorithm for the automated surface observing system. Preprints, *15th Int. Conf. on Interactive Information and Processing Systems for Meteorology, Oceanography, and Hydrology*, Dallas, TX, Amer. Meteor. Soc., 193–196.

Rasmussen, R. M., J. Vivekanandan, J. Cole, B. Myers, and C. Masters, 1999: The estimation of snowfall rate using visibility. *J. Appl. Meteor.*, 38, 1542–1563, doi:10.1175/1520-0450(1999)038<1542:TEOSRU>2.0.CO;2.

Rasmussen, R., M. Dixon, S. Vasiloff, F. Hage, S. Knight, J. Vivekanandan, and M. Xu, 2003: Snow nowcasting using a real-time correlation of radar reflectivity with snow gauge accumulation. *J. Appl. Meteor.*,42, 20–36, doi: 10.1175/1520-0450(2003)042<0020:SNUART>2.0.CO;2

Rasmussen, R., M. Dixon, F. Hage, J. Cole, C. Wade, J. Tuttle, S. McGettigan, T. Carty, L. Stevenson, W. Fellner, S. Knight, E. Karplus, and N. Rehak, 2001: Weather Support to Deicing Decision Making (WSDDM): A Winter Weather Nowcasting System. *Bull. Amer. Meteor. Soc.*, 82, 579–596,

Rasmussen, R., B. Baker, J. Kochendorfer, T. Meyers, S. Landolt, A. P. Fischer, J. Black, J. M. Thériault, P. Kucera, D. Gochis, C. Smith, R. Nitu, M. Hall, K. Ikeda, and E. Gutmann, 2012: How Well Are We Measuring Snow: The NOAA/FAA/ NCAR Winter Precipitation Test Bed. *Bull. Amer. Meteor. Soc.*, 93, 811–829.

Rasmussen, R., M. Politovich, J. Marwitz, W. Sand, J. McGinley, J. Smart, R. Pielke, S. Rutledge, D. Wesley, G. Stossmeister, B. Bernstein, K. Elmore, N. Powell, E. Westwater, B. B. Stankov, and D. Burrows, 1992: Winter Icing and Storms Project (WISP). *Bull. Amer. Meteor. Soc.*, 73, 951–974.

Raytheon, 2016: *AWIPS CAVE-D2D user's manual: AWIPS II operational build 13.4.1. Raytheon Doc.* AWP.MAN.UM.A2-OB13.4.1, 609 pp. [Available online at www.unidata.ucar.edu/software/awips2 / doc/CAVE_D2D_Manual.pdf.].

Reehorst, A. L., D. J. Brinker, and T. P. Ratvasky, C. C. Ryerson and G. G. Koenig, 2005: *The NASA Icing Remote Sensing System. NASA/TM*—2005-213591. Paper # 80776. 11 pp.

Reineman, B. D., L. Lenain, and W. K. Melville, 2016: The Use of Ship-Launched Fixed-Wing UAVs for Measuring the Marine Atmospheric Boundary Layer and Ocean Surface Processes. *J. Atmos. Oceanic Technol.*, 33, 2029–2052.

Reineman, B. D., L. Lenain, N. M. Statom, and W.K. Melville, 2013: Development and Testing of Instrumentation for UAV-Based Flux Measurements within Terrestrial and Marine Atmospheric Boundary Layers. *J. Atmos. Oceanic Technol.*, 30, 1295–1319.

Reitebuch, O., 2012: Wind lidar for atmospheric research. Atmospheric Physics – Background, Methods, Trends, Prediction, U. Schumann, Ed., Springer, 487-507.

Roberts, R. D., and S. Rutledge, 2003: Nowcasting storm initiation and growth using GOES-8 and WSR-88D data. *Wea. Forecasting*, 18, 562-584.

Roberts, R. D., T. Saxen, C. Mueller, J. Wilson, A. Crook, J. Sun, and S. Henry, 1999: Operational application and use of NCAR's thunderstorm nowcasting system. Preprints, *Int. Conf. on Interactive Information and Processing Systems*, Dallas, TX, Amer. Meteor. Soc., 158-161.

Roquelaure, S. and T. Bergot, 2008: A Local Ensemble Prediction System for Fog and Low Clouds: Construction, Bayesian Model Averaging Calibration, and Validation. *J. Appl. Meteor. Climatol.*, 47, 3072–3088.

Roquelaure, S. and T. Bergot, 2009: Contributions from a Local Ensemble Prediction System (LEPS) for Improving Fog and Low Cloud Forecasts at Airports. *Wea. Forecasting*, 24, 39–52.

Roquelaure, S., and T. Bergot, 2007: Seasonal sensitivity on COBEL-ISBA local forecast system for fog and low clouds. *Pure Appl. Geophys.*, 164, 1283–1301.

Rose, S. F., P. V. Hobbs, J. D. Locatelli, and M. T. Stoelinga, 2004: A 10-Yr Climatology Relating the Locations of Reported Tornadoes to the Quadrants of Upper-Level Jet Streaks. *Wea. Forecasting*, 19, 301–309.

Rudack, D. E. and J. E. Ghirardelli, 2010: A Comparative Verification of Localized Aviation Model Output Statistics Program (LAMP) and Numerical Weather Prediction (NWP) Model Forecasts of Ceiling Height and Visibility. *Wea. Forecasting*, 25, 1161–1178.

Rudra, R., Dickinson, W. T., Ahmed, S. I., Patel, P., Zhou, J., & Gharabaghi, B., 2015: Changes in Rainfall Extremes in Ontario. Inter. J. of Environ. Res., 9 (4), 1117-1372.

Ryerson, W. R. and J.P. Hacker, 2014: The Potential for Mesoscale Visibility Predictions with a Multimodel Ensemble. *Wea. Forecasting*, 29, 543–562.

Ryzhkov, A. V., D. S. Zrnic, J. C. Hubbert, V. N. Bringi, J. Vivekanandan, and E.A. Brandes, 2002: Polarimetric Radar Observations and Interpretation of Co-Cross-PolarCorrelation Coefficients. *J. Atmos. Oceanic Technol.*, 19, 340–354.

Ryzhkov, A. V., M. R. Kumjian, S. M. Ganson, and P. Zhang, 2013: Polarimetric Radar Characteristics of Melting Hail. Part II: Practical Implications. *J. Appl. Meteor. Climatol.*, 52, 2871–2886.

Santel, D., 2010: The impact of satellite-derived polar winds on lower-latitude forecasts. *Mon. Wea. Rev.*, 123-139.

Santek, D., 2010: The Impact of Satellite-Derived Polar Winds on Lower-Latitude Forecasts.*Mon. Wea. Rev.*,138, 123–139.

Sathe, A., J. Mann, J. Gottschall, and M.S. Courtney, 2011: Can Wind Lidars Measure Turbulence? *J. Atmos. Oceanic Technol.*, 28, 853–868.

Sattar, A. M., Elhakeem, M., Gerges, B. N., Gharabaghi, B., & Gultepe, I. 2018: Wind-Induced Air-Flow Patterns in an Urban Setting: Observations and Numerical Modeling. *Pure and Applied Geophysics*, DOI: 10.1007/s00024-018-1846-5.

Schmit, T.J., P. Griffith, M.M. Gunshor, J.M. Daniels, S.J. Goodman, and W.J. Lebair, 2017: A Closer Look at the ABI on the GOES-R Series. *Bull. Amer. Meteor. Soc.*, 98, 681–698.

Schmit, T. J., M. M. Gunshor, W. P. Menzel, J. Li, S. Bachmeier, and J. J. Gurka, 2005: Introducing the next-generation Advanced Baseline Imager on GOES-R. *Bull. Amer. Meteor. Soc.*, 86, 1079–1096.

Schreiner, A. J., D. A. Unger, W. P. Menzel, G. P. Ellrod, K. I. Strabala, and J. L. Pellett, 1993: A comparison of ground and satellite observations of cloud cover. *Bull. Amer. Meteor. Soc.*, 74, 1851-1861.

Schultz, P., and M. K. Politovich, 1992: Toward the improvement of aircraft-icing forecasts for the continental United States. *Wea. Forecasting*, 7, 491–500.

Schultz, P., and M. K. Politovich, 1992: Toward the improvement of aircraft-icing forecasts for the continental United States. *Wea.Forecasting*, 7, 491–500.

Schuur, T. J., H. Park, A. V. Ryzhkov, and H. D. Reeves, 2012: Classification of Precipitation Types during Transitional Winter Weather Using the RUC Model and Polarimetric Radar Retrievals. *J. Appl. Meteor. Climatol.*, 51, 763–779.

Schumann, U., K. Graf, H. Mannstein, and B. Mayer, 2012: Contrails: Visible aviation induced climate impact. *Atmospheric Physics – Background, Methods, Trends, Prediction*, U. Schumann, Ed., Springer, 239-257.

Schumann, U., B. Mayer, K. Graf, and H. Mannstein, 2012: A Parametric Radiative Forcing Model for Contrail Cirrus. *J. Appl. Meteor. Climatol.*, 51, 1391–1406.

Schumann, U. and A. J. Heymsfield, 2017: On the Life Cycle of Individual Contrails and Contrail Cirrus. *Meteorological Monographs*, 58, 3.1–3.24.

Schumann, U., and B. Mayer, 2017: Sensitivity of surface temperature to radiative forcing by contrail cirrus in a radiative-mixing model. *Atm. Chem. Phys.*, 17, 13833–13848.

Schwartz, B., 1996: The quantitative use of PIREPs in developing aviation weather guidance products. *Wea. Forecasting*, 11, 372-384, doi:10.1175/1520-434(1996)011,0372:TQUOPI.2.0.CO;2.

Schwartz, B. E., and S. G. Benjamin, 1995: A comparison of temperature and wind measurements from ACARS equipped aircraft and rawinsondes. *Wea. Forecasting*, 10, 528–544.

Seity Y, Brousseau P, S. Malardel, G. Hello, P. Benard, F. Bouttier, V. Lac C,Masson, 2011. The AROME–France convective-scale operational model. *Mon. Weather Rev.* 139: 976–991.

Selz, T. and G. C. Craig, 2015: Upscale Error Growth in a High-Resolution Simulation of a Summertime Weather Event over Europe. *Mon. Wea. Rev.*, 143, 813–827.

Serke, D., Politovich, M., Reehorst, A., and Gaydos, A., 2008: "The Use of X-band Radar to Support theDetection of In-Flight Icing Hazards by the NASA Icing Remote Sensing System During AIRS-II," *Proc. SPIE 7088, #18*, 2008.

Serke, D., E. Hall, J. Bogna, A.Jordan, S. Abdo, K. Baker, T.Seitel, M. Nelson, R. Ware, F. McDonough, M. Politovich 2014: Supercooled liquid water content profiling case studies with a new vibrating wire sonde compared to a ground-based microwave radiometer. *Atmospheric Research* 149, 77–87.

Sharman, R.D. & Trier, S.B. 2018: Influences of Gravity Waves on Convectively Induced Turbulence (CIT): A Review. *Pure and Appl. Geophys.* https://doi.org/10.1007/s00024-018-1849-2 .

Sharman, R., 2016: Nature of aviation turbulence. Aviation Turbulence: Processes, Detection, Prediction, R. Sharman and T. Lane, Eds., Springer, 3-30.

Sharman, R., and T. Lane, 2016: *Aviation Turbulence: Processes, Detection, Prediction. Springer*, 523 pp.

Sharman, R., and J. M. Pearson, 2017: Prediction of energy dissipation rates for aviation turbulence. Part I: Forecasting non-convective turbulence. *J. Appl. Meteor. Climatol.*, 56, 317–337.

Sharman, R., S. B. Trier, T. P. Lane, and J. D. Doyle, 2012: Sources and dynamics of turbulence in the upper troposphere and lower stratosphere: A review. *Geophys. Res. Lett.*, 39, L12803, doi:10.1029/2012GL051996.

Sharman, R., L. B. Cornman, G. Meymaris, J. Pearson, and T. Farrar, 2014: Description and derived climatologies of automated in situ eddy dissipation rate reports of atmospheric turbulence. *J. Appl. Meteor. Climatol.*, 53, 1416–1432, doi:10.1175/JAMC-D-13-0329.1.

Sharman, R., C. Tebaldi, G. Wiener, and J. Wolff, 2006: An integrated approach to mid- and upper-level turbulence forecasting. *Wea. Forecasting*, 21, 268–287.

Sieglaff, J. M., L. M. Cronce, W. F. Feltz, K. M. Bedka, M. J. Pavolonis, and A. K. Heidinger, 2011: Nowcasting Convective Storm Initiation Using Satellite-Based Box-Averaged Cloud-Top Cooling and Cloud-Type Trends. *J. Appl. Meteor. Climatol.*, 50, 110–126.

Sillmann, J., V. V. Kharin, X. Zhang, F. V. Zwiers, and D. Bronaugh 2013a: Climate extremes indices in the CMIP5 multimodel ensemble: Part 1: Model evaluation in the present climate. *J. Geophy. Res.-Atmosphere*, V 118, 1716-1733.

Sillmann, J., V. V. Kharin, F. W. Zwiers, X. Zhang, and D. Bronaugh, 2013b: Climate extreme indices in the CMIP5 multi-model ensemble. Part 2: Future projections, *J. Geophys. Res.*, accepted doi:10.1002/jgrd.50188.

Silva, W. L., F. A. Albuquerque Neto, G. B. França, and M. Matschinske. 2016. "Conceptual Model for Runway Change Procedure in Guarulhos International Airport Based on SODAR Data." *The Aeronautical Journal* 120 (1227): 725–734. doi:10.1017/aer.2016.33.

Simpson, J. J., G. L. Hufford , R. Servranckx, J. Berg, and D. Pieri, 2003: Airborne Asian dust: Case study of long-range transport and implications for the detection of volcanic ash. *Wea. Forecasting*, 18, 121–141.

Simpson, J. J., G. L. Hufford, D. C. Pieri, and J. Berg, 2000: Failures in detecting volcanic ash from satellite-based technique. *Remote Sens. Environ.*, 72, 191–217.

Sims, D. L., C. B. Fidalgo and T. C. Carty, 2000: Integrated Icing Diagnostic Algorithm assessment at regional airlines. *9th Conference on Aviation, Range, and Aerospace Meteorology*. AMS 2000 Annual Meeting. Preprints, #4.16.

Skofronick-Jackson, G., W.A. Petersen, W. Berg, C. Kidd, E.F. Stocker, D.B. Kirschbaum, R. Kakar, S.A. Braun, G.J. Huffman, T. Iguchi, P.E. Kirstetter, C. Kummerow, R. Meneghini, R. Oki, W.S. Olson, Y.N. Takayabu, K. Furukawa, and T. Wilheit, 2017: The Global Precipitation Measurement (GPM) Mission for Science and Society. *Bull. Amer. Meteor. Soc.*, 98, 1679–1695.

Smith, W. L., 2014: *4-D cloud properties from passive satellite data and applications to resolve the flight icing threat to aircraft*. PhD Dissertation, University of Wisconsin-Madison, July 22, 15 pp.

Smith, W. L., P. Minnis, C. Fleeger, D. Spangenberg, R. Palikonda, and L. Nguyen, 2012: Determining the Flight Icing Threat to Aircraft with Single-Layer Cloud Parameters Derived from Operational Satellite Data. *J. Appl. Meteor. Climatol.*, 51, 1794–1810.

Smith, T. M., V. Lakshmanan, G. J. Stumpf, K. L. Ortega, K. Hondl, K. Cooper, K.M. Calhoun, D.M. Kingfield, K.L. Manross, R. Toomey, and J. Brogden, 2016: Multi-Radar Multi-Sensor (MRMS) Severe Weather and Aviation Products: Initial Operating Capabilities. *Bull. Amer. Meteor. Soc.*, 97, 1617–1630.

Soden, B. J., S. A. Ackerman, DOC Starr, and S. H. Melfi, and R. A. Ferrare, 1994: Comparison

of upper tropospheric water vapor from GOES, Raman lidar, and cross-chain loran atmospheric sounding system measurements. *J. Geoph. Res.*, 99, D10, 21005-21016.

Sokol, Z., and P. Zacharov, 2012: Nowcasting of precipitation by an NWP model using assimilation of extrapolated radar reflectivity. *Quart. J. Roy. Meteor. Soc.*, 138, 1072–1082.

Solheim, F., J. Godwin and R. Ware, 1998: Passive ground-based remote sensing of atmospheric temperature, water vapor, and cloud liquid water profiles by a frequency synthesized microwave radiometer, *Met. Zeit.*, 7, 370-376.

Song, J.-I., S. S. Yum, K.-H. Chang, B.-G. Kim and B.-J. Kim, 2018: Development of a new visibility parameterization based on long term in-situ measurement of fog (cloud) microphysics at a mountainous site in Korea, *J. of Pure and Applied Geophysics*, In press..

Sorenson, J. E., 1964: *Synoptic patterns for clear air turbulence*. UAL Meteorology Circular 56, 64 pp. [Available from Dept. of Atmospheric Science, Colorado State University, Fort Collins, CO 80523.]

Spangenberg, D. A., P. Minnis, S. T. Bedka, R. Palikonda, D. P. Duda, and F. G. Rose, 2013: Contrail radiative forcing over the Northern Hemisphere from 2006 Aqua MODIS data. *Geophys. Res. Lett.*, 40, doi:10.1002/grl.50168, 595-600.

Stano, G. T., K. K. Fuell, and G. J. Jedlovec, 2010: NASA SPoRT GOES-R Proving Ground activities. Preprints, *Sixth Annual Symp. on Future National Operational Environmental Satellite Systems: NPOESS and GOES-R*, Atlanta, GA, Amer. Meteor. Soc., 8.2. Available att https://ams.confex.com/ams/90annual/techprogram/.

Steiner, M., W. Deierling, K. Ikeda, M. Robinson, A. Klein, J. Bewley and R. Bass, 2016: Air traffic impacts caused by lightning safety procedures, AIAA 2016-4213. *AIAA Aviation 2016 conference*. Washington DC. 13-17 June 2016. Doi: 10.2514/6.2016-4213.

Stickland, J. J., 1998: *An assessment of two algorithms for automatic measurement and reporting of turbulence from commercial public transport aircraft*. Rep. to the ICAO METLINK Study Group, Bureau of Meteorology, Melbourne, Australia, 42 pp.

Stobie, J., A. Moosakhanian, P. Jackson, and W. N. Brown, 2008: Evolution of FAA's Weather and Radar Processor (WARP) into the Next Generation Air Transportation System (NextGen). *13th*

Conference on Aviation, Range and Aerospace Meteorology, 21-24 January 2008, New Orleans, Amer. Met. Soc.

Stoelinga, M.T., and T.T. Warner, 1999: Nonhydrostatic, meso-beta scale model simulations of cloud ceiling and visibility for an east coast winter precipitation event. *J. Appl. Meteor.*, 38, 385-404.

Storer, L. N., Williams, P. D., & Joshi, M. M., 2017: Global response of clear-air turbulence to climate change. *Geophysical Research Letters*, 44, 9976–9984. https://doi.org/10.1002/2017GL074618.

Strapp, J. W., A. Korolev, T. Ratvasky, R. Potts, A. Protat, P. May, A. Ackerman, A. Fridlind, P. Minnis, J. Haggerty, J. T. Riley, L. E. Lilie, and G. A. Isaac, 2016: *The high ice water content study of deep convective clouds: Report on science and technical plan*. Final Report. DOT/FAA/TC-14/31, 92 pp. Available at http://www.tc.faa.gov/its/worldpac/techrpt/tc14-31.pdf.

Sumner, J., and C. Mason, 2006: A Turbulence-Based Model for Resolving Velocity and Temperature Profiles in the Atmospheric Surface Layer, *Wind Energy*, 30, 317-340. https://doi.org/10.1260/030952406779295462.

Sun, J., M. Xue, J.W. Wilson, I. Zawadzki, S.P. Ballard, J. Onvlee-Hooimeyer, P. Joe, D.M. Barker, P. Li, B. Golding, M. Xu, and J. Pinto, 2014: Use of NWP for Nowcasting Convective Precipitation: Recent Progress and Challenges. *Bull. Amer. Meteor. Soc.*, 95, 409–426.

Sun-Mack, S., Minnis, P., Smith, W. L., Hong, G., Chen, Y.: Detection of single and multilayer clouds in an artificial neural network approach, Proc. *SPIE 10424, Remote Sensing of Clouds and the Atmosphere XXII*, 1042408 (13 October 2017); doi: 10.1117/12.2277397; https://doi.org/10.1117/12.2277397.

Tafferner, A., T. Hauf, C. Leifeld, T. Hafner, H. Leykauf, and U. Voigt, 2003: ADWICE: Advanced Diagnosis and Warning System for Aircraft Icing Environments. *Wea. Forecasting*, 18, 184–203

Tag, P. M., R. L. Bankert, and L. R. Brody, 2000: An AVHRR multiple cloud-type classification package. *J. of Appl. Meteor.*, 39, 125-134.

Tan, I. and T. Storelvmo, 2016: Sensitivity Study on the Influence of Cloud Microphysical Parameters on Mixed-Phase Cloud Thermodynamic Phase Partitioning in CAM5. *J. Atmos. Sci.*, 73, 709–728.

Tardif, R. and R.M. Rasmussen, 2007: Event-Based Climatology and Typology of Fog in the New York City Region. *J. Appl. Meteor. Climatol.*, 46, 1141–1168.

Teixeira, J., and Coauthors, 2008: Parameterization of the atmospheric boundary layer: A view from just above the inversion. *Bull. Amer. Meteor. Soc.*, 89, 453–458.

Thompson, G., R. T. Bruintjes, B. G. Brown, and F. Hage, 1997: Intercomparison of In-Flight Icing Algorithms. Part I: WISP94 Real-Time Icing Prediction and Evaluation Program. *Wea. Forecasting*, 12, 878–889.

Thompson, G., M. K. Politovich, and R. M. Rasmussen, 2017: A Numerical Weather Model's Ability to Predict Characteristics of Aircraft Icing Environments. *Wea. Forecasting*, 32, 207–221.

Thobois, L, Cariou, J. P., & Gultepe, I. 2018. Review of lidar based applications for aviation weather. Pure and Applied Geophysics. (submitted).

Tomita, H., 2008: New Microphysical Schemes with Five and Six Categories by Diagnostic Generation of Cloud Ice. Journal of the Meteorological Society of Japan. Ser. II, Special Issue: *The International Workshop on High-Resolution and Cloud Modeling*, 2006, 86A, 121-142.

TC, 2004: *Small and large aircraft; Aircraft critical surface contamination training for aircrew and ground crew*. TP 10643E, 12/2004. Ottawa, Ont., Canada. 138 pp.

Trier, S. B., R. D. Sharman, and T. P. Lane, 2012: Influences of moist convection on a cold-season outbreak of clear-air turbulence (CAT). *Mon. Wea. Rev.*, 140, 2477–2496.

Tucker, S. C., C. J. Senff, A. M. Weickmann, W. A. Brewer, R. M. Banta, S. P. Sandberg, D. C. Law, and R. M. Hardesty, 2009: Doppler Lidar Estimation of Mixing Height Using Turbulence, Shear, and Aerosol Profiles. *J. Atmos. Oceanic Technol.*, 26, 673–688.

Turcotte, M.-F., and R. Verret, 1999: In-flight icing and turbulence forecasts for aviation. Proc. *Sixth Workshop on Operational Meteorology*, Halifax, NS, Canada, Canadian Meteorological and Oceanographic Society, 53–56.

Turner, J., and D. E. Warren, 1989: Cloud track winds in the polar regions from sequences of AVHRR images. *Int. J. Remote Sens.*, 10, 695–703.

Turner, D., *Clough, S., Liljegren, J., Clothiaux, E., Cady-Pereira, K., & Gaustad, K. 2007): Retrieving Liquid Water Path and Precipitable Water Vapor from the Atmospheric Radiation Measurement (ARM) Microwave Radiometers*, TGRS.

Turp, D., and P. Gill, 2008: Developments in numerical clear air turbulence forecasting at the U.K. Met Office. Preprints, *13thConf. on Aviation, Range and Aerospace Meteorology*, New Orleans, LA, Amer. Meteor. Soc., P3.10A. [Available online at http://ams.confex.com/ams/pdfpapers/131782.pdf.]

Uccellini, L. W. and D. R. Johnson, 1979: The Coupling of Upper and Lower Tropospheric Jet Streaks and Implications for the Development of Severe Convective Storms. *Mon. Wea. Rev.*, 107, 682–703.

Uccellini, L. W., 1980: On the Role of Upper Tropospheric Jet Streaks and Leeside Cyclogenesis in the Development of Low-Level Jets in the Great Plains. *Mon. Wea. Rev.*, 108, 1689–1696.

Van den Berg, G. P. 2008. "Wind Turbine Power and Sound in Relation to Atmospheric Stability." *Wind Energy* 11.2 (2008): 151–169. doi:10.1002/we.240.

Van den Berg, G. P. 2008. "Wind Turbine Power and Sound in Relation to Atmospheric Stability." *Wind Energy* 11.2 (2008): 151–169. doi:10.1002/we.240

Van Den Broeke, M. S., D. M. Tobin, and M. R. Kumjian, 2016: Polarimetric Radar Observations of Precipitation Type and Rate from the 2–3 March 2014 Winter Storm in Oklahoma and Arkansas. *Wea. & Forecasting*, 31, 1179–1196.

Van Den Broeke, M. S., 2016: Polarimetric Variability of Classic Supercell Storms as a Function of Environment. *J. Appl. Meteor. Climatol.*, 55, 1907–1925.

Velden, C., J. Daniels, D. Stettner, D. Santek, J. Key, J. Dunion, K. Holmlund, G. Dengel, W. Bresky, and P. Menzel, 2005: Recent Innovations in Deriving Tropospheric Winds from Meteorological Satellites. *Bull. Amer. Meteor. Soc.*, 86, 205–224.

Velden, C. S., C. M. Hayden, S. Nieman, W. P. Menzel, S. Wanzong, and J. Goerss, 1997: Upper-tropospheric winds derived from geostationary satellite water vapor observations. *Bull. Amer. Meteor. Soc.*, 78, 173-195.

Velden, C. S., T. L. Olander, and S. Wanzong, 1998: The impact of multispectral GOES-8 wind information on Atlantic tropical cyclone track forecasts in 1995. Part I: Dataset methodology, description, and case analysis. *Mon. Wea. Rev.*, 126, 1202-1218.

Verlinden, K. L. and D. R. Bright, 2017: Using the Second-Generation GEFS Reforecasts to Predict

Ceiling, Visibility, and Aviation Flight Category. *Wea. Forecasting*, 32, 1765–1780.

Westwater, E. (1978). The accuracy of water vapor and cloud liquiddeter minations by dual-frequency ground-based microwave radiometry. *Radio Sci*. 13, 677–685.

Vislocky, R. L. and J. M. Fritsch, 1995: Generalized Additive Models versus Linear Regression in Generating Probabilistic MOS Forecasts of Aviation Weather Parameters. *Wea. Forecasting*, 10, 669–680.

Vislocky, R. L. and J. M. Fritsch, 1997: An Automated, Observations-Based System for Short-Term Prediction of Ceiling and Visibility. *Wea. Forecasting*, 12, 31–43.

.Vivekanandan, J., G. Zhang, and M.K. Politovich, 2001: An Assessment of Droplet Size and Liquid Water Content Derived from Dual-Wavelength Radar Measurements to the Application of Aircraft Icing Detection. *J. Atmos. Oceanic Technol.*, 18, 1787–1798.

Vrancken, P. S., 2016: Airborne remote detection of turbulence with forward-pointing LIDAR. In: *Aviation Turbulence: Processes, Detection, and Prediction*. R. D. Sharman and T. P. Lane, Eds., Chapter 22, 443-464. Springer.

Walker, John R; MacKenzie, Wayne M, JR; Mecikalski, John R; Jewett, Christopher P., 2012: An Enhanced Geostationary Satellite–Based Convective Initiation Algorithm for 0–2-h Nowcasting with Object Tracking. *Journal of Applied Meteorology and Climatology*. 1931-1949.

Wang, L., and C. Cao, 2008: On-orbit calibration assessment of AVHRR longwave channels on MetOp-A using IASI. IEEE Trans. *Geosci. Remote Sens.*, 46, 4005–4013.

Wang, L., Y. Han, D. Tremblay, F.Weng, and M.Goldberg, 2012: Intercomparison of NPP/CrIS radiances with VIIRS, AIRS, and IASI: A post-launch calibration assessment. Earth Observing Missions and Sensors: Development, Implementation, and Characterization II, H. Shimoda et al.,Eds., International Society for Optical Engineering (*SPIE Proceedings*, Vol. 8528), 85280J, doi:10.1117/12.978769.

Warner, T. T., 2011: *Numerical Weather and Climate Prediction*. Cambridge, 526 pp.

Ware, R., Cimini, D., Campos, E., Giuliani, G., Albers, S., Nelson, M., Koch, S. E., Joe, P., & Cober, S. (2013). Thermodynamic and liquid profiling during the 2010 Winter Olympics. *Atmos. Research*. 132-133, 278-290.

Weber, M. E., and M. L. Stone, 1995: Low altitude wind shear detection using airport surveillance radars. *IEEE Aerosp. Electron. Syst. Mag.*, 10, 3–9, doi:10.1109/62.387970.

Weisman, M. L., C. Davis, W. Wang, K. W. Manning, and J. B. Klemp, 2008: Experiences with 0–36-h explicit convective forecasts with the WRF-ARW model. *Wea. Forecasting*, 23, 407–437.

Wen, Y., P. Kirstetter, J. J. Gourley, Y. Hong, A. Behrangi, and Z. Flamig, 2017: Evaluation of MRMS Snowfall Products over the Western United States. *J. Hydrometeor.*, 18, 1707–1713.

Weygandt, S., T. Smirnova, S. Benjamin, K. Brundage, S. Sahm, C. Alexander, and B. Schwartz, 2009: The High Resolution Rapid Refresh (HRRR): An hourly updated convection resolving model utilizing radar reflectivity assimilation from the RUC/RR. *23rd Conf. on Weather Analysis and Forecasting/19th Conf. on Numerical Weather Prediction*, Omaha, NE, Amer. Meteor. Soc., 15A.6.

Whiteman, D. N., S. H. Melfi, and R. A. Ferrare, 1992: Raman lidar system for the measuremen of water vapor and aerosols in the earth's atmosphere. *Appl. Opt.* 31, 3068-3082.

Wick, G., T. Hock, P. Neiman, H. VÖmel, M. Black, and J. Spackman, 2018: The NCAR/NOAA Global Hawk Dropsonde System. *J. Atmos. Oceanic Technol.* doi:10.1175/JTECH-D-17-0225.1, in press.

Williams, J. K., and G. Meymaris, 2016: Remote turbulence detection using ground-based Doppler radar, 2016: Aviation turbulence forecast verification. *Aviation Turbulence: Processes, Detection, Prediction*, R. Sharman and T. Lane, Eds., Springer, 149-177.

Williams, J. K., 2014: Using random forests to diagnose aviation turbulence. *Mach. Learn.*, 95, 51–70, doi:10.1007/s10994-013-5346-7.

Williams, P. D., 2017: Increased light, moderate, and severe clear-air turbulence in response to climate change. Adv. *Atmos. Sci.*, 34, 576-586. https://doi.org/10.1007/s00376-017-6268-2.

Williams, P. D., and M. M. Joshi 2013: Intensification of winter transatlantic aviation turbulence in response to climate change. *Nature Climate Change*. Published online: 8 April 2013. DOI: 10.1038/NCLIMATE1866. 644-647.

Williams, P. D., 2016: Transatlantic flight times and climate change. *Environmental Research Letters*. 11 (2016) doi:10.1088/1748-9326/11/2/024008.

Wilson, J. W., 1966: *Movement and predictability of radar echoes*. National Severe Storms Laboratory Tech. Memo. ERTM-NSSL-28, 30 pp.

Wilson, J. W., N. A. Crook, C. K. Mueller, J. Sun, and M. Dixon, 1998: Nowcasting thunderstorms: A status report. *Bull. Amer. Meteor. Soc.*, 79, 2079–2099.

Wilson, F. W., and R. H. Gramzow, 1991: The redesigned Low Level Wind Shear Alert System. Preprints, *4th Int. Conf. on Aviation Weather Systems*, Paris, France, 370-375

Wilson, J. W., Roberts, R. D., Kessinger, C, and McCarthy, J. (1984): Microburst structure and evaluation of Doppler radar for airport wind shear detection. *J. Climate and Appl. Meteorol.*, 23, 898-915.

Wilson, J. W., and Wakimoto, R. M. (1982). The discovery of the downburst: T. T. Fijita's contribution. *Bull. Amer. Meteorol. Soc.*, 82(1), 49-62.

Wilson, J. W., E. Ebert, T. Saxen, R. Roberts, C. Mueller, M. Sleigh, C. Pierce, and A. Seed, 2004: Sydney 2000 Forecast Demonstration Project: Convective storm nowcasting. *Wea. Forecasting*, 19, 131–150.

Wilson, J. W., and R. D. Roberts, 2006: Summary of convective storm initiation and evolution during IHOP: Observational and modeling perspective. *Mon. Wea. Rev.*, 134, 23–47.

Wirth, M., 2012: Measuring water vapor with Differential Absorption Lidar. *In Atmospheric Physics – Background, Methods, Trends, Prediction*, U. Schumann, Ed., Springer, 465-476.

Wolfson, M. M., Delanoy, R. L., Forman, B. E., Hallowell, R. G., Pawlak, M. L., and Smith, P. D. (1944). Automated microburst wind-shear prediction. *The Lincoln Laboratory Journal*, 7(2), 399-426.

Wolfson, M. M. and D. A. Clark, 2006: *Advanced Aviation Weather Forecasts*. The Lincoln Laboratory Journal, 16, No.1, pp. 31-58.

Wolfson, M. M., W. J. Dupree, R. Rasmussen, M.Steiner, S. Benjamin, S. Weygandt, 2008: Consolidated Storm Prediction for Aviation (CoSPA), *AMS 13th Conference on Aviation,Range, and Aerospace Meteorology*, NewOrleans, LA, 2008.

Wong, M., W. C. Skamarock, P. H. Lauritzen, and R. B. Stull, 2013: A Cell-Integrated Semi-Lagrangian Semi-Implicit Shallow-Water Model (CSLAM-SW) with Conservative and Consistent Transport. *Mon. Wea. Rev.*, 141, 2545–2560.

Woodley, W. L., T. J. Henderson, B. Vonnegut, G. Gordon, R. Breidenthal, and S. M. Holle,

1991: Aircraft-produced ice particles (APIPs) in supercooled clouds and the probable mechanism for their production. *J. Appl. Meteor.*, 30, 1469-1489

Wulfmeyer, V., 1999: Investigation of Turbulent Processes in the Lower Troposphere with Water Vapor DIAL and Radar–RASS. *J. Atmos. Sci.*, 56, 1055–1076.

Wulfmeyer, V., 1998: Ground-based differential absorption lidar for water-vapor and temperature profiling: Development and specifications of a high-performance laser transmitter. *Appl. Opt.*, 37, 3804–3824.

Wulfmeyer, V., and J. Bosenberg, 1996: Single-mode operation of an injection seeded alexandrite ring laser for application in water-vapor and temperature differential absorption lidar. *Opt. Lett.*, 21, 1150– 1152.

Wulfmeyer, V., and J. Bosenberg, 1998: Ground-based differential absorption lidar for water-vapor profiling: Assessment of accuracy, resolution, and meteorological applications. *Appl. Opt.*, 37, 3825–3844.

Wulfmeyer, V., S. Lehmann, C. Senff, and S. Schmitz, 1995: Injection seeded alexandrite ring laser: Performance and application in a water-vapor differential absorption lidar. *Opt. Lett.*, 20, 638–640.

Wurman, J., D. Dowell, Y. Richardson, P. Markowski, E. Rasmussen, D. Burgess, L. Wicker, and H.B. Bluestein, 2012: The Second Verification of the Origins of Rotation in Tornadoes Experiment: VORTEX2. *Bull. Amer. Meteor. Soc.*, 93, 1147–1170.

Yang, B., Qian, Y., Lin, G., Leung, R., and Zhang, Y.: Some issues in uncertainty quantification and parameter tuning: a case study of convective parameterization scheme in the WRF regional climate model, Atmos. Chem. Phys., 12, 2409-2427, https://doi.org/10.5194/acp-12-2409-2012, 2012.

Yang, J., Z. Zhang, C. Wei, F. Lu, and Q. Guo, 2017: Introducing the New Generation of Chinese Geostationary Weather Satellites, Fengyun-4. *Bull. Amer. Meteor. Soc.*, 98, 1637–1658. https://doi. org/10.1175/BAMS-D-16-0065.1

Yano, J., M. Z. Ziemia ski, M. Cullen, P. Termonia, J. Onvlee, L. Bengtsson, A. Carrassi, R. Davy, A. Deluca, S. L. Gray, V. Homar, M. Köhler, S. Krichak, S. Michaelides, V. T. Phillips, P. M. Soares, and A. A. Wyszogrodzki, 2018: Scientific Challenges of Convective-Scale Numerical Weather Prediction. *Bull. Amer. Meteor. Soc.*,99, 699–710, https://doi. org/10.1175/BAMS-D-17-0125.1

Yost, C. R., K. M. Bedka, P. Minnis, L. Nguyen, J. W. Strapp, R. Palikonda, K. Khlopenkov, D. Spangenberg, William L. Smith, A. Protat, and J. Delanoe, 2017: A Prototype Method for Diagnosing High Ice Water Content Probability Using Satellite Imager Data. https://doi.org/10.5194/amt-2017-367. *J. of Atmos. Meas. Tech.* In Press.

Zhang, J., and Coauthors, 2011: National Mosaic and Multi-Sensor QPE (NMQ) system: Description, results, and future plans. *Bull. Amer. Meteor. Soc.*, 92, 1321–1338, doi:10.1175/2011BAMS-D-11-00047.1.

Zang, J., and Coauthors, 2016: Multi-Radar Multi-Sensor (MRMS) quantitative precipitation estimation: Initial operating capabilities. *Bull. Amer. Meteor. Soc.,* 97, 621–637, doi:10.1175/BAMS-D-14-00174.1.

Zhou, B., J. Du, J. McQueen ,G. Dimego, G. Manikin, B. Ferrier, Z.Toth, H. Juang, M.Hart, and J. Han, 2004: An Introduction to NCEP SREF Aviation Project, *11th Conference on Aviation Range and Aerospace*, Oct 4-8, Hyannis, MA, Amer. Meteor. Soc. Presentation. 10 pp.

Zhou, B. and J. Du, 2010: Fog Prediction from a Multimodel Mesoscale Ensemble Prediction System. *Wea. Forecasting*, 25, 303–322.

Zhou, B., J. Du, J. McQueen, and G. Dimego, 2009: Ensemble forecast of ceiling, visibility, and fog with NCEP Short-Range Ensemble Forecast system (SREF). Preprints. *Aviation, Range, and Aerospace Meteorology Special Symp. on Weather–Air Traffic Management Integration*, Phoenix, AZ, Amer. Meteor. Soc., 4.5. [Available online at http://www.emc.ncep. noaa.gov/.mmb/SREF/AMS_2009CV_fog.pdf.]

Gutemberg B. França received a B.S. degree in physics from the Federal University of Mato Grosso do Sul, Campo Grande, Brazil, in 1985, the M.S. degree from the National Institute for Space Research (INPE), São José dos Campos, Brazil, in 1988, and the Ph.D. degree from the University of Dundee, Dundee, U.K., in 1994. From 1997 to 2013, he was an Associate Professor with the Department of Meteorology, Federal University of Rio de Janeiro, Rio de Janeiro, Brazil, where he became a Professor in 2014 and has been coordinating the Applied Meteorological Laboratory since 2014. His research interests include nowcasting models and quantitative remote sensing. Prof. França is an Associate Editor of the International Journal of Remote Sensing.

Francisco L. de Albuquerque Neto, graduated as an aviator officer from the Brazilian Air Force Academy, Pirassununga, Brazil in 1976, the Command and General Staff Course at the Air Force General Staff Command School, Rio de Janeiro, Brazil in 1993, the course of Higher Studies in Politics and Strategy, at the Escola Superior de Guerra (ESG) in 2001, the M.S. in Aerospace Sciences from the Air Force University, Rio de Janeiro, Brazil in 2009 and a Doctorate degree in Civil Engineering from the Federal University Rio de Janeiro (UFRJ) in 2016. Collaborates as a researcher at the Applied Meteorology Laboratory of the Meteorology Department at UFRJ since 2014 and with the Institute of Electrical Engineering of the Federal University of Maranhão since 2020. His research interests include the application of remote sensors and modeling in the areas of micrometeorology, aeronautical meteorology, pollutant dispersion, and wind energy.
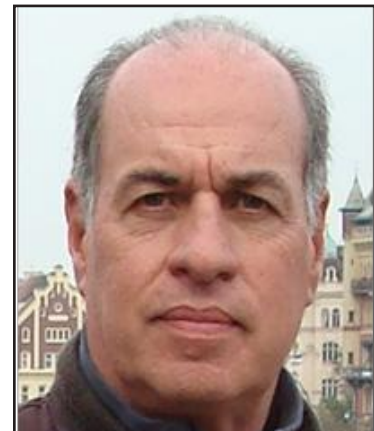
Haroldo F. de Campos Velho received a B.S. degree in Chemical Engineering from the Pontifical Catholic University of Rio Grande do Sul (PUCRS), Brazil, in 1982; D.Sc. (1992) and M.Sc. (1988) degrees in Mechanical Engineering on nuclear reactor physics and computational fluid dynamics, respectively, from the Federal University of Rio Grande do Sul (UFRGS), Brazil, in 1988 and 1992. He was a visiting scientist for the Instituto di Cosmo-Geofisica (Turim, Italy), in 1997, and the Department. of Atmospheric Science of Colorado State University (USA), in 1998. He is a senior researcher of the National Institute for Space Research (INPE). He was Associate Director for Space and Environment of the INPE (2008- 2010). His research interests include machine learning applications, atmospheric turbulence modeling, data assimilation, inverse problems, and scientific computing.

Weather nowcasting is an essential activity for many sectors of society. Aviation meteorology is one of the most relevant activities for this kind of prediction. The book deals with the description and applications of computer codes using mesoscale atmospheric numerical models, machine learning algorithms, and hybrid models - combining those two mentioned approaches. Applications range from convective complexes, airport ceiling and visibility, clear air turbulence, wind conditions, and a final chapter with a review of challenges for aviation meteorology.

The text is of interest to professionals, graduate students, and operational meteorological centers. Most of the chapters are results from a research program between the Department of Meteorology of the Federal University of Rio de Janeiro (UFRJ) and the Department of Airspace Control (DECEA), a division of the Brazilian air force. The joint project between UFRJ and DECEA, named "Cátedra" project of aeronautical meteorology, is a very good example of the effort to address priority topics selected by an operational player and the academic advanced techniques.

Techniques and applications are explained clearly, with the intention to make the text the most self-content as possible.

UFRJ